

Special Issue Reprint

Mass Spectrometry for Biomedical and Food Analysis

Edited by
Wen Ma and Xianjiang Li

mdpi.com/journal/molecules

Mass Spectrometry for Biomedical and Food Analysis

Mass Spectrometry for Biomedical and Food Analysis

Editors

Wen Ma

Xianjiang Li



Basel • Beijing • Wuhan • Barcelona • Belgrade • Novi Sad • Cluj • Manchester

Editors

Wen Ma

School of Pharmaceutical

Sciences

Peking Univeristy

Beijing

China

Xianjiang Li

Food Safety Laboratory

National Institute

of Metrology

Beijing

China

Editorial Office

MDPI

St. Alban-Anlage 66

4052 Basel, Switzerland

This is a reprint of articles from the Special Issue published online in the open access journal *Molecules* (ISSN 1420-3049) (available at: www.mdpi.com/journal/molecules/special_issues/XY0HF5IUFP).

For citation purposes, cite each article independently as indicated on the article page online and as indicated below:

Lastname, A.A.; Lastname, B.B. Article Title. <i>Journal Name</i> Year , <i>Volume Number</i> , Page Range.
--

ISBN 978-3-7258-0700-0 (Hbk)

ISBN 978-3-7258-0699-7 (PDF)

doi.org/10.3390/books978-3-7258-0699-7

Cover image courtesy of Xianjiang Li

© 2024 by the authors. Articles in this book are Open Access and distributed under the Creative Commons Attribution (CC BY) license. The book as a whole is distributed by MDPI under the terms and conditions of the Creative Commons Attribution-NonCommercial-NoDerivs (CC BY-NC-ND) license.

Contents

About the Editors	vii
Preface	ix
Xianjiang Li and Wen Ma Mass Spectrometry for Biomedical and Food Analysis Reprinted from: <i>Molecules</i> 2024 , 29, 1290, doi:10.3390/molecules29061290	1
Tuo Qin, Xiaojuan Rong, Xiaohui Zhang, Lingfei Kong, Yutong Kang and Xuanlin Liu et al. Lipid Mediators Metabolic Chaos of Asthmatic Mice Reversed by Rosmarinic Acid Reprinted from: <i>Molecules</i> 2023 , 28, 3827, doi:10.3390/molecules28093827	5
Madhuri Jayathirtha, Taniya Jayaweera, Danielle Whitham, Isabelle Sullivan, Brîndușa Alina Petre and Costel C. Darie et al. Two-Dimensional-PAGE Coupled with nLC-MS/MS-Based Identification of Differentially Expressed Proteins and Tumorigenic Pathways in MCF7 Breast Cancer Cells Transfected for JTB Protein Silencing Reprinted from: <i>Molecules</i> 2023 , 28, 7501, doi:10.3390/molecules28227501	19
Piotr Kośliński, Robert Pluskota, Marcin Koba, Zygmunt Siedlecki and Maciej Śniegocki Comparative Analysis of Amino Acid Profiles in Patients with Glioblastoma and Meningioma Using Liquid Chromatography Electrospray Ionization Tandem Mass Spectrometry (LC-ESI-MS/MS) Reprinted from: <i>Molecules</i> 2023 , 28, 7699, doi:10.3390/molecules28237699	51
Mariachiara Bianco, Giovanni Ventura, Cosima Damiana Calvano, Ilario Losito, Tommaso R. I. Cataldi and Antonio Monopoli Matrix Selection Strategies for MALDI-TOF MS/MS Characterization of Cyclic Tetrapyrroles in Blood and Food Samples Reprinted from: <i>Molecules</i> 2024 , 29, 868, doi:10.3390/molecules29040868	69
Mingxia Liu, Wen Ma, Yi He, Zuoli Sun and Jian Yang Recent Progress in Mass Spectrometry-Based Metabolomics in Major Depressive Disorder Research Reprinted from: <i>Molecules</i> 2023 , 28, 7430, doi:10.3390/molecules28217430	84
Chen He, Qin Gao, Changwen Ye, Guotao Yang, Pengfei Zhang and Rongchao Yang et al. Development of a Purity Certified Reference Material for Vinyl Acetate Reprinted from: <i>Molecules</i> 2023 , 28, 6245, doi:10.3390/molecules28176245	106
Xianjiang Li, Wei Zhang, Xiao Li, Shukun Zhou, Mengling Tu and Yunxiao Zhu et al. Purity Assessment of Dinotefuran Using Mass Balance and Quantitative Nuclear Magnetic Resonance Reprinted from: <i>Molecules</i> 2023 , 28, 3884, doi:10.3390/molecules28093884	122
Xiao Li, Ling Shi, Panshu Song, Wei Cai, Ximing Luo and Bo Zhao Certification of New Selenium-Enriched Yeast and Supplement Reference Materials for Selenomethionine Using Two Independent Measurement Strategies Reprinted from: <i>Molecules</i> 2024 , 29, 235, doi:10.3390/molecules29010235	133
Yue Wang, Tingjie Huang, Tao Zhang, Xiaoping Ma, Guangshuo Zhou and Meiyao Chi et al. Residue Levels and Dietary Intake Risk Assessments of 139 Pesticides in Agricultural Produce Using the m-PFC Method Based on SBA-15-C ₁₈ with GC-MS/MS Reprinted from: <i>Molecules</i> 2023 , 28, 2480, doi:10.3390/molecules28062480	145

Kangcong Li, Yan Gao, Xiuqin Li, Yan Zhang, Benfeng Zhu and Qinghe Zhang Fragmentation Pathway of Organophosphorus Flame Retardants by Liquid Chromatography–Orbitrap-Based High-Resolution Mass Spectrometry Reprinted from: <i>Molecules</i> 2024 , <i>29</i> , 680, doi:10.3390/molecules29030680	159
Jiali Fan, Feng Liu, Wenhua Ji, Xiao Wang and Lili Li Comprehensive Investigation of Ginsenosides in the Steamed <i>Panax quinquefolius</i> with Different Processing Conditions Using LC-MS Reprinted from: <i>Molecules</i> 2024 , <i>29</i> , 623, doi:10.3390/molecules29030623	172
Zeyang Liu, Susu Pan, Peize Wu, Ming Li and Dapeng Liang Determination of A1 and A2 β -Casein in Milk Using Characteristic Thermolytic Peptides via Liquid Chromatography-Mass Spectrometry Reprinted from: <i>Molecules</i> 2023 , <i>28</i> , 5200, doi:10.3390/molecules28135200	188

About the Editors

Wen Ma

Wen Ma received her B.S. degree from Wuhan University and a Ph.D. degree from Peking University. She is now an associate researcher at the State Key Laboratory of Natural and Biomimetic Drugs, School of Pharmaceutical Sciences, Peking University. Her current research interests focus on the design of novel nanomaterials and nanodevices for biomedical applications based on laser desorption/ionization mass spectrometry (LDI-MS) and liquid chromatography mass spectrometry (LC-MS). She has chaired or participated in five projects from the National Natural Science Foundation of China and State Key Laboratory. She has been authorized 5 national invention patents and published 41 papers on journals, such as *Small Methods*, *Chem. Eng. J.*, *Chem. Sci.*, *Molecules*, and so on. She also works as an editor for *J. Anal. Test.* and invited as reviewer for 25 journals including *Small Methods*, *Food Chem.*, *Talanta*, *Chem-Asian J.*, and so on.

Xianjiang Li

Xianjiang Li received his Ph.D. degree from Peking University and then worked as a post-doc researcher at the National Institute of Metrology (NIM). After that, he worked as a visiting scientist at Bureau International des Poids et Mesures (BIPM). Now, he is an associate research fellow at NIM and was nominated as Youth Talent by the State Administration for Market Regulation. His current research interests include high-accuracy method development for the food safety and development of certified reference materials. He has chaired one project from the National Natural Science Foundation of China and participated in four projects from National Key R&D Program of China. He has published 62 papers with more than 2200 citations (h-index=29), including 6 in *Food Chem.*, 2 on *Coord. Chem. Rev.*, and 1 in *Trends Food Sci. Technol.* He also wrote chapters in three English books and one Chinese book. He also works as an editor for *Metrology*, *J. Anal. Test.*, *Adv. Argochem*, and *Food Innov. Adv.*, as well as a guest editor for *Separations* and *Molecules*. He is invited as reviewer for 37 journals, including *Food Chem.*, *Food Control*, *J. Hazard. Mater.*, *Environ. Sci. Nano*, and so on.

Preface

Mass Spectrometry was initially developed to determine the molecular weight. It is becoming more and more powerful and widely used in complex analysis. Mass-spectrometry-based technology is one of the frontiers in biomedical and food analysis, especially in the era of metabolomics, foodomics, and so on.

This is the reprint of a Special Issue of *Molecules*, titled “Mass Spectrometry for Biomedical and Food Analysis”, which was organized by two guest editors. Biomedical and food analysis has always been an important topic and received remarkably positive feedback from numerous geographically diverse scientists. The sensitive and accurate detection of related components (metabolites, proteins/peptides, drugs, nutrient contents, pesticides, and so on) is vitally important to explaining the molecular mechanisms of biological functions that guarantee food safety and people’s health. As a result, five works focused on biomedical analysis and seven focused on food analysis in this reprint. In biomedical analysis, topics covered active drug and tumor biomarker discovery, metabolic pathways, novel matrices, and depressive disorder treatment. In food aspects, topics included certified reference material development, pesticide residue analysis methods, fragmentation pathways of flame retardants, as well as the identification and detection of nutritional components. All 12 contributions covered the latest advances and we hope it will benefit readers in this field.

We would like to thank all the authors for their excellent contributions. The efforts of the reviewers greatly contribute to the quality of the published work. We would also like to thank the editorial staff of MDPI for their professional support. This work was supported by the State Administration for Market Regulation (QNBJ202306) and the National Natural Science Foundation of China (grant no. 22004004).

Wen Ma and Xianjiang Li
Editors

Editorial

Mass Spectrometry for Biomedical and Food Analysis

Xianjiang Li ^{1,*}  and Wen Ma ^{2,*} 

- ¹ Key Laboratory of Chemical Metrology and Applications on Nutrition and Health for State Market Regulation, Division of Metrology in Chemistry, National Institute of Metrology, Beijing 100029, China
- ² State Key Laboratory of Natural and Biomimetic Drugs, School of Pharmaceutical Sciences, Peking University, Beijing 100191, China
- * Correspondence: lixianjiang@nim.ac.cn (X.L.); wen.ma@bjmu.edu.cn (W.M.); Tel.: +86-10-64524737

1. Introduction

Biomedical and food analysis has always been an important topic that closely relates to health. The sensitive and accurate detection of related components (metabolites, proteins/peptides, drugs, nutrient contents, pesticides, and so on) are critical in understanding the molecular mechanism of biological functions and guaranteeing food safety and people's health [1]. However, the inevitable complexity of the practical matrix has encouraged researchers to continuously exert significant effort in developing innovative methods with accuracy, rapidity, and simplicity [2]. Relying on its high accuracy, great sensitivity and versatility, and reliable qualitative and quantitative ability, mass spectrometry-related technology is perfect for biomedical and food analysis [3]. On the other hand, sample preparation plays an essential role in analyte enrichment and interference removal, further increasing specificity and sensitivity [4]. Moreover, certified reference materials are essential to guarantee reliable and comparable results [5].

This Special Issue gathers the latest research trends in biomedical and food analysis. By collecting the contributions of specialists in the field, this Special Issue aims to advance knowledge and increase the expertise on biomedical analysis, pharmaceutical science, and food chemistry.

2. Summary of Published Articles

This Special Issue includes twelve manuscripts which address the latest advances, including five on biomedical research and seven on food analysis.

Nature is a bank of active compounds among which humans have been seeking drugs [6]. *Hyssopus cuspidatus* Boriss is a traditional Uyghur medicine for the treatment of asthma. Dr. Tie (contribution 1) demystified its molecular mechanism and revealed its pharmacology with an asthmatic mice model. Rosmarinic acid (RosA), the main active constituent, could regulate cytokine levels and inhibit the signaling pathway to suppress inflammation, such as TNF- α and IL-4. Additionally, the animal ethology score and lung histology analysis confirmed its potency. Moreover, some other constituents neutralized the side reaction caused by RosA. Further in-depth research is needed to make RosA a treatment for asthma in humans. Together with medical treatment, early diagnosis is very helpful. Therefore, novel biomarker discovery is a very meaningful topic, especially differentially expressed genes/proteins of cancers. Neagu's group (contribution 2) used 2D-PAGE-nLC-MS/MS to identify the differences in tumorigenic pathways with MCF7 breast cancer cells that were silenced with the human jumping translocation breakpoint. Their results demonstrated the tumor-suppressive function of this gene that might be a tumor biomarker for breast cancer. Related signaling and metabolic pathways included EMT, ERK/MAPK, PI3K/AKT, Wnt/ β -catenin, mTOR, C-MYC, NF- κ B, IFN- γ and IFN- α responses, UPR, and glycolysis/gluconeogenesis. Accordingly, LC-MS-based omics is a powerful tool [7,8], especially for disease diagnosis. Metabolites can reflect many pathological or internal changes in biochemical pathways at the molecular level [9]. Dr. Kośliński



Citation: Li, X.; Ma, W. Mass Spectrometry for Biomedical and Food Analysis. *Molecules* **2024**, *29*, 1290. <https://doi.org/10.3390/molecules29061290>

Received: 7 March 2024

Accepted: 13 March 2024

Published: 14 March 2024



Copyright: © 2024 by the authors. Licensee MDPI, Basel, Switzerland. This article is an open access article distributed under the terms and conditions of the Creative Commons Attribution (CC BY) license (<https://creativecommons.org/licenses/by/4.0/>).

(contribution 3) used them to develop an amino acid metabolic profile method for glioblastoma and meningioma diagnosis. From the ROV curve results, four targets (lysine, histidine, α -aminoadipic acid, and phenylalanine) demonstrated statistically significant differences, especially phenylalanine. Furthermore, cysteine turned out to be the most important in the decision-making algorithm of the classification tree. These results indicate the importance of mass spectrometry in marker discovery. Compared to LC-MS, matrix-assisted laser desorption/ionization (MALDI) has major advantages in time and throughput. Antonio Monopoli and colleagues (contribution 4) analyzed cyclic tetrapyrroles in blood, bovine liver, fish liver, and mussel samples with different matrixes. In detail, α -cyano-4-chlorocinnamic acid was more effective than proton transfer and electron transfer matrices for protoporphyrin analysis, whereas α -cyano-4-hydroxycinnamic acid facilitated the better detection of heme b and c. This work paved the way for better understanding of the cyclic tetrapyrroles in biological samples. Dr. Liu (contribution 5) comprehensively summarized the recent progress in major depressive disorder research from four dimensions, including analytical platforms, strategies, key metabolites, and antidepressant treatment. In this manuscript, key metabolic challenges are described, and current challenges and prospects are discussed. She hopes this work will stimulate further advances in the field of major depressive disorder research with MS-based metabolomics.

Certified reference material (CRM) is very important in guaranteeing the reliability of detection [10]. Especially, pure CRM is located at the top of the metrological traceability chain [11]. Dr. Ma (contribution 6) developed a vinyl acetate CRM (GBW (E) 062710) that is a restricted substance in food products. For pure CRM development, the identification and quantification of structurally related impurities represent a large bottleneck [12,13]. Three structurally related impurities were elucidated and their correction factors were calculated in the vinyl acetate CRM. Finally, its purity was assigned using the mass balance method with a value of 99.90% and expanded uncertainty of 0.30%. Similarly, Dr. Li (contribution 7) carried out purity assessment of dinotefuran, which is a widely used pesticide. Eventually, the DNT CRM was assigned a mass fraction of 995 mg/g with both mass balance and quantitative nuclear magnetic resonance spectroscopy. During real sample analysis, matrix components affect the accuracy of the final results. Thus, matrix CRMs are very important to realize consensus values. Mr. Li and coworkers (contribution 8) used both HPLC-ICP-MS and HPLC-ESI-MS/MS methods to certificate selenium-enriched yeast reference material. Both methods yielded consistent results for the selenium supplement and the certified value of selenomethionine was 716 mg/kg with expanded uncertainties of 36 mg/kg.

Pesticide residue is a tough problem in food safety, especially during simultaneous analysis of hundreds of them [14,15]. Dr. Zou (contribution 9) proposed an m-PFC method with an SBA-15- C_{18} sorbent. This method was reliable for 139 pesticides. Moreover, 314 samples of nine types of fruits and vegetables were analyzed to assess dietary intake risk. In detail, procymidone most often exceeded the MRLs and tebuconazole was most frequently found. Organophosphorus flame retardants (OPFRs) are another common residue in foods. Due to their large numbers of variants, the high-resolution mass spectrometry-based screening method is very popular. One important prerequisite for novel OPFR discovery is the elucidation of their fragmentation pathway. Dr. Li with her team (contribution 10) found that alkyl and halogenated OPFRs underwent three McLafferty hydrogen rearrangements and aromatic OPFRs cleaved not only the C-O bond but also the P-O bond. Moreover, the substituents had a large effect on the cleavage, as shown by the figures. These fragmentation laws can provide great help in screening OPFR pollutants.

In addition to hazardous residue, two manuscripts focused on nutritional components. Dr. Li (contribution 11) investigated the ginsenoside profile in steamed *Panax quinquefolius* using UPLC-Q-TOF-MS. In total, 175 ginsenosides were identified, and 10 new ginsenosides, and 3 new aglycones were discovered. They also mentioned that the steaming temperature had a larger influence than time on the chemical components after principal component analysis. Some typical position changes and configuration inversion were elucidated simultaneously. The most abundant protein in milk is β -casein, and A1 is one variant that

has a histidine moiety in the 67th position. A1 β -casein is harmful for humans; therefore, high specificity is very important in distinguishing all variants. Dr. Li (contribution 12) reported a simple thermolytic digested method to produce characteristic peptides without any denaturing reagents. Thermolysin was chosen for digestion at 60 °C for 4 h. These shorter thermolytic peptides with 11 or 18 amino acid moieties are more suitable for LC-MS analysis than tryptic characteristic peptides with 49 amino acid moieties. This method was successfully applied to commercial milk samples.

3. Conclusions

The twelve articles published in this Special Issue cover the latest advances in mass spectrometry for biomedical and food analysis. As we can see, high-resolution omics is very useful in finding biomarkers and revealing their mechanism. Moreover, novel CRM development is a trend in dealing with new contaminants in food analysis. We hope these Special Issues tracking the recent progress will provide beneficial information to readers.

Author Contributions: Conceptualization and writing, X.L.; writing—review and editing, W.M. All authors have read and agreed to the published version of the manuscript.

Funding: This work was financially supported by the State Administration for Market Regulation (QNB202306) and the National Natural Science Foundation of China (Grant No. 22004004).

Acknowledgments: Xianjiang Li and Wen Ma thank all the authors for their excellent contributions. The efforts of the reviewers are acknowledged as contributing greatly to the quality of this Special Issue. We were very satisfied with the review process and management of the Special Issue, and all those involved are appreciated.

Conflicts of Interest: The authors declare no conflicts of interest.

List of Contributions:

1. Qin, T.; Rong, X.; Zhang, X.; Kong, L.; Kang, Y.; Liu, X.; Hu, M.; Liang, H.; Tie, C. Lipid Mediators Metabolic Chaos of Asthmatic Mice Reversed by Rosmarinic Acid. *Molecules* **2023**, *28*, 3827. <https://doi.org/10.3390/molecules28093827>.
2. Jayathirtha, M.; Jayaweera, T.; Whitham, D.; Sullivan, I.; Petre, B.A.; Darie, C.C.; Neagu, A.-N. Two-Dimensional-PAGE Coupled with nLC-MS/MS-Based Identification of Differentially Expressed Proteins and Tumorigenic Pathways in MCF7 Breast Cancer Cells Transfected for JTB Protein Silencing. *Molecules* **2023**, *28*, 7501. <https://doi.org/10.3390/molecules28227501>.
3. Kośliński, P.; Pluskota, R.; Koba, M.; Siedlecki, Z.; Śniegocki, M. Comparative Analysis of Amino Acid Profiles in Patients with Glioblastoma and Meningioma Using Liquid Chromatography Electrospray Ionization Tandem Mass Spectrometry (LC-ESI-MS/MS). *Molecules* **2023**, *28*, 7699. <https://doi.org/10.3390/molecules28237699>.
4. Bianco, M.; Ventura, G.; Calvano, C.D.; Losito, I.; Cataldi, T.R.I.; Monopoli, A. Matrix Selection Strategies for MALDI-TOF MS/MS Characterization of Cyclic Tetrapyrroles in Blood and Food Samples. *Molecules* **2024**, *29*, 868. <https://doi.org/10.3390/molecules29040868>.
5. Liu, M.; Ma, W.; He, Y.; Sun, Z.; Yang, J. Recent Progress in Mass Spectrometry-Based Metabolomics in Major Depressive Disorder Research. *Molecules* **2023**, *28*, 7430. <https://doi.org/10.3390/molecules28217430>.
6. He, C.; Gao, Q.; Ye, C.; Yang, G.; Zhang, P.; Yang, R.; Zhang, Q.; Ma, K. Development of a Purity Certified Reference Material for Vinyl Acetate. *Molecules* **2023**, *28*, 6245. <https://doi.org/10.3390/molecules28176245>.
7. Li, X.; Zhang, W.; Li, X.; Zhou, S.; Tu, M.; Zhu, Y.; Li, H. Purity Assessment of Dinotefuran Using Mass Balance and Quantitative Nuclear Magnetic Resonance. *Molecules* **2023**, *28*, 3884. <https://doi.org/10.3390/molecules28093884>.
8. Li, X.; Shi, L.; Song, P.; Cai, W.; Luo, X.; Zhao, B. Certification of New Selenium-Enriched Yeast and Supplement Reference Materials for Selenomethionine Using Two Independent Measurement Strategies. *Molecules* **2024**, *29*, 235. <https://doi.org/10.3390/molecules29010235>.
9. Wang, Y.; Huang, T.; Zhang, T.; Ma, X.; Zhou, G.; Chi, M.; Geng, X.; Yuan, C.; Zou, N. Residue Levels and Dietary Intake Risk Assessments of 139 Pesticides in Agricultural Produce Using the m-PFC Method Based on SBA-15-C18 with GC-MS/MS. *Molecules* **2023**, *28*, 2480. <https://doi.org/10.3390/molecules28062480>.

10. Li, K.; Gao, Y.; Li, X.; Zhang, Y.; Zhu, B.; Zhang, Q. Fragmentation Pathway of Organophosphorus Flame Retardants by Liquid Chromatography–Orbitrap-Based High-Resolution Mass Spectrometry. *Molecules* **2024**, *29*, 680. <https://doi.org/10.3390/molecules29030680>.
11. Fan, J.; Liu, F.; Ji, W.; Wang, X.; Li, L. Comprehensive Investigation of Ginsenosides in the Steamed *Panax quinquefolius* with Different Processing Conditions Using LC-MS. *Molecules* **2024**, *29*, 623. <https://doi.org/10.3390/molecules29030623>.
12. Liu, Z.; Pan, S.; Wu, P.; Li, M.; Liang, D. Determination of A1 and A2 β -Casein in Milk Using Characteristic Thermolytic Peptides via Liquid Chromatography-Mass Spectrometry. *Molecules* **2023**, *28*, 5200. <https://doi.org/10.3390/molecules28135200>.

References

1. Mitchell, E.A.D.; Mulhauser, B.; Mulot, M.; Mutabazi, A.; Glauser, G.; Aebi, A. A worldwide survey of neonicotinoids in honey. *Science* **2017**, *358*, 109–111. [CrossRef] [PubMed]
2. Ma, W.; Yang, B.; Li, J.; Li, X. Amino-functional metal-organic framework as a general applicable adsorbent for simultaneous enrichment of nine neonicotinoids. *Chem. Eng. J.* **2022**, *434*, 134629. [CrossRef]
3. Yang, J.; Guo, W.; Xu, X.; Zhao, L.; Xu, Y.; Wang, Y. Analysis of Fatty Acid in Biological Samples Using Liquid Chromatography–Quadrupole-Orbitrap Mass Spectrometry Under Parallel Reaction Monitoring Mode. *J. Anal. Test.* **2024**, *in press*. [CrossRef]
4. Wu, Y.; Han, L.; Wu, X.; Jiang, W.; Liao, H.; Xu, Z.; Pan, C. Trends and perspectives on general Pesticide analytical chemistry. *Adv. Agrochem.* **2022**, *1*, 113–124. [CrossRef]
5. Zheng, F.; Zhao, X.; Zeng, Z.; Wang, L.; Lv, W.; Wang, Q.; Xu, G. Development of a plasma pseudotargeted metabolomics method based on ultra-high-performance liquid chromatography–mass spectrometry. *Nat. Protoc.* **2020**, *15*, 2519–2537. [CrossRef] [PubMed]
6. Ren, Z.; Yang, H.; Zhu, C.; Fan, D.; Deng, J. Dietary phytochemicals: As a potential natural source for treatment of Alzheimer’s Disease. *Food Innov. Adv.* **2023**, *2*, 36–43. [CrossRef]
7. Yang, S.; Mi, L.; Wang, K.; Wang, X.; Wu, J.; Wang, M.; Xu, Z. Comparative metabolomics analysis in the clean label ingredient of NFC spine grape juice processed by mild heating vs high pressure processing. *Food Innov. Adv.* **2023**, *2*, 95–105. [CrossRef]
8. Balkir, P.; Kemahlioglu, K.; Yucel, U. Foodomics: A new approach in food quality and safety. *Trends Food Sci. Technol.* **2021**, *108*, 49–57. [CrossRef]
9. Li, M.; Yang, L.; Bai, Y.; Liu, H. Analytical Methods in Lipidomics and Their Applications. *Anal. Chem.* **2013**, *86*, 161–175. [CrossRef] [PubMed]
10. Lippa, K.A.; Duewer, D.L.; Nelson, M.A.; Davies, S.R.; Mackay, L.G. The role of the CCQM OAWG in providing SI traceable calibrators for organic chemical measurements. *Accred. Qual. Assur.* **2019**, *24*, 407–415. [CrossRef]
11. Tu, M.; Zhang, W.; Zhu, Y.; Ma, W.; Li, X.; Zhou, S.; Li, H.; Li, X. Accurate quantification of pure thiacloprid with mass balance and quantitative H-NMR. *J. Anal. Test.* **2024**, *8*, 1–8. [CrossRef]
12. *ISO 33407-2024*; Guidance for the Production of Pure Organic Substance Certified Reference Materials. International Organization for Standardization: Geneva, Switzerland, 2024.
13. Maienfisch, P. Challenges and risks associated with impurity profiles in technical grade crop protection products produced semi-synthetically from natural products. *Adv. Agrochem.* **2022**, *1*, 148–156. [CrossRef]
14. Wang, X.; Zhang, W.; Wang, M.; Ma, Y.; Han, Y.; Deng, B.; Gao, M.; Tong, J.; Shen, S.; Feng, D. Simultaneous determination of ten neonicotinoid pesticides in vegetables by dispersed solid-phase extraction coupled with ultra performance liquid chromatography-tandem mass spectrometry. *Chin. J. Anal. Lab.* **2023**, *42*, 897–902. [CrossRef]
15. Rajski, L.; Petromelidou, S.; Diaz-Galiano, F.J.; Ferrer, C.; Fernandez-Alba, A.R. Improving the simultaneous target and non-target analysis LC-amenable pesticide residues using high speed Orbitrap mass spectrometry with combined multiple acquisition modes. *Talanta* **2021**, *228*, 122241. [CrossRef] [PubMed]

Disclaimer/Publisher’s Note: The statements, opinions and data contained in all publications are solely those of the individual author(s) and contributor(s) and not of MDPI and/or the editor(s). MDPI and/or the editor(s) disclaim responsibility for any injury to people or property resulting from any ideas, methods, instructions or products referred to in the content.

Article

Lipid Mediators Metabolic Chaos of Asthmatic Mice Reversed by Rosmarinic Acid

Tuo Qin ^{1,2}, Xiaojuan Rong ^{3,*}, Xiaohui Zhang ⁴, Lingfei Kong ^{1,2}, Yutong Kang ³, Xuanlin Liu ³, Mengying Hu ³, Handong Liang ¹ and Cai Tie ^{1,2,*}

¹ State Key Laboratory Coal Resources and Safe Mining, China University of Mining and Technology-Beijing, Ding11 Xueyuan Road, Beijing 100083, China

² School of Chemical and Environmental Engineering, China University of Mining and Technology-Beijing, Ding11 Xueyuan Road, Beijing 100083, China

³ Xinjiang Institute of Material Medica, South Xinhua Road 140, Urumqi 830004, China

⁴ State Key Laboratory of Natural and Biomimetic Drugs, Peking University, 38 Xueyuan Road, Beijing 100191, China

* Correspondence: rxj141021@163.com (X.R.); tiecai@cumtb.edu.cn (C.T.); Tel.: +86-10-62339522 (C.T.)

Abstract: Background and objective: Asthma is a common chronic inflammatory disease of the airways with no known cure. Lipid mediators (LMs) are a kind of inflammatory signaling molecules which are believed to be involved in the development of asthma. *Hyssopus cuspidatus* Boriss. is a traditional Uyghur medicine, which is widely used in the treatment of asthma and other respiratory diseases. Extraction of *Hyssopus cuspidatus* Boriss. was reported to neutralize asthma symptoms. The purpose of the study was to investigate both the anti-inflammatory and immunoregulation properties of the *Hyssopus cuspidatus* Boriss. extract (SXCF) and its main active constituent, rosmarinic acid (RosA), in vivo. The effect of RosA, a major constituent of SXCF, was evaluated on an asthmatic model, with both anti-inflammatory and immunoregulation properties. Materials and methods: Anti-inflammatory effect of SXCF and RosA was assessed using OVA-induced asthma model mice by UPLC-MS/MS method. Results: Overall, RosA played a critical role in anti-asthma treatment. In total, 90% of LMs species that were significantly regulated by SXCF were covered. On the most important LMs associated with asthma, RosA equivalent induced similar effects as SXCF did. It is believed that some constituents in SXCF could neutralize RosA excessive impacts on LMs.

Keywords: asthma; lipid mediators (LMs); rosmarinic acid (RosA); inflammation



Citation: Qin, T.; Rong, X.; Zhang, X.; Kong, L.; Kang, Y.; Liu, X.; Hu, M.; Liang, H.; Tie, C. Lipid Mediators Metabolic Chaos of Asthmatic Mice Reversed by Rosmarinic Acid.

Molecules **2023**, *28*, 3827. <https://doi.org/10.3390/molecules28093827>

Academic Editor: Domenico Trombetta

Received: 27 February 2023

Revised: 17 April 2023

Accepted: 26 April 2023

Published: 30 April 2023



Copyright: © 2023 by the authors. Licensee MDPI, Basel, Switzerland. This article is an open access article distributed under the terms and conditions of the Creative Commons Attribution (CC BY) license (<https://creativecommons.org/licenses/by/4.0/>).

1. Introduction

Bronchial asthma is a chronic inflammatory airway disease, with typical clinical manifestations of recurring symptoms (including cough, wheezing, and chest tightness). Asthma is a chronic inflammation influenced by a variety of cells [1]. Currently, approximately 300 million people suffer from asthma worldwide [2]. Widely accepted treatments for asthma are inhaled bronchodilators and glucocorticoids [3]. A significant portion of asthma patients is well-controlled. The medicines help asthma patients control symptoms but cannot cure the disease. What is worse, 5% to 10% of asthma patients remain poorly controlled [4]. Both pharmaceutical academics and industry professionals are devoted to developing novel medicine to treat asthma. For those people who had been living in areas with a high prevalence of asthma for centuries, effective treatment options were developed, which led to a clue for the discovery of a new medicine. Xinjiang province is a historical asthma high prevalence area due to the desert climate. Uyghur medicine developed distinctive therapy solutions for asthma based on hundreds of years of treatment experience. *Hyssopus cuspidatus* Boriss. has been used to relieve cough, asthma and dispelling dampness for a long time in Uighur medicine. Many studies have proven the efficacy of *Hyssopus cuspidatus* Boriss. in treatment of Bronchial asthma [5,6]. Phenolic acid

Rosmarinic acid (RosA) was determined to be one of the prime components in *Hyssopus cuspidatus* Boriss, with apparent anti-inflammatory effects in asthma [7,8]. RosA has been shown to have several potential therapeutic applications, including as an anti-allergic, anti-inflammatory, and antimicrobial agent [9]. It has also been studied for its potential to help with allergies, asthma, and other respiratory conditions. RosA works by inhibiting the production and activity of proinflammatory cytokines and enzymes in the body [10]. These cytokines and enzymes are responsible for triggering and sustaining the inflammatory response. It was reported that RosA protects the lung by inhibiting the cyclooxygenase (COX) and lipoxygenase (LOX) activities and complement activation [11,12]. Due to the limited knowledge on SXCF and RosA mechanism, the development of *Hyssopus cuspidatus* Boriss. was delayed [13].

LMs are potent signaling molecules that regulate multiple cellular responses through receptor-mediated pathways, including cell growth and death as well as inflammation/infection. Asthma is characterized by chronic inflammation of the airways in which there is an overabundance of eosinophils, mast cells, and activated T helper lymphocytes [14]. These inflammatory cells release mediators that then trigger bronchoconstriction, mucus secretion, and remodeling [14]. Th2 cytokines typically induce inflammation in asthma by promoting the production of additional inflammatory mediators, other cytokines and chemokines [15]. Torres. R et al. reported that Prostaglandin E₂(PGE₂) inhibited mast cell activity by activating the E-prostanoid 2 (EP2) receptor by regulating the PGE₂-EP2-mast cell axis [16]. Leukotrienes (LTs) are a type of powerful proinflammatory molecules; they can cause bronchial smooth muscle contraction, increase vascular permeability, airway mucus secretion, chemotactic inflammatory cell infiltration, airway remodeling, etc. [17]. A large number of studies have shown that levels of LTs in asthma patients are higher than those of normal patients, whether in disease onset or stable stage [18]. The imbalance of LMs is associated with partial lesions of the airway, blood vessels and lung parenchyma.

After systemic LMs profiling containing Linoleic acid, arachidonic acid-related LMs products were produced. This revealed the differential impacts on the dysregulation of asthma modeling between SXCF and RosA. RosA was believed to be a mainly effective constituent of SXCF. However, some side reaction effects would be induced by RosA, which could be neutralized by other constituents in SXCF. It was believed that some constituents of SXCF neutralized the side reaction caused by RosA while maintaining the effects.

2. Results

2.1. Enrichment Analysis

In order to analyze 68 intersection targets between RosA target and asthma-related targets, GO and KEGG enrichment analyses were carried out. The top 10 significant biological processes (BP), cellular compositions (CC), and molecular functions (MF) are displayed in Figure 1B. BPs are mainly related to response to oxidative stress, cellular response to chemical stress, etc. CCs are mainly related to membrane raft, membrane micro domain, etc. MFs are mainly related to endopeptidase activity, metallopeptidase activity, etc. KEGG pathway analyses were performed to investigate the mechanism of RosA in treating asthma, and the top 30 significant pathways are shown in Figure 1A. It was determined that the pathways (removing the pathways related to cancer and those not related to asthma) were mainly enriched in the inflammatory factor pathway (IL-17 signaling pathway, TNF signaling pathway), arachidonic acid metabolism pathway, and so on.

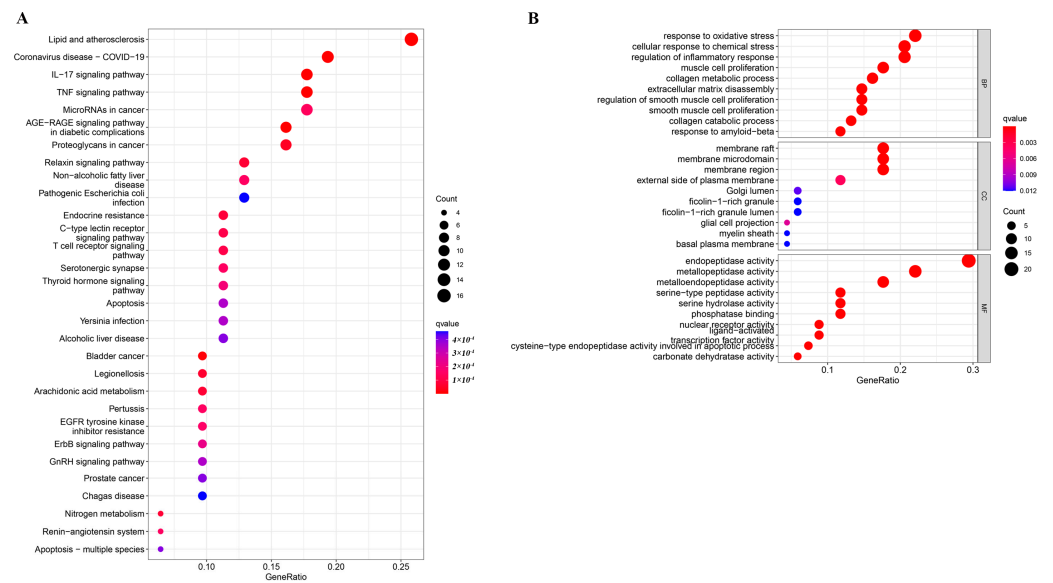


Figure 1. Enrichment analysis of key modules (A): Kyoto Encyclopedia of Genes and Genomes (KEGG); (B): Gene ontology (GO).

2.2. Animal Ethology

After OVA sensitizing, the mice were observed for sneezing, scratching, and wheezing and scored according to the following scoring method. No sneezing: 0 point; sneezing < 4 times: 1 point; sneezing 4–10 times: 2 points; sneezing > 11 times: 3 points. No scratching: 0 point; mild scratching: 1 point; moderate scratching: 2 points; severe scratching: 3 points. No wheezing: 0 points, mild wheezing: 1 point; moderate wheezing: 2 points; severe wheezing: 3 points. Animal ethology of different groups were shown in Figure 2.

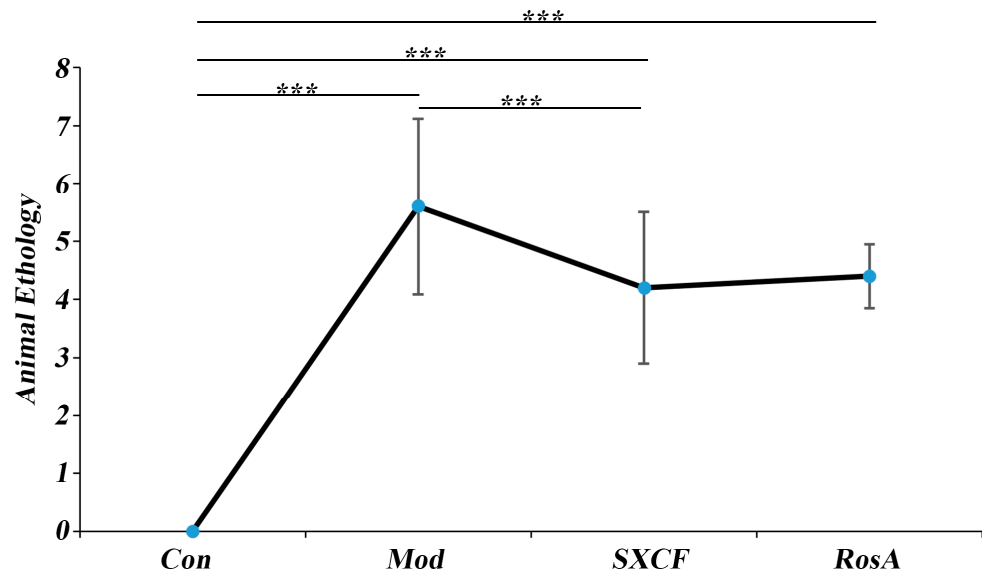


Figure 2. Animal Ethology of Different Groups. ***: $p < 0.001$.

2.3. Histology and Serology

Compared to control mice, the bronchi and blood vessels of asthma mice were infiltrated by a large number of inflammatory cells with mucosal epithelial degeneration and mucosal thickening (Figure 3A–D). With RosA and SXCF treatment, inflammatory cell infiltration, bronchial epithelial degeneration, and mucosal thickening were significantly inhibited.

Based on the histological changes observed in this experiment, the severity of pulmonary injury was graded using the following main indicators: peribronchial and perivascular inflammatory cell infiltration, bronchial obstruction, and interstitial inflammatory cell infiltration (Table 1).

Immunoglobulin E (IgE) is a key immunoglobulin in the pathogenesis of IgE-mediated related allergic diseases. As shown in Figure 3E, the serum IgE of the model group was almost twice that of the control group with p value < 0.05 , which proves that the model group was successfully established.

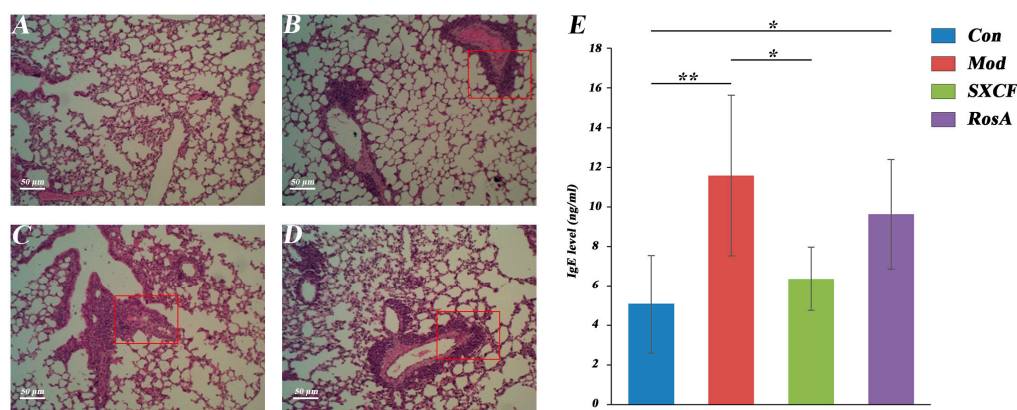


Figure 3. Lung Histology Analysis of Different Groups. (A): Con group; (B): Mod group; (C): SXCF group; (D): RosA group; (E): IgE content in serum. *: $p < 0.05$, **: $p < 0.01$.

Table 1. Analysis of mice pulmonary injury.

Group ($n = 5$)	Grading Score for Pulmonary Injury			
	--	+	++	+++
Con	5	0	0	0
Mod	0	1	2	2
SXCF	0	4	1	0
RosA	0	3	2	0

--: The morphology of the lung tissue was normal, and no abnormal changes were seen. +: Mild pathological changes in a small portion of lung tissue (bronchi, pulmonary interstitium). ++: Moderate pathological changes in a portion of lung tissue (bronchi, pulmonary interstitium). +++: Large pathological changes in the majority of lung tissue (bronchi, pulmonary interstitium).

2.4. Regulated Cytokine Levels of Target Organ

The levels of inflammatory and immune-related cytokines in the BALF of mice in each group were measured. As shown in Figure 4, a significant increase in TNF- α was observed ($p < 0.05$). TNF- α is a cytokine with various biological functions. It is mainly produced by activated monocytes, macrophages and lymphocytes, and participates in various inflammatory reactions. TNF- α can induce inflammation and immune cell infiltration, increase vascular permeability [19], and promote the expression of adhesion molecules in vascular endothelial cells [20]. TNF- α is one of the most important inflammatory cytokines which is produced by macrophages and mast cells through the IgE-mediated pathway and also induces Th2 cells to produce IL-4 [21].

IL-4 is a cytokine with various biological functions. IL-4 plays an important role in the activation and differentiation of CD4⁺ T cells. It stimulates the development of Th2 cells, which produce specific cytokines and participate in the humoral immune response. At the same time, it can also inhibit the development of Th1 cells, which participate in cellular immune responses [22–24]. Our result showed that IL-4 level nearly doubled in the model group, which means that the model was established successfully.

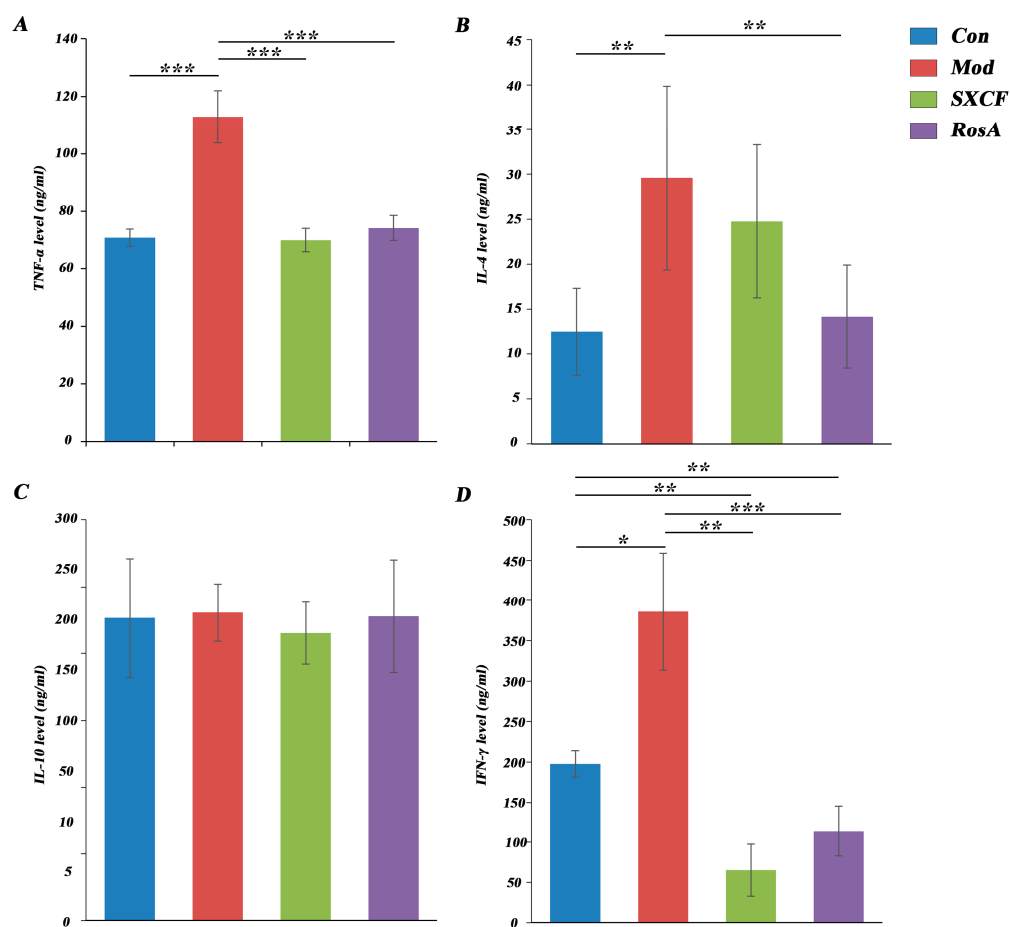


Figure 4. Cytokine content of different groups in BALF. (A): TNF- α level; (B): IL-4 level; (C): IL-10 level; (D): IFN- γ level. *: $p < 0.05$, **: $p < 0.01$, and ***: $p < 0.001$.

The IFN- γ level was significantly increased in OVA-induced mice compared to that of the control group. In the intervention groups, IFN- γ levels have a significant downregulation. It should be observed that IFN- γ level in both intervention groups was lower than that in control group. IFN- γ plays a complex role in regulating inflammation. While it can stimulate the production of pro-inflammatory cytokines, such as TNF- α and IL-1 β , it can also inhibit the production of IL-4, IL-5, and IL-13, which are involved in the development of allergic and eosinophilic inflammation [25,26].

2.5. Characterization of Target Organ LMs Metabolism Network

The impacts on the LMs metabolism network in lung tissue and serum induced by modeling and medical intervention were obtained with PCA analysis. As shown in Figure 5A, the LMs metabolism network in the lung was restored partially both with SXCF and RosA. As shown in Figure 5B, similar regulation in serum was observed with SXCF treatment. However, RosA caused excessive regulation in serum.

As shown in Figure 5C,D, the heatmap validated the PCA results. In lung tissue, LMs decreased close to the control group both with SXCF and RosA treatment. In serum, limited recovery to the control group was obtained.

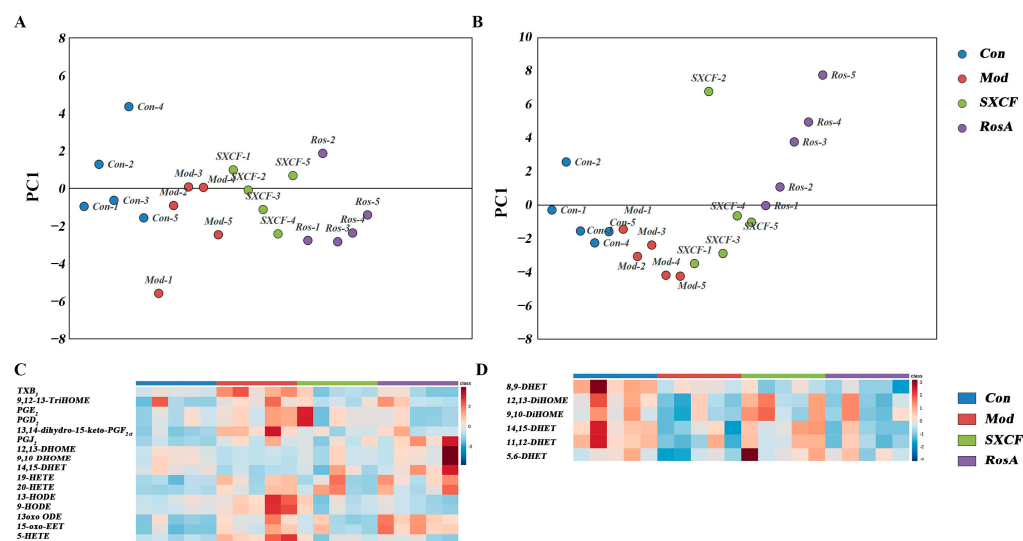


Figure 5. LMs regulation of OVA-induced asthma group and the control group. ((A) One-dimensional PCA score scatter plot of lung tissue. (B) One-dimensional PCA score scatter plot of serum. (C) Heatmap of lung tissue. (D) Heatmap of serum).

3. Discussion

Asthma can affect people of all ages and there is no cure for it. Therefore, suppressing inflammation by inhibiting inflammatory mediators is a reasonable treatment for asthma.

Natural products are increasingly recognized as valuable sources of pharmacotherapeutic agents for treating chronic diseases or for their biological activity. RosA is a phenolic compound found in plants and possessing anti-inflammatory properties [9]. RosA has been determined to significantly reduce airway inflammation, decrease the levels of Th1 cytokines and Th2 cytokines, and inhibit the activation of signaling pathways associated with inflammation, such as MAPK and NF- κ B [27]. RosA has also been shown to reduce the infiltration of inflammatory cells into the airways, such as eosinophils and neutrophils, which are commonly found in the lungs of individuals with asthma [28].

Early research has shown a strong correlation between Th2 cytokine expression and allergic asthma. Regulation of Th2 cytokines is essential for the development of common allergic responses such as asthma. These cytokines trigger inflammatory responses, which can increase IgE secretion and inflammatory cell recruitment [29]. These symptoms are the primary pathophysiological indicators of allergic airway conditions. IL-4 has shown the effect of inhibiting the production of Th1 cells that secrete IFN- γ [30]. Our results indicate that RosA induced more downregulation of IL-4 compared with SXCF, corresponding to higher level of IFN- γ (Figure 4), and IgE was downregulated as low as control group after SXCF treatment (Figure 3E), which means SXCF exhibits greater anti-asthmatic potential.

Remarkable parts of LMs were regulated by both RosA and SXCF in asthmatic mice and PLS-DA were carried out to discover those LMs impacted by modelling. As shown in Figure 6A, 16 LMs of lung tissue were determined to change significantly with OVA sensitization compared with Con group ($p < 0.05$). With SXCF treatment, 50% (8 of 16) of LMs were significantly changed compared with the Mod group, 87.5% (7 of 8) of these LMs overlapped with those significantly changed by RosA ($p < 0.05$); the regulation direction was basically the same. It can be observed in Figure 6C that the effect of SXCF on the metabolism network of LMs was mainly confined to the metabolites of Linoleic acid. RosA has a broader impact; 62.5% (10 of 16) of LMs were significantly regulated by RosA ($p < 0.05$). We determined that only 9,10-DiHOME and 12,13-DiHOME were upregulated by SXCF and RosA compared with most of these downregulated LMs.

As shown in Figure 6B, only a limited fraction of LMs changed significantly in serum after OVA stimulation. In total, 50% (3 of 6) LMs were reversed by SXCF. Only 33% (2 of 6) were regulated by RosA. It was believed that LMs changes in serum would be minimized

by dilution effects, as metabolites pool from diverse organs. It should be noted that one LM (5,6-DHET) was reversed, and another LM (8,9-DHET) decreased further by RosA treatment.

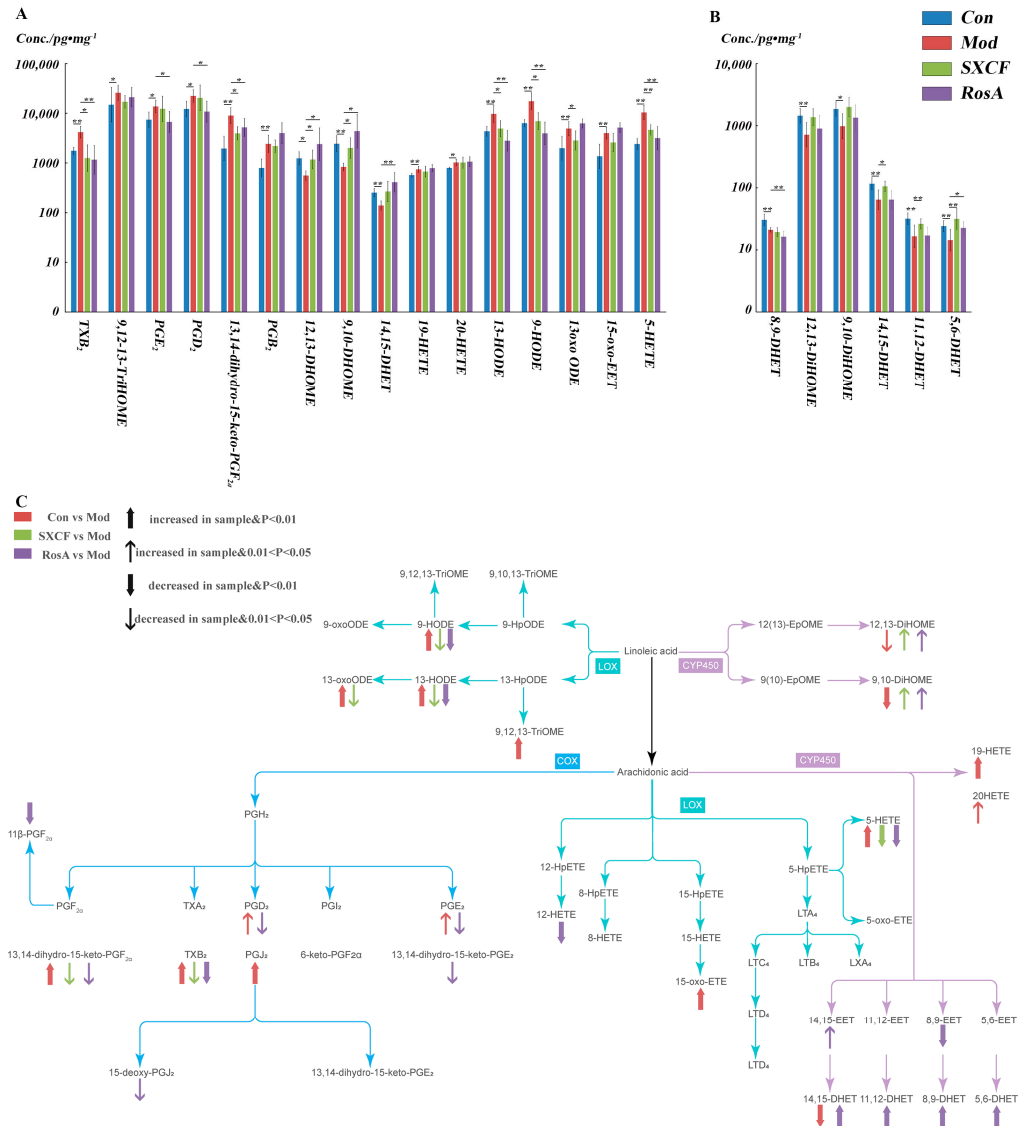


Figure 6. A&B: Different LMs Regulation between SXFC and RosA in target organ (A) and serum (B). All the LMs shown in the figure were determined to be significantly changed between Con group and Mod group ($p < 0.05$). *: $p < 0.05$ and **: $p < 0.01$. (C): LMs detected in target organ with their metabolism pathway and variations among different groups.

3.1. RosA Induced Equal Effects on Key-LMs as SXCF

We can observe that most of the LMs show the same trend, such as TXB₂, 9-HODE, 9,10-DHOME, and 12,13-DHOME (Figure 7). Both RosA and SXCF regulation ratios (R_r) were mostly distributed from 0.75–1.25 (Table 2).

The most impacted LMs were filtered by p value and VIP score. TXB₂ was the most important LMs after SXCF treatment and RosA treatment (VIP > 1.5). As shown in Figure 4, compared to the Mod group, the TXB₂ level had a significant reversal upon SXCF administration and RosA administration, even lower than that of the control group.

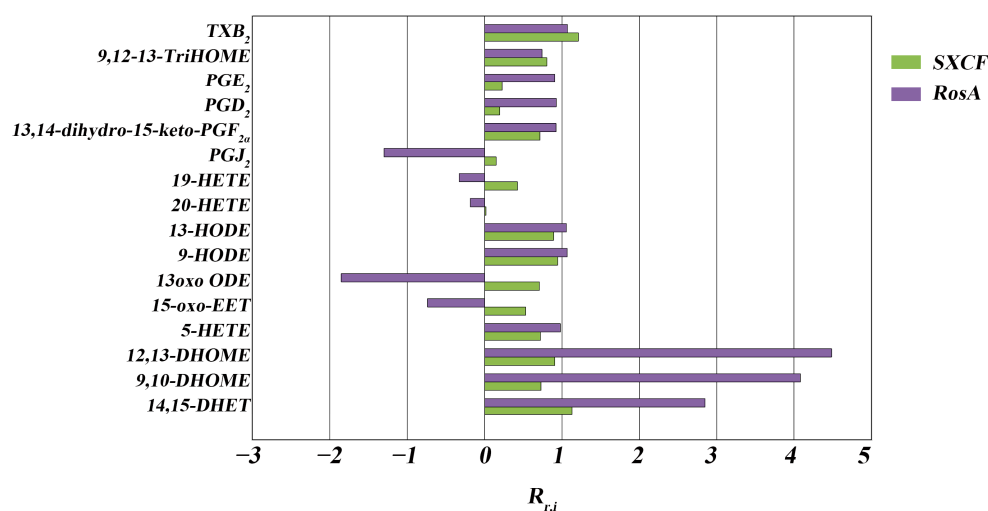


Figure 7. The LMs regulation ratios (R_r) of SXCF and RosA. LMs shown in the figure were significantly regulated in the Mod group compared with the Con group. $R_{r,i} = \frac{C_m - C_i}{C_m - C_c}$, C_m : Concentration of LMs in Mod group; C_i : Concentration of LMs in SXCF or RosA group; C_c : Concentration of LMs in Con group.

Table 2. LMs regulation summary.

Group	$R_{r,i} > 125\%$	$75\% < R_{r,i} < 125\%$	$0 < R_{r,i} < 75\%$	$R_{r,i} < 0$
SXCF	0	10	6	0
RosA	3	7	1	5

TXA₂ is very unstable in aqueous solution; it is hydrated to biological inactivity within about 30 s. In most studies, the TXB₂ level was extensively examined to reflect the level of TXA₂. TXA₂ is a powerful vascular inflammatory factor, and previous research demonstrated that TXA₂ inhibits dendritic cell-dependent proliferation of T cells and weakens the dendritic cell–T cell adhesion, which proved that RosA and SXCF can reduce inflammation by downregulating TXA₂ to reach therapeutic effect [31,32]. The release of TXA₂ from macrophages was stimulated by IgE, and TXA₂ subsequently stimulated the TNF- α production by human alveolar macrophages [33]. As shown in Figure 4A, TNF- α was downregulated significantly with SXCF and RosA treatment ($p > 0.05$). IgE also has a downregulation in both SXCF group and RosA group. Hayashi et al. reported that TXA₂ plays an important role in airway allergic inflammation, which is related to the infiltration of Th2 lymphocytes and eosinophils [34]. These findings suggest that TXA₂ induced IL-4 upregulation. In Figure 6A, TXA₂ is higher in SXCF group, which is consistent with the increase in IL-4 levels in SXCF group (Figure 4B).

HODEs are generated through the oxidation of linoleic acid and arachidonic acid and have been shown to regulate the inflammation in vascular wall [35]. 13-HODE and 9-HODE are two of the most commonly studied HODEs. They are involved in a variety of physiological processes, including inflammation and angiogenesis [36,37]. The activity of HODEs is regulated by Th2 cytokines, and IL-4 plays an important role in the synthesis of HODEs [38]. As shown in Figures 4B and 6A, HODEs levels are lower in RosA, which means that RosA prevented the formation of HODEs by inhibition of IL-4.

3.2. SXCF Reduced the Side Reactions by Neutralizing Parts of RosA Regulation on LMs Metabolic Network

We can also observe the difference between SXCF group and RosA group (Table 2). RosA has excessive regulation on some of these LMs, such as 14,15-DHET, 12,13-DHOME, and 9,10-DHOME ($R_{r,RosA} > 125\%$). These excessive regulations may be the main factor of side reactions of RosA.

DHOMEs are metabolized by linoleic acid through soluble epoxide hydrolase (sEH) and CYP450 epoxygenases [39]. These metabolites induced oxidative stress and chemotaxis of human neutrophils and aggravated lung inflammation in asthmatic mice [40] and also appeared in the airways of adults with asthma following bronchial provocation with an allergen [41]. As reported, intraperitoneal injection of DHOMEs increased pulmonary inflammation manifested as the increase in IgE levels and the decrease in regulatory T cells in the lungs [40]. Here, we showed that overregulated DHOMEs were accompanied by a high level of IgE in RosA groups, which shows the side effect of RosA (Figures 3E and 7).

EETs are known for their anti-inflammatory effect and vascular function [42,43]. 14,15-EET is a lipid mediator produced by the metabolism of arachidonic acid. It is a bioactive molecule that regulates intracellular signaling and physiological processes through interactions with G protein-coupled receptors [44]. 14,15-EET is involved in various physiological and pathological processes, including cardiovascular diseases and inflammation [45]. Studies have shown that 14,15-EET has protective effects on the cardiovascular system, including lowering blood pressure, antiplatelet aggregation, and involvement in vasodilation and angiogenesis [42,43]. Additionally, 14,15-EET has anti-inflammatory and anti-oxidative stress effects, which can alleviate inflammatory reactions and tissue damage caused by oxidative stress [46]. DHETs are the stable metabolites of the EETs, and 14,15-EET is converted to 14,15-DHET almost entirely in six hours [43]. 14,15-DHET is a biologically active molecule that plays a role in regulating various physiological processes, including blood pressure regulation, inflammation, and pain perception. It is also involved in the regulation of vascular tone and endothelial function [47,48]. Studies have shown that 14,15-DHET has anti-inflammatory effects and is involved in the resolution of inflammation [49]. Additionally, it has been suggested that 14,15-DHET may have therapeutic potential in the treatment of various diseases, including hypertension [50] and cardiovascular disease [51]. As shown in Figure 4A, the 14,15-DHET levels increased significantly in the RosA group ($p < 0.05$) and also increased in the SXCF group, which proved the anti-inflammatory effect of SXCF and RosA. Furthermore, 14,15-EET has been shown to have a hypotensive impact [52], while elevated EETs and DHETs levels are associated with ischemic stroke [53]. As shown in Figure 5, 14,15-DHET was overregulated in the RosA group. Excessive secretion of 14,15-DHET may increase the risk of incident ischemic stroke. It is believed some constituents in SXCF besides RosA may neutralize excessive impacts of RosA on LMs.

4. Materials and Methods

4.1. Materials

MS-grade water, acetonitrile, formic acid, acetic acid, and methanol were purchased from Fisher Scientific (Waltham, MA, USA). Isopropanol was obtained from Honeywell (West Valley City, UT, USA). Glycerol, Ovalbumin (OVA) and Butylated hydroxytoluene (BHT) were purchased from Sigma-Aldrich (Milwaukee, WI, USA). Internal standards were purchased from Cayman (Ann Arbor, MI, USA). IL-4, IL-10, TNF- α , IFN- γ , and IgE ELISA kits were purchased from Lianke (Shaoxing, China). Waters MAX SPE cartridges (Milford, MA, USA) and BCA kit (Rockford, IL, USA) were also obtained.

4.2. Methods

4.2.1. Network Pharmacology

We entered the keyword “rosmarinic acid” into PubChem (<https://pubchem.ncbi.nlm.nih.gov/>, accessed on 6 July 2022) and obtained Isomeric SMILES of RosA.

Isomeric SMILES of RosA was imported into the Swiss Target Prediction website (<http://www.swisstargetprediction.ch/>, accessed on 6 July 2022) to predict RosA target proteins.

We entered “asthma” in the GeneCards (<http://www.genecards.org/>, accessed on 6 July 2022) database and DrugBank (<https://go.drugbank.com/>, accessed on 6 July 2022) database to predict potential asthma target.

The intersection targets of the RosA and asthma were input into the R software 4.1.1(R Foundation for Statistical Computing, Vienna, Austria) data package to perform Gene Ontology (GO) enrichment analysis and Kyoto Encyclopedia of Genes and Genomes (KEGG) pathway analysis on the effective targets of the RosA to explore the biological process and signaling pathway of treating asthma with RosA.

4.2.2. Animals and Preparation of Asthma Model

All the animal experiments were approved by the Animal Care and Use Committee of Xinjiang Medical University, Ethics Committee of Xinjiang Medical University (IACUC-20210603-07). After 3 days of experimental feeding, mice were randomly divided into four groups, Con group, Mod group, SXCF group, RosA group, with five mice per group.

On 1st and 8th day, mice of group Mod, SXCF, and RosA were OVA-sensitized twice by an intraperitoneal injection of 0.2 mL OVA sensitization solution (0.5 mg/mL in aluminum hydroxide gum saline diluent). Con group mice were injected with 0.2 mL saline. From the 15th to 21st day, the Mod group was orally administered with 0.5% CMC-Na, group SXCF and group RosA mice were orally administered with SXCF (10 mg/mL, 100 mg/kg) and RosA solution (0.5 mg/mL, 5 mg/kg) equal to SXCF dose (4.8% *m/v* which was measured by UPLC-MS.), respectively. After one hour, group B, C and D were challenged by nebulized OVA (10 mg/mL) for 30 min; Con group mice were challenged by saline. Mice received this treatment once a day and had free access to food and water during the study period.

4.2.3. Hematoxylin and Eosin Staining

For lung histology, lungs were dissected, fixed in 4% paraformaldehyde, paraffin-embedded, sectioned, stained with hematoxylin and eosin, and analyzed under a light microscope.

4.2.4. Cytokine Detection

TNF- α , IFN- γ , IL-4, and IL-10 levels in BALF and serum IgE were measured by specific ELISA kits purchased from Lianke (Shaoxing, China).

4.2.5. Sample Preparation

A total of 50 μ L of serum was thawed on ice and 70 μ L 10% glycerol aqueous solution was added. Samples were diluted to 1 mL with 25% acetonitrile aqueous solution.

A total of 10 mg of ground lung tissue was mixed with 250 μ L acetonitrile. After centrifugation at 15,000 rpm for 5 min, 200 μ L supernatant was transferred to a tube containing 70 μ L 10% glycerol aqueous solution. Samples were diluted to 1 mL final volume (containing 20 μ g BHT and 0.5 ng IS) with 25% acetonitrile aqueous solution.

Solid-phase extraction cartridges were equilibrated with 3 mL acetonitrile and 3 mL 25% acetonitrile aqueous solution. Samples were loaded onto conditioned cartridges. The cartridge was washed with 25% acetonitrile aqueous solution and acetonitrile. LMs were eluted with acetonitrile containing 1% formic acid. The elution was concentrated with a vacuum concentrator. Purified samples were stored at -80 °C before UPLC-MRM analysis.

All samples were reconditioned with 50 μ L acetonitrile/methanol (50/50, *v/v*) for injection.

The remaining 100 μ L of supernatant of lung tissue was mixed with 100 μ L of water and applied for protein quantitation by BCA kit.

4.2.6. UPLC-MS/MS Conditions

LC-MS/MS analysis was performed on a AB SCIEX Triple Quad 5500+ MS (Framingham, MA, USA) coupled with a Thermo Scientific Dionex Ultimate 3000 UHPLC (Waltham, MA, USA). A Waters ACQUITY UPLC BEH C18 (2.1 \times 50 mm) (Milford, MA, USA) was applied. The column temperature was set as 40 °C. Mobile phase A was 0.1% formic acid aqueous solution; mobile phase B was ACN/IPA (9/1 *v/v*). Gradient elution conditions

are shown in Table 3. The flow rate was 0.4 mL/min. The injection volume was 5 μ L. Data acquisition was performed in negative ion mode equipped with an ESI source.

Table 3. Gradient Elution program for LMs analysis.

Time/min	A%	B%
0	75	25
1	75	25
8	5	95
8.5	5	95
8.51	75	25
10	75	25

4.2.7. Data Analysis

The data acquisition was carried out with Analyst 1.7.1 (AB SCIEX, Framingham, MA, USA). Integration and quantification were achieved with OS-Q V1.6 (AB SCIEX, Framingham, MA, USA). Principal component analysis was conducted with EZinfo (Waters, Milford, MA, USA). T-tests were performed by IBM SPSS (Armonk, NY, USA). Heatmaps were utilized using the Metaboanalyst 5.0 (<http://www.metaboanalyst.ca/>, accessed on 30 June 2022).

5. Conclusions

According to the results, both SXCF and RosA had the effect of asthma control and inflammation reduction by regulation of LMs associated with cytokine production and leukocyte chemotaxis. This proved that RosA can exert therapeutic functions against asthma as the main constituent of SXCF. LMs overregulation of target organ induced by RosA was neutralized by other constituents in SXCF. There are other substances synergistically enhancing its anti-asthma efficacy in the SXCF, which is better than the equivalent RosA. While further research is needed to understand RosA's full potential as a treatment for asthma in humans, the existing evidence shows that RosA may be a viable natural product for managing asthma symptoms and inhibiting airway inflammation, and SXCF has the potential to be an asthma treatment option with accessibility, adherence, and safety.

Author Contributions: C.T.: Project administration, Conceptualization, Methodology, Writing—Review and Editing. X.R.: Project administration, Conceptualization, Methodology. T.Q.: Writing—Original Draft, Formal analysis, Investigation, Data Curation, Visualization. L.K.: Validation, Investigation, Y.K.: Investigation, Resources. X.L.: Investigation, Resources. M.H.: Investigation, Resources. X.Z.: Supervision, Formal analysis. H.L.: Funding acquisition, Supervision. All authors have read and agreed to the published version of the manuscript.

Funding: This work was supported by National Natural Science Foundation of China (No. 81960752, China), the Open Fund of the State Key Laboratory Coal Resources and Safe Mining (No. SKL-CRSM21KFA11, China), Tianshan Youth Project (No. 2020Q047, China).

Institutional Review Board Statement: All the animal experiments were approved by the Animal Care and Use Committee of Xinjiang Medical University. Ethics Committee of Xinjiang Medical University (IACUC-20210603-07).

Informed Consent Statement: Not applicable.

Data Availability Statement: The data presented in this study are available on request from the corresponding author.

Conflicts of Interest: The authors declare no conflict of interest.

Sample Availability: Not applicable.

References

1. Ray, A.; Raundhal, M.; Oriss, T.B.; Ray, P.; Wenzel, S.E. Current concepts of severe asthma. *J. Clin. Investig.* **2016**, *126*, 2394–2403. [CrossRef] [PubMed]
2. Katsumoto, T.R.; Kudo, M.; Chen, C.; Sundaram, A.; Callahan, E.C.; Zhu, J.W.; Lin, J.; Rosen, C.E.; Manz, B.N.; Lee, J.W.; et al. The phosphatase CD148 promotes airway hyperresponsiveness through SRC family kinases. *J. Clin. Investig.* **2013**, *123*, 2037–2048. [CrossRef] [PubMed]
3. van Staa, T.-P.; Bishop, N.; Leufkens, H.G.; Cooper, C. Are inhaled corticosteroids associated with an increased risk of fracture in children? *Osteoporos. Int.* **2004**, *15*, 785–791. [CrossRef] [PubMed]
4. Lavoie, K.L.; Cartier, A.; Labrecque, M.; Bacon, S.L.; Lemiere, C.; Malo, J.L.; Lacoste, G.; Barone, S.; Verrier, P.; Ditto, B. Are psychiatric disorders associated with worse asthma control and quality of life in asthma patients? *Respir. Med.* **2005**, *99*, 1249–1257. [CrossRef] [PubMed]
5. Yuan, F.; Liu, R.; Hu, M.; Rong, X.; Bai, L.; Xu, L.; Mao, Y.; Hasimu, H.; Sun, Y.; He, J. JAX2, an ethanol extract of *Hyssopus cuspidatus* Boriss, can prevent bronchial asthma by inhibiting MAPK/NF-kappaB inflammatory signaling. *Phytomedicine* **2019**, *57*, 305–314. [CrossRef] [PubMed]
6. Xie, C.; Gul, A.; Yu, H.; Huang, X.; Deng, L.; Pan, Y.; Ni, S.; Nurahmat, M.; Abduwaki, M.; Luo, Q. Integrated systems pharmacology and transcriptomics to dissect the mechanisms of Loki Zupa decoction in the treatment of murine allergic asthma. *J. Ethnopharmacol.* **2022**, *294*, 115351. [CrossRef] [PubMed]
7. Micovic, T.; Katanic Stankovic, J.S.; Bauer, R.; Nost, X.; Markovic, Z.; Milenkovic, D.; Jakovljevic, V.; Tomovic, M.; Bradic, J.; Stesevic, D.; et al. In vitro, in vivo and in silico evaluation of the anti-inflammatory potential of *Hyssopus officinalis* L. subsp. *aristatus* (Godr.) Nyman (Lamiaceae). *J. Ethnopharmacol.* **2022**, *293*, 115201. [CrossRef] [PubMed]
8. Han, X.; Li, L.; Diao, J. Qualitative and quantitative analyses of labiatic acid, apigenin and buddleoside in *Hyssopus officinalis* by high-performance thin-layer chromatography. *JPC-J. Planar Chromatogr.-Mod. TLC* **2021**, *34*, 45–53. [CrossRef]
9. Takano, H.; Osakabe, N.; Sanbongi, C.; Yanagisawa, R.; Inoue, K.-I.; Yasuda, A.; Natsume, M.; Baba, S.; Ichiishi, E.-I.; Yoshikawa, T. Extract of *Perilla frutescens* Enriched for Rosmarinic Acid, a Polyphenolic Phytochemical, Inhibits Seasonal Allergic Rhinoconjunctivitis in Humans. *Exp. Biol. Med.* **2004**, *229*, 247–254. [CrossRef]
10. Zhang, M.; Li, N.; Cai, R.; Gu, J.; Xie, F.; Wei, H.; Lu, C.; Wu, D. Rosmarinic acid protects mice from imiquimod induced psoriasis-like skin lesions by inhibiting the IL-23/Th17 axis via regulating Jak2/Stat3 signaling pathway. *Phytother. Res. PTR* **2021**, *35*, 4526–4537. [CrossRef]
11. Kelm, M.; Nair, M.; Strasburg, G.; DeWitt, D. Antioxidant and cyclooxygenase inhibitory phenolic compounds from *Ocimum sanctum* Linn. *Phytomedicine* **2000**, *7*, 7–13. [CrossRef] [PubMed]
12. Sanbongi, C.; Takano, H.; Osakabe, N.; Sasa, N.; Natsume, M.; Yanagisawa, R.; Inoue, K.I.; Sadakane, K.; Ichinose, T.; Yoshikawa, T. Rosmarinic acid in perilla extract inhibits allergic inflammation induced by mite allergen, in a mouse model. *Clin. Exp. Allergy* **2004**, *34*, 971–977. [CrossRef] [PubMed]
13. Liang, Z.; Wu, L.; Deng, X.; Liang, Q.; Xu, Y.; Deng, R.; Lv, L.; Ji, M.; Hao, Z.; He, J. The Antioxidant Rosmarinic Acid Ameliorates Oxidative Lung Damage in Experimental Allergic Asthma via Modulation of NADPH Oxidases and Antioxidant Enzymes. *Inflammation* **2020**, *43*, 1902–1912. [CrossRef] [PubMed]
14. Hamid, Q.; Tulic, M. Immunobiology of Asthma. *Annu. Rev. Physiol.* **2009**, *71*, 489–507. [CrossRef] [PubMed]
15. Barnes, P.J. Th2 cytokines and asthma: An introduction. *Respir. Res.* **2001**, *2*, 64. [CrossRef]
16. Torres, R.; Picado, C.; de Mora, F. The PGE2-EP2-mast cell axis: An antiasthma mechanism. *Mol. Immunol.* **2015**, *63*, 61–68. [CrossRef]
17. Shin, K.; Hwang, J.J.; Kwon, B.I.; Kheradmand, F.; Corry, D.B.; Lee, S.H. Leukotriene enhanced allergic lung inflammation through induction of chemokine production. *Clin. Exp. Med.* **2015**, *15*, 233–244. [CrossRef]
18. Gauvreau, G.M.; Boulet, L.P.; FitzGerald, J.M.; Cockcroft, D.W.; Davis, B.E.; Leigh, R.; Tanaka, M.; Fourre, J.A.; Tanaka, M.; Nabata, T.; et al. A dual CysLT1/2 antagonist attenuates allergen-induced airway responses in subjects with mild allergic asthma. *Allergy* **2016**, *71*, 1721–1727. [CrossRef]
19. Zhang, H.; Park, Y.; Wu, J.; Chen, X.; Lee, S.; Yang, J.; Dellsperger, K.C.; Zhang, C. Role of TNF- α in vascular dysfunction. *Clin. Sci.* **2009**, *116*, 219–230. [CrossRef]
20. Willerson, J.T.; Ridker, P.M. Inflammation as a cardiovascular risk factor. *Circulation* **2004**, *109* (Suppl. S1), II2–II10. [CrossRef]
21. Liu, L.Y.; Bates, M.E.; Jarjour, N.N.; Busse, W.W.; Bertics, P.J.; Kelly, E.A.B. Generation of Th1 and Th2 Chemokines by Human Eosinophils: Evidence for a Critical Role of TNF- α 1. *J. Immunol.* **2007**, *179*, 4840–4848. [CrossRef] [PubMed]
22. Paul, W.E. Interleukin 4: Signalling mechanisms and control of T cell differentiation. *Ciba Found. Symp.* **1997**, *204*, 208–216, discussion 216–9. [CrossRef] [PubMed]
23. Kapsenberg, M.L. Dendritic-cell control of pathogen-driven T-cell polarization. *Nat. Rev. Immunol.* **2003**, *3*, 984–993. [CrossRef] [PubMed]
24. Zhao, J.; Lloyd, C.M.; Noble, A. Th17 responses in chronic allergic airway inflammation abrogate regulatory T-cell-mediated tolerance and contribute to airway remodeling. *Mucosal Immunol.* **2013**, *6*, 335–346. [CrossRef]
25. Schroder, K.; Hertzog, P.J.; Ravasi, T.; Hume, D.A. Interferon-gamma: An overview of signals, mechanisms and functions. *J. Leukoc. Biol.* **2004**, *75*, 163–189. [CrossRef] [PubMed]
26. Billiau, A.; Matthys, P. Interferon-gamma: A historical perspective. *Cytokine Growth Factor Rev.* **2009**, *20*, 97–113. [CrossRef]


27. Xavier, C.P.R.; Lima, C.F.; Fernandes-Ferreira, M.; Pereira-Wilson, C. Salvia Fruticosa, Salvia Officinalis, and Rosmarinic Acid Induce Apoptosis and Inhibit Proliferation of Human Colorectal Cell Lines: The Role in MAPK/ERK Pathway. *Nutr. Cancer* **2009**, *61*, 564–571. [CrossRef] [PubMed]
28. Luo, C.; Zou, L.; Sun, H.; Peng, J.; Gao, C.; Bao, L.; Ji, R.; Jin, Y.; Sun, S. A review of the anti-inflammatory effects of rosmarinic acid on inflammatory diseases. *Front. Pharmacol.* **2020**, *11*, 153. [CrossRef]
29. O'Garra, A. Cytokines induce the development of functionally heterogeneous T helper cell subsets. *Immunity* **1998**, *8*, 275–283. [CrossRef]
30. Yanagihara, Y.; Ikizawa, K.; Kajiwara, K.; Koshio, T.; Basaki, Y.; Akiyama, K. Functional significance of IL-4 receptor on B cells in IL-4-induced human IgE production. *J. Allergy Clin. Immunol.* **1995**, *96* (Suppl. S6), 1145–1151. [CrossRef]
31. Kabashima, K.; Murata, T.; Tanaka, H.; Matsuoka, T.; Sakata, D.; Yoshida, N.; Katagiri, K.; Kinashi, T.; Tanaka, T.; Miyasaka, M.; et al. Thromboxane A2 modulates interaction of dendritic cells and T cells and regulates acquired immunity. *Nat. Immunol.* **2003**, *4*, 694–701. [CrossRef] [PubMed]
32. Conti, P.; Caraffa, A.; Gallenga, C.; Ross, R.; Kritas, S.; Frydas, I.; Younes, A.; Di Emidio, P.; Ronconi, G.; Toniato, E. IL-1 induces thromboxane-A2 (TxA2) in COVID-19 causing inflammation and micro-thrombi: Inhibitory effect of the IL-1 receptor antagonist (IL-1Ra). *J. Biol. Regul. Homeost. Agents* **2020**, *34*, 1623–1627. [CrossRef] [PubMed]
33. Storch, J.; MacDermot, J. IgE and IgG are synergistic in antigen-mediated release of thromboxane from human lung macrophages. *Cell. Immunol.* **1991**, *134*, 138–146. [CrossRef] [PubMed]
34. Hayashi, M.; Koya, T.; Kawakami, H.; Sakagami, T.; Hasegawa, T.; Kagamu, H.; Takada, T.; Sakai, Y.; Suzuki, E.; Gelfand, E.W.; et al. A prostacyclin agonist with thromboxane inhibitory activity for airway allergic inflammation in mice. *Clin. Exp. Allergy* **2010**, *40*, 317–326. [CrossRef] [PubMed]
35. Kikut, J.; Komorniak, N.; Ziętek, M.; Palma, J.; Szczuko, M. Inflammation with the participation of arachidonic (AA) and linoleic acid (LA) derivatives (HETEs and HODEs) is necessary in the course of a normal reproductive cycle and pregnancy. *J. Reprod. Immunol.* **2020**, *141*, 103177. [CrossRef]
36. Eling, T.E.; Glasgow, W.C. Cellular proliferation and lipid metabolism: Importance of lipoxygenases in modulating epidermal growth factor-dependent mitogenesis. *Cancer Metastasis Rev.* **1994**, *13*, 397–410. [CrossRef]
37. Schneider, M.; Wortmann, M.; Mandal, P.K.; Arpornchayanon, W.; Jannasch, K.; Alves, F.; Strieth, S.; Conrad, M.; Beck, H. Absence of Glutathione Peroxidase 4 Affects Tumor Angiogenesis through Increased 12/15-Lipoxygenase Activity. *Neoplasia* **2010**, *12*, 254–263. [CrossRef]
38. Kühn, H.; O'Donnell, V.B. Inflammation and immune regulation by 12/15-lipoxygenases. *Prog. Lipid Res.* **2006**, *45*, 334–356. [CrossRef]
39. Hildreth, K.; Kodani, S.D.; Hammock, B.D.; Zhao, L. Cytochrome P450-derived linoleic acid metabolites EpOMEs and DiHOMEs: A review of recent studies. *J. Nutr. Biochem.* **2020**, *86*, 108484. [CrossRef]
40. Levan, S.R.; Stamnes, K.A.; Lin, D.L.; Panzer, A.R.; Fukui, E.; McCauley, K.; Fujimura, K.E.; McKean, M.; Ownby, D.R.; Zoratti, E.M.; et al. Elevated faecal 12,13-diHOME concentration in neonates at high risk for asthma is produced by gut bacteria and impedes immune tolerance. *Nat. Microbiol.* **2019**, *4*, 1851–1861. [CrossRef]
41. Lundström, S.L.; Yang, J.; Källberg, H.J.; Thunberg, S.; Gafvelin, G.; Haeggström, J.Z.; Grönneberg, R.; Grunewald, J.; van Hage, M.; Hammock, B.D.; et al. Allergic Asthmatics Show Divergent Lipid Mediator Profiles from Healthy Controls Both at Baseline and following Birch Pollen Provocation. *PLoS ONE* **2012**, *7*, e33780. [CrossRef] [PubMed]
42. Chen, X.; Li, Z.; Zhang, B.; Liu, T.; Yao, W.; Wan, L.; Zhang, C.; Zhang, Y. Antinociception role of 14,15-epoxyeicosatrienoic acid in a central post-stroke pain model in rats mediated by anti-inflammation and anti-apoptosis effect. *Neurochem. Int.* **2022**, *154*, 105291. [CrossRef] [PubMed]
43. Sudhakar, V.; Shaw, S.; Imig, J.D. Epoxyeicosatrienoic acid analogs and vascular function. *Curr. Med. Chem.* **2010**, *17*, 1181–1190. [CrossRef] [PubMed]
44. Liu, X.; Qian, Z.-Y.; Xie, F.; Fan, W.; Nelson, J.W.; Xiao, X.; Kaul, S.; Barnes, A.P.; Alkayed, N.J. Functional screening for G protein-coupled receptor targets of 14,15-epoxyeicosatrienoic acid. *Prostaglandins Other Lipid Mediat.* **2017**, *132*, 31–40. [CrossRef]
45. Askari, A.A.; Thomson, S.; Edin, M.L.; Lih, F.B.; Zeldin, D.C.; Bishop-Bailey, D. Basal and inducible anti-inflammatory epoxygenase activity in endothelial cells. *Biochem. Biophys. Res. Commun.* **2014**, *446*, 633–637. [CrossRef]
46. Li, Y.; Yu, G.; Yuan, S.; Tan, C.; Xie, J.; Ding, Y.; Lian, P.; Fu, L.; Hou, Q.; Xu, B.; et al. 14,15-Epoxyeicosatrienoic acid suppresses cigarette smoke condensate-induced inflammation in lung epithelial cells by inhibiting autophagy. *Am. J. Physiol. Lung Cell. Mol. Physiol.* **2016**, *311*, L970–L980. [CrossRef]
47. VanRollins, M.; Kaduce, T.L.; Knapp, H.R.; Spector, A.A. 14,15-Epoxyeicosatrienoic acid metabolism in endothelial cells. *J. Lipid Res.* **1993**, *34*, 1931–1942. [CrossRef]
48. Fang, X.; Moore, S.A.; Stoll, L.L.; Rich, G.; Kaduce, T.L.; Weintraub, N.L.; Spector, A.A. 14,15-Epoxyeicosatrienoic acid inhibits prostaglandin E2 production in vascular smooth muscle cells. *Am. J. Physiol.-Heart Circ. Physiol.* **1998**, *275*, H2113–H2121. [CrossRef]
49. Biliktu, M.; Senol, S.P.; Temiz-Resitoglu, M.; Guden, D.S.; Horat, M.F.; Sahan-Firat, S.; Sevim, S.; Tunctan, B. Pharmacological inhibition of soluble epoxide hydrolase attenuates chronic experimental autoimmune encephalomyelitis by modulating inflammatory and anti-inflammatory pathways in an inflammasome-dependent and -independent manner. *Inflammopharmacology* **2020**, *28*, 1509–1524. [CrossRef]

50. Imig, J.D.; Zhao, X.; Capdevila, J.H.; Morisseau, C.; Hammock, B.D. Soluble Epoxide Hydrolase Inhibition Lowers Arterial Blood Pressure in Angiotensin II Hypertension. *Hypertension* **2002**, *39*, 690–694. [CrossRef]
51. Theken, K.N.; Schuck, R.N.; Edin, M.L.; Tran, B.; Ellis, K.; Bass, A.; Lih, F.B.; Tomer, K.B.; Poloyac, S.M.; Wu, M.C.; et al. Evaluation of cytochrome P450-derived eicosanoids in humans with stable atherosclerotic cardiovascular disease. *Atherosclerosis* **2012**, *222*, 530–536. [CrossRef] [PubMed]
52. Walkowska, A.; Červenka, L.; Imig, J.D.; Falck, J.R.; Sadowski, J.; Kompanowska-Jezierska, E. Early renal vasodilator and hypotensive action of epoxyeicosatrienoic acid analog (EET-A) and 20-HETE receptor blocker (AAA) in spontaneously hypertensive rats. *Front. Physiol.* **2021**, *12*, 622882. [CrossRef] [PubMed]
53. Lemaitre, R.N.; Jensen, P.N.; Zeigler, M.; Fretts, A.M.; Umans, J.G.; Howard, B.V.; Sitlani, C.M.; McKnight, B.; Gharib, S.A.; King, I.B.; et al. Plasma epoxyeicosatrienoic acids and diabetes-related cardiovascular disease: The cardiovascular health study. *eBioMedicine* **2022**, *83*, 104189. [CrossRef] [PubMed]

Disclaimer/Publisher’s Note: The statements, opinions and data contained in all publications are solely those of the individual author(s) and contributor(s) and not of MDPI and/or the editor(s). MDPI and/or the editor(s) disclaim responsibility for any injury to people or property resulting from any ideas, methods, instructions or products referred to in the content.

Article

Two-Dimensional-PAGE Coupled with nLC-MS/MS-Based Identification of Differentially Expressed Proteins and Tumorigenic Pathways in MCF7 Breast Cancer Cells Transfected for JTB Protein Silencing

Madhuri Jayathirtha ¹, Taniya Jayaweera ¹, Danielle Whitham ¹ , Isabelle Sullivan ¹, Brîndușa Alina Petre ^{1,2,3,*}, Costel C. Darie ¹  and Anca-Narcisa Neagu ^{4,*}

- ¹ Biochemistry & Proteomics Laboratories, Department of Chemistry and Biomolecular Science, Clarkson University, 8 Clarkson Avenue, Potsdam, NY 13699, USA; jayathm@clarkson.edu (M.J.); jayawetm@clarkson.edu (T.J.); whithad@clarkson.edu (D.W.); sullivil@clarkson.edu (I.S.); cdarie@clarkson.edu (C.C.D.)
- ² Laboratory of Biochemistry, Department of Chemistry, “Alexandru Ioan Cuza” University of Iasi, Carol I Blvd, No. 11, 700506 Iasi, Romania
- ³ Center for Fundamental Research and Experimental Development in Translation Medicine—TRANSCEND, Regional Institute of Oncology, 700483 Iasi, Romania
- ⁴ Laboratory of Animal Histology, Faculty of Biology, “Alexandru Ioan Cuza” University of Iasi, Carol I Blvd, No. 22, 700505 Iasi, Romania
- * Correspondence: bpetre@clarkson.edu (B.A.P.); aneagu@uaic.ro (A.-N.N.)



Citation: Jayathirtha, M.; Jayaweera, T.; Whitham, D.; Sullivan, I.; Petre, B.A.; Darie, C.C.; Neagu, A.-N. Two-Dimensional-PAGE Coupled with nLC-MS/MS-Based Identification of Differentially Expressed Proteins and Tumorigenic Pathways in MCF7 Breast Cancer Cells Transfected for JTB Protein Silencing. *Molecules* **2023**, *28*, 7501. <https://doi.org/10.3390/molecules28227501>

Academic Editors: George Grant, Xianjiang Li and Wen Ma

Received: 27 September 2023
Revised: 29 October 2023
Accepted: 31 October 2023
Published: 9 November 2023



Copyright: © 2023 by the authors. Licensee MDPI, Basel, Switzerland. This article is an open access article distributed under the terms and conditions of the Creative Commons Attribution (CC BY) license (<https://creativecommons.org/licenses/by/4.0/>).

Abstract: The identification of new cancer-associated genes/proteins, the characterization of their expression variation, the interactomics-based assessment of differentially expressed genes/proteins (DEGs/DEPs), and understanding the tumorigenic pathways and biological processes involved in BC genesis and progression are necessary and possible by the rapid and recent advances in bioinformatics and molecular profiling strategies. Taking into account the opinion of other authors, as well as based on our own team's *in vitro* studies, we suggest that the human jumping translocation breakpoint (hJTB) protein might be considered as a tumor biomarker for BC and should be studied as a target for BC therapy. In this study, we identify DEPs, carcinogenic pathways, and biological processes associated with JTB silencing, using 2D-PAGE coupled with nano-liquid chromatography tandem mass spectrometry (nLC-MS/MS) proteomics applied to a MCF7 breast cancer cell line, for complementing and completing our previous results based on SDS-PAGE, as well as *in-solution* proteomics of MCF7 cells transfected for JTB downregulation. The functions of significant DEPs are analyzed using GSEA and KEGG analyses. Almost all DEPs exert pro-tumorigenic effects in the JTB^{low} condition, sustaining the tumor suppressive function of JTB. Thus, the identified DEPs are involved in several signaling and metabolic pathways that play pro-tumorigenic roles: EMT, ERK/MAPK, PI3K/AKT, Wnt/ β -catenin, mTOR, C-MYC, NF- κ B, IFN- γ and IFN- α responses, UPR, and glycolysis/gluconeogenesis. These pathways sustain cancer cell growth, adhesion, survival, proliferation, invasion, metastasis, resistance to apoptosis, tight junctions and cytoskeleton reorganization, the maintenance of stemness, metabolic reprogramming, survival in a hostile environment, and sustain a poor clinical outcome. In conclusion, JTB silencing might increase the neoplastic phenotype and behavior of the MCF7 BC cell line. The data is available via ProteomeXchange with the identifier PXD046265.

Keywords: breast cancer (BC); MCF7; JTB protein silencing; overexpressed JTB interactome; down-regulated JTB interactome; tumorigenic pathways

1. Introduction

Discovering and validating novel biomarkers, especially for early cancer diagnosis, as well as molecular targets for advanced therapies in breast cancer (BC), necessitate

the handling of accurate gene expression datasets [1]. The identification of new cancer-associated regulatory genes/proteins, the characterization of their expression variations, the interactomics-based assessment of differentially expressed genes/proteins (DEGs/DEPs), and understanding the tumorigenic pathways and biological processes involved in BC genesis and progression are possible by the rapid and recent advances in bioinformatics and molecular profiling strategies or analytical techniques, especially based on high-throughput sequencing and mass spectrometry (MS) developments.

In 1999, Hatakeyama et al. reported the human jumping translocation breakpoint (hJTB) as a novel transmembrane protein gene at locus 1q21, a region called the epidermal differentiation complex (EDC), involved in unbalanced jumping translocation, suggesting the JTB's association with tumor progression [2]. Moreover, Tyszkiewicz et al. (2014) showed that the EDC molecules were involved in important mechanisms in adenocarcinomas [3], while other authors showed that chromosomal translocations were a hallmark for cancer [4], jumping translocations (JTs) being usually identified in tumors [5]. In 2007, Kanome et al. stated that JTB is a transmembrane protein with an unknown function; however, the authors observed that JTB expression was suppressed in many tumor types, emphasizing its role in the malignant transformation of cells [6]. Platica et al. (2000) showed that hJTB cDNA had a 100% homology with prostate androgen-regulated (PAR) gene isolated from an androgen-resistant prostate cancer cell line [7]. The same authors reported that PAR/JTB expression was upregulated in all studied prostatic carcinoma cell lines compared with normal prostatic tissue, in androgen-resistant prostate cancer cell lines in comparison with androgen-sensitive prostate cells, in MCF7 and T47D BC cell lines, as well as in all the primary breast tumors studied compared to their normal counterparts. Moreover, Platica et al. (2011) observed that the downregulation of PAR levels in DU145 cells resulted in defects in centrosome segregation, failed cytokinesis and chromosome alignment, and an increased number of apoptotic cells, polyploidy, and aberrant mitosis that could lead to genomic instability and tumorigenesis [8]. These authors suggested that the PAR overexpression in several human cancers might be a putative target for therapy. Pan et al. (2009) showed that JTB may play a critical role in liver carcinogenesis [9]. Functionally, JTB has been reported as a regulator of mitochondrial function, cell growth, cell death and apoptosis, as well as being a protein involved in cytokinesis/cell cycle activities [6,8].

MCF7 is a middle aggressive and non-invasive BC cell line that has been used for membrane protein enrichment proteomic analyses [10] as well as for the identification of dysregulated signaling pathways and cellular targets of different compounds with anti-tumorigenic activity [11]. We also show that the upregulated expression of DEPs in the JTB^{low} condition, investigated by SDS-PAGE followed by nLC-MS/MS proteomics in a transfected MCF7 BC cell line, promotes cancer cell viability, motility, proliferation, invasion, the ability to survive in hostile environments, metabolic reprogramming, and the escaping of tumor cells from host immune control, leading to a more invasive phenotype for MCF7 cells. Several downregulated DEPs in a low-JTB condition also promote the invasive phenotype of MCF7 cells, sustaining cell proliferation, migration, invasion, and tumorigenesis [12]. Several DEPs identified during JTB silencing by in-solution digestion followed by nLC-MS/MS that were complementary to the initial in-gel based ones [12], especially upregulated proteins, are known to emphasize pro-tumorigenic activities in a downregulated state [13].

Taking into account the previously cited references [2,6–9], as well as based on our own team's studies [12–15], we suggest that the JTB protein might be a tumor biomarker for BC and should be studied as a target for cancer therapy. In this study, we identify the DEPs and carcinogenic pathways associated with JTB silencing, using 2D-PAGE coupled with nano-liquid chromatography-tandem mass spectrometry (nLC-MS/MS) proteomics applied to the MCF7 breast cancer cell line, for complementing and completing our previous results based on SDS-PAGE [12], as well as the in-solution proteomics of MCF7 cells transfected for JTB downregulation [13]. We concluded that almost all DEPs exert pro-

tumorigenic effects in JTB^{low} conditions, sustaining the tumor suppressive function of JTB. The function of DEPs has been analyzed using GSEA and KEGG, while STRING analysis has been applied to construct the protein-protein interaction network of the JTB^{low}-related proteins that exert a PT activity. The identified DEPs are involved in several signaling and metabolic pathways and biological processes that exert pro-tumorigenic (PT) roles: EMT, tight junction, cytoskeleton organization, ERK/MAPK, PI3K/AKT, Wnt/ β -catenin, mTOR, c-MYC, NF- κ B, IFN- γ and IFN- α response, UPR, and metabolic reprogramming.

2. Results and Discussion

Using 2D-PAGE coupled with nLC-MS/MS proteomics, the present study identified 45 significantly dysregulated proteins, 37 upregulated and 8 downregulated, in the MCF7 BC cell line transfected for JTB silencing. The workflow for cellular proteomics followed by 2D-polyacrylamide gel (2D-PAGE) coupled with nLC-MS/MS analysis of the cell lysates is presented in the Figure 1.

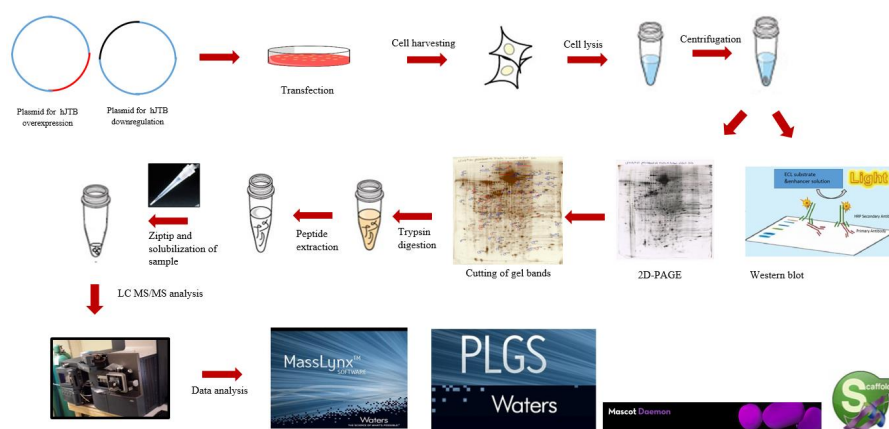


Figure 1. The workflow for cellular proteomics followed by 2D-polyacrylamide gel (2D-PAGE) coupled with nLC-MS/MS analysis of the cell lysates.

There were 131 dysregulated spots in the control_shRNA vs. sh_JTB and 153 differences in the control vs. sh_JTB (Figures 2 and 3). A total of 284 spots were selected for Nano LC-MS/MS analysis, as previously described [16].

We only analyzed proteins that have a protein score of above 40 and p -value < 0.05 . HSPB1, HSPA4, MCM6, ACTB, ACTN1, PFN2, TUBA1A, EEF2, PCK1, PCK2, GPI, FARSB, GARS1, LARS1, RARS1, PSMC6, CCT2, CCT3, IFIT1, PTBP1, DDX19A, UTY, NCAM2, RHBDD1, CS, LAMTOR3, OGA, ZNF114, PA2G4, SRM, GSTM3, NCKAP1, PRDX3, REB8A, RAB8B, RAB15 and RAB35 are overexpressed, while TUBB4B, CAPN2, ELFN2, SLC9AR1, ANXA4, YWHAZ, YWHAE, and PSMB9 proteins were found to be significantly downregulated. GSEA analysis was performed for the downregulated JTB condition using the H (hallmark gene sets) collection in MSigDB. Analysis of the H collection revealed four upregulated pathways, including proteins important for interferon alpha response (IFN- α), interferon gamma response (IFN- γ), Myc targets V1, and unfolded protein response (UPR). Two downregulated pathways comprised proteins involved in estrogen response late and estrogen response early pathways (Table 1). We also performed Kyoto Encyclopedia of Genes and Genomes (KEGG) analysis and here we emphasized the enriched biological processes in pro-tumorigenic proteins identified in downregulated JTB conditions using GeneCodis website (<https://genecodis.genyo.es/>, accessed on 22 October 2023). There were 25 upregulated and two downregulated proteins with pro-tumorigenic (PT) potential, which were then submitted for protein-protein interaction (PPI) network construction with Search Tool for the Retrieval of Interacting Genes/Proteins (STRING) database (<https://string-db.org/>, accessed on 22 October 2023), to analyze the specific interaction network associated with the JTB^{low} condition in the transfected MCF7 BC cell line. A total of 27 nodes and 69 edges were mapped in the PPI network, with an average

node degree of 5.11, an average local clustering coefficient of 0.632, and a PPI enrichment p -value 6.44×10^{-12} .

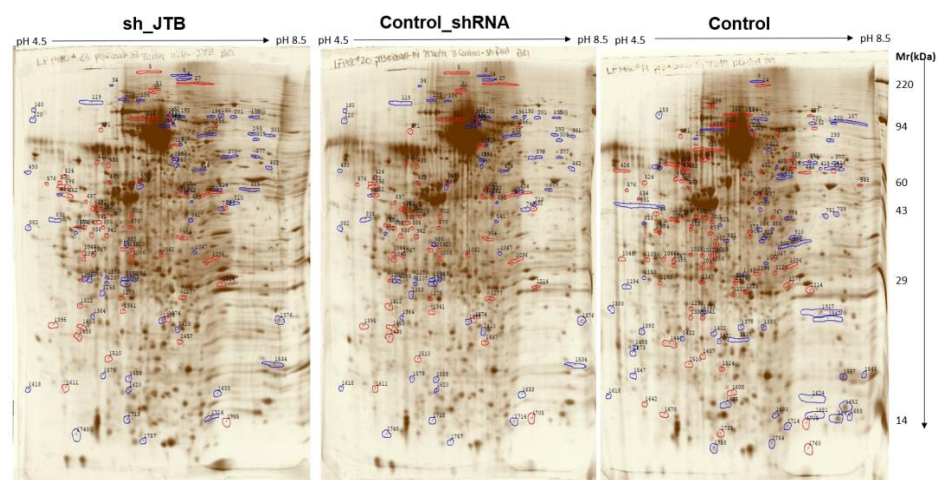


Figure 2. Images of sh_JTB (left), control_shRNA (middle), control (right) silver stained 2D polyacrylamide gels. Polypeptide spots increased in each compared gels (top vs. bottom) are shown in blue, while spots decreased are outlined in red.

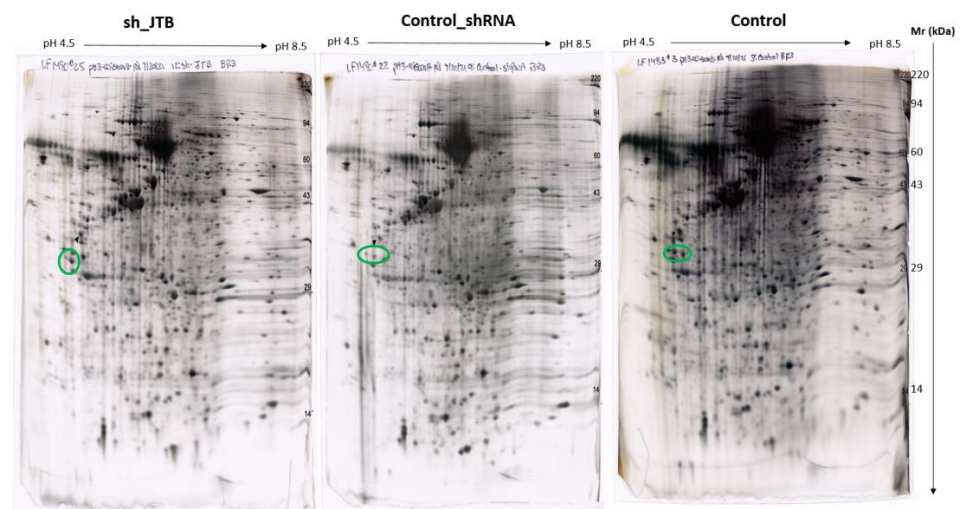


Figure 3. Images of sh_JTB (left), control_shRNA (middle), control (right) silver stained 2D polyacrylamide gels. The circles on each 2D-polyacrylamide gel shows the location of Isoelectric focusing internal standard TROPOMYOSIN of Mw: 33000 and a pI of 5.2.

Table 1. Significant up and downregulated pathways in the downregulated JTB condition in the MCF7 BC cell line, according to GSEA with FDR < 25%.

	Pathways	NES	FDR q-Val
Upregulated	INTERFERON_ALPHA_RESPONSE (IFN- α)	1.52	0.223
	INTERFERON_GAMMA_RESPONSE (IFN- γ)	1.47	0.165
	MYC_TARGETS_V1	1.04	0.971
Downregulated	UNFOLDED_PROTEIN_RESPONSE	1	0.831
	ESTROGEN_RESPONSE_LATE	-1.17	1
	ESTROGEN_RESPONSE_EARLY	-1.07	0.948

To emphasize the role of the JTB-interactome, we analysed the pro-tumorigenic (PT) and anti-tumorigenic (AT) function of these proteins, as well as the neoplastic dysregulated pathways and biological processes (Table 2).

Table 2. Deregulated DEPs, neoplastic roles, and biological processes expressed in response to JTB downregulation in MCF7 BC cell line.

Gene Name	Gene Description	Role	Expression in Malignancies and Putative Neoplastic Effects	Pathways	Neoplastic Condition
		Proteins enriched in phenotype of low JTB expression condition			
HSPB1/HSP27	Heat shock 27 kDa protein 1	protein folding/CMPE, cell adhesion, cell migration, cytoskeleton dependent intracellular transport, cell death in response to OS, programmed cell death	overexpressed in many cancers [17]; including BC [18]	PT APOPTOSIS, regulates EMT process and NF-κB activity [18]	poor clinical outcome, cell invasion, metastasis, resistance to apoptosis [17]; participates in maintenance of BCSCs [18]
HSPA4/HSP70/Apg-2	Heat shock 70 kDa protein family A (HSP70) member 4 isoform a variant	molecular chaperone, induced by oncogenic stress, autophagy, regulation of protein ubiquitination, cadherin binding, cell adhesion molecule binding, MHC class II protein complex binding [19]	overexpressed in many cancers, including HCC [19], CRC [20], HNSC [21], involved in progression of BC [22], GC [23]	PT MTORC1_SIGNALING; associated with CSCs properties via chaperones for EMT-associated proteins, inducing migration [23]; silencing reduced activation of PI3K/Akt signaling and increase in apoptosis [20]; activates mTOR pathway [21]	facilitates cancer cell survival, inhibits apoptosis, promotes proliferation, immune regulation [19], accumulation of misfolded proteins, ROS, and DNA damage [21], considered as a necroptosis-related gene in BC that activates cell cycle [22]
MCM6	Minichromosome maintenance complex component 6	significant DNA replication regulator, plays a key role in cell cycle progression [24]	overexpressed in many cancers [25]: BC, CRC, HCC [25], glioma, endometrial adenocarcinoma, cervical cancer, Merkel cell carcinoma, lung cancer [24]	PT promotes EMT and activates MEK/ERK signaling, sustaining carcinogenesis [24,25]	sensitive, specific biomarker for GSTM cancer, involved in cell proliferation, metastasis, migration, invasion, immune response [24,25]
POTEF/POTEACTIN/ACTB	POTE ankyrin domain family member F/Beta-actin	cytoskeleton protein that belongs to the actin family, involved in motility, polarity, chemotaxis and immune cell infiltration [26]	expressed in many cancers: BC cell lines, overexpressed in CRPC [27]	PT A]; represses the AT effect of Toll-like receptor (TLR) signaling pathway [27,28]; involved in cell migration by NF-κB and Wnt/β-catenin pathway [26]	promotes cell growth [27], migration, invasion [26]

Table 2. Cont.

Gene Name	Gene Description	Role	Expression in Malignancies and Putative Neoplastic Effects	Pathways	Neoplastic Condition
ACTN1	Alpha-actinin-1 (isoform X5)	actin cross-linking protein involved in cytokinesis, cell adhesion and migration [29]	overexpressed in BC tissue, BL-BC cell lines [30], GC [29]	PT AKT/GSK3β/β-catenin pathway and FAK/Src/IAK2/STAT3 signaling [29]	promotes cell proliferation, invasion, migration, and inhibits apoptosis [29]; loss of polarity by cytoskeleton reorganization and E-cadherin-based adhesion, lack of ER expression and poor survival in BL-BC [30]
PFN2	Profilin-2 (isoform b)	actin binding protein involved in cytoskeleton organization, vesicle mediated transport, signaling, cell junction organization, cell motility	overexpressed in TNBC [31], ESCC [32]	PT EMT [31]	promotes cell proliferation, migration and invasion of TNBC cells [31]
EEF2	Eukaryotic elongation factor 2	translation elongation factor involved in polypeptide chain elongation step, cell cycle progression	highly expressed in various malignant tumors: BC [33], GC, CRC, esophageal, pancreatic, PCa, HNSCC, GBM [34], LSCC tissues and cell lines [35]	PT UPR; promotes G2/M progression in cell cycle activating Akt signaling [34], CDC2/Cyclin B1 and EMT-related proteins [35]	associated with node positivity [33]; plays an oncogenic role, promotes cancer cell growth [34], migration, invasion [35]
1KHB/PCK1/PEPCK-C (cytoplasmic isoenzyme)	Phosphoenolpyruvate carboxykinase 1 (PEPCK) Complex With Nonhydrolyzable GTP Analog, Mad Data (chain A)	rate-limiting gluconeogenesis enzyme	oncogene overexpressed in colon cancer and melanoma [36]; downregulated and tumor suppressor in gluconeogenic tissues (liver and kidney): HCC [36] and ccRCC [37]	PT GLYCOLYSIS; acts via AMPK/p27 ^{Kip1} axis [36]; depletion promotes EMT in HCC [38]	promotes cell proliferation via mTORC1 (oncogenic function) [39]; AT in kidney and liver: suppressed ccRCC cell growth and metastasis, inhibited tumorigenesis by blocking aerobic glycolysis pathway [37]; suppresses liver tumor growth, cell cycle progression and proliferation [36]

Table 2. Cont.

Gene Name	Gene Description	Role	Expression in Malignancies and Putative Neoplastic Effects	Pathways	Neoplastic Condition
PCK2/PEPCK-M (mitochondrial isoenzyme)	Phosphoenolpyruvate carboxykinase	rate-limiting gluconeogenesis enzyme	overexpressed many cancers, including ER ⁺ BC [40], lung, prostate, thyroid, bladder, BC, cervical cancer [41]	REACTOME_GLUONEOGENESIS; activation of mTORC1 and E2F1 pathways [40]; silencing contributes to cellular senescence, inhibiting EMT in BC cells [42]	promotes tumor growth, proliferation and cell cycle progression [40]
FARSB/HSPC173	Phenylalanyl-tRNA ligase beta subunit	cytoplasmic aminoacyl-tRNA synthetase (ARS/AARS) involved in tRNA metabolic process, amino acid metabolic process, protein-containing complex assembly	overexpressed in in tumor samples compared to adjacent normal tissues [43]; GC [44]	aminoacyl-tRNA synthesis pathway [44]	promotes cancer progression, poor prognosis, metastasis [44]; worse patient survival in BC [43]
GARS1	Glycyl-tRNA synthetase 1	cytoplasmic and mitochondrial ARS	overexpressed in tumor samples compared to adjacent normal tissues [43], displays androgen-dependent transcriptional initiation in several hormone-responsive cells, overexpressed in PCa [45]	may deactivate ERK signaling pathway [45]	worse patient survival in BC [43]; could induce tumor regression [45]
LARS1	Leucyl-tRNA synthetase 1 (Editing Domain)	cytoplasmic ARS	overexpressed in some cancers: myeloid leukemia, pancreatic cancer, renal, cervical, skin cancer [45], lung cancer cell lines and tissues [46]	senses intracellular leucine levels to activate mTORC1 pathway [45]	lower patient survival in BC [43], promotes cell proliferation, growth [45], and migration [46]

Table 2. Cont.

Gene Name	Gene Description	Role	Expression in Malignancies and Putative Neoplastic Effects	Pathways	Neoplastic Condition
RARS1	Arginyl-tRNA synthetase 1	cytoplasmic ARS involved in protein synthesis	important tumorigenic activity, overexpressed in hepatoma cells [47], associated with an increased risk of BC [45]	PT impairment of AIMP1/EMAPII secretion in MCF7 cells [48]	lower patient survival in BC [43], increases growth rate in hepatoma cells, induces stem cell-like features in head and neck tumors [47]
PSMC6	Proteasome subunit p42/proteasome 26S subunit ATPase 6	protein catabolic process, regulation of DNA-template transcription, protein-containing complex assembly	highly upregulated in LUAD [49], BC tissues, especially in luminal cancer [50]	PT MTORC1_SIGNALING; REACTOME_REGULATION_OF_MITOTIC_CELL_CYCLE; activation of Wnt signaling via degrading AXIN proteins [49]	oncogenic effect [50], poor prognosis, silencing inhibits cell growth, migration and invasion [49]
CCT2/CCTβ	Chaperonin containing TCP1 Subunit 2	involved in cell cycle regulation, protein folding and binding biological processes [51]	overexpressed in various tumors and cell lines, such as HER2+ BC, liver, prostate, cholecyst, lung, CRC, BC [51], glioblastoma [52]	PT P53 signaling [51]	worse prognosis, especially in luminal A subtype, promotes cell growth/survival, invasion and proliferation [51]
CCT3/TRIC	Cytosolic chaperonin containing t-complex polypeptide 1 (TCP1) subunit 3/TCP1 ring complex (hTRIC5), partial	molecular chaperone involved in proteostasis, folding of tubulin and actins and many proteins involved in cancer [53], cell division, proliferation andapoptosis [52]	overexpressed in some tumors: BC, HCC, LUAD and LUSC, NSCLC, cervical and CRC, AML, multiple myeloma, papillary thyroid carcinoma, melanoma, GC [52]	PT might regulate IGF-1 signaling; actin cytoskeletal signaling, and PTEN signaling, Wnt/β-catenin, JAK2/STAT3, PI3K/Akt [52]	oncogene, promotes cell growth, survival, proliferation, cell cycle progression and anti-apoptosis [52]
IFIT1	Interferon-induced protein with tetraatricopeptide repeats 1 (isoform 2)	inflammation-related protein, RNA-binding protein modulated by JAK/STAT pathway [54], involved in regulation of translation [55]	overexpressed in PDAC [54], OSCC [56]	PT INTERFERON_GAMMA_RESPONSE; UPR; EMT [56], Wnt/β-catenin activation [54], increasing levels of p-EGFR and p-Akt [56]	increases cell proliferation, migration, invasion [54], tumor growth, regional and distant metastasis [56]

Table 2. Cont.

Gene Name	Gene Description	Role	Expression in Malignancies and Putative Neoplastic Effects	Pathways	Neoplastic Condition
PTBP1/hnRNP1	Polypyrimidine tract-binding protein 1 (isoform a)	RNA-binding protein, key factor in the control of RNA metabolism, regulates mRNA alternative splicing (AS) events, mRNA stability, mRNA localization [57]	overexpressed in human epithelial ovarian tumors, BC tissues and cell lines, glioblastomas [57], LUAD tissues and cell lines [58]	PT regulates PTEN-PI3K/Akt and autophagy [57]; enhances EGFR signaling, MAPK, hypoxia inducible factor-1 α pathways [59]; associated with HSP progress [58]	associated with breast tumorigenesis, promotes tumor cell growth, invasion and maintenance of metastasis [57], regulates apoptosis and cell proliferation [59]
DDX19A	DEAD-box helicase 19A/ATP-dependent RNA helicase DDX19A	RNA helicases involved in RNA metabolic process including transcription, RNA transport, RNA degradation [60]	overexpressed in CSCC [60], BC cell lines [61]	PT induces EMT [60]	promotes cell migration, invasion, metastasis, NOX1 expression and ROS production [60]
GPI	Glucose-6-phosphate isomerase/neuroleukin	cytoplasmic glycolytic-related enzyme, secreted in ECM of cancer cells it is called autocrine motility factor (AMF) [62] and functions as a cytokine or growth factor [63]	overexpressed in BC [63], LUAD/NSCLC, glioblastoma, ccRCC [64], GC [62]	PT REACTOME_GLUONEOGENESIS; OXFOS; glycolysis and gluconeogenesis [64], correlated with cell cycle regulatory genes, immune cell infiltration, gene alteration, ferroptosis genes [63]; AMF induces EMT [65]	involved in cell cycle, cell proliferation, correlates with immune infiltration, cell migration, invasion [64]; silencing suppressed proliferation, migration, invasion, glycolysis, and induced apoptosis [62]
TUBA1A	Tubulin alpha-1a	cell division, cell movement, microtubule based process, cell junction organization, cytoskeleton organization and cytoskeleton dependent intracellular transport	upregulated in BC tissues [66], GC [67]	PT involved in infiltration of macrophages to the tumor microenvironment [67], involved in EMT related to re-organization of cell-cell contact [68]	overexpression was correlated with poor overall survival and a more aggressive phenotype in GC [67]

Table 2. Cont.

Gene Name	Gene Description	Role	Expression in Malignancies and Putative Neoplastic Effects	Pathways	Neoplastic Condition
UTY/KDM6C	Ubiquitously transcribed tetrapeptide repeat protein Y-linked transcript variant 83	member of lysine (K)-specific dimethylase (KDM6) family that act as dynamic regulators of gene expression by histone demethylation [69], chromatin organization, anatomical structure development, gene transcription regulation [70]	not controversial	REACTOME_CHROMATIN_MODIFYING_ENZYMES, transcriptional dysregulation in cancer (KEGG)	oncogenic or tumor suppressive roles [70]
NCAM2	Neural cell adhesion molecule 2	involved in cell adhesion, differentiation and anatomical structure development	overexpressed in some prostate and BC cell lines, such as ER-dependent BC cell lines MCF7 and T47D [71]	not known	not known
RHBDD1	Rhomboid-related protein 4 isoform X1/rhomboid domain-containing protein 1	intramembrane/cytoplasmic-cleaving serine protease involved in intracellular protein transport, programmed cell death, protein catabolic process, cell differentiation, cell growth, protein maturation, participates in ER quality control system [72] and regulation of mitochondrial membrane remodeling [73]	highly upregulated in BC, CRC tissue and cell lines [72]	positive correlation with p-Akt and CDK2 [72], c-Jun [73]	important in tumorigenesis, poor prognosis in ER+, ER+PR+, HER2+, and TNBC, inhibits apoptosis by activation of c-Jun and Bcl-3 [73]; deletion suppresses BC cell survival, migration, invasion, cycle progression and G1/S phase transition and increases apoptosis and ERAD [72]

Table 2. Cont.

Gene Name	Gene Description	Role	Expression in Malignancies and Putative Neoplastic Effects	Pathways	Neoplastic Condition
CS	Citrate synthase	rate-limiting respiratory enzyme in the TCA cycle, involved in cell lipid metabolism (conversion of glucose to lipids) and mitochondrial function [74]	overexpressed in various cancers: PCa [74], pancreatic ductal carcinoma [75], ovarian carcinoma [76]; downregulated in human cervical carcinoma cells [77]	OXPHOS; lipid metabolism signaling [74]; downregulation could induce EMT [77]	aggressive tumor progression, poor prognosis, increases cell proliferation, growth, colony formation, migration, invasion, and cell cycle [74]; silencing induces reduction of cell proliferation, invasion, migration, and enhances apoptosis [76], cells being unable to grow or proliferate in response to extracellular growth factors [78]
LAMTOR3/ MAPKSP1/MP1	Late endosomal/lysosomal adaptor, MAPK and MTOR activator 3/mitogen activated protein kinase scaffold protein 1/MEK partner 1	member of the Ragulator complex involved in multiple signaling pathways that acts as a scaffold protein complex [79]	overexpressed in ER+ and ER- BC cell lines and in non-tumorigenic mammary epithelial cell lines [80]; downregulated in KIRC [79]	considered to be a convergence point for MAPK and mTOR pathways [81]; targeting MEK1/MP1/ERK1/BCL2 axis may improve clinical outcome of MLCC patients [82]	required for pro-survival signaling from PI3K/AKT pathway in ER+ BC cells [80]; upregulation induces BCL2 expression (anti-apoptotic protein) [82]
OGA	Protein O-GlcNAcase (isoform a)	involved in protein glycosylation and protein catabolic process	overexpressed in numerous cancers [83]	drives aerobic glycolysis and tumor growth by inhibiting PKM2 [83]	enhances tumor progression [83];
ZNF114	ZNF114 protein, partial	DNA-binding protein involved in transcription; member of KRAB-ZEPs family of transcription regulators [84]	overexpressed in ccRCC [85]	pluripotency maintenance; repression of differentiation gene DPYSL4 [86]	involved in maintenance of cell pluripotency and stemness [84,86]; shorter overall survival [85]

Table 2. Cont.

Gene Name	Gene Description	Role	Expression in Malignancies and Putative Neoplastic Effects	Pathways	Neoplastic Condition
PA2G4/EBP1	Proliferation associated protein 2G4/ErbB3-binding protein 1	found in cytoplasm and nucleus, regulates cell growth and differentiation, being a ribosomal constituent, transcriptional regulator, RNA/DNA-binding protein, mediates rRNA processing, DNA transcription, mRNA translation, protein stability and signal transduction [87]	overexpressed in HCC, cervical cancer, CC, NPC, salivary ACC, downregulated in HER2+ BC and bladder cancer [87]	PT tumor formation via Ebp1/p38/HIF1 α signaling and proto-oncogene MDM2-mediated downregulation of p53, promotes EMT [87]	intensively involved in tumorigenesis and cancer progression/metastasis, promotes cell proliferation and soft agar colony generation [87]
SRM	spermidine synthase	essential polyamine for cell proliferation, differentiation, development [88], regulation of gene expression, apoptosis, cell cycle progression and signaling pathways [89]	biosynthesis is upregulated in BC and contribute to disease progression [89], overexpression in CRC [90]	PT MYC_TARGETS_V2; interferes with mTOR and RAS oncogenic pathways [88], c-MYC target [91] and C/ERP β may serve as regulators of SRM [90]	cell growth [89]
GSTM3	Glutathione S-transferase mu3	enzyme involved in xenobiotic metabolism/detoxification, apoptosis inhibition [92], regulates ROS and participates in OS-mediated pathology [93]	mRNA expression level high in HER2+ or ER+ BC [93], overexpressed in cervical cancer, colon cancer [92]	PT EMT inducer [94], cellular stress response via NF- κ B and MAPK pathway during tumor progression [92]	cancer cell maintenance, survival and tumor progression [92]

Table 2. Cont.

Gene Name	Gene Description	Role	Expression in Malignancies and Putative Neoplastic Effects	Pathways	Neoplastic Condition
NCKAP1/NAP1	Noncatalytic region of tyrosine kinase (Nck)-associated protein 1	<p>associates with Src homology 3 (SH3) domain of NCK protein that localizes along the lamellipodia and mediates contact-cell dependent migration [95]; member of WASF3 regulatory complex [96]; involved in cytoskeleton organization through actin polymerization, programmed cell death, signaling, cell differentiation and protein-containing complex assembly</p>	<p>overexpressed in NSCLC [95]; downregulated in ccRCC [97]</p> <p>PT</p>	<p>ribosomal signaling, OXPPOS, TGF-β, EMT-related signaling pathways [97]; involved in HSP90-mediated invasion and metastasis by provoking MMP9 activation and EMT [95]</p>	<p>overexpression is associated with poorer survival in BC patients; essential for cell motility, adhesion, invasion and metastasis [95]; knockdown in BC cell lines, MDA-MB-231 and Hs578T, leads to a significant reduction in invasion and suppresses metastasis [96]; tumor suppressive in ccRCC [97] and HCC [98]</p>
PRDX3	Thioredoxin-dependent peroxide reductase, mitochondrial isoform a precursor	<p>mitochondrial member of the antioxidant family of thioredoxin peroxidase [99] required for mitochondrial homeostasis [100]</p>	<p>overexpressed in HCC, malignant mesothelioma, BC, PCa, lung cancer, cervical carcinoma [99]; overexpression associated with ER and PR [100]</p> <p>PT</p>	<p>OXPPOS; defense against H2O2 produced by mitochondrial respiratory chain [99], c-Myc target gene [100]</p>	<p>tumor promoting effects [99], involved in regulation of cell proliferation, differentiation and antioxidant function, overexpression protects cells from oxidative stress and apoptosis [100]</p>

Table 2. Cont.

Gene Name	Gene Description	Role	Expression in Malignancies and Putative Neoplastic Effects	Pathways	Neoplastic Condition
RAB8A	Ras-related protein Rab-8A	intracellular protein transport, intracellular membrane trafficking, autophagy, vesicle-mediated transport, signaling, cell differentiation, membrane organization	overexpressed in BC tissues [101]	PT activates AKT and ERK1/2 signaling pathways [101]	increases cell growth, proliferation, migration, invasion [101]
RAB8B	Ras-related protein Rab-8B	member of the Rab small G protein family, immune system process, intracellular trafficking, peroxisome organization, vesicle-mediated transport, signaling, cell junction organization, membrane organization, protein localization to plasma membrane	overexpressed in TC [102]	PT required for Wnt/ β -catenin signaling [103]	overexpression and loss of functioning adherence junction accelerate tumorigenesis in testis [102]
RAB15	Ras-related protein Rab-15 (isoform AN2)	involved in trafficking of cargos through the apical recycling endosome (ARE) to mediate transcytosis [104]	overexpressed in liver cancer cells [105]	PT regulates the endocytic recycling pathway [106]	associated with the susceptibility of cells to DNA damage-induced cell death [105]
RAB35	Ras-related protein Rab-35 (isoform 1)	Rab GTPase located in plasma membrane/endosomes, involved in vesicular trafficking, actin dynamics, cytokinesis, apical-basal polarity, endocytosis, phagocytosis, autophagy, exosome release [107]	overexpressed in OC [107]	PT activator of PI3K/AKT pathway [107]	oncogenic protein, enhances BC cells invasion and metastasis [107]

Table 2. Cont.

Gene Name	Gene Description	Role	Expression in Malignancies and Putative Neoplastic Effects	Pathways	Neoplastic Condition
Proteins with downregulated expression in phenotype of low JTB expression condition					
TUBB4B	tubulin beta-4B chain	constituent of microtubules involved in mitotic cycle, immune system process and cytoskeleton organization	overexpressed in membranes of stem cells enriched cultures, PCa, OC, glioblastoma, metastatic CRC [108]	PT	downregulation is essential for the initiation of EMT [108], for microtubule-VIM interaction and contributes to the maintenance of polarity in migrating cells [108] decreased level correlates with increased cell migration [109]
CAPN2	Calpain 2/ m-calpain	calcium-dependent, non-lysosomal cysteine protease involved in lipid metabolic process, cytoskeleton organization, programmed cell death, cell differentiation, protein catabolic process, protein maturation and anatomical structure development	overexpressed in various malignancies: CRPC cell lines (DU145, PC3), BL and TNBC [110], RCC [111], PC [112]	AT	acts via AKT/mTOR signaling pathway [111], and regulates Wnt/ β -catenin signaling pathway-mediated EMT [112]; silencing may inhibit EMT [111,112] oncogene involved in carcinogenesis and tumor progression, and metastasis silencing inhibits cell proliferation, migration and invasion by reducing MMP-2 and MMP-9 activation and regulation of invadopodia dynamics [111]
ELFN2/LRRC62	Extracellular leucine rich repeat and fibronectin type III domain-containing 2/protein phosphatase 1 regulatory subunit 29	putative oncogene, hypomethylation gene [113]	overexpressed in GC tissues and cell lines [114]; oncogene in GBM [113]	AT	interacts with Aurka and eukaryotic translation initiation factor 2 subunit alpha (EIF2 α) and regulates the kinase activity of Aurka to promote cell autophagy [113] knockdown inhibits cell proliferation, migration, invasion, increases E-cadherin and decreases N-cadherin [114]
SLC9AR1/NHERF1/ERB50	Solute carrier (SLC) family 9 (Na(+)/H(+) exchanger), member 3 regulator 1/sodium-hydrogen exchanger regulatory factor 1/ERM-binding phosphoprotein	multifunctional cytoplasmic adaptor involved in growth factor signaling [115]; interacts with several proteins related to the estrogen pathway and tumorigenesis: EGFR, PTEN, PDGFR, beta catenin, EZR [116]	in BC acts as a tumor suppressor protein; oncogene in glioma and other cancers; overexpressed in PCa tissue and cell lines [117]	AT/PT	knockdown suppresses proliferation and migration of metastatic PCa cells and promotes apoptosis [117]

Table 2. Cont.

Gene Name	Gene Description	Role	Expression in Malignancies and Putative Neoplastic Effects	Pathways	Neoplastic Condition
ANXA4	Annexin 4/lipocortin IV/endonexin I [120]	intracellular Ca ²⁺ -sensor that modulates membrane permeability and membrane trafficking, participates in cell growth, apoptosis [121], cell cycle and anticoagulation [122]	overexpressed in various tumors: chemoresistant LC, ESCC, GC, CRC, PCC, gallbladder, HCC, cholangiocarcinoma, BC, RCC, OCCC, laryngeal and PCa, MM [121,123], cervical cancer [120]	AT overexpressed, is related to AKT, CDK1, and tumor suppressor p21 [122]	knockdown attenuates migration in OC and BC cells [121]
YWHAE	14-3-3 protein epsilon	mitochondrial import stimulation factor L subunit [124] involved in mitotic cell cycle, intracellular protein transport, nucleocytoplasmic transport, signaling, cell differentiation, cell motility and transmembrane transport	overexpressed in BC tissue [124]	AT MITOTIC_SPINDLE; MYC_TARGETS_V1	knockdown reduces expression of Snail and Twist [124]
YWHAZ	tyrosine 3-monoxygenase/tryptophan 5-monoxygenase activation protein zeta	central hub protein involved in many signal transduction pathways [125]	oncogene overexpressed in multiple cancers: HCC, CRC, LUAD, BC [125], urothelial carcinomas [126]	AT UPR	knockdown decreases cell growth, proliferation, invasion, enhances apoptosis and tamoxifen-induced inhibition of cell viability [125]

Table 2. Cont.

Gene Name	Gene Description	Role	Expression in Malignancies and Putative Neoplastic Effects	Pathways	Neoplastic Condition
PSMB9/LMP2	Proteasome 20S subunit 9 beta/low molecular weight protein 2	immunoproteasome functions; major enzyme in ubiquitin-dependent protein degradation and inactivation [127]	overexpressed in tumor tissues; LGG [127]; deficient in uLMS [128]	PT	defective expression contributes to abnormal cell proliferation and tumor progression [128]

Abbreviations: ACC—adenoid cystic carcinoma; AJ—APICAL_JUNCTION; AT—anti-tumorigenic; BC—breast cancer; BCSCs—breast cancer stem cells; CC—colon cancer; ccRCC/KIRC—clear cell renal cell carcinoma/kidney renal clear cell carcinoma; CDK2—cyclin-dependent kinase 2; CMPP—chaperone-mediated proteins folding; CRC—colorectal cancer; CRPC—castration-resistant prostate cancer; CSCC—cervical squamous cell carcinoma; DCIS—ductal carcinoma in situ; EMT—epithelial-mesenchymal transition pathway; ERAD—endoplasmic reticulum-associated degradation; ERK—extracellular signal-regulated kinase; ESCC—esophageal squamous cell carcinoma; EZReztin; FAK—focal adhesion kinase; GBM—glioblastoma multiforme; GC—gastric cancer; HCC—hepatocellular carcinoma; HNSC—head and neck squamous carcinoma; IAP—inhibitory of apoptosis proteins; KRAB-ZFPs—Krüppel-associated box domain zinc finger proteins; LC—lung cancer; LGG—low grade glioma; LSCC—lung squamous cell carcinoma; LUAD—lung adenocarcinoma; LUSC—lung squamous cell carcinoma; MAPK—mitogen-activated protein kinase; MDM2—mouse double minute 2 homolog/E3 ubiquitin-protein ligase; MM—malignant mesothelioma; MMP9—matrix metalloproteinase 9; mTOR—mammalian target of rapamycin; NOX1—NADPH oxidase 1; NPC—nasopharyngeal carcinoma; NSCLC—non-small-cell lung cancer; OCCC—ovarian clear cell carcinoma; OSCC—oral squamous cell carcinoma; OXPPOS—oxidative phosphorylation pathway; PCC—pancreatic cancer; PCa—prostate cancer; PDAC—pancreatic ductal adenocarcinoma; PT—pro-tumorigenic; PTEN—phosphatase and tensin homolog; ROS—reactive oxygen species pathway; SRC—sarcoma; TCA—tricarboxylic acid; TGF- β —transforming growth factor beta; uLMS—uterine leiomyosarcoma; UPR—unfolded protein response; VIM—vimentin.

Analyzing the data from Table 2, we observed that 38 DEPs emphasize a pro-tumorigenic (PT) role and 5 DEPs are known to have anti-tumorigenic (AT) activity in the MCF7 BC cell line transfected for JTB downregulation.

2.1. JTB Silencing Is Associated with Neoplastic Abilities of MCF7 Transfected Cells

The epithelial-mesenchymal transition (EMT) process facilitates the local invasion in cancer. We identified a plethora of upregulated and downregulated DEPs directly or indirectly involved in EMT process: HSPB1, HSPA4, MCM6, ACTN1, PFN2, EEF2, IFIT1, DDX19A, GPI, TUBA1A, CS, PA2G4, GSTM3, NCKAP1, and TUBB4B (Table 2). According to previously published data, HSPB1 and HSPA4 are members of the HSP family that promote EMT in association with the increased invasiveness of cancer cells [13]. Also, the EMT process is subjected to metabolic regulation, while the metabolic pathways adapt to cellular changes during the EMT. The mammalian or mechanistic target of rapamycin (mTOR) pathway becomes aberrant in various types of cancer. The hyperactivation of mTOR signaling pathway promotes cell proliferation and metabolic reprogramming that initiates tumorigenesis and progression [129]. HSPA4, PCK1, PCK2, LARS1, PSMC6, LAMTOR3, SRM, and SLC9AR1 proteins are involved in mTOR pathway activation in MCF7 cells transfected for JTB silencing. The mitogen-activated protein kinase (MAPK) signaling pathway regulates proliferation, differentiation, apoptosis and stress responses, while the overexpression of extracellular signal-regulated kinases ERK1 and ERK2 is critical in cancer development and progression [130]. We identified MCM6, PCK1, LAMTOR3, GSM3, and REB8A as pro-tumorigenic proteins involved in ERK/MAPK signaling pathways in the JTB^{low} condition. Also, the phosphatidylinositol-3-kinase (PI3K/AKT) pathway is one of the most hyper-activated intracellular pathways in many human cancers, contributing to carcinogenesis, cell proliferation, invasion and metastasis [131]. HSPA4, CCT3, PTBP1, and RAB35 are pro-tumorigenic proteins involved in PI3K/AKT pathway. The Wnt/ β -catenin signaling pathway facilitates cancer stem cell renewal, cell proliferation and differentiation, being involved in carcinogenesis and therapy response [132]. Several DEPs, such as POTEF/ACTB, PSMC6, CCT3, IFIT1, and RAB8B are dysregulated proteins involved in Wnt/ β -catenin signaling pathway, which emphasize pro-tumorigenic activities. NF- κ B is an important signaling pathway involved in cancer development and progression, which controls the expression of several target genes and mediates cancer cell proliferation, survival and angiogenesis [133]. Thus, HSPB1/HSP27 and POTEF have been identified as proto-oncogenic proteins involved in this pathway. The unfolded protein response (UPR) is known as a pro-survival mechanism involved in progression of several cancers, such as BC, prostate cancer, and glioblastoma multiforme [134]. Here, JTB silencing was associated with UPR-related proteins, such as EEF2 and IFIT1.

The vesicle transport regulators play key roles in tumor progression, including uncontrolled cell growth, invasion and metastasis [104]. Ras-related proteins, small GTP-binding proteins of the Rab family, are dysregulated in malignant cells, affecting intracellular and membrane traffic, as well as proliferation and metastasis, reducing the survival rate of patients [101]. Ras-related protein Rab-8A (RAB8A) and Ras-related protein Rab-8B (RAB8B) were significantly upregulated in this experiment. Gene ontology enrichment analysis identified the following biological processes enriched in these upregulated proteins: vesicle docking involved in exocytosis, regulation of exocytosis, regulation of protein transport, protein secretion, protein import into peroxisome membrane, Golgi vesicle fusion to target membrane, protein localization to plasma membrane and cell junction organization. RABA8 was reported as overexpressed in BC tissues [101], while RAB8B was upregulated in TC [102]. The RAB8A silencing inhibits the proliferation, migration and invasion of BC cells through suppression of AKT and ERK1/2 phosphorylation [101]. RAB8B is required for the Wnt/ β -catenin signaling pathway [103], while its overexpression promotes the activity and internalization by caveolar endocytosis of LRP6, a member of the low-density lipoprotein receptor superfamily of cell-surface receptors, which is involved in cell proliferation, migration, and metastasis [135]. RAB15 is involved in trafficking cargo through the

apical recycling endosome (ARE) to mediate transcytosis [104]. It is overexpressed in liver cancer cells [105] and is associated with the susceptibility of cells to DNA damage-induced cell death [105]. RAB35 is an oncogenic protein that enhances the invasion and metastasis of BC cells [107].

KEGG pathway analysis (Figure 4) also emphasized the following enriched pathways in the MCF7 BC cell line transfected for JTB downregulation: KEGG_Tight junction and KEGG_Regulation of actin cytoskeleton. De Abreu Pereira et al. (2022) showed that highly expressed proteins and biological processes in HCC-1954 (HER2+), a very invasive and metastatic BC cell line, are classified as tight junctions and cytoskeleton proteins, as compared to an MCF7 BC cell line that emphasized proteins related to proteasome and histones in correlation with the higher rate of mutation in MCF7 BC cells [10].

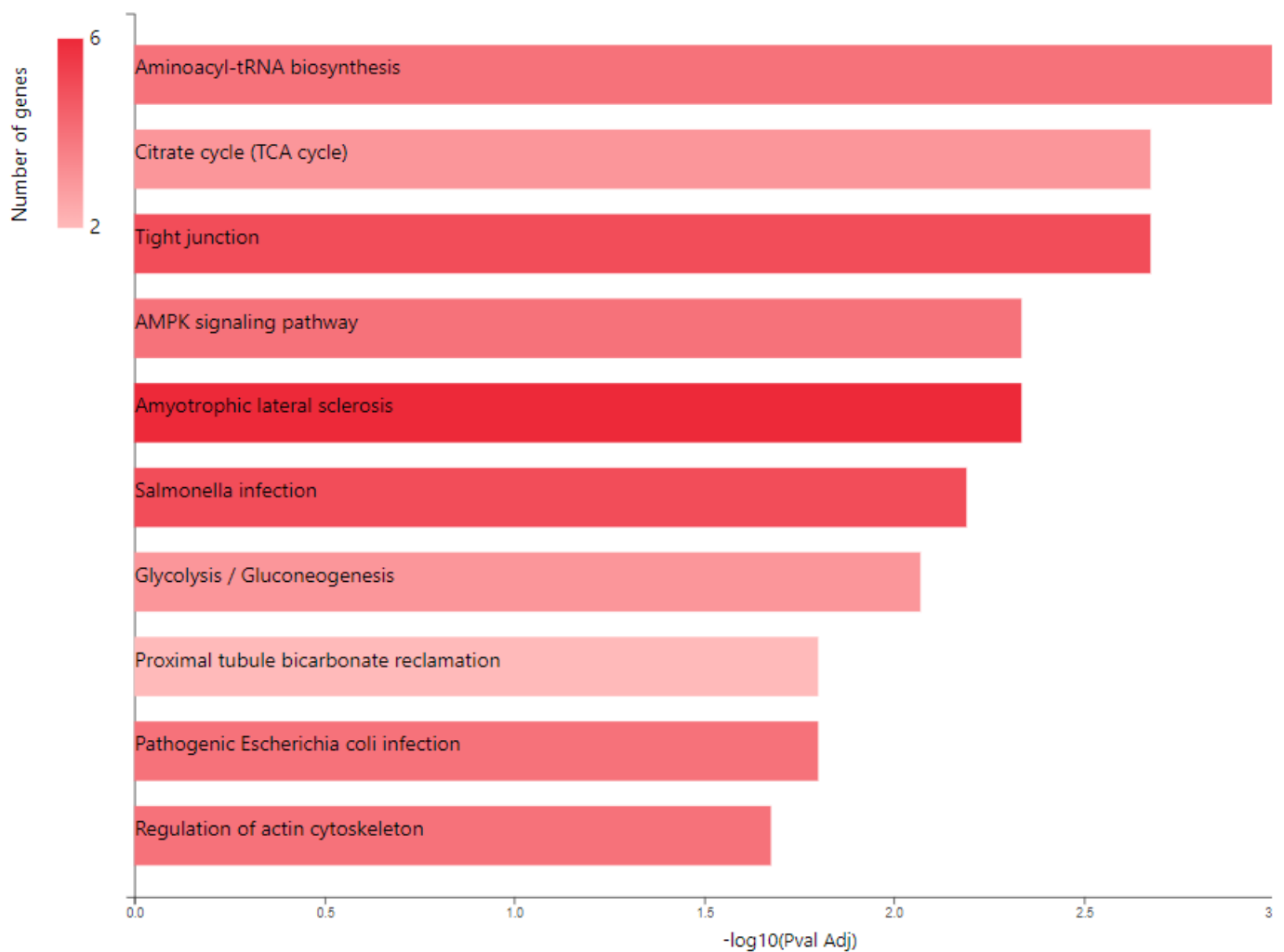


Figure 4. Cont.

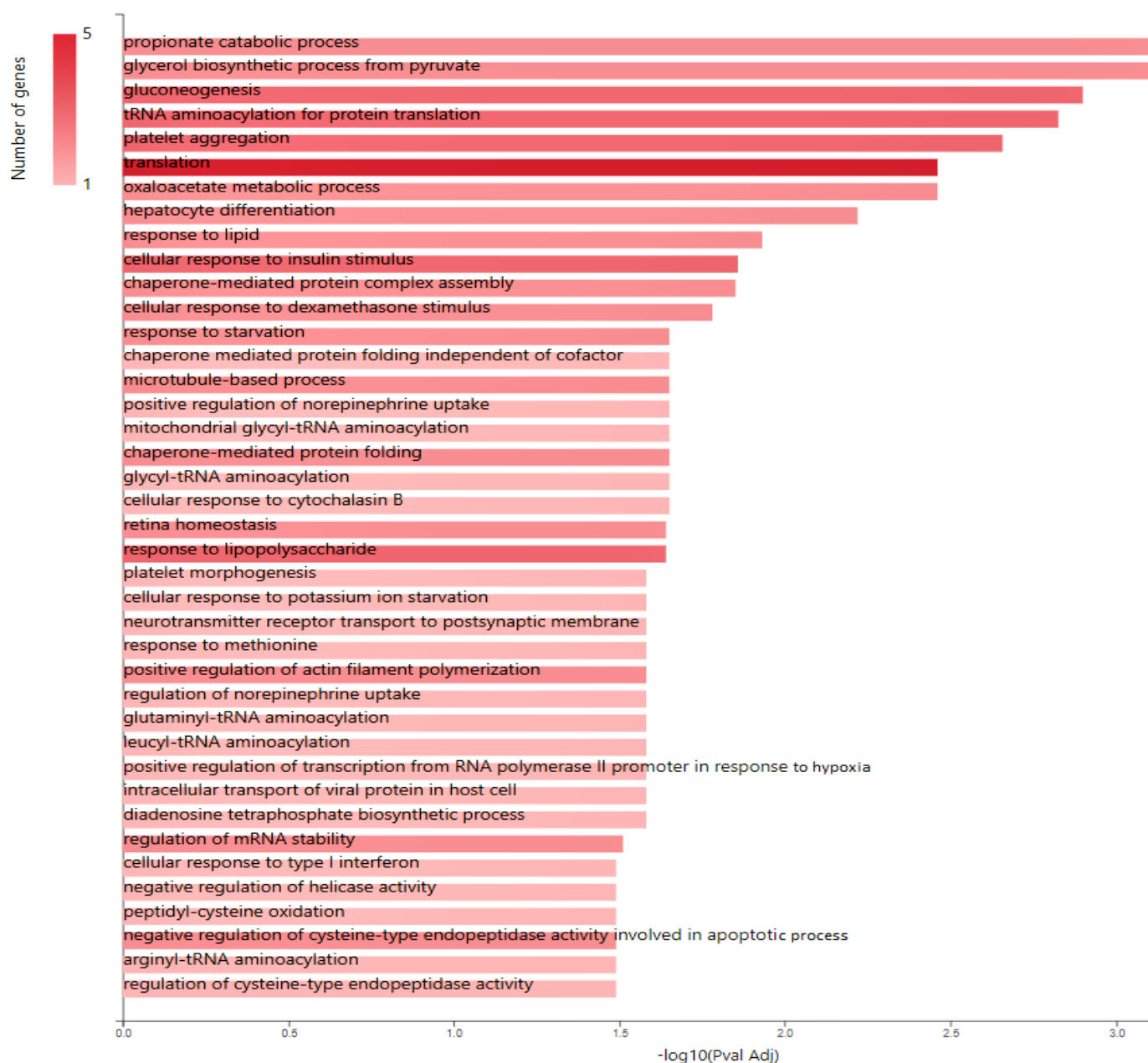


Figure 4. KEGG pathway analysis of pro-tumorigenic (PT) proteins in downregulated JTB condition; **B.** Gene ontology (GO) enrichment analysis of proteins in MCF7 BC cell line transfected for JTB downregulation: biological processes (BP) enriched in PT proteins. The analysis was performed using GeneCodis website (<https://genecodis.genyo.es/>, accessed on 22 October 2023).

2.2. Glucose Metabolism Reprogramming in JTB Downregulated Condition

Multiple cancer cell metabolic pathways are reprogrammed and adapted to sustain cell proliferation, tumor growth, and metastasis in tumor progression, especially under a nutrient deprivation condition. KEGG pathway analysis (Figure 4) emphasized several metabolic enriched pathways in the MCF7 BC cell line transfected for JTB downregulation: TCA cycle (KEGG_Citrate cycle/TCA cycle) and Glycolysis/Gluconeogenesis (KEGG_Glycolysis/Gluconeogenesis), while GO analysis showed as upregulated: gluconeogenesis (GO_BP Gluconeogenesis) and pyruvate metabolism (GO_BP_Glycerol biosynthetic process from pyruvate). The highlighted dysregulation of propionate metabolism (GO_BP Propionate catabolic process) is also known to contribute to a pro-aggressive state in BC cells, increasing cancer cell metastatic ability [136]. Phosphoenolpyruvate (PEP)

carboxykinases (PCK1/PEPCK-C, cytosolic isoform, and PCK2/PEPCK-M, mitochondrial isoform) have been shown to be multifunctional enzymes, critical for the growth of certain cancers [137], sustaining cell cycle progression and cell proliferation [39,40]. Thus, in the absence of glucose, cancer cells may synthesize essential metabolites using abbreviated forms of gluconeogenesis, as a reverse phase of glycolysis, especially by PCK1 and PCK2 expression [137], both well known for their key roles in gluconeogenesis and regulation of TCA cycle flux [39]. PCK1 has been reported as a tumor-suppressor in cancers arising from gluconeogenic tissues/organs, such as liver and kidney, while it acts as a tumor promoter in many human cancers arising in non-gluconeogenic tissues [138]. Consequently, PCK1 was reported as an overexpressed oncogene in colon, thyroid, breast, lung, urinary tract, and melanoma cancers [36], while it was found as a downregulated tumor suppressor in tumors arising in gluconeogenic tissues of liver and kidney, such as in HCC [36], and ccRCC [37]. Here we showed that MCF7 cells transfected for JTB downregulation markedly upregulated cytosolic PCK1, which was described as a molecular hub that regulates glycolysis, TCA cycle and gluconeogenesis to increase glycogenesis via gluconeogenesis [139]. PCK1, as a key rate-limiting enzyme in gluconeogenesis, catalyzes the conversion of oxaloacetate (OAA) to PEP (GO_BP oxaloacetate metabolic process) [138] and links the TCA and glycolysis/gluconeogenesis [40]. The expression of PGK1 leads to the biosynthesis of glucose-6-phosphate (G6P) that can be used by different pathways, including conversion to glucose, glycolysis, pentose phosphate pathway (PPP) or glycogenesis [139]. Glucose-6-phosphate isomerase (GPI) that interconverts G6P and fructose-6-phosphate (F6P) is also overexpressed in the downregulated JTB condition (GO_BP Gluconeogenesis). Cyttoplasmic GPI is a glycolytic-related enzyme secreted in the extracellular matrix (ECM) of cancer cells, where it is called an autocrine motility factor (AMF) [62], and functions as a cytokine or growth factor [63]. GPI is overexpressed in BC [63], LUAD/NSCLC, glioblastoma, ccRCC [64], and GC [62]. This glycolytic enzyme is involved in cell cycle, cell proliferation, correlates with immune infiltration, cell migration and invasion [64], while silencing suppressed proliferation, migration, invasion, glycolysis, and induced apoptosis (GO_BP Negative regulation of cysteine-type endopeptidase activity involved in apoptotic process) [62]. PCK1 also enhances the PPP, which produces ribose-5-phosphate for nucleotide synthesis and NADPH for biosynthetic pathways [138]. Abundant NADPH ensures high levels of reduced glutathione (GSH) [139], known for its important intracellular antioxidant role, which acts as a regulator of cellular redox state as well as a controller of cell differentiation, proliferation, apoptosis, ferroptosis and immune function [140].

Cancer cells utilize glutamine metabolism for energy generation as well as to synthesize molecules that are essential for cancer growth and progression [141], such as nucleotides and fatty acids, which regulate redox balance in cancer cells [142]. PEPCKs increase the synthesis of ribose from non-carbohydrate sources, such as glutamine [39] as well as the serine and other amino acid synthesis [143]. Also, PCK1 helps regulate triglyceride/fatty acid cycle (GO_BP Regulation of lipid biosynthetic process) and development of insulin resistance (GO_BP Cellular response to insulin stimulus), being involved in glyceroneogenesis (GO_BP Glycerol biosynthetic pathway from pyruvate) and re-esterification of free fatty acids [144]. PEPCK-M is reported as a key mediator for the synthesis of glycerol phosphate from non-carbohydrate precursors, being important to maintain level of glycerophospholipids as major constituents of bio-membranes [145]. The effects of PEPCK on glucose metabolism and cancer cell proliferation are partially mediated by activation of mechanistic target of rapamycin (mTORC1) [39], which is regulated by glucose, growth factors and amino acids and is coupled to the insulin/IGF-1 (insulin-like growth factor 1) signaling pathway [146]. Thus, the mitochondrial phosphoenolpyruvate carboxykinase (PEPCK-M/PCK2), known to enhance cell proliferation and response to stress or nutrient/glucose restriction/deprivation in cancer cells (GO_BP Response to starvation) compared to PCK1 that functions primarily in gluconeogenesis, promotes tumor growth in ER+ BC through regulation of mTOR pathway (GO_BP Positive regulation of mTOR signaling) [40]. AMP-activated protein kinase (AMPK) is an "energy sensor"/metabolic regulator

involved in lipogenesis, glycolysis, TCA cycle, cell cycle progression, and mitochondrial dynamics [147]. PCK1 dysregulation may promote cell proliferation via inactivation of AMPK (KEGG_AMPK signaling pathway), known as a tumor suppressor [36] but was recently reconsidered as a putative oncogene [148]. PCK1-directed glycogen metabolic program regulates differentiation and maintenance of CD8⁺ T cells that are essential for protective immunity against cancer [139] (GO_BP Positive regulation of memory T cell differentiation). PEPCK is known to be activated in response to acidosis. The acid-induced PEPCK provides glucose for acid-base homeostasis (GO_BP Positive regulation of transcription from RNA polymerase II promoter in response to acidic pH) [149]. In conclusion, PCK enzymes are involved in gluconeogenesis, glyceroneogenesis, serine biosynthesis, and amino acid metabolism, targeting the increase of glucose level that contributes to the development and progression of many types of cancer arising in non-gluconeogenic tissues/organs [150]. 25 upregulated DEPs with PT activity (HSPB1, HSPA4, ACTB, ACTN1, PFN2, EEF2, PCK1, PCK2, FARSB, GARS1, LARS1, RARS1, PSMC6, CCT2, IFIT1, PTBP1, GPI, TUBA1A, UTY, CS, PA2G4, NCKAP1, PRDX3, RAB8A, and RAB35) and two down-regulated DEPs (TUBB4B and PSMB9) were submitted for PPI network construction with STRING database (<https://string-db.org/>, accessed on 22 October 2023), to highlight the specific interaction network associated with the JTB^{low} condition in transfected MCF7 BC cell line (Figure 5). This enrichment indicates that these proteins with PT potential are biological connected, as a group.

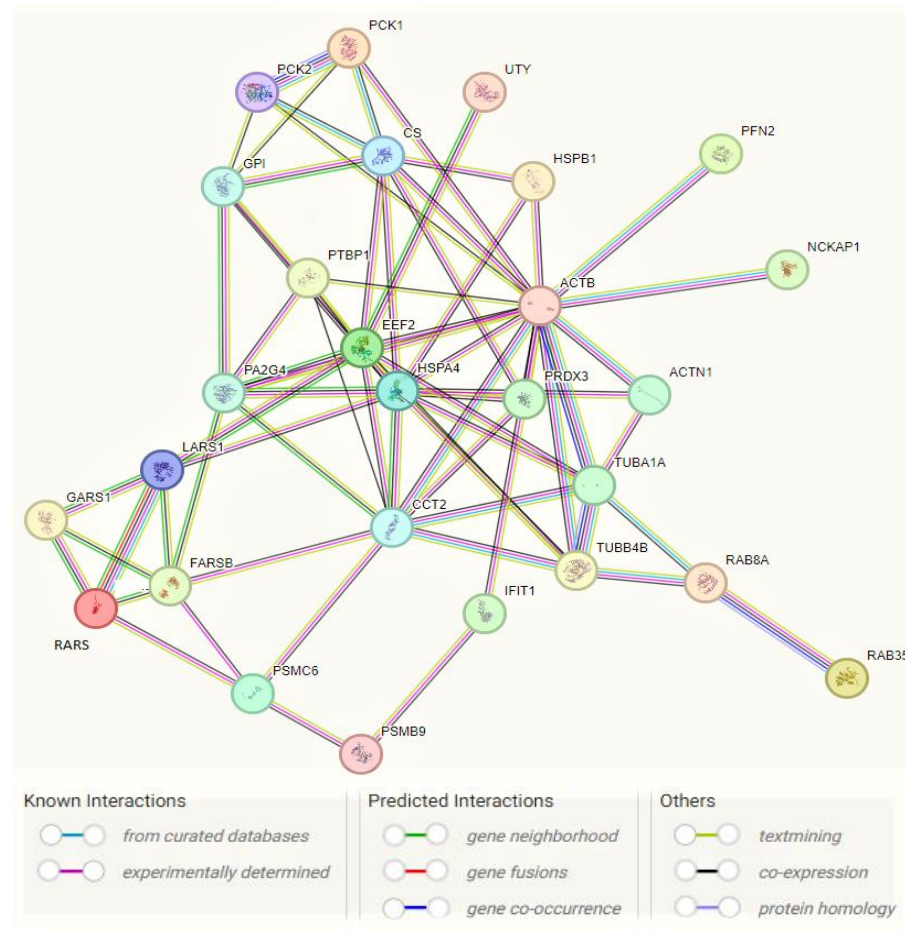


Figure 5. Interaction network of pro-tumorigenic (PT) proteins in MCF7 BC cell line transfected for JTB silencing, by means of STRING on-line database (<https://string-db.org/>, accessed on 22 October 2023). A total of 27 nodes and 69 edges were mapped in the PPI network with a PPI enrichment p -value of 6.44×10^{-12} .

The main results of this experiment are synthesized in the Figure 6.

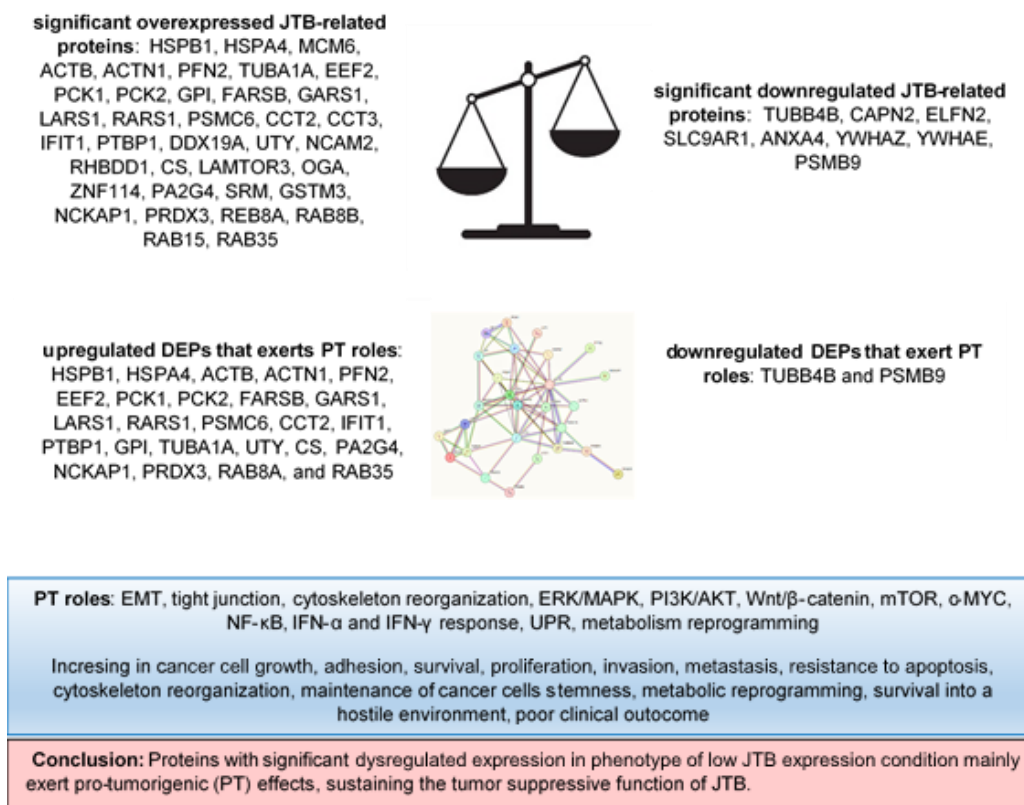


Figure 6. DEPs and their pro-tumorigenic (PT) activity in MCF7 BC cell line transfected for JTB silencing.

3. Materials and Methods

MCF7 cell culture, the transfection of hJTB plasmids and the collection of cell lysates was described previously [12] and briefly described below.

3.1. Cell Culture

MCF7 cell lines were purchased from American Type Culture Collection (HTB-22 ATCC) and grown in RPMI medium supplemented with 10% FBS, 0.2% Gentamicin, 1% Penicillin-Streptomycin and 0.2% Amphotericin (growth media) at 37 °C. The cells were grown until they reached 70–80% confluency and were transiently transfected with JTB shRNA plasmid for downregulation.

3.2. Plasmids for Downregulation

Four plasmids were custom made by Creative Biogene, Shirley, NY, USA. Three shRNA plasmids containing GCTTTGATGGAACAACGCTTA sequence, with forward sequencing primer of 5'-CCGACAACCACTACCTGA-3' and reverse primer of 5'-CTCTACAAATGTG-GTATGGC-3', GCAAATCGAGTCCATATAGCT sequence, with forward primer 5'-CCGAC-AACCACTACCTGA-3' and reverse primer of 5'-CTCTACAAATGTGGTATGGC-3', and GTGCAGGAAGAGAAGCTGTCA sequence with 5'-CCGACAACCACTACCTGA-3' and reverse primer of 5'-CTCTACAAATGTGGTATGGC-3', all targeting the hJTB mRNA respectively. The fourth plasmid was a control plasmid with a scramble sequence GCTTCGCGC-CGTAGTCTTA with forward primer 5'-CCGACAACCACTACCTGA-3' and reverse primer of 5'-CTCTACAAATGTGGTATGGC-3'. These plasmids were further customized to have an eGFP tag with Puromycin antibiotic resistance gene.

3.3. Transfection into MCF7 Cells

As stated in [12], Lipofectamine™ 3000/DNA and DNA/Plasmid (10 µg/µL) complexes were prepared in Opti-MEM Reduced Serum Media (Invitrogen, Waltham, MA, USA) for each condition and added directly to the cells in culture medium. Cells were allowed to grow for 48–72 h after which they were collected. 70% transient transfection efficiency was confirmed by visualizing the green fluorescence emitted by the eGFP using a confocal microscope (Figure S1).

3.4. Western Blot Analysis

Cell lysates from both the control and downregulated JTB condition were collected using a lysis buffer. The lysates were then incubated on ice for 30 min and centrifuged at 14,000 rpm for 20 min. The protein samples were quantified using Bradford Assay. Lysates containing 20 µg of proteins were run in a 14% SDS-polyacrylamide gels and transferred to nitrocellulose membranes. The blots were incubated with blocking buffer containing 5% milk and 0.1% tween-20 overnight at 4 °C with shaking. Primary antibody (JTB Polyclonal Antibody—PA5-52307, Invitrogen, Waltham, MA, USA) was added and incubated for 1 h with constant shaking. Secondary antibody (mouse anti-rabbit IgG-HRP sc-2357, Santa Cruz Biotechnology, Inc., Dallas TX, USA) was added and incubated for 1 h with constant shaking. After each incubation, the blots were washed thrice with TBS-T (1X TBS buffer, containing 0.05% tween-20) for 10 min each with constant shaking. Finally, the enhanced chemi-luminescent substrate (Pierce™ ECL Western Blotting Substrate—32106, ThermoFisher, Waltham, MA, USA) was added and the blot was analyzed using a CCD Imager. For normalization, mouse GAPDH monoclonal antibody (51332, cell-signaling technology, Danvers, MA, USA) was added and incubated for 1 h, followed by the addition of goat anti-mouse IgG-HRP (sc-2005, Santa Cruz Biotechnology) and the addition of ECL substrate. Image J software was used for the detection and comparison of the intensity of the bands (Figure S2).

3.5. 2D-PAGE & Proteomic Analysis

We used three biological replicates for the downregulated JTB condition. Two controls were used for the comparison: control ($n = 3$), control_shRNA ($n = 3$) and sh_JTB ($n = 3$). These conditions were analyzed in 2D-PAGE by Kendrick Labs, Inc. (Madison, WI, USA) and nanoLC-MS/MS as previously described [13]. The computer comparison was done for the average of three samples (3 vs. 3)—control_shRNA vs. sh_JTB ($n = 3$) and Control vs. sh_JTB ($n = 3$). The dysregulated spots were selected based on the criteria of having a fold increase or decrease of ≥ 1.7 and p value of ≤ 0.05 . The data processing was done using PLGS software (v. 2.4) to convert them to pkl files and Mascot Daemon software (v. 2.5.1) was used to identify the dysregulated proteins. Finally, Gene Set Enrichment Analysis (GSEA) analysis was done to identify the dysregulated pathways as previously described [13].

3.6. Data Sharing

Mascot data will be provided upon request, according to Clarkson University Material Transfer Agreement. The mass spectrometry data have been deposited to the ProteomeX-change Consortium via PRIDE partner repository with the dataset identifier PXD046265.4.

4. Conclusions

The jumping translocation breakpoint (JTB) protein has been reported as a regulator of mitochondrial function, cell growth, cell death and apoptosis, as well as a protein involved in cytokinesis/cell cycle. Some authors detected JTB as an overexpressed gene/protein in several malignant tissues and cancer cell lines, including liver cancer, prostate cancer, and BC, showing that this gene may suffer from unbalanced jumping translocation that leads to aberrant products, highlighting that the JTB downregulation/silencing increases cancer cell motility, anti-apoptosis, and promotes genomic instability and tumorigenesis. We also

showed that the upregulated expression of DEPs in the JTB^{low} condition, investigated by SDS-PAGE followed by nLC-MS/MS proteomics in transfected MCF7 BC cell line, may promote cancer cell viability, motility, proliferation, invasion, ability to survive into hostile environment, metabolic reprogramming, escaping of tumor cells from host immune control, leading to a more invasive phenotype for MCF7 cells. Several downregulated DEPs in the JTB^{low} condition also promoted the invasive phenotype of MCF7 cells, sustaining cell proliferation, migration, invasion, and tumorigenesis. A plethora of DEPs identified during JTB silencing by in-solution digestion followed by nLC-MS/MS have been complementary and completed the list of DEPs identified by SDS-PAGE proteomics [12]. In this last case especially, upregulated proteins emphasized pro-tumorigenic activities in downregulated JTB state [13].

Using 2D-PAGE coupled with nLC-MS/MS proteomics, the present study identified 45 significantly dysregulated proteins, of which 37 were upregulated and 8 downregulated, in MCF7 BC cell line transfected for downregulated JTB condition. HSPB1, HSPA4, MCM6, ACTB, ACTN1, PFN2, TUBA1A, EEF2, PCK1, PCK2, GPI, FARSB, GARS1, LARS1, RARS1, PSMC6, CCT2, CCT3, IFIT1, PTBP1, DDX19A, UTY, NCAM2, RHBDD1, CS, LAMTOR3, OGA, ZNF114, PA2G4, SRM, GSTM3, NCKAP1, PRDX3, REB8A, RAB8B, RAB15 and RAB35 have been overexpressed, while TUBB4B, CAPN2, ELFN2, SLC9AR1, ANXA4, YWHAZ, YWHAE, and PSMB9 proteins were found to be significantly downregulated. GSEA revealed four upregulated pathways, including proteins important for interferon alpha (IFN- α) response, interferon gamma (IFN- γ) response, Myc targets V1, and unfolded protein response (UPR). Two downregulated pathways comprised proteins involved in estrogen response late and estrogen response early pathways. Almost all DEPs identified in this experiment exert pro-tumorigenic effects in the JTB^{low} condition, sustaining the tumor suppressive function of JTB. Thus, the identified DEPs are involved in several signaling and metabolic pathways that exert pro-tumorigenic roles: EMT, ERK/MAPK, PI3K/AKT, Wnt/ β -catenin, mTOR, C-MYC, NF- κ B, IFN- γ and IFN- α response, UPR, and glycolysis/gluconeogenesis. These pathways sustain cancer cell growth, adhesion, survival, proliferation, invasion, metastasis, resistance to apoptosis, cytoskeleton reorganization, maintenance of stemness, metabolic reprogramming, survival in a hostile environment, and a poor clinical outcome. In conclusion, JTB silencing might increase the neoplastic phenotype and behavior of MCF7 BC cell line.

Analysis of upregulation of JTB was systematic, complementary and comprehensive: in-solution digestion, 1-D-PAGE and 2D-PAGE, followed by proteomics. Analysis of JTB silencing was also systematic, complementary and comprehensive: in-solution digestion and 1D-PAGE, and now 2D-PAGE, followed by proteomics. Additional, complementary or better methods can also be used, at the sample level, or at the instrumentation level. The current in-solution and gel-based analysis can be complemented, among others, by peptidomics analysis, phosphoproteomics analysis, or analysis of stable and transient protein-protein interactions. At the instrumentation level, 2D-UPLC could be one option, and newer, more performant mass spectrometers could also be used.

Overall, taking into account the opinion of other authors, as well as based on our own team's in vitro studies, we suggest that JTB protein might be considered as a tumor biomarker for BC and should be studied as a target for BC therapy.

Supplementary Materials: The following supporting information can be downloaded at: <https://www.mdpi.com/article/10.3390/molecules28227501/s1>, Figure S1. Confocal microscope images showing conformation of transient transfection for control (A) and JTB downregulated condition (B). Left panel is the Bright Field (BF) mode, middle panel is the GFP mode and the right panel is a merge between BF and GFP modes. Figure S2. Downregulation confirmation of hJTB compared to control samples with (A) showing the downregulation of JTB protein at ~45 kDa in MCF7 cells treated with sh plasmids compared to control using commercially available full length hJTB antibody from Invitrogen; (B) shows GAPDH used as the loading control at 37 kDa.

Author Contributions: Conceptualization, M.J. and C.C.D.; writing—original draft preparation, M.J., A.-N.N., D.W., I.S., B.A.P., T.J. and C.C.D.; writing—review and editing, M.J., A.-N.N., D.W., I.S., B.A.P., T.J. and C.C.D.; funding acquisition, C.C.D. All authors have read and agreed to the published version of the manuscript.

Funding: This publication was supported in part by the National Cancer Institute of the National Institutes of Health under Award Number R15CA260126. The content is solely the responsibility of the authors and does not necessarily represent the official views of the National Institutes of Health.

Institutional Review Board Statement: Not applicable.

Informed Consent Statement: Not applicable.

Data Availability Statement: The mass spectrometry data have been deposited to the ProteomeX-change Consortium via PRIDE partner repository with the dataset identifier PXD046265.

Acknowledgments: The authors thank the members of the Biochemistry & Proteomics Laboratories for the pleasant working environment. CCD would like to thank the Fulbright Commission USA-Romania (CCD host, Brindusa Alina Petre guest) and to the Erasmus+ Exchange Program between Clarkson University and Al. I. Cuza Iasi, Romania (Tess Cassler at Clarkson and Alina Malanciu & Gina Marinescu at Al. I. Cuza Iasi).

Conflicts of Interest: The authors declare no conflict of interest.

References

1. Ali, R.; Sultan, A.; Ishrat, R.; Haque, S.; Khan, N.J.; Prieto, M.A. Identification of New Key Genes and Their Association with Breast Cancer Occurrence and Poor Survival Using In Silico and In Vitro Methods. *Biomedicines* **2023**, *11*, 1271. [CrossRef] [PubMed]
2. Hatakeyama, S.; Osawa, M.; Omine, M.; Ishikawa, F. JTB: A novel membrane protein gene at 1q21 rearranged in a jumping translocation. *Oncogene* **1999**, *18*, 2085–2090. [CrossRef] [PubMed]
3. Tyszkiewicz, T.; Jarzab, M.; Szymczyk, C.; Kowal, M.; Krajewska, J.; Jaworska, M.; Fraczek, M.; Krajewska, A.; Hadas, E.; Swierniak, M.; et al. Epidermal differentiation complex (locus 1q21) gene expression in head and neck cancer and normal mucosa. *Folia Histochem. et Cytobiol.* **2014**, *52*, 79–89. [CrossRef] [PubMed]
4. Hogenbirk, M.A.; Heideman, M.R.; de Rink, I.; Velds, A.; Kerkhoven, R.M.; Wessels, L.F.A.; Jacobs, H. Defining chromosomal translocation risks in cancer. *Proc. Natl. Acad. Sci. USA* **2016**, *113*, E3649–E3656. [CrossRef] [PubMed]
5. Stankiewicz, P.; Cheung, S.; Shaw, C.; Saleki, R.; Szigeti, K.; Lupski, J. The donor chromosome breakpoint for a jumping translocation is associated with large low-copy repeats in 21q21.3. *Cytogenet. Genome Res.* **2003**, *101*, 118–123. [CrossRef]
6. Kanome, T.; Itoh, N.; Ishikawa, F.; Mori, K.; Kim-Kaneyama, J.R.; Nose, K.; Shibamura, M. Characterization of Jumping translocation breakpoint (JTB) gene product isolated as a TGF- β 1-inducible clone involved in regulation of mitochondrial function, cell growth and cell death. *Oncogene* **2007**, *26*, 5991–6001. [CrossRef]
7. Platica, O.; Chen, S.; Ivan, E.; Lopingco, M.C.; Holland, J.F.; Platica, M. PAR, a novel androgen regulated gene, ubiquitously expressed in normal and malignant cells. *Int. J. Oncol.* **2000**, *16*, 1055–1116. [CrossRef]
8. Platica, M.; Ionescu, A.; Ivan, E.; Holland, J.F.; Mandeli, J.; Platica, O. PAR, a protein involved in the cell cycle, is functionally related to chromosomal passenger proteins. *Int. J. Oncol.* **2011**, *38*, 777–785. [CrossRef]
9. Pan, J.-S.; Cai, J.-Y.; Xie, C.-X.; Zhou, F.; Zhang, Z.-P.; Dong, J.; Xu, H.-Z.; Shi, H.-X.; Ren, J.-L. Interacting with HBsAg compromises resistance of Jumping translocation breakpoint protein to ultraviolet radiation-induced apoptosis in 293FT cells. *Cancer Lett.* **2009**, *285*, 151–156. [CrossRef]
10. de Abreu Pereira, D.; Sandim, V.; Fernandes, T.F.; Almeida, V.H.; Rocha, M.R.; do Amaral, R.J.; Rossi, M.I.D.; Kalume, D.E.; Zingali, R.B. Proteomic Analysis of HCC-1954 and MCF-7 Cell Lines Highlights Crosstalk between α v and β 1 Integrins, E-Cadherin and HER-2. *Int. J. Mol. Sci.* **2022**, *23*, 10194. [CrossRef]
11. Somasekhara, D.; Dammali, M.; Nadumane, V.K. Proteomic Analysis of Human Breast Cancer MCF-7 Cells to Identify Cellular Targets of the Anticancer Pigment OR3 from *Streptomyces coelicolor* JUACT03. *Appl. Biochem. Biotechnol.* **2023**, *195*, 236–252.
12. Jayathirtha, M.; Whitham, D.; Alwine, S.; Donnelly, M.; Neagu, A.-N.; Darie, C.C. Investigating the Function of Human Jumping Translocation Breakpoint Protein (hJTB) and Its Interacting Partners through In-Solution Proteomics of MCF7 Cells. *Molecules* **2022**, *27*, 8301. [CrossRef]
13. Jayathirtha, M.; Neagu, A.-N.; Whitham, D.; Alwine, S.; Darie, C.C. Investigation of the effects of overexpression of jumping translocation breakpoint (JTB) protein in MCF7 cells for potential use as a biomarker in breast cancer. *Am. J. Cancer Res.* **2022**, *12*, 1784–1823.
14. Jayathirtha, M.; Channaveerappa, D.; Darie, C. Investigation and Characterization of the Jumping Translocation Breakpoint (JTB) Protein using Mass Spectrometry based Proteomics. *FASEB J.* **2021**, *35*. [CrossRef]

15. Jayathirtha, M.; Neagu, A.-N.; Whitham, D.; Alwine, S.; Darie, C.C. Investigation of the effects of downregulation of jumping translocation breakpoint (JTB) protein expression in MCF7 cells for potential use as a biomarker in breast cancer. *Am. J. Cancer Res.* **2022**, *12*, 4373–4398. [PubMed]
16. Aslebagh, R.; Channaveerappa, D.; Arcaro, K.F.; Darie, C.C. Comparative two-dimensional polyacrylamide gel electrophoresis (2D-PAGE) of human milk to identify dysregulated proteins in breast cancer. *Electrophoresis* **2018**, *39*, 1723–1734. [CrossRef]
17. Arrigo, A.-P.; Gibert, B. HspB1, HspB5 and HspB4 in Human Cancers: Potent Oncogenic Role of Some of Their Client Proteins. *Cancers* **2014**, *6*, 333–365. [CrossRef] [PubMed]
18. Wei, L.; Liu, T.T.; Wang, H.H.; Hong, H.M.; Yu, A.L.; Feng, H.P.; Chang, W.W. Hsp27 participates in the maintenance of breast cancer stem cells through regulation of epithelial-mesenchymal transition and nuclear factor- κ B. *Breast Cancer Res.* **2011**, *13*, R101. [CrossRef] [PubMed]
19. Shang, B.-B.; Chen, J.; Wang, Z.-G.; Liu, H. Significant correlation between HSPA4 and prognosis and immune regulation in hepatocellular carcinoma. *PeerJ* **2021**, *9*, e12315. [CrossRef]
20. Zhang, M.; Dai, W.; Li, Z.; Tang, L.; Chen, J.; Chen, C. HSPA4 Knockdown Retarded Progression and Development of Colorectal Cancer. *Cancer Manag. Res.* **2021**, *13*, 4679–4690. [CrossRef]
21. Fan, G.; Tu, Y.; Wu, N.; Xiao, H. The expression profiles and prognostic values of HSPs family members in Head and neck cancer. *Cancer Cell Int.* **2020**, *20*, 220. [CrossRef] [PubMed]
22. Xu, Y.; Wu, Q.; Tang, Z.; Tan, Z.; Pu, D.; Tan, W.; Zhang, W.; Liu, S. Comprehensive Analysis of Necroptosis-Related Genes as Prognostic Factors and Immunological Biomarkers in Breast Cancer. *J. Pers. Med.* **2022**, *13*, 44. [CrossRef] [PubMed]
23. Morisaki, T.; Yashiro, M.; Kakehashi, A.; Inagaki, A.; Kinoshita, H.; Fukuoka, T.; Kasashima, H.; Masuda, G.; Sakurai, K.; Kubo, N.; et al. Comparative proteomics analysis of gastric cancer stem cells. *PLoS ONE* **2014**, *9*, e110736. [CrossRef] [PubMed]
24. Zeng, T.; Guan, Y.; Li, Y.-K.; Wu, Q.; Tang, X.-J.; Zeng, X.; Ling, H.; Zou, J. The DNA replication regulator MCM6: An emerging cancer biomarker and target. *Clin. Chim. Acta* **2021**, *517*, 92–98. [CrossRef]
25. Liu, M.; Hu, Q.; Tu, M.; Wang, X.; Yang, Z.; Yang, G.; Luo, R. MCM6 promotes metastasis of hepatocellular carcinoma via MEK/ERK pathway and serves as a novel serum biomarker for early recurrence. *J. Exp. Clin. Cancer Res.* **2018**, *37*, 10. [CrossRef]
26. Gu, Y.; Tang, S.; Wang, Z.; Cai, L.; Lian, H.; Shen, Y.; Zhou, Y. A pan-cancer analysis of the prognostic and immunological role of β -actin (ACTB) in human cancers. *Bioengineered* **2021**, *12*, 6166–6185. [CrossRef]
27. Misawa, A.; Takayama, K.I.; Fujimura, T.; Homma, Y.; Suzuki, Y.; Inoue, S. Androgen-induced lncRNA POTEf-AS1 regulates apoptosis-related pathway to facilitate cell survival in prostate cancer cells. *Cancer Sci.* **2017**, *108*, 373–379. [CrossRef]
28. Javaid, N.; Choi, S. Toll-like Receptors from the Perspective of Cancer Treatment. *Cancers* **2020**, *12*, 297. [CrossRef]
29. Zhang, S.; Wang, J.; Chen, T.; Wang, J.; Wang, Y.; Yu, Z.; Zhao, K.; Zheng, K.; Chen, Y.; Wang, Z.; et al. α -Actinin1 promotes tumorigenesis and epithelial-mesenchymal transition of gastric cancer via the AKT/GSK3 β / β -Catenin pathway. *Bioengineered* **2021**, *12*, 5688–5704. [CrossRef]
30. Kovac, B.; Mäkelä, T.P.; Vallenius, T. Increased α -actinin-1 destabilizes E-cadherin-based adhesions and associates with poor prognosis in basal-like breast cancer. *PLoS ONE* **2018**, *13*, e0196986. [CrossRef]
31. Ling, Y.; Cao, Q.; Liu, Y.; Zhao, J.; Zhao, Y.; Li, K.; Chen, Z.; Du, X.; Huo, X.; Kang, H.; et al. Profilin 2 (PFN2) promotes the proliferation, migration, invasion and epithelial-to-mesenchymal transition of triple negative breast cancer cells. *Breast Cancer* **2021**, *28*, 368–378. [CrossRef]
32. Cui, X.-B.; Zhang, S.-M.; Xu, Y.-X.; Dang, H.-W.; Liu, C.-X.; Wang, L.-H.; Yang, L.; Hu, J.-M.; Liang, W.-H.; Jiang, J.-F.; et al. PFN2, a novel marker of unfavorable prognosis, is a potential therapeutic target involved in esophageal squamous cell carcinoma. *J. Transl. Med.* **2016**, *14*, 137. [CrossRef] [PubMed]
33. Meric-Bernstam, F.; Chen, H.; Akcakanat, A.; Do, K.-A.; Lluch, A.; Hennessy, B.T.; Hortobagyi, G.N.; Mills, G.B.; Gonzalez-Angulo, A.M. Aberrations in translational regulation are associated with poor prognosis in hormone receptor-positive breast cancer. *Breast Cancer Res.* **2012**, *14*, R138. [CrossRef]
34. Oji, Y.; Tatsumi, N.; Fukuda, M.; Nakatsuka, S.-I.; Aoyagi, S.; Hirata, E.; Nanchi, I.; Fujiki, F.; Nakajima, H.; Yamamoto, Y.; et al. The translation elongation factor eEF2 is a novel tumor-associated antigen overexpressed in various types of cancers. *Int. J. Oncol.* **2014**, *44*, 1461–1469. [CrossRef]
35. Song, Y.; Sun, B.; Hao, L.; Hu, J.; Du, S.; Zhou, X.; Zhang, L.; Liu, L.; Gong, L.; Chi, X.; et al. Elevated eukaryotic elongation factor 2 expression is involved in proliferation and invasion of lung squamous cell carcinoma. *Oncotarget* **2016**, *7*, 58470–58482. [CrossRef] [PubMed]
36. Tuo, L.; Xiang, J.; Pan, X.; Hu, J.; Tang, H.; Liang, L.; Xia, J.; Hu, Y.; Zhang, W.; Huang, A.; et al. PCK1 negatively regulates cell cycle progression and hepatoma cell proliferation via the AMPK/p27Kip1 axis. *J. Exp. Clin. Cancer Res.* **2019**, *38*, 50. [CrossRef]
37. Shi, L.; An, S.; Liu, Y.; Liu, J.; Wang, F. PCK1 Regulates Glycolysis and Tumor Progression in Clear Cell Renal Cell Carcinoma Through LDHA. *OncoTargets Ther.* **2020**, *13*, 2613–2627. [CrossRef] [PubMed]
38. Liu, R.; Gou, D.; Xiang, J.; Pan, X.; Gao, Q.; Zhou, P.; Liu, Y.; Hu, J.; Wang, K.; Tang, N. O-GlcNAc modified-TIP60/KAT5 is required for PCK1 deficiency-induced HCC metastasis. *Oncogene* **2021**, *40*, 6707–6719. [CrossRef]
39. Montal, E.D.; Dewi, R.; Bhalla, K.; Ou, L.; Hwang, B.J.; Ropell, A.E.; Gordon, C.; Liu, W.-J.; DeBerardinis, R.J.; Sudderth, J.; et al. PEPCCK Coordinates the Regulation of Central Carbon Metabolism to Promote Cancer Cell Growth. *Mol. Cell* **2015**, *60*, 571–583. [CrossRef]

40. Hsu, H.; Chu, P.; Chang, T.; Huang, K.; Hung, W.; Jiang, S.S.; Lin, H.; Tsai, H. Mitochondrial phosphoenolpyruvate carboxykinase promotes tumor growth in estrogen receptor-positive breast cancer via regulation of the mTOR pathway. *Cancer Med.* **2022**, *12*, 1588–1601. [CrossRef]
41. Wang, Z.; Dong, C. Gluconeogenesis in Cancer: Function and Regulation of PEPCK, FBPase, and G6Pase. *Trends Cancer* **2019**, *5*, 30–45. [CrossRef]
42. Ma, X.; Gao, Y.; Liu, J.; Xu, L.; Liu, W.; Huna, A.; Wang, X.; Gong, W. Low expression of PCK2 in breast tumors contributes to better prognosis by inducing senescence of cancer cells. *IUBMB Life* **2022**, *74*, 896–907. [CrossRef] [PubMed]
43. Sangha, A.K.; Kantidakis, T. The Aminoacyl-tRNA Synthetase and tRNA Expression Levels Are Deregulated in Cancer and Correlate Independently with Patient Survival. *Curr. Issues Mol. Biol.* **2022**, *44*, 3001–3017. [CrossRef]
44. Gao, X.; Guo, R.; Li, Y.; Kang, G.; Wu, Y.; Cheng, J.; Jia, J.; Wang, W.; Li, Z.; Wang, A.; et al. Contribution of upregulated aminoacyl-tRNA biosynthesis to metabolic dysregulation in gastric cancer. *J. Gastroenterol. Hepatol.* **2021**, *36*, 3113–3126. [CrossRef]
45. Sung, Y.; Yoon, I.; Han, J.M.; Kim, S. Functional and pathologic association of aminoacyl-tRNA synthetases with cancer. *Exp. Mol. Med.* **2022**, *54*, 553–566. [CrossRef] [PubMed]
46. Shin, S.H.; Kim, H.S.; Jung, S.H.; Xu, H.D.; Jeong, Y.B.; Chung, Y.J. Implication of leucyl-tRNA synthetase 1 (LARS1) over-expression in growth and migration of lung cancer cells detected by siRNA targeted knock-down analysis. *Exp. Mol. Med.* **2008**, *40*, 229–236. [CrossRef] [PubMed]
47. Khan, K.; Gogonea, V.; Fox, P.L. Aminoacyl-tRNA synthetases of the multi-tRNA synthetase complex and their role in tumorigenesis. *Transl. Oncol.* **2022**, *19*, 101392. [CrossRef]
48. Bottoni, A.; Vignali, C.; Piccin, D.; Tagliati, F.; Luchin, A.; Zatelli, M.C.; Uberti, E.C.D. Proteasomes and RARS modulate AIMP1/EMAP II secretion in human cancer cell lines. *J. Cell. Physiol.* **2007**, *212*, 293–297. [CrossRef]
49. Zhang, J.-Y.; Shi, K.-Z.; Liao, X.-Y.; Li, S.-J.; Bao, D.; Qian, Y.; Li, D.-J. The Silence of PSMC6 Inhibits Cell Growth and Metastasis in Lung Adenocarcinoma. *BioMed Res. Int.* **2021**, *2021*, 9922185. [CrossRef]
50. Kao, T.-J.; Wu, C.-C.; Phan, N.N.; Liu, Y.-H.; Ta, H.D.K.; Anuraga, G.; Wu, Y.-F.; Lee, K.-H.; Chuang, J.-Y.; Wang, C.-Y. Prognoses and genomic analyses of proteasome 26S subunit, ATPase (PSMC) family genes in clinical breast cancer. *Ageing* **2021**, *13*, 17970. [CrossRef]
51. Liu, Q.; Qi, Y.; Kong, X.; Wang, X.; Zhang, W.; Zhai, J.; Yang, Y.; Fang, Y.; Wang, J. Molecular and Clinical Characterization of CCT2 Expression and Prognosis via Large-Scale Transcriptome Profile of Breast Cancer. *Front. Oncol.* **2021**, *11*, 614497. [CrossRef] [PubMed]
52. Liu, W.; Lu, Y.; Yan, X.; Lu, Q.; Sun, Y.; Wan, X.; Li, Y.; Zhao, J.; Li, Y.; Jiang, G. Current understanding on the role of CCT3 in cancer research. *Front. Oncol.* **2022**, *12*, 961733. [CrossRef] [PubMed]
53. Boudiaf-Benmammar, C.; Cresteil, T.; Melki, R. The cytosolic chaperonin CCT/TRiC and cancer cell proliferation. *PLoS ONE* **2013**, *8*, e60895.
54. Li, T.H.; Zhao, B.B.; Qin, C.; Wang, Y.Y.; Li, Z.R.; Cao, H.T.; Yang, X.Y.; Zhou, X.T.; Wang, W.B. IFIT1 modulates the proliferation, migration and invasion of pancreatic cancer cells via Wnt/ β -catenin signaling. *Cell. Oncol.* **2021**, *44*, 1425–1437. [CrossRef]
55. Danish, H.H.; Goyal, S.; Taunk, N.K.; Wu, H.; Moran, M.S.; Haffty, B.G. Interferon-induced protein with tetratricopeptide repeats 1 (IFIT1) as a prognostic marker for local control in T1-2 N0 breast cancer treated with breast-conserving surgery and radiation therapy (BCS + RT). *Breast J.* **2013**, *19*, 231–239. [CrossRef]
56. Pidugu, V.K.; Wu, M.-M.; Yen, A.-H.; Pidugu, H.B.; Chang, K.-W.; Liu, C.-J.; Lee, T.-C. IFIT1 and IFIT3 promote oral squamous cell carcinoma metastasis and contribute to the anti-tumor effect of gefitinib via enhancing p-EGFR recycling. *Oncogene* **2019**, *38*, 3232–3247. [CrossRef]
57. Wang, X.; Li, Y.; Fan, Y.; Yu, X.; Mao, X.; Jin, F. PTBP1 promotes the growth of breast cancer cells through the PTEN/Akt pathway and autophagy. *J. Cell. Physiol.* **2018**, *233*, 8930–8939. [CrossRef]
58. Li, S.; Shen, L.; Huang, L.; Lei, S.; Cai, X.; Breitzig, M.; Zhang, B.; Yang, A.; Ji, W.; Huang, M.; et al. PTBP1 enhances exon11a skipping in Mena pre-mRNA to promote migration and invasion in lung carcinoma cells. *Biochim. Biophys. Acta BBA-Genet. Regul. Mech.* **2019**, *1862*, 858–869.
59. Zhu, W.; Zhou, B.-L.; Rong, L.-J.; Ye, L.; Xu, H.-J.; Zhou, Y.; Yan, X.-J.; Liu, W.-D.; Zhu, B.; Wang, L.; et al. Roles of PTBP1 in alternative splicing, glycolysis, and oncogenesis. *J. Zhejiang Univ. Sci. B* **2020**, *21*, 122–136. [PubMed]
60. Jiang, Y.; Wang, B.; Li, Y.; Shen, J.; Wei, Y.; Li, H.; Chen, S.; Yang, H.; Zeng, F.; Liu, C.; et al. DDX19A Promotes Metastasis of Cervical Squamous Cell Carcinoma by Inducing NOX1-Mediated ROS Production. *Front. Oncol.* **2021**, *11*, 6299744. [CrossRef]
61. Cai, W.; Xiong Chen, Z.; Rane, G.; Satendra Singh, S.; Choo, Z.E.; Wang, C.; Yuan, Y.; Zea Tan, T.; Arfuso, F.; Yap, C.T.; et al. Wanted DEAD/H or Alive: Helicases Winding Up in Cancers. *JNCI J. Natl. Cancer Inst.* **2017**, *109*, djw278.
62. Ma, Y.-T.; Xing, X.-F.; Dong, B.; Cheng, X.-J.; Guo, T.; Du, H.; Wen, X.-Z.; Ji, J.-F. Higher autocrine motility factor/glucose-6-phosphate isomerase expression is associated with tumorigenesis and poorer prognosis in gastric cancer. *Cancer Manag. Res.* **2018**, *10*, 4969–4980. [CrossRef]
63. Zeng, J.; Yi, J.; Tan, S.; Zeng, Y.; Zou, L.; Zhang, C.; Liu, L.; Yi, P.; Fan, P.; Yu, J. GPI: An indicator for immune infiltrates and prognosis of human breast cancer from a comprehensive analysis. *Front. Endocrinol.* **2022**, *13*, 995972. [CrossRef] [PubMed]
64. Han, J.; Deng, X.; Sun, R.; Luo, M.; Liang, M.; Gu, B.; Zhang, T.; Peng, Z.; Lu, Y.; Tian, C.; et al. GPI Is a Prognostic Biomarker and Correlates With Immune Infiltrates in Lung Adenocarcinoma. *Front. Oncol.* **2021**, *11*, 752642.

65. Gallardo-Pérez, J.C.; Rivero-Segura, N.A.; Marín-Hernández, A.; Moreno-Sánchez, R.; Rodríguez-Enríquez, S. GPI/AMF inhibition blocks the development of the metastatic phenotype of mature multi-cellular tumor spheroids. *Biochim. Biophys. Acta BBA-Mol. Cell Res.* **2014**, *1843*, 1043–1053.
66. Nami, B.; Wang, Z. Genetics and Expression Profile of the Tubulin Gene Superfamily in Breast Cancer Subtypes and Its Relation to Taxane Resistance. *Cancers* **2018**, *10*, 274. [CrossRef] [PubMed]
67. Wang, D.; Jiao, Z.; Ji, Y.; Zhang, S. Elevated TUBA1A Might Indicate the Clinical Outcomes of Patients with Gastric Cancer, Being Associated with the Infiltration of Macrophages in the Tumor Immune Microenvironment. *J. Gastrointest. Liver Dis.* **2020**, *29*, 509–522. [CrossRef]
68. Liang, L.; Sun, H.; Zhang, W.; Zhang, M.; Yang, X.; Kuang, R.; Zheng, H. Meta-Analysis of EMT Datasets Reveals Different Types of EMT. *PLoS ONE* **2016**, *11*, e0156839.
69. Hua, C.; Chen, J.; Li, S.; Zhou, J.; Fu, J.; Sun, W.; Wang, W. KDM6 Demethylases and Their Roles in Human Cancers. *Front. Oncol.* **2021**, *11*, 779918.
70. Sterling, J.; Menezes, S.V.; Abbassi, R.H.; Munoz, L. Histone lysine demethylases and their functions in cancer. *Int. J. Cancer* **2020**, *148*, 2375–2388.
71. Takahashi, S.; Kato, K.; Nakamura, K.; Nakano, R.; Kubota, K.; Hamada, H. Neural cell adhesion molecule 2 as a target molecule for prostate and breast cancer gene therapy. *Cancer Sci.* **2011**, *102*, 808–814. [CrossRef] [PubMed]
72. Zhang, X.; Zhao, Y.; Wang, C.; Ju, H.; Liu, W.; Zhang, X.; Miao, S.; Wang, L.; Sun, Q.; Song, W. Rhomboid domain-containing protein 1 promotes breast cancer progression by regulating the p-Akt and CDK2 levels. *Cell Commun. Signal.* **2018**, *16*, 65. [PubMed]
73. Ren, X.; Song, W.; Liu, W.; Guan, X.; Miao, F.; Miao, S.; Wang, L. Rhomboid domain containing 1 inhibits cell apoptosis by upregulating AP-1 activity and its downstream target Bcl-3. *FEBS Lett.* **2013**, *587*, 1793–1798. [CrossRef] [PubMed]
74. Cai, Z.; Deng, Y.; Ye, J.; Zhuo, Y.; Liu, Z.; Liang, Y.; Zhang, H.; Zhu, X.; Luo, Y.; Feng, Y.; et al. Aberrant Expression of Citrate Synthase is Linked to Disease Progression and Clinical Outcome in Prostate Cancer. *Cancer Manag. Res.* **2020**, *12*, 6149–6163. [PubMed]
75. Schlichtholz, B.; Turyn, J.; Goyke, E.; Biernacki, M.; Jaskiewicz, K.; Sledzinski, Z.; Swierczynski, J. Enhanced Citrate Synthase Activity in Human Pancreatic Cancer. *Pancreas* **2005**, *30*, 99–104. [CrossRef]
76. Chen, L.; Liu, T.; Zhou, J.; Wang, Y.; Wang, X.; Di, W.; Zhang, S. Citrate synthase expression affects tumor phenotype and drug resistance in human ovarian carcinoma. *PLoS ONE* **2014**, *9*, e115708.
77. Lin, C.-C.; Cheng, T.-L.; Tsai, W.-H.; Tsai, H.-J.; Hu, K.-H.; Chang, H.-C.; Yeh, C.-W.; Chen, Y.-C.; Liao, C.-C.; Chang, W.-T. Loss of the respiratory enzyme citrate synthase directly links the Warburg effect to tumor malignancy. *Sci. Rep.* **2012**, *2*, 785.
78. MacPherson, S.; Horkoff, M.; Gravel, C.; Hoffmann, T.; Zuber, J.; Lum, J.J. STAT3 Regulation of Citrate Synthase Is Essential during the Initiation of Lymphocyte Cell Growth. *Cell Rep.* **2017**, *19*, 910–918. [CrossRef]
79. Gong, Y.; Lv, Y.; Xu, F.; Xiu, Y.; Lu, Y.; Liu, Z.; Deng, L. LAMTOR3 is a prognostic biomarker in kidney renal clear cell carcinoma. *J. Clin. Lab. Anal.* **2022**, *36*, e24648.
80. Marina, M.; Wang, L.; Conrad, S.E. The scaffold protein MEK Partner 1 is required for the survival of estrogen receptor positive breast cancer cells. *Cell Commun. Signal.* **2012**, *10*, 18. [CrossRef]
81. De Araujo, M.E.; Erhart, G.; Buck, K.; Müller-Holzner, E.; Hubalek, M.; Fiegl, H.; Campa, D.; Canzian, F.; Eilber, U.; Chang-Claude, J.; et al. Polymorphisms in the gene regions of the adaptor complex LAMTOR2/LAMTOR3 and their association with breast cancer risk. *PLoS ONE* **2013**, *8*, e53768. [CrossRef] [PubMed]
82. Kwon, O.S.; Hong, S.K.; Kwon, S.J.; Go, Y.H.; Oh, E.; Cha, H.J. BCL2 induced by LAMTOR3/MAPK is a druggable target of chemoradioresistance in mesenchymal lung cancer. *Cancer Lett.* **2017**, *403*, 48–58. [CrossRef] [PubMed]
83. Singh, J.P.; Qian, K.; Lee, J.S.; Zhou, J.; Han, X.; Zhang, B.; Ong, Q.; Ni, W.; Jiang, M.; Ruan, H.B.; et al. O-GlcNAcase targets pyruvate kinase M2 to regulate tumor growth. *Oncogene* **2020**, *39*, 560–573. [CrossRef] [PubMed]
84. Olechnowicz, A.; Oleksiewicz, U.; Machnik, M. KRAB-ZFPs and cancer stem cells identity. *Genes Dis.* **2022**, *10*, 1820–1832. [CrossRef] [PubMed]
85. Pan, Q.; Wang, L.; Zhang, H.; Liang, C.; Li, B. Identification of a 5-Genes Signature Predicting Progression and Prognosis of Clear Cell Renal Cell Carcinoma. *Med. Sci. Monit.* **2019**, *25*, 4401–4413. [CrossRef]
86. Oleksiewicz, U.; Gładych, M.; Raman, A.T.; Heyn, H.; Mereu, E.; Chlebanowska, P.; Andrzejewska, A.; Sozańska, B.; Samant, N.; Fałk, K.; et al. TRIM28 and Interacting KRAB-ZNFs Control Self-Renewal of Human Pluripotent Stem Cells through Epigenetic Repression of Pro-differentiation Genes. *Stem Cell Rep.* **2017**, *9*, 2065–2080. [CrossRef]
87. Sun, S.; Liu, Y.; Zhou, M.; Wen, J.; Xue, L.; Han, S.; Liang, J.; Wang, Y.; Wei, Y.; Yu, J.; et al. PA2G4 promotes the metastasis of hepatocellular carcinoma by stabilizing FYN mRNA in a YTHDF2-dependent manner. *Cell Biosci.* **2022**, *12*, 55. [CrossRef]
88. Novita Sari, I.; Setiawan, T.; Seock Kim, K.; Toni Wijaya, Y.; Won Cho, K.; Young Kwon, H. Metabolism and function of polyamines in cancer progression. *Cancer Lett.* **2021**, *519*, 91–104. [CrossRef]
89. Akinyele, O.; Wallace, H.M. Characterising the Response of Human Breast Cancer Cells to Polyamine Modulation. *Biomolecules* **2021**, *11*, 743. [CrossRef]

90. Snezhkina, A.V.; Krasnov, G.S.; Lipatova, A.V.; Sadritdinova, A.F.; Kardymon, O.L.; Fedorova, M.S.; Melnikova, N.V.; Stepanov, O.A.; Zaretsky, A.R.; Kaprin, A.D. The Dysregulation of Polyamine Metabolism in Colorectal Cancer Is Associated with Overexpression of c-Myc and C/EBP β rather than Enterotoxigenic *Bacteroides fragilis* Infection. *Oxidative Med. Cell. Longev.* **2016**, *2016*, 2353560. [CrossRef]
91. Gamble, L.D.; Hogarty, M.D.; Liu, X.; Ziegler, D.S.; Marshall, G.; Norris, M.D.; Haber, M. Polyamine pathway inhibition as a novel therapeutic approach to treating neuroblastoma. *Front. Oncol.* **2012**, *2*, 162. [CrossRef] [PubMed]
92. Checa-Rojas, A.; Delgadillo-Silva, L.F.; Velasco-Herrera, M.d.C.; Andrade-Domínguez, A.; Gil, J.; Santillán, O.; Lozano, L.; Toledo-Leyva, A.; Ramírez-Torres, A.; Talamas-Rohana, P.; et al. GSTM3 and GSTP1: Novel players driving tumor progression in cervical cancer. *Oncotarget* **2018**, *9*, 21696–21714. [CrossRef] [PubMed]
93. Wang, S.; Yang, J.; You, L.; Dai, M.; Zhao, Y. GSTM3 Function and Polymorphism in Cancer: Emerging but Promising. *Cancer Manag. Res.* **2020**, *12*, 10377–10388. [CrossRef] [PubMed]
94. Di Lollo, V.; Canciello, A.; Orsini, M.; Bernabò, N.; Ancora, M.; Federico, M.; Curini, V.; Mattioli, M.; Russo, V.; Mauro, A.; et al. Transcriptomic and computational analysis identified LPA metabolism, KLHL14 and KCNE3 as novel regulators of Epithelial-Mesenchymal Transition. *Sci. Rep.* **2020**, *10*, 4180. [CrossRef] [PubMed]
95. Xiong, Y.; He, L.; Shay, C.; Lang, L.; Loveless, J.; Yu, J.; Chemmalakuzhy, R.; Jiang, H.; Liu, M.; Teng, Y. Nck-associated protein 1 associates with HSP90 to drive metastasis in human non-small-cell lung cancer. *J. Exp. Clin. Cancer Res.* **2019**, *38*, 122. [CrossRef]
96. Teng, Y.; Qin, H.; Bahassan, A.; Bendzun, N.G.; Kennedy, E.J.; Cowell, J.K. The WASF3-NCKAP1-CYFIP1 Complex Is Essential for Breast Cancer Metastasis. *Cancer Res.* **2016**, *76*, 5133–5142. [CrossRef]
97. Chen, J.; Ge, J.; Zhang, W.; Xie, X.; Zhong, X.; Tang, S. NCKAP1 is a Prognostic Biomarker for Inhibition of Cell Growth in Clear Cell Renal Cell Carcinoma. *Front. Genet.* **2022**, *13*, 764957. [CrossRef]
98. Zhong, X.P.; Kan, A.; Ling, Y.H.; Lu, L.H.; Mei, J.; Wei, W.; Li, S.H.; Guo, R.P. NCKAP1 improves patient outcome and inhibits cell growth by enhancing Rb1/p53 activation in hepatocellular carcinoma. *Cell Death Dis.* **2019**, *10*, 369. [CrossRef]
99. Nicolussi, A.; D’Inzeo, S.; Capalbo, C.; Giannini, G.; Coppa, A. The role of peroxiredoxins in cancer. *Mol. Clin. Oncol.* **2017**, *6*, 139–153. [CrossRef]
100. Park, M.H.; Jo, M.; Kim, Y.R.; Lee, C.-K.; Hong, J.T. Roles of peroxiredoxins in cancer, neurodegenerative diseases and inflammatory diseases. *Pharmacol. Ther.* **2016**, *163*, 1–23. [CrossRef]
101. Liu, Y.; Zhang, Z.; Gao, X.; Ma, Q.; Yu, Z.; Huang, S. Rab8A promotes breast cancer progression by increasing surface expression of Tropomyosin-related kinase B. *Cancer Lett.* **2022**, *535*, 215629. [CrossRef] [PubMed]
102. Aboubakr, H.; Lavanya, S.; Thirupathi, M.; Rohini, R.; Sarita, R. Human Rab8b Protein as a Cancer Target—An In Silico Study. *J. Comput. Sci. Syst. Biol.* **2016**, *9*, 132–149.
103. Demir, K.; Kirsch, N.; Beretta, C.A.; Erdmann, G.; Ingelfinger, D.; Moro, E.; Argenton, F.; Carl, M.; Niehrs, C.; Boutros, M. RAB8B Is Required for Activity and Caveolar Endocytosis of LRP6. *Cell Rep.* **2013**, *4*, 1224–1234. [CrossRef] [PubMed]
104. Tzeng, H.-T.; Wang, Y.-C. Rab-mediated vesicle trafficking in cancer. *J. Biomed. Sci.* **2016**, *23*, 70. [CrossRef]
105. Jia, N.; Song, Z.; Chen, B.; Cheng, J.; Zhou, W. A Novel Circular RNA circCSPP1 Promotes Liver Cancer Progression by Sponging miR-1182. *Oncotargets Ther.* **2021**, *14*, 2829–2838. [CrossRef]
106. Nishimura, N.; Pham, T.V.H.; Hartomo, T.B.; Lee, M.J.; Hasegawa, D.; Takeda, H.; Kawasaki, K.; Kosaka, Y.; Yamamoto, T.; Morikawa, S.; et al. Rab15 expression correlates with retinoic acid-induced differentiation of neuroblastoma cells. *Oncol. Rep.* **2011**, *26*, 145–151. [CrossRef]
107. Villagomez, F.R.; Medina-Contreras, O.; Cerna-Cortes, J.F.; Patino-Lopez, G. The role of the oncogenic Rab35 in cancer invasion, metastasis, and immune evasion, especially in leukemia. *Small GTPases* **2020**, *11*, 334–345. [CrossRef]
108. Dharmapal, D.; Jyothy, A.; Mohan, A.; Balagopal, P.G.; George, N.A.; Sebastian, P.; Maliekal, T.T.; Sengupta, S. β -Tubulin Isotype, TUBB4B, Regulates The Maintenance of Cancer Stem Cells. *Front. Oncol.* **2021**, *11*, 788024. [CrossRef]
109. Sobierajska, K.; Ciszewski, W.M.; Wawro, M.E.; Wiczorek-Szukala, K.; Boncela, J.; Papiewska-Pajak, I.; Niewiarowska, J.; Kowalska, M.A. TUBB4B Downregulation Is Critical for Increasing Migration of Metastatic Colon Cancer Cells. *Cells* **2019**, *8*, 810. [CrossRef]
110. Li, P.; Miao, C.; Liang, C.; Shao, P.; Wang, Z.; Li, J. Silencing CAPN2 Expression Inhibited Castration-Resistant Prostate Cancer Cells Proliferation and Invasion via AKT/mTOR Signal Pathway. *BioMed Res. Int.* **2017**, *2017*, 2593674. [CrossRef]
111. Miao, C.; Liang, C.; Tian, Y.; Xu, A.; Zhu, J.; Zhao, K.; Zhang, J.; Hua, Y.; Liu, S.; Dong, H.; et al. Overexpression of CAPN2 promotes cell metastasis and proliferation via AKT/mTOR signaling in renal cell carcinoma. *Oncotarget* **2017**, *8*, 97811–97821. [CrossRef]
112. Peng, X.; Yang, R.; Song, J.; Wang, X.; Dong, W. Calpain2 Upregulation Regulates EMT-Mediated Pancreatic Cancer Metastasis via the Wnt/ β -Catenin Signaling Pathway. *Front. Med.* **2022**, *9*, 783592. [CrossRef]
113. Liu, C.; Haijuan, F.; Liu, X.; Lei, Q.; Zhang, Y.; She, X.; Liu, Q.; Liu, Q.; Sun, Y.; Li, G.; et al. LINC00470 Coordinates the Epigenetic Regulation of ELFN2 to Distract GBM Cells Autophagy. *Mol. Ther.* **2018**, *26*, 2267–2281. [CrossRef] [PubMed]
114. Zhang, Y.Q.; Zhang, J.J.; Song, H.J.; Li, D.W. Overexpression of CST4 promotes gastric cancer aggressiveness by activating the ELFN2 signaling pathway. *Am. J. Cancer Res.* **2017**, *7*, 2290–2304. [PubMed]
115. Wang, B.; Yang, Y.; Friedman, P.A. Na/H Exchange Regulatory Factor 1, a Novel AKT-associating Protein, Regulates Extracellular Signal-regulated Kinase Signaling through a B-Raf-Mediated Pathway. *Mol. Biol. Cell* **2008**, *19*, 1637–1645. [CrossRef]

116. Crocarno, S.; Binato, R.; Santos, E.; de Paula, B.; Abdelhay, E. Translational Results of Zo-NANtax: A Phase II Trial of Neoadjuvant Zoledronic Acid in HER2-Positive Breast Cancer. *Int. J. Mol. Sci.* **2022**, *23*, 15515. [CrossRef] [PubMed]
117. Ma, Q.; Jiao, Y.; Hao, Y.; Yan, S.; Lyu, N.; Gao, H.; Li, D.; Liu, Q.; Zheng, J.; Song, N. Targeting of NHERF1 through RNA interference inhibits the proliferation and migration of metastatic prostate cancer cells. *Oncol. Lett.* **2016**, *11*, 1149–1154. [CrossRef] [PubMed]
118. Jia, Z.; Zhu, H.; Sun, H.; Hua, Y.; Zhang, G.; Jiang, J.; Wang, X. Adipose Mesenchymal Stem Cell-Derived Exosomal microRNA-1236 Reduces Resistance of Breast Cancer Cells to Cisplatin by Suppressing SLC9A1 and the Wnt/ β -Catenin Signaling. *Cancer Manag. Res.* **2020**, *12*, 8733–8744. [CrossRef]
119. Takahashi, Y.; Morales, F.C.; Kreimann, E.L.; Georgescu, M.-M. PTEN tumor suppressor associates with NHERF proteins to attenuate PDGF receptor signaling. *EMBO J.* **2006**, *25*, 910–920. [CrossRef]
120. Choi, C.H.; Chung, J.-Y.; Chung, E.J.; Sears, J.D.; Lee, J.-W.; Bae, D.-S.; Hewitt, S.M. Prognostic significance of annexin A2 and annexin A4 expression in patients with cervical cancer. *BMC Cancer* **2016**, *16*, 448. [CrossRef]
121. Yao, H.; Sun, C.; Hu, Z.; Wang, W. The role of annexin A4 in cancer. *Front. Biosci. Landmark Ed.* **2016**, *21*, 949–957. [PubMed]
122. Lin, L.-L.; Huang, H.-C.; Juan, H.-F. Revealing the Molecular Mechanism of Gastric Cancer Marker Annexin A4 in Cancer Cell Proliferation Using Exon Arrays. *PLoS ONE* **2012**, *7*, e44615. [CrossRef] [PubMed]
123. Wei, B.; Guo, C.; Liu, S.; Sun, M.Z. Annexin A4 and cancer. *Clin. Chim. Acta Int. J. Clin. Chem.* **2015**, *447*, 72–78. [CrossRef] [PubMed]
124. Yang, Y.F.; Lee, Y.C.; Wang, Y.Y.; Wang, C.H.; Hou, M.F.; Yuan, S.S.F. YWHAE promotes proliferation, metastasis, and chemoresistance in breast cancer cells. *Kaohsiung J. Med. Sci.* **2019**, *35*, 408–416. [CrossRef]
125. Gan, Y.; Ye, F.; He, X.-X. The role of YWHAZ in cancer: A maze of opportunities and challenges. *J. Cancer* **2020**, *11*, 2252–2264. [CrossRef]
126. Yu, C.C.; Li, C.F.; Chen, I.H.; Lai, M.T.; Lin, Z.J.; Korla, P.K.; Chai, C.Y.; Ko, G.; Chen, C.M.; Hwang, T. YWHAZ amplification/overexpression defines aggressive bladder cancer and contributes to chemo-/radio-resistance by suppressing caspase-mediated apoptosis. *J. Pathol.* **2019**, *248*, 476–487. [CrossRef]
127. Liu, J.; Yang, X.; Ji, Q.; Yang, L.; Li, J.; Long, X.; Ye, M.; Huang, K.; Zhu, X. Immune Characteristics and Prognosis Analysis of the Proteasome 20S Subunit Beta 9 in Lower-Grade Gliomas. *Front. Oncol.* **2022**, *12*, 875131. [CrossRef]
128. Hayashi, T.; Horiuchi, A.; Sano, K.; Hiraoka, N.; Kasai, M.; Ichimura, T.; Sudo, T.; Tagawa, Y.-I.; Nishimura, R.; Ishiko, O.; et al. Potential role of LMP2 as tumor-suppressor defines new targets for uterine leiomyosarcoma therapy. *Sci. Rep.* **2011**, *1*, 180. [CrossRef]
129. Tian, T.; Li, X.; Zhang, J. mTOR Signaling in Cancer and mTOR Inhibitors in Solid Tumor Targeting Therapy. *Int. J. Mol. Sci.* **2019**, *20*, 755. [CrossRef]
130. Guo, Y.J.; Pan, W.W.; Liu, S.B.; Shen, Z.F.; Xu, Y.; Hu, L.L. ERK/MAPK signalling pathway and tumorigenesis. *Exp. Ther. Med.* **2020**, *19*, 1997–2007. [CrossRef]
131. Rascio, F.; Spadaccino, F.; Rocchetti, M.T.; Castellano, G.; Stallone, G.; Netti, G.S.; Ranieri, E. The Pathogenic Role of PI3K/AKT Pathway in Cancer and Drug Resistance: An Updated Review. *Cancers* **2021**, *13*, 3949. [CrossRef] [PubMed]
132. Zhang, Y.; Wang, X. Targeting the Wnt/ β -catenin signaling pathway in cancer. *J. Hematol. Oncol.* **2020**, *13*, 165. [CrossRef]
133. Xia, L.; Tan, S.; Zhou, Y.; Lin, J.; Wang, H.; Oyang, L.; Tian, Y.; Liu, L.; Su, M.; Wang, H.; et al. Role of the NF κ B-signaling pathway in cancer. *OncoTargets Ther.* **2018**, *11*, 2063–2073. [CrossRef] [PubMed]
134. Madden, E.; Logue, S.E.; Healy, S.J.; Manie, S.; Samali, A. The role of the unfolded protein response in cancer progression: From oncogenesis to chemoresistance. *Biol. Cell* **2019**, *111*, 1–17. [CrossRef] [PubMed]
135. Alrefaei, A.F.; Abu-Elmagd, M. LRP6 Receptor Plays Essential Functions in Development and Human Diseases. *Genes* **2022**, *13*, 120. [CrossRef]
136. Gomes, A.P.; Ilter, D.; Low, V.; Drapela, S.; Schild, T.; Mullarky, E.; Han, J.; Elia, I.; Broekaert, D.; Rosenzweig, A.; et al. Altered propionate metabolism contributes to tumour progression and aggressiveness. *Nat. Metab.* **2022**, *4*, 435–443. [CrossRef]
137. Grasmann, G.; Smolle, E.; Olschewski, H.; Leithner, K. Gluconeogenesis in cancer cells—Repurposing of a starvation-induced metabolic pathway? *Biochim. Biophys. Acta BBA-Rev. Cancer* **2019**, *1872*, 24–36. [CrossRef]
138. Li, X.; Han, M.; Zhang, H.; Liu, F.; Pan, Y.; Zhu, J.; Liao, Z.; Chen, X.; Zhang, B. Structures and biological functions of zinc finger proteins and their roles in hepatocellular carcinoma. *Biomark. Res.* **2022**, *10*, 2. [CrossRef]
139. Ma, R.; Ji, T.; Zhang, H.; Dong, W.; Chen, X.; Xu, P.; Chen, D.; Liang, X.; Yin, X.; Liu, Y.; et al. A Pck1-directed glycogen metabolic program regulates formation and maintenance of memory CD8⁺ T cells. *Nat. Cell Biol.* **2018**, *20*, 21–27. [CrossRef] [PubMed]
140. Kennedy, L.; Sandhu, J.K.; Harper, M.-E.; Cuperlovic-Culf, M. Role of Glutathione in Cancer: From Mechanisms to Therapies. *Biomolecules* **2020**, *10*, 1429. [CrossRef]
141. Halama, A.; Suhre, K. Advancing Cancer Treatment by Targeting Glutamine Metabolism—A Roadmap. *Cancers* **2022**, *14*, 553. [CrossRef]
142. Altman, B.J.; Stine, Z.E.; Dang, C.V. From Krebs to clinic: Glutamine metabolism to cancer therapy. *Nat. Rev. Cancer* **2016**, *16*, 619–634. [PubMed]
143. Liu, M.-X.; Jin, L.; Sun, S.-J.; Liu, P.; Feng, X.; Cheng, Z.-L.; Liu, W.-R.; Guan, K.-L.; Shi, Y.-H.; Yuan, H.-X.; et al. Metabolic reprogramming by PCK1 promotes TCA cataplerosis, oxidative stress and apoptosis in liver cancer cells and suppresses hepatocellular carcinoma. *Oncogene* **2018**, *37*, 1637–1653. [CrossRef]

144. Millward, C.A.; DeSantis, D.; Hsieh, C.-W.; Heaney, J.D.; Pisano, S.; Olswang, Y.; Reshef, L.; Beidelschies, M.; Puchowicz, M.; Croniger, C.M. Phosphoenolpyruvate carboxykinase (Pck1) helps regulate the triglyceride/fatty acid cycle and development of insulin resistance in mice. *J. Lipid Res.* **2010**, *51*, 1452–1463. [CrossRef]
145. Leithner, K.; Triebel, A.; Trötz Müller, M.; Hinteregger, B.; Leko, P.; Wieser, B.I.; Grasmann, G.; Bertsch, A.L.; Züllig, T.; Stacher, E.; et al. The glycerol backbone of phospholipids derives from noncarbohydrate precursors in starved lung cancer cells. *Proc. Natl. Acad. Sci. USA* **2018**, *115*, 6225–6230. [CrossRef] [PubMed]
146. Sadria, M.; Layton, A.T. Interactions among mTORC, AMPK and SIRT: A computational model for cell energy balance and metabolism. *Cell Commun. Signal.* **2021**, *19*, 57. [CrossRef] [PubMed]
147. Hsu, C.-C.; Peng, D.; Cai, Z.; Lin, H.-K. AMPK signaling and its targeting in cancer progression and treatment. *Semin. Cancer Biol.* **2022**, *85*, 52–68.
148. Penugurti, V.; Mishra, Y.G.; Manavathi, B. AMPK: An odyssey of a metabolic regulator, a tumor suppressor, and now a contextual oncogene. *Biochim. Biophys. Acta BBA-Rev. Cancer* **2022**, *1877*, 188785. [CrossRef]
149. Furukawa, F.; Tseng, Y.-C.; Liu, S.-T.; Chou, Y.-L.; Lin, C.-C.; Sung, P.-H.; Uchida, K.; Lin, L.-Y.; Hwang, P.-P. Induction of Phosphoenolpyruvate Carboxykinase (PEPCK) during Acute Acidosis and Its Role in Acid Secretion by V-ATPase-Expressing Ionocytes. *Int. J. Biol. Sci.* **2015**, *11*, 712–725. [CrossRef]
150. Yu, S.; Meng, S.; Xiang, M.; Ma, H. Phosphoenolpyruvate carboxykinase in cell metabolism: Roles and mechanisms beyond gluconeogenesis. *Mol. Metab.* **2021**, *53*, 101257. [CrossRef]

Disclaimer/Publisher's Note: The statements, opinions and data contained in all publications are solely those of the individual author(s) and contributor(s) and not of MDPI and/or the editor(s). MDPI and/or the editor(s) disclaim responsibility for any injury to people or property resulting from any ideas, methods, instructions or products referred to in the content.

Article

Comparative Analysis of Amino Acid Profiles in Patients with Glioblastoma and Meningioma Using Liquid Chromatography Electrospray Ionization Tandem Mass Spectrometry (LC-ESI-MS/MS)

Piotr Kośliński ^{1,*} , Robert Pluskota ¹ , Marcin Koba ¹ , Zygmunt Siedlecki ² and Maciej Śniegocki ²

¹ Department of Toxicology and Bromatology, Collegium Medicum in Bydgoszcz, Nicolaus Copernicus University in Toruń, dr. A. Jurasza 2, 85-089 Bydgoszcz, Poland; pluskota.r@gmail.com (R.P.); kobamar@cm.umk.pl (M.K.)

² Department of Neurosurgery, Neurotraumatology and Pediatric Neurosurgery, Collegium Medicum in Bydgoszcz, Nicolaus Copernicus University in Toruń, 85-094 Bydgoszcz, Poland; siedlecki@cm.umk.pl (Z.S.); sniegocki@cm.umk.pl (M.Ś.)

* Correspondence: piotr.koslinski@cm.umk.pl

Abstract: Brain tumors account for 1% of all cancers diagnosed de novo. Due to the specificity of the anatomical area in which they grow, they can cause significant neurological disorders and lead to poor functional status and disability. Regardless of the results of biochemical markers of intracranial neoplasms, they are currently of no diagnostic significance. The aim of the study was to use LC-ESI-MS/MS in conjunction with multivariate statistical analyses to examine changes in amino acid metabolic profiles between patients with glioblastoma, meningioma, and a group of patients treated for osteoarthritis of the spine as a control group. Comparative analysis of amino acids between patients with glioblastoma, meningioma, and the control group allowed for the identification of statistically significant differences in the amino acid profile, including both exogenous and endogenous amino acids. The amino acids that showed statistically significant differences (lysine, histidine, α -amino adipic acid, phenylalanine) were evaluated for diagnostic usefulness based on the ROC curve. The best results were obtained for phenylalanine. Classification trees were used to build a model allowing for the correct classification of patients into the study group (patients with glioblastoma multiforme) and the control group, in which cysteine turned out to be the most important amino acid in the decision-making algorithm. Our results indicate amino acids that may prove valuable, used alone or in combination, toward improving the diagnosis of patients with glioma and meningioma. To better assess the potential utility of these markers, their performance requires further validation in a larger cohort of samples.

Keywords: glioblastoma; meningioma; amino acid; biomarkers; LC-MS



Citation: Kośliński, P.; Pluskota, R.; Koba, M.; Siedlecki, Z.; Śniegocki, M. Comparative Analysis of Amino Acid Profiles in Patients with Glioblastoma and Meningioma Using Liquid Chromatography Electrospray Ionization Tandem Mass Spectrometry (LC-ESI-MS/MS). *Molecules* **2023**, *28*, 7699. <https://doi.org/10.3390/molecules28237699>

Academic Editors: Xianjiang Li and Wen Ma

Received: 4 October 2023

Revised: 20 November 2023

Accepted: 21 November 2023

Published: 22 November 2023



Copyright: © 2023 by the authors. Licensee MDPI, Basel, Switzerland. This article is an open access article distributed under the terms and conditions of the Creative Commons Attribution (CC BY) license (<https://creativecommons.org/licenses/by/4.0/>).

1. Introduction

Intracranial neoplasms account for 2% of cancers, and deaths during these cancers account for 3% of all cancer deaths worldwide. Gliomas are among the most common CNS neoplasms and the most common primary malignant tumors. From a practical point of view, glial tumors are divided into low-grade gliomas (LGGs) and high-grade gliomas (HGGs) [1–5]. LGGs are diagnosed in the younger age group and grow slowly, but usually infiltratively. They are most often located within the temporal and frontal lobes and within the insula. The median survival time from diagnosis is seven years [6–8]. An HGG, in turn, is much more common in older people who are most often diagnosed with GBM (grade 4 according to the WHO). GBM is an aggressive tumor that grows dynamically and leads to a progressive decline in neurological performance. The average survival of patients with an HGG is 16 to 36 months [4,5,9].

Meningiomas are the most common primary intracranial neoplasms. Most often, meningiomas are solitary intracranial tumors that arise without obvious risk factors. However, possible factors contributing to the development of meningiomas include radiation therapy, inflammation, intracranial trauma, and hormonal disorders [10–12].

Clinical symptoms of intracranial tumors have a twofold pathophysiological basis. Firstly, they result from increased intracranial pressure (ICP) and are non-specific, and secondly, they are related to the location of the lesion and depend on the neural centers and tracts occupied or compressed by the tumor. The most common symptom of all intracranial tumors is progressive neurological deficit [13,14].

The emergence and development of intracranial tumors are conditioned by genetic, molecular, cellular, and biochemical mechanisms. As in the case of any carcinogenesis, including CNS tumors, their growth is a multi-stage process underpinned by genetic mutations [15].

Imaging tests (MRI, CT) are the basic method of monitoring the course and treatment of brain tumors, while biochemical markers determined in urine and body fluids have limited use so far. Previous studies indicate the possibility of using various compounds as potential biomarkers in CNS tumors, such as interleukins [16,17], the S100 Protein Superfamily [18–22], proteins reacting in the acute phase and other markers of inflammatory proteins [19,22–25], and panels of peptides and proteins [24,26,27]. Despite many studies, none of the biomarkers are ready for direct clinical implementation. A key criterion for the potential clinical value of a candidate cancer biomarker is the consistency and strength of the association between the biomarker and the treatment outcome or disease of interest and the extent to which this represents a diagnostic improvement over methods already in use. The intensity of work on potential biomarkers of CNS tumors is reflected in the number of scientific works, the summary and critical analysis of which can be found in review works [28–30].

Metabolomics is a complementary approach to genomics and proteomics focused on the comprehensive profiling of all small molecular weight metabolites in biofluids, tissues, and cells. Metabolomics approaches can be targeted or non-targeted. Untargeted metabolomics focuses on the unbiased, hypothesis-free analysis of all detectable metabolites from a biological sample. Although this approach allows for the identification of a large pool of potentially relevant metabolites, the approach often represents a trade-off between specificity, selectivity, and analysis time. Targeted metabolomics refers to the quantitative measurement of a select group of metabolites (e.g., amino acids) in order to investigate specific metabolic pathways or validate biomarkers identified using non-targeted metabolic profiling. Once a potentially relevant metabolic pathway has been identified using an untargeted approach, targeted metabolic profiling appears advisable to increase the number of metabolites associated with that particular pathway [31,32].

A wide range of analytical techniques are available for the qualitative and quantitative determination of metabolites; however, the most commonly used analytical techniques in cancer metabolomics are MS and NMR spectroscopy.

NMR spectroscopy is a quantitative, high-throughput technology that provides both qualitative and quantitative information, making it a useful tool in metabolomics research. Despite the many advantages of NMR spectroscopy, due to its relatively low sensitivity and poor dynamic range, it is not suitable for the detection of metabolites present in trace amounts. Most metabolomics studies of brain tumors are based on NMR spectroscopy, which allows for the observation of changes in metabolism related to tumor development and differentiation of the degree of malignancy [31–35].

Mass spectrometry (MS) provides a valuable analytical platform for metabolomics due to its high sensitivity and wide dynamic range. With the dissemination of this technology to routine medical laboratories, it has become possible to measure low molecular weight metabolites for diagnostic purposes. The use of LC-MS/MS methods for small molecules in biological fluids is becoming increasingly preferred because they have higher sensitivity and better reliability in complex biological fluids. Recent studies have shown that the use

of metabolomic analysis with mass spectrometry detection allowed the identification of biomarkers differentiating patients with CNS tumors from healthy people or enabling the differentiation of low- and high-grade tumors [34,36–41].

There are several ways to assess changes in the metabolome in patients with CNS tumors: through the metabolome of plasma collected from an antecubital vein or the metabolomic analysis of blood collected from resected tumor tissue or cerebrospinal fluid [31,32,38–40,42]. Griffin et al.'s review summarizes progress in the field of human brain tumor metabolomics research using tissue sections using both *ex vivo* and *in vivo* approaches [43]. Another approach to assessing changes in metabolism was presented in the work of Xiong et al., who used the method of collecting intraoperative blood samples from the artery located directly above the brain tumor and the vein located directly behind the brain tumor [44].

Amino acids (AAs) are the building blocks of various biomacromolecules, as well as functional regulators of various metabolic processes. The altered metabolism of AAs promotes the proliferation of tumors and contribute to their immune escape and resistance to treatment. From a clinical point of view, it is estimated that changes in amino acid concentrations observed in specific body fluids provide the opportunity to develop new diagnostic and prognostic markers [45,46]. Early diagnostic blood markers are biomarkers that can be used to predict the development of cancer in an individual, many years before clinical or radiological signs are noticed. These markers can be useful for screening patients at risk. A prognostic biomarker is defined as a clinical or biological characteristic that provides information on the most probable patient health outcome irrespective of the treatment [29].

The aim of the study is to evaluate the potential of targeted dual-control serum amino acid metabolomics analysis in the diagnosis of patients with glioma and meningioma. In pilot studies, other groups have explored the use of a metabolomics approach to distinguish patients with glioblastoma and meningioma from healthy controls. However, to the best of our knowledge, no metabolomics study based on targeted amino acid analysis has attempted to remove the confounding effects of common pathophysiology, such as a generalized immune response.

The present study used high-performance liquid chromatography–mass spectrometry (HPLC-MS) coupled with multivariate statistical analyses to accurately identify unique changes in amino acid metabolomic profiles that distinguish glioma patients from meningioma patients and other diseases that may be associated with overall inflammation, e.g., degenerative spine disease.

2. Results

2.1. Comparison of the Control Group and Cancer Patients

The first stage of the study was to compare amino acid concentrations between patients diagnosed with glioblastoma and the control group. A comparative analysis of the analyzed AAs between patients with glioblastoma and the control group allowed the identification of statistically significant differences between the study groups. Statistically significant differences were observed both among endogenous (Figure 1) and exogenous (Figure 2) amino acids.

Among endogenous AAs, statistically significant differences concerned SER ($p = 0.002245$), ARG ($p = 0.009292$), CIT ($p = 0.000000$), ASN ($p = 0.000939$), GLY ($p = 0.017846$), GABA ($p = 0.000000$), SAR ($p = 0.019362$), ABA ($p = 0.001831$), ORN ($p = 0.000012$), and ASP ($p = 0.000214$).

In the case of exogenous amino acids, statistically significant differences were observed for THR ($p = 0.000032$), MET ($p = 0.000190$), LYS ($p = 0.000000$), HIS ($p = 0.000011$), AAA ($p = 0.000021$), LEU ($p = 0.036077$), PHE ($p = 0.000001$), ILE ($p = 0.000728$), C-C ($p = 0.000037$), and TYR ($p = 0.000007$).

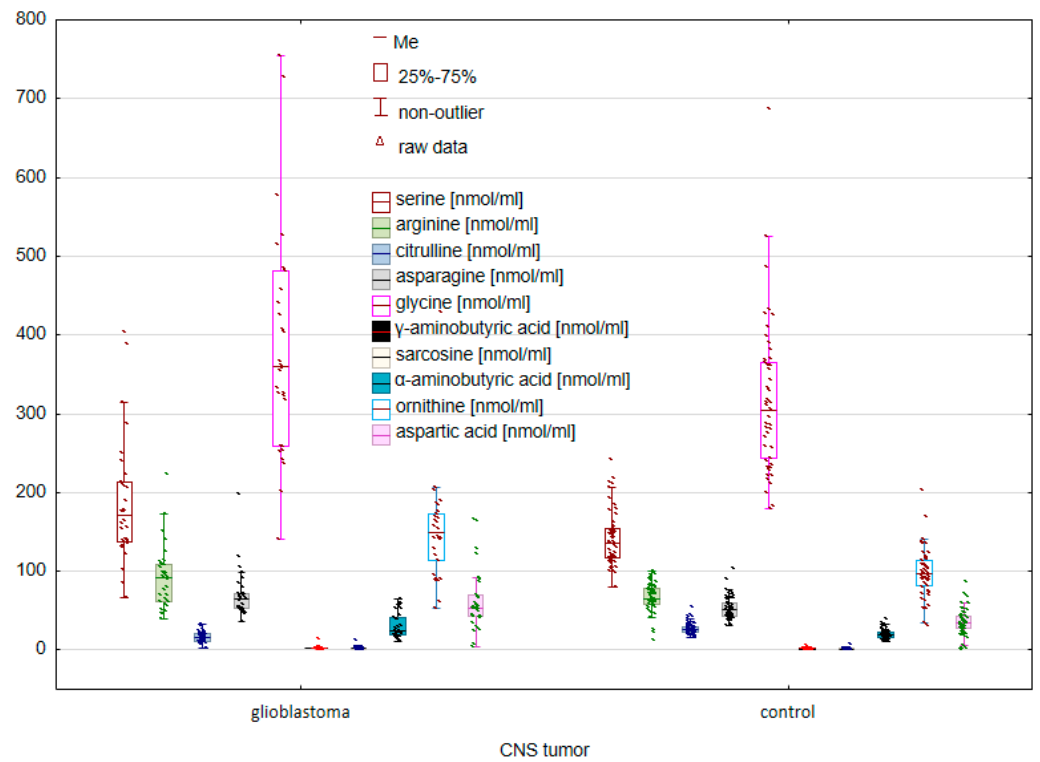


Figure 1. Comparison of endogenous AAs between controls and cancer patients with glioblastoma.

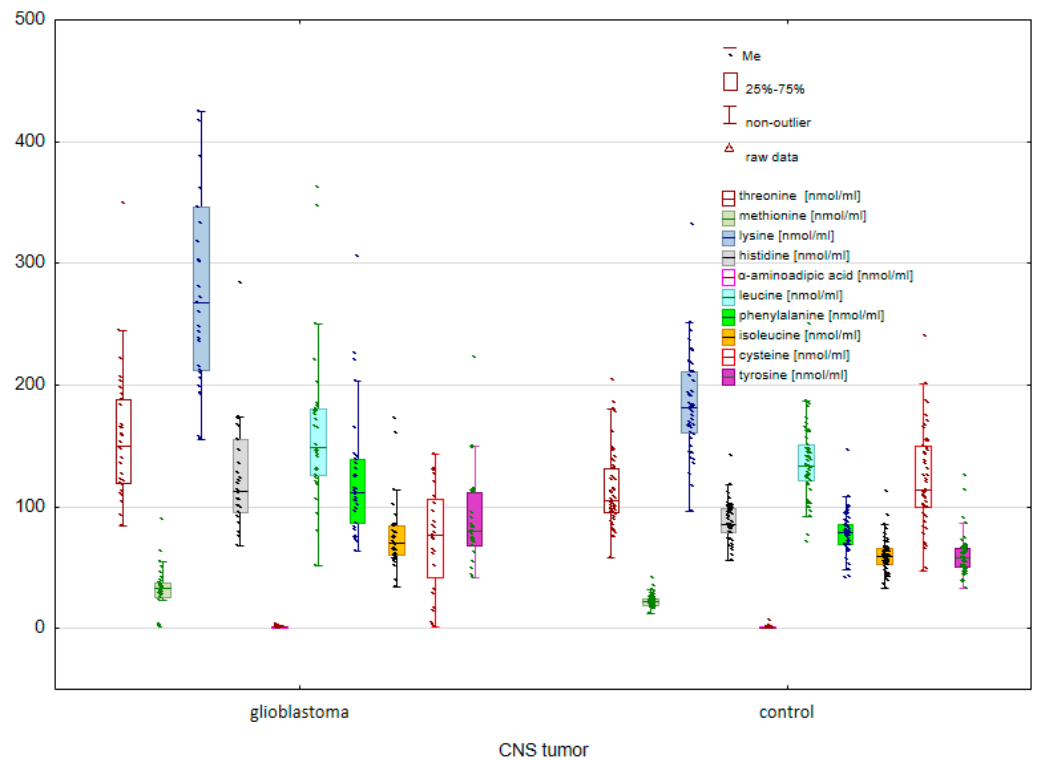


Figure 2. Comparison of exogenous AAs between controls and cancer patients with glioblastoma.

In the next stage, the concentrations of the tested amino acids were compared between the group of patients with meningioma and the control group. The U Mann–Whitney U test allowed us to identify statistically significant differences between the study groups (Figures 3 and 4).

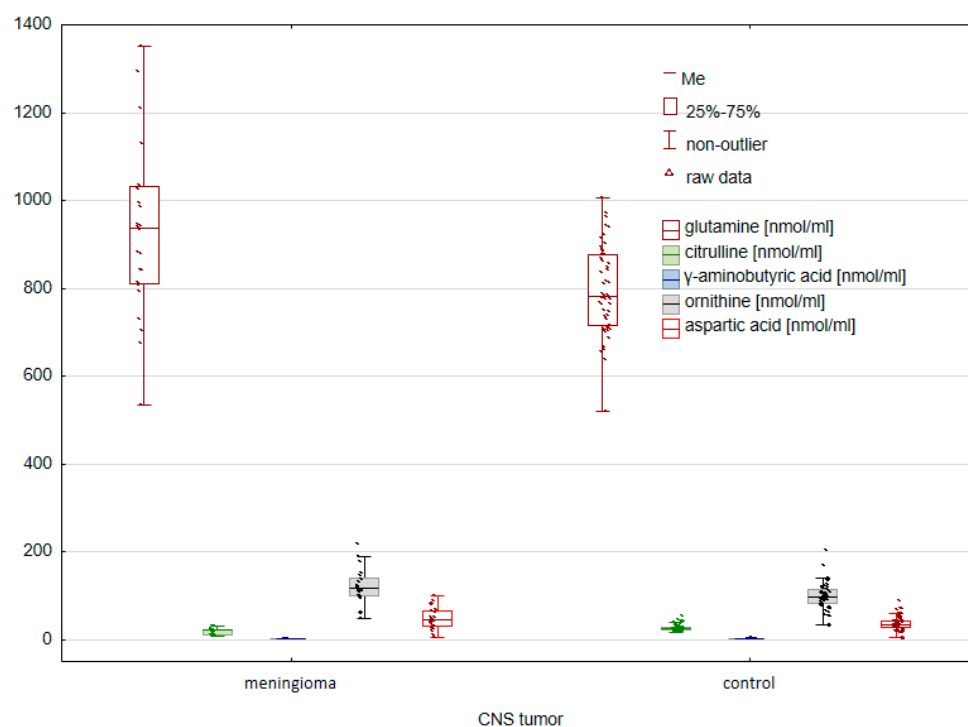


Figure 3. Comparison of endogenous AAs between controls and cancer patients with meningioma.

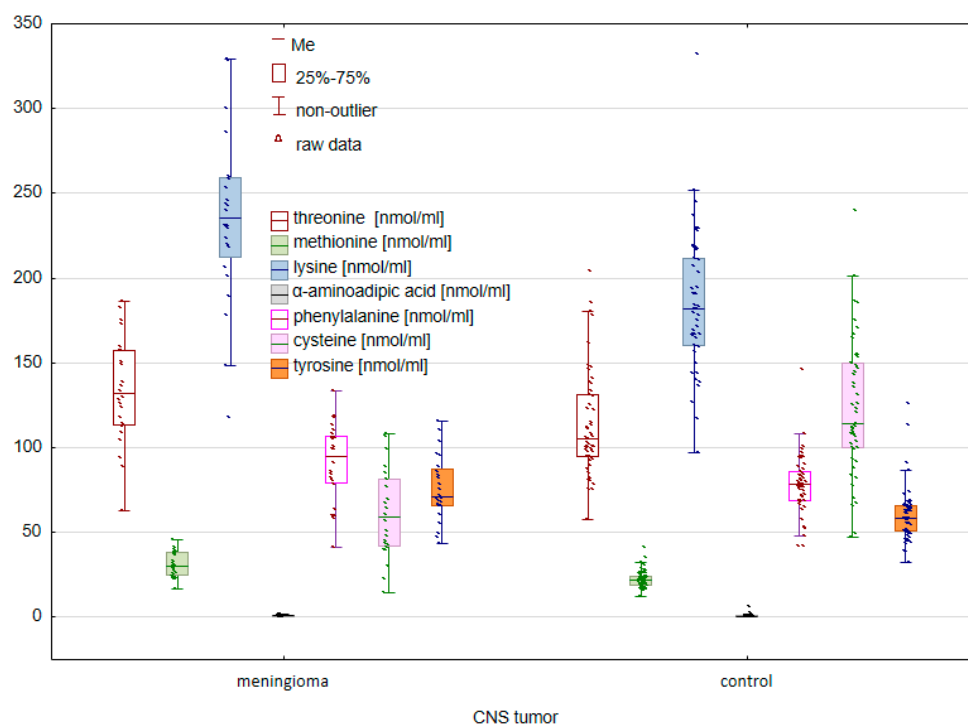


Figure 4. Comparison of exogenous AAs between controls and cancer patients with meningioma.

In the case of endogenous amino acids, significant differences were found for GLN ($p = 0.001167$), CIT ($p = 0.000028$), GABA ($p = 0.000145$), ORN ($p = 0.005893$), and ASP ($p = 0.049001$). A comparison of the group of patients with glioma and the control group also allowed for the confirmation of statistically significant differences for such exogenous amino acids such as THR ($p = 0.005100$), MET ($p = 0.000003$), LYS ($p = 0.000019$), AAA ($p = 0.007040$), PHE ($p = 0.007552$), C-C ($p = 0.000000$), and TYR ($p = 0.000349$).

To eliminate the influence of the variability related to the sex of the studied groups on the observed differences in amino acid concentrations, a comparison was made taking into account the division by sex. The obtained results made it possible to isolate those amino acids for which statistically significant differences were found between the study group of cancer patients and the control group, both in the group of women and men.

When comparing the group of patients with glioblastoma with the control group, statistically significant differences after post hoc analysis were observed for lysine, histidine, α -aminoadipic acid, and phenylalanine (Table 1). In the case of meningioma patients, compared to the control group, statistically significant differences in the group of women and men were observed only for lysine (women p -value = 0.0032; men p -value = 0.0120). Figures 5–8 illustrate the observed differences for amino acids with statistically significant differences, both in the group of men and women.

Table 1. Statistically significant differences between cancer group glioblastoma and the control in with regard to sex.

Compounds	Women p -Value	Men p -Value
lysine	0.0059	0.0000
histidine	0.0250	0.0004
α -aminoadipic acid	0.0026	0.0060
phenylalanine	0.0088	0.0001

In Figure 5, the highest lysine concentration can be observed in glioma patients compared to the controls and meningioma patients. Similar relationships of amino acid concentrations (i.e., the highest in patients with glioma and the lowest in the control group) between the studied groups can be observed in the case of histidine (Figure 6) and phenylalanine (Figure 7).

Only in the case of α -aminoadipic acid was the concentration of this amino acid higher in the group of men in patients with meningioma compared to the group with glioma and the control group (Figure 8).

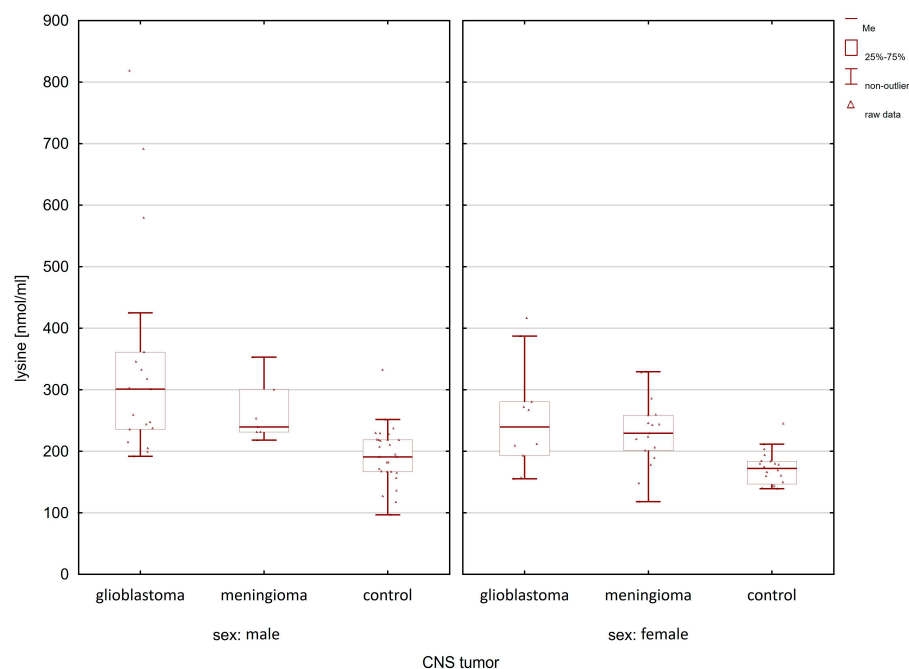


Figure 5. Comparison of lysine concentrations between glioma patients, meningioma patients, and the control group in the male and female group.

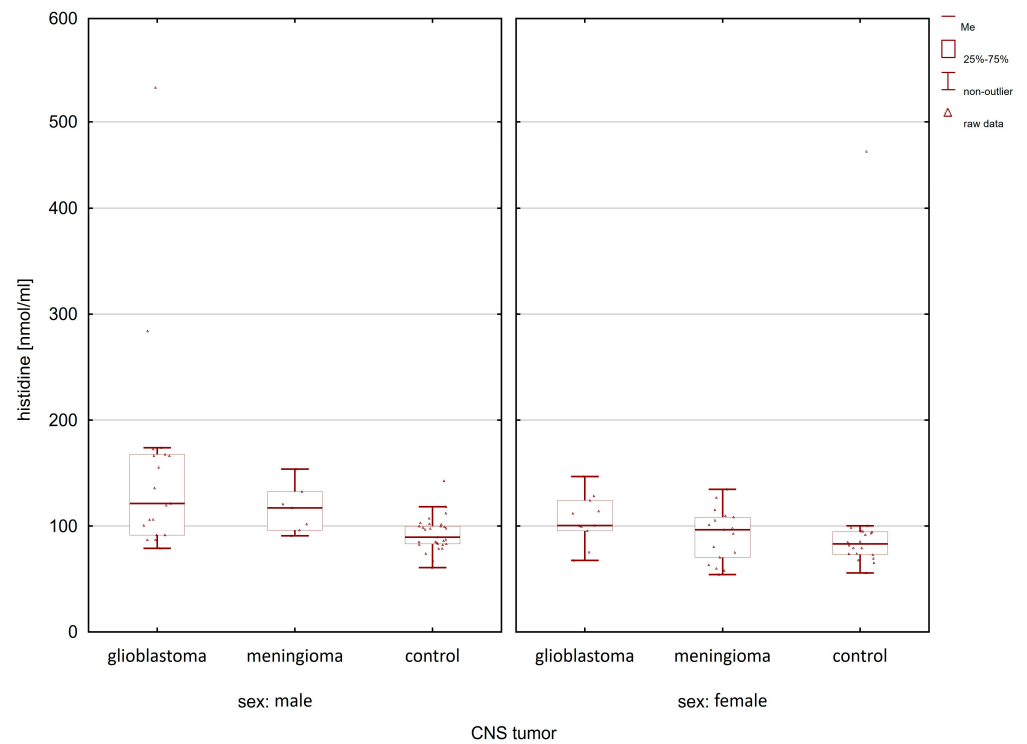


Figure 6. Comparison of histidine concentrations between glioma patients, meningioma patients, and the control group in the male and female group.

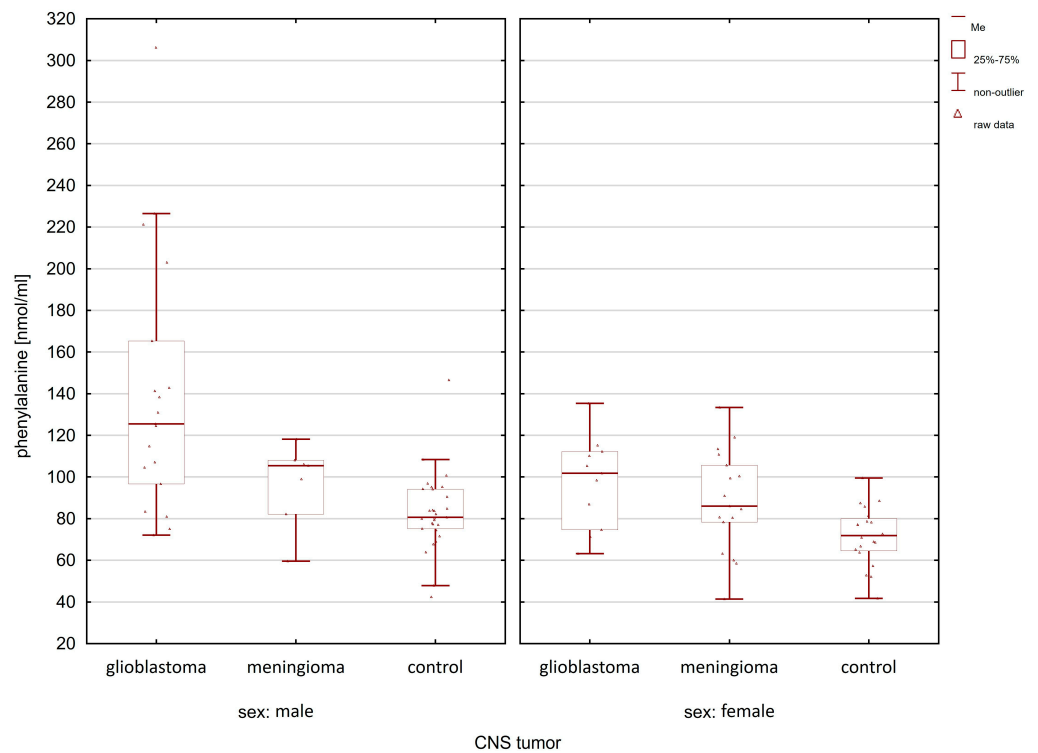


Figure 7. Comparison of phenylalanine concentrations between glioma patients, meningioma patients, and the control group in the male and female group.

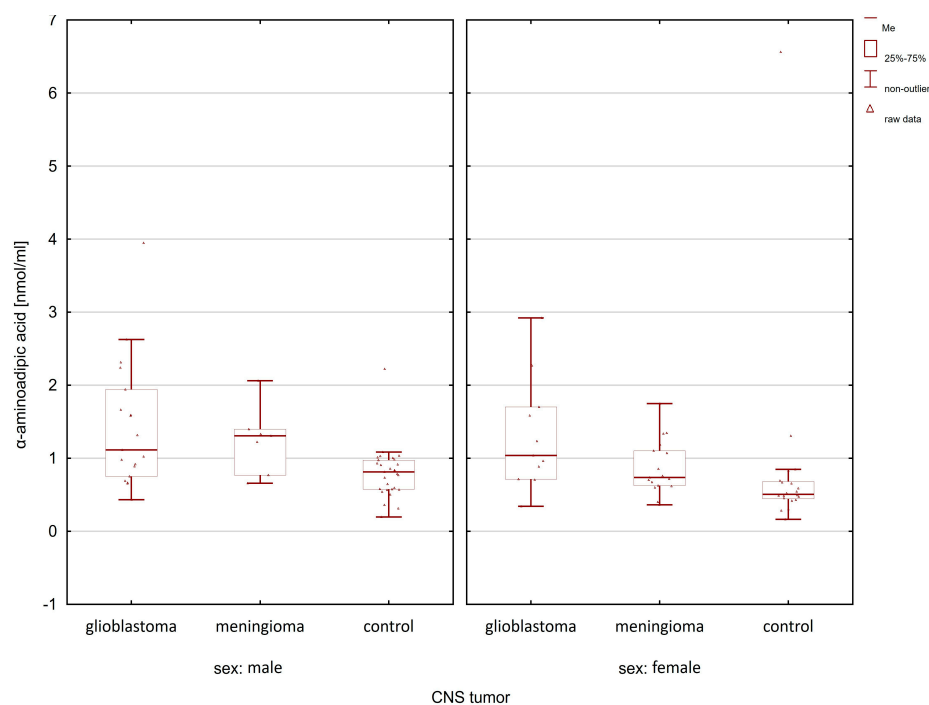


Figure 8. Comparison of α -aminoadipic acid concentrations between glioma patients, meningioma patients, and the control group in the male and female group.

2.2. Classification Analysis

2.2.1. Receiver Operating Characteristic Curves

The next part of the analysis started to build a classification model that will classify patients as healthy or suffering from glioblastoma of the CNS with the highest efficiency. Receiver operating characteristic (ROC) analysis is a useful tool for evaluating the accuracy of a model's prediction by plotting the sensitivity versus (1-specificity) a classification test. The model of the classification of patients into the group with glioblastoma and the control group included those AAs in which statistically significant differences were found between the study group and the control group, both in the group of women and men. Visualizations of the obtained results are presented in Figure 9.

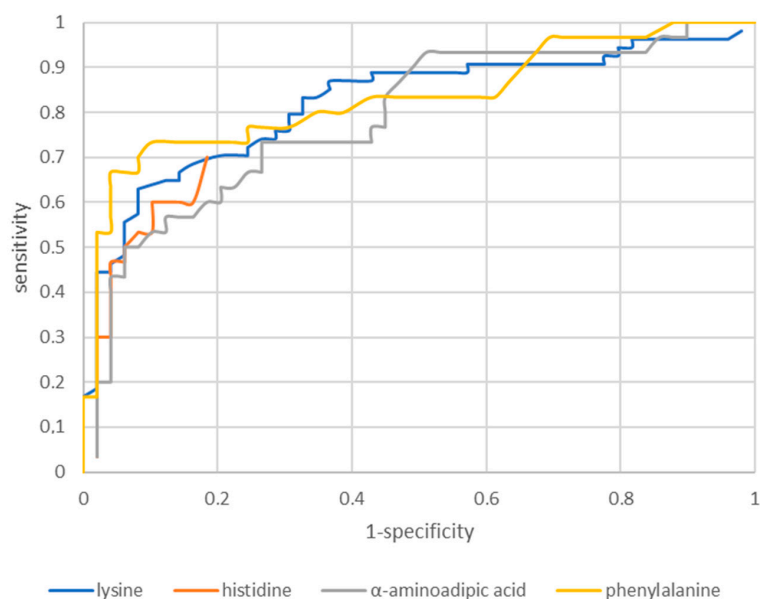


Figure 9. Visualizations of sensitivity and the specific model of ROC analysis.

Then, the accuracy of the model was assessed in relation to the concentration of the analyzed amino acids. The obtained results are illustrated in Figure 10.

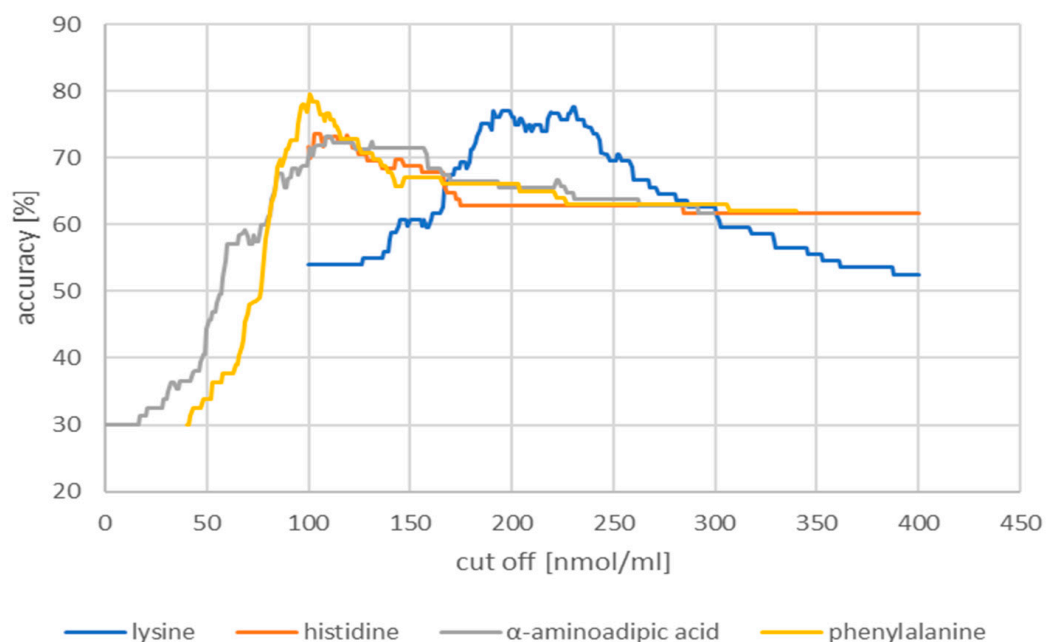


Figure 10. Visualizations of the accuracy model of ROC analysis.

The obtained cut-off, accuracy, sensitivity, and specificity values of the tested amino acids obtained using the ROC curve are summarized in Table 2.

Table 2. Classification parameters of a model based on the ROC.

	Cut-off (nmol/mL)	Accuracy (%)	Sensitivity (%)	Specificity (%)
Lysine	230.00	77.7	63.0	91.8
Histidine	103.00	73.7	60.0	89.8
α -aminoadipic acid	1.09	73.2	50.0	91.8
Phenylalanine	101.00	79.5	66.7	95.9

2.2.2. Decision Trees

The analysis was aimed at showing which amino acids would allow for a better classification of patients into a group with glioblastoma and a control group of healthy people. Classification trees are used to build predictive models (predicting subsequent data based on the model based on previously provided information) and descriptive models. The significance plot of the model variables based on standardized data primarily indicates the concentration of cysteine, citrulline, and glutamine (Figure 11).

Importantly, the use of a model based on the above parameters gives a much better chance of correctly diagnosing a person with glioblastoma than diagnosing the same cancer in a healthy person (Figure 12).

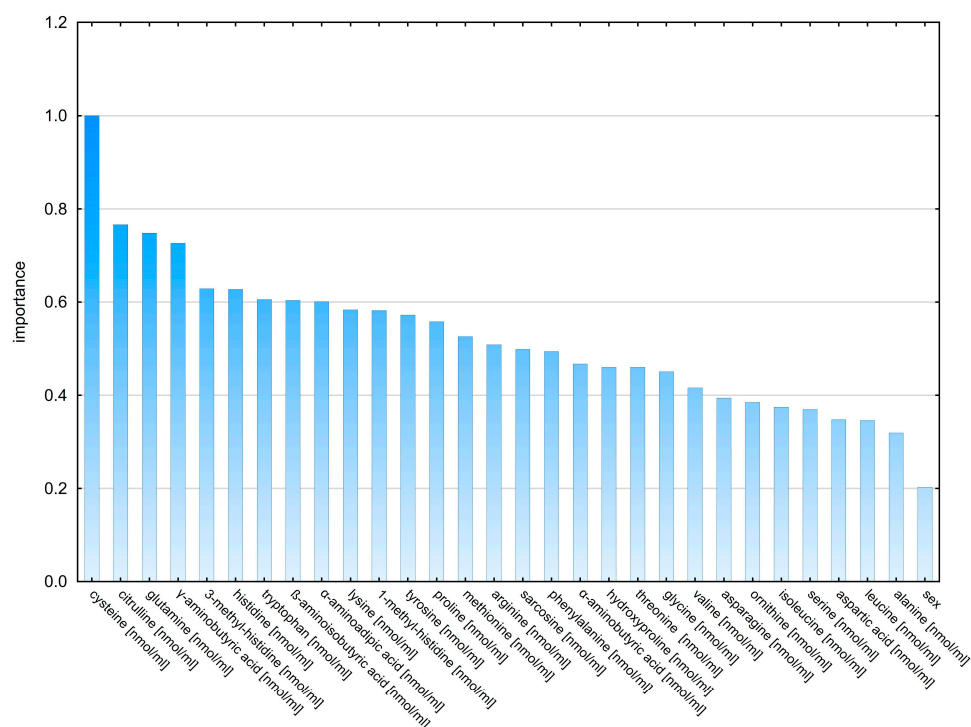


Figure 11. Graph of the validity of model variables based on aggregated data.

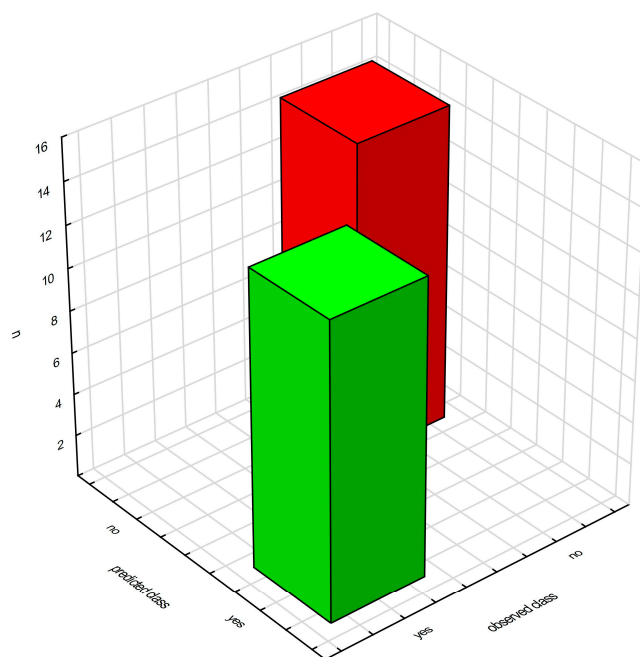


Figure 12. Matrix of patient classification made by a model based on aggregated data. Green—glioma patients correctly classified. Red—control group classified as healthy.

3. Discussion

Many research projects focus on finding prognostic or diagnostic biomarkers for central nervous system tumors, including meningiomas and gliomas. Currently, classical metabolic pathways such as the citric acid cycle (TCA), glycolysis, and arachidonic acid/inflammatory pathway have been well-studied in glioma. However, in recent years, attention has also been paid to understanding new metabolic changes in glioma cells, such as metabolic changes in IDH mutant cells, amino acid metabolism, or nucleotide metabolism. Many

characteristic metabolites have been discovered in glioma, such as 2-HG, fumaric acid, succinic acid, sarcosine, glycine, glutamine, aspartic acid, choline, serine, glucose, lactic acid, and polyamines, which suggest the dysregulation of multiple metabolic pathways (e.g., glycolysis, TCA, glutaminolysis, pentose phosphate pathway, fatty acid metabolism, amino acid metabolism) [34,36,37,47–51].

This study was designed to evaluate changes in amino acid profiles between patients with glioblastoma, meningioma, and the control group. Available studies indicate that dysregulated AA metabolism is not characteristic of a given type of cancer. The selection of the study groups (glioblastoma vs. meninges vs. a group of patients treated for osteoarthritis of the spine as a control group) was aimed at capturing possible differences in the profiles of the tested amino acids, depending on the type of cancer.

The conducted analysis allowed the observation of statistically significant differences between the study groups. When we compare the changes in the amino acid profiles of the glioblastoma and meningioma patients to the controls, we can see a group of amino acids that differ in both cases. This applies to endogenous amino acids (CIT, GABA, ORN, ASP) and exogenous (THR, MET, LYS, AAA, PHE, C-C, and TYR). In the case of glioblastoma, we observe additional amino acids differentiating the study group and the control group, including SER, ARG, ASN, GLY, SAR, and ABA. This points to a more altered amino acid metabolism in the glioblastoma group. In the case of meningioma, attention is paid to glutamine, whose elevated concentration is observed in comparison with the control group. In patients with glioblastoma, these differences are not statistically significant. In most cases, we observe a higher concentration of amino acids in groups of cancer patients compared to the control group. Lower concentrations were observed with cysteine, the concentration of which is statistically significantly lower in patients with glioblastoma compared to the control group. In turn, the concentration of cysteine is reduced in both glioblastoma and meningioma patients compared to the control group.

The biomarker should be resistant to inter- and intra-individual factors, such as gender. Therefore, in the proposed study, the study groups of both cancer patients and the control group were divided by gender. Among the compounds that showed statistically significant differences, only lysine, histidine, α -amino adipic acid, and phenylalanine differentiated patients with glioblastoma from healthy ones both in the group of men and women. In patients with meningioma, differences in the group of men and women concerned only lysine.

The AAs that showed statistically significant differences were evaluated for diagnostic usefulness. The diagnostic usefulness of AAs determined in the identification of glioblastoma was assessed based on the ROC curve with the proposed cut-off point and area under the AUC curve. Sensitivity, specificity, and accuracy are given for the designated cut-off points. The best results were obtained for phenylalanine. The ROC graph for phenylalanine showed a sensitivity of 66.7%, a specificity of 95.9%, and an accuracy of 79.5% for the proposed cut-off of 101.00 nmol/mL. The other analyzed amino acids were characterized by similar parameters of lysine (cut-off point 230 nmol/mL, sensitivity 77.7%, specificity 63%, accuracy 91.8%), histidine (cut-off point 103 nmol/mL, sensitivity 73.7%, specificity 60%, accuracy 89.8%), and α -amino adipic acid (cut-off 1.09 nmol/mL, sensitivity 73.2%, specificity 50%, accuracy 91.8%).

In the next stage of the research, classification trees were used, which allowed us to build a model allowing for the correct classification of patients into the study group (patients with glioblastoma) and the control group (healthy individuals) (Figure 11). Cysteine turned out to be the most important amino acid in the decision-making algorithm, followed by a group of three amino acids (citrulline, glutamine, γ -aminobutyric acid).

Analyzing the results of our research, it seems that the most important amino acids in terms of diagnostic decisions are lysine, amino adipic acid, histidine, and phenylalanine. The higher concentration of lysine observed in our study in patients with glioma and meningioma, considering the division by gender, was also observed in patients with head and neck cancers and sarcoma [52–54]. Toklu et al. found high levels of serum lysine in

high-grade glioma patients [55]. Mören et al. observed that serum lysine levels of high-grade glioma patients decreased during radiotherapy when the disease is indolent [56]. It is worth noting that in patients with glioblastoma, we also found statistically significantly higher concentrations of amino adipic acid, which is a poorly characterized product of lysine degradation and may appear in the circulation because of the degradation of whole tissue or plasma proteins. The ϵ -amino group of lysine residues in proteins can undergo deamination to form an intermediate lysine, which during subsequent oxidation forms amino adipic acid. Available data indicate that plasma amino adipic acid plays a role in the modulation of glucose levels through a compensatory response to hyperglycemia, resulting in increased insulin secretion in early insulin resistance [57]. Cadoni et al. noted a high level of amino adipic acid in the serum of patients with a reduced risk of advanced head and neck cancer [54]. Toklu et al. did not observe statistically significant differences in amino adipic acid between high-grade glioma and the control group determined in serum and brain tissue [55].

We found high levels of serum histidine in glioblastoma patients compared to the controls. This was parallel with the result of Toklu et al., where histidine levels were elevated in patients with high-grade glioblastoma [55]. Previous studies found that low plasma levels of histidine were observed in patients with shorter overall survival in glioblastoma patients. The potential role of histidine in the neoplastic process is not clear. It is believed that some AAs seemingly unrelated to the cancer process are used to increase the rate of uptake of other AAs. The upregulation of amino acid transporters in cancer maintains amino acid pools at levels that support its malignant characteristics. This can be highlighted by several examples: the export of glutamine to drive leucine uptake, asparagine for serine, arginine, and histidine, and glutamate for cystine [58].

The results of our study indicate an altered metabolism of phenylalanine in both glioblastoma and meningioma patients. In addition, we showed the statistical significance of phenylalanine differentiating patients with glioblastoma and the control group, considering a division by gender. Phenylalanine was also characterized by the best diagnostic values in the case of patients with glioblastoma. Phenylalanine is the precursor of tyrosine, an important AA for the biosynthesis of neurotransmitters like L-DOPA (L-3,4-dihydroxyphenylalanine) and catecholamines dopamine, epinephrine, and norepinephrine. Available research results indicate an increased concentration of phenylalanine in cancer, which reflects increased muscle proteolysis. For example, elevated levels of phenylalanine have been observed in squamous cell carcinoma of the head and neck [54] and hepatocellular carcinoma [59]. In a study comparing metabolites produced and consumed by glioma, Xiong et al. indicated phenylalanine as one of the metabolites intensively consumed by glioma cells [44]. The reason for the increase in phenylalanine levels in cancer is not fully understood. It is believed to be related to inflammation, the activation of the immune system, and increased levels of markers of immune activation, including tumor necrosis factor (STNF R75) and neopterin [60]. Phenylalanine is required to produce tyrosine. This conversion is catalyzed by the enzyme phenylalanine hydroxylase (EC 1.14.16.1), which functions primarily in the liver but has been shown to be active in other tissues of the body, including the brain. It has also been observed that phenylalanine hydroxylase activity may be sensitive to inflammation or cancer [61,62].

4. Materials and Methods

4.1. Subjects and Serum Samples

This study included 54 patients treated surgically for intracranial tumors in the Department of Neurosurgery, Neurotraumatology, and Paediatric Neurosurgery at the University Hospital No. 1, Collegium Medicum of the Nicolaus Copernicus University. The histological types of tumors in the examined patients were glial tumors and meningiomas. Table 3 shows the clinical and demographic characteristics of the study group.

Table 3. Clinical and demographic characteristics of the study group.

CNS Tumor	Glioma (n = 30)	Meningioma (n = 24)
Age	62.5	59.6
Sex		
– Female	11 (36.67%)	17 (70.83%)
– Male	19 (63.33%)	7 (29.17%)
WHO Classification		
– HGG (4. WHO)	30	
– Meningothelial meningiomas (1. WHO)		13
– Transitional meningiomas (1. WHO)		3
– Fibroblastic meningiomas (1. WHO)		3
– Atypical meningiomas (2. WHO)		5

The control group consisted of 49 people (29 men, 20 women) treated for osteoarthritis of the spine. The exclusion criteria for the control group were past or current neoplastic disease and (similarly to the study group) a surgical procedure performed less than 30 days ago. This study was conducted in accordance with all internationally approved human testing guidelines and was in accordance with the Declaration of Helsinki. The Ethics Committee of the Nicolaus Copernicus University in Toruń and Collegium Medicum in Bydgoszcz approved this study (consent number KB 499/2021).

4.2. Sample Preparation

Antecubital whole-blood samples were drawn from a peripheral vein in the morning hours (always between 7 and 8 a.m.). Overnight fasting and 15 min of rest before the blood test were obligatory. Blood collected in the tube was kept for 30 min. Serum from the blood after clotting was separated, centrifuged, and frozen at $-80\text{ }^{\circ}\text{C}$ until analysis was performed. The EZ:faast amino acid analysis kit was utilized for serum sample preparation.

The EZ:faast amino acid analysis procedure consists of a solid phase extraction step followed by derivatization and a liquid/liquid extraction. The solid phase extraction is performed via a sorbent-packed tip that binds amino acids while allowing interfering compounds to flow through. Amino acids on sorbent are then extruded into the sample vial and quickly derivatized with a reagent at room temperature in an aqueous solution. Derivatized amino acids concomitantly migrate to the organic layer for additional separation from interfering compounds. The organic layer is then removed, evaporated, and re-dissolved in an aqueous mobile phase and analyzed on an LC-MS system.

4.3. Instrumentation and Conditions

The quantitative and qualitative analyses of samples were performed using High-Performance Liquid Chromatograph Nexera XR LC-20 AD pump (Shimadzu, Kyoto, Japan) and a Nexera XR SIL-20AC autosampler (Shimadzu, Kyoto, Japan) coupled with a mass spectrometer equipped with an electrospray ion source (ESI), an LCMS-8045 Mass Spectrometer (Shimadzu, Kyoto, Japan). The instrument was controlled, and recorded data were processed using LabSolutions LCMS Ver.5.6 software.

Chromatographic separation was carried on the EZ:faast amino acid analysis–mass spectrometry column ($250 \times 3.0\text{ mm}$, $4\text{ }\mu\text{m}$) at a column temperature of $35\text{ }^{\circ}\text{C}$ with the corresponding binary mobile phase. Solvent A was 10 mM ammonium formate in water

and solvent B was 10 mM ammonium formate in methanol. The mobile phase flow was 0.25 mL/min and took place in a gradient system: 68% B–83% B in 13 min. The injection volume was 1 μ L. The mass spectrometry (MS) data were acquired in positive ion mode. Multiple reacting monitoring was used for quantification by monitoring the ion transition of amino acids.

Selected mass spectrometry parameters are summarized in Table 4.

Table 4. Amino acids, AA abbreviated name, retention time (min.), transitions chosen for each compound.

Compound Name	Abbreviated Name	t _R (min)	Quantification Transition
Serine	SER	3.885	233.9 > 146.00
Glutamine	GLN	3.468	275.1 > 172.00
Arginine	ARG	3.557	303.1 > 69.00
Citrulline	CIT	3.549	304.1 > 156.00
Homoarginine	HARG (IS)	3.753	317.10 > 84.00
Asparagine	ASN	3.985	243.10 > 157.00
1-Methyl-L-histidine	1MHIS	4.201	298.1 > 96.00
3-Methyl-L-histidine	3MHIS	4.235	298.1 > 210.00
4-Hydroxyproline	HYP	4.183	260.1 > 172.1
Glycine	GLY	4.423	203.9 > 144.00
Threonine	THR	4.482	248.10 > 160.00
Alanine	ALA	5.347	218.00 > 130.00
Gamma-aminobutyric acid	GABA	5.739	232.00 > 172.00
Sarcosine	SAR	5.948	217.90 > 88.00
Beta-aminoisobutyric acid	BAIB	6.202	232.00 > 172.00
α -Aminobutyric acid	ABA	6.567	232.00 > 172.00
Ornithine	ORN	6.795	347.00 > 287.00
Methionine	MET	7.085	227.9 > 190.10
Methionine-d3	Met-d3 (IS)	7.030	281.1 > 193.00
Proline	PRO	7.130	244.00 > 156.00
Lysine	LYS	7.743	361.00 > 301.10
Aspartic acid	ASP	7.753	304.00 > 216.10
Histidine	HIS	7.826	370.10 > 196.00
Valine	VAL	8.116	246.00 > 158.00
Glutamic acid	GLU	8.223	317.50 > 172.10
Tryptophan	TRP	8.468	333.10 > 245.10
α -Amino adipic acid	AAA	9.202	332.00 > 244.10
Leucine	LEU	9.593	260.00 > 172.10
Phenylalanine	PHE	9.679	294.10 > 206.10
Isoleucine	ILE	9.997	260.00 > 172.10
Homophenylalanine	HPHE (IS)	11.224	308.00 > 220.00
Cystine	C-C	11.402	497.00 > 248.00
Tyrosine	TYR	11.999	395.90 > 136.00

4.4. Reagents and Solvents

The EZ:faastTM amino acid analysis kit was obtained from Phenomenex, Inc. (Torrance, CA, USA). HPLC grade methanol was obtained from Merck (Darmstadt, Germany). Ammonium acetate and formic acid of analytical grade were purchased from Sigma-Aldrich Co. (St. Louis, MO, USA) with purity greater than 99%. Water was deionized and purified using a Milli-Q system (Millipore, Bedford, MA, USA) and used to prepare all aqueous solutions.

Calibration curves for each AA were constructed in a range from 0.01 to 75 nmol/mL. Calculation and calibration are based on an internal standard method. The kit contains as an internal standard an AA mixture of homoarginine (HARG), methionine-d3 (Met-d3), and homophenylalanine (HPHE).

4.5. Statistical Analysis

The statistical analysis was performed using Statistica 13.1 (StatSoft) and Excel 365 (Microsoft). The type of distribution was examined using the Shapiro–Wilk test. The Levene test was used to test the homogeneity of variance. The Kruskal–Wallis test and multiple comparisons of mean ranks for all trials were used to assess differences between more than two groups. Relationships between variables were described using the Spearman coefficient in the event of statistically significant differences. The data were visualized using a box plot. Principal component analysis (PCA) was used to classify correlation coefficients. The correlation matrix was used as the input. To isolate the number of principal components, Cattella's and Kaiser's criteria were used.

The receiver operating characteristic (ROC) curves were prepared using the concentration values of amino acid compounds. Sensitivity (SEN), specificity (SPE), and accuracy (Acc) were used to evaluate the model. The general models of regression and classification trees were used to build the classification model. The collected data were divided by a 4:1 ratio into a learning and testing group. Cross-validation was used to verify the effectiveness of the models. All analyses were performed at a significance level of 5% ($\alpha = 0.05$).

5. Conclusions

A comparative analysis of AAs between patients with glioblastoma, meningioma, and the control group allowed for the identification of statistically significant differences between the study groups.

A comparison of the amino acid profile between patients with glioma and the control group allowed for the identification of differences in both endogenous amino acids (SER, ARG, CIT, ASN, GLY, GABA, SAR, ABA, ORN, ASP) and exogenous amino acids (THR, MET, LYS, HIS, AAA, LEU, PHE, ILE, CC, TYR). Similarly, when comparing the amino acid profiles of patients with meningioma to the control group, the differences observed concerned endogenous amino acids (GLN, CIT, GABA, ORN, ASP) and exogenous amino acids (THR, MET, LYS, AAA, PHE, C-C, TYR). When comparing the amino acid profile by gender, only lysine showed statistically significantly higher concentrations in the group of patients with glioma and in the group of patients with meningioma compared to the control group. In the group of glioma patients, differences in amino acid profiles by gender also concerned histidine, α -amino adipic acid, and phenylalanine. However, no statistically significant differences were observed when comparing amino acid profiles between the groups of patients with glioma and meningioma. The AAs that showed statistically significant differences were evaluated for diagnostic usefulness. The best results were obtained for phenylalanine.

This study showed that amino acids may be involved in the mechanisms underlying the pathogenesis of glioblastoma and meningioma and may also be considered potential indicators of some pathways altered in CNS neoplastic diseases. However, given the multifactorial, heterogeneous, and complex nature of these diseases, further work with a larger study group is needed to correlate the results of previous studies with possible other malignancies to see if the amino acid profile of meningiomas and gliomas can be considered characteristic of these diseases.

Author Contributions: Conceptualization, P.K.; methodology, P.K.; validation, P.K.; formal analysis, R.P. and P.K.; investigation, P.K.; resources, Z.S. and M.Ś.; writing—original draft preparation, P.K.; writing—review and editing, P.K., R.P. and M.K.; visualization, P.K.; supervision, P.K.; project administration, P.K.; funding acquisition, M.K. All authors have read and agreed to the published version of the manuscript.

Funding: This research received no external funding.

Institutional Review Board Statement: The study was conducted in accordance with the Declaration of Helsinki and approved by the Ethics Committee of the Nicolaus Copernicus University in Toruń and Collegium Medicum in Bydgoszcz (consent number KB 499/2021).

Informed Consent Statement: Informed consent was obtained from all subjects involved in the study.

Data Availability Statement: Data are unavailable due to privacy or ethical restrictions.

Conflicts of Interest: The authors declare no conflict of interest.

References

1. Fisher, J.L.; Schwartzbaum, J.A.; Wrensch, M.; Wiemels, J.L. Epidemiology of Brain Tumors. *Neurol. Clin.* **2007**, *25*, 867–890. [CrossRef] [PubMed]
2. Darlix, A.; Zouaoui, S.; Rigau, V.; Bessaoud, F.; Figarella-Branger, D.; Mathieu-Daudé, H.; Trétarre, B.; Bauchet, F.; Duffau, H.; Taillandier, L.; et al. Epidemiology for Primary Brain Tumors: A Nationwide Population-Based Study. *J. Neurooncol.* **2017**, *131*, 525–546. [CrossRef] [PubMed]
3. Polly, F.P.; Shil, S.K.; Hossain, M.A.; Ayman, A.; Jang, Y.M. Detection and Classification of HGG and LGG Brain Tumor Using Machine Learning. In Proceedings of the 2018 International Conference on Information Networking (ICOIN), Chiang Mai, Thailand, 10–12 January 2018; pp. 813–817. [CrossRef]
4. Ohgaki, H.; Kleihues, P. Epidemiology and Etiology of Gliomas. *Acta Neuropathol.* **2005**, *109*, 93–108. [CrossRef] [PubMed]
5. Ostrom, Q.T.; Cioffi, G.; Waite, K.; Kruchko, C.; Barnholtz-Sloan, J.S. CBTRUS Statistical Report: Primary Brain and Other Central Nervous System Tumors Diagnosed in the United States in 2014–2018. *Neuro-oncology* **2021**, *23*, III1–III105. [CrossRef]
6. Cao, J.; Yan, W.; Zhan, Z.; Hong, X.; Yan, H. Epidemiology and Risk Stratification of Low-Grade Gliomas in the United States, 2004–2019: A Competing-Risk Regression Model for Survival Analysis. *Front. Oncol.* **2023**, *13*, 1079597. [CrossRef] [PubMed]
7. Diwanji, T.P.; Engelman, A.; Snider, J.W.; Mohindra, P. Epidemiology, Diagnosis, and Optimal Management of Glioma in Adolescents and Young Adults. *Adolesc. Health Med. Ther.* **2017**, *8*, 99–113. [CrossRef]
8. Claus, E.B.; Black, P.M. Survival Rates and Patterns of Care for Patients Diagnosed with Supratentorial Low-Grade Gliomas: Data from the SEER Program, 1973–2001. *Cancer* **2006**, *106*, 1358–1363. [CrossRef]
9. Han, S.; Liu, Y.; Cai, S.J.; Qian, M.; Ding, J.; Larion, M.; Gilbert, M.R.; Yang, C. IDH Mutation in Glioma: Molecular Mechanisms and Potential Therapeutic Targets. *Br. J. Cancer* **2020**, *122*, 1580–1589. [CrossRef]
10. Wiemels, J.; Wrensch, M.; Claus, E.B. Epidemiology and Etiology of Meningioma. *J. Neurooncol.* **2010**, *99*, 307–314. [CrossRef]
11. Yamanaka, R.; Hayano, A.; Kanayama, T. Radiation-Induced Meningiomas: An Exhaustive Review of the Literature. *World Neurosurg.* **2017**, *97*, 635–644.e8. [CrossRef]
12. Franz, G. Immunohistochemical Detection of Female Sex Hormone Receptors in Meningiomas: Correlation with Clinical and Histological Features Clinical Study. *Neurosurgery* **1992**, *33*, 212.
13. Alentorn, A.; Hoang-Xuan, K.; Mikkelsen, T. Presenting Signs and Symptoms in Brain Tumors. In *Handbook of Clinical Neurology*; Elsevier: Amsterdam, The Netherlands, 2016; Volume 134, pp. 19–26; ISBN 9780128029978.
14. Snyder, H.; Robinson, K.; Shah, D.; Brennan, R.; Handrigan, M. Signs and Symptoms of Patients with Brain Tumors Presenting to the Emergency Department. *J. Emerg. Med.* **1993**, *11*, 253–258. [CrossRef] [PubMed]
15. Huse, J.T.; Holland, E.C. Targeting Brain Cancer: Advances in the Molecular Pathology of Malignant Glioma and Medulloblastoma. *Nat. Rev. Cancer* **2010**, *10*, 319–331. [CrossRef] [PubMed]
16. Doroudchi, M.; Pische, Z.G.; Malekzadeh, M.; Golmoghaddam, H.; Taghipour, M.; Ghaderi, A. Elevated Serum IL-17A but Not IL-6 in Glioma versus Meningioma and Schwannoma. *Asian Pac. J. Cancer Prev.* **2013**, *14*, 5225–5230. [CrossRef]
17. Holst, C.B.; Christensen, I.J.; Skjøth-Rasmussen, J.; Hamerlik, P.; Poulsen, H.S.; Johansen, J.S. Systemic Immune Modulation in Gliomas: Prognostic Value of Plasma IL-6, YKL-40, and Genetic Variation in YKL-40. *Front. Oncol.* **2020**, *10*, 478. [CrossRef]
18. Popescu, I.D.; Codrici, E.; Albulescu, L.; Mihai, S.; Enciu, A.M.; Albulescu, R.; Tanase, C.P. Potential Serum Biomarkers for Glioblastoma Diagnostic Assessed by Proteomic Approaches. *Proteome Sci.* **2014**, *12*, 47. [CrossRef]
19. Gautam, P.; Nair, S.C.; Gupta, M.K.; Sharma, R.; Polisetty, R.V.; Uppin, M.S.; Sundaram, C.; Puligopu, A.K.; Ankathi, P.; Purohit, A.K.; et al. Proteins with Altered Levels in Plasma from Glioblastoma Patients as Revealed by ITRAQ-Based Quantitative Proteomic Analysis. *PLoS ONE* **2012**, *7*, e46153. [CrossRef]
20. Arora, A.; Patil, V.; Kundu, P.; Kondaiah, P.; Hegde, A.S.; Arivazhagan, A.; Santosh, V.; Pal, D.; Somasundaram, K. Serum Biomarkers Identification by ITRAQ and Verification by MRM: S100A8/S100A9 Levels Predict Tumor-Stroma Involvement and Prognosis in Glioblastoma. *Sci. Rep.* **2019**, *9*, 2749. [CrossRef]
21. Gielen, P.R.; Schulte, B.M.; Kers-Rebel, E.D.; Verrijp, K.; Bossman, S.A.J.F.H.; Ter Laan, M.; Wesseling, P.; Adema, G.J. Elevated Levels of Polymorphonuclear Myeloid-Derived Suppressor Cells in Patients with Glioblastoma Highly Express S100A8/9 and Arginase and Suppress T Cell Function. *Neuro-oncology* **2016**, *18*, 1253–1264. [CrossRef]
22. Lyubimova, N.V.; Toms, M.G.; Popova, E.E.; Bondarenko, Y.V.; Krat, V.B.; Kushlinskii, N.E.; Blokhin, N.N. Neurospecificity Proteins in the Serum of Patients with Brain Tumors. *Bull. Exp. Biol. Med.* **2010**, *150*, 678–681.
23. Gollapalli, K.; Ray, S.; Srivastava, R.; Renu, D.; Singh, P.; Dhali, S.; Bajpai Dikshit, J.; Srikanth, R.; Moiyadi, A.; Srivastava, S. Investigation of Serum Proteome Alterations in Human Glioblastoma Multiforme. *Proteomics* **2012**, *12*, 2378–2390. [CrossRef] [PubMed]
24. Wang, P.F.; Meng, Z.; Song, H.W.; Yao, K.; Duan, Z.J.; Yu, C.J.; Li, S.W.; Yan, C.X. Preoperative Changes in Hematological Markers and Predictors of Glioma Grade and Survival. *Front. Pharmacol.* **2018**, *9*, 886. [CrossRef] [PubMed]







25. Nijaguna, M.B.; Schröder, C.; Patil, V.; Shwetha, S.D.; Hegde, A.S.; Chandramouli, B.A.; Arivazhagan, A.; Santosh, V.; Hoheisel, J.D.; Somasundaram, K. Definition of a Serum Marker Panel for Glioblastoma Discrimination and Identification of Interleukin 1 β in the Microglial Secretome as a Novel Mediator of Endothelial Cell Survival Induced by C-Reactive Protein. *J. Proteom.* **2015**, *128*, 251–261. [CrossRef] [PubMed]
26. Zheng, S.H.; Huang, J.L.; Chen, M.; Wang, B.L.; Ou, Q.S.; Huang, S.Y. Diagnostic Value of Preoperative Inflammatory Markers in Patients with Glioma: A Multicenter Cohort Study. *J. Neurosurg.* **2018**, *129*, 583–592. [CrossRef] [PubMed]
27. Carlsson, A.; Persson, O.; Ingvarsson, J.; Widegren, B.; Salford, L.; Borrebaeck, C.A.K.; Wingren, C. Plasma Proteome Profiling Reveals Biomarker Patterns Associated with Prognosis and Therapy Selection in Glioblastoma Multiforme Patients. *Proteom. Clin. Appl.* **2010**, *4*, 591–602. [CrossRef]
28. Linhares, P.; Carvalho, B.; Vaz, R.; Costa, B.M. Glioblastoma: Is There Any Blood Biomarker with True Clinical Relevance? *Int. J. Mol. Sci.* **2020**, *21*, 5809. [CrossRef]
29. Ali, H.; Harting, R.; de Vries, R.; Ali, M.; Wurdinger, T.; Best, M.G. Blood-Based Biomarkers for Glioma in the Context of Gliomagenesis: A Systematic Review. *Front. Oncol.* **2021**, *11*, 665235. [CrossRef]
30. Śledzińska, P.; Bebyn, M.G.; Furtak, J.; Kowalewski, J.; Lewandowska, M.A. Prognostic and Predictive Biomarkers in Gliomas. *Int. J. Mol. Sci.* **2021**, *22*, 10373. [CrossRef]
31. Maher, E.A.; Marin-Valencia, I.; Bachoo, R.M.; Mashimo, T.; Raisanen, J.; Hatanpaa, K.J.; Jindal, A.; Jeffrey, F.M.; Choi, C.; Madden, C.; et al. Metabolism of [U-13C]Glucose in Human Brain Tumors in Vivo. *NMR Biomed.* **2012**, *25*, 1234–1244. [CrossRef]
32. Mashimo, T.; Pichumani, K.; Vemireddy, V.; Hatanpaa, K.J.; Singh, D.K.; Sirasanagandla, S.; Nannepaga, S.; Piccirillo, S.G.; Kovacs, Z.; Foong, C.; et al. Acetate Is a Bioenergetic Substrate for Human Glioblastoma and Brain Metastases. *Cell* **2014**, *159*, 1603–1614. [CrossRef]
33. Baranovičová, E.; Galanda, T.; Galanda, M.; Hatok, J.; Kolarovszki, B.; Richterová, R.; Račay, P. Metabolomic Profiling of Blood Plasma in Patients with Primary Brain Tumours: Basal Plasma Metabolites Correlated with Tumour Grade and Plasma Biomarker Analysis Predicts Feasibility of the Successful Statistical Discrimination from Healthy Subjects—A Preliminary Study. *IUBMB Life* **2019**, *71*, 1994–2002. [CrossRef] [PubMed]
34. Pandey, R.; Cafilisch, L.; Lodi, A.; Brenner, A.J.; Tiziani, S. Metabolomic Signature of Brain Cancer. *Mol. Carcinog.* **2017**, *56*, 2355–2371. [CrossRef]
35. Masalha, W.; Daka, K.; Woerner, J.; Pompe, N.; Weber, S.; Delev, D.; Krüger, M.T.; Schnell, O.; Beck, J.; Heiland, D.H.; et al. Metabolic Alterations in Meningioma Reflect the Clinical Course. *BMC Cancer* **2021**, *21*, 211. [CrossRef] [PubMed]
36. Ferrasi, A.C.; Puttini, R.; Galvani, A.F.; Hamamoto Filho, P.T.; Delafiori, J.; Argente, V.D.; de Oliveira, A.N.; Dias-Audibert, F.L.; Catharino, R.R.; Silva, O.C.; et al. Metabolomics Approach Reveals Important Glioblastoma Plasma Biomarkers for Tumor Biology. *Int. J. Mol. Sci.* **2023**, *24*, 8813. [CrossRef] [PubMed]
37. Chinnaiyan, P.; Kensicki, E.; Bloom, G.; Prabhu, A.; Sarcar, B.; Kahali, S.; Eschrich, S.; Qu, X.; Forsyth, P.; Gillies, R. The Metabolomic Signature of Malignant Glioma Reflects Accelerated Anabolic Metabolism. *Cancer Res.* **2012**, *72*, 5878–5888. [CrossRef]
38. Huang, J.; Weinstein, S.J.; Kitahara, C.M.; Karoly, E.D.; Sampson, J.N.; Albanes, D. A Prospective Study of Serum Metabolites and Glioma Risk. *Oncotarget* **2017**, *8*, 70366–70377. [CrossRef]
39. Locasale, J.W.; Melman, T.; Song, S.; Yang, X.; Swanson, K.D.; Cantley, L.C.; Wong, E.T.; Asara, J.M. Metabolomics of Human Cerebrospinal Fluid Identifies Signatures of Malignant Glioma. *Mol. Cell. Proteom.* **2012**, *11*, M111.014688. [CrossRef]
40. Nakamizo, S.; Sasayama, T.; Shinohara, M.; Irino, Y.; Nishiumi, S.; Nishihara, M.; Tanaka, H.; Tanaka, K.; Mizukawa, K.; Itoh, T.; et al. GC/MS-Based Metabolomic Analysis of Cerebrospinal Fluid (CSF) from Glioma Patients. *J. Neurooncol.* **2013**, *113*, 65–74. [CrossRef]
41. Kurokawa, G.A.; Hamamoto Filho, P.T.; Delafiori, J.; Galvani, A.F.; de Oliveira, A.N.; Dias-Audibert, F.L.; Catharino, R.R.; Pardini, M.I.M.C.; Zanini, M.A.; Lima, E.d.O.; et al. Differential Plasma Metabolites between High- and Low-Grade Meningioma Cases. *Int. J. Mol. Sci.* **2023**, *24*, 394. [CrossRef]
42. Patti, G.J.; Yanes, O.; Siuzdak, G. Metabolomics: The Apogee of the Omics Trilogy. *Nat. Rev. Mol. Cell Biol.* **2012**, *13*, 263–269. [CrossRef]
43. Griffin, J.L.; Kauppinen, R.A. A Metabolomics Perspective of Human Brain Tumours. *FEBS J.* **2007**, *274*, 1132–1139. [CrossRef] [PubMed]
44. Xiong, N.; Gao, X.; Zhao, H.; Cai, F.; Zhang, F.-C.; Yuan, Y.; Liu, W.; He, F.; Zacharias, L.G.; Lin, H.; et al. Using Arterial–Venous Analysis to Characterize Cancer Metabolic Consumption in Patients. *Nat. Commun.* **2020**, *11*, 3169. [CrossRef]
45. Wei, Z.; Liu, X.; Cheng, C.; Yu, W.; Yi, P. Metabolism of Amino Acids in Cancer. *Front. Cell Dev. Biol.* **2021**, *8*, 603837. [CrossRef]
46. Chen, S.; Jiang, J.; Shen, A.; Miao, Y.; Cao, Y.; Zhang, Y.; Cong, P.; Gao, P. Rewired Metabolism of Amino Acids and Its Roles in Glioma Pathology. *Metabolites* **2022**, *12*, 918. [CrossRef]
47. Bernhard, C.; Reita, D.; Martin, S.; Entz-Werle, N.; Dontenwill, M. Glioblastoma Metabolism: Insights and Therapeutic Strategies. *Int. J. Mol. Sci.* **2023**, *24*, 9137. [CrossRef] [PubMed]
48. Danzi, F.; Pacchiana, R.; Mafficini, A.; Scupoli, M.T.; Scarpa, A.; Donadelli, M.; Fiore, A. To Metabolomics and beyond: A Technological Portfolio to Investigate Cancer Metabolism. *Signal Transduct. Target. Ther.* **2023**, *8*, 137. [CrossRef] [PubMed]
49. Wang, X.; Yang, K.; Xie, Q.; Wu, Q.; Mack, S.C.; Shi, Y.; Kim, L.J.Y.; Prager, B.C.; Flavahan, W.A.; Liu, X.; et al. Purine Synthesis Promotes Maintenance of Brain Tumor Initiating Cells in Glioma. *Nat. Neurosci.* **2017**, *20*, 661–673. [CrossRef]

50. Palanichamy, K.; Thirumoorthy, K.; Kanji, S.; Gordon, N.; Singh, R.; Jacob, J.R.; Sebastian, N.; Litzenberg, K.T.; Patel, D.; Bassett, E.; et al. Methionine and Kynurenine Activate Oncogenic Kinases in Glioblastoma, and Methionine Deprivation Compromises Proliferation. *Clin. Cancer Res.* **2016**, *22*, 3513–3523. [CrossRef]
51. Prabhu, A.; Sarcar, B.; Kahali, S.; Yuan, Z.; Johnson, J.J.; Adam, K.P.; Kensicki, E.; Chinnaiyan, P. Cysteine Catabolism: A Novel Metabolic Pathway Contributing to Glioblastoma Growth. *Cancer Res.* **2014**, *74*, 787–796. [CrossRef]
52. Dols, M.C.; Domínguez López, M.; Ramírez Plaza, C.; Pérez Miranda, E.; Gil Calle, S.; Chamorro, E.V.; Alés Díaz, I.; Pino, A.M.; García, J.A.; Calderón, V.G. Specific Alterations in the Serum Amino Acid Profile of Patients with Lung Cancer and Head and Neck Cancer. *Oncologica* **2006**, *29*, 283–290.
53. Jia, B.; Wang, W.; Lin, S.; Shi, L.; Li, Y.; Gu, Y.; Gao, F.; Qin, Y. The Free Amino Acid Profiles and Metabolic Biomarkers of Predicting the Chemotherapeutic Response in Advanced Sarcoma Patients. *Clin. Transl. Oncol.* **2020**, *22*, 2213–2221. [CrossRef] [PubMed]
54. Cadoni, G.; Giraldi, L.; Chiarla, C.; Gervasoni, J.; Persichilli, S.; Primiano, A.; Settini, S.; Galli, J.; Paludetti, G.; Arzani, D.; et al. Prognostic Role of Serum Amino Acids in Head and Neck Cancer. *Dis. Markers* **2020**, *2020*, 2291759. [CrossRef] [PubMed]
55. Toklu, S.; Kemerdere, R.; Kacira, T.; Gurses, M.S.; Benli Aksungar, F.; Tanriverdi, T. Tissue and Plasma Free Amino Acid Detection by LC-MS/MS Method in High Grade Glioma Patients. *J. Neurooncol* **2023**, *163*, 293–300. [CrossRef] [PubMed]
56. Mören, L.; Wibom, C.; Bergström, P.; Johansson, M.; Antti, H.; Bergenheim, A.T. Characterization of the Serum Metabolome Following Radiation Treatment in Patients with High-Grade Gliomas. *Radiat. Oncol.* **2016**, *11*, 51. [CrossRef]
57. Wang, T.J.; Ngo, D.; Psychogios, N.; Dejam, A.; Larson, M.G.; Vasan, R.S.; Ghorbani, A.; O’sullivan, J.; Cheng, S.; Rhee, E.P.; et al. 2-Amino adipic Acid Is a Biomarker for Diabetes Risk. *J. Clin. Investig.* **2013**, *123*, 4309. [CrossRef]
58. Vettore, L.; Westbrook, R.L.; Tennant, D.A. New Aspects of Amino Acid Metabolism in Cancer. *Br. J. Cancer* **2020**, *122*, 150–156. [CrossRef]
59. Watanabe, A.; Higashi, T.; Sakata, T.; Nagashima, H. Serum Amino Acid Levels in Patients With Hepatocellular Carcinoma. *Cancer* **1984**, *54*, 1875–1882. [CrossRef]
60. Diez-Ruiz, A.; Titz, G.P.; Zangerle, R.; Baier-Bitterlich, G.; Wachter, H.; Fuchs, D. Soluble Receptors for Tumour Necrosis Factor in Clinical Laboratory Diagnosis. *Eur. J. Haematol.* **1995**, *54*, 1–8. [CrossRef]
61. Neurauter, G.; Grahmann, A.V.; Klieber, M.; Zeimet, A.; Ledochowski, M.; Sperner-Unterweger, B.; Fuchs, D. Serum Phenylalanine Concentrations in Patients with Ovarian Carcinoma Correlate with Concentrations of Immune Activation Markers and of Isoprostane-8. *Cancer Lett.* **2008**, *272*, 141–147. [CrossRef]
62. Ploder, M.; Neurauter, G.; Spittler, A.; Schroecksnadel, K.; Roth, E.; Fuchs, D. Serum Phenylalanine in Patients Post Trauma and with Sepsis Correlate to Neopterin Concentrations. *Amino Acids* **2008**, *35*, 303–307. [CrossRef]

Disclaimer/Publisher’s Note: The statements, opinions and data contained in all publications are solely those of the individual author(s) and contributor(s) and not of MDPI and/or the editor(s). MDPI and/or the editor(s) disclaim responsibility for any injury to people or property resulting from any ideas, methods, instructions or products referred to in the content.

Article

Matrix Selection Strategies for MALDI-TOF MS/MS Characterization of Cyclic Tetrapyrroles in Blood and Food Samples

Mariachiara Bianco ¹, Giovanni Ventura ¹, Cosima Damiana Calvano ^{1,2,*}, Ilario Losito ^{1,2},
Tommaso R. I. Cataldi ^{1,2} and Antonio Monopoli ^{1,*}

¹ Department of Chemistry, University of Bari Aldo Moro, 70126 Bari, Italy; mariachiara.bianco@uniba.it (M.B.); giovanni.ventura@uniba.it (G.V.); ilario.losito@uniba.it (I.L.); tommaso.cataldi@uniba.it (T.R.I.C.)

² Interdepartmental Research Center (SMART), University of Bari Aldo Moro, 70126 Bari, Italy

* Correspondence: cosimadamiana.calvano@uniba.it (C.D.C.); antonio.monopoli@uniba.it (A.M.)

Abstract: Cyclic tetrapyrrole derivatives such as porphyrins, chlorins, corrins (compounds with a corrin core), and phthalocyanines are a family of molecules containing four pyrrole rings usually coordinating a metal ion (Mg, Cu, Fe, Zn, etc.). Here, we report the characterization of some representative cyclic tetrapyrrole derivatives by MALDI-ToF/ToF MS analyses, including heme b and c, phthalocyanines, and protoporphyrins after proper matrix selection. Both neutral and acidic matrices were evaluated to assess potential demetallation, adduct formation, and fragmentation. While chlorophylls exhibited magnesium demetallation in acidic matrices, cyclic tetrapyrroles with Fe, Zn, Co, Cu, or Ni remained steadfast against demetallation across all conditions. Phthalocyanines and protoporphyrins were also detectable without a matrix using laser desorption ionization (LDI); however, the incorporation of matrices achieved the highest ionization yield, enhanced sensitivity, and negligible fragmentation. Three standard proteins, i.e., myoglobin, hemoglobin, and cytochrome c, were analyzed either intact or enzymatically digested, yielding heme b and heme c ions along with accompanying peptides. Furthermore, we successfully detected and characterized heme b in real samples, including blood, bovine and cod liver, and mussel. As a result, MALDI MS/MS emerged as a powerful tool for straightforward cyclic tetrapyrrole identification, even in highly complex samples. Our work paves the way for a more comprehensive understanding of cyclic tetrapyrroles in biological and industrial settings, including the geochemical field, as these compounds are a source of significant geological and geochemical information in sediments and crude oils.

Keywords: phthalocyanine; heme; blood; food; MALDI MS/MS



Citation: Bianco, M.; Ventura, G.; Calvano, C.D.; Losito, I.; Cataldi, T.R.I.; Monopoli, A. Matrix Selection Strategies for MALDI-TOF MS/MS Characterization of Cyclic Tetrapyrroles in Blood and Food Samples. *Molecules* **2024**, *29*, 868. <https://doi.org/10.3390/molecules29040868>

Academic Editors: Wen Ma and Xianjiang Li

Received: 30 December 2023

Revised: 5 February 2024

Accepted: 11 February 2024

Published: 15 February 2024



Copyright: © 2024 by the authors. Licensee MDPI, Basel, Switzerland. This article is an open access article distributed under the terms and conditions of the Creative Commons Attribution (CC BY) license (<https://creativecommons.org/licenses/by/4.0/>).

1. Introduction

Porphyrins are a group of macromolecules participating in the biosynthesis of numerous fundamental biomolecules, such as vitamin B₁₂ [1] and heme [2]. At the heart of all porphyrins lies a central tetrapyrrolic ring, *porphine* (Figure 1A), held together by methane bridges. The unique identity of each porphyrin species stems from its side chain substituents, which can be alkyl, alkene, or carboxylic acid groups. As an example, protoporphyrin IX (Figure 1B) [3] is an organic compound classified as a porphyrin containing four methyl (M), two vinyl (V), and two propionic acidic (P) groups; it plays an important role in living organisms as a precursor of heme b (Figure 1C) and chlorophyll. Many metal ions can be incorporated into porphyrins generating metalloporphyrins, whose stability can vary dramatically. For instance, Mg(II) porphyrins are easily demetallated by weak acidic conditions, being the most labile metalloporphyrins [4]. Naturally occurring porphyrinic molecules constitute the most important class of biological cofactors present as green pigments in chloroplasts [5] or red pigments in hemoglobin (heme b), myoglobin (heme b), and cytochrome c (heme c) [6,7]. Heme, the iron-containing prosthetic group of

many proteins, including hemoglobin, is essential for oxygen transport and other crucial biological processes. However, the redox activity of iron and the hydrophobic nature of protoporphyrin IX can lead to cytotoxicity effects, which can be minimized when heme is bound to proteins. Therefore, analyzing unbound heme levels in patient plasma samples can provide valuable insights into conditions like hemolysis, where heme is released from its bound state [7–9].

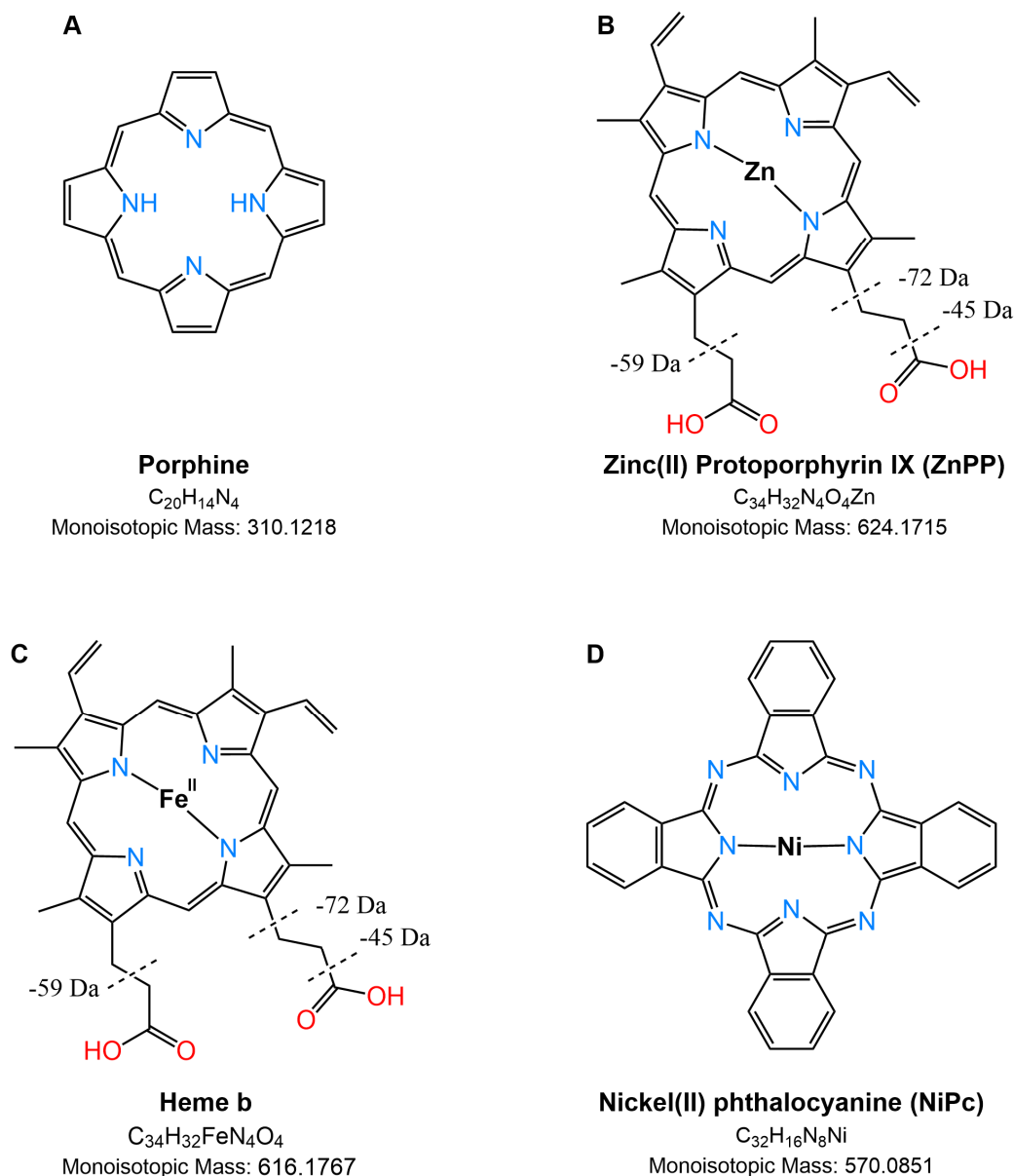


Figure 1. Structures of some compounds investigated with porphine core (A), such as Zinc(II) protoporphyrin IX (ZnPP) (B), heme b (C), and nickel(II) phthalocyanine (D). The major neutral losses of ZnPP and heme b are reported as dashed lines; note that some ions could be generated from the concurrent loss of reported fragments (see Table 1).

Synthetic porphyrins and aromatic tetrapyrrole (i.e., corrole) complexes have been proposed for diverse applications, serving as biomimetic models, catalysts for many reactions [10], sensors [11], and therapeutic agents [12]. Phthalocyanines (Figure 1D), which are closely related to porphyrins, have rich synthetic chemistry and have been widely used as dyes for textiles and paper, as blue and green colors in liquid crystal displays, as photoconductors in laser printers, and as absorbers and *p*-conductors in organic solar

cells [13]. Such an outstanding collection of properties allows porphyrin derivatives to be applied to different transducers, ranging from nano-gravimetric to optical devices, and empowering the conception of multiple transduction chemical sensors onto the same sensing layer. The ability to modify the structure of the macrocycle by synthetic alteration of the various components of the porphyrin ring, including the molecular skeleton, substituents, and coordinated metals/metalloids in the ligand, offers a vast range of possibilities for creating porphyrinoid-based systems with precisely tailored properties. This provides the opportunity to generate a massive library of such systems with finely tuned properties [14].

Optical spectroscopic techniques such as UV–vis spectrophotometry, chemiluminescence, and fluorescence are widely preferred for the identification of these porphyrinic compounds, due to their extensive system of delocalized π electrons and fluorescent nature [15,16]. However, these currently used techniques may not guarantee a high level of selectivity. This is because they do not provide detailed information on the molecular structure of the analyzed compounds. This can be a limiting factor when examining newly synthesized derivatives. Additionally, in complex natural samples, interference from other pigments and degradation by-products may occur. A more selective method for the separation of cyclic tetrapyrroles and related compounds is reversed-phase high-performance liquid chromatography [17] coupled with mass spectrometry (RP-HPLC-MS) [18,19], even if, due to the time-consuming sample treatment and experimental setup, routine analyses of a significant number of samples become unaffordable. In this context, matrix-assisted laser desorption/ionization (MALDI) time-of-flight (ToF) MS can offer a fast and selective technique for the identification of cyclic tetrapyrroles thanks to well-recognized features, such as speedy and simple sample preparation, tolerance to salts, and high sensitivity [20]. Indeed, recent works employing MALDI-MS for the analysis of cyclic tetrapyrrole derivatives have been published [8,21–26]. We have also deeply demonstrated that a major challenge in the MS analysis of porphyrinic compounds is to preserve the original metallation state during the analysis, avoiding demetallation or trans-metallation of metalloporphyrins and metallation of free-base porphyrins [27–29]. Reflecting the extensive conjugation of these systems and the nature of the coordinating metal cation, numerous ionization pathways can occur during the MALDI process. Thus, the properties of the MALDI matrix (proton or electron transfer) can be crucial to their successful ionization [30].

To guarantee a high degree of selectivity through molecular mass, isotopic distribution, and structure-specific fragmentation, accurate tandem mass spectrometry is needed, but detailed structural studies by MALDI MS/MS investigation are limited. Here, we report the examination and comparison of various recognized MALDI matrices for the identification and characterization of several porphine-derived compounds, also employing tandem MS analysis. The results demonstrate that MALDI MS/MS also allowed the complete, rapid, and incisive description of these compounds in complex food and biological samples after selecting the best matrix for each group.

2. Results and Discussion

2.1. Matrix Evaluation for Protoporphyrin Analysis by MALDI MS

In the first step, the desorption/ionization efficiency of representative matrices for analyzing a synthetic Co(II) protoporphyrin was evaluated and the results obtained with and without a matrix were compared. Alongside conventional low-proton-affinity (PA) acidic matrices such as α -cyano-4-hydroxycinnamic acid (CHCA) and α -cyano-4-chlorocinnamic acid (CCICA), known to facilitate magnesium porphyrin demetallation [28], neutral or electron transfer (ET) matrices like DCTB (trans-2-[3-(4-t-butyl-phenyl)-2-methyl-2-propenylidene]malononitrile), DAN (1,5-diaminonaphthalene), and TER (2,2':5',2''-terthiophene) were tested to ensure the stability of the central metal ion and to identify potential matrix-related interfering peaks in the low m/z range ($<1000 m/z$). Figure 2 displays the MALDI MS spectra of CoPP (cobalt chloride (II) Protoporphyrin IX) in positive ion mode, using DAN (A), CCICA (B), DCTB (C), and TER (D) as matrices, or in LDI mode (E). In all cases, CoPP was detected as the base peak at m/z 619.18, except for the

MALDI spectrum obtained using DAN as the matrix (Figure 2A), where the main peak (*) is generated from an interfering matrix ion. From the MALDI mass spectra, it is clear that Co-porphyrin is relatively stable and a demetallation reaction does not occur when also employing acidic matrices. Indeed, Buchler et al. [31] developed a stability index (S) to evaluate the stability of metal–porphyrin complexes, which is related to certain metal properties, i.e., Pauling electronegativity (PE), valence (V), and ionic radius expressed in Å (R). The index S can be calculated as $S = ((PE \times V)/R)$. The higher the stability index, the lower the possibility of demetallation in the solution. Considering the relevant values for Mg(II) (R = 0.72 Å, PE = 1.31, V = 2), Co(II) (R = 0.65 Å, PE = 1.88, V = 2), and Zn(II) (R = 0.74 Å, PE = 1.65, V = 2), the porphyrin cycles containing Co and Zn as the central metals are more stable than the one containing Mg, with the stability index, S being, respectively, 5.78 (Co) > 4.46 (Zn) > 3.64 (Mg).

As evidenced in the insets of Figure 2, alongside the $M^{+\bullet}$ at m/z 619.18, the $M + 1$ isotope exhibited a relative abundance of ca 85% in Figure 2B,C, which is higher than the expected natural isotopic abundance of 36.8%, thus indicating the major contribution of a simultaneously formed protonated molecule ($[M + H]^+$). Thus, while DAN (A) and TER (D) could drive the ionization process towards the formation of the odd electron molecular ion with nearly 100% yield as in LDI mode (E), using CCICA (B) and DCTB (C), a concurrent ionization with the formation of a protonated adduct was observed. Proton transfer (PT) ions tend to be energetically preferred for the classical matrices CCICA and CHCA, which have acidic sites, while ET ions can be dominant for other matrices (DCTB, DAN, TER), and both types may appear in the same spectrum. The propensity for gas-phase PT or ET depends on the relative ionization energies, electron and proton affinities, and basicity of the interacting partners, even if the interconversion reactions are likely for many matrices in the early plume being rather low in energy [32]. In our case, ET is the favored mechanism considering the highly aromatic feature of all cyclic tetrapyrroles, but it competes with PT when CCICA and DCTB are used as matrices likely due to the presence of two carboxylic end residues in the PPIX structure (see Figure 1B). The intensity of the CoPP is highest when analyzed with CCICA (B) and is comparable to LDI (C) when using DAN (A) and DCTB (C), even if fewer matrix-related peaks or fragment ions occurred using the latter matrix instead of DAN and LDI, respectively. TER (D) gave rise to the lowest signal in terms of intensity. It should be noted an increased contribution from the peak at m/z 618.17 that corresponds to $[M - H]^+$ for DCTB, suggesting that also a PT from analyte to matrix can compete with the ET process. Indeed, the loss of a hydrogen radical (H^\bullet) from the retinol molecular radical cation was already reported by Cole et al. [33] and by O'Connor et al. [34] in chlorophyll-a, facilitated by the generation of thermodynamically favored conjugated structures. To avoid this further complication, CCICA exhibited the best performance as the PT matrix and DAN as the ET matrix for CoPP. Overlapping results were obtained for the other investigated standard of Zn(II) Protoporphyrin IX (ZnPP), thus confirming our findings. Then, we tested these matrices for tandem MS acquisition to verify if useful spectra for structural information could be attained. All the matrices were able to generate very similar fragmentation patterns, even if CCICA produced spectra with higher intensity, so we referred to this matrix. Figure 3 reports the MS/MS spectrum of CoPP (A) and ZnPP (B) in positive ion mode. The fragmentation pattern of the porphyrins is dominated by cleavages of the side chain substituents, so the investigation of the product ion MALDI spectrum allows the identification of the substituent groups. In analogy with ESI-MS/MS [17], an acetic acid substituent typically eliminates a neutral H_2CO_2 (46 Da) while a propionic acid substituent loses preferentially a $H_3C_2O_2$ radical ($[CH_2COOH]^\bullet$ 59 Da) group. Porphyrins containing both acetic and propionic acid substituents show a combination of both pathways. The same findings apply to both ZnPP and CoPP, and the main product ions identified in Figure 3 are listed in Table 1.

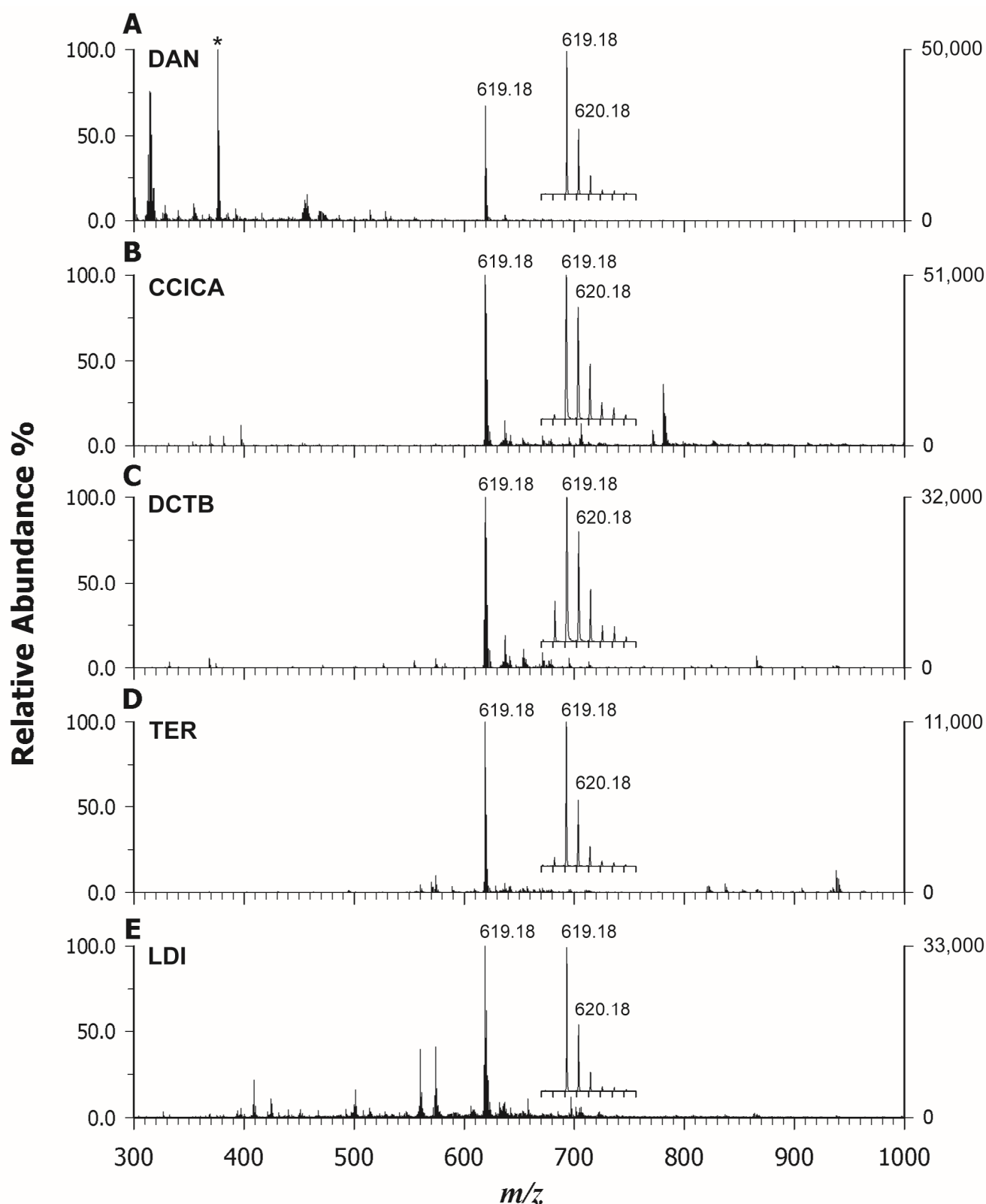


Figure 2. Positive ion mass spectra by MALDI-ToF MS of a CoPP using (A) DAN, (B) CCICA, (C) DCTB, and (D) TER as matrices. LDI mode is reported in (E). The expanded isotopic pattern of the odd-electron $[M]^{+\bullet}$ radical at m/z 619.18 is shown in the inset, (*) main peak.

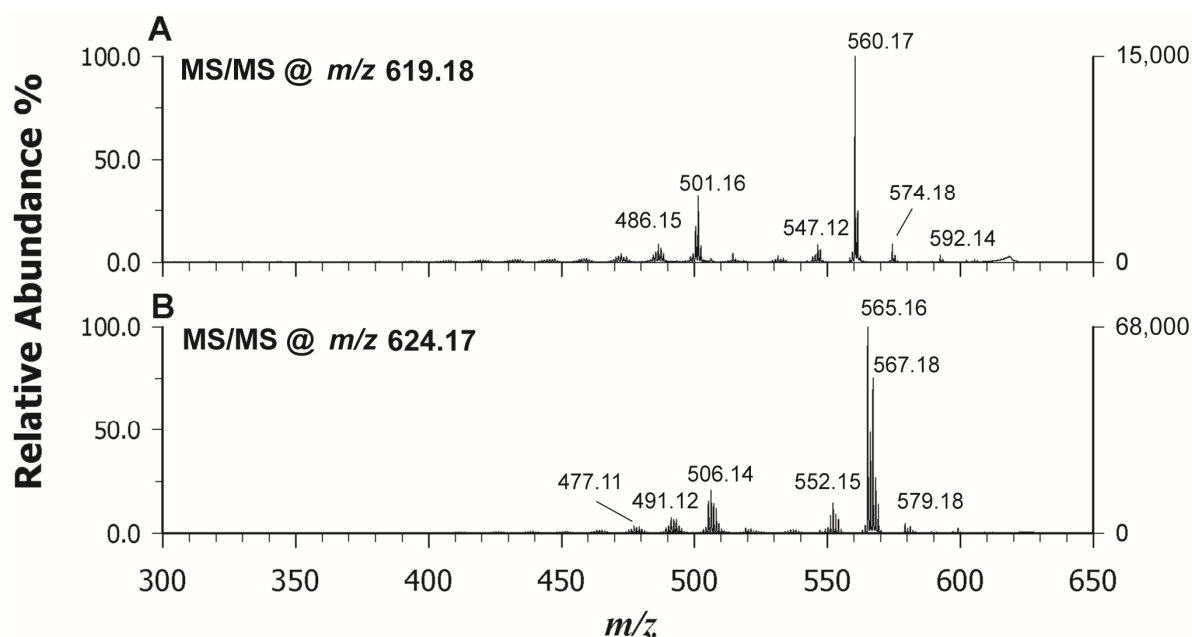


Figure 3. MALDI-ToF/ToF tandem mass spectra in positive ion mode of CoPP at m/z 619.18 (A) and ZnPP at m/z 624.17 (B). CCICA was used as a matrix; peaks are indicated according to their m/z value and their identities are given in Table 1.

Table 1. Product ions summary of Co(II) and Zn(II) protoporphyrins, both in positive ion mode, obtained by MALDI MS/MS using CCICA as a matrix (see Figure 3).

Product Ions	Proposed Formula	Loss of Chemical Species	Theoretical m/z Value	MALDI MS/MS m/z	Relative Intensity%
CoPP ($[C_{34}H_{32}CoN_4O_4]^+$) at m/z 619.180					
B	$[C_{32}H_{29}CoN_4O_4]^+$	$[CH_2CH]^•$	592.156	592.14	5.2
C	$[C_{33}H_{31}CoN_4O_2]^+$	$[HCO_2]^•$	574.177	574.18	9.2
D	$[C_{32}H_{29}CoN_4O_2]^+$	$[CH_2COOH]^•$	560.162	560.17	100
E	$[C_{31}H_{28}CoN_4O_2]^+$	$[CH_2CHCOOH]$	547.154	547.12	6.4
F	$[C_{30}H_{26}CoN_4]^+$	$2 \times [CH_2COOH]^•$	501.148	501.16	32.3
G	$[C_{29}H_{23}CoN_4]^+$	$[C_5H_9O_4]^•$	486.125	486.15	8.7
ZnPP ($[C_{34}H_{32}ZnN_4O_4]^+$) at m/z 624.172					
B	$[C_{33}H_{31}ZnN_4O_2]^+$	$[HCO_2]^•$	579.174	579.18	2.3
C	$[C_{32}H_{29}ZnN_4O_2]^+$	$[CH_2COOH]^•$	565.158	565.16	100
D	$[C_{31}H_{28}ZnN_4O_2]^+$	$[CH_2CHCOOH]$	552.150	552.15	14.6
E	$[C_{30}H_{26}ZnN_4]^+$	$2 \times [CH_2COOH]^•$	506.145	506.14	20.7
F	$[C_{29}H_{23}ZnN_4]^+$	$[C_5H_9O_4]^•$	491.121	491.12	7.6
G	$[C_{28}H_{21}ZnN_4]^+$	$[C_6H_{11}O_4]^•$	477.106	477.11	3.6

2.2. MALDI MS(/MS) of Phthalocyanines

Phthalocyanines (Pcs) are largely employed in several applications in modern technology from sensors [11] to cultural heritage in street art [35] for their interesting spectroscopic, optical, and electrical properties in addition to chemical and thermal stability. Also in this case, the MALDI MS analysis offers the advantage of a fast analysis with high sensitivity that can provide structural information on chemical species and relative quantification information during the synthesis of novel Pcs with improved performance. In a previous study [36], metal phthalocyanines (MPcs) have been used as a matrix for the analysis of small molecules (<500 Da) able to form spotless peaks free of interference of MPc–analyte adducts in a mass region of >1000 Da. Due to the highly conjugated π system, MPcs show

a Soret absorption band between 290 nm and 450 nm, and thus they can easily absorb laser energy. For this reason, we should expect that PCs can be detected well also in the LDI modality. Indeed, after exploring all the ET or PT matrices listed in the Section 3, we confirmed that the three investigated PCs with different central metal ions (Cu vs. Ni) or different lateral substituents were significantly ionized in LDI mode with high intensity and without matrix ion interference. Figure 4 reports the LDI spectra in positive mode of Copper (II) phthalocyanine (CuPc) (A), Nickel(II) phthalocyanine (NiPc) (B), and Nickel(II) 2,9,16,23-tetraphenoxy-29H-31H-phthalocyanine (NiPcPhe) (C). In all cases, the base peak detected for each compound was represented by the radical cation at m/z 575.08 (CuPc), 570.09 (NiPc), and 938.19 (NiPcPhe), reflecting the natural isotopic pattern. The use of matrices did not add any improvement, since the occurrence of interfering ions was experienced together with the concurrent formation of protonated adduct that complicated the spectrum. Moreover, the PCs have scarce solubility in the common organic solvents used to dissolve matrices, so, in some cases, on-target precipitation reactions were also surveyed. The MS/MS analyses of the selected compounds were also carried out in LDI mode and Figure 5 reports the relevant spectra of CuPc (A), NiPc (B), and NiPcPhe (C). The tandem mass spectra did not provide useful information on the structure since PCs have great thermal stability and usually spectral studies on metal phthalocyanine are established to be meagre. However, our findings were in agreement with the NIST library, where very similar electron ionization spectra of CuPc [37] and NiPc [38] are found. Some tentative fragmentation mechanisms and attributions were proposed by Achar et al. [39] reporting GC–MS studies of nickel phthalocyanine sheet polymer. The MALDI spectrum of the substituted NiPcPhe looks different, since fragments linked to the consecutive losses of phenyl and phenoxy alongside CO residues were detected in the m/z range 600–863 (Figure 5C). In this case, MALDI MS/MS can be exploited to obtain more information on the nature of substituents.

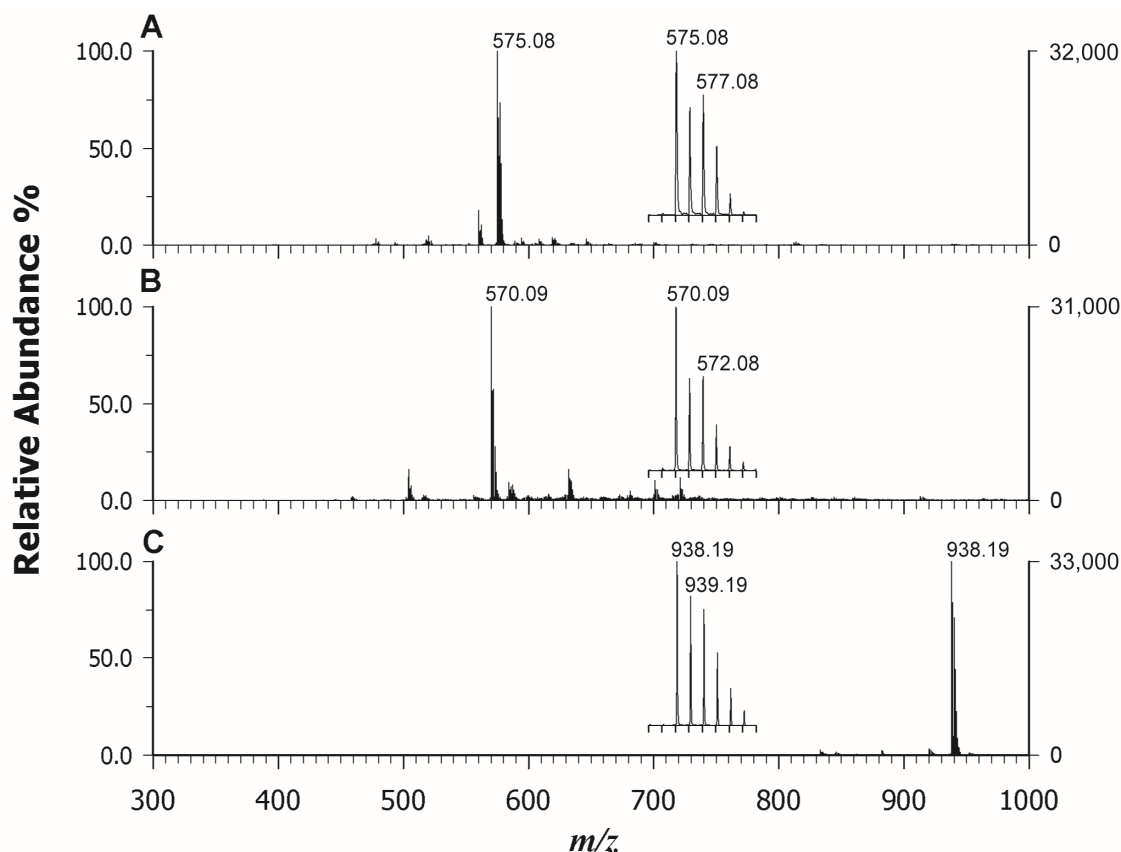


Figure 4. LDI-ToF mass spectra in positive ion mode of CuPc (A), NiPc (B), and NiPcPhe (C) with corresponding insets on the base peak.

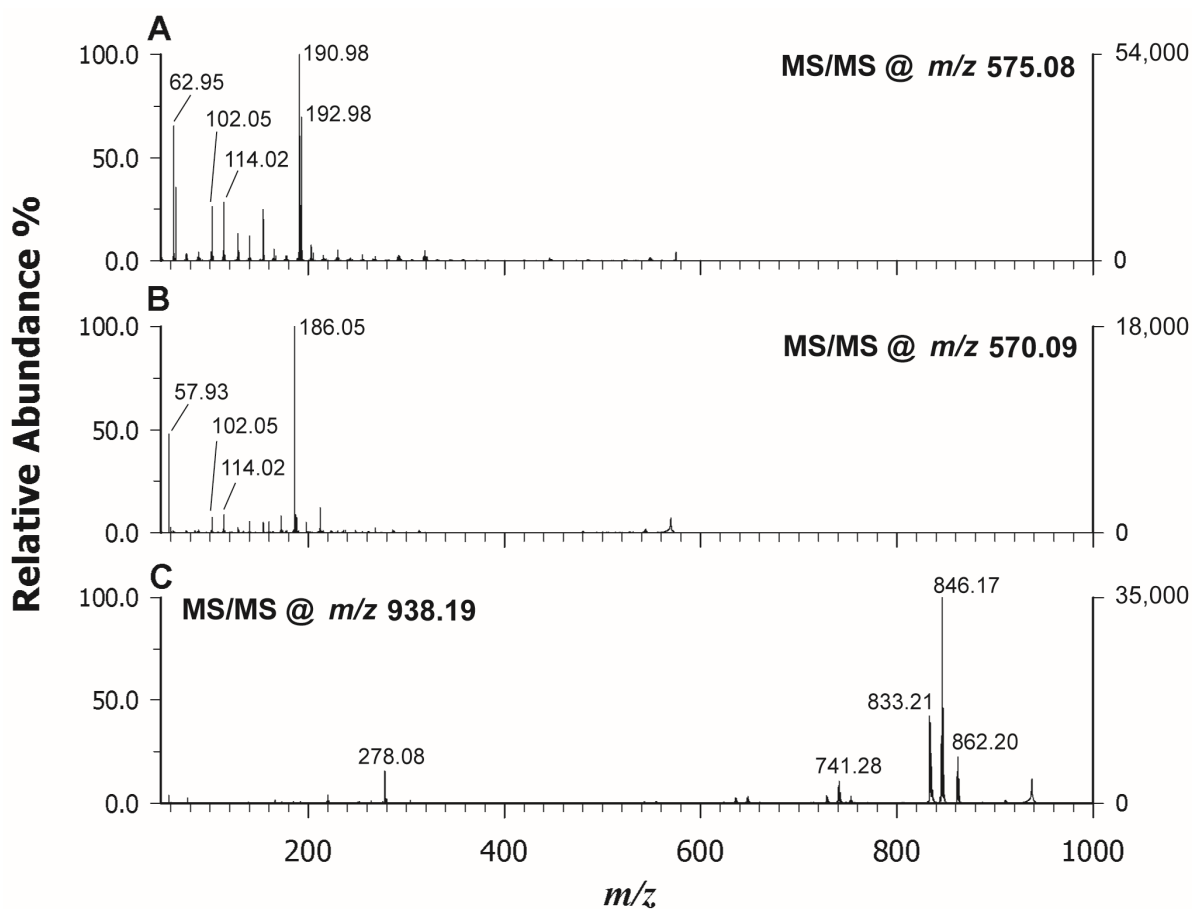


Figure 5. LDI-ToF/ToF mass spectra in positive ion mode of CuPc at m/z 575.08 (A), NiPc at m/z 570.09 (B), and NiPcPhe at m/z 938.19 (C).

2.3. MALDI MS(/MS) of Heme b and c in Standards and Real Samples

A complete characterization of the heme molecule is important, as it can provide a rapid method of disease detection, structural information on unusual heme groups, evidence on association of drugs with heme groups, or data on hemoproteins with specific biological functions [40,41]. Myoglobin and hemoglobin were here used as reference materials containing the heme b moiety, while cytochrome C (Cyt C) was chosen as a reference for heme c. After screening ET and PT matrices (see Figures S1 and S2), we noticed that heme was successfully and efficiently detected by employing PT matrices such as CCICA and CHCA. Furthermore, the use of this last matrix allowed us to systematically obtain suppression of other interfering species in support of heme ionization. In Figure 6, the MALDI MS spectra in the low m/z regions of hemoglobin (A), myoglobin (B), and cytochrome c (C) using CHCA as a matrix are reported. In detail, the intact analyte heme b (Figure 6A,B) was identified at m/z 616.18, which can be rationalized by admitting the occurrence of an Fe^{3+} ion within the intact porphyrin cycle, such as $[\text{C}_{34}\text{H}_{32}\text{O}_4\text{FeN}_4]^+$. Indeed, it is known that the Fe^{2+} within the cycle easily oxidizes in the air or during the analyses [42]. A comparison between the theoretical intensity of the second isotopic peak of heme b (40% of the peak at m/z 616) and that obtained experimentally (ca 60–70%) clearly shows, in both cases, the presence of an unknown ionic species formed at m/z 617.18. This phenomenon can be partially explained as the overlapping problem of isobaric species which causes a change in the apparent isotopic distribution, as proved by Yang et al. [24] comparing the high-resolution mode ($\sim 800,000$) in MALDI FT-ICR-MS and low-resolution mode (~ 8000).

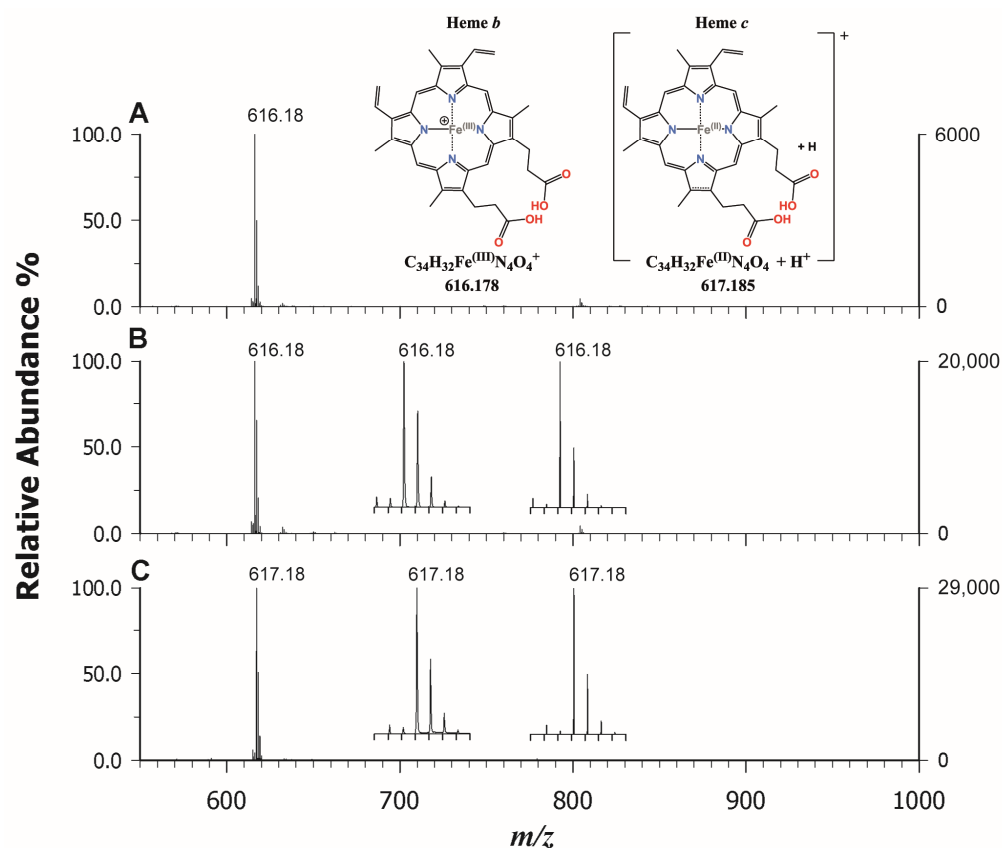


Figure 6. MALDI-ToF mass spectra in positive ion mode using CHCA as a matrix of heme b in hemoglobin (A), in myoglobin (B), and heme c in cytochrome C (C). The comparison between experimental and theoretical mass spectra is shown in the insets of plots (B) and (C).

Upon examining Figure 6C, it is evident that the signal at m/z 617.18 represents the base peak in the dissociation of heme from cytochrome c. This signal poses a challenging explanation, as it requires the rupture of two covalent and two coordination bonds to release the porphyrin complex heme c. In the literature, it is reported that this species can be generated in electrospray (ESI) by collisionally induced dissociation (CID) following the ionization of intact cytochrome c [42]. In the MALDI process, the iron reduction within the complex may be due either to the relatively high electron affinity of the metalloporphyrins or to the presence of free electrons in the plume; however, an excess of energy is required to simulate CID conditions. When analyzing cytochrome C at low concentrations (<0.1 mg/mL) using our experimental setup, no signal attributable to heme c was detected until higher concentrations (1.0 mg/mL) were investigated. These findings suggest that the greater presence of neutral species within the MALDI plume, due to the concentration increase of the protein by a factor of 10, together with the higher laser energy used compared to hemoglobin and myoglobin, can permit the breaking of the covalent bonds releasing heme c. According to Crestoni et al. [43], the protonation of heme occurs at the level of one of the vinyl groups. We were intrigued by this odd behavior of heme c, and therefore we also investigated the complex bound to protein after its digestion by trypsin, following a classical bottom-up approach for peptide mass fingerprinting (PMF). The proteolysis was carried out on hemoglobin, myoglobin, and cytochrome c, and both CCICA and CHCA were employed as matrices. Also in this case, the use of CHCA allowed us to ionize the heme group very well alongside the peptides arising from each protein, which were still detectable but with less intensity. As an example, Figure 7 reports the PMF of Cyt C analyzed by using CCICA (A) and CHCA (B). It is possible to observe the occurrence of heme c at m/z 617.18 at a higher intensity in Figure 7B compared to Figure 7A where CCICA was employed, also confirming the efficacy of CHCA in ionizing the heme group in the complex

sample. Further, it is interesting to note the base peak in Figure 7B at m/z 1633.50 which corresponds to a peptide ambiguously assigned to the sequence IFVQKCAQCHTVEK or CAQCHTVEK combined with a heme group [44]. To confirm the attribution, M/MS was performed, and the results are reported in Figure 7C. The manual inspection of the spectrum identifies the origin of the peak as CAQCHTVEK + heme, since some y ions bear the heme moiety [44] which was correspondingly observed as an intense fragment ion at m/z 616.17. Very fascinatingly, the energy applied for the dissociation of peptides is likely similar to the energy required to simulate CID conditions in ESI, and indeed the ion was detected as in hemoglobin and myoglobin [42]. The main difference between CHCA and CCICA relies on the different ionization yields of heme and heme-modified peptides. The coverage of PMF was higher using CCICA (88% vs. 66 % for cyt C), but the detection of iron-containing peptides was greatly enhanced without any further time-consuming enrichment procedure [45].

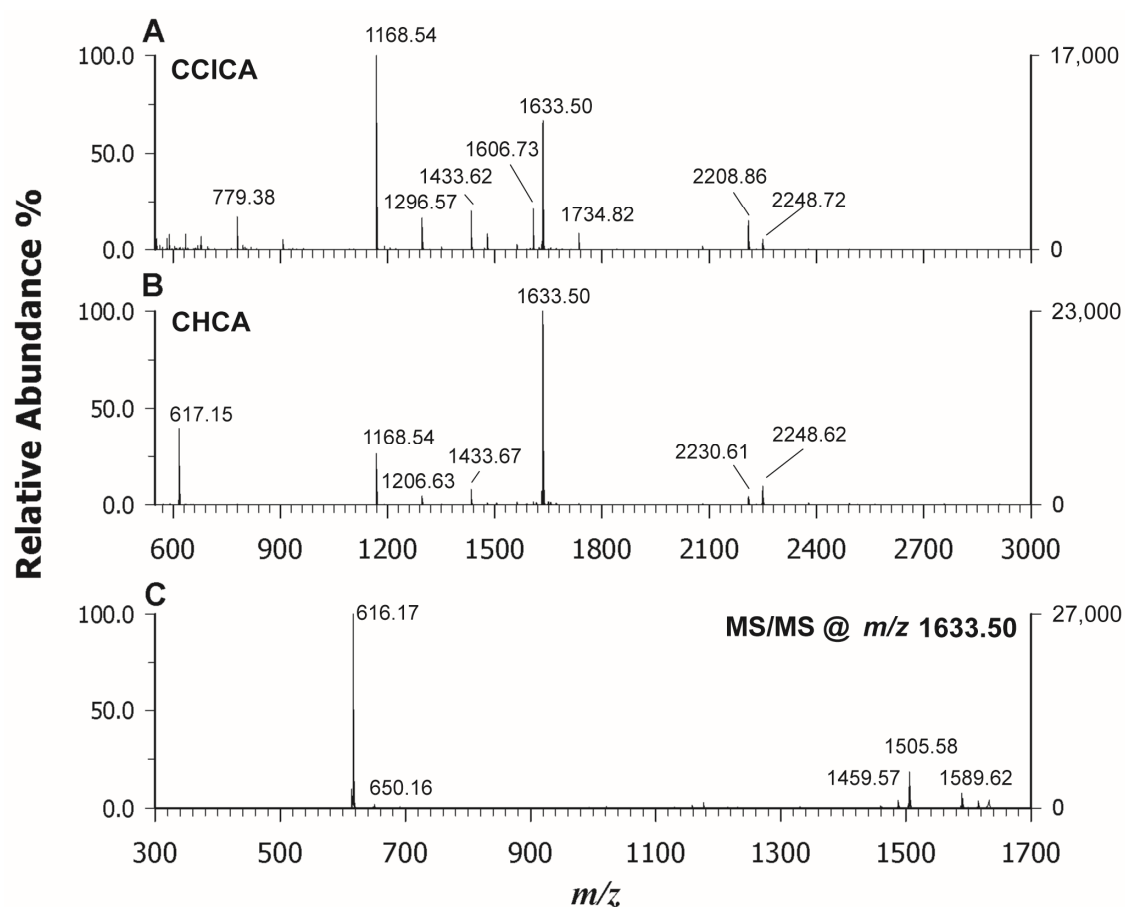


Figure 7. MALDI-ToF mass spectra in positive ion mode of a tryptic digest of cytochrome C analyzed using CCICA (A) and CHCA (B) as a matrix. The tandem MS spectrum of heme-modified peptide detected at m/z 1633.50 using CHCA as a matrix is shown in plot (C).

Given the excellent properties of CHCA in the ionizing heme group, it was chosen for its analysis and MS(/MS) characterization on real samples. Figure 8 shows the MALDI MS spectra of blood (A), bovine liver (B), fish liver (C), and mussel (D) simply diluted in water as described in the Section 3. In all cases, the ion at m/z 616.18 was the base peak, suggesting the occurrence of heme b as an unbounded group likely in hemoglobin and myoglobin (in the liver). To confirm the attribution of heme, MS/MS data were collected for each sample and Figure 8E reports the spectrum of heme b in blood analyzed using an isolation window ± 3 m/z units wide. The fragmentation spectrum obtained is identical to that obtained for heme b extracted from hemoglobin standard protein (see Figure S3).

As can be seen, the base peak is represented by the ion fragment at m/z 557.15, due to a β -cleavage from one of the two carboxyl substituents with loss of a carboxymethyl radical and formation of the porphyrin radical cation stabilized by a π conjugated system which allows the delocalization of the unpaired electron. Another important peak is represented by the ion at m/z 543.14, a radical cation formed following the homolytic breaking of the bond between the porphyrin macrocycle and one propionic group. All other fragments, resulting from homolytic bond breaks, are explained in the inset of Figure S3. Some signals, however, are more difficult to interpret as the peak at m/z 498.15, for example, resulting from the simultaneous loss of both propionic groups, should be at m/z 499.15. One possible explanation may be the choice of the large isolation window which includes both m/z 616 and 617, as we also perceived the fragment at m/z 498.15 in the MS/MS spectrum of heme c.

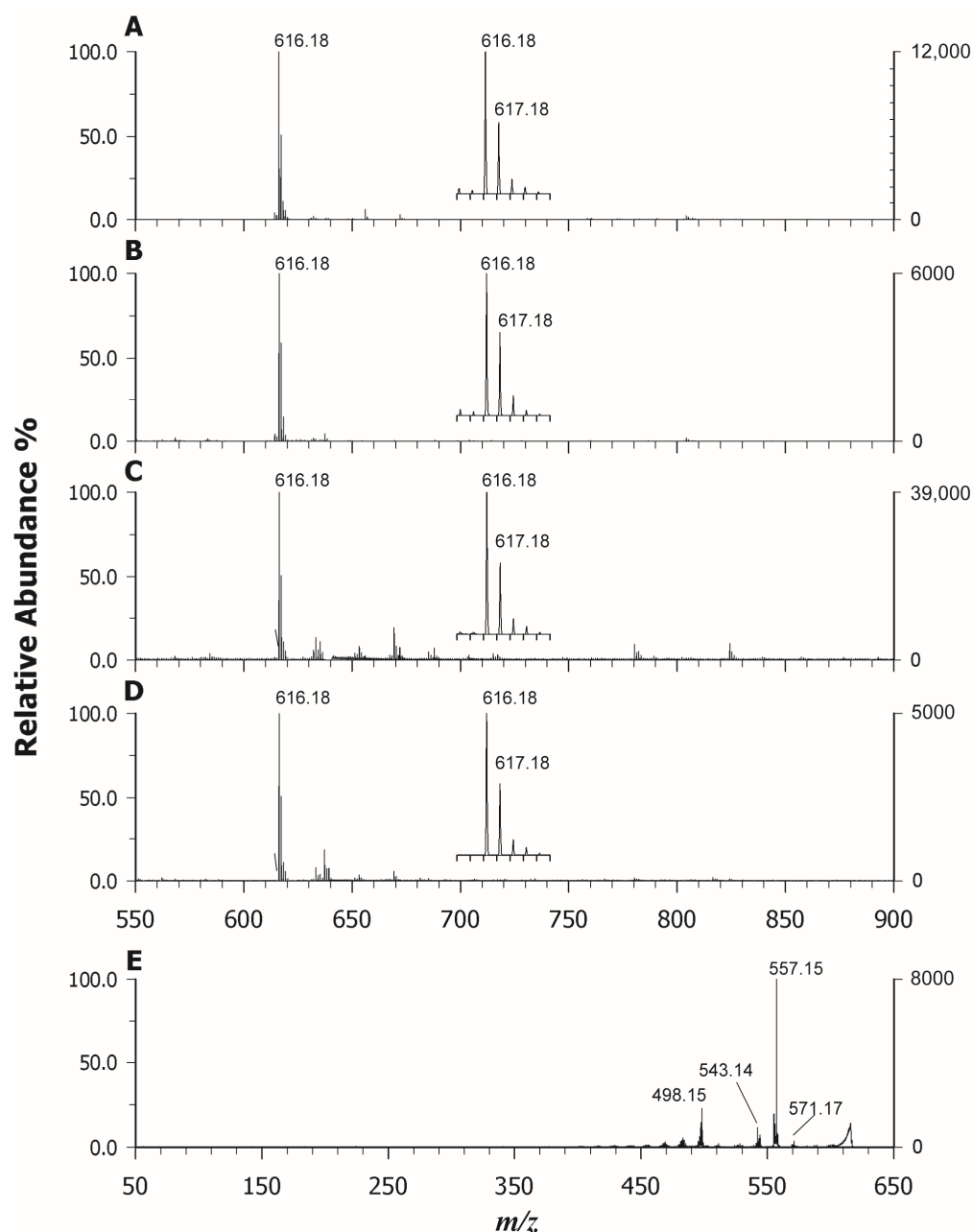


Figure 8. MALDI-ToF mass spectra in positive ion mode of blood (A), bovine liver (B), fish liver (C), and mussel (D) using CHCA as a matrix. (E) Tandem MS spectrum of heme b at m/z 616.18 using CHCA as a matrix.

3. Materials and Methods

3.1. Chemicals

Water, acetone, acetonitrile, trifluoroacetic acid (TFA), 2,2':5',2''-terthiophene (TER), 1,5-diaminonaphthalene (DAN), trans-2-[3-(4-t-butyl-phenyl)-2-methyl-2-propenyldiene] malononitrile (DCTB), 4-hydroxy- α -cyano cinnamic acid (CHCA), 4-chloro- α -cyano cinnamic acid (CCICA), Nickel(II) phthalocyanine (NiPc), Nickel(II) 2,9,16,23-tetraphenoxy-29H-31H-phthalocyanine (NiPcPhe), Cu(II) phthalocyanine (CuPc), Zinc(II) Protoporphyrin IX (ZnPP), Cobalt chloride (II) Protoporphyrin IX (CoPP), cytochrome c (horse heart), myoglobin, human hemoglobin, and proteomic-grade trypsin, were obtained from Sigma-Aldrich (Milan, Italy). Livers of cod and bovine as well as mussel were purchased from a local supermarket. Plasma was drawn from a healthy voluntary subject. All solvents used were LC-MS grade. A mass standards kit containing bradykinin (2–9 clip), angiotensin I, glu1-fibrinopeptide, ACTH (1–17, 18–39, 7–38 clips) for calibration was purchased from AB Sciex (Concord, ON, Canada).

3.2. Instrumentation

All experiments were performed using a 5800 MALDI ToF/ToF analyzer (AB SCIEX, Darmstadt, Germany) equipped with a neodymium-doped yttrium lithium fluoride (Nd:YLF) laser (345 nm), in reflectron positive mode with a typical mass accuracy of 5 ppm. In MS and MS/MS mode, 1000 laser shots were normally accumulated by a random rastering pattern at laser pulse rates of 400 and 1000 Hz, respectively; the mass spectra shown in this paper were averaged on at least five single mass spectra (1000 laser shots each). MS/MS experiments were performed setting a potential difference of 1 kV between the source and the collision cell; collision-induced dissociation (CID) modality was activated using argon as the collision gas with a medium pressure of 10^{-6} Torr. The delayed extraction (DE) time was set at 400 ns. The laser fluences used were fixed close to the laser threshold for each matrix within a range of 1.9–2.5 J/m². DataExplorer software 4.0 (AB Sciex) was used to control the acquisitions and to perform the initial elaboration of data, while SigmaPlot 14.0 was used to graph the final mass spectra. ChemDraw Pro 8.0.3 (CambridgeSoft Corporation, Cambridge, MA, USA) was employed to draw chemical structures.

3.3. Sample Preparation

3.3.1. Standard Phthalocyanines and Protoporphyrins

Nickel(II) phthalocyanine, Nickel(II) 2,9,16,23-tetraphenoxy-29H-31H-phthalocyanine, Copper(II) phthalocyanine, and Zinc(II) protoporphyrin IX were prepared at 1 mg/mL concentration in THF. For cobalt chloride (II) protoporphyrin IX, a 0.5 mg/mL solution was prepared since it tended to precipitate at higher concentrations. For MALDI analyses, 5 μ L of the resulting solutions were mixed with an equal volume of each matrix solution (DAN, DCTB, TER, CHCA, and CCICA, 5 mg/mL in acetone); 1 μ L of this solution was then spotted onto a MALDI plate and allowed to dry. Analyses also in LDI modality were carried out by depositing 1 μ L of each standard solution directly on the target.

3.3.2. Standard Hemoglobin, Myoglobin, and Cytochrome c

Human hemoglobin, bovine myoglobin, and cytochrome c were prepared at a concentration of 0.5 mg/mL in water. For tryptic digestion, 50 μ L of each solution was added with 2.5 μ L of trypsin 0.1 g/L and incubated overnight in a thermo-shaker at 37 °C under stirring at 400 rpm. Alternatively, these solutions were subjected to microwave digestion at 37 °C for 1 h (800 W output at 60 Hz, AC 220–240 V) but digestion yield was not reproducible so only the samples digested overnight are discussed here. For MALDI analyses, 5 μ L of the resulting solution (before and after digestion) were mixed with an equal volume of each matrix solution (DAN, CHCA, CCICA, DCTB, 10 mg/mL in 70:30 ACN:0.1% TFA); 1 μ L of this solution was then spotted on to a MALDI plate and allowed to dry. Unless otherwise specified, the dried-droplet method was used throughout this work. Analyses in

LDI modality were also carried out. **WARNING:** Caution should be taken when handling DAN due to possible carcinogenetic effects. Exposure to the chemical should be minimized and fume hoods should always be used.

3.3.3. Heme in Blood and Food Samples

Blood samples were diluted 50 times with water and analyzed as such. Bovine and cod liver and mussel were homogenized in a mortar, and then 5 mg of each were dissolved in 1 mL of water. After centrifugation ($4300\times g$ for 10 min) the supernatant was collected and analyzed as such. All samples were also digested; 50 μL of each solution was added to 2.5 μL of trypsin 0.1 g/L and incubated overnight at 37 °C under stirring at 400 rpm. For MALDI analyses, 5 μL of the resulting solution (before and after digestion) were mixed with an equal volume of each matrix solution (CHCA and CCICA, 10 mg/mL in 70:30 ACN:0.1% TFA); 1 μL of this solution was then spotted on to a MALDI plate and allowed to dry.

4. Conclusions

In this study, we conducted a characterization of porphine-derivative compounds using MALDI MS/MS in positive ion mode, following a careful selection of the appropriate matrix. Our findings reveal that ET or PT matrices can be employed for protoporphyrin analysis, but for enhanced signals in both MS and MS/MS acquisitions, CCICA proves to be more effective. In the case of phthalocyanines, the LDI-MS is consistently preferable, mitigating interference from matrix-related peaks. This is crucial as phthalocyanines absorb laser energy significantly, allowing desorption and adequate internal energy for successive fragmentation. Despite the inherent stability of these compounds, achieving robust fragmentation spectra becomes challenging unless substituted phthalocyanine variants are explored. For the ionization of heme b and c, CHCA stands out as a MALDI matrix, demonstrating great utility in the analysis of iron-containing peptides. Remarkably, CHCA facilitates the easy detection of heme b even in complex samples such as blood and food, eliminating the need for time-consuming pre-treatment. By simply diluting the sample and applying CHCA as a matrix, we achieved reliable results. As we continue to explore the vast realm of porphyrin-like metabolites in nature or newly synthesized compounds, our study underscores the potency of MALDI-MS/MS when coupled with the right matrix. This combination proves to be a robust and sensitive technique for the successful characterization of these compounds in biological samples.

Supplementary Materials: The following supporting information can be downloaded at: <https://www.mdpi.com/article/10.3390/molecules29040868/s1>. Figure S1. MALDI-ToF mass spectra in positive ion mode using 2-[(2E)-3-(4-tert-butylphenyl)-2-methylprop-2-enylidene]malononitrile (DCTB) as a matrix of heme b in hemoglobin (A), in myoglobin (B), and heme c in cytochrome C (C). Figure S2. MALDI-ToF mass spectra in positive ion mode using CCICA as a matrix of heme b in hemoglobin (A), in myoglobin (B), and heme c in cytochrome C (C). Figure S3. Tandem MS spectrum of heme b from hemoglobin standard protein at m/z 616.18 using CHCA as a matrix.

Author Contributions: Conceptualization, C.D.C. and A.M.; Methodology, M.B., G.V., C.D.C. and A.M.; Formal Analysis, G.V. and M.B.; Investigation, M.B., G.V. and C.D.C.; Data Curation: G.V. and M.B.; Writing—Original Draft Preparation, C.D.C. and A.M.; Writing—Review and Editing, I.L. and T.R.I.C.; Funding Acquisition, T.R.I.C. All authors have read and agreed to the published version of the manuscript.

Funding: This work was supported by the project PONa3_00395/1 “BIOSCIENZE & SALUTE (B&H)” of Italian Ministero per l’Istruzione, l’Università e la Ricerca (MIUR).

Data Availability Statement: The authors confirm that most of the data supporting the findings of this study are available within the article and its supplementary material. Raw data are available from the corresponding authors (C.D.C. and A.M.) on request.

Conflicts of Interest: The authors declare no conflict of interest.

References



1. Watanabe, F.; Yabuta, Y.; Bito, T.; Teng, F. Vitamin B12-containing plant food sources for vegetarians. *Nutrients* **2014**, *6*, 1861–1873. [CrossRef]
2. Hopp, M.T.; Schmalohr, B.F.; Kühl, T.; Detzel, M.S.; Wißbrock, A.; Imhof, D. Heme Determination and Quantification Methods and Their Suitability for Practical Applications and Everyday Use. *Anal. Chem.* **2020**, *92*, 9429–9440. [CrossRef] [PubMed]
3. Caughey, W.S.; Ibers, J.A. Crystal and Molecular Structure of the Free Base Porphyrin, Protoporphyrin IX Dimethyl Ester. *J. Am. Chem. Soc.* **1977**, *99*, 6639–6645. [CrossRef] [PubMed]
4. Calvano, C.D.; Ventura, G.; Cataldi, T.R.I.; Palmisano, F. Improvement of chlorophyll identification in foodstuffs by MALDI ToF/ToF mass spectrometry using 1,5-diaminonaphthalene electron transfer secondary reaction matrix. *Anal. Bioanal. Chem.* **2015**, *407*, 6369–6379. [CrossRef] [PubMed]
5. Huang, S.C.; Hung, C.F.; Wu, W.B.; Chen, B.H. Determination of chlorophylls and their derivatives in *Gynostemma pentaphyllum* Makino by liquid chromatography-mass spectrometry. *J. Pharm. Biomed. Anal.* **2008**, *48*, 105–112. [CrossRef]
6. Carlsson, M.L.R.; Kanagarajan, S.; Bülow, L.; Zhu, L.H. Plant based production of myoglobin—A novel source of the muscle heme-protein. *Sci. Rep.* **2020**, *10*, 920. [CrossRef]
7. Xing, Y.; Gao, S.; Zhang, X.; Zang, J. Dietary Heme-Containing Proteins: Structures, Applications, and Challenges. *Foods* **2022**, *11*, 3594. [CrossRef]
8. Shan, L.; Xu, X.; Zhang, J.; Cai, P.; Gao, H.; Lu, Y.; Shi, J.; Guo, Y.; Su, Y. Increased hemoglobin and heme in MALDI-TOF MS analysis induce ferroptosis and promote degeneration of herniated human nucleus pulposus. *Mol. Med.* **2021**, *27*, 103. [CrossRef]
9. Hooda, J.; Shah, A.; Zhang, L. Heme, an essential nutrient from dietary proteins, critically impacts diverse physiological and pathological processes. *Nutrients* **2014**, *6*, 1080–1102. [CrossRef]
10. Gu, S.; Marianov, A.N.; Lu, T.; Zhong, J. A review of the development of porphyrin-based catalysts for electrochemical CO₂ reduction. *Chem. Eng. J.* **2023**, *470*, 144249. [CrossRef]
11. Paolesse, R.; Nardis, S.; Monti, D.; Stefanelli, M.; Di Natale, C. Porphyrinoids for Chemical Sensor Applications. *Chem. Rev.* **2017**, *117*, 2517–2583. [CrossRef]
12. Teo, R.D.; Hwang, J.Y.; Termini, J.; Gross, Z.; Gray, H.B. Fighting Cancer with Corroles. *Chem. Rev.* **2017**, *117*, 2711. [CrossRef] [PubMed]
13. Gregory, P. Industrial applications of phthalocyanines. *J. Porphyr. Phthalocyanines* **2000**, *4*, 432–437. [CrossRef]
14. Fernández, C.C.; Williams, F.J. Reactions involving the central cavity of porphyrin molecules attached to self-assembled monolayers. *Inorganica Chim. Acta* **2023**, *556*, 121678. [CrossRef]
15. Zheng, W.; Shan, N.; Yu, L.; Wang, X. UV-visible, fluorescence and EPR properties of porphyrins and metalloporphyrins. *Dye Pigment.* **2008**, *77*, 153–157. [CrossRef]
16. Wang, J.; Tan, S.; Liang, Q.; Guan, H.; Han, Q.; Ding, M. Selective separation of bovine hemoglobin using magnetic mesoporous rare-earth silicate microspheres. *Talanta* **2019**, *204*, 792–801. [CrossRef]
17. Fateen, E.; Abd-Elfattah, A.; Gouda, A.; Ragab, L.; Nazim, W. Porphyrins profile by high performance liquid chromatography/electrospray ionization tandem mass spectrometry for the diagnosis of porphyria. *Egypt. J. Med. Hum. Genet.* **2011**, *12*, 49–58. [CrossRef]
18. Woltering, M.; Tulipani, S.; Boreham, C.J.; Walshe, J.; Schwark, L.; Grice, K. Simultaneous quantitative analysis of Ni, VO, Cu, Zn and Mn geoporphyrins by liquid chromatography-high resolution multistage mass spectrometry: Method development and validation. *Chem. Geol.* **2016**, *441*, 81–91. [CrossRef]
19. Magi, E.; Ianni, C.; Rivarolo, P.; Frache, R. Determination of porphyrins and metalloporphyrins using liquid chromatography–diode array detection and mass spectrometry. *J. Chromatogr. A* **2001**, *905*, 141–149. [CrossRef]
20. Monopoli, A.; Calvano, C.D.; Nacci, A.; Palmisano, F. Boronic acid chemistry in MALDI MS: A step forward in designing a reactive matrix with molecular recognition capabilities. *Chem. Commun.* **2014**, *50*, 4322–4324. [CrossRef]
21. Bradshaw, R.; Bleay, S.; Clench, M.R.; Francese, S. Direct detection of blood in fingerprints by MALDI MS profiling and Imaging. *Sci. Justice* **2014**, *54*, 110–117. [CrossRef]
22. Srinivasan, N.; Haney, C.A.; Lindsey, J.S.; Zhang, W.; Chait, B.T. Investigation of MALDI-TOF Mass Spectrometry of Diverse Synthetic Metalloporphyrins, Phthalocyanines and Multiporphyrin Arrays. *J. Porphyr. Phthalocyanines* **1999**, *3*, 283–291. [CrossRef]
23. Kim, T.; Lee, J.; Kim, J. Effect of laser intensity on the apparent isotope patterns of heme and peptide ions in MALDI-TOF MS. *Int. J. Mass. Spectrom.* **2015**, *376*, 13–18. [CrossRef]
24. Yang, H.J.; Park, K.H.; Shin, S.; Lee, J.H.; Park, S.; Kim, H.S.; Kim, J. Characterization of heme ions using MALDI-TOF MS and MALDI FT-ICR MS. *Int. J. Mass. Spectrom.* **2013**, *343*, 37–44. [CrossRef]
25. Whiteaker, J.R.; Fenselau, C.C.; Fetterolf, D.; Steele, D.; Wilson, D. Quantitative Determination of Heme for Forensic Characterization of *Bacillus* Spores Using Matrix-Assisted Laser Desorption/Ionization Time-of-Flight Mass Spectrometry. *Anal. Chem.* **2004**, *76*, 2836–2841. [CrossRef]
26. Yin, Z.; Sun, B.; Wang, X.; Cheng, X.; Hang, W.; Huang, B. Comprehensive analysis of metalloporphyrins via high irradiance laser ionization time-of-flight mass spectrometry. *J. Anal. At. Spectrom.* **2014**, *29*, 1714–1719. [CrossRef]
27. Calvano, C.D.; Ventura, G.; Palmisano, F.; Cataldi, T.R.I. 4-Chloro- α -cyanocinnamic acid is an efficient soft matrix for cyanocobalamin detection in foodstuffs by matrix-assisted laser desorption/ionization mass spectrometry (MALDI MS). *J. Mass Spectrom.* **2016**, *51*, 841–848. [CrossRef] [PubMed]

28. Calvano, C.D.; Ventura, G.; Trotta, M.; Bianco, G.; Cataldi, T.R.I.; Palmisano, F. Electron-Transfer Secondary Reaction Matrices for MALDI MS Analysis of Bacteriochlorophyll a in Rhodobacter sphaeroides and Its Zinc and Copper Analogue Pigments. *J. Am. Soc. Mass Spectrom.* **2017**, *28*, 125–135. [CrossRef] [PubMed]
29. Calvano, C.D.; Capozzi, M.A.M.; Punzi, A.; Farinola, G.M.; Cataldi, T.R.I.; Palmisano, F. 1,5-Diaminonaphthalene is a Highly Performing Electron-Transfer Secondary-Reaction Matrix for Laser Desorption Ionization Mass Spectrometry of Indolenine-Based Croconaines. *ACS Omega* **2018**, *3*, 17821–17827. [CrossRef]
30. Calvano, C.D.; Monopoli, A.; Cataldi, T.R.I.; Palmisano, F. MALDI matrices for low molecular weight compounds: An endless story? *Anal. Bioanal. Chem.* **2018**, *410*, 4015–4038. [CrossRef]
31. Buchler, J.W. Static coordination chemistry of metalloporphyrins. In *Porphyrins and Metalloporphyrins*; Smith, K.M.E., Ed.; Elsevier: Amsterdam, The Netherlands, 1975; pp. 157–231.
32. Knochenmuss, R. An Introduction to MALDI Ionization Mechanisms for Users of Mass Spectrometry Imaging. In *MALDI Mass Spectrometry Imaging: From Fundamentals to Spatial Omics*; Porta Siegel, T., Ed.; The Royal Society of Chemistry: London, UK, 2021; pp. 1–19.
33. Nazim Boutaghou, M.; Cole, R.B. 9,10-Diphenylanthracene as a matrix for MALDI-MS electron transfer secondary reactions. *J. Mass Spectrom.* **2012**, *47*, 995–1003. [CrossRef]
34. Wei, J.; Li, H.; Barrow, M.P.; O'Connor, P.B. Structural characterization of chlorophyll-a by high resolution tandem mass spectrometry. *J. Am. Soc. Mass Spectrom.* **2013**, *24*, 753–760. [CrossRef]
35. Rigante, E.C.L.; Calvano, C.D.; Picca, R.A.; Modugno, F.; Cataldi, T.R.I. An insight into spray paints for street art: Chemical characterization of two yellow varnishes by spectroscopic and MS-based spectrometric techniques. *Vacuum* **2023**, *215*, 112350. [CrossRef]
36. Zhang, S.; Chen, Y.; Liu, J.A.; Xiong, S.X.; Wang, G.H.; Chen, J.; Yang, G.Q. New matrix of MALDI-TOF MS for analysis of small molecules. *Chin. Chem. Lett.* **2009**, *20*, 1495–1497. [CrossRef]
37. Copper Phthalocyanine, CI 74160. Available online: <https://webbook.nist.gov/cgi/inchi?ID=C147148&Mask=200#Mass-Spec> (accessed on 28 December 2023).
38. Nickel Phthalocyanine. Available online: <https://webbook.nist.gov/cgi/inchi?ID=C14055028&Mask=200> (accessed on 28 December 2023).
39. Achar, B.N.; Fohlen, G.M.; Lokesh, K.S. Degradation study on the thermally stable nickel phthalocyanine sheet polymer. *Polym. Degrad. Stab.* **2003**, *80*, 427–433. [CrossRef]
40. Pashynska, V.A.; Van Den Heuvel, H.; Claeys, M.; Kosevich, M.V. Characterization of noncovalent complexes of antimalarial agents of the artemisinin-type and Fe(III)-Heme by electrospray mass spectrometry and collisional activation tandem mass spectrometry. *J. Am. Soc. Mass Spectrom.* **2004**, *15*, 1181–1190. [CrossRef] [PubMed]
41. Demirev, P.A.; Feldman, A.B.; Kongkasuriyachai, D.; Scholl, P.; Sullivan, D.; Kumar, N. Detection of Malaria Parasites in Blood by Laser Desorption Mass Spectrometry. *Anal. Chem.* **2002**, *74*, 3262–3266. [CrossRef] [PubMed]
42. Li, Y.T.; Hsieh, Y.L.; Henion, J.D.; Ganem, B. Studies on heme binding in myoglobin, hemoglobin, and cytochrome c by ion spray mass spectrometry. *J. Am. Soc. Mass Spectrom.* **1993**, *4*, 631–637. [CrossRef] [PubMed]
43. Chiavarino, B.; Crestoni, M.E.; Fornarini, S.; Rovira, C. Protonated Heme. *Chem.—A Eur. J.* **2007**, *13*, 776–785. [CrossRef]
44. Shin, S.; Yang, H.J.; Kim, J.H.; Kim, J.; Lee, J.H.; Park, K.H.; Kim, H.S.; Kim, J. Clarification of a peak at m/z 1634 from tryptically digested cytochrome c. *J. Mass Spectrom.* **2012**, *47*, 1576–1581. [CrossRef]
45. Zhang, H.; Yang, F.; Qian, W.J.; Brown, R.N.; Wang, Y.; Merkley, E.D.; Park, J.H.; Monroe, M.E.; Purvine, S.O.; Moore, R.J.; et al. Identification of c-Type Heme-Containing Peptides Using Non-Activated Immobilized Metal Affinity Chromatography Resin Enrichment and Higher-Energy Collisional Dissociation. *Anal. Chem.* **2011**, *83*, 7260–7268. [CrossRef] [PubMed]

Disclaimer/Publisher's Note: The statements, opinions and data contained in all publications are solely those of the individual author(s) and contributor(s) and not of MDPI and/or the editor(s). MDPI and/or the editor(s) disclaim responsibility for any injury to people or property resulting from any ideas, methods, instructions or products referred to in the content.

Review

Recent Progress in Mass Spectrometry-Based Metabolomics in Major Depressive Disorder Research

Mingxia Liu ^{1,2} , Wen Ma ³ , Yi He ^{1,2}, Zuoli Sun ^{1,2,*} and Jian Yang ^{1,2,*}

¹ Beijing Key Laboratory of Mental Disorders, National Clinical Research Center for Mental Disorders, National Center for Mental Disorders, Beijing Anding Hospital, Capital Medical University, Beijing 100088, China; liumingxia14@mails.ucas.ac.cn

² Advanced Innovation Center for Human Brain Protection, Capital Medical University, Beijing 100069, China

³ State Key Laboratory of Natural and Biomimetic Drugs, School of Pharmaceutical Sciences, Peking University, Beijing 100191, China

* Correspondence: sunzuoli@mail.ccmu.edu.cn (Z.S.); yangjian@ccmu.edu.cn (J.Y.)

Abstract: Major depressive disorder (MDD) is a serious mental illness with a heavy social burden, but its underlying molecular mechanisms remain unclear. Mass spectrometry (MS)-based metabolomics is providing new insights into the heterogeneous pathophysiology, diagnosis, treatment, and prognosis of MDD by revealing multi-parametric biomarker signatures at the metabolite level. In this comprehensive review, recent developments of MS-based metabolomics in MDD research are summarized from the perspective of analytical platforms (liquid chromatography-MS, gas chromatography-MS, supercritical fluid chromatography-MS, etc.), strategies (untargeted, targeted, and pseudotargeted metabolomics), key metabolite changes (monoamine neurotransmitters, amino acids, lipids, etc.), and antidepressant treatments (both western and traditional Chinese medicines). Depression subphenotypes, comorbid depression, and multi-omics approaches are also highlighted to stimulate further advances in MS-based metabolomics in the field of MDD research.

Keywords: major depressive disorder; mass spectrometry; metabolomics; biomarkers



Citation: Liu, M.; Ma, W.; He, Y.; Sun, Z.; Yang, J. Recent Progress in Mass Spectrometry-Based Metabolomics in Major Depressive Disorder Research. *Molecules* **2023**, *28*, 7430. <https://doi.org/10.3390/molecules28217430>

Academic Editors: Igor Jerković and Susy Piovesana

Received: 25 September 2023

Revised: 24 October 2023

Accepted: 2 November 2023

Published: 4 November 2023



Copyright: © 2023 by the authors. Licensee MDPI, Basel, Switzerland. This article is an open access article distributed under the terms and conditions of the Creative Commons Attribution (CC BY) license (<https://creativecommons.org/licenses/by/4.0/>).

1. Introduction

Major depressive disorder (MDD) is a debilitating and widespread psychiatric illness characterized by enduring and substantial feelings of sadness, inferiority, and despair [1]. Notably, the World Health Organization has listed depression as the third leading cause of disease burden across the world and has predicted that the disease will rank first by 2030 [2]. However, due to the complicated pathogenesis of depression and the lack of pathophysiological biomarkers, the diagnosis and treatment of MDD using subjective evaluation and “trial-and-error” approaches often involve considerable error rates [3].

Metabolites are the downstream products of transcription and translation, and changes in those closest to a given phenotype can reflect many pathological or internal changes in biochemical pathways [4]. Metabolic disorders are considered to be an etiological factor in MDD, and metabolite analysis can certainly improve our understanding of the many pathological processes involved in MDD [5,6]. Metabolomics is the culmination of the cascade of “omics” technologies. It combines advanced analytical instrumentations with pattern recognition algorithms to reveal and monitor changes in metabolite profiles in subjects based on their disease status or response to medical or other interventions [7]. Advances in metabolomics have opened new avenues for exploring mechanisms related to MDD.

The main analytical platforms in metabolomics are nuclear magnetic resonance (NMR) and mass spectrometry (MS) [8]. NMR enables non-invasive analysis and relatively fast and straightforward metabolite annotation, but is less sensitive than MS. In-depth explanations and discussions of NMR-based metabolomics can be found in various excellent

studies and reviews [9–11]. MS is widely used in metabolomics analyses. It combines rapidly developing separation technologies—primarily liquid chromatography (LC) and gas chromatography (GC)—to allow qualitative and quantitative analysis of multiple organic molecules in complex biological matrices (serum, plasma, urine, tissue, etc.) with high specificity, sensitivity, and throughput, and low sample consumption [12]. Given these advantages, the applications of MS in metabolomics research have grown exponentially in recent years.

This review focuses on advances in research into MDD using MS-based metabolomics. Common analytical procedures and key metabolic changes during pathogenesis and treatment are described, and current challenges and prospects are discussed with a view to enhancing research into this condition.

A search of electronic literature bases from 2020 to August 2023 (PubMed [$n = 170$] and Web of Science [$n = 192$]) was conducted using the keywords “depression”, “metabolomics”, and “mass spectrometry”. After a preliminary review of these studies, articles in which the disease studied was not depression or the research method was not metabolomics were excluded. In addition, the reference lists of all identified studies were manually searched to identify any additional studies. Finally, 142 studies that met our criteria were identified, and these reports were reviewed. Figure 1 summarizes the numbers of studies in our review for the different MS-based analytical platforms and metabolomics strategies.

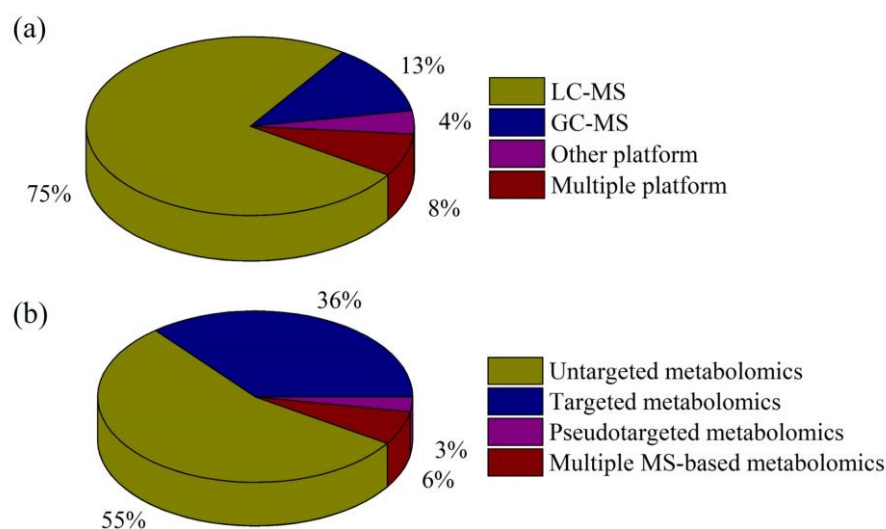


Figure 1. Percentages of reviewed, published studies utilizing various (a) MS-based analytical platforms and (b) metabolomics strategies.

2. MS-Based Metabolomics Platforms in Depression Research

2.1. MS Platforms in Depression Research

Current state-of-the-art metabolomics technologies are mostly based on MS. Due to the need for measurement of isomers, isobars, and structurally similar analogs, chromatographic MS is preferred for metabolite profiling. LC-MS and GC-MS are the two primary platforms used in metabolomics research into depression, although other platforms, such as supercritical fluid chromatography-MS (SFC-MS) and capillary electrophoresis-MS (CE-MS), also play significant roles (Figure 1a).

2.1.1. LC-MS

LC-MS is capable of detecting most compounds, including non-volatile and thermally labile metabolites, with or without derivatization and is, thus, the most frequently used platform in metabolomics analysis of depression. LC-MS analysis uses various types of columns, including reverse phase (RP-LC-MS; e.g., C18, C8, and C30 columns), normal phase (NP-LC-MS), and hydrophilic interaction (HILIC-LC-MS). RP and HILIC are mainly

used for separation of weakly polar and polar compounds, respectively. Recently, an all-in-one-injection HILIC-MS/MS method was developed for the simultaneous determination of 20 purine and pyrimidine metabolites and used to show greatly disturbed purine metabolism in the serum and hippocampus of depressed mice [13]. Our group established a convenient LC-MS/MS method for the simultaneous measurement of 18 amino acid enantiomers using a conventional octadecylsilane RP column and chiral derivatization reagent. Significant differences in glycine, L-threonine, and D-methionine between late-life depression patients and controls were revealed by this method [14]. Sensitive Profiling ChemoSelective Derivatization Carboxylomics (SPCSDCarboxyl) was proposed by Zhou's group in 2023 for the analysis of carboxylic acids using 5-(diisopropylamino) amyamine derivatization and ultra-performance LC-quadrupole time-of-flight MS (UHPLC-Q-TOF/MS) [15]. Two hundred and eight metabolites were identified in the serum of depressed patients using SPCSDCarboxyl, and a combination of proline, 1-pyrroline-5-carboxylate, and glutamic acid could distinguish between patients and healthy controls. Mocking et al. measured 399 metabolites in patients with recurrent MDD using an established LC-MS/MS platform, and 80% of the recurring metabolic predictors belonged to the phospholipid, sphingomyelin, glycosphingolipid, eicosanoid, microbiome, or purine pathways [16].

2.1.2. GC-MS

GC-MS is suitable for the analysis of volatile organic compounds (VOCs), although derivatization is required to increase the thermal stability and volatility of non-volatile compounds and to reduce their polarity. Due to the high reproducibility of electron ionization in MS, GC-MS can utilize many mass spectra libraries, which enables relatively easy identification of peaks. Several studies have shown that urinary metabolite biomarkers identified by GC-MS can identify post-stroke depression (PSD) in stroke survivors [17]. A biomarker panel consisting of glyceric acid, tyrosine, and azelaic acid was identified in middle-aged and elderly patients with PSD [18,19]. Solid-phase microextraction and GC-MS were used to analyze urinary VOCs and semi-VOCs in patients with late-life major depressive and anxiety disorders. The combined indicators dimethylsulfone, phenethyl isothiocyanate, hexanoic acid, texanol, and texanol isomers showed excellent performance in evaluating MDD and/or agoraphobia in the elderly [20].

2.1.3. Other Chromatography-MS Platforms

Interest in SFC-MS in depression research has grown in recent years due to its excellent separation capabilities and environmental friendliness. It shows remarkable performance in the analysis of lipids. In-line supercritical fluid extraction coupled with SFC-MS/MS method was used to rapidly separate 23 inflammation-related lipids in brain tissue of depressed rats within 15 min. Six pro-inflammatory lipids increased in depressed rats, while six anti-inflammatory lipids decreased [21]. Analysis of VOCs in exhaled breath using proton-transfer-reaction MS (PTR-MS) is a hot topic in the field of depression research, given its advantageous real-time, in-line, and non-invasive attributes. Lueno et al. conducted the first PTR-MS study of the differences in VOCs in exhaled breath in MDD patients and healthy controls. There were significant differences in several masses between the groups, with $m/z = 69, 74, 93,$ and 94 being identified as potential high-accuracy biomarkers [22]. This group then applied breathomics (one of the newest branches of metabolomics) using untargeted PTR-MS to explore changes in biochemical patterns and metabolic pathways related to MDD. A total of 23 differential exhaled metabolites were significantly altered in MDD patients, and these were mapped to five metabolic pathways [23]. Recently, an interesting study from Frodl's group used PTR-MS to analyze gut-brain axis VOCs and distinguish between schizophrenia, MDD, and healthy controls [24]. CE-MS is a powerful tool that combines the high separation capability and low sample consumption of CE with the identification capabilities of MS. Okamoto et al. used CE and Fourier transform MS to identify differential patterns of serum metabolites in MDD patients with and without

type 2 diabetes mellitus, indicating that this comorbidity can affect metabolic pathways and alter the distribution of serum metabolites in MDD patients [25].

2.1.4. Combined Chromatography-MS Platforms

A single analytical technique cannot encompass all metabolites, given their wide-ranging physicochemical properties and broad concentration ranges. For example, Xie's group used GC-MS to characterize differential metabolites in the olfactory bulb (OB) of rats with chronic unpredictable mild stress (CUMS). Disruption of lipid and purine metabolisms was demonstrated, which may be related to dysfunction of the OB [26]. Subsequently, Zhou's group used LC-MS to investigate metabolic changes in the OB of mice and, in contrast to the previous GC-MS results, demonstrated disruption of the tryptophan-5-hydroxytryptamine pathway [27]. These findings show that different analytical techniques can highlight different metabolic perspectives, and it is necessary to adopt multiple chromatography-MS platforms in the search for new depression biomarkers and molecular mechanisms. A combination of GC-MS and LC-MS/MS was used to analyze metabolite profiles in plasma, urine, and cerebrospinal fluid (CSF) of patients with treatment-refractory depression and suicidal behavior [28]. A significant proportion of patients showed treatable abnormalities, while no healthy controls exhibited metabolic abnormalities. A metabolome-wide association study using two separate UHPLC-MS/MS injections and one GC/MS injection of each sample found that the level of lauroylcarnitine in serum was decreased in patients with depression, which may indicate fatty acid oxidation and/or mitochondrial dysfunction in depression [29].

2.2. Metabolomics Strategies in Depression Research

Metabolomics is a branch of "omics" technology focusing on high-throughput identification and quantification of small molecule metabolites (<1500 Da). It can describe specific multi-parameter characteristics of the heterogeneous pathophysiological mechanisms underlying depression. There are three main MS-based metabolomics approaches in depression research: untargeted, targeted, and pseudotargeted analyses (Figure 1b).

2.2.1. Untargeted Metabolomics

Untargeted methods are typically used in metabolomics studies for the detection and discovery of small organic compounds, with high-resolution MS (HRMS) using Orbitrap or Q-TOF instruments providing full-scan information, accurate masses, and tandem MS details of the metabolites. Although untargeted metabolomics suffers from high complexity, poor repeatability, and limited linear range, it remains the first choice for the metabolite discovery stage because it is unbiased and has high coverage. Jiao et al. used the classic untargeted metabolomics technique (UHPLC-Q-TOF-MS) to investigate the antidepressant-like effects of Jiaotaiwan on rats [30]. Changes in the metabolite profile of rat serum before and after administration were analyzed using multiple statistical approaches. The most important biomarkers associated with depression were identified via principal component analysis, partial least squares discriminant analysis, and heatmap analysis. Pathway analysis then revealed that the therapeutic effect of Jiaotaiwan on depression may involve the regulation of amino acid, glycerophospholipid, and energy metabolisms. Untargeted metabolomics was also used to identify O-acetyl-L-carnitine, L-aspartic acid, fumarate, and alanine as peripheral biomarkers in patients with MDD [31]. To clarify the metabolites involved in specific pathways, a stable isotope-resolved metabolomics method was developed and applied in depression research for the first time by Qin's group [32]. The stable isotope tracer $^{13}\text{C}_6$ -glucose was prepared and introduced into a CUMS rat model, and labeled metabolites were detected by LC-MS using HILIC and T3 chromatography columns. Twenty-eight of the 78 labeled metabolites related to energy metabolism in the model group differed significantly from the control group.

2.2.2. Targeted Metabolomics

Targeted metabolomics based on triple-quadrupole MS (TQMS) is generally used in the verification phase to confirm the identity of, and to quantify, compounds of interest. When using multiple reaction monitoring (MRM) mode, targeted analysis is characterized by high sensitivity, strong specificity, good repeatability, and wide linear range, but it is limited by its relatively narrow coverage of metabolites. However, continuous development of ionization efficiency, scanning rate, and other parameters has enabled the simultaneous analysis of dozens to hundreds of metabolites by TQMS. Energy-related metabolites, carnitine, amino acids, and biogenic amines were quantified in the ventral hippocampus of rats with chronic mild stress (CMS) using LC-MS/MS. Glycolysis and the tricarboxylic acid cycle were particularly involved in defining vulnerability to stress [33]. To avoid the addition of internal standards and corresponding analogs, Chen et al. developed a targeted metabolomics method involving relative quantification based on HILIC-MS/MS and the quality control-based random forest signal correction algorithm [34]. Nineteen metabolites were simultaneously determined in the serum of MDD patients, the changes in urocanic acid being reported for the first time.

2.2.3. Pseudotargeted Metabolomics

The recently developed pseudotargeted metabolomics approach combines the benefits of targeted and untargeted analyses. By extracting MRM transitions from biological samples, pseudotargeted profiling offers higher coverage of metabolites than targeted profiling. Furthermore, the use of selected ion monitoring (SRM) mode gives pseudotargeted profiling a wider linear range and better data quality than untargeted profiling. However, some limitations of pseudotargeted metabolomics still need to be addressed. For example, a combination of HRMS and TQMS is usually required, some detected metabolites cannot be identified, and it is only semi-quantitative [35]. There are many applications of targeted and untargeted metabolomics in studies of depression, but only a few studies have used pseudotargeted methods. In 2020, Yang et al. described a segment data-dependent acquisition (SDDA)-based pseudotargeted approach for analysis of depressed rats treated with liquiritin [36]. A total of 502 MRM transitions were detected, and five metabolic pathways were found to be related to depression. This same research group subsequently developed comprehensive pseudotargeted lipidomics methods based on SDDA and two- or three-phase liquid extraction to elucidate the differential lipids related to depression. Broadening the lipid coverage and addressing analyte co-elution enabled 53 and 61 differential variables to be identified in the plasma of depressed rats in these studies [37,38]. Yang et al. also described a green and efficient ultra-high performance supercritical fluid chromatography-MS (UHPSFC-MS/MS)-based pseudotargeted lipidomics method that detected 758 lipids within 8 min [39]. This method had a shorter analytical runtime, narrower peaks, higher sensitivity, and better separation of lipid isomers than the UHPLC-MS/MS-based pseudotargeted method. Applications of the pseudotargeted metabolomics approach in depression research are still in their infancy but show great potential.

2.2.4. Combined Metabolomics Strategies

Increasing attempts are being made to determine the complete metabolite profile for depression by combining multiple MS-based metabolomic approaches. Untargeted methods are often used as an initial screening assay in clinical biomarker discovery studies, with only those metabolites showing significant differences being confirmed using targeted, quantitative assays. Lee et al. profiled serum metabolites using an untargeted method, identifying 14 metabolites with differences between MDD and control groups [40]. The efficacy of endogenous acetylcarnitine for the diagnosis of depression and determination of remission status was then confirmed using a targeted SRM approach. Similarly, Wang et al. used untargeted serum metabolomics and pathway analysis to show that abnormal amino acid metabolism in mice with chronic social defeat stress (CSDS) is related to their abnormal behavior, and the reduction in leucine revealed by targeted metabolomics is specifically

and positively related to the social interaction rate [41]. The antidepressant mechanism of the Chaihu–Baishao herb pair was investigated using combined untargeted and targeted analyses [42]. Twenty-one metabolic pathways that were synergistically regulated by Chaihu–Baishao were identified via cortex metabolomics based on UPLC-Q-Orbitrap/MS, and the crucial impact on the purine metabolism pathway was quantitatively confirmed by UPLC-MS/MS in MRM mode.

3. Key Metabolic Changes in Depression

Advances in MS-based metabolomics techniques have been crucial in driving the progress of research into depression. Recent applications of MS-based metabolomics in depression biomarker discovery and elucidation of pathogenic mechanisms are summarized below.

3.1. Monoamine Neurotransmitters

The “monoamine hypothesis” is important in the study of depression, and the development of the majority of clinical antidepressants has been based on monoamine neurotransmitters [43]. Although considerable progress has been made in this area, the underlying mechanisms remain unclear and treatments are increasingly controversial. Monoamine neurotransmitters can interact with other metabolic pathways in depression. The “monoamine (5-HT)-Glutamate/GABA long neural circuit”, proposed by Li, holds the view that monoaminergic and non-monoaminergic mechanisms form a long neural circuit that mediates rapid antidepressant effects [44]. Li et al., using LC-MS/MS, studied changes in neurotransmitters and their related metabolites in GABAergic, serotonergic, and catecholaminergic pathways in the nucleus accumbens of CUMS-induced anhedonia-like rats [45]. The level of 5-hydroxytryptamine in anhedonia-susceptible rats increased, while dopamine did not change significantly. Xu et al. found that gut microbiota (GM) can activate monoamines via stimulating the enteroendocrine cells to produce 5-hydroxytryptamine, dopamine, and norepinephrine, which can affect the central nervous system. The brain in turn can regulate gastrointestinal functions through the neuro-immune-endocrine system [46]. Using LC-MS/MS, Zhong’s group showed that *Morinda officinalis* oligosaccharides alleviated depression via the tryptophan-5-hydroxytryptophan-serotonin metabolic pathway in the GM [47]. In addition, monoamine neurotransmitters are intertwined with numerous new depression pathways, such as inflammation, oxidative stress, neurotrophins, and neurogenesis. In-depth explanation and discussion can refer to some excellent works and reviews [5,43].

3.2. Amino Acids

Amino acids and their metabolites are fundamental substrates and regulators in many metabolic pathways and some have been identified as biomarkers of depression. Untargeted GC-MS identified significant changes in L-alanine, L-glutamic acid, glycine, L-methionine, L-phenylalanine, L-valine, L-isoleucine, and L-norleucine in the main stress-targeted tissues of CUMS-induced mice [48]. High levels of glutamic acid, aspartic acid, and glycine and low levels of 3-hydroxykynurenine were quantified by LC-MS in serum of MDD patients, and the levels of glutamic acid and phenylalanine correlated with the severity of depression [49]. Significant negative associations of the branched-chain amino acids valine and leucine with depression were identified using untargeted metabolomics [50]. Increased glutamate, decreased dopamine, and altered trends in γ -aminobutyric acid in the habenula of CUMS-susceptible and -resilient rats were identified using LC-MS/MS [51].

Disruption of the tryptophan pathway plays a crucial role in MDD. Tryptophan is metabolized alongside the kynurenine, serotonin, and microbial pathways. Brum et al. found that levels of all tryptophan catabolites were reduced in the plasma of patients with MDD, bipolar depression (BD), and schizophrenia (SCZ), but these metabolites could not be used to distinguish between the disorders [52]. A similar conclusion was also reached by Liu et al. [53]. Yun et al. studied the relationship between the tryptophan–kynurenine pathway

and the painful physical symptoms of MDD [54]. Patients with such symptoms exhibited higher kynurenine, quinolinic acid, and kynurenine/tryptophan ratios than those without. Tryptophan metabolism is central to communication between the GM and the brain in depression [55]. LC-MS/MS showed that kynurenine and 3-hydroxycaninuric acid increased significantly along the gut–brain axis of depressive-like rats subjected to chronic restraint stress (CRS) [56]. The tryptophan–kynurenine pathway is also linked to the inflammatory state of patients with MDD [57]. Haroon et al. analyzed kynurenine pathway metabolites and inflammatory markers in the plasma and CSF of depressed patients [58]. Kynurenine and kynurenine/tryptophan in plasma, and kynurenine, kynurenic acid, and quinolinic acid in CSF were closely related to plasma tumor necrosis factor. Pau et al. replicated and expanded upon these findings by evaluating more metabolites and suggesting that the levels of some peripheral kynurenine pathway metabolites might serve as proxies for central kynurenine pathway metabolites in patients with MDD [59]. Zheng et al. also found that C-reactive protein and kynurenic acid/quinolinic acid are independently associated with white matter integrity in MDD [60]. Some studies indicate that therapy can affect tryptophan metabolism. Tateishi et al. reported that levels of kynurenine, kynurenic acid, and kynurenine/tryptophan ratio in plasma of patients with treatment-resistant depression were unchanged after repetitive transcranial magnetic stimulation treatment [61]; however, Ryan et al. reported that the kynurenic acid pathway was mobilized by electroconvulsive therapy [62].

3.3. Lipids

Lipids are a broad class of biomolecules with essential roles in many cellular processes, including molecular signal transduction, energy storage, and cell membrane formation. Advanced MS-based lipidomics methods have deepened our understanding of the lipidome in the central and peripheral nervous systems and its associations with depression [6]. Miao et al. identified lipid networks associated with the risk of depression using untargeted LC-MS lipid analysis [63]. For example, lower levels of sphingomyelins and glycerophospholipids and higher levels of lysophospholipids were associated with the incidence and/or prevalence of depression. An LC-MS lipidomics study identified 13 differentially expressed lipids in the plasma of adult female MDD and BD patients and could distinguish between these conditions with medium confidence (area under the curve [AUC] was 0.860) [64]. Similarly, a panel of 111 lipid species was capable of distinguishing SCZ from MDD (AUC = 0.920) [65]. Glycerophospholipids are critical components of neuronal membranes and eukaryote cellular membranes. LC-MS lipid metabolite profiling in the hippocampus of PSD rats showed 50 key metabolites were reduced, and these were mainly involved in glycerophospholipid metabolism (particularly cardiolipin metabolism) [66]. Glycerophospholipid metabolism was also associated with the pathogenesis of PSD in humans [67,68]. Various lipidomics studies have confirmed that peripheral and central glycerophospholipid metabolism disorders are involved in the pathogenesis of depression via the microbiome–gut–brain axis [69–72]. Jiang et al. used UHPLC-Q-TOF-MS to investigate plasma metabolite biomarkers in young MDD patients and identified phosphatidylcholine as a female-specific biomarker (AUC = 0.957) [73]. Schumacher et al. found that ceramide concentration in the plasma of MDD patients correlated with the severity of MDD, and neutralization of ceramides abrogated depressive behavior in mice [74]. Untargeted UHPLC-MS metabolomics revealed that phosphatidylserine (16:0/16:1) and phosphatidic acid (18:1/18:0) were significantly increased in plasma of MDD patients [75].

3.4. Energy Metabolism

Many studies have shown that energy metabolism is impaired in patients with depression. This may point towards new treatments for the condition. Most of the body's energy comes from the tricarboxylic acid cycle, oxidative phosphorylation, and glycolysis [76]. Wang et al. demonstrated, using metabolomics, that the tricarboxylic acid cycle was inhibited in mice exposed to CSDS and in patients with first-episode depression [77]. The altered

metabolism of acylcarnitines may link mitochondrial dysfunction to depression via impairment of fatty acid β -oxidation [78]. Lower levels of acetyl-L-carnitine and medium- and long-chain acylcarnitines and higher levels of L-carnitine and L-carnitine/acetyl-L-carnitine ratio were found in the plasma of depressed patients, but these differences disappeared after treatment [79,80]. Acylcarnitine profiles also help to distinguish different phenotypic subtypes of MDD, such as core depression, anxious depression, and neurovegetative symptoms of melancholia [81]. Given that glycogen is the main energy source for most higher organisms, Qin's group used stable isotope-resolved metabolomics with a $^{13}\text{C}_6$ -glucose tracer to reveal the blockage of the tricarboxylic acid cycle and abnormal activation of gluconeogenesis in rats with CUMS and in corticosteroid-induced PC12 cells [82–86].

3.5. Gut Microbiota and Metabolomics

The relationship between the GM and depression is a particular focus of psychobiology research, but the underlying molecular mechanisms remain unclear [87]. A combination of 16S rRNA gene sequencing and MS-based metabolomics is often used to investigate these GM mechanisms in patients with depression and in CUMS, CSDS, and CRS mouse models [88]. Growing evidence from this toolkit of clinical studies and animal models suggests that GM compositions (e.g., the phylum Firmicutes and genera *Bacteroides* and *Lactobacillus*) and related metabolites (e.g., short-chain fatty acids and tryptophan metabolism) are disordered in depression along the brain–gut–microbiota axis. For example, Xie et al. found that two crucial tryptophan metabolism-related metabolites (tryptophan and 5-hydroxytryptophan) were reduced in the feces of CSDS mice, and these compounds were associated with *Lactobacillus* [89]. Zhang et al. showed that *Bacteroides* species enriched in the GM of MDD patients had differing effects on the susceptibility to depressive behaviors [90]. This was partly explained by the different changes in tryptophan pathway metabolites and neurotransmitters along the gut–brain axis. The relationship between microbial metabolites in feces and neurotransmitters in the prefrontal cortex of depressed mice was also explored using targeted metabolomics [91]. This suggested that the disruption of microbial metabolites may affect prefrontal cortex neurotransmitter levels, leading to depressive episodes. This same phenomenon—simultaneous changes in brain and gut metabolism in CUMS rats—was also observed by Hu et al. [92]. Our group used whole-genome shotgun metagenomic and untargeted metabolomic methods to identify disturbed microbial genes (in *Bacteroides*, *Blautia*, and *Eubacterium*) and fecal metabolites (γ -aminobutyrate, phenylalanine, and tryptophan) in MDD patients [93]. The antidepressant effect of chenodeoxycholic acid regulated by *Blautia* and *Eubacterium* has also been studied [94]. Table 1 summarizes the GM-related metabolites that have been reported to be associated with depression.

Table 1. Examples of metabolites associated with gut microbiota that have been reported to be associated with depression.

Gut Microbiome Profiling Method	Gut Microbiota	Metabolomics Method	Metabolic Pathway	Subject/Sample Type	Reference
16S rRNA gene sequencing	Phylum Firmicutes and genus <i>Lactobacillus</i>	Targeted metabolomics/UHPLC-MS/MS	Tryptophan metabolism	Mice (CSDS)/feces and hippocampus	[89]
16S rRNA gene sequencing and metagenomic analysis	<i>Lachnospiraceae</i>	Untargeted metabolomics/UPLC-Q-TOF-MS and targeted metabolomics/UPLC-MS/MS	Glycerophospholipid metabolism and γ -aminobutyric acid	Mice (CUMS)/feces, liver, and hippocampus	[72]
16S rRNA gene sequencing and metagenomic analysis	Phylum Firmicutes	Untargeted metabolomics/UPLC-Q-TOF-MS and targeted metabolomics/UPLC-MS/MS	Glycerophospholipid metabolism, tryptophan pathway, and short-chain fatty acids	Mice (CRS)/feces, serum, and hippocampus	[71]

Table 1. Cont.

Gut Microbiome Profiling Method	Gut Microbiota	Metabolomics Method	Metabolic Pathway	Subject/Sample Type	Reference
16S rRNA gene sequencing	Phylum Firmicutes	Untargeted metabolomics/UPLC-Q-TOF-MS	Inflammation-related metabolites	MDD patients/serum and feces	[95]
16S rRNA gene sequencing	Phylum Firmicutes	Untargeted metabolomics/GC-MS and LC-MS	Glycerophospholipid metabolism	Cynomolgus macaque of depression/feces, peripheral, and brain tissue	[69]
16S rRNA gene sequencing	Genus <i>Allobaculum</i> and family <i>Ruminococcaceae</i>	Targeted metabolomics/LC-MS/MS and GC-MS	Acetic acid, propionic acid, pentanoic acid, norepinephrine, 5-hydroxy indole acetic acid, and 5-hydroxy tryptamine	Mice (CRS)/feces and hypothalamus	[96]
16S rRNA gene sequencing	Ten genera (most of them belonged to phylum Firmicutes)	Targeted metabolomics/GC-MS and untargeted metabolomics/LC-Q-Orbitrap/MS	Short chain fatty acids	Rats (PSD)/feces and prefrontal cortex	[97]
16S rRNA gene sequencing	Phylum Firmicutes, genus <i>Blautia</i> , and <i>Streptococcus</i>	Untargeted metabolomics/GC-MS	Lipid metabolism	Rats (PSD)/feces	[98]
16S rRNA gene sequencing	<i>Actinobacteria</i> and <i>Bacteroidetes</i>	Untargeted metabolomics/LC-Q-Orbitrap/MS and GC-MS	Glycerophospholipids	Mice (CSDS)/feces and prefrontal cortex	[70]
Whole-genome shotgun metagenomic	Genus <i>Bacteroides</i> , genera <i>Blautia</i> , and <i>Eubacterium</i>	Untargeted metabolomics/GC-MS	Amino acid metabolism (γ -aminobutyrate, phenylalanine, and tryptophan)	MDD patients/feces	[93]
Viral metagenomics	<i>Microviridae</i> , <i>Podoviridae</i> , and <i>Siphoviridae</i>	Targeted metabolomics/UPLC-MS/MS	Tryptophan metabolism	Mice (CRS)/feces	[99]
16S rDNA amplification sequencing	<i>Deferribacteres</i> , <i>Proteobacteria</i> , <i>Verrucomicrobia</i> , <i>Actinobacteria</i> , <i>Desulfovibrio</i> , <i>Clostridium_IV</i> , <i>Helicobacter</i> , <i>Pseudoflavonifractor</i> , and <i>Akkermansia</i>	Untargeted metabolomics/LC-MS/MS	Lipid metabolites, glycerophospholipid metabolism Pathway, and the retrograde endocannabinoid signaling pathway	Atherosclerosis co-depression mice/feces	[100]
16S rRNA gene sequencing	<i>Turicibacteraceae</i> , <i>Turicibacterales</i> , and <i>Turicibacter</i>	Targeted metabolomics/UPLC-MS/MS	Bile acids metabolism	MDD patients/blood and feces	[101]
Metagenomics sequencing	<i>Ruminococcus bromii</i> , <i>Lactococcus chungangensis</i> , and <i>Streptococcus gallolyticus</i>	Targeted metabolomics/HPLC-MS/MS	Lipid, vitamin, and carbohydrate metabolism	MDD patients/blood and feces	[102]
16S rRNA gene sequencing	<i>Bacteroides</i>	Untargeted metabolomics/UPLC-Q-TOF-MS and targeted metabolomics/UPLC-MS/MS	Tryptophan pathway metabolites and neurotransmitters	MDD patients/feces, serum, and tissue samples	[90]
16S rRNA gene sequencing	Phylum Firmicute, <i>Bacteroidetes</i> , genus <i>Faecalibacterium</i> , <i>Roseburia</i> , <i>Subdoligranulum</i> , and <i>Agathobacter</i>	Untargeted metabolomics/UPLC-Q-TOF-MS	Alpha-linolenic acid metabolism, biosynthesis of unsaturated fatty acids, ATP-binding cassette transporters, and bile secretion	Systemic lupus erythematosus patients with depression/feces	[103]
16S rRNA gene sequencing	<i>Streptococcus</i> , <i>Phascolarctobacterium</i> , <i>Akkermansia</i> , <i>Coprococcus</i> , and <i>Streptococcus</i>	Targeted metabolomics/LC-MS/MS	Indole-3-carboxyaldehyde	MDD patients/feces	[104]
16S ribosomal RNA gene sequencing	Family <i>Lachnospiraceae</i> , <i>Muribaculaceae</i> , and <i>Oscillospiraceae</i>	Untargeted metabolomics/LC-Q-Orbitrap/MS	Lipid and amino acid metabolism	Rats (CUMS, CRS, SD, and LH)/feces	[88]
16S rRNA gene sequencing	<i>Alistipes indistinctus</i> , <i>Bacteroides ovatus</i> , and <i>Alistipes senegalensis</i>	Untargeted metabolomics/LC-Q-Orbitrap/MS	D-pinitol, indoxyl sulfate, trimethylamine-oxide, and 3 alpha, 7 alpha-dihydroxy-12-oxocholanoic acid	Rats (CUMS)/feces	[105]

Abbreviations: major depressive disorder (MDD), chronic social-defeat stress (CSDS), chronic unpredictable mild stress (CUMS), chronic restraint stress (CRS), post-stroke depression (PSD), social defeat (SD), and learned helplessness (LH).

4. Metabolomics in Antidepressant Treatment Response

Given the phenotypic complexity of patients' responses to antidepressants, clinical symptoms and "trial-and-error" approaches are insufficient to guide treatment selection for individual patients. Pharmacotherapy is generally the first-choice treatment for MDD. Crucially, the metabolic status of MDD patients exhibiting a response to pharmacotherapy (including remission) appears to differ from non-responsive patients [106]. Pharmacometabolomics (the application of metabolomics in the study of drug effects) has been used to map the effects of antidepressants on metabolite profiles and has provided new insights into the mechanisms of action of various therapies. Some of the studies that have evaluated metabolite changes in animal models and clinical patients following antidepressant treatment are summarized in Table 2. Pharmacological medications have alleviated abnormalities of amino acid, energy, and lipid metabolisms and GM-derived metabolites induced by depression.

Table 2. Applications of metabolomics in the analysis of treatments for depressive disorders.

Treatment	Subject/Sample Type	Analytical Platform	Metabolic Pathway	Reference	
Western medicine	Citalopram, escitalopram	MDD patients/plasma	Targeted metabolomics/LC-MS/MS and flow-injection analysis-MS/MS	Mitochondrial energetics (acylcarnitine metabolism, transport, and β -oxidation) and lipid membrane remodeling	[107]
	Escitalopram	MDD patients/plasma	Targeted metabolomics/LC-MS/MS	Oxysterols	[108]
	Escitalopram	MDD patients/plasma and feces	Untargeted metabolomics/GC-MS	Amino acids and fatty acids	[109]
	Clomipramine	Rats with ultrasound model of depression/frontal cortex and hippocampus	Targeted metabolomics/LC-MS/MS	Alanine, aspartate, and glutamate pathways	[110]
	Fluoxetine hydrochloride	Depression patients/serum	Untargeted metabolomics/UPLC-Q-TOF-MS	Amino acid metabolism, energy metabolism, and lipid metabolism	[111]
	Ketamine	Treatment-resistant depression patients/plasma	Targeted metabolomics/LC-MS/MS and flow injection analysis-MS/MS	Lipid metabolism	[112]
	Ketamine	Mice (CVS)/hippocampus and prefrontal cortex	Untargeted Metabolomics/UPLC-Q-Orbitrap/MS	Sphingolipids, glycerolipids, and fatty acyls	[113]
	Ketamine	Humans/plasma and CSF, mice/plasma and brain	Targeted metabolomics/LC-MS/MS	LAT1, IDO1, NAD ⁺ , the nitric oxide (NO) signaling pathway, and sphingolipid rheostat	[114]
Traditional Chinese medicine	Bupleurum Chinese DC-Paeonia Lactiflora Pall Herb Pair	Rats (CUMS)/cortex	Untargeted metabolomics/UPLC-Q-Orbitrap/MS and targeted metabolomics/UPLC-MS/MS	Purine metabolism	[42]
	Chaigui Granules	Rats (CUMS)/peripheral blood mononuclear cell	Untargeted metabolomics/UPLC-Q-Orbitrap/MS	Purine metabolism	[115]
	Xiaoyao San	Rats (CUMS)/hippocampus	Untargeted metabolomics/UPLC-Q-Orbitrap/MS	Glucose catabolism	[116]
	Xiaoyao San	Rats (CUMS)/hippocampus	Untargeted metabolomics/GC-MS	D-glutamine and D-glutamate metabolism, arginine biosynthesis and alanine, aspartate, and glutamate metabolism	[117]
	Xiaoyao San	Depressed patients/plasma	Untargeted metabolomics/GC-MS	Oxalic and stearic acids	[118]
	Xiaoyao San	Rats (CUMS)/liver	Untargeted metabolomics/UHPLC-Q-Orbitrap/MS	Glutamine, glutamate, and energy metabolism	[119]
	Xiaoyao Pills	Rats (CUMS)/feces, brain, and plasma	Untargeted metabolomics/GC-MS	Metabolites from gut microbiota (benzoic acid, liquiritigenin, glycyrrhetic acid, and saikogenin D) and fatty acids amide Hydrolase	[120]

Table 2. Cont.

Treatment	Subject/Sample Type	Analytical Platform	Metabolic Pathway	Reference
Jia Wei Xiao Yao San	Mice (CRS)/brain	Untargeted metabolomics/LC-TOF-MS and GC-MS	Purine metabolism	[121]
Crocin	Mice (CUMS)/serum, tissues, and feces	Targeted metabolomics/UPLC-Q-TOF/MS	Intestinal flora and tryptophan metabolism	[122]
Schisandrin	Mice (LPS)/feces	Targeted metabolomics/GC-MS/MS	Short chain fatty acid	[123]
Tongxiyaofang polysaccharide	Mice (CUS)/colon microflora	Untargeted metabolomics/UPLC-Q-TOF-MS	Bacterial community and bile acid metabolism	[124]
Morinda officinalis oligosaccharides	Rats (CUMS)/plasma, brain, and feces	Targeted metabolomics/HPLC-MS/MS	Gut microbiota, serotonin, and 5-hydroxytryptophan	[47]
Chaihu-Shugan-San	Mice (CUMS)/serum and liver	Targeted metabolomics/UHPLC-MS/MS	Gut microbiota, bile acids hyocholic acid, and 7-ketodeoxycholic acid	[125]
Zhi-Zi-Chi decoctions	Rats (CUMS)/cecal contents, ileum, and hippocampus	Targeted metabolomics/LC-MS/MS and UHPLC-Q-TOF/MS	Butyrate	[126]
Banxia Xiexin decoction	Atherosclerosis co-depression Mice/hippocampus and prefrontal cortex tissues	Untargeted metabolomics/UPLC-Q-Orbitrap/MS	Glycerophospholipid metabolism, lysophosphatidylcholine, and LPC (20:4) (rep)	[127]
Paeoniflorin	Rats (CUMS)/urine	Untargeted metabolomics/UPLC-Q-Orbitrap/MS	Citrate cycle	[128]
Jiaotaiwan	Rats (CUMS)/serum	Untargeted Metabolomics/UPLC-Q-TOF/MS	Amino acid, glycerophospholipid, and energy metabolism	[30]
Albiflorin	Mice (CUMS, OBX, and LPS)/hippocampus	Targeted metabolomics/UPLC-MS/MS	Phospholipid and tryptophan metabolism	[129]
Xiang-Su Volatile Oil	Menopausal rats by ovariectomy (CUMS)/plasma	Untargeted metabolomics/GC-MS	Phenylalanine, tyrosine, and tryptophan biosynthesis, tyrosine, and tryptophan metabolism	[130]
Huang-lian Jie-du Decoction	Mice (CUMS)/hippocampus, cortex, striatum, and amygdala	Targeted metabolomics/LC-MS/MS	Tryptophan metabolism	[131]
Berberine	Mice (CUMS)/hippocampus, prefrontal cortex, striatum, and amygdala tissues	Untargeted metabolomics/UPLC-Q-TOF/MS and targeted metabolomics/LC-MS/MS	Tryptophan metabolism	[132]
Berberine	Rats (CUMS)/feces	Targeted metabolomics/GC-MS	Short chain fatty acids and monoamine neurotransmitters	[133]
Quercetin	Rats (CUMS)/liver	Untargeted metabolomics/UPLC-MS	Methionine metabolism, bile acid metabolism, and phosphatidylcholine biosynthesis	[134]
Acanthopanax senticosus	Mice (CUMS)/liver	Untargeted metabolomics/GC-MS	Glycine, serine, threonine, starch, and sucrose metabolism	[135]
Radix Bupleuri-Radix Paeoniae Alba	Rats (CUMS)/serum	Untargeted metabolomics/UPLC-Q-Orbitrap/MS	Energy, amino acid, and lipid metabolism	[136]
Bupleurum chinense DC-Paeonia lactiflora Pall	Rats (CUMS)/serum	Untargeted metabolomics/UPLC-Q-Orbitrap/MS	Saikogenin F and benzoic acid	[137]
Baihe-Dihuang Tang	Rats (CUMS)/brain	Untargeted metabolomics/UPLC-Q-TOF/MS and targeted metabolomics/LC-MS/MS	L-glutamate, xanthine, and adenine	[138]

Table 2. Cont.

Treatment	Subject/Sample Type	Analytical Platform	Metabolic Pathway	Reference
L-Theanine	Rats (CUMS)/serum and hippocampal	Untargeted metabolomics/UPLC-Q-TOF-MS and targeted metabolomics/HILC-MS/MS	Amino acid metabolism and lipid metabolism	[139]
Ferulic acid and feruloylated oligosaccharides	Mice (LPS)/serum	Untargeted metabolomics/UPLC-Q-Orbitrap/MS	Phenylalanine, tyrosine, and tryptophan biosynthesis, phenylalanine, and caffeine metabolism	[140]
DL-3-n-butylphthalide	Mice (CSDS)/brain	Targeted metabolomics/LC-MS/MS	Energy metabolism	[141]
Edaravone	Mice (CSDS)/hippocampal and medial prefrontal cortex	Targeted metabolomics/LC-MS/MS	Energy metabolism	[142]
Bifid triple viable capsule	Rats (CUMS)/serum and hippocampal	Untargeted metabolomics/UPLC-Q-TOF-MS	Biosynthesis of unsaturated fatty acids, glycerophospholipid, linoleic acid, and arachidonic acid metabolism	[143]
Bifidobacterium breve CCFM1025	MDD patients/serum and feces	Targeted metabolomics/UHPLC-MS/MS	Gut microbiome and tryptophan metabolism	[144]
Akkermansia muciniphila	Mice (CRS)/serum	Untargeted metabolomics/UHPLC-Q-Orbitrap MS	Hormone and neurotransmitter	[145]
Lactobacillus	Depression mice induced by Ampicillin/cecum content	Targeted metabolomics/GC-MS/MS	Short-chain fatty acids	[146]
Rifaximin	Rats (CUMS)/hippocampus	Targeted metabolomics/LC-MS/MS	Tryptophan metabolism	[147]
Bacillus coagulans Unique IS-2	Rats (CUMS)/plasma	Targeted metabolomics/UPLC-Q-TOF-MS	L-Tryptophan, L-kynurenine, kynurenic-acid, 3-hydroxyanthranilic acid, acetate, propionate, and butyrate	[148]
Aerobic exercise	Rats (CUMS)/serum	Untargeted metabolomics/UPLC-Q-Orbitrap/MS	Amino acid and energy metabolism	[149]
Electroconvulsive therapy	Depressed patients/plasma	Targeted metabolomics/LC-MS	Tryptophan and kynurenine metabolites	[62]
Repetitive transcranial magnetic stimulation	Mice (CUMS)/stool, plasma, prefrontal cortex, and hippocampus	Targeted metabolomics/GC-MS	Polyunsaturated fatty acids	[150]
Repetitive transcranial magnetic stimulation	Treatment-resistant depression patients/plasma	Targeted metabolomics/LC-MS	Kynurenine metabolites	[61]

Other

Abbreviations: major depressive disorder (MDD), chronic unpredictable mild stress (CUMS), chronic restraint stress (CRS), chronic unpredictable stress (CUS), chronic social defeat stress (CSDS), chronic variable stress (CVS), olfactory bulbectomy (OBX), lipopolysaccharide (LPS).

4.1. Western Medicines

Several notable western medicines have contributed significantly to the management of depression, although their mechanisms of action are not fully understood. Escitalopram is one example. It is a commonly used antidepressant of the selective serotonin reuptake inhibitor (SSRI) class, but the response varies between individuals. The mechanism of citalopram/escitalopram was studied using metabolomics targeted at 180 metabolites, and changes in the profiles of acylcarnitine, lipids, and amino acids indicated that mitochondrial energetics and lipid membrane remodeling are implicated in the SSRI treatment response [107]. Recently, our group conducted an LC-MS/MS study on the relationship between plasma oxysterol levels and the effectiveness of escitalopram antidepressant treatment. Oxysterols, especially 27-hydroxycholesterol, decreased in responders and increased in non-responders following escitalopram treatment. This suggests that 27-hydroxycholesterol has potential as an escitalopram response indicator during MDD treatment [108]. We also explored the role of the GM in determining escitalopram treatment efficacy in MDD patients [109]. Such microbiota-centered perspective could potentially

improve antidepressant efficacy in clinical practice. The antidepressant effects of ketamine have received increasing attention since the United States Food and Drug Administration approved (S)-ketamine nasal spray in March 2019 [151,152]. Zhou et al. analyzed changes in lipid compositions in mice with induced chronic variable stress (CVS) and found that disruption of sphingolipids, glycerolipids, and fatty acyls was partially corrected by administration of (S)-ketamine [113]. MS-based metabolomics has been used to analyze the efficacy of various synthetic antidepressants and has made a significant contribution to improving the treatment of depression.

4.2. Traditional Chinese Medicines

Traditional Chinese medicines (TCMs) exhibiting desirable antidepressive effects have gradually attracted more attention because of their strong safety profiles. However, due to the multi-component, multi-target, and multi-channel nature of TCMs, elucidation of their mechanisms of action is challenging. MS-based metabolomics provides a new way to elucidate these mechanisms holistically [153]. For the first time, in 2021, a combination of pharmacodynamics and urine metabolomics based on UPLC-Q-TOF-MS was used to investigate the antidepressant effect of *Millettia speciosa* Champ [154]. L-isoleucine, sebacic acid, and allantoin were identified as potential pharmacodynamic biomarkers related to the efficacy of this TCM. Similarly, LC-MS-based metabolomics of peripheral blood mononuclear cells (PBMCs) was used to investigate the antidepressant mechanism of Chaigui granules [115]. Their antidepressant effects were attributed to improved immune function and regulation of the purine metabolic pathway in PBMCs. The metabolomics analysis of TCMs in Table 2 exhibits a systemic metabolic shift in amino acids (such as alanine, aspartate, glutamate, tryptophan, etc.), organic acids (oxalic acids, stearic acids, bile acid, etc.), and purine, phospholipid, etc. These differential metabolites are mainly involved in amino acid metabolism, lipid metabolism, energy metabolism, gut microbiota metabolism, etc. Such integration of metabolomics with other analytical strategies has provided new insights into the mechanisms of many TCMs and promoted their use as modern treatments for depression.

4.3. Other Treatments

Given the high proportion of refractory or treatment-resistant cases of depression, there is an urgent need for the development of new antidepressants. Metabolomics is an effective strategy in this field. L-theanine is a bioactive component of green tea and a food additive with health benefits. Zhu et al. systematically explored the antidepressant effects of L-theanine in a CUMS rat model using LC-MS/MS and enzyme-linked immunosorbent assay (ELISA) techniques [139]. Untargeted UPLC-Q-TOF-MS highlighted 28 metabolites that changed significantly during L-theanine treatment, while targeted HILIC-MS/MS identified these key amino acids and neurotransmitters and, consequently, their related pathways. By clarifying these preventive mechanisms, this study laid a foundation for the use of L-theanine in the treatment of children and adolescents with depression. Some probiotics also exhibit antidepressant effects and have fewer side effects, have less of an associated stigma, and are less addictive than conventional antidepressants [155]. The therapeutic effect of bifid triple viable probiotic capsules was evaluated in a CUMS rat model, and untargeted metabolomics revealed that the observed reduction in depression-like behavior may be related to endothelin-1 or CREB signaling [143].

5. Perspectives and Conclusions

MDD is a highly heterogeneous condition, but the use of metabolomics to identify specific biological characteristics of clinical sub-phenotypes is expected to improve personalized diagnostic capabilities. Brydges et al. used three metabolomics platforms to evaluate the correlation between metabolomic markers and three symptom dimensions of MDD (melancholic, anxious distress, and immunometabolic) [156]. These symptoms exhibited specific and minimally overlapping metabolomic signatures, suggesting that the

multifaceted disruption of the delicate balance between the GM, dietary lipids, and host lipid metabolism may be a cause of specific MDD symptoms. It is clear that further detailed MS metabolomics studies of the various subtypes of depression are likely to improve clinical diagnosis.

In addition to subtypes of depression, increasing attention has been paid to metabolomics-based research of comorbid depression. Investigation of comorbid depression in mice under social fear conditions suggested that changes in sphingolipid metabolism in the brain may be related to the short- and long-term pathophysiology of social anxiety disorder [157]. The effects and mechanisms of Jiaotaiwan treatment of diabetes mellitus accompanied by depression, and of albiflorin and paeoniflorin in the treatment of cancer-related depression, have been evaluated using MS-based metabolomics, providing greater understanding of the mechanisms of antidepressant therapies [158,159]. Metabolomics is expected to be increasingly used in research into various diseases complicated by depression.

Due to the complexity of the pathogenesis of MDD, the integration of metabolomics with other “omics” technologies is becoming increasingly necessary. Recent studies have combined genomics and metabolomics to characterize various aspects of early- and adult-onset MDD, including adult MDD suicide attempts [160–163]. Integrated proteomics and metabolomics were used to explore antidepressant treatments in animal models and MDD patients [164,165]. Multi-omics methods will improve our understanding and treatment of MDD and enhance prevention strategies, enabling the considerable advancement of precision medicine [166].

Recent advances in MS-based metabolomics platforms have facilitated a more intensive study of depression. This review summarizes the main findings of the most recent studies in this field focusing on the applied platforms (LC-MS, GC-MS, SFC-MS, etc.) and strategies (untargeted, targeted, and pseudotargeted approaches). Key metabolic changes (in monoamine neurotransmitters, amino acids, lipids, energy metabolism, and GM-related metabolism) and the application of metabolomics in antidepressant treatments in western medicines and TCMs are also reviewed. Depression sub-phenotypes, comorbid depression, and multi-omics approaches are also discussed. We expect this review to stimulate new developments in MS-based metabolomics in the field of depression research.

Author Contributions: Conceptualization, M.L. and Z.S.; writing—original draft preparation, M.L.; writing—review and editing, W.M. and Y.H.; supervision, Z.S. and J.Y.; funding acquisition, M.L., Z.S., J.Y. and W.M. All authors have read and agreed to the published version of the manuscript.

Funding: This research was funded by the R&D Program of Beijing Municipal Education Commission (KM202310025007), the National Natural Science Foundation of China (No. 82171525, 82171526), Beijing Talents Project (2020A38), Beijing Key Laboratory of Mental Disorders, Code: 2021JSJB02.

Institutional Review Board Statement: Not applicable.

Informed Consent Statement: Not applicable.

Data Availability Statement: Not applicable.

Conflicts of Interest: The authors declare no conflict of interest.

References

1. Beurel, E.; Toups, M.; Nemeroff, C.B. The bidirectional relationship of depression and inflammation: Double trouble. *Neuron* **2020**, *107*, 234–256. [CrossRef]
2. World Health Organization. Depression. Available online: <https://www.who.int/news-room/fact-sheets/detail/> (accessed on 25 July 2021).
3. Marwaha, S.; Palmer, E.; Suppes, T.; Cons, E.; Young, A.H.; Upthegrove, R. Novel and emerging treatments for major depression. *Lancet* **2023**, *401*, 141–153. [CrossRef] [PubMed]
4. Qiu, S.; Guo, S.F.; Yang, Q.; Xie, Y.Q.; Tang, S.Q.; Zhang, A.H. Innovation in identifying metabolites from complex metabolome—Highlights of recent analytical platforms and protocols. *Front. Chem.* **2023**, *11*, 1129717. [CrossRef] [PubMed]
5. Fries, G.R.; Saldana, V.A.; Finnstein, J.; Rein, T. Molecular pathways of major depressive disorder converge on the synapse. *Mol. Psychiatry* **2023**, *28*, 284–297. [CrossRef] [PubMed]

6. Pinto, B.; Conde, T.; Domingues, I.; Domingues, M.R. Adaptation of lipid profiling in depression disease and treatment: A critical review. *Int. J. Mol. Sci.* **2022**, *23*, 2032. [CrossRef]
7. Duan, J.J.; Xie, P. The potential for metabolomics in the study and treatment of major depressive disorder and related conditions. *Expert Rev. Proteom.* **2020**, *17*, 309–322. [CrossRef]
8. Letertre, M.P.M.; Dervilly, G.; Giraudeau, P. Combined nuclear magnetic resonance spectroscopy and mass spectrometry approaches for metabolomics. *Anal. Chem.* **2021**, *93*, 500–518. [CrossRef]
9. Edison, A.S.; Colonna, M.; Gouveia, G.J.; Holderman, N.R.; Judge, M.T.; Shen, X.N.; Zhang, S.C. NMR: Unique strengths that enhance modern metabolomics research. *Anal. Chem.* **2021**, *93*, 478–499. [CrossRef]
10. Xie, X.F.; Shi, Y.; Ma, L.; Yang, W.Q.; Pu, J.C.; Shen, Y.Q.; Liu, Y.Y.; Zhang, H.P.; Lv, F.J.; Hu, L.B. Altered neurometabolite levels in the brains of patients with depression: A systematic analysis of magnetic resonance spectroscopy studies. *J. Affect. Disord.* **2023**, *328*, 95–102. [CrossRef]
11. Rydin, A.O.; Milaneschi, Y.; Quax, R.; Li, J.; Bosch, J.A.; Schoevers, R.A.; Giltay, E.J.; Penninx, B.W.J.H.; Lamers, F. A network analysis of depressive symptoms and metabolomics. *Psychol. Med.* **2023**, 1–10, (Online ahead of print). [CrossRef]
12. Collins, S.L.; Koo, I.; Peters, J.M.; Smith, P.B.; Patterson, A.D. Current challenges and recent developments in mass spectrometry-based metabolomics. *Annu. Rev. Anal. Chem.* **2021**, *14*, 467–487. [CrossRef]
13. Lu, Z.; Li, S.; Aa, N.; Zhang, Y.; Zhang, R.; Xu, C.; Zhang, S.; Kong, X.; Wang, G.; Aa, J.; et al. Quantitative analysis of 20 purine and pyrimidine metabolites by HILIC-MS/MS in the serum and hippocampus of depressed mice. *J. Pharm. Biomed. Anal.* **2022**, *219*, 114886. [CrossRef]
14. Liu, M.; He, J.; Ruan, C.; Pan, W.; Mao, P.; Sun, Z.; Wang, G.; Yang, J. Simultaneous measurement of amino acid enantiomers in the serum of late-life depression patients using convenient LC-MS/MS method with N(alpha)-(5-fluoro-2,4-dinitrophenyl)-l-leucinamide derivatization. *J. Pharm. Biomed. Anal.* **2023**, *230*, 115387. [CrossRef]
15. Bian, X.; Zhou, N.; Zhao, Y.; Fang, Y.; Li, N.; Zhang, X.; Wang, X.; Li, Y.; Wu, J.L.; Zhou, T. Identification of proline, 1-pyrroline-5-carboxylate and glutamic acid as biomarkers of depression reflecting brain metabolism using carboxylomics, a new metabolomics method. *Psychiat. Clin. Neuros.* **2023**, *77*, 196–204. [CrossRef]
16. Mocking, R.J.T.; Naviaux, J.C.; Li, K.; Wang, L.; Monk, J.M.; Bright, A.T.; Figueroa, C.A.; Schene, A.H.; Ruhé, H.G.; Assies, J.; et al. Metabolic features of recurrent major depressive disorder in remission, and the risk of future recurrence. *Transl. Psychiatry* **2021**, *11*, 37. [CrossRef]
17. Cai, W.; Wang, X.F.; Wei, X.F.; Zhang, J.R.; Hu, C.; Ma, W.; Shen, W.D. Does urinary metabolite signature act as a biomarker of post-stroke depression? *Front. Psychiatry* **2022**, *13*, 928076. [CrossRef] [PubMed]
18. Xie, J.; Han, Y.; Hong, Y.L.; Li, W.W.; Pei, Q.L.; Zhou, X.Y.; Zhang, B.B.; Wang, Y. Identification of potential metabolite markers for middle-aged patients with post-stroke depression using urine metabolomics. *Neuropsych. Dis. Treat.* **2020**, *16*, 2017–2024. [CrossRef] [PubMed]
19. Chen, J.; Lv, Y.N.; Li, X.B.; Xiong, J.J.; Liang, H.T.; Xie, L.; Wan, C.Y.; Chen, Y.Q.; Wang, H.S.; Liu, P.; et al. Urinary metabolite signatures for predicting elderly stroke survivors with depression. *Neuropsychiatr. Dis. Treat.* **2021**, *17*, 925–933. [CrossRef] [PubMed]
20. Fujita, A.; Ihara, K.; Kawai, H.; Obuchi, S.; Watanabe, Y.; Hirano, H.; Fujiwara, Y.; Takeda, Y.; Tanaka, M.; Kato, K. A novel set of volatile urinary biomarkers for late-life major depressive and anxiety disorders upon the progression of frailty: A pilot study. *Discov. Ment. Health* **2022**, *2*, 20. [CrossRef]
21. Jin, W.; Yang, J.; Liu, D.; Zhong, Q.; Zhou, T. Determination of inflammation-related lipids in depressive rats by on-line supercritical fluid extraction-supercritical fluid chromatography-tandem mass spectrometry. *J. Pharm. Biomed. Anal.* **2021**, *203*, 114210. [CrossRef]
22. Lueno, M.; Dobrowolny, H.; Gescher, D.; Gbaoui, L.; Meyer-Lotz, G.; Hoeschen, C.; Frodl, T. Volatile organic compounds from breath differ between patients with major depression and healthy controls. *Front. Psychiatry* **2022**, *13*, 819607. [CrossRef] [PubMed]
23. Gbaoui, L.; Facht, M.; Lueno, M.; Meyer-Lotz, G.; Frodl, T.; Hoeschen, C. Breathomics profiling of metabolic pathways affected by major depression: Possibilities and limitations. *Front. Psychiatry* **2022**, *13*, 1061326. [CrossRef]
24. Henning, D.; Lueno, M.; Jiang, C.; Meyer-Lotz, G.; Hoeschen, C.; Frodl, T. Gut-brain axis volatile organic compounds derived from breath distinguish between schizophrenia and major depressive disorder. *J. Psychiatry Neurosci.* **2023**, *48*, E117–E125. [CrossRef] [PubMed]
25. Okamoto, N.; Hoshikawa, T.; Ikenouchi, A.; Natsuyama, T.; Fujii, R.; Igata, R.; Tesen, H.; Konishi, Y.; Honma, Y.; Harada, M.; et al. Comparison of serum metabolomics pathways and patterns between patients with major depressive disorder with and without type 2 diabetes mellitus: An exploratory study. *J. Integr. Neurosci.* **2023**, *22*, 13. [CrossRef]
26. He, Y.; Wang, Y.; Wu, Z.; Lan, T.; Tian, Y.; Chen, X.; Li, Y.; Dang, R.; Bai, M.; Cheng, K.; et al. Metabolomic abnormalities of purine and lipids implicated olfactory bulb dysfunction of CUMS depressive rats. *Metab. Brain Dis.* **2020**, *35*, 649–659. [CrossRef]
27. Chen, G.; Zhou, S.; Chen, Q.; Liu, M.; Dong, M.; Hou, J.; Zhou, B. Tryptophan-5-HT pathway disorder was uncovered in the olfactory bulb of a depression mice model by metabolomic analysis. *Front. Mol. Neurosci.* **2022**, *15*, 965697. [CrossRef] [PubMed]
28. Pan, L.A.; Segreti, A.M.; Wroblewski, J.; Shaw, A.; Hyland, K.; Hughes, M.; Finegold, D.N.; Naviaux, R.K.; Brent, D.A.; Vockley, J.; et al. Metabolomic disorders: Confirmed presence of potentially treatable abnormalities in patients with treatment refractory depression and suicidal behavior. *Psychol. Med.* **2022**, *11*, 1–9. [CrossRef]

29. Zacharias, H.U.; Hertel, J.; Johar, H.; Pietzner, M.; Lukaschek, K.; Atasoy, S.; Kunze, S.; Völzke, H.; Nauck, M.; Friedrich, N.; et al. A metabolome-wide association study in the general population reveals decreased levels of serum laurycarnitine in people with depression. *Mol. Psychiatry* **2021**, *26*, 7372–7383. [CrossRef]
30. Jiao, Z.; Zhao, H.; Huang, W.; Liang, R.; Liu, Y.; Li, Z.; Li, L.; Xu, Y.; Gao, S.; Gao, S.; et al. An investigation of the antidepressant-like effect of Jiaotaiwan in rats by nontargeted metabolomics based on ultra-high-performance liquid chromatography quadrupole time-of-flight mass spectrometry. *J. Sep. Sci.* **2021**, *44*, 645–655. [CrossRef]
31. Wu, Z.; Yu, H.; Tian, Y.; Wang, Y.; He, Y.; Lan, T.; Li, Y.; Bai, M.; Chen, X.; Chen, Z.; et al. Non-targeted metabolomics profiling of plasma samples from patients with major depressive disorder. *Front. Psychiatry* **2021**, *12*, 810302. [CrossRef] [PubMed]
32. Linghu, T.; Gao, Y.; Li, A.; Shi, B.; Tian, J.; Qin, X. A unique insight for energy metabolism disorders in depression based on chronic unpredictable mild stress rats using stable isotope-resolved metabolomics. *J. Pharm. Biomed. Anal.* **2020**, *191*, 113588. [CrossRef]
33. Brivio, P.; Audano, M.; Gallo, M.T.; Gruca, P.; Lason, M.; Litwa, E.; Fumagalli, F.; Papp, M.; Mitro, N.; Calabrese, F. Metabolomic signature and mitochondrial dynamics outline the difference between vulnerability and resilience to chronic stress. *Transl. Psychiatry* **2022**, *12*, 87. [CrossRef]
34. Chen, H.; Xie, H.; Huang, S.; Xiao, T.; Wang, Z.; Ni, X.; Deng, S.; Lu, H.; Hu, J.; Li, L.; et al. Development of mass spectrometry-based relatively quantitative targeted method for amino acids and neurotransmitters: Applications in the diagnosis of major depression. *J. Pharm. Biomed. Anal.* **2021**, *194*, 113773. [CrossRef]
35. Zheng, F.; Zhao, X.; Zeng, Z.; Wang, L.; Lv, W.; Wang, Q.; Xu, G. Development of a plasma pseudotargeted metabolomics method based on ultra-high-performance liquid chromatography-mass spectrometry. *Nat. Protoc.* **2020**, *15*, 2519–2537. [CrossRef] [PubMed]
36. Yang, J.; Jin, W.; Liu, D.; Zhong, Q.; Zhou, T. Enhanced pseudotargeted analysis using a segment data dependent acquisition strategy by liquid chromatography-tandem mass spectrometry for a metabolomics study of liquiritin in the treatment of depression. *J. Sep. Sci.* **2020**, *43*, 2088–2096. [CrossRef] [PubMed]
37. Huang, M.; Zhou, T. Comprehensive pseudotargeted metabolomics analysis based on two-phase liquid extraction-UHPLC-MS/MS for the investigation of depressive rats. *J. Sep. Sci.* **2022**, *45*, 2977–2986. [CrossRef] [PubMed]
38. Liu, D.; Yang, J.; Jin, W.; Zhong, Q.; Zhou, T. A high coverage pseudotargeted lipidomics method based on three-phase liquid extraction and segment data-dependent acquisition using UHPLC-MS/MS with application to a study of depression rats. *Anal. Bioanal. Chem.* **2021**, *413*, 3975–3986. [CrossRef] [PubMed]
39. Yang, J.; Liu, D.; Jin, W.; Zhong, Q.; Zhou, T. A green and efficient pseudotargeted lipidomics method for the study of depression based on ultra-high performance supercritical fluid chromatography-tandem mass spectrometry. *J. Pharm. Biomed. Anal.* **2021**, *192*, 113646. [CrossRef]
40. Lee, S.; Mun, S.; Lee, Y.R.; Choi, H.; Joo, E.J.; Kang, H.G.; Lee, J. Discovery and validation of acetyl-L-carnitine in serum for diagnosis of major depressive disorder and remission status through metabolomic approach. *Front. Psychiatry* **2022**, *13*, 1002828. [CrossRef]
41. Wang, Q.; Wu, Z.; Xiang, H.; Zhou, Y.; Qin, X.; Tian, J. Revealing the role of leucine in improving the social avoidance behavior of depression through a combination of untargeted and targeted metabolomics. *Food Funct.* **2023**, *14*, 6397–6409. [CrossRef]
42. Chen, J.; Li, T.; Qin, X.; Du, G.; Zhou, Y. Integration of non-targeted metabolomics and targeted quantitative analysis to elucidate the synergistic antidepressant effect of Bupleurum Chinense DC-Paeonia Lactiflora Pall Herb Pair by regulating purine metabolism. *Front. Pharmacol.* **2022**, *13*, 900459. [CrossRef] [PubMed]
43. Jiang, Y.; Zou, D.; Li, Y.; Gu, S.; Dong, J.; Ma, X.; Xu, S.; Wang, F.; Huang, J.H. Monoamine neurotransmitters control basic emotions and affect major depressive disorders. *Pharmaceuticals* **2022**, *15*, 1203. [CrossRef] [PubMed]
44. Li, Y.F. A hypothesis of monoamine (5-HT) – Glutamate/GABA long neural circuit: Aiming for fast-onset antidepressant discovery. *Pharmacol. Therapeut.* **2020**, *208*, 107494. [CrossRef]
45. Li, Y.; Chen, Z.; Zhao, J.; Yu, H.; Chen, X.; He, Y.; Tian, Y.; Wang, Y.; Chen, C.; Cheng, K.; et al. Neurotransmitter and related metabolic profiling in the nucleus accumbens of chronic unpredictable mild stress-induced anhedonia-like rats. *Front. Behav. Neurosci.* **2022**, *16*, 862683. [CrossRef] [PubMed]
46. Xu, Q.Y.; Jiang, M.C.; Gu, S.M.; Zhang, X.L.; Feng, G.K.; Ma, X.J.; Xu, S.J.; Wu, E.X.; Huang, J.S.; Wang, F.S. Metabolomics changes in brain-gut axis after unpredictable chronic mild stress. *Psychopharmacology* **2022**, *239*, 729–743. [CrossRef] [PubMed]
47. Zhang, Z.W.; Gao, C.S.; Zhang, H.; Yang, J.; Wang, Y.P.; Pan, L.B.; Yu, H.; He, C.Y.; Luo, H.B.; Zhao, Z.X.; et al. Morinda officinalis oligosaccharides increase serotonin in the brain and ameliorate depression via promoting 5-hydroxytryptophan production in the gut microbiota. *Acta Pharm. Sin. B* **2022**, *12*, 3298–3312. [CrossRef] [PubMed]
48. Geng, C.; Guo, Y.; Wang, C.; Liao, D.; Han, W.; Zhang, J.; Jiang, P. Systematic impacts of chronic unpredictable mild stress on metabolomics in rats. *Sci. Rep.* **2020**, *10*, 700. [CrossRef]
49. Ho, C.S.H.; Tay, G.W.N.; Wee, H.N.; Ching, J. The utility of amino acid metabolites in the diagnosis of major depressive disorder and correlations with depression severity. *Int. J. Mol. Sci.* **2023**, *24*, 2231. [CrossRef]
50. Whipp, A.M.; Heinonen-Guzejev, M.; Pietiläinen, K.H.; van Kamp, I.; Kaprio, J. Branched-chain amino acids linked to depression in young adults. *Front. Neurosci.* **2022**, *16*, 935858. [CrossRef]

51. Tian, Y.; Wu, Z.; Wang, Y.; Chen, C.; He, Y.; Lan, T.; Li, Y.; Bai, M.; Yu, H.; Chen, X.; et al. Alterations of neurotransmitters and related metabolites in the habenula from CUMS-susceptible and -resilient rats. *Biochem. Biophys. Res. Commun.* **2021**, *534*, 422–428. [CrossRef]
52. Brum, M.; Nieberler, M.; Kehrwald, C.; Knopf, K.; Brunkhorst-Kanaan, N.; Etyemez, S.; Allers, K.A.; Bittner, R.A.; Slattery, D.A.; McNeill, R.V.; et al. Phase—And disorder-specific differences in peripheral metabolites of the kynurenine pathway in major depression, bipolar affective disorder and schizophrenia. *World J. Biol. Psychiatry* **2023**, *24*, 564–577. [CrossRef]
53. Liu, J.C.; Yu, H.; Li, R.; Zhou, C.H.; Shi, Q.Q.; Guo, L.; He, H. A preliminary comparison of plasma tryptophan metabolites and medium- and long-chain fatty acids in adult patients with major depressive disorder and schizophrenia. *Medicina* **2023**, *59*, 413. [CrossRef] [PubMed]
54. Yun, Y.; Zhang, Q.; Zhao, W.; Ma, T.; Fan, H.; Bai, L.; Ma, B.; Qi, S.; Wang, Z.; An, H.; et al. Relationship between the tryptophan-kynurenine pathway and painful physical symptoms in patients with major depressive disorder. *J. Psychosom. Res.* **2022**, *163*, 111069. [CrossRef] [PubMed]
55. Liaqat, H.; Parveen, A.; Kim, S.Y. Neuroprotective natural products' regulatory effects on depression via gut-brain axis targeting tryptophan. *Nutrients* **2022**, *14*, 3270. [CrossRef] [PubMed]
56. Li, C.C.; Ye, F.; Xu, C.X.; Jiang, N.; Chang, Q.; Liu, X.M.; Pan, R.L. Tryptophan-kynurenine metabolic characterization in the gut and brain of depressive-like rats induced by chronic restraint stress. *J. Affect. Disord.* **2023**, *328*, 273–286. [CrossRef]
57. Arteaga-Henriquez, G.; Burger, B.; Weidinger, E.; Grosse, L.; Moll, N.; Schuetze, G.; Schwarz, M.; Wijkhuijs, A.; Op de Beeck, G.; Berghmans, R.; et al. Activation and deactivation steps in the tryptophan breakdown pathway in major depressive disorder: A link to the monocyte inflammatory state of patients. *Prog. Neuropsychopharmacol. Biol. Psychiatry* **2021**, *107*, 110226. [CrossRef] [PubMed]
58. Haroon, E.; Welle, J.R.; Woolwine, B.J.; Goldsmith, D.R.; Baer, W.; Patel, T.; Felger, J.C.; Miller, A.H. Associations among peripheral and central kynurenine pathway metabolites and inflammation in depression. *Neuropsychopharmacology* **2020**, *45*, 998–1007. [CrossRef]
59. Paul, E.R.; Schwieler, L.; Erhardt, S.; Boda, S.; Trepici, A.; Kampe, R.; Asratian, A.; Holm, L.; Yngve, A.; Dantzer, R.; et al. Peripheral and central kynurenine pathway abnormalities in major depression. *Brain Behav. Immun.* **2022**, *101*, 136–145. [CrossRef]
60. Zheng, H.; Teague, T.K.; Yeh, F.-C.; Burrows, K.; Figueroa-Hall, L.K.; Aupperle, R.L.; Khalsa, S.S.; Paulus, M.P.; Savitz, J. C- Reactive protein and the kynurenic acid to quinolinic acid ratio are independently associated with white matter integrity in major depressive disorder. *Brain Behav. Immun.* **2022**, *105*, 180–189. [CrossRef]
61. Tateishi, H.; Setoyama, D.; Kang, D.; Matsushima, J.; Kojima, R.; Fujii, Y.; Mawatari, S.; Kikuchi, J.; Sakemura, Y.; Fukuchi, J.; et al. The changes in kynurenine metabolites induced by rTMS in treatment-resistant depression: A pilot study. *J. Psychiatr. Res.* **2021**, *138*, 194–199. [CrossRef]
62. Ryan, K.M.; Allers, K.A.; McLoughlin, D.M.; Harkin, A. Tryptophan metabolite concentrations in depressed patients before and after electroconvulsive therapy. *Brain Behav. Immun.* **2020**, *83*, 153–162. [CrossRef]
63. Miao, G.; Deen, J.; Struzeski, J.B.; Chen, M.; Zhang, Y.; Cole, S.A.; Fretts, A.M.; Lee, E.T.; Howard, B.V.; Fiehn, O.; et al. Plasma lipidomic profile of depressive symptoms: A longitudinal study in a large sample of community-dwelling American Indians in the strong heart study. *Mol. Psychiatry* **2023**, *28*, 2480–2489. [CrossRef] [PubMed]
64. Zhang, T.; Guo, L.; Li, R.; Wang, F.; Yang, W.M.; Yang, J.B.; Cui, Z.Q.; Zhou, C.H.; Chen, Y.H.; Yu, H.; et al. Alterations of plasma lipids in adult women with major depressive disorder and bipolar depression. *Front. Psychiatry* **2022**, *13*, 927817. [CrossRef] [PubMed]
65. Wang, F.; Guo, L.; Zhang, T.; Cui, Z.Q.; Wang, J.K.; Zhang, C.; Xue, F.; Zhou, C.H.; Li, B.J.; Tan, Q.R.; et al. Alterations in plasma lipidomic profiles in adult patients with schizophrenia and major depressive disorder. *Medicina-Lithuania* **2022**, *58*, 1509. [CrossRef] [PubMed]
66. Jiang, W.; Chen, J.; Gong, L.; Liu, F.; Zhao, H.; Mu, J. Alteration of glycerophospholipid metabolism in hippocampus of post-stroke depression rats. *Neurochem. Res.* **2022**, *47*, 2052–2063. [CrossRef]
67. Wen, L.L.; Yan, C.M.; Zheng, W.C.; Li, Y.; Wang, Y.H.; Qu, M. Metabolic alterations and related biological functions of post-stroke depression in ischemic stroke patients. *Neuropsych. Dis. Treat.* **2023**, *19*, 1555–1564. [CrossRef]
68. Mao, Q.; Tian, T.; Chen, J.; Guo, X.; Zhang, X.; Zou, T. Serum metabolic profiling of late-pregnant women with antenatal depressive symptoms. *Front. Psychiatry* **2021**, *12*, 679451. [CrossRef]
69. Zheng, P.; Wu, J.; Zhang, H.; Perry, S.W.; Yin, B.; Tan, X.; Chai, T.; Liang, W.; Huang, Y.; Li, Y.; et al. The gut microbiome modulates gut-brain axis glycerophospholipid metabolism in a region-specific manner in a nonhuman primate model of depression. *Mol. Psychiatry* **2021**, *26*, 2380–2392. [CrossRef]
70. Gong, X.; Huang, C.; Yang, X.; Chen, J.; Pu, J.; He, Y.; Xie, P. Altered fecal metabolites and colonic glycerophospholipids were associated with abnormal composition of gut microbiota in a depression model of mice. *Front. Neurosci.* **2021**, *15*, 701355. [CrossRef]
71. Tian, T.; Mao, Q.; Xie, J.; Wang, Y.; Shao, W.H.; Zhong, Q.; Chen, J.J. Multi-omics data reveals the disturbance of glycerophospholipid metabolism caused by disordered gut microbiota in depressed mice. *J. Adv. Res.* **2022**, *39*, 135–145. [CrossRef]
72. Xie, J.; Zhong, Q.; Wu, W.T.; Chen, J.J. Multi-omics data reveals the important role of glycerophospholipid metabolism in the crosstalk between gut and brain in depression. *J. Transl. Med.* **2023**, *21*, 93. [CrossRef] [PubMed]

73. Jiang, Y.; Qin, M.; Teng, T.; Li, X.; Yu, Y.; Wang, J.; Wu, H.; He, Y.; Zhou, X.; Xie, P. Identification of sex-specific plasma biomarkers using metabolomics for major depressive disorder in children and adolescents. *Front. Psychiatry* **2022**, *13*, 929207. [CrossRef] [PubMed]
74. Schumacher, F.; Edwards, M.J.; Mühle, C.; Carpinteiro, A.; Wilson, G.C.; Wilker, B.; Soddemann, M.; Keitsch, S.; Scherbaum, N.; Müller, B.W.; et al. Ceramide levels in blood plasma correlate with major depressive disorder severity and its neutralization abrogates depressive behavior in mice. *J. Biol. Chem.* **2022**, *298*, 102185. [CrossRef] [PubMed]
75. Homorogan, C.; Nitusca, D.; Enatescu, V.; Schubart, P.; Moraru, C.; Socaciu, C.; Marian, C. Untargeted plasma metabolomic profiling in patients with major depressive disorder using ultra-high performance liquid chromatography coupled with mass spectrometry. *Metabolites* **2021**, *11*, 466. [CrossRef]
76. Gu, X.; Ke, S.; Wang, Q.; Zhuang, T.; Xia, C.; Xu, Y.; Yang, L.; Zhou, M. Energy metabolism in major depressive disorder: Recent advances from omics technologies and imaging. *Biomed. Pharmacother.* **2021**, *141*, 111869. [CrossRef]
77. Wang, C.; Cui, C.; Xu, P.; Zhu, L.; Xue, H.; Chen, B.; Jiang, P. Targeting PDK2 rescues stress-induced impaired brain energy metabolism. *Mol. Psychiatry* **2023**. (Online ahead of print). [CrossRef]
78. Liu, T.; Deng, K.; Xue, Y.; Yang, R.; Yang, R.; Gong, Z.; Tang, M. Carnitine and depression. *Front. Nutr.* **2022**, *9*, 853058. [CrossRef]
79. Ait Tayeb, A.E.K.; Colle, R.; El-Asmar, K.; Chappell, K.; Acquaviva-Bourdain, C.; David, D.J.; Trabado, S.; Chanson, P.; Feve, B.; Becquemont, L.; et al. Plasma acetyl-l-carnitine and l-carnitine in major depressive episodes: A case-control study before and after treatment. *Psychol. Med.* **2023**, *53*, 2307–2316. [CrossRef]
80. Ait Tayeb, A.E.K.; Colle, R.; Chappell, K.; El-Asmar, K.; Acquaviva-Bourdain, C.; David, D.J.; Trabado, S.; Chanson, P.; Feve, B.; Becquemont, L.; et al. Metabolomic profiles of 38 acylcarnitines in major depressive episodes before and after treatment. *Psychol. Med.* **2023**. (Online ahead of print). [CrossRef]
81. Ahmed, A.T.; MahmoudianDehkordi, S.; Bhattacharyya, S.; Arnold, M.; Liu, D.; Neavin, D.; Moseley, M.A.; Thompson, J.W.; Williams, L.S.J.; Louie, G.; et al. Acylcarnitine metabolomic profiles inform clinically-defined major depressive phenotypes. *J. Affect. Disord.* **2020**, *264*, 90–97. [CrossRef]
82. Linghu, T.; Zhao, Y.; Wu, W.; Gao, Y.; Tian, J.; Qin, X. Novel targets for ameliorating energy metabolism disorders in depression through stable isotope-resolved metabolomics. *Biochim. Biophys. Acta. Bioenerg.* **2022**, *1863*, 148578. [CrossRef] [PubMed]
83. Ling-Hu, T.; Liu, S.B.; Gao, Y.; Han, Y.M.; Tian, J.S.; Qin, X.M. Stable isotope-resolved metabolomics reveals the abnormal brain glucose catabolism in depression based on chronic unpredictable mild stress rats. *J. Proteome Res.* **2021**, *20*, 3549–3558. [CrossRef] [PubMed]
84. Tian, J.S.; Zhao, Y.H.; Ling-Hu, T.; Wu, W.Z.; Wang, X.X.; Ji, C.; Zhao, W.D.; Han, Y.M.; Qin, X.M. A novel insight for high-rate and low-efficiency glucose metabolism in depression through stable isotope-resolved metabolomics in CUMS-induced rats. *J. Affect. Disord.* **2023**, *331*, 121–129. [CrossRef]
85. Tian, J.S.; Wu, W.Z.; Liu, S.B.; Ling-Hu, T.; Zhao, Y.H.; Gao, Y.; Qin, X.M. Stable isotope-resolved metabolomics studies on corticosteroid-induced PC12 cells: A strategy for evaluating glucose catabolism in an in vitro model of depression. *J. Proteome Res.* **2022**, *21*, 788–797. [CrossRef]
86. Ji, C.; Zhao, W.D.; Zheng, J.; Zhou, S.; Tian, J.S.; Han, Y.M.; Qin, X.M. Mechanism of the effect of Xiaoyao powder treatment on exercise capacity of depressed rats—A stable isotope tracer metabolomic study. *J. Liq. Chromatogr. R. T.* **2022**, *45*, 143–155. [CrossRef]
87. Liu, L.; Wang, H.; Chen, X.; Zhang, Y.; Zhang, H.; Xie, P. Gut microbiota and its metabolites in depression: From pathogenesis to treatment. *EBioMedicine* **2023**, *90*, 104527. [CrossRef]
88. Liu, X.; Li, X.; Teng, T.; Jiang, Y.; Xiang, Y.; Fan, L.; Yu, Y.; Zhou, X.; Xie, P. Comparative analysis of gut microbiota and fecal metabolome features among multiple depressive animal models. *J. Affect. Disord.* **2022**, *314*, 103–111. [CrossRef]
89. Xie, J.; Wu, W.T.; Chen, J.J.; Zhong, Q.; Wu, D.; Niu, L.; Wang, S.; Zeng, Y.; Wang, Y. Tryptophan metabolism as bridge between gut microbiota and brain in chronic social defeat stress-induced depression mice. *Front. Cell. Infect. Microbiol.* **2023**, *13*, 1121445. [CrossRef]
90. Zhang, Y.; Fan, Q.; Hou, Y.; Zhang, X.; Yin, Z.; Cai, X.; Wei, W.; Wang, J.; He, D.; Wang, G.; et al. Bacteroides species differentially modulate depression-like behavior via gut-brain metabolic signaling. *Brain Behav. Immun.* **2022**, *102*, 11–22. [CrossRef]
91. Xie, J.; Wang, Y.; Zhong, Q.; Bai, S.J.; Zhou, C.J.; Tian, T.; Chen, J.J. Associations between disordered microbial metabolites and changes of neurotransmitters in depressed mice. *Front. Cell. Infect. Microbiol.* **2022**, *12*, 906303. [CrossRef]
92. Hu, Z.Y.; Zhao, P.H.; Liao, A.M.; Pan, L.; Zhang, J.; Dong, Y.Q.; Huang, J.H.; He, W.W.; Ou, X.Q. Fermented wheat germ alleviates depression-like behavior in rats with chronic and unpredictable mild stress. *Foods* **2023**, *12*, 920. [CrossRef]
93. Yang, J.; Zheng, P.; Li, Y.; Wu, J.; Tan, X.M.; Zhou, J.J.; Sun, Z.L.; Chen, X.; Zhang, G.F.; Zhang, H.P.; et al. Landscapes of bacterial and metabolic signatures and their interaction in major depressive disorders. *Sci. Adv.* **2020**, *6*, eaba8555. [CrossRef] [PubMed]
94. Li, H.; Zhu, X.; Xu, J.; Li, L.; Kan, W.; Bao, H.; Xu, J.; Wang, W.; Yang, Y.; Chen, P.; et al. The FXR mediated anti-depression effect of CDCA underpinned its therapeutic potentiation for MDD. *Int. Immunopharmacol.* **2023**, *115*, 109626. [CrossRef] [PubMed]
95. Bai, S.J.; Xie, J.; Bai, H.L.; Tian, T.; Zou, T.; Chen, J.J. Gut microbiota-derived inflammation-related serum metabolites as potential biomarkers for major depressive disorder. *J. Inflamm. Res.* **2021**, *14*, 3755–3766. [CrossRef]
96. Wu, M.; Tian, T.; Mao, Q.; Zou, T.; Zhou, C.J.; Xie, J.; Chen, J.J. Associations between disordered gut microbiota and changes of neurotransmitters and short-chain fatty acids in depressed mice. *Transl. Psychiat.* **2020**, *10*, 350. [CrossRef]

97. Jiang, W.; Chen, J.; Gong, L.; Liu, F.; Zhao, H.; Yan, Z.; Li, Y.; Zhang, J.; Xiao, M.; Mu, J. Microbiota-derived short-chain fatty acids may participate in post-stroke depression by regulating host's lipid metabolism. *J. Psychiatr. Res.* **2023**, *161*, 426–434. [CrossRef] [PubMed]
98. Jiang, W.; Gong, L.; Liu, F.; Ren, Y.; Mu, J. Alteration of gut microbiome and correlated lipid metabolism in post-stroke depression. *Front. Cell. Infect. Microbiol.* **2021**, *11*, 663967. [CrossRef]
99. Duan, J.; Wang, W.; Jiang, T.; Bai, X.; Liu, C. Viral metagenomics combined with metabolomics reveals the role of gut viruses in mouse model of depression. *Front. Microbiol.* **2022**, *13*, 1046894. [CrossRef]
100. Hu, K.; Liao, X.X.; Wu, X.Y.; Wang, R.; Hu, Z.W.; Liu, S.Y.; He, W.F.; Zhou, J.J. Effects of the lipid metabolites and the gut microbiota in ApoE^{-/-} mice on atherosclerosis co-depression from the microbiota-gut-brain axis. *Front. Mol. Biosci.* **2022**, *9*, 786492. [CrossRef]
101. Sun, N.; Zhang, J.; Wang, J.; Liu, Z.; Wang, X.; Kang, P.; Yang, C.; Liu, P.; Zhang, K. Abnormal gut microbiota and bile acids in patients with first-episode major depressive disorder and correlation analysis. *Psychiatry Clin. Neurosci.* **2022**, *76*, 321–328. [CrossRef]
102. Zhao, H.; Jin, K.; Jiang, C.; Pan, F.; Wu, J.; Luan, H.; Zhao, Z.; Chen, J.; Mou, T.; Wang, Z.; et al. A pilot exploration of multi-omics research of gut microbiome in major depressive disorders. *Transl. Psychiatry* **2022**, *12*, 8. [CrossRef] [PubMed]
103. Yao, H.; Yang, H.; Wang, Y.; Xing, Q.; Yan, L.; Chai, Y. Gut microbiome and fecal metabolic alteration in systemic lupus erythematosus patients with depression. *Front. Cell. Infect. Microbiol.* **2022**, *12*, 1040211. [CrossRef]
104. Zhang, X.; Hou, Y.; Li, Y.; Wei, W.; Cai, X.; Shao, H.; Yuan, Y.; Zheng, X. Taxonomic and metabolic signatures of gut microbiota for assessing the severity of depression and anxiety in major depressive disorder patients. *Neuroscience* **2022**, *496*, 179–189. [CrossRef] [PubMed]
105. Li, Y.; Li, J.; Cheng, R.; Liu, H.; Zhao, Y.; Liu, Y.; Chen, Y.; Sun, Z.; Zhai, Z.; Wu, M.; et al. Alteration of the gut microbiome and correlated metabolism in a rat model of long-term depression. *Front. Cell. Infect. Microbiol.* **2023**, *13*, 1116277. [CrossRef] [PubMed]
106. Pu, J.; Liu, Y.; Gui, S.; Tian, L.; Yu, Y.; Wang, D.; Zhong, X.; Chen, W.; Chen, X.; Chen, Y.; et al. Effects of pharmacological treatment on metabolomic alterations in animal models of depression. *Transl. Psychiatry* **2022**, *12*, 175. [CrossRef]
107. MahmoudianDehkordi, S.; Ahmed, A.T.; Bhattacharyya, S.; Han, X.; Baillie, R.A.; Arnold, M.; Skime, M.K.; John-Williams, L.S.; Moseley, M.A.; Thompson, J.W.; et al. Alterations in acylcarnitines, amines, and lipids inform about the mechanism of action of citalopram/escitalopram in major depression. *Transl. Psychiat.* **2021**, *11*, 153. [CrossRef]
108. Sun, Z.; Yang, J.; Zhou, J.; Zhou, J.; Feng, L.; Feng, Y.; He, Y.; Liu, M.; Li, Y.; Wang, G.; et al. Tissue-specific oxysterols as predictors of antidepressant (Escitalopram) treatment response in patients with major depressive disorder. *Biol. Psychiatry Glob. Open Sci.* **2023**, *3*, 663–672. [CrossRef]
109. Wang, Y.; Zhou, J.; Ye, J.; Sun, Z.; He, Y.; Zhao, Y.; Ren, S.; Zhang, G.; Liu, M.; Zheng, P.; et al. Multi-omics reveal microbial determinants impacting the treatment outcome of antidepressants in major depressive disorder. *Microbiome* **2023**, *11*, 195. [CrossRef]
110. Abramova, O.; Zorkina, Y.; Syunyakov, T.; Zubkov, E.; Ushakova, V.; Silantyev, A.; Soloveva, K.; Gurina, O.; Majouga, A.; Morozova, A.; et al. Brain metabolic profile after intranasal vs. intraperitoneal clomipramine treatment in rats with ultrasound model of depression. *Int. J. Mol. Sci.* **2021**, *22*, 9598. [CrossRef] [PubMed]
111. Shen, D.; Zhao, H.; Gao, S.; Li, Y.; Cheng, Q.; Bi, C.; Zhou, Z.; Li, Y.; Yu, C. Clinical serum metabolomics study on fluoxetine hydrochloride for depression. *Neurosci. Lett.* **2021**, *746*, 135585. [CrossRef]
112. Singh, B.; MahmoudianDehkordi, S.; Voort, J.L.V.; Han, X.; Port, J.D.; Frye, M.A.; Kaddurah-Daouk, R. Metabolomic signatures of intravenous racemic ketamine associated remission in treatment-resistant depression: A pilot hypothesis generating study. *Psychiat. Res.* **2022**, *314*, 114655. [CrossRef]
113. Zhou, C.; Zhao, X.; Ma, X.; Ma, H.; Li, R.; Hu, G.; Wang, H.; Peng, Z.; Cai, M. Effects of (S)-ketamine on depression-like behaviors in a chronic variable stress model: A role of brain lipidome. *Front. Cell. Neurosci.* **2023**, *17*, 1114914. [CrossRef]
114. Moaddel, R.; Zanos, P.; Farmer, C.A.; Kadriu, B.; Morris, P.J.; Lovett, J.; Acevedo-Diaz, E.E.; Cavanaugh, G.W.; Yuan, P.; Yavi, M.; et al. Comparative metabolomic analysis in plasma and cerebrospinal fluid of humans and in plasma and brain of mice following antidepressant-dose ketamine administration. *Transl. Psychiat.* **2022**, *12*, 179. [CrossRef] [PubMed]
115. Huang, D.; Wang, L.; Wu, Y.; Qin, X.; Du, G.; Zhou, Y. Metabolomics based on peripheral blood mononuclear cells to dissect the mechanisms of chaigui granules for treating depression. *ACS Omega* **2022**, *7*, 8466–8482. [CrossRef] [PubMed]
116. Wu, W.Z.; Ting, L.H.; Zhao, Y.H.; Zhao, W.D.; Ji, C.; Tian, J.S.; Ren, Y.; Qin, X.M. A unique insight for Xiaoyao San exerts antidepressant effects by modulating hippocampal glucose catabolism using stable isotope-resolved metabolomics. *J. Ethnopharmacol.* **2023**, *300*, 115702. [CrossRef] [PubMed]
117. Liu, X.; Wei, F.; Liu, H.; Zhao, S.; Du, G.; Qin, X. Integrating hippocampal metabolomics and network pharmacology deciphers the antidepressant mechanisms of Xiaoyaosan. *J. Ethnopharmacol.* **2021**, *268*, 113549. [CrossRef]
118. Liu, X.; Liu, C.; Tian, J.; Gao, X.; Li, K.; Du, G.; Qin, X. Plasma metabolomics of depressed patients and treatment with Xiaoyaosan based on mass spectrometry technique. *J. Ethnopharmacol.* **2020**, *246*, 112219. [CrossRef]
119. Chen, C.; Yin, Q.; Tian, J.; Gao, X.; Qin, X.; Du, G.; Zhou, Y. Studies on the potential link between antidepressant effect of Xiaoyao San and its pharmacological activity of hepatoprotection based on multi-platform metabolomics. *J. Ethnopharmacol.* **2020**, *249*, 112432. [CrossRef]

120. Zhang, Z.W.; Han, P.; Fu, J.; Yu, H.; Xu, H.; Hu, J.C.; Lu, J.Y.; Yang, X.Y.; Zhang, H.J.; Bu, M.M.; et al. Gut microbiota-based metabolites of Xiaoyao Pills (a typical Traditional Chinese medicine) ameliorate depression by inhibiting fatty acid amide hydrolase levels in brain. *J. Ethnopharmacol.* **2023**, *313*, 116555. [CrossRef]
121. Ji, S.; Han, S.; Yu, L.; Du, L.; You, Y.; Chen, J.; Wang, M.; Wu, S.; Li, S.; Sun, X.; et al. Jia Wei Xiao Yao San ameliorates chronic stress-induced depression-like behaviors in mice by regulating the gut microbiome and brain metabolome in relation to purine metabolism. *Phytomedicine* **2022**, *98*, 153940. [CrossRef] [PubMed]
122. Lin, S.; Li, Q.; Xu, Z.; Chen, Z.; Tao, Y.; Tong, Y.; Wang, T.; Chen, S.; Wang, P. Detection of the role of intestinal flora and tryptophan metabolism involved in antidepressant-like actions of crocetin based on a multi-omics approach. *Psychopharmacology (Berl)* **2022**, *239*, 3657–3677. [CrossRef]
123. Sun, Y.; Yan, T.; Gong, G.; Li, Y.; Zhang, J.; Wu, B.; Bi, K.; Jia, Y. Antidepressant-like effects of Schisandrin on lipopolysaccharide-induced mice: Gut microbiota, short chain fatty acid and TLR4/NF-kappaB signaling pathway. *Int. Immunopharmacol.* **2020**, *89*, 107029. [CrossRef]
124. Chen, H.; Kan, Q.; Zhao, L.; Ye, G.; He, X.; Tang, H.; Shi, F.; Zou, Y.; Liang, X.; Song, X.; et al. Prophylactic effect of Tongxieyaofang polysaccharide on depressive behavior in adolescent male mice with chronic unpredictable stress through the microbiome-gut-brain axis. *Biomed. Pharmacother.* **2023**, *161*, 114525. [CrossRef] [PubMed]
125. Ma, C.; Yuan, D.; Renaud, S.J.; Zhou, T.; Yang, F.; Liou, Y.; Qiu, X.; Zhou, L.; Guo, Y. Chaihu-shugan-san alleviates depression-like behavior in mice exposed to chronic unpredictable stress by altering the gut microbiota and levels of the bile acids hyocholic acid and 7-ketoDCA. *Front. Pharmacol.* **2022**, *13*, 1040591. [CrossRef]
126. Liu, J.; Fang, Y.; Cui, L.; Wang, Z.; Luo, Y.; Gao, C.; Ge, W.; Huang, T.; Wen, J.; Zhou, T. Butyrate emerges as a crucial effector of Zhi-Zi-Chi decoctions to ameliorate depression via multiple pathways of brain-gut axis. *Biomed. Pharmacother.* **2022**, *149*, 112861. [CrossRef]
127. Liao, X.X.; Hu, K.; Xie, X.H.; Wen, Y.L.; Wang, R.; Hu, Z.W.; Zhou, Y.L.; Li, J.J.; Wu, M.K.; Yu, J.X.; et al. Banxia Xiexin decoction alleviates AS co-depression disease by regulating the gut microbiome-lipid metabolic axis. *J. Ethnopharmacol.* **2023**, *313*, 116468. [CrossRef]
128. Lei, C.; Chen, Z.; Fan, L.; Xue, Z.; Chen, J.; Wang, X.; Huang, Z.; Men, Y.; Yu, M.; Liu, Y.; et al. Integrating metabolomics and network analysis for exploring the mechanism underlying the antidepressant activity of Paeoniflorin in rats with CUMS-induced depression. *Front. Pharmacol.* **2022**, *13*, 904190. [CrossRef] [PubMed]
129. Wang, Q.S.; Yan, K.; Li, K.D.; Gao, L.N.; Wang, X.; Liu, H.B.; Zhang, Z.G.; Li, K.F.; Cui, Y.L. Targeting hippocampal phospholipid and tryptophan metabolism for antidepressant-like effects of albiflorin. *Phytomedicine* **2021**, *92*, 153735. [CrossRef]
130. Li, Y.; Yang, X.; Chen, S.; Wu, L.; Zhou, J.; Jia, K.; Ju, W. Integrated network pharmacology and GC-MS-based metabolomics to investigate the effect of Xiang-Su volatile oil against menopausal depression. *Front. Pharmacol.* **2021**, *12*, 765638. [CrossRef] [PubMed]
131. Qu, S.Y.; Li, X.Y.; Heng, X.; Qi, Y.Y.; Ge, P.Y.; Ni, S.J.; Yao, Z.Y.; Guo, R.; Yang, N.Y.; Cao, Y.; et al. Analysis of antidepressant activity of Huang-Lian Jie-Du decoction through network pharmacology and metabolomics. *Front. Pharmacol.* **2021**, *12*, 619268. [CrossRef]
132. Ge, P.Y.; Qu, S.Y.; Ni, S.J.; Yao, Z.Y.; Qi, Y.Y.; Zhao, X.; Guo, R.; Yang, N.Y.; Zhang, Q.C.; Zhu, H.X. Berberine ameliorates depression-like behavior in CUMS mice by activating TPH1 and inhibiting IDO1-associated with tryptophan metabolism. *Phytother. Res.* **2022**, *37*, 342–357. [CrossRef] [PubMed]
133. Huang, M.; He, Y.; Tian, L.; Yu, L.; Cheng, Q.; Li, Z.; Gao, L.; Gao, S.; Yu, C. Gut microbiota-SCFAs-brain axis associated with the antidepressant activity of berberine in CUMS rats. *J. Affect. Disord.* **2023**, *325*, 141–150. [CrossRef] [PubMed]
134. Jia, S.; Wang, R.; Zhang, D.; Guan, Z.; Ding, T.; Zhang, J.; Zhao, X. Quercetin modulates the liver metabolic profile in a chronic unpredictable mild stress rat model based on metabolomics technology. *Food Funct.* **2023**, *14*, 1726–1739. [CrossRef]
135. Gu, X.Y.; Zhang, G.Y.; Wang, Q.X.; Song, J.; Li, Y.; Xia, C.Y.; Zhang, T.; Yang, L.; Sun, J.J.; Zhou, M.M. Integrated network pharmacology and hepatic metabolomics to reveal the mechanism of *Acanthopanax senticosus* against major depressive disorder. *Front. Cell Dev. Biol.* **2022**, *10*, 900637. [CrossRef] [PubMed]
136. Zhou, Y.; Li, T.; Zhu, S.; Gong, W.; Qin, X.; Du, G. Study on antidepressant mechanism of Radix Bupleuri–Radix Paeoniae Alba herb pair by metabolomics combined with 1H nuclear magnetic resonance and ultra-high-performance liquid chromatography-tandem mass spectrometry detection technology. *J. Pharm. Pharmacol.* **2021**, *73*, 1262–1273. [CrossRef]
137. Chen, C.; Tian, J.; Gao, X.; Qin, X.; Du, G.; Zhou, Y. An integrated strategy to study the combination mechanisms of Bupleurum chinense DC and Paeonia lactiflora Pall for treating depression based on correlation analysis between serum chemical components profiles and endogenous metabolites profiles. *J. Ethnopharmacol.* **2023**, *305*, 116068. [CrossRef] [PubMed]
138. Gu, S.; Mou, T.T.; Chen, J.; Wang, J.; Zhang, Y.; Cui, M.R.; Hao, W.Q.; Sun, Y.; Zhang, C.Q.; Zhao, T.T.; et al. Develop a stepwise integrated method to screen biomarkers of Baihe-Dihuang Tang on the treatment of depression in rats applying with composition screened, untargeted, and targeted metabolomics analysis. *J. Sep. Sci.* **2022**, *43*, 1656–1671. [CrossRef]
139. Zhu, Y.; Wang, F.; Han, J.; Zhao, Y.; Yu, M.; Ma, M.; Yu, Z. Untargeted and targeted mass spectrometry reveal the effects of theanine on the central and peripheral metabolomics of chronic unpredictable mild stress-induced depression in juvenile rats. *J. Pharm. Anal.* **2023**, *13*, 73–87. [CrossRef]


140. Deng, L.; Zhou, X.; Tao, G.; Hao, W.; Wang, L.; Lan, Z.; Song, Y.; Wu, M.; Huang, J.Q. Ferulic acid and feruloylated oligosaccharides alleviate anxiety and depression symptom via regulating gut microbiome and microbial metabolism. *Food Res. Int.* **2022**, *162*, 111887. [CrossRef]
141. Wang, W.; Wang, T.; Bai, S.; Chen, Z.; Qi, X.; Xie, P. DL-3-n-butylphthalide attenuates mouse behavioral deficits to chronic social defeat stress by regulating energy metabolism via AKT/CREB signaling pathway. *Transl. Psychiat.* **2020**, *10*, 49. [CrossRef]
142. Dang, R.; Wang, M.; Li, X.; Wang, H.; Liu, L.; Wu, Q.; Zhao, J.; Ji, P.; Zhong, L.; Licinio, J.; et al. Edaravone ameliorates depressive and anxiety-like behaviors via Sirt1/Nrf2/HO-1/Gpx4 pathway. *J. Neuroinflamm.* **2022**, *19*, 41. [CrossRef]
143. Bu, Q.; Zhang, J.; Guo, X.; Feng, Y.; Yan, H.; Cheng, W.; Feng, Z.; Cao, M. The antidepressant effects and serum metabolomics of bifid triple viable capsule in a rat model of chronic unpredictable mild stress. *Front. Nutr.* **2022**, *9*, 947697. [CrossRef] [PubMed]
144. Tian, P.; Chen, Y.; Zhu, H.; Wang, L.; Qian, X.; Zou, R.; Zhao, J.; Zhang, H.; Qian, L.; Wang, Q.; et al. Bifidobacterium breve CCFM1025 attenuates major depression disorder via regulating gut microbiome and tryptophan metabolism: A randomized clinical trial. *Brain Behav. Immun.* **2022**, *100*, 233–241. [CrossRef]
145. Ding, Y.; Bu, F.; Chen, T.; Shi, G.; Yuan, X.; Feng, Z.; Duan, Z.; Wang, R.; Zhang, S.; Wang, Q.; et al. A next-generation probiotic: Akkermansia muciniphila ameliorates chronic stress-induced depressive-like behavior in mice by regulating gut microbiota and metabolites. *Appl. Microbiol. Biot.* **2021**, *105*, 8411–8426. [CrossRef]
146. Tsai, W.H.; Yeh, W.L.; Chou, C.H.; Wu, C.L.; Lai, C.H.; Yeh, Y.T.; Liao, C.A.; Wu, C.C. Suppressive effects of Lactobacillus on depression through regulating the gut microbiota and metabolites in C57BL/6J mice induced by Ampicillin. *Biomedicines* **2023**, *11*, 1068. [CrossRef]
147. Cheng, S.; Zhu, Z.; Li, H.; Wang, W.; Jiang, Z.; Pan, F.; Liu, D.; Ho, R.C.M.; Ho, C.S.H. Rifaximin ameliorates depression-like behaviour in chronic unpredictable mild stress rats by regulating intestinal microbiota and hippocampal tryptophan metabolism. *J. Affect. Disord.* **2023**, *329*, 30–41. [CrossRef] [PubMed]
148. Satti, S.; Palepu, M.S.K.; Singh, A.A.; Jaiswal, Y.; Dash, S.P.; Gajula, S.N.R.; Chaganti, S.; Samanthula, G.; Sonti, R.; Dandekar, M.P. Anxiolytic- and antidepressant-like effects of Bacillus coagulans Unique IS-2 mediate via reshaping of microbiome gut-brain axis in rats. *Neurochem. Int.* **2023**, *163*, 105483. [CrossRef]
149. Liu, X.; Han, Y.; Zhou, S.; Tian, J.; Qin, X.; Ji, C.; Zhao, W.; Chen, A. Serum metabolomic responses to aerobic exercise in rats under chronic unpredictable mild stress. *Sci. Rep.* **2022**, *12*, 4888. [CrossRef] [PubMed]
150. Zhou, C.H.; Chen, Y.H.; Xue, S.S.; Shi, Q.Q.; Guo, L.; Yu, H.; Xue, F.; Cai, M.; Wang, H.N.; Peng, Z.W. rTMS ameliorates depressive-like behaviors and regulates the gut microbiome and medium- and long-chain fatty acids in mice exposed to chronic unpredictable mild stress. *CNS Neurosci. Ther.* **2023**, *29*, 1–18. [CrossRef]
151. Cristea, I.A.; Naudet, F. US Food and Drug Administration approval of esketamine and brexanolone. *Lancet Psychiat.* **2019**, *6*, 975–977. [CrossRef]
152. Hashimoto, K.; Chaki, S. Ketamine and its metabolites: Potential as novel treatments for depression. *Neuropharmacology* **2023**, *230*, 109492. [CrossRef]
153. Gu, X.; Gao, X.; Cheng, J.; Xia, C.; Xu, Y.; Yang, L.; Zhou, M. Emerging application of metabolomics on Chinese herbal medicine for depressive disorder. *Biomed. Pharmacother.* **2021**, *141*, 111866. [CrossRef] [PubMed]
154. Zhang, C.; Mo, Y.Y.; Feng, S.S.; Meng, M.W.; Chen, S.Y.; Huang, H.M.; Ling, X.; Song, H.; Liang, Y.H.; Ou, S.F.; et al. Urinary metabolomics study of anti-depressive mechanisms of Millettia speciosa Champ on rats with chronic unpredictable mild stress-induced depression. *J. Pharm. Biomed. Anal.* **2021**, *205*, 114338. [CrossRef]
155. Ng, Q.X.; Lim, Y.L.; Yaow, C.Y.L.; Ng, W.K.; Thumboo, J.; Liew, T.M. Effect of probiotic supplementation on gut microbiota in patients with major depressive disorders: A systematic review. *Nutrients* **2023**, *15*, 1351. [CrossRef] [PubMed]
156. Brydges, C.R.; Bhattacharyya, S.; Dehkordi, S.M.; Milaneschi, Y.; Penninx, B.; Jansen, R.; Kristal, B.S.; Han, X.; Arnold, M.; Kastenmuller, G.; et al. Metabolomic and inflammatory signatures of symptom dimensions in major depression. *Brain Behav. Immun.* **2022**, *102*, 42–52. [CrossRef] [PubMed]
157. Zoicas, I.; Mühle, C.; Schumacher, F.; Kleuser, B.; Kornhuber, J. Development of comorbid depression after social fear conditioning in mice and its effects on brain sphingolipid metabolism. *Cells* **2023**, *12*, 1355. [CrossRef]
158. Tang, Y.; Su, H.; Wang, H.; Lu, F.; Nie, K.; Wang, Z.; Huang, W.; Dong, H. The effect and mechanism of Jiao-tai-wan in the treatment of diabetes mellitus with depression based on network pharmacology and experimental analysis. *Mol. Med.* **2021**, *27*, 154. [CrossRef]
159. Zhao, D.P.; Zhang, J.J.; Zhu, Y.; He, C.; Fei, W.T.; Yue, N.; Wang, C.L.; Wang, L.Y. Study of antidepressant-like effects of Albiflorin and Paeoniflorin through metabolomics from the perspective of cancer-related depression. *Front. Neurol.* **2022**, *13*, 828612. [CrossRef]
160. Grant, C.W.; Barreto, E.F.; Kumar, R.; Kaddurah-Daouk, R.; Skime, M.; Mayes, T.; Carmody, T.; Biernacka, J.; Wang, L.; Weinshilboum, R.; et al. Multi-omics characterization of early- and adult-onset major depressive disorder. *J. Pers. Med.* **2022**, *12*, 412. [CrossRef]
161. Grant, C.W.; Wilton, A.R.; Kaddurah-Daouk, R.; Skime, M.; Biernacka, J.; Mayes, T.; Carmody, T.; Wang, L.; Lazaridis, K.; Weinshilboum, R.; et al. Network science approach elucidates integrative genomic-metabolomic signature of antidepressant response and lifetime history of attempted suicide in adults with major depressive disorder. *Front. Pharmacol.* **2022**, *13*, 984383. [CrossRef]

162. Joyce, J.B.; Grant, C.W.; Liu, D.; MahmoudianDehkordi, S.; Kaddurah-Daouk, R.; Skime, M.; Biernacka, J.; Frye, M.A.; Mayes, T.; Carmody, T.; et al. Multi-omics driven predictions of response to acute phase combination antidepressant therapy: A machine learning approach with cross-trial replication. *Transl. Psychiatry* **2021**, *11*, 513. [CrossRef]
163. Hernandez-Baixauli, J.; Puigbò, P.; Abasolo, N.; Palacios-Jordan, H.; Foguet-Romero, E.; Suñol, D.; Galofré, M.; Caimari, A.; Baselga-Escudero, L.; Bas, J.M.D.; et al. Alterations in metabolome and microbiome associated with an early stress stage in male wistar rats: A multi-omics approach. *Int. J. Mol. Sci.* **2021**, *22*, 12931. [CrossRef] [PubMed]
164. Hamilton, P.J.; Chen, E.Y.; Tolstikov, V.; Peña, C.J.; Picone, J.A.; Shah, P.; Panagopoulos, K.; Strat, A.N.; Walker, D.M.; Lorsch, Z.S.; et al. Chronic stress and antidepressant treatment alter purine metabolism and beta oxidation within mouse brain and serum. *Sci. Rep.* **2020**, *10*, 18134. [CrossRef]
165. Zheng, Y.; Zhang, L.; He, S.; Xie, Z.; Zhang, J.; Ge, C.; Sun, G.; Huang, J.; Li, H. Integrated module of multidimensional omics for peripheral biomarkers (iMORE) in patients with major depressive disorder: Rationale and design of a prospective multicentre cohort study. *BMJ Open* **2022**, *12*, e067447. [CrossRef] [PubMed]
166. Sathyanarayanan, A.; Mueller, T.T.; Ali Moni, M.; Schueler, K.; Baune, B.T.; Lio, P.; Mehta, D.; Baune, B.T.; Dierssen, M.; Ebert, B.; et al. Multi-omics data integration methods and their applications in psychiatric disorders. *Eur. Neuropsychopharm.* **2023**, *69*, 26–46. [CrossRef] [PubMed]

Disclaimer/Publisher's Note: The statements, opinions and data contained in all publications are solely those of the individual author(s) and contributor(s) and not of MDPI and/or the editor(s). MDPI and/or the editor(s) disclaim responsibility for any injury to people or property resulting from any ideas, methods, instructions or products referred to in the content.

Article

Development of a Purity Certified Reference Material for Vinyl Acetate

Chen He ¹, Qin Gao ¹, Changwen Ye ¹, Guotao Yang ¹, Pengfei Zhang ¹, Rongchao Yang ¹, Qing Zhang ^{1,*} and Kang Ma ^{2,*} 

¹ Zhengzhou Tobacco Research Institute of China National Tobacco Corporation, Zhengzhou 450001, China; hechen2012@sina.com (C.H.); mtjj20200601@163.com (Q.G.); yectsrc@163.com (C.Y.); ygt3315@163.com (G.Y.); yczhangpf@163.com (P.Z.); yangrongchao2760@126.com (R.Y.)

² Division of Chemical Metrology and Analytical Science, National Institute of Metrology, Beijing 100013, China

* Correspondence: ocu@236.net (Q.Z.); makang@nim.ac.cn (K.M.)

Abstract: Vinyl acetate is a restricted substance in food products. The quantification of the organic impurities in vinyl acetate is a major problem due to its activity, instability, and volatility. In this paper, while using the mass balance method to determine the purity of vinyl acetate, an improved method was established for the determination of the content of three impurities in vinyl acetate reference material, and the GC-FID peak area normalization for vinyl acetate was calibrated. The three trace organic impurities were identified by gas chromatography tandem high-resolution mass spectrometry to be methyl acetate, ethyl acetate, and vinyl propionate. The content and relative correction factors for the three organic impurities were measured. The purity of vinyl acetate determined by the mass balance method was 99.90% with an expanded uncertainty of 0.30%, and the total content of organic impurities was 0.08% with a relative correction factor of 1.23%. The vinyl acetate reference material has been approved as a national certified reference material in China as GBW (E) 062710.

Keywords: vinyl acetate; mass balance method; purity; certified reference materials; uncertainty



Citation: He, C.; Gao, Q.; Ye, C.; Yang, G.; Zhang, P.; Yang, R.; Zhang, Q.; Ma, K. Development of a Purity Certified Reference Material for Vinyl Acetate. *Molecules* **2023**, *28*, 6245. <https://doi.org/10.3390/molecules28176245>

Academic Editor: Alfonso Jimenez

Received: 27 July 2023

Revised: 21 August 2023

Accepted: 22 August 2023

Published: 25 August 2023



Copyright: © 2023 by the authors. Licensee MDPI, Basel, Switzerland. This article is an open access article distributed under the terms and conditions of the Creative Commons Attribution (CC BY) license (<https://creativecommons.org/licenses/by/4.0/>).

1. Introduction

Vinyl acetate is a colorless, flammable liquid with a sweet, ether flavor. Because of the presence of carbon–carbon double bonds, vinyl acetate is active, and chemical reactions, such as addition and polymerization reactions, are prone to occurring [1]. In industry, vinyl acetate is mainly used as a polymer or copolymer monomer in the synthesis of polyvinyl acetate homopolymer emulsions, vinyl acetate ethylene copolymer emulsions, ethylene vinyl alcohol copolymer emulsions, and other common adhesives that are widely used in the food, construction, and other industries [2–5]. Vinyl acetate is irritating to the eyes, skin, mucous membranes, and upper respiratory tract, and long-term exposure can anesthetize nerves. It has been proven that vinyl acetate is carcinogenic to animals, and it is classified as a class 2B carcinogen [6,7]. The food, construction, and other industries in China have restrictions on the allowable content of vinyl acetate in specific industrial products [8]. Therefore, analytical methods for the accurate measurement of vinyl acetate are required in order to provide quality assurance for commercial products. Currently, the reported analysis methods include the saponification [9], thermo-gravimetric [10], nuclear magnetic resonance (NMR) spectroscopy [11], infrared spectroscopy [12], and gas chromatography (GC) [13] methods. Because of its high accuracy and sensitivity, chromatography is a common method for the quantitative determination of vinyl acetate, and several chromatographic methods have been reported for the quantitative determination of vinyl acetate in food contact materials [14], plastics [15], and white latex [16]. However, chromatographic quantification usually requires a certified reference material (CRM) to prepare a standard solution. Therefore, it is necessary to establish a measurement method for a vinyl acetate

CRM and to use this vinyl acetate CRM to make the currently used methods more accurate and convenient.

There have been few reports of purity determination methods for vinyl acetate. Accurate purity determination methods are the basis for the development of CRMs, and play an important role in the establishment of measurement traceability, the calibration of instruments, and verification methods [17,18]. Therefore, CRMs have important uses in food, medicine, and other fields [19–21].

In the development of CRMs, the quantitative nuclear magnetic resonance (q-NMR) [22,23], thermal analysis [24,25], and mass balance [26–29] methods are commonly used methods for measuring the purity of organic substances. The mass balance method is generally considered to be a relatively high-precision method for purity determination, and can be directly traced back to the SI units of mass (kg) and amount of substance (mol). The mass balance method is one of the main methods for determining the purity of substances in the Organic Analysis Work Group of the International Bureau of Weights and Measures [30]. The mass balance method is also one of the methods for determining the purity of pharmaceutical reference substances that is recommended by the World Health Organization and the European Pharmacopoeia [31,32]. Mass balance, high performance liquid chromatography (HPLC), and differential scanning calorimetry (DSC) were used by Kang Ma et al. to determine the purity of a theophylline CRM, and the accuracy of the mass balance method was shown to be better than that of the other methods [33]. With the mass balance method, HPLC and GC are frequently used to measure organic components. A mass balance method combined with gas chromatography–mass spectrometry was used by Wang et al. [34] to determine the content of benzene and to investigate the accuracy of DSC and q-NMR measurements. The mass balance method was used by Chen et al. to assign purity to four unsaturated fatty acid esters; the gas chromatographic area normalization method was used to determine the content of the main components; and the content of volatile impurities, moisture, and non-volatile impurities was calculated [35]. However, because of the nonlinear response of the detector, the percentages calculated from the peak areas were not equal to the percentages of each component. Therefore, a correction factor was introduced by Wang et al. to correct the values for the purity obtained by area normalization to produce more accurate measurement results [36].

However, it is still a challenge to determine vinyl acetate's purity using the mass balance method, which can mainly be attributed to the difficulty of identifying and quantifying the organic impurities in vinyl acetate. This difficulty occurs because vinyl acetate and the organic impurities in it have small molecular weights and are difficult to separate.

Therefore, in the present study, a new pure CRM for vinyl acetate was developed, and a mass balance method was established to determine the purity of the vinyl acetate. The gas chromatographic area normalization results were corrected and recalculated by characterizing and calculating the relative correction factors for three organic impurities in vinyl acetate. In addition, a homogeneity test and stability study were carried out on the prepared vinyl acetate CRM, and the uncertainty of the CRM was evaluated.

2. Results and Discussion

2.1. Characterization of the CRM Candidate

2.1.1. Mass Spectrometry (MS) Analysis

The mass spectrometry analysis of the CRM candidate was performed in positive ion mode, and the results are shown in Figure 1. Figure 1a shows the low-resolution spectrum. According to the molecular structure of vinyl acetate, the molecular ion $[\text{CH}_3\text{COOCH}=\text{CH}_2]^+$ undergoes homolytic and heterolytic decomposition under the bombardment of electrons, forming the fragment ion $\text{CH}_3\text{C}=\text{O}^+$. Therefore, the strong peak at $m/z = 43$ corresponded to the fragment ion $\text{CH}_3\text{C}=\text{O}^+$.

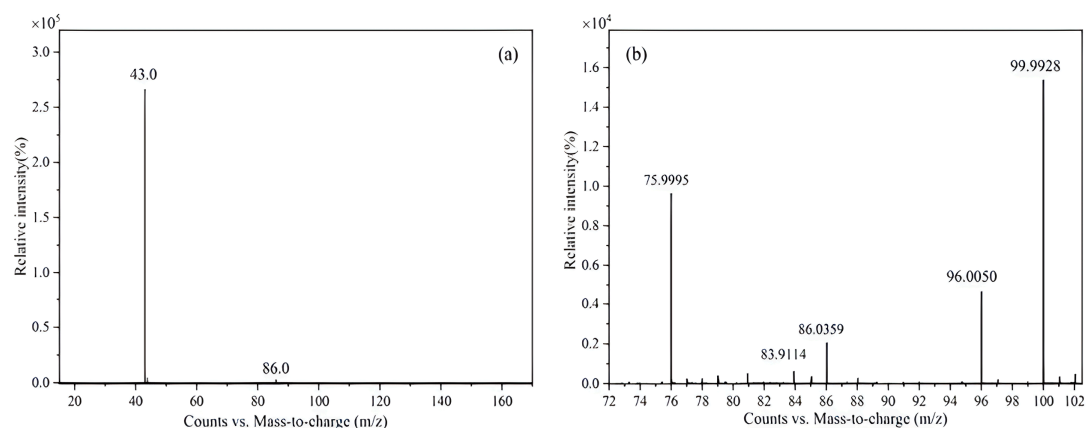


Figure 1. Mass spectrometry results of CRM candidate: (a) low-resolution mass spectrum; (b) high-resolution mass spectrum (m/z 75.9995, m/z 96.0050, and m/z 99.9928 are the molecular ion peaks of the reference ions).

High-resolution mass spectrometry was used to accurately measure the molecular weights of the compounds, and the results are shown in Figure 1b. $m/z = 86.0395$ corresponded to the molecular ion peak for vinyl acetate. The measured molecular weight of vinyl acetate was detected to be 86.0359, with a theoretical value of 86.0362 and a relative analytical error of 3.85×10^{-6} , which can be considered to be consistent with $C_4H_6O_2$.

2.1.2. Fourier Transform Infrared Spectroscopy (FT-IR) Analysis

Figure 2 shows the infrared spectrum of a CRM candidate. It can be seen from Figure 2 that the absorption peaks at 3094.1 and 1431.6 cm^{-1} are the C-H stretching and bending vibrations, respectively, in the carbon–carbon double bond, and the absorption peak at 1647.5 cm^{-1} is the C-C stretching vibration of the carbon–carbon double bond. This result indicates that there may be an alkene structure in the molecule. The absorption peak at 1762.0 cm^{-1} is the C=O stretching vibration of a carboxylate, and the absorption peaks at 1219.5 and 1021.0 cm^{-1} are the C-O stretching vibrations in a carboxylate, indicating that there may be a carboxylate structure in the molecule. The absorption peak at 1371.5 cm^{-1} is the C-H bending vibration of a methyl group, indicating that there may be a methyl structure in the molecule. Comparing Figure 2b with the standard infrared spectra of vinyl acetate indicates that the spectra were basically consistent.

2.1.3. NMR Analysis

Figure 3a shows the ^1H NMR spectrum of a CRM candidate. The chemical shifts (δ , ppm) of the four proton signals were as follows: δ 7.26 (1H, dd, $J = 6.0, 14.0$ Hz) was the proton signal of C3; δ 4.88 (1H, dd, $J = 1.5, 14.0$ Hz) and δ 4.56 (1H, dd, $J = 2.0, 6.2$ Hz) were the proton signals of C4 in the carbon–carbon double bond; and δ 2.13 (3H, s) was the proton signal of the methyl group.

Figure 3b shows the chemical shift (δ , ppm) of the carbon signal: δ 77.02 was the carbon signal of the solvent CDCl_3 , δ 167.89 was the carbon signal for the carbonyl group (C2); δ 141.15 and 97.50 were the double-bonded carbon signals, δ 141.15 corresponded to the tertiary C3, δ 97.50 corresponded to the secondary C4, and δ 20.54 was the carbon signal of the methyl group (C1). According to the above analysis, the results were basically consistent with vinyl acetate.

2.2. Purity Determination by the Mass Balance Method

2.2.1. Qualitative Analysis of Organic Impurities

The organic impurities in the vinyl acetate CRM candidate were analyzed by MS-TOF, and the results are shown in Figure 4.

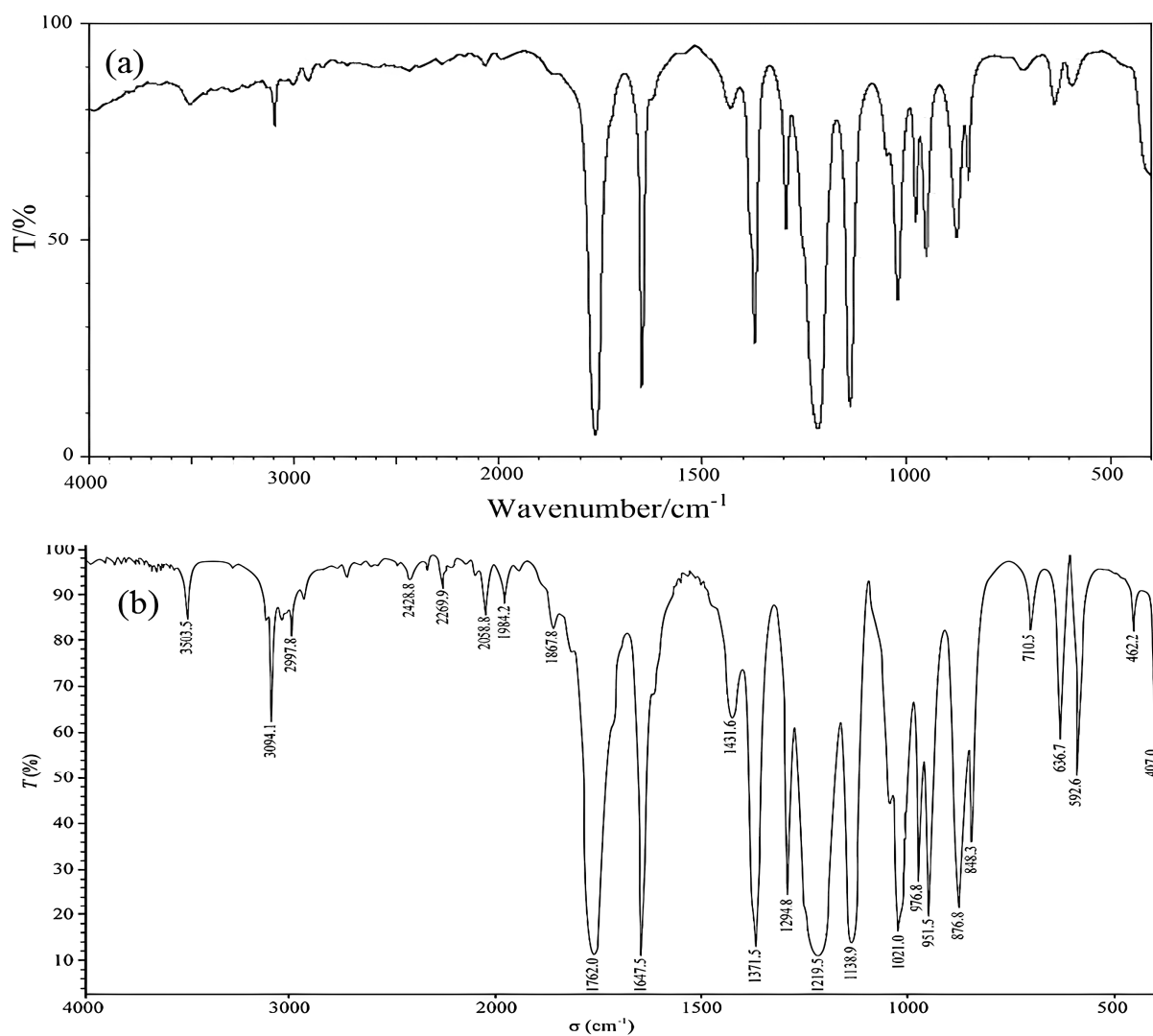


Figure 2. Infrared spectra of vinyl acetate: (a) infrared standard spectrum of vinyl acetate; (b) infrared spectra of CRM candidate.

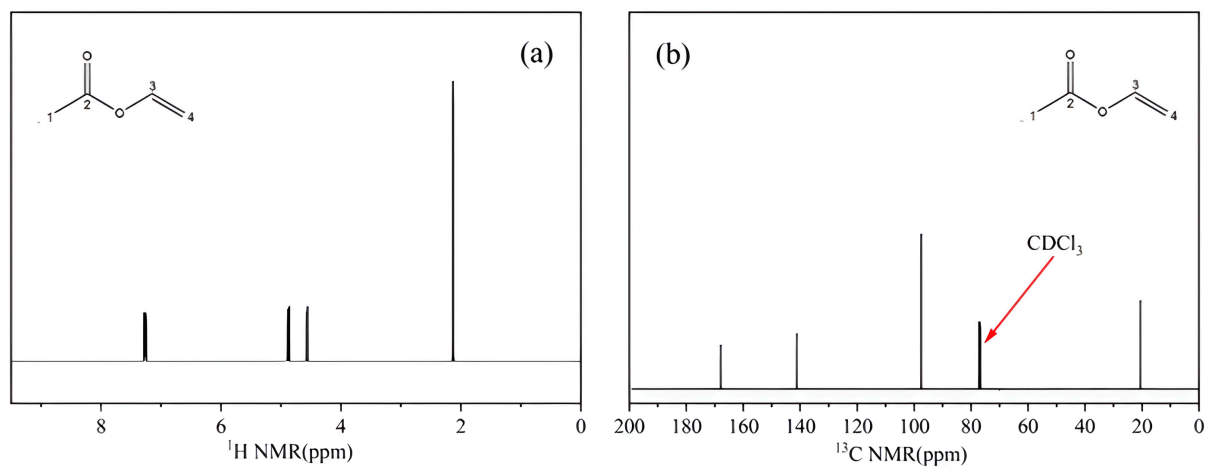


Figure 3. NMR spectra of CRM candidate: (a) ^1H NMR spectra, (b) ^{13}C NMR spectra.

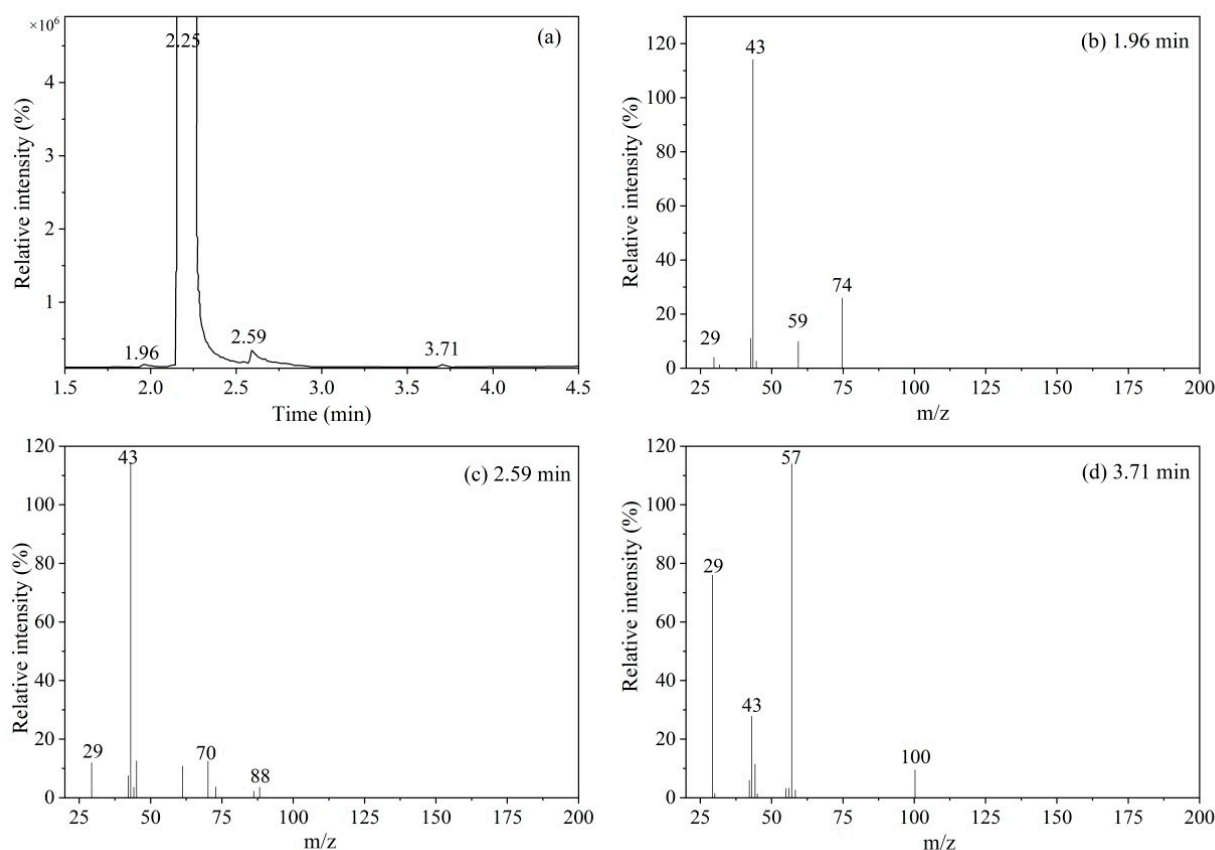


Figure 4. MS-TOF analysis results: (a) total ion chromatogram of CRM candidate; (b) mass spectrum of impurity #1; (c) mass spectrum of impurity #2; and (d) mass spectrum of impurity #3.

Figure 4a shows the total ion chromatogram (TIC) of a vinyl acetate candidate. It can be seen from the figure that there are four components in the candidate: the main peak at 2.25 min is vinyl acetate and the peaks at 1.96, 2.59, and 3.71 min are three organic impurities, numbered 1#, 2#, and 3#, respectively. The three impurities were analyzed by high-resolution mass spectrometry, and the results are shown in Figure 4b–d. The following conclusions can be drawn in accordance with Table 1: (1) In Figure 4b, m/z 74 is the molecular ion peak of $\text{CH}_3\text{COOCH}_3$, m/z 59 is the free radical $\text{CH}_3\text{COO}^\bullet$ formed after $[\text{CH}_3\text{COOCH}_3]^\bullet$ is cleaved to remove CH_3^\bullet , m/z 43 is the ion peak of $\text{CH}_3\text{C}\equiv\text{O}^+$ formed after cleavage, and m/z 29 is the ion peak of $\text{CH}_3\text{CH}_2^\bullet$ cleavage; therefore, impurity #1 may be methyl acetate. (2) In Figure 4c, m/z 88 is the molecular ion peak of $\text{CH}_3\text{COOCH}_2\text{CH}_3$, and m/z 70, m/z 43, and m/z 61 are the fragment ions $\text{HC}\equiv\text{COCH}_2\text{CH}_3^+$, $\text{CH}_3\text{COOH}_2^+$, and $\text{CH}_3\text{C}\equiv\text{O}^+$, respectively, formed after cleavage and rearrangement of the radical $[\text{CH}_3\text{COOCH}_2\text{CH}_3]^\bullet$; therefore, impurity #2 is ethyl acetate. (3) In Figure 4d, m/z 100 is the molecular ion peak of $\text{CH}_3\text{CH}_2\text{COOCH}=\text{CH}_2$ and m/z 57, m/z 43, and m/z 29 are the fragment ions $\text{CH}_3\text{CH}_2\text{C}\equiv\text{O}^+$, $\text{CH}_3\text{C}\equiv\text{O}^+$, and $\text{CH}_3\text{CH}_2^\bullet$, respectively, formed after the cleavage of $\text{CH}_3\text{CH}_2\text{COOCH}=\text{CH}_2$; therefore, impurity #3 is vinyl propionate.

The results of the mass spectrometry analysis were verified by gas chromatography experiments, and the results are shown in Figure 5. Figure 5a shows a typical chromatogram. The retention times of the three impurities were 12.52, 15.86, and 18.49 min. A comparison of these results with the spectra after the addition of methyl acetate, ethyl acetate, and vinyl propionate standard samples indicated that the impurity with a response time of 12.52 min was methyl acetate, the impurity with a response time of 15.86 min was ethyl acetate, and the impurity with a response time of 18.49 min was vinyl propionate (Figure 5b–d), which was consistent with the mass spectrometry results.

Table 1. High-resolution mass spectrometry data on three impurities in vinyl acetate.

Impurity No.	Retention Time	Measured Value (m/z)	Theoretical Value (m/z)	Elemental Composition
Vinyl acetate	2.25 min	86.0366	86.0362	$C_4H_6O_2$
		43.0177	43.0178	C_2H_3O
Impurity #1	1.96 min	74.0361	74.0362	$C_3H_6O_2$
		59.0124	59.0128	$C_2H_3O_2$
		43.0177	43.0178	C_2H_3O
Impurity #2	2.59 min	88.0520	88.0519	$C_4H_8O_2$
		70.0410	70.0143	C_4H_6O
		61.0281	61.0284	$C_2H_5O_2$
		43.0174	43.0178	C_2H_3O
Impurity #3	3.71 min	100.02	100.02	$C_5H_8O_2$
		57.0337	57.0335	C_3H_5O
		43.0176	43.0178	C_2H_3O
		29.0382	29.0386	C_2H_5

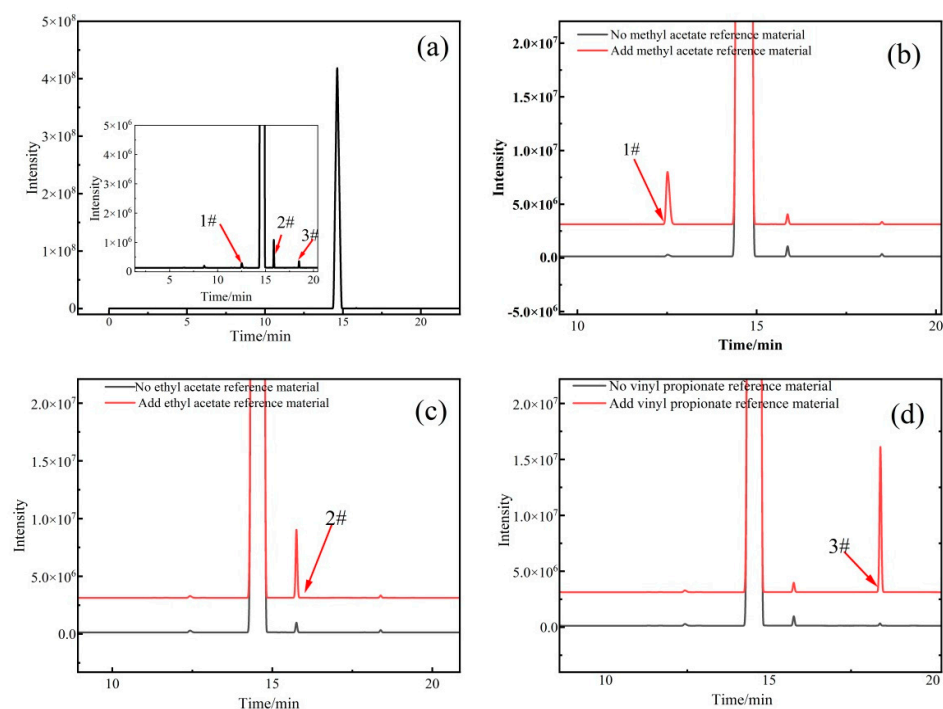


Figure 5. Results of the gas chromatography spike experiment: (a) mass spectrogram of vinyl acetate sample; (b) comparison before and after adding methyl acetate standard solution to the vinyl acetate CRM; (c) comparison before and after adding ethyl acetate standard solution to the vinyl acetate CRM; (d) comparison before and after adding vinyl propionate standard solution to the vinyl acetate CRM.

2.2.2. Purity Determined by Mass Balance Method

Figure 6 shows a typical chromatogram of vinyl acetate, in which the main peak at 14.40 min is vinyl acetate and the peaks at 12.52, 15.86, and 18.49 min are impurities. The area normalization method was used to integrate each peak area and to determine the concentration of the analyte. The results are shown in Table 2. The concentration of vinyl acetate was 99.92%. Because of the non-linear response of the GC detector, the results of the area normalization method depended on the magnitude of the response of each component on the detector, and, therefore, a relative correction factor was required in order to correct the area normalization results to achieve more accurate determination.

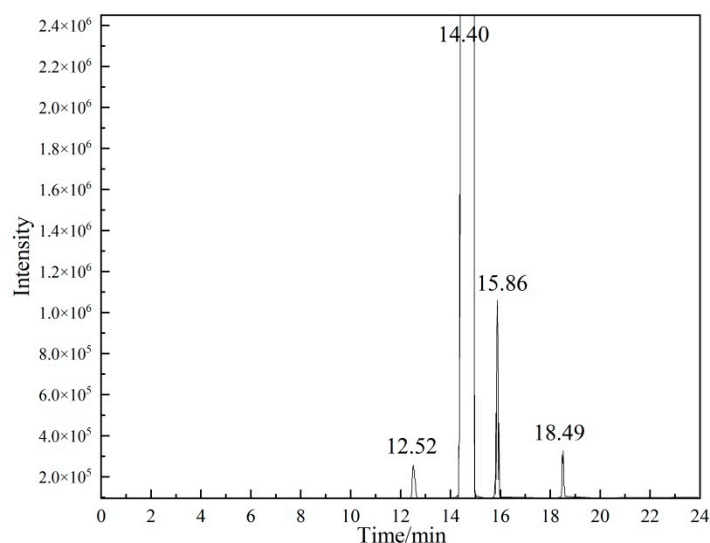


Figure 6. Gas chromatography area normalization of the vinyl acetate CRM.

Table 2. Purity of the analytes, determined using the mass balance method.

Measurement	Retention Time (min)	A_i	Concentration (%)	f_i (%)	Concentration (Calibration %)	RSD (%)
Methyl acetate	12.52	9,315,686	0.02	0.86	--	--
Ethyl acetate	15.86	33,948,215	0.05	0.83	--	--
Vinyl propionate	18.49	7,934,083	0.01	1.23	--	--
Vinyl acetate (P_0)	14.40	63,973,339,424	99.92	--	99.93	0.0029
x_w					0.030	0.0015
x_a					0.0012	0.00011
P_{MB}					99.0	0.018

Calibration solutions were prepared according to the concentration ratio of each component in the vinyl acetate CRM, and were then detected by GC. Relative correction factor f_i values of 0.86, 0.83, and 1.23 were calculated for the three impurities according to Equation (3), as shown in Table 2. By substituting the correction factors into Equation (2), the concentration of vinyl acetate was determined to be 99.93%.

$$P(\%) = \left(1 - \sum_{i=1} P_{im}\right) (1 - P_w - P_n - P_a) \times 100\% \quad (1)$$

$$P_0 = \frac{A_0}{A_0 + \sum_{i=1} f_i A_i} \quad (2)$$

↑ Characterize organic impurities and measure relative correction factors

$$f_i = \frac{A_s \times m_i}{A_i \times m_s} \quad (3)$$

The results regarding the analysis of moisture and organic acids are shown in Table 2. The moisture content was 0.03% with a standard deviation of 0.0015%, the organic acid content was 0.0012% with a standard deviation of 0.00011%, and the content of non-volatile impurities was 0.00016%. As the percentage of non-volatile impurities was very low, it could not affect the initial assignment or uncertainty evaluation of vinyl acetate, so the effect of these impurities was ignored. Finally, the purity of the vinyl acetate CRM, using the mass balance method (Equation (1)), was determined to be 99.90%.

2.3. Homogeneity and Stability Test

The homogeneity results for the vinyl acetate CRM are summarized in Table 3. The data were estimated using analysis of variance (F-test) according to ISO Guide 35:2017 [37], as shown in Table 4. The mean square value between the S_1^2 groups and the mean square value within the S_2^2 groups were calculated, and the corresponding F value was 2.01, which was smaller than the critical value F_{crit} (2.04), indicating that the homogeneity of the vinyl acetate CRM did not differ significantly during the period of the experiment. The uncertainty u_{bb} of uniformity was calculated using Equation (4).

$$u_{bb} = \sqrt{\frac{(S_1^2 - S_2^2)}{n}} \quad (4)$$

where S_1^2 is the mean square error between groups, S_2^2 is the mean square error within a group, and n is the number of measurements.

Table 3. Homogeneity results for the vinyl acetate CRM (%).

Number	1	2	3	Means
1	99.89	99.88	99.90	99.89
2	99.89	99.87	99.91	99.89
3	99.87	99.90	99.89	99.89
4	99.87	99.93	99.90	99.90
5	99.90	99.91	99.93	99.91
6	99.91	99.89	99.88	99.89
7	99.91	99.90	99.92	99.91
8	99.90	99.87	99.88	99.88
9	99.93	99.91	99.93	99.92
10	99.91	99.88	99.90	99.90
11	99.90	99.88	99.89	99.89
12	99.89	99.90	99.90	99.90
13	99.88	99.89	99.89	99.89
14	99.92	99.90	99.92	99.91
15	99.90	99.92	99.90	99.91
Overall mean			99.90	
Standard deviation			0.017	

Table 4. ANOVA analysis of homogeneity results.

Parameters	Values
Mean square between groups	$S_1^2 = 0.00043$
Mean square within groups	$S_2^2 = 0.00022$
F	$F = S_1^2/S_2^2 = 2.01$
$F_{0.05}(14, 30)$	2.04
Conclusion	$F < F_{0.05}(14, 30)$

In the stability test, a vinyl acetate CRM was continuously monitored for 12 months during storage, and the relationship between the measurement results and the monitoring time is shown in Figure 7. The measurement results were linearly fitted to show the stability trend, and regression analysis statistical tests were performed on the data. According to ISO guideline 35:2007 [38], the t test was used to calculate the significance of the slope a , where $s(a)$ is the uncertainty of the slope a , as calculated using Equations (5) and (6).

$$s^2 = \frac{\sum_1^n (y_i - b - ax_i)^2}{n - 2} \quad (5)$$

$$s_{(a)} = \frac{s}{\sqrt{\sum_1^n (x_i - \bar{x})^2}} \quad (6)$$

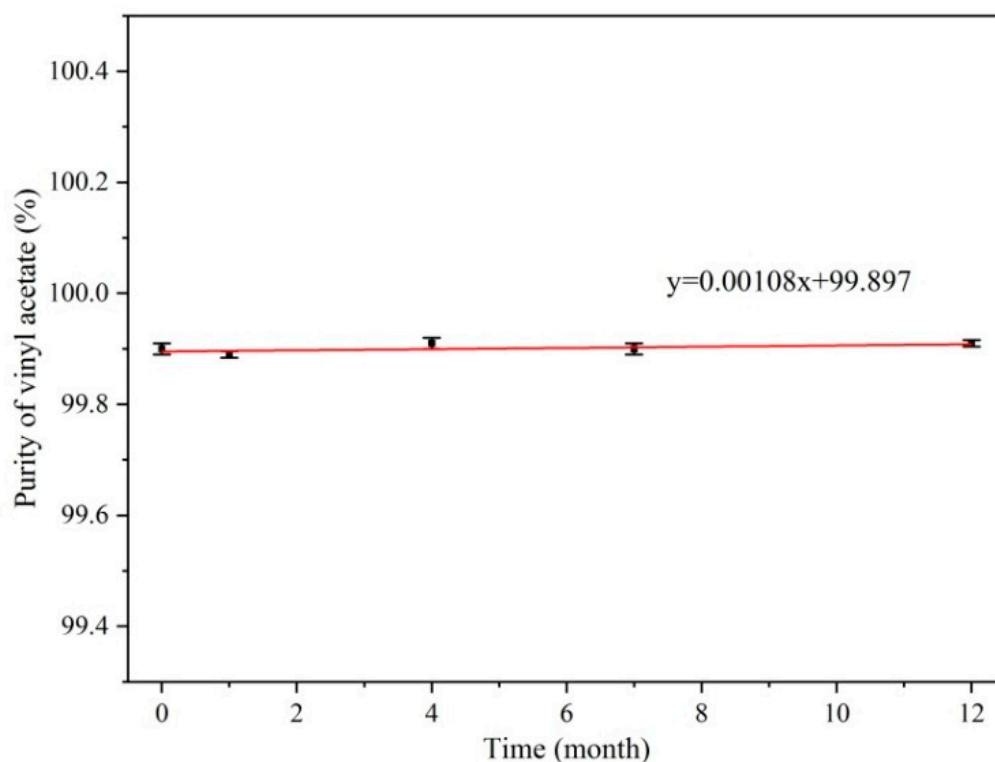


Figure 7. Stability test results.

$t_{0.95,3}$ is the critical t -value at a 95% confidence level and three degrees of freedom. The calculation result satisfied $|a| < t_{0.95,3}^{0.05} \times s_{(a)}$, and no significant change in the stability was found under long-term storage and simulated transport conditions. The results indicate that the CRM can be stored stably at -4 °C for 12 months. The uncertainty (u_s) was calculated using Equation (7), where T represents the duration of the long-term stability study.

$$u_s = s_{(a)} \times T \quad (7)$$

2.4. Uncertainty Estimation

2.4.1. Uncertainty of the Mass Balance Method

According to the ISO Guidelines for the Expression of Uncertainty in Measurement [39], the uncertainty of the mass balance method u_{MB} mainly comes from principal component measurement $u(P_0)$, moisture measurement $u(x_w)$, and organic acid measurement. The detection $u(x_a)$ and the measurement $u(x_n)$ of less volatile impurities can be evaluated using Equation (8).

$$u_{MB} = P_{MB} \times \sqrt{u(P_0)^2 + \frac{u(x_w)^2 + u(x_a)^2 + u(x_n)^2}{(1 - x_w - x_a - x_n)^2}} \quad (8)$$

For the main components analyzed by GC-FID, the combined uncertainty $u(P_0)$ can be evaluated as:

$$u(P_0) = \sqrt{u_{rel,1}^2 + u_{rel,2}^2} \quad (9)$$

where $u_{rel,1}$ represents the uncertainty introduced by the repeatability of the measurement, which is usually equal to the relative standard deviation of the measurement, and $u_{rel,2}$ represents the uncertainty introduced by the limit of detection (LOD) of GC-FID.

The uncertainty in the water measurement $u(x_w)$, using the Karl Fischer coulomb method, can be calculated by the following formula:

$$u(x_w) = x_w \sqrt{u_1^2 + \left[\frac{u(m)}{m}\right]^2 + \left[\frac{u(W)}{W}\right]^2 + \left[\frac{u(f)}{f}\right]^2} \quad (10)$$

where u_1 represents the relative standard uncertainty introduced by measurement repeatability; $u(m)$ represents the uncertainty of the sample's quality; $u(W)$ represents the standard uncertainty of the quality of water; and $u(f)$ represents the uncertainty of the correction factor, calculated from the uncertainty of the moisture reference material.

The uncertainty $u(x_a)$ introduced by the titration method for the organic acid measurement was equal to the relative standard deviation of the repeated determinations.

The calculation results for the various uncertainties are shown in Table 5, and the uncertainty introduced by the mass balance method was 0.105%.

Table 5. Uncertainties of the parameters in the mass balance method.

Uncertainty Symbols	$u(x_w)$	$u(x_a)$	$u_{rel,1}$	$u_{rel,2}$	$u(P_0)$	u_{MB}
Results	0.0015%	0.00011%	0.009%	0.105%	0.105%	0.105%

2.4.2. Combined Uncertainty

According to ISO guideline 35, the combined uncertainty u_{CRM} for a vinyl acetate CRM includes the uncertainty in the homogeneity test; the uncertainty in the stability study; and the uncertainty in the fixed value, as calculated from Equation (11) [32].

$$u_{CRM} = \sqrt{u_{bb}^2 + u_{ls}^2 + u_{MB}^2} \quad (11)$$

where u_{bb} is the uncertainty of the uniformity test, u_{ls} is the uncertainty of the stability test, and u_{MB} is the uncertainty of the mass balance legal value. Table 6 summarizes the sources of uncertainty and the results of the assessment. When the confidence probability was 95%, the expansion factor was 2, and the expansion uncertainty U_{CRM} of the vinyl acetate CRM was 0.3%.

Table 6. Uncertainty evaluation of vinyl acetate CRM.

Uncertainty Symbols	Uncertainty Sources	Results
u_{bb}	Homogeneity test	0.00849%
u_{ls}	Long-term stability study	0.00930%
u_{MB}	Mass balance method	0.105%
$u(P_0)$	GC-FID	0.105%
u_{CRM}	Combined uncertainty	0.11%
U_{CRM}	Expanded combined uncertainty	0.3%

3. Materials and Methods

3.1. Apparatus and Materials

Low-resolution mass spectrometry (Agilent 6890N-5973N GC/MS, USA), high-resolution mass spectrometry (Agilent 7890A/7200 Q-TOF GC/MS, USA), superconducting nuclear magnetic resonance spectroscopy (Bruker AV-500, USA), and Fourier transform infrared spectrometry (Thermo Fisher, Waltham, MA, USA, Thermo Nicolet In10MX-Iz10, USA) were used to characterize the CRM candidate; gas chromatography was also performed on an Agilent 6890N-5973N GC/MS instrument (Agilent Technologies, Santa Clara,

CA, USA) equipped with a flame ionization detector (FID). The present study also employed a Karl Fischer automatic moisture analyzer (Mettler C30, Mettler Toledo, Zurich, Switzerland), an inductively coupled plasma mass spectrometer (Agilent 7500a, USA), and a potentiometric titrator (Mettler T50, Mettler Toledo, Switzerland).

The CRM candidate material for vinyl acetate required for the experiment was commissioned from the Beijing Oriental Organic Chemical Factory. Methyl acetate, ethyl acetate, and vinyl propionate were all standard products produced by Dr. Ehrenstorfer, Germany. The Karl Fischer reagent (without pyridine) had a titer of approximately 2–5 mg/mL. All other reagents used were of analytical grade or higher.

3.2. Methods

3.2.1. Preparation of CRM Candidate

Because of the instability and toxicity of vinyl acetate, the raw materials for vinyl acetate used in this study were prepared by the Beijing Dongfang Organic Chemical Factory (Beijing, China), the main information about the reagents can be obtained from the Table S1.

Preparation method: Acetic acid, ethylene, and oxygen underwent a gas phase reaction under the action of a catalyst. After the reaction was completed, the obtained mixture was purified by rectification three times, and finally, vinyl acetate raw material was obtained. The material was cooled to $-18\text{ }^{\circ}\text{C}$ and dispensed into 2 mL brown ampoules under nitrogen protection, and the ampoules were immediately sealed. The same batch of vinyl acetate feedstock was used to fill 450 vials of CRM candidate before being stored at $4\text{ }^{\circ}\text{C}$.

3.2.2. Characterization of the CRM Candidate

(1) MS analysis

The CRM candidate was characterized by MS, and the molecular weights were determined. A 250 μL sample of CRM was introduced to a DB-5MS capillary column ($30\text{ m} \times 0.25\text{ mm} \times 0.25\text{ }\mu\text{m}$) for separation. The experimental conditions were as follows: The carrier gas was helium; the flow rate in constant flow mode was 1 mL/min; the inlet temperature was $200\text{ }^{\circ}\text{C}$; the ion source temperature was $230\text{ }^{\circ}\text{C}$; the quadrupole temperature was $150\text{ }^{\circ}\text{C}$; the transfer line temperature was $250\text{ }^{\circ}\text{C}$; the split ratio was 100:1; the ionization method was electron bombardment ionization (EI) (70 eV); and the heating program progressed from an initial temperature of $35\text{ }^{\circ}\text{C}$ to the target temperature over 10 min. The range of mass $m/z = 30\text{--}350$ was scanned using a one-level full scan.

(2) FT-IR

FT-IR spectroscopy was used to characterize the structures of the CRM candidate. Samples were prepared using the liquid film method, and infrared spectra were collected using the attenuated total reflection (ATR) technique using the infrared wavelength of polystyrene as a reference. All infrared spectra were acquired in the range of $4000\text{--}400\text{ cm}^{-1}$ at a resolution of 4.000 cm^{-1} .

(3) NMR

A sample of the CRM candidate (0.5 mg) was weighed and dissolved in 0.50 mL of CDCl_3 , and the proton and carbon spectra were acquired by means of superconducting NMR.

3.2.3. Mass Balance Method

The mass balance method involves the measurement of the major components in a sample, as well as moisture, less volatile impurities, and organic acids. According to the con-

tent of each component, the purity of vinyl acetate can be calculated by Equation (12) [40].

$$P(\%) = \left(1 - \sum_{i=1}^n P_{im}\right) (1 - P_w - P_n - P_a) \times 100\%$$

Determination of water content by Karl Fischer
 Determination of non-volatile impurities by ICP-MS
 Determination of acid content by potentiometric titration
 1. GC-TOF confirms three kinds of organic impurities
 2. Area percentages of impurities were calibrated

(12)

where P_{im} , P_w , P_n , and P_a are the contents of organic impurities, water, non-volatile impurities, and organic acids, respectively, in the raw material.

(1) Qualitative analysis of organic components

The organic impurities in vinyl acetate were characterized by high-resolution mass spectrometry, and the results were verified by gas chromatography. The experimental conditions for the high-resolution mass spectrometry were the same as those described in Section 3.2.2 (1).

For the GC conditions (the instrument model used was an Agilent 6890N-5973N GC/MS), 1 μ L of vinyl acetate solution was separated using a J&W DB-624 capillary column (60 m \times 0.32 mm \times 0.25 μ m). The experimental conditions were as follows: carrier gas helium; flow rate of 1 mL/min in constant flow mode; inlet temperature of 200 $^{\circ}$ C; ion source temperature of 230 $^{\circ}$ C; quadrupole temperature of 150 $^{\circ}$ C; transfer line temperature of 200 $^{\circ}$ C; and split ratio of 10:1. Temperature programming conditions were as follows: The initial temperature was 40 $^{\circ}$ C, the temperature was raised to 50 $^{\circ}$ C at a rate of 2 $^{\circ}$ C/min, and then the temperature was raised to 140 $^{\circ}$ C at a rate of 5 $^{\circ}$ C/min before being maintained for 1 min.

(2) Determination of organic components

The gas chromatography area normalization method was used to measure the contents of organic components in the CRM candidate, and the experimental conditions were the same as those described in Section 3.2.3 (1). The organic component after introducing the correction factor can be calculated from Equation (13).

$$P_0 = \frac{A_0}{A_0 + \sum_{i=1}^n f_i A_i} \quad (13)$$

where P_0 is the content of the main component; A_0 represents the peak areas of the main components; and f_i , A_i ($i = 1 - n$) represent the relative correction factors and peak areas of the organic impurities, respectively. The experimental conditions were the same as those used for the gas chromatography spiked experiment.

$$f_i = \frac{A_s \times m_i}{A_i \times m_s} \quad (14)$$

where A_s is the peak area of the standard substance, A_i is the peak area of impurity i , m_s is the mass of the standard substance, and m_i is the mass of impurity i .

(3) Determination of water

Because vinyl acetate is prone to polymerization when heated, the Karl Fischer coulometric method was chosen to measure the water content in the CRM candidate. First, 100 mL of Karl Fischer reagent was added into the calibrated instrument, the vibration frequency of the oscillator was set to 155 r/min, and the solution was mixed evenly. Then, approximately 1 mL of vinyl acetate CRM was added and reacted to the end point under the protection of nitrogen. A blank experiment was performed to ensure the accuracy of the test data.

(4) Determination of inorganic impurities

The mass fraction of inorganic impurities in the CRM candidate was measured using ICP-MS. The instrument parameters were as follows: the radio frequency power was 1300 W; the carrier gas flow rate was 1.20 L/min; the sampling rate was 0.1 r/s; and the measurement was repeated three times in the full quantitative analysis mode. The measurement method was as follows: 1 mL of candidate CRM was transferred to a 10 mL volumetric flask, diluted to volume with deionized water, shaken well, and used directly for ICP-MS.

(5) Determination of acid

A Mettler T50 potentiometric titrator was used to measure the content of organic acids. The measurement method was as follows: 1.5 mL of vinyl acetate solution was added to the potentiometric titrator, and calibrated sodium hydroxide solution was automatically added dropwise to the titration end point. To ensure the accuracy of the experimental data, a DG113-SC non-aqueous titration composite electrode was used to monitor the titration end point.

3.3. Homogeneity and Stability Test

According to the packing sequence, a total of 15 bottles of samples were randomly selected, with five bottles of vinyl acetate CRM candidate samples taken from each of the front, middle, and back. Each bottle was tested three times using the established GC-FID method. One-way analysis of variance (ANOVA) was used to test the homogeneity of the sample values. Comparison of the calculated value of F with the critical value of F (with a confidence level of 95%) determined whether there was a significant difference in homogeneity.

Because of the unstable nature of vinyl acetate, self-polymerization reactions may occur during long-term storage to affect the purity; therefore, monitoring the stability of vinyl acetate CRMs is the key to ensuring the quality of the measurements. The packaged vinyl acetate CRM candidate products were stored at 4 °C in the dark. Following the principle of dense first and thin later, and the concentrations were measured after 0, 1, 4, 7, and 12 months of storage. The purity of the vinyl acetate CRM products was measured by GC-FID, and the samples were measured three times at each time point.

Statistical Analyses

The homogeneity test data were analyzed by ANOVA (F-test). The F-value was calculated according to Equation (15), where S_1^2 is the mean square error between groups and S_2^2 is the mean square error within a group.

$$F = \frac{S_1^2}{S_2^2} \quad (15)$$

The stability studies were assessed by performing ANOVA (t -test) on linear regression data to determine the stability trends in CRM candidate purity. Statistical tests for regression analysis were performed on the stability measurements. We compared the absolute value of the slope (a) with the product of t the critical value and the slope uncertainty $s(a)$. The calculation of $s(a)$ is shown in Equations (5) and (6), which are mentioned in Section 2.3.

4. Conclusions

In this experiment, the raw materials were processed and produced, following the existing production process, and the filling and heat-sealing procedures were strictly controlled to prepare the vinyl acetate CRM. GC-MS, FT-IR, and NMR spectrometry were used to characterize the CRM candidate. Gas chromatography tandem high-resolution mass spectrometry indicated that the organic impurities in the vinyl acetate candidate were methyl acetate, ethyl acetate, and vinyl propionate. The correction factors for the three impurities were calculated, and the concentrations of the main components were determined by the gas chromatographic area normalization method. The mass balance method was used to determine the purity of vinyl acetate, and the extended uncertainty was calculated. A homogeneity and stability test indicated that the vinyl acetate CRM had good homogeneity and could be stored stably for 12 months. This study will rectify the lack of available vinyl acetate purity reference materials in China, provides a method for the comprehensive purity analysis of vinyl acetate, and can be used to develop certified reference materials with metrological traceability to SI units, and vinyl acetate certified reference material classification certificate available in File S2.

Supplementary Materials: The following supporting information can be downloaded at: <https://www.mdpi.com/article/10.3390/molecules28176245/s1>, Table S1: Concentration of some domestic and foreign vinyl acetate reagent labels; File S2: Vinyl Acetate certified reference material classification certificate.

Author Contributions: Conceptualization, methodology, investigation, project administration, data curation, C.H.; software, writing—original draft preparation, data curation, Q.G.; data curation, methodology, C.Y.; formal analysis, data curation, G.Y.; investigation, data curation, P.Z.; supervision, R.Y.; project administration, supervision, Q.Z.; writing—review and editing, K.M. All authors have read and agreed to the published version of the manuscript.

Funding: This research received no external funding.

Institutional Review Board Statement: Not applicable.

Informed Consent Statement: Not applicable.

Data Availability Statement: Data sharing is not applicable.

Conflicts of Interest: The authors declare no conflict of interest.

Sample Availability: Samples of the compounds are not available from the authors.

References

1. Neurock, M.; Tysoe, W.T. Mechanistic Insights in the Catalytic Synthesis of Vinyl Acetate on Palladium and Gold/Palladium Alloy Surfaces. *Top. Catal.* **2013**, *56*, 19. [CrossRef]
2. França De Sá, S.; Viana, C.; Ferreira, J.L. Tracing Poly(Vinyl Acetate) Emulsions by Infrared and Raman Spectroscopies: Identification of Spectral Markers. *Polymers* **2021**, *13*, 3609. [CrossRef] [PubMed]
3. Petrocelli, F.P.; Cordeiro, C.F. *Continuous Process for the Production of Vinyl Acetate-Ethylene Emulsion Copolymers, Macromolecular Symposia*; Wiley Online Library: Hoboken, NJ, USA, 2000; pp. 39–52.
4. Maes, C.; Luyten, W.; Herremans, G.; Peeters, R.; Carleer, R.; Buntinx, M. Recent Updates on the Barrier Properties of Ethylene Vinyl Alcohol Copolymer (EVOH): A Review. *Polym. Rev.* **2018**, *58*, 209–246. [CrossRef]
5. Zhang, Y.; Pang, B.; Yang, S.; Fang, W.; Yang, S.; Yuan, T.-Q.; Sun, R.-C. Improvement in Wood Bonding Strength of Poly (Vinyl Acetate-Butyl Acrylate) Emulsion by Controlling the Amount of Redox Initiator. *Materials* **2018**, *11*, 89. [CrossRef] [PubMed]
6. Bogdanffy, M.S.; Sarangapani, R.; Plowchalk, D.R.; Jarabek, A.; Andersen, M.E. A biologically based risk assessment for vinyl acetate-induced cancer and noncancer inhalation toxicity. *Toxicol. Sci.* **1999**, *51*, 19–35. [CrossRef]
7. Bogdanffy, M.S.; Valentine, R. Differentiating between local cytotoxicity, mitogenesis, and genotoxicity in carcinogen risk assessments: The case of vinyl acetate. *Toxicol. Lett.* **2003**, *140–141*, 83–98. [CrossRef]
8. Liu, A.-F.; Zhao, J.-Y.; Liu, L.; Shen, M.-J.; Lei, P.-N. Headspace-GC Determination of 1-Hexene, 1-Octene and Vinyl Acetate Migrated from Polyethylene Food-Contacting Materials into Food Simulants. *Phys. Test. Chem. Anal. (Part B Chem. Anal.)* **2020**, *56*, 1073–1078.



9. Bianchi, O.; Oliveira, R.V.B.; Fiorio, R.; Martins, J.D.N.; Zattera, A.J.; Canto, L.B. Assessment of Avrami, Ozawa and Avrami–Ozawa equations for determination of EVA crosslinking kinetics from DSC measurements. *Polym. Test.* **2008**, *27*, 722–729. [CrossRef]
10. Wenwei, Z.; Xiaoguang, Z.; Li, Y.; Yuefang, Z.; Jiazhen, S. Determination of the vinyl acetate content in ethylene-vinyl acetate copolymers by thermogravimetric analysis. *Polymer* **1994**, *35*, 3348–3350. [CrossRef]
11. Beshah, K. Microstructural analysis of ethylene-vinyl acetate copolymer by 2D NMR spectroscopy. *Macromolecules* **1992**, *25*, 5597–5600. [CrossRef]
12. Meszlényi, G.; Körtvélyessy, G. Direct determination of vinyl acetate content of ethylene-vinyl acetate copolymers in thick films by infrared spectroscopy. *Polym. Test.* **1999**, *18*, 551–557. [CrossRef]
13. Koopmans, R.J.; van der Linden, R.; Vansant, E.F. Quantitative determination of the vinylacetate content in ethylene vinyl-acetate copolymers—A critical review. *Polym. Eng. Sci.* **1982**, *22*, 878–882. [CrossRef]
14. Sun, D.-Z.; Lu, C.-Q.; Zuo, Y.; Qin, Z.-M. Head-Space GC Determination of Formamide in Children’s Articles Made of Plastic of Copolymer of Ethylene and Vinyl Acetate. *Phys. Test. Chem. Anal. (Part B Chem. Anal.)* **2014**, *50*, 199–201.
15. Pang, A.-Q.; Chen, C.-W. Pyrolytic Gas Chromatography Analyzes Vinyl Acetate Content in EVA. *Tech. Text.* **2000**, *7*, 36–39.
16. Shi, M.-J.; Zhang, J. Introduction and Evaluation for the Determination Methods of Vinyl Acetate Content. *Plastics* **2008**, *37*, 59+108–110.
17. Wise, S.A. What is novel about certified reference materials? *Anal. Bioanal. Chem.* **2018**, *410*, 2045–2049. [CrossRef]
18. Gong, H.; Huang, T.; Yang, Y.; Wang, H. Purity determination and uncertainty evaluation of folic acid by mass balance method. *Talanta* **2012**, *101*, 96–103. [CrossRef]
19. Ulberth, F. Certified reference materials for inorganic and organic contaminants in environmental matrices. *Anal. Bioanal. Chem.* **2006**, *386*, 1121–1136. [CrossRef]
20. Hyung, S.-W.; Lee, C.-H.; Kim, B. Development of certified reference materials for accurate determination of fluoroquinolone antibiotics in chicken meat. *Food Chem.* **2017**, *229*, 472–478. [CrossRef]
21. Zhou, J.; Zhao, Y.; Wang, M.; Yang, M.; Wang, T. Production of matrix certified reference material for analysis of salbutamol residue in mutton. *Microchem. J.* **2022**, *175*, 107151. [CrossRef]
22. Chen, W.; Jin, W.; Fang, H.; Chen, H.; Chen, X.; Zhang, Y.; Hong, Z. Development of a new taurine purity certified reference material. *Microchem. J.* **2022**, *181*, 107761. [CrossRef]
23. Davies, S.R.; Jones, K.; Goldys, A.; Alamgir, M.; Chan, B.K.H.; Elgindy, C.; Mitchell, P.S.R.; Tarrant, G.J.; Krishnaswami, M.R.; Luo, Y.; et al. Purity assessment of organic calibration standards using a combination of quantitative NMR and mass balance. *Anal. Bioanal. Chem.* **2015**, *407*, 3103–3113. [CrossRef] [PubMed]
24. Gao, J.-M.; Ding, L.-X.; Hu, C.-Q. A comparative uncertainty study of the purity assessment of chemical reference substances using differential scanning calorimetry (DSC) and mass balance method. *Thermochim. Acta* **2011**, *525*, 1–8. [CrossRef]
25. Wang, F.; Zhang, Y.; Wu, Q.; Xiao, W.; Zhu, J.; Ding, Y. Purity determination and uncertainty estimation of natural products sourcing chemical reference substances by high-performance liquid chromatography and differential scanning calorimetry. *Microchem. J.* **2021**, *166*, 106257. [CrossRef]
26. Nogueira, R.; Garrido, B.C.; Borges, R.M.; Silva, G.E.B.; Queiroz, S.M.; Cunha, V.S. Development of a new sodium diclofenac certified reference material using the mass balance approach and ¹H qNMR to determine the certified property value. *Eur. J. Pharm. Sci.* **2013**, *48*, 502–513. [CrossRef]
27. Davies, S.R.; Alamgir, M.; Chan, B.K.H.; Dang, T.; Jones, K.; Krishnaswami, M.; Luo, Y.; Mitchell, P.S.R.; Moawad, M.; Swan, H.; et al. The development of an efficient mass balance approach for the purity assignment of organic calibration standards. *Anal. Bioanal. Chem.* **2015**, *407*, 7983–7993. [CrossRef]
28. Lee, S.; Kwon, H.-J. Purity Assessment of Monosaccharides using Mass Balance Method. *Bulletin of the Korean Chemical Society* **2020**, *41*, 1002–1008. [CrossRef]
29. Wang, S.; Wu, P.; Li, M.; Huang, T.; Shi, N.; Feng, L.; Li, H. Mass balance method for SI-traceable purity assignment of synthetic oxytocin. *J. Pharm. Biomed. Anal.* **2022**, *207*, 114401. [CrossRef]
30. Westwood, S.; Choteau, T.; Daireaux, A.; Josephs, R.D.; Wielgosz, R.I. Mass Balance Method for the SI Value Assignment of the Purity of Organic Compounds. *Anal. Chem.* **2013**, *85*, 3118–3126. [CrossRef]
31. Liu, H.; Cheow, P.S.; Yong, S.; Chen, Y.; Liu, Q.; Teo, T.L.; Lee, T.K. Determination of purity values of amino acid reference materials by mass balance method: An approach to the quantification of related structure impurities. *Anal. Bioanal. Chem.* **2020**, *412*, 8023–8037. [CrossRef]
32. Zhou, J.; Li, F.; Wang, M.; Yan, C.; Yang, M.; Wang, T.; Zhang, L. Preparation of clorprenaline certified reference material: Purity determination and uncertainty evaluation. *Microchem. J.* **2022**, *179*, 107502. [CrossRef]
33. Ma, K.; Wang, H.; Zhao, M.; Xing, J. Purity determination and uncertainty evaluation of theophylline by mass balance method, high performance liquid chromatography and differential scanning calorimetry. *Anal. Chim. Acta* **2009**, *650*, 227–233. [CrossRef] [PubMed]
34. Wang, J.; Zhang, W.; Huang, T.; Su, P.; Yang, Y. Quantification of a volatile deuterated compound by the differential scanning calorimetry combined with quantitative nuclear magnetic resonance and its verification by the mass balance method combined with gas chromatography-mass spectrometry. *Talanta* **2022**, *246*, 123538. [CrossRef] [PubMed]

35. Chen, W.; Jin, W.; Zhang, Y.; Fang, H.; Chen, H.; Hong, Z.; Huang, X. Development of certified reference materials for four polyunsaturated fatty acid esters. *Food Chem.* **2022**, *389*, 133006. [CrossRef] [PubMed]
36. Wang, S.; Wang, S.; Li, P.; Li, L.; Ye, J. Establishment of SI-traceable purity assessment of Fumonisin B1 using a combination of quantitative ¹H NMR and mass balance. *Microchem. J.* **2023**, *185*, 108282. [CrossRef]
37. Kumar, A.; Misra, D.K. A Review on the Statistical Methods and Implementation to Homogeneity Assessment of Certified Reference Materials in Relation to Uncertainty. *Mapan* **2020**, *35*, 457–470. [CrossRef]
38. Zhou, J.; Yang, M.; Li, F.; Wang, M.; Zhang, Y.; Wei, M.; Li, X.; Qi, X.; Bai, X.; Chai, Y. Development of matrix certified reference material for accurate determination of docosahexaenoic acid in milk powder. *Food Chem.* **2023**, *406*, 135012. [CrossRef]
39. Huang, T.; Li, H.; Zhang, W. Metrological technical specification for purity assessment of organic pure substance certified reference materials in China. *Accredit. Qual. Assur.* **2021**, *26*, 279–284. [CrossRef]
40. Quan, C. Establishment of the purity values of carbohydrate certified reference materials using quantitative nuclear magnetic resonance and mass balance approach. *Food Chem.* **2014**, *153*, 378–386. [CrossRef]

Disclaimer/Publisher’s Note: The statements, opinions and data contained in all publications are solely those of the individual author(s) and contributor(s) and not of MDPI and/or the editor(s). MDPI and/or the editor(s) disclaim responsibility for any injury to people or property resulting from any ideas, methods, instructions or products referred to in the content.

Article

Purity Assessment of Dinotefuran Using Mass Balance and Quantitative Nuclear Magnetic Resonance

Xianjiang Li ^{1,*} , Wei Zhang ¹, Xiao Li ¹ , Shukun Zhou ¹, Mengling Tu ¹, Yunxiao Zhu ^{1,2} and Hongmei Li ¹

¹ Key Laboratory of Chemical Metrology and Applications on Nutrition and Health for State Market Regulation, Division of Metrology in Chemistry, National Institute of Metrology, Beijing 100029, China

² State Key Laboratory of Heavy Oil Processing, College of Chemical Engineering and Environment, China University of Petroleum, Beijing 102249, China

* Correspondence: lixianjiang@nim.ac.cn; Tel.: +86-10-6452-4737

Abstract: Dinotefuran (DNT) belongs to the third-generation neonicotinoid pesticides, which are among the most common residuals in a variety of food commodities. To guarantee accurate quantification and traceability of results in food samples, certified reference materials (CRMs) are the indispensable benchmark. In this work, a DNT CRM was characterized and its purity was assessed by two independent methods, including mass balance (MB) and quantitative nuclear magnetic resonance spectroscopy (qNMR). The mass fraction of moisture was 0.33 mg/g, the inorganic impurity was 0.01 mg/g, and no detectable organic solvent was detected. Benzoic acid was chosen as the internal standard for qNMR. Its mass fraction was 997.9 mg/g and 992.9 mg/g by MB and qNMR, respectively. Eventually, the DNT CRM was assigned a mass fraction of 995 mg/g, with expanded uncertainty of 5 mg/g ($k = 2$). This CRM can be used to prepare calibrant solutions and is applicable to national routine monitoring of DNT residuals in agro-products and food.

Keywords: dinotefuran; certified reference material; mass balance; quantitative nuclear magnetic resonance spectroscopy



Citation: Li, X.; Zhang, W.; Li, X.; Zhou, S.; Tu, M.; Zhu, Y.; Li, H. Purity Assessment of Dinotefuran Using Mass Balance and Quantitative Nuclear Magnetic Resonance. *Molecules* **2023**, *28*, 3884. <https://doi.org/10.3390/molecules28093884>

Academic Editor: Susy Piovesana

Received: 16 March 2023

Revised: 19 April 2023

Accepted: 24 April 2023

Published: 4 May 2023



Copyright: © 2023 by the authors. Licensee MDPI, Basel, Switzerland. This article is an open access article distributed under the terms and conditions of the Creative Commons Attribution (CC BY) license (<https://creativecommons.org/licenses/by/4.0/>).

1. Introduction

Neonicotinoid (NEO) insecticides are very efficient in pest control and have accounted for one-fourth of the global insecticide market since 2019 [1]. This family includes imidacloprid, acetamiprid, nitenpyram, thiamethoxam, clothianidin, thiacloprid, dinotefuran (DNT), cycloxaprid, and some new members. Dinotefuran is the common name for (RS)-1-methyl-2-nitro-3-(tetrahydro-3-furylmethyl) guanidine, with the CAS registry number 165252-70-0. As the first commercially available member of the third-generation neonicotinoids (furanicotinyl class) by Mitsui Chemicals [2], DNT has no chloride and sulfur elements and has the same good broad-spectrum insecticidal activity [3]. It is postulated that DNT affects the insect's nicotinic acetylcholine binding in a mode different from that of the other NEOs. Additionally, it has little neonicotinoid effect on fruit quality and a lower ecological risk [4]. The formulated DNT products are widely applied to soil, foliage, nursery boxes, and paddy water by drench, spray, and broadcast treatments. After two decades of global use, DNT has been one of the most frequently detected residual insecticides in food commodities, including melons [5], oranges [6], cabbage [7], honey [8], cantaloupes [9], water [10], etc. Because it has good water solubility, it can penetrate into food tissues. With its heavy usage and wide contamination, deep safety concerns arise with DNT. Further studies have shown that DNT and metabolites already exist in human teeth [11], urine [12], and sera [13]. The Joint FAO/WHO Meeting on Pesticide Residues report estimated that the acceptable daily intake for humans was 0–0.2 mg/kg bw. France has banned the usage of five NEOs since 2018 [14], and DNT is promising to take their roles. The National Institutes of Health reported that NEOs could bind to the nicotinic acetylcholine receptor in mammals and lead to serious neurotoxicity [15]. A recent report showed that exposure to

DNT and metabolites may also increase the possibility of liver cancer [16]. China issued a national food safety standard (GB 2763-2021) to forbid its intensive use, and DNT residues were strictly restricted in 52 kinds of foodstuff. The routine monitoring of residual DNT is indispensable for food safety and human wellbeing.

Because of the polarity of DNT ($\log P = -0.55$) [17], liquid chromatography–ultraviolet detection (LC-UV) [18] and liquid chromatography–mass spectrometry (LC-MS) [19–21] are widely used techniques. In addition to the detection method, calibrants are also indispensable for accurate results. In China, thousands of vegetable and fruit samples were collected from markets and tested in authorized laboratories for DNT-related health risk assessment. The National Metrology Institute shoulders the responsibility of developing CRMs to guarantee accuracy and traceability [22]. Therefore, a National Key R&D Program of China (2019YFC1604801) was launched to develop pesticide CRMs. DNT was included because of its importance for food safety concerns.

Purity CRM are located at the top of the metrological traceability chain and are highly necessary to guarantee the reliability of detection. As a result, purity assessment of a DNT CRM is a prerequisite for calibrant solutions and following reliable measurements. The mass balance (MB) and quantitative nuclear magnetic resonance (qNMR) methods are internationally recognized primary methods for the purity assessment of organic materials. MB is an indirect method whereby the mass fraction can be directly traced back to the International System of Units (SI) [23]. By this strategy, the mass fraction can be calculated by subtracting all of the impurities from 1000 mg/g, typically including related structural impurities, water, residual organic solvents, and inorganic impurities. The accuracy of MB strongly depends on baseline separation and the method sensitivity of each impurity. Meanwhile, qNMR is a direct method whereby the mass fraction is assigned with a well-characterized SI-traceable internal standard [24]. Hydrogen is the most widely used element for qNMR. The selection of the internal standard and quantitative hydrogen is critical for this method. Value assignments of organic CRMs commonly adopt a combined methodology of MB and qNMR to provide a solid result.

In this work, an extensive purity assessment of a DNT CRM was implemented with both MB and qNMR methods for the first time. In the MB method, structurally related impurities were determined by LC-UV. The other impurities (i.e., volatile organic compounds, water, and inorganic elements) were quantified by purge-trapping gas chromatography–mass spectrometry (PT-GC-MS), Karl Fischer titration, thermogravimetric analysis (TGA), and inductively coupled plasma mass spectrometry (ICP-MS). In the qNMR method, the mass fraction was calculated by the selected hydrogen peaks from benzoic acid (internal standard) and the sample. This DNT CRM could trace to the SI unit, and the associated uncertainty contribution of the two methods was carefully evaluated. As far as we know, this is the first reported pure CRM of DNT.

2. Results and Discussion

2.1. Qualitative Characterization

The aim of qualitative characterization was to verify the identity of the DNT material. The IR spectrum shown in Figure 1a is consistent with the reported spectrum from Jiang's book [25]. The characteristic absorption peaks can be attributed to typical functional groups in DNT. In detail, the peak at 3300 cm^{-1} was attributed to -NH- stretching vibration, the peak at 2900 cm^{-1} to -N-CH₃ stretching vibration, the peak at 1610 cm^{-1} to -C=N- stretching vibration, the peak at 1550 cm^{-1} to -NO₂ stretching vibration, and the peak at 1143 cm^{-1} to -C-O-C stretching vibration.

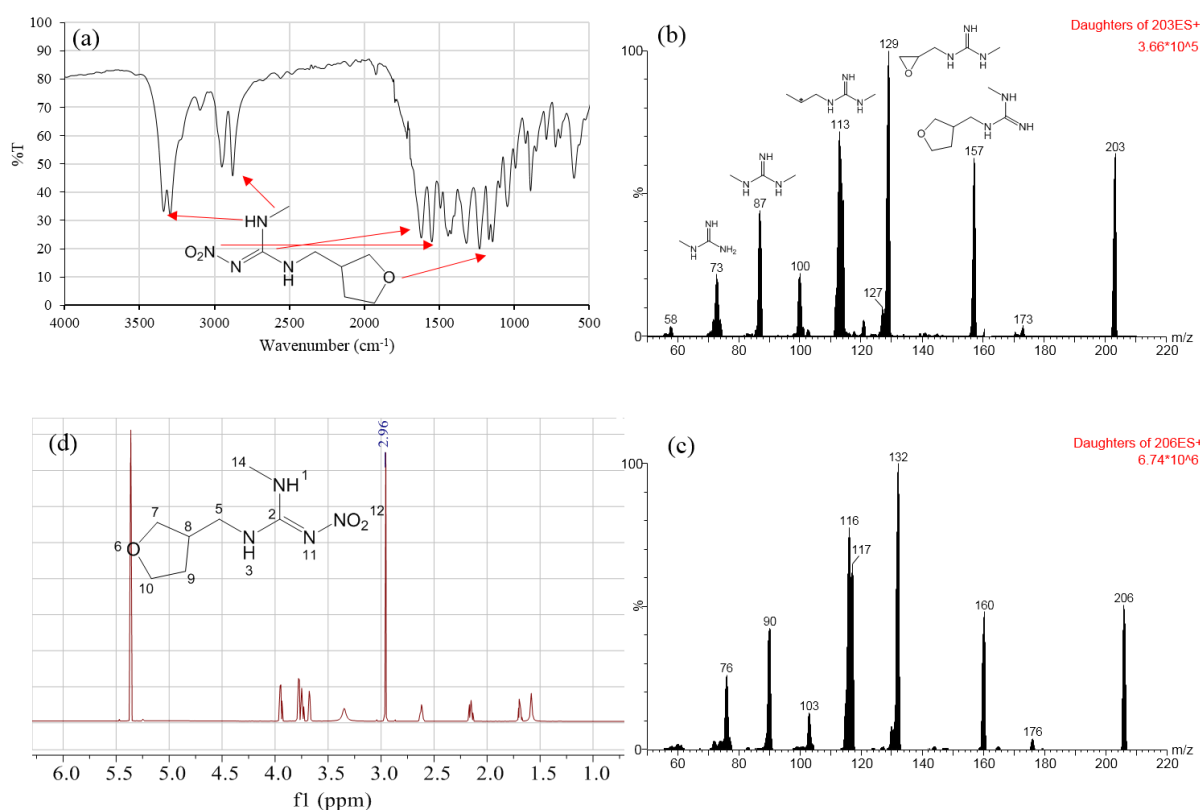


Figure 1. Characterization of DNT: (a) IR spectrum, (b) MS/MS spectrum of DNT, (c) MS/MS spectrum of DNT- d_3 , (d) ^1H NMR spectrum.

For the full-scan spectrum, the precursor ions (m/z 203 and 206) of DNT and DNT- d_3 were detected by Waters TQ-S. Then, the precursor ions were fragmented to record the product ions (Figure 1b). The typical product ions of DNT were 157 for $[\text{M}+\text{H}-\text{NO}_2]^+$ and 129 for $[\text{M}+\text{H}-\text{C}_2\text{H}_4-\text{NO}_2]^+$, in accordance with spectrum from MassBank with the ID EQ310801 [26]. Additionally, the typical daughter ions of DNT- d_3 were 160 and 132 (Figure 1c). DNT- d_3 had three deuterium atoms in the methyl group. All of the captured ions in DNT- d_3 were 3 m/z heavier than those of DNT. This indicated that the deuterium guanidine structure was quite stable. The mass deviations of the daughter ions helped in the elucidation of the fragmentation process. The chemical structures of typical ions are demonstrated in Figure 1b.

Figure 1d shows the ^1H spectrum of DNT. The proton shifts were H-5 (3.32 ppm, 2H), H-7 (3.61 ppm, 1H; 3.74 ppm, 1H), H-8 (2.58 ppm, 3H), H-9 (1.65 ppm, 1H; 2.10 ppm, 1H), H-10 (3.70 ppm, 1H; 3.89 ppm, 1H), and H-14 (2.96 ppm, 3H). Additionally, the chemical shift of the residual solvent in methylene chloride- d_2 was 5.32 and 1.68 ppm. The ^{13}C spectrum of DNT is shown in Figure S2. The chemical shifts were 158.68, 71.00, 67.58, 44.84, 38.34, 29.58, and 28.01 ppm, which matched the predicted spectrum from MestReNova (V12.0).

The above results are in accordance with the findings of a previous report [2], so the candidate material was DNT.

2.2. Quantitative Analysis by Mass Balance

2.2.1. Contents of Structurally Related Impurities

From the above acquired fragment ions and calculated neutral losses, some hints were useful for the structural elucidation. Sodium adducts and non-covalent dimer ions were observed for all peaks. The DNT and other peaks had many similarities in the fragment ions. The ion m/z 87.0796 appeared in all analytes.

The challenge of determining structurally related impurities was the baseline separation of the main component from every impurity [27]. Different columns and combinations of eluents with various gradient programs were intensively explored to baseline separate all impurities as much as possible. The details of the impurity identification and quantification were included in our previous work [28]. At last, two byproduct impurities and one stereoisomer were identified. Because these impurities had quite similar chemical structures to DNT, relative quantitation was carried out by the normalization of the peak area in the chromatogram. The maximum adsorption wavelengths were 267 nm, 268 nm, 270 nm, and 269 nm for four peaks. The purity of DNT was 99.82%, with a relative standard deviation (RSD) of 0.004%, under the wavelength of 269 nm. The calculated standard uncertainty was 0.004%, including the contribution from repeatability (u_1) and the difference in the UV response factor (u_2) (Table S1). The LOD and LOQ were 5 µg/L and 20 µg/L for the developed LC method, respectively. Good linearity was achieved for DNT, with concentrations ranging from 20 µg/L to 400,000 µg/L. Analogue elucidation not only provides the mass fraction in MB but also guides the selection of the quantitative hydrogen peak in qNMR.

2.2.2. Mass Fraction of Residual Organic Solvent

The residual organic solvent was determined by the PT-GC-MS method. Pure water was tested as a blank sample. After background subtraction, the results showed that no detectable organic solvent was present in the DNT material.

2.2.3. Mass Fraction of Water

From the synthesis pathway of DNT, water is used as a solvent for some polar precursors [2]. DNT has good solubility in methanol; therefore, direct addition instead of oven-assisted Karl Fischer titration was used. The blank value was determined with dummy addition to compensate for the adventitious water introduced during the sample loading, which was then subtracted from the mass of water determined in the DNT sample. From the result, the mass fraction of water was 0.33 mg/g, with an RSD of 6.0%. This value was proposed in rectangular distribution, and the standard uncertainty was 0.190 mg/g. The trace water content may come from residual solvent or moisture in the air during storage.

2.2.4. Determination of the Mass Fraction of Inorganic Impurities

As shown by the TGA curve in Figure S1, the weight of the DNT was kept constant after 650 °C. The final weight was almost zero, and the total content of inorganic impurities was below the instrument sensitivity (0.1 µg). This indicated the presence of no detectible inorganic impurities in DNT according to the TGA method. Meanwhile, for ICP-MS, it had better sensitivity. A semi-quantitative analysis mode was performed for preliminary screening for the inorganic elements. As shown in Table S2, the total mass fraction of inorganic impurities was only 0.01 mg/g according to the ICP-MS method. The associated standard uncertainty was estimated as 0.005 mg/g.

2.2.5. Mass Fraction by MB

Using the MB method, the mass fraction of DNT was calculated by subtracting the contents of all impurities from 1000 mg/g, as shown in Equation (1):

$$P_{MB} = [1 - (P_W + P_{NV} + P_{OS})] \times P_{HPLC} \quad (1)$$

where P_{HPLC} is the content of DNT measured by LC-UV (99.82%), P_W is the content of water (0.33 mg/g), P_{OS} is the content of residual organic solvent (0 mg/g), and P_{NV} is the content of inorganic impurities (0.01 mg/g). Ultimately, the mass fraction of DNT was determined to be 997.9 mg/g.

2.3. Quantitative Analysis by qNMR

The equation for qNMR was as follows:

$$P_{qNMR} = \frac{I_{DNT}}{I_{Std}} \frac{n_{Std}}{n_{DNT}} \frac{M_{DNT}}{M_{Std}} \frac{m_{Std}}{m_{DNT}} P_{Std} \quad (2)$$

where m_{std} and m_{DNT} are the weight of benzoic acid and DNT, respectively, M_{std} and M_{DNT} are the molecular weight of benzoic acid and DNT, respectively, n_{std} and n_{DNT} are the number of hydrogens in the quantification peaks of benzoic acid and DNT, respectively, I_{std} and I_{DNT} are the integrated signal intensities of the quantification peaks of benzoic acid and DNT, respectively, and P_{std} and P_{qNMR} are the mass fraction of benzoic acid and DNT, respectively.

The mass fraction of DNT was directly assigned to the benzoic acid CRM using the relative integral ratios of the selected hydrogen signals of benzoic acid and DNT. Because the second impurity had one more furan ring in the methyl group of DNT, this methyl hydrogen was a good choice for quantification without overlapping with the second impurity. Moreover, the aromatic hydrogen of benzoic acid (7.39–7.82 ppm 3H) and the methyl hydrogen of DNT (2.96 ppm 3H) were isolated from the other peaks and exhibited good peak symmetry for precise integration in Figure 2. Hence, these hydrogen peaks were chosen for quantification. The mass fraction of DNT was 992.9 mg/g, with an RSD of 0.03% in six duplicates.

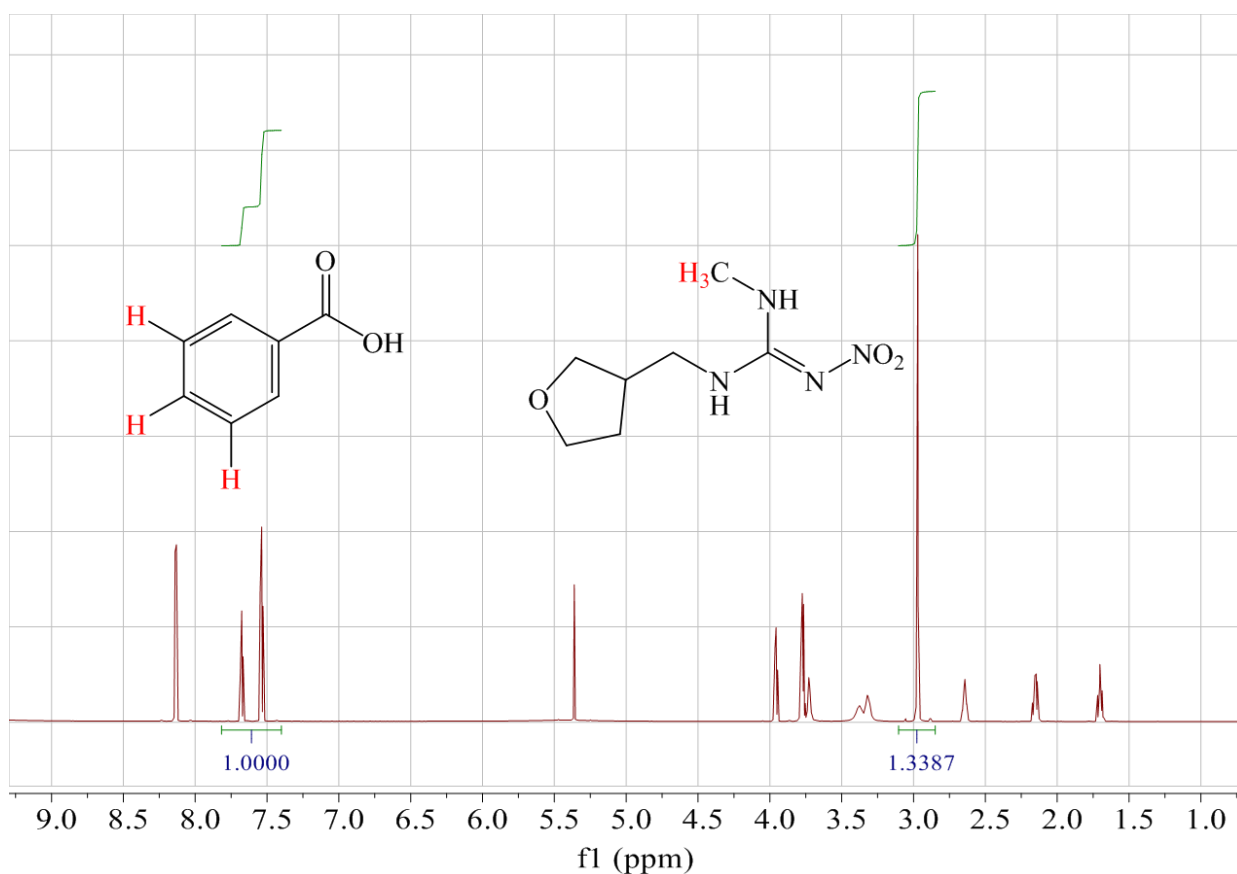


Figure 2. $^1\text{H-NMR}$ spectra of DNT and benzoic acid.

2.4. Value Assignment

It is desirable to obtain consistent values from two independent methods, while the mass fraction determined by the MB method was a little higher than that determined by the qNMR method. This situation is common, because impurities are hardly comprehensively quantified in the MB method [29]. Finally, the mass fraction of the DNT CRM was 995 mg/g, taking the mean value of the MB and qNMR methods.

2.5. Uncertainty Evaluation

The uncertainty was evaluated according to the metrological technical specification for purity assessment of certified reference materials—organic purity certified reference materials (JJF 1855-2020) and the general and statistical principles for characterization of reference materials (JJF 1343-2022). In detail, the contribution to the uncertainty of characterization was from the methods of qNMR and MB, with their main influencing parameters. For the MB method, the combined standard uncertainty (u_{MB}) was obtained by quadratic combination of the uncertainties from all detectable impurities, as shown in Equation (3):

$$u_{MB} = P_{MB} \times \sqrt{u_{rel,HPLC}^2 + \frac{u_W^2 + u_{NV}^2 + u_{OS}^2}{(1 - P_W - P_{NV} - P_{OS})^2}} \quad (3)$$

where $u_{rel,HPLC}$ is the relative uncertainty from LC-UV (0.004%), u_W is the uncertainty from the water content (0.190 mg/g), u_{NV} is the uncertainty from inorganic impurities (0.005 mg/g), and u_{OS} is the uncertainty from residual organic solvent (0 mg/g). At last, the uncertainty of MB was 0.2 mg/g.

For qNMR, the uncertainty budget of DNT was 0.3 mg/g, originating from Equation (4):

$$u_{qNMR} = P_{qNMR} \sqrt{\left(\frac{u(I_{TMX}/I_{std})}{I_{TMX}/I_{std}}\right)^2 + \left(\frac{u(M_{TMX})}{M_{TMX}}\right)^2 + \left(\frac{u(M_{std})}{M_{std}}\right)^2 + \left(\frac{u(m_{TMX})}{m_{TMX}}\right)^2 + \left(\frac{u(m_{std})}{m_{std}}\right)^2 + \left(\frac{u(P_{std})}{P_{std}}\right)^2} \quad (4)$$

These two methods were regarded as having unequal precision. So, the standard uncertainty (u_{char}) of characterization was half of the square root of the sum of squares of the purity bias and uncertainty from the two methods, as shown in Equation (5):

$$u_{char} = \sqrt{(P_{MB} - P_{qNMR})^2 + u_{MB}^2 + u_{qNMR}^2}/2 \quad (5)$$

Finally, the standard uncertainty of DNT characterization (u_{char}) was 3 mg/g. The details are described in Table 1. The expanded uncertainty u_{char} was calculated by multiplying the u_{char} by the cover factor ($k = 2$) at a confidence level of 95%. As a result, the expanded uncertainty of the DNT characterization was 5 mg/g ($k = 2$).

Table 1. Uncertainty budget.

	Subitem	Value	$u_{(xi)}$
MB	P_{HPLC} (%)	99.82	0.004
	P_W (mg/g)	0.33	0.190
	P_{OS} (mg/g)	0	0
	P_{NV} (mg/g)	0.01	0.005
	P_{MB} (mg/g)	997.9	0.2
qNMR	M_{std} (g/mol)	124.1368	0.00411
	M_{TMX} (g/mol)	202.2115	0.00435
	m_{TMX} (mg)	7.4559	0.00029
	m_{std} (mg)	3.1701	0.00029
	P_{std} (mg/g)	999.9	0.09
	I_{TMX}/I_{std}	1.3387	0.00036
	P_{qNMR} (mg/g)	992.9	0.3
	P_{char}	995	3

3. Materials and Methods

3.1. Chemicals and Materials

HPLC-grade acetonitrile (ACN) was obtained from Merck (Darmstadt, Germany). The DNT candidate material and DNT-d₃ were bought from Toronto Research Chemicals (Nanjing, China) and Alta Scientific (Tianjin, China), respectively. The stock solution of DNT was prepared at a concentration of 0.4 mg/mL with ACN and stored at −20 °C in the dark. Water was supplied by Hangzhou Wahaha Group Co., Ltd. (Zhejiang, China). KBr for infrared (IR) was supplied by Aladdin (Shanghai, China). Methylene chloride-d₂ was obtained from Sigma-Aldrich (St. Louis, MO, USA). The water content (GBW13517, 50.7 mg/g, $U = 0.6$ mg/g, $k = 2$) and benzoic acid (GBW06148, 99.991%, $U = 0.024\%$, $k = 2$) CRMs were obtained from the National Institute of Metrology (Beijing, China). The tuning solution (part no. 5184-3566) and calibration standard (part no. 8500-6940) for ICP-MS were obtained from Agilent Technology (Tokyo, Japan).

3.2. Instruments

A Shimadzu LC-20A (Kyoto, Japan) was used for the analysis of the main components and structurally related impurities. It was equipped with an Agilent ZORBAX Eclipse plus C₈ column (5 μm particle size, 4.6 mm × 250 mm). A Waters UPLC TQ-S system (Manchester, UK) was used for qualitative analysis. The residual organic solvent was quantified on a Thermo Scientific Trace 1310-TSQ 8000 EVO (Austin, TX, USA) with a Lumin AQUATEk 100 purge and trap concentrator (Mason, OH, USA). Separation was performed on a DB-624 column (30 m × 0.320 mm × 1.80 μm). The moisture content was determined using a Mettler-Toledo C30S Karl Fischer titrator (Greifensee, Switzerland). TGA tests were carried out on a PerkinElmer Pyris 1 (Waltham, MA, USA), and ICP-MS was conducted on an Agilent 8800 (Tokyo, Japan). IR was tested using a PerkinElmer 100 N (Waltham, MA, USA). A Bruker Ascend™ 800 NMR nuclear magnetic resonance spectrometer (Billerica, MA, USA) was applied for characterization and quantification. A quadruple inverse 5 mm CPQCI cryo-probe was equipped with for the ¹H spectrum. The Bruker NMR software TopSpin 3.1 was used for data processing. Samples were weighed using a Mettler-Toledo XP205 or UMX2 balance (Greifensee, Switzerland). An IKA HS260 was used for material homogenization (Staufen, Germany).

3.3. Qualitative Characterization

3.3.1. IR Spectrometry

KBr crystal was dried in advance and milled with DNT to form a homogeneous mixture. Then, the powder mixture was pressed into a tablet for IR spectroscopy. Data were collected in the wavenumber range of 600–4000 cm^{−1}, with 24 accumulations, and then compared with the reported spectra from the literature.

3.3.2. LC-MS/MS Analysis

DNT and DNT-d₃ were analyzed with the UPLC TQ-S system. The solution was directly injected via the Intellistart™ system, with a constant flow (10 μL/min). The instrument parameters were operated as described in a previous report [7]. First, a full scan was carried out to find their precursor ions in the range of 100–300 *m/z*. Then, the collision energy was set to 10 to find their fragmented ions. The differences in the fragmented ions were helpful for explanation of the fragmentation pathways.

3.3.3. NMR Analysis

Considering its solubility, methylene chloride-d₂ was selected as the deuterated solvent. DNT (5 mg) was weighed into a glass vial and mixed with 1 mL of methylene chloride-d₂ for complete dissolution. Afterward, 0.6 mL of the solution was pipetted into an NMR tube for characterization. The ¹H spectra were collected with a 30° flip angle, 26 s relaxation delay, and zg30 pulse sequence. The pulse offset was 5.25 ppm, which was the midpoint of the selected quantitative hydrogen atoms. Data were collected with

32 repetitions of 64 K complex points. For the ^{13}C spectrum, a 2 s relaxation delay and 1024 repetitions were applied. The head of the NMR probe was maintained at 296 K. TopSpin 3.1 was used for data processing.

3.4. Quantitative Analysis by Mass Balance

3.4.1. Determination of Structurally Related Impurities

The comprehensive detection of structurally related impurities using liquid chromatographic methods is the key part of the mass balance method [30]. Their contents were closely related to industrial synthetic processes. Here, the contents of these impurities were determined by the LC-UV method. DNT stock solution was directly injected without dilution. The LC conditions were as described in our previous report [28]. All tests were carried out in triplicate and followed with solvent blank injections to avoid any carryover effect. Signal-to-noise ratios of 3 and 10 were chosen to determine the limit of detection (LOD) and the limit of quantification (LOQ) of the developed method, respectively. The contents of structurally related impurities were based on the normalized peak area of all detected peaks with the same wavelength. Because the signal intensity of impurities relied on the wavelength of UV detector, an uncertainty was introduced according to the Standard JF 1855-2020 [31].

3.4.2. Residual Organic Solvent Determination

Residual organic solvents were quantitatively determined by the PT-GC-MS method. Solid DNT was gravimetrically dissolved in 40 mL of H_2O at a concentration of 1 mg/g. The PT sample parameters were as follows: purge temperature 20 °C, purge time 11 min, purge flow 40 mL/min, desorb preheat temperature 245 °C, desorb temperature 250 °C, desorb time 2 min, drain flow 300 mL/min, bake temperature 280 °C, and injection volume 25 mL. For the GC part, the oven temperature was programmed as follows: started from 40 °C and kept for 3 min, increased by 20 °C/min to 230 °C, and kept for 2 min. The carrier gas was helium at a flow rate of 1 mL/min through the column. For the MS part, the ion source and transfer-line temperatures were kept at 230 °C.

3.4.3. Water Determination

Residual water was determined by Karl Fischer coulometric titration with a diaphragmless electrode. The method conditions were as follows: polarization current 5 μA , end voltage 100 mV, and minimum titration time 30 s. In detail, the water CRM was precisely weighed and loaded into the titration cell to verify its accuracy. Then, solid DNT (about 50 mg) was precisely weighed and added for the determination of water. Five replicates were performed for DNT. The blank value was obtained without the introduction of DNT samples and was subtracted from the measured value.

3.4.4. Inorganic Impurity Determination

Both the TGA and ICP-MS methods were adopted to determine inorganic impurities. In TGA, the heating program started from 30 °C and increased to 750 °C at a rate of 30 °C/min. First, an empty pan was tested to draw a thermographic baseline of the program. Then, about 5 mg of DNT was loaded to record the weight loss during continuous combustion. The residual weight was regarded as the total of inorganic impurities. In ICP-MS, the trace levels of the 70 most common elements were individually analyzed. By this method, the DNT solution was gravimetrically prepared at about 5 mg/g and infused for analysis. The instrument parameters were the same as before [32].

3.5. Quantitative Analysis by qNMR

In addition to MB, qNMR provided an orthogonal approach for the purity assessment of DNT. It overcame the problem that impurities may not be detected by MB. For qNMR, an internal standard CRM (benzoic acid) was necessary for accurate quantification. In addition to the traceability to the SI unit, there should be no overlapping peaks between

DNT and the internal standard. Here, DNT (7 mg) and benzoic acid (3 mg) were accurately weighed and dissolved by methylene chloride-d₂. After complete dissolution, the mixture was transferred into an NMR tube. The parameters of the instrument were the same as described in Section 3.3.3.

4. Conclusions

The pure DNT CRM was comprehensively investigated with SI-traceable purity assessment for the first time. Qualitative characterization by IR, LC-MS/MS, and H-NMR confirmed the structural identity of DNT. Its purity was determined by both MB and qNMR, with a mass fraction of 995 mg/g and expanded uncertainty of 5 mg/g. In MB, four classes of potential impurities were extensively quantified. The mass fraction of moisture was 0.33 mg/g, while that of inorganic impurities was 0.01 mg/g, and no detectable organic solvent was detected. In qNMR, benzoic acid was used as an internal standard for direct assignment. The selected hydrogen in DNT had no overlap with any of the four structurally related impurities. The assigned purity value of the DNT can be traceable to the SI unit via an unbreakable traceability chain. This new DNT CRM will contribute to more accurate and traceable results from labs.

Supplementary Materials: The following supporting information can be downloaded at: <https://www.mdpi.com/article/10.3390/molecules28093884/s1>, Figure S1: TGA curve of DNT, Figure S2: The ¹³C spectrum of DNT, Table S1: Uncertainty from the difference in UV response factor, Table S2: Concentrations of inorganic impurities.

Author Contributions: Conceptualization, formal analysis, methodology, data curation, investigation, writing—original draft, X.L. (Xianjiang Li); qNMR data curation, W.Z.; PT-GC-MS data curation, S.Z.; ICP-MS data curation, X.L. (Xiao Li); writing—review and editing, X.L. (Xianjiang Li), M.T. and Y.Z.; funding acquisition and project administration, H.L. All authors have read and agreed to the published version of the manuscript.

Funding: This work was supported by the National Key R&D Program of China (2019YFC1604801).

Institutional Review Board Statement: Not applicable.

Informed Consent Statement: Not applicable.

Data Availability Statement: Data sharing not applicable.

Conflicts of Interest: The authors declare no conflict of interest.

Sample Availability: Samples of the compounds are not available from the authors.

References

1. Sparks, T.C.; Crossthwaite, A.J.; Nauen, R.; Banba, S.; Cordova, D.; Earley, F.; Ebbinghaus-Kintscher, U.; Fujioka, S.; Hirao, A.; Karmon, D.; et al. Insecticides, biologics and nematicides: Updates to IRAC's mode of action classification—a tool for resistance management. *Pestic. Biochem. Phys.* **2020**, *167*, 104587. [CrossRef]
2. Wakita, T.; Kinoshita, K.; Yamada, E.; Yasui, N.; Kawahara, N.; Naoi, A.; Nakaya, M.; Ebihara, K.; Matsuno, H.; Kodaka, K. The discovery of dinotefuran: A novel neonicotinoid. *Pest Manag. Sci.* **2003**, *59*, 1016–1022. [CrossRef] [PubMed]
3. Jeschke, P.; Nauen, R. Neonicotinoids—From zero to hero in insecticide chemistry. *Pest Manag. Sci.* **2008**, *64*, 1084–1098. [CrossRef] [PubMed]
4. Deng, Y.; Liu, R.; Zheng, M.; Wang, Z.; Yu, S.; Zhou, Y.; Zhou, Z.; Diao, J. From the First to Third Generation of Neonicotinoids: Implication for Saving the Loss of Fruit Quality and Flavor by Pesticide Applications. *J. Agric. Food. Chem.* **2022**, *70*, 15415–15429. [CrossRef] [PubMed]
5. Rahman, M.M.; Park, J.-H.; Abd El-Aty, A.M.; Choi, J.-H.; Yang, A.; Park, K.H.; Nashir Uddin Al Mahmud, M.; Im, G.-J.; Shim, J.-H. Feasibility and application of an HPLC/UV-D to determine dinotefuran and its shorter wavelength metabolites residues in melon with tandem mass confirmation. *Food Chem.* **2013**, *136*, 1038–1046. [CrossRef]
6. Yang, Z.; Zhang, K.; Chen, L.; Liu, B.; Zhang, Q.; Zhang, H.; Sun, C.; Hu, D. Determination of Dinotefuran and Its Metabolites in Orange Pulp, Orange Peel, and Whole Orange Using Liquid Chromatography-Tandem Mass Spectrometry. *J. AOAC Int.* **2017**, *100*, 1551–1558. [CrossRef]

7. Yang, B.; Ma, W.; Wang, S.; Shi, L.; Li, X.; Ma, Z.; Zhang, Q.; Li, H. Determination of eight neonicotinoid insecticides in Chinese cabbage using a modified QuEChERS method combined with ultra performance liquid chromatography-tandem mass spectrometry. *Food Chem.* **2022**, *387*, 132935. [CrossRef]
8. Mitchell, E.A.D.; Mulhauser, B.; Mulot, M.; Mutabazi, A.; Glauser, G.; Aebi, A. A worldwide survey of neonicotinoids in honey. *Science* **2017**, *358*, 109–111. [CrossRef]
9. Chen, M.; Tao, L.; McLean, J.; Lu, C. Quantitative Analysis of Neonicotinoid Insecticide Residues in Foods: Implication for Dietary Exposures. *J. Agric. Food. Chem.* **2014**, *62*, 6082–6090. [CrossRef]
10. Ma, W.; Yang, B.; Li, J.; Li, X. Amino-functional metal-organic framework as a general applicable adsorbent for simultaneous enrichment of nine neonicotinoids. *Chem. Eng. J.* **2022**, *434*, 134629. [CrossRef]
11. Zhang, N.; Wang, B.; Zhang, Z.; Chen, X.; Huang, Y.; Liu, Q.; Zhang, H. Occurrence of neonicotinoid insecticides and their metabolites in tooth samples collected from south China: Associations with periodontitis. *Chemosphere* **2021**, *264*, 128498. [CrossRef] [PubMed]
12. Zhang, T.; Song, S.; Bai, X.; He, Y.; Zhang, B.; Gui, M.; Kannan, K.; Lu, S.; Huang, Y.; Sun, H. A nationwide survey of urinary concentrations of neonicotinoid insecticides in China. *Environ. Int.* **2019**, *132*, 105114. [CrossRef] [PubMed]
13. Yamamuro, T.; Ohta, H.; Aoyama, M.; Watanabe, D. Simultaneous determination of neonicotinoid insecticides in human serum and urine using diatomaceous earth-assisted extraction and liquid chromatography–tandem mass spectrometry. *J. Chromatogr. B* **2014**, *969*, 85–94. [CrossRef] [PubMed]
14. France Bans All Uses of Neonicotinoid Pesticides. Available online: <https://cen.acs.org/environment/pesticides/France-bans-uses-neonicotinoid-pesticides/96/i36> (accessed on 1 April 2023).
15. Cimino, A.M.; Boyles, A.L.; Thayer, K.A.; Perry, M.J. Effects of Neonicotinoid Pesticide Exposure on Human Health: A Systematic Review. *Environ. Health Persp.* **2017**, *125*, 155–162. [CrossRef]
16. Zhang, H.; Zhang, R.; Zeng, X.; Wang, X.; Wang, D.; Jia, H.; Xu, W.; Gao, Y. Exposure to neonicotinoid insecticides and their characteristic metabolites: Association with human liver cancer. *Environ. Res.* **2022**, *208*, 112703. [CrossRef]
17. United States Environmental Protection Agency. *Dinotefuran*; United States Environmental Protection Agency: Washington, DC, USA, 2004.
18. Carbonell-Rozas, L.; Lara, F.J.; del Olmo Iruela, M.; Garcia-Campana, A.M. Capillary liquid chromatography as an effective method for the determination of seven neonicotinoid residues in honey samples. *J. Sep. Sci.* **2020**, *43*, 3847–3855. [CrossRef]
19. Yang, Y.; Ma, X.; Yang, C.; Wang, Y.; Cheng, J.; Zhao, J.; Dong, X.; Zhang, Q. Eco-friendly and acid-resistant magnetic porous carbon derived from ZIF-67 and corn stalk waste for effective removal of imidacloprid and thiamethoxam from water. *Chem. Eng. J.* **2022**, *430*, 132999. [CrossRef]
20. Zuo, J.; Cai, R.; An, Y.; Tang, H. Simultaneous Quantification of Five Stereoisomeric Hexoses in Nine Biological Matrices Using Ultrahigh Performance Liquid Chromatography with Tandem Mass Spectrometry. *J. Anal. Test.* **2020**, *4*, 249–256. [CrossRef]
21. Yang, B.; Wang, S.; Ma, W.; Li, G.; Tu, M.; Ma, Z.; Zhang, Q.; Li, H.; Li, X. Simultaneous Determination of Neonicotinoid and Carbamate Pesticides in Freeze-Dried Cabbage by Modified QuEChERS and Ultra-Performance Liquid Chromatography–Tandem Mass Spectrometry. *Foods* **2023**, *12*, 699. [CrossRef]
22. Juhász, E. The role of certified reference materials in metrology. *Measurement* **1986**, *4*, 104–110. [CrossRef]
23. Westwood, S.; Choteau, T.; Dairea, A.; Josephs, R.D.; Wielgosz, R.I. Mass Balance Method for the SI Value Assignment of the Purity of Organic Compounds. *Anal. Chem.* **2013**, *85*, 3118–3126. [CrossRef] [PubMed]
24. Mahajan, S.; Singh, I.P. Determining and reporting purity of organic molecules: Why qNMR. *Magn. Reson. Chem.* **2013**, *51*, 76–81. [CrossRef] [PubMed]
25. Jiang, Y.; Huang, X.; Wang, X.; Zhang, Y. Insecticides. In *Pesticides Analysis Manual*, 1st ed.; Chemical Industry Press: Beijing, China, 2012; pp. 205–207.
26. Dinotefuran; LC-ESI-QFT.; MS2; CE: 15; R=35000; [M+H]⁺. MassBank: Swiss Federal Institute of Aquatic Science and Technology. 2015. Available online: https://massbank.eu/MassBank/RecordDisplay?id=MSBNK-Eawag_Additional_Specs-ET220203 (accessed on 1 April 2023).
27. Chen, J.-B.; Zhao, X.; Zhang, Z.; Chen, Y.; Fu, X.; Liu, Y. Separation and characterization of the impurities in 3,3-diamino-4,4-azoxyfurazan by ultrahigh-performance liquid chromatography combined with Qorbitrap mass spectrometry. *Microchem. J.* **2021**, *170*, 106647. [CrossRef]
28. Li, X.; Ma, W.; Yang, B.; Tu, M.; Zhang, Q.; Li, H. Impurity Profiling of Dinotefuran by High Resolution Mass Spectrometry and SIRIUS Tool. *Molecules* **2022**, *27*, 5251. [CrossRef] [PubMed]
29. Lippa, K.A.; Duewer, D.L.; Nelson, M.A.; Davies, S.R.; Mackay, L.G. The role of the CCQM OAWG in providing SI traceable calibrators for organic chemical measurements. *Accredit. Qual. Assur.* **2019**, *24*, 407–415. [CrossRef]
30. Li, X.; Yang, B.; Ma, W.; Tu, M.; Zhang, Y.; Ma, Z.; Zhang, Q.; Li, H. Impurity identification in thiamethoxam by high resolution mass spectrometry and computer assisted elucidation. *Anal. Bioanal. Chem.* **2022**, *414*, 7203–7210. [CrossRef]

31. *JFJ 1855–2020*; Metrological Technical Specification for Purity Assessment of Certified Reference Materials–Organic Purity Certified Reference Materials. Standards Press of China: Beijing, China, 2020.
32. Li, X.; Li, H.; Zhang, W.; Li, X.; Zhang, Q.; Guo, Z.; Li, X.; Song, S.; Zhao, G. Development of patulin certified reference material using mass balance and quantitative NMR. *World Mycotoxin J.* **2021**, *15*, 135–142. [CrossRef]

Disclaimer/Publisher’s Note: The statements, opinions and data contained in all publications are solely those of the individual author(s) and contributor(s) and not of MDPI and/or the editor(s). MDPI and/or the editor(s) disclaim responsibility for any injury to people or property resulting from any ideas, methods, instructions or products referred to in the content.

Article

Certification of New Selenium-Enriched Yeast and Supplement Reference Materials for Selenomethionine Using Two Independent Measurement Strategies

Xiao Li ^{1,2} , Ling Shi ², Panshu Song ², Wei Cai ² , Ximing Luo ^{1,*} and Bo Zhao ^{2,*}¹ School of Ocean Sciences, China University of Geosciences (Beijing), Beijing 100083, China; lixiao@nim.ac.cn² Division of Chemical Metrology and Analytical Science, National Institute of Metrology, Beijing 100029, China; shiling@nim.ac.cn (L.S.); songpsh@nim.ac.cn (P.S.); caiwei@nim.ac.cn (W.C.)

* Correspondence: luoxm@cugb.edu.cn (X.L.); zhaobo@nim.ac.cn (B.Z.); Tel.: +86-10-6452-4721 (B.Z.)

Abstract: Selenium-enriched yeast possesses the unique ability of transforming chemical selenium, such as sodium selenite, into a biologically active form, which mitigates its toxic effects on the human body. The transformation product of this process, selenomethionine, can be safely and effectively absorbed and utilized by the human body; hence, it has been spiked into a selenium-enriched supplement. This study employs two distinct measurement strategies to determine the selenomethionine content in two candidate reference materials, a selenium-enriched yeast powder and supplement, using both organic and inorganic mass spectrometry. The concentrations of selenomethionine in the selenium-enriched yeast were determined using HPLC-ICP-MS and HPLC-ESI-MS/MS, with mass fractions measured at 718 mg SeMet kg⁻¹ and 715 mg SeMet kg⁻¹, respectively. Notably, both methods yielded consistent results for the selenium supplement, with a selenomethionine mass fraction of 59 mg SeMet kg⁻¹. Ultimately, the certified values of these candidate reference materials were determined as 716 mg kg⁻¹ and 59 mg SeMet kg⁻¹ with expanded uncertainties of 36 mg SeMet kg⁻¹ ($k = 2$) and 5 mg SeMet kg⁻¹ ($k = 2$), respectively. The development of these candidate reference materials serves as a valuable reference for diverse methods aiming to determine the value of organic selenium speciation in complex food substrates.

Keywords: selenium speciation; selenomethionine; certified reference material; HPLC-ICP-MS; HPLC-ESI-MS/MS



Citation: Li, X.; Shi, L.; Song, P.; Cai, W.; Luo, X.; Zhao, B. Certification of New Selenium-Enriched Yeast and Supplement Reference Materials for Selenomethionine Using Two Independent Measurement Strategies. *Molecules* **2024**, *29*, 235. <https://doi.org/10.3390/molecules29010235>

Academic Editor: Michael G. Kontominas

Received: 5 December 2023

Revised: 26 December 2023

Accepted: 30 December 2023

Published: 1 January 2024



Copyright: © 2024 by the authors. Licensee MDPI, Basel, Switzerland. This article is an open access article distributed under the terms and conditions of the Creative Commons Attribution (CC BY) license (<https://creativecommons.org/licenses/by/4.0/>).

1. Introduction

Selenium was first discovered and named by the Swedish chemist Jöns Jacob Berzelius in 1817. It was not until 1973 that the World Health Organization officially recognized selenium as an essential trace element for the human body [1]. Numerous studies have shown that selenium has a variety of beneficial functions, including improving immunity, exhibiting anti-oxidation and anti-tumor properties, and protecting cells [2]. The maximum safe dietary selenium intake is suggested as 400 mg per day. A level of ~40 mg daily is suggested as the minimum amount required and an intake of <11 mg daily will definitely put a person at risk of deficiency problems [3]. China is a typical country with selenium deficiency, and the distribution of selenium on the Earth's surface is uneven. In areas with serious selenium deficiency, such as Northeast China, the low content of selenium in food has led to endemic diseases, such as Keshan disease and Kaschin-Beck disease [4]. Selenium in food can be divided into inorganic selenium and organic selenium. The utilization rate of organic selenium in animal bodies is much higher than that of inorganic selenium [5]. An insufficient or excessive intake of selenium may cause adverse effects on the human body [6]. Natural foods, such as selenium-rich plants, are an effective way to increase selenium intake, while they may not be enough to meet the recommended daily intake for the human body [7]. Therefore, studies on understanding the enrichment process of

selenium in plants, animals, and microorganisms and comparing the composition of natural selenium-rich foods and artificially transformed selenium-rich foods have been carried out to find suitable selenium-rich products to supplement the human body's demand for selenium [8].

Natural selenium-rich foods are primarily derived from organic selenium-rich raw materials formed by the biotransformation of crops in inorganic-selenium-rich soils [9]. In general, natural selenium-rich foods include selenium-rich tea [10], selenium-rich rice [11], selenium-rich garlic [12], and other similar products. Artificial conversion, on the other hand, involves using plants, animals, and microorganisms as transformants to convert inorganic selenium into organic selenium [13], which can then be processed and used to produce selenium-rich foods, such as selenium-rich eggs [14] and selenium-rich pork [15]. As far as we know, the content and biological activity of selenium in natural selenium-containing compounds found in plants and animals are relatively lower than those of selenium in the synthesized selenium-containing compounds [16]. Selenium-enriched yeast, as a source of organic selenium, has a higher bioavailability and better safety compared to inorganic selenium, and is an ideal selenium supplement with broad application prospects. It can be used as a nutrient-rich additive in health-food products and as a starter to prepare selenium-rich food [17]. SeMet is the main component of organic selenium in selenium-rich yeast that accounts for more than half of the organic selenium content [18]. Selenium supplements contain selenium in different chemical forms. The current evidence favors SeMet over the other forms of selenium. Therefore, in the majority of supplements, selenium is present as SeMet [19].

At present, chromatographic separation methods, such as gas chromatography (GC) [20], high-performance liquid chromatography (HPLC) [21], and capillary electrophoresis (CE) [22], are commonly employed to detect SeMet in food owing to their advantages of high selectivity and sensitivity. Among these methods, liquid chromatography is the most important separation method, which is often coupled with various detection techniques, such as high-performance liquid chromatography-inductively coupled plasma mass spectrometry (HPLC-ICP-MS) [21], high-performance liquid chromatography-atomic fluorescence spectroscopy (HPLC-AFS) [23], and HPLC-fluorescence detection [24].

The compliance with respect to the quality can be very well assured by the use of certified reference materials (CRMs) [25]. In this paper, to ensure the accurate and reliable quantification of SeMet in selenium-enriched nutritional supplements, the first certified reference materials for SeMet based on a selenium-enriched yeast and supplement are developed. The selenium-enriched yeast and supplement were purchased from the market, and the candidate material of the CRMs were obtained through homogenization and sieving. The certified value of the CRMs were determined by HPLC-ICP-MS/MS and HPLC-ESI-MS/MS approaches. The homogeneity and stability under storage and transportation conditions of the CRM were monitored, and their associated uncertainties were taken into account in the total uncertainty. The development of the two mentioned substances' standard matrices address the gap in the research of relevant CRMs for food in China. The uncertainty levels of these substances are on par with internationally established CRM levels.

2. Results and Discussion

2.1. Optimization of the Extraction Method

2.1.1. Enzyme Screening

As demonstrated by Ma et al. [26], the use of a combination of protease XIV with other enzymes not only failed to increase the extraction efficiency, but also enhanced the blank levels of Se species. Thus, only protease XIV was utilized for SeMet extraction in the following studies.

2.1.2. Optimization of the Solvent for the Enzyme Solution Based on Enzymatic Hydrolysis

This study demonstrated that overnight enzymatic hydrolysis yields a SeMet recovery rate of less than 50%. To enhance the stability of the target compound, the laboratory utilized 0.1 M Tris-HCl, 0.1% trifluoroacetic acid (TFA), 5 mmol/L citric acid, and ultrapure water as the solvents for enzyme preparation. The results reveal that, when 0.1 M Tris-HCl was employed as the solvent, the spike recovery of SeMet was 102.3%, markedly higher than the recovery rates obtained with the other three solvents (0.1% TFA: 67.1%; 5 mmol/L citric acid: 73.9%; and ultrapure water: 44.7%). Consequently, 0.1 M Tris-HCl was selected as the solvent for enzyme preparation in the experiment.

2.1.3. Ultrasound-Assisted Enzymatic Hydrolysis

To mitigate the potential contamination issues stemming from Tris-HCl of the ion source of HPLC-ESI-MS/MS, the laboratory devised an ultrasound-assisted enzymatic hydrolysis method for extracting SeMet from selenium-enriched yeast. This involved weighing 0.2 g of the sample and adding 5 g of the protease XIV enzyme solution (10 mg mL^{-1}). The mixture was then sonicated at $37 \text{ }^\circ\text{C}$ for 1 h. Following centrifugation at 8000 rpm for 10 min, the supernatant was extracted. Subsequently, another 5 g of the enzyme solution was added to the centrifuge tube, and the extraction process was repeated. The supernatants from both centrifugations were combined and filtered through a $0.2 \text{ }\mu\text{m}$ polyethersulfone (PES) membrane and used for analysis. The results demonstrate that, with this pretreatment method, the recovery of the target compound reached 97.9%.

2.2. Optimization of the Mobile Phase and Chromatographic Column

Due to the structural and property similarities between selenium and arsenic species, this experiment initially attempted to utilize a PRP-X100 anion exchange column as the chromatographic column. Diammonium hydrogen phosphate (Figure 1a), an ideal mobile phase for arsenic speciation analysis, was compared with two previously reported mobile phases (citric acid [6] (Figure 1b) and ammonium dihydrogen phosphate [27] (Figure 1c)). Through the optimization of the concentration, pH, and flow rate of different mobile phases, the results demonstrate that the chromatographic separation and analysis time were optimal when using diammonium hydrogen phosphate as the mobile phase.

Considering that selenate, as a commonly occurring selenium species in the samples, tends to have a prolonged retention time, which significantly affects the analysis efficiency, our laboratory explored the use of a C_{18} reversed-phase column. This approach involves the rapid elution of inorganic selenium, effectively reducing the analysis time for selenium species. The use of an OSAKA SODA CAPCELL PAK C_{18} reversed-phase column with a mobile phase consisting of 10 mmol/L sodium 1-butananesulfonic acid, 8 mmol/L tetramethylammonium hydroxide pentahydrate, 5 mmol/L malonic acid, and 5% MeOH at a pH of 4.0 exhibited the shortest analysis time and superior separation efficiency. Therefore, these chromatographic conditions were selected for the separation of the selenium species in this study (Figure 1d).

2.3. Reproducibility, Linear Relationship, and Detection Limits

The instrument conditions of HPLC-ICP-MS were optimized through instrument tuning. After that, a series of SeMet standard solutions ($0.5, 5, 25, 50,$ and 100 ng g^{-1}) were analyzed for linearity assessment. Within the concentration range of $0.5\text{--}100 \text{ ng/g}$, the linear correlation coefficient between the peak area of SeMet and its concentration was calculated to be 0.9995. The instrument's LOD was determined as 0.23 ng g^{-1} based on the calculation of 3 times of signal-to-noise ratio (SNR), and the LOQ of the instrument was established as 0.71 ng g^{-1} based on 10 times of SNR. The precision of the developed method, evaluated using a 25 ng g^{-1} SeMet standard solution, demonstrated a relative standard deviation (RSD) of 0.52% ($n = 6$).

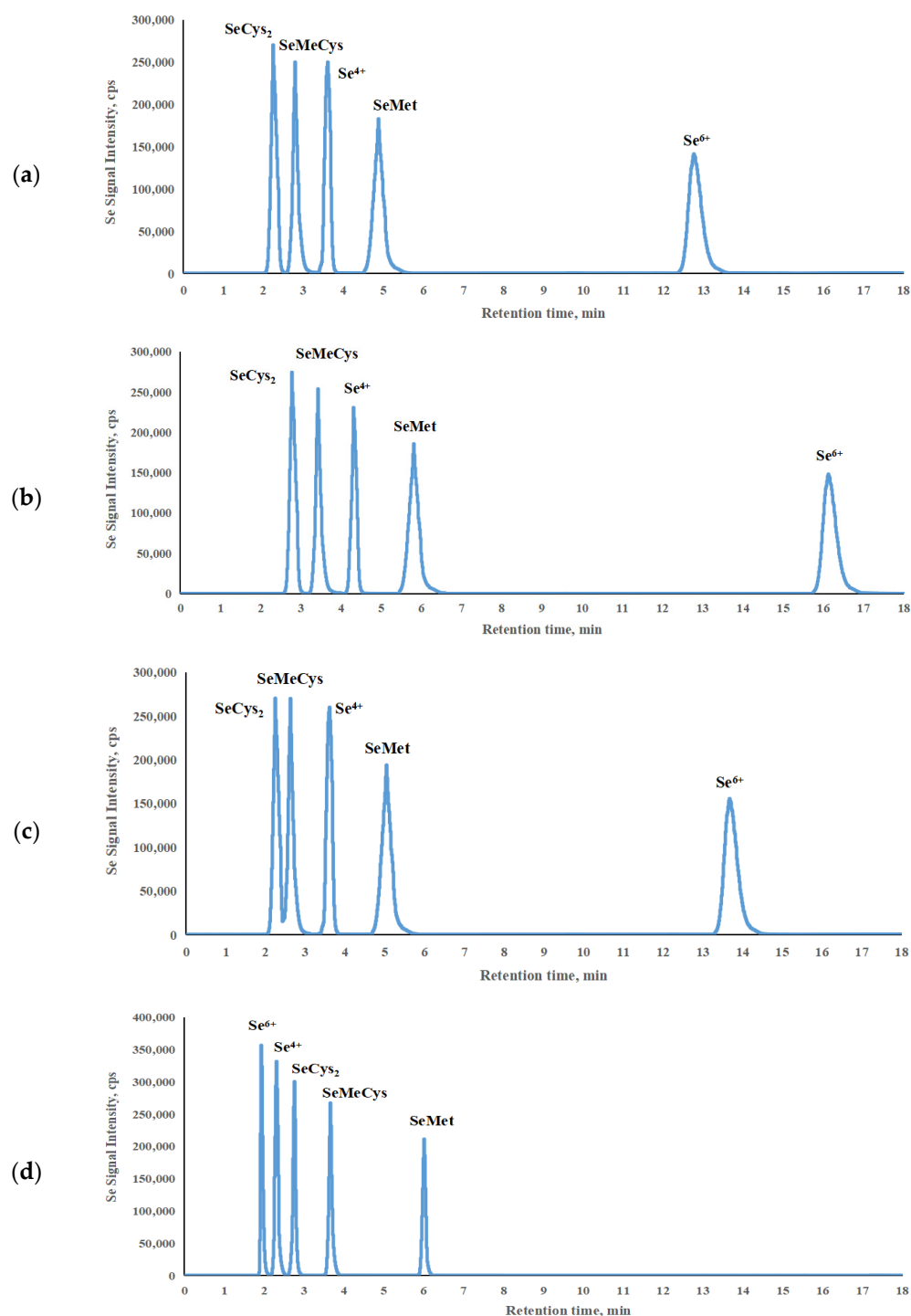


Figure 1. The chromatographic separation results of the different mobile phases and chromatographic column. (a) 40 mmol/L diammonium hydrogen phosphate with the anion exchange column; (b) 5 mmol/L citric acid with the anion exchange column; (c) 60 mmol/L ammonium dihydrogen phosphate with the anion exchange column and (d) A total of 10 mmol/L sodium 1-butanedisulfonic acid, 8 mmol/L tetramethylammonium hydroxide pentahydrate, and 5 mmol/L malonic acid with the C_{18} column.

In the HPLC-ESI-MS/MS analysis, a highly favorable linear correlation coefficient of 0.9998 was achieved for a series of standard solutions with the same concentrations mentioned above. The instrument's LOD was found to be 0.5 ng g^{-1} , while the LOQ was determined to be 1.7 ng g^{-1} . In addition, at a SeMet standard solution concentration

of 25 ng g⁻¹, the precision, as indicated by the relative standard deviation (RSD) of the method, was exceptionally low at 1.2% ($n = 6$). This demonstrates the method's high precision and reliability in quantifying SeMet concentrations.

2.4. Homogeneity Test

The homogeneity of the candidate certified reference materials (CRMs) for SeMet was evaluated using the HPLC-ICP-MS method. Homogeneity testing was conducted on 11 units for each of the two CRM substance candidates. For each unit, two parallel samples were taken and subjected to analysis. The calculated F values for SeMet ($F_{\text{calculated-yeast}} = 1.59$ and $F_{\text{calculated-supplement}} = 1.16$) were found to be lower than the critical value of $F_{0.05(10, 11)} = 2.85$, indicating that no significant differences were evident within and between the sample packets. Thus, it can be concluded that the homogeneity for the CRM candidates was satisfied. The uncertainty introduced by heterogeneity (u_{bb}) was assessed based on the inhomogeneity among the bottles (M_{among}) and within the bottles (M_{within}). The u_{bb} was calculated as shown in Equation (1):

$$u_{bb} = \sqrt{(M_{\text{among}} - M_{\text{within}})/n} \quad (1)$$

2.5. Stability Monitoring

To assess the stability of the candidate reference materials, both long-term and short-term stability outcomes were evaluated under storage conditions of -20 °C for 12 months and transport temperatures of 50 °C for 5 days. The stability was assessed through a regression line analysis. The t-test results indicate that the SeMet content in both CRMs displayed no statistically significant instability, neither within the elapsed time of 12 months nor under extreme temperatures. The uncertainties for both long-term and short-term stability outcomes were calculated using the following Equation (2).

$$u_{lts} = s(\beta_1) \times t_l; u_{sts} = s(\beta_1) \times t_s \quad (2)$$

where $s(\beta_1)$ is the standard deviation (SD) of the slope β_1 and t represents the monitoring time of long-term and short-term stability outcomes.

2.6. Value Assignment

The certified value of SeMet concentration was obtained through two independent measurement methods, HPLC-ICP-MS and ESI-HPLC-MS/MS. The concentrations of selenomethionine in the selenium-enriched yeast were determined as 718 mg SeMet kg⁻¹ and 715 mg SeMet kg⁻¹, respectively, while the selenomethionine mass fractions in the selenium supplement were determined as 59 mg SeMet kg⁻¹ by both methods. Statistical tests, including Dixon's Q test and Cochran's test, were performed, and no data were excluded. Due to the equal accuracy of the results obtained from both measurement methods, the certified values of the selenium-enriched yeast powder and supplement were established as 716 mg/kg and 59 mg/kg, respectively, which represent the average values of the two measurement results.

2.7. Uncertainty Assessment

The uncertainty outcomes of the certified SeMet value in the selenium-enriched yeast and supplement were evaluated in accordance with the ISO Guide 35 "Reference materials—Guidance for characterization and assessment of homogeneity and stability", and were based on the combination of uncertainties associated with characterization (u_{char}), possible variations between packets (u_{bb}), long-term stability (u_{lts}), and short-term stability (u_{sts}).

The uncertainties related to the standard solution, sample preparation, and measurement repeatability were all taken into account in the characterization uncertainty. Among them, the uncertainty of preparing the standard solution (u_{std}) included three components: u_{CRM} for the uncertainty of the CRMs for SeMet, $u_{m\text{CRM}}$ for the precision of weighing the

CRMs, and $u_{mCRMsol}$ for the precision of weighing the solvent. The formula for u_{std} is as shown in Equation (3):

$$u_{std} = \sqrt{u_{CRM}^2 + u_{mCRM}^2 + u_{mCRMsol}^2} \quad (3)$$

The uncertainty of preparing the sample u_{sam} included u_{msam} and $u_{msamsol}$. Here, u_{msam} represents the uncertainty from the weighing of the sample and $u_{msamsol}$ represents the uncertainty from the weighing of the solvent for the sample. The formula for u_{sam} is as shown in Equation (4):

$$u_{sam} = \sqrt{u_{msam}^2 + u_{msamsol}^2} \quad (4)$$

The uncertainty of the measurement results according to the instrument stability and sample preparation procedures from the measurement repeatability for HPLC-ICP-MS (u_{AICP}) and ESI-HPLC-MS/MS (u_{AESI}) are calculated using the following Equations (5) and (6), respectively:

$$u_{AICP} = \sqrt{\sum_{i=1}^n (x - \bar{x})^2 / n(n-1)} \quad (5)$$

$$u_{AESI} = \sqrt{\sum_{i=1}^n (x - \bar{x})^2 / n(n-1)} \quad (6)$$

where x is the result of the subsamples, \bar{x} is the average test result of all subsamples, and n is the number of measurement repetitions.

The combined uncertainty outcomes of the definite values of HPLC-ICP-MS $u_{charICP}$ and ESI-HPLC-MS/MS $u_{charESI}$ are calculated using u_{AICP} , u_{AESI} , u_{std} , and u_{sam} , as shown in Equations (7) and (8), respectively:

$$u_{charICP} = \sqrt{u_{std}^2 + u_{sam}^2 + u_{AICP}^2} \quad (7)$$

$$u_{charESI} = \sqrt{u_{std}^2 + u_{sam}^2 + u_{AESI}^2} \quad (8)$$

As the results obtained from two independent measurement methods reveal equal precision values, the combined relative uncertainty of the definite value of u_{char} is calculated using $u_{charICP}$ and $u_{charESI}$, as shown in Equation (9):

$$u_{char} = \sqrt{u_{charICP}^2 + u_{charESI}^2} \quad (9)$$

The combined uncertainty of the certified u_C is calculated as shown in Equation (10):

$$u_C = \sqrt{u_{char}^2 + u_{bb}^2 + u_{lts}^2 + u_{sts}^2} \quad (10)$$

Finally, the expanded uncertainty U_{CRM} values were calculated as 36 mg/kg and 5 mg/kg according to the following Equation (11):

$$U_{CRM} = u_C \times k (k = 2) \quad (11)$$

The uncertainty values of SeMet in the selenium-enriched yeast powder and supplement CRMs are shown in Tables 1 and 2, respectively. Ultimately, the expanded uncertainties of these candidate reference materials were calculated as 36 mg SeMet kg⁻¹ ($k = 2$) and 5 mg SeMet kg⁻¹ ($k = 2$), respectively, which were as low as the uncertainties of the selenomethionine CRMs produced by other National Metrology Institutes.

Table 1. Uncertainty values of SeMet in the selenium-enriched yeast powder CRM.

Source of Uncertainty	Uncertainty Item	Typical Value (mg/kg)
Homogeneity test	u_{bb}	9
Long-term stability study	u_{lts}	13
Short-term stability study	u_{sts}	8
Standard deviation of the mean values measured by HPLC-ICP-MS	u_{AICP}	4.15
Standard deviation of the mean values measured by ESI-HPLC-MS/MS	u_{AESI}	7.88
Standard solution preparation	u_{std}	9.31
Sample preparation	u_{sam}	0.68
Relative combined uncertainty	u_c	18
U_{CRM}	U_{CRM}	36

Table 2. Uncertainty values of SeMet in the selenium-enriched supplement CRM.

Source of Uncertainty	Uncertainty Item	Typical Value (mg/kg)
Homogeneity test	u_{bb}	1
Long-term stability study	u_{lts}	1
Short-term stability study	u_{sts}	1
Standard deviation of the mean values measured by HPLC-ICP-MS	u_{AICP}	1.27
Standard deviation of the mean values measured by ESI-HPLC-MS/MS	u_{AESI}	1.75
Standard solution preparation	u_{std}	0.77
Sample preparation	u_{sam}	0.06
Relative combined uncertainty	u_c	2.5
U_{CRM}	U_{CRM}	5

3. Materials and Methods

3.1. Candidate Reference Materials

The selenium-enriched yeast powder samples were purchased from a commercial supplier. The raw material for the selenium-enriched supplement was obtained through the preliminary screening of various commercially supplements. It was confirmed that the composition included organic selenium in the form of SeMet. Some products are falsely advertised as containing only inorganic selenium components. Therefore, they cannot be considered as raw materials. To ensure homogeneity, the samples were sieved using a 100-mesh sieve and then thoroughly mixed for 1 h in a V-type aluminum alloy mixer. The resulting mixture was divided into 200 packets, each containing 5 g of the selenium-enriched yeast powder or supplement, and sealed within aluminum bags. To prevent contamination by pathogenic or spoilage microorganisms, the candidates of the standard material were sterilized under ^{60}Co exposure, delivering an absorbed dose of approximately 2.5 kGy. The irradiated samples were subsequently stored at a temperature of $-20\text{ }^\circ\text{C}$ to ensure long-term preservation.

3.2. Materials and Apparatus

The CRM of selenomethionine in water, GBW10034, was developed by the National Institute of Metrology (Beijing, China) and has a certified value of $(39.4 \pm 1.0)\ \mu\text{g g}^{-1}$ as Se. A selenium-enriched yeast CRM, SELM-1, which was purchased from the National Research Council Canada (NRC, Ottawa, Canada), was used for the method validation. The certified value of SeMet was $(3190 \pm 260)\ \text{mg kg}^{-1}$. Protease XIV from Sigma-Aldrich Inc. (St. Louis, MO, USA) was employed for the extraction of SeMet from the yeast sample. HPLC-grade methanol, obtained from Thermo Fisher Scientific (Carlsbad, CA, USA), was used as the organic solvent. Ultrapure water was produced using a Milli-Q Integral 5 system

(Millipore Corp., Burlington, MA, USA) and was utilized for the preparation of all samples and standard solutions. For the mobile phase preparation, HPLC-grade 1-butananesulfonic acid sodium salt, malonic acid (Regent Plus, 99%), and tetramethylammonium hydroxide pentahydrate (HPLC-grade) were supplied by Merck (Darmstadt, Germany).

The ultrasound-assisted extractions were conducted using an ultrasonic bath (KQ-500GDV, Kun Shan Ultrasonic Instruments Co., Ltd., Kunshan, Jiangsu, China). Shaking was performed using a WS20 shaking incubator (Wiggens, Straubenhardt, Germany). The extracts obtained from the samples were centrifuged using a Universal 320R centrifuge (Hettich, Tuttlingen, Germany). Se determination was carried out using an ICP-MS apparatus (8800, Agilent Technologies, Santa Clara, CA, USA) equipped with a collision cell, a Scott double-pass spray chamber, and a PFA nebulizer. The Agilent 1290 HPLC system (Santa Clara, CA, USA) outlet was directly connected to the MicroMist nebulizer of the ICP-MS/MS via PEEK capillary tubing for SeMet determination. Liquid chromatography tandem with triplequad 3500 mass spectrometer was also employed for the value assignment of SeMet in the yeast powder and supplement.

3.3. Preparation of the Standard Solutions

The stock standard solution was prepared by the gravimetric weighing of a certain amount of GBW10034 in ultrapure water to achieve a concentration of 1 mg kg^{-1} . It was then sealed in ampoules and stored at a temperature of $4 \text{ }^{\circ}\text{C}$.

3.4. Selenomethionine Extraction

To characterize the content values of SeMet in the yeast powder and supplement using (HPLC-ICP-MS and ESI-HPLC-MS/MS), two different extraction methods were developed.

3.4.1. Extraction Method for the HPLC-ICP-MS Analysis

For the HPLC-ICP-MS analysis, 0.2 g of the sample was placed into a 15 mL polypropylene centrifuge tube. Subsequently, 15 mg of protease XIV in 2 mL of 0.1 M Tris-HCl buffer adjusted to a pH of 6.5 was added. The mixture was vortexed for 1 minute and shaken at 180 rpm for 20 h at $37 \text{ }^{\circ}\text{C}$, with vigorous shaking every 60 min. Following this, the mixture was centrifuged at 8000 rpm for 10 min and then filtered through a $0.22 \text{ }\mu\text{m}$ PES filter before the HPLC-ICP-MS/MS analysis.

3.4.2. Extraction Method for the ESI-HPLC-MS/MS Analysis

For the ESI-HPLC-MS/MS analysis, an enzymatic hydrolysis method assisted by ultrasound was employed to ensure the stability of SeMet. Therefore, 0.2 g of sample was introduced into a 15 mL polypropylene centrifuge tube. Subsequently, 20 mg of protease XIV was added to 2 mL of ultrapure water. The mixture underwent vortexing for 1 minute, followed by ultrasound treatment for 1 h in a $37 \text{ }^{\circ}\text{C}$ water bath, with vigorous shaking every 20 min. After this, the mixture underwent centrifugation at 8000 rpm for 10 min. The extracts were then filtered through a $0.22 \text{ }\mu\text{m}$ PES filter before the ESI-HPLC-MS/MS analysis. It is noteworthy that the Tris-HCl buffer was deliberately excluded from this method to prevent the potential contamination of the ESI.

3.5. Determination of SeMet by HPLC-ICP-MS

For the analysis of SeMet using HPLC-ICP-MS, the outlet of the HPLC column was directly connected to the MicroMist nebulizer of the ICP-MS/MS instrument (Agilent 8800, Tokyo, Japan) using a PEEK capillary tube. To guarantee precise measurements, the instrument operating conditions were optimized using a mixed solution containing Li, Y, Ce, Tl, and Co elements at a concentration of 1 ng g^{-1} .

The chromatographic separation of SeMet was conducted using an Agilent 1290 HPLC system (Santa Clara, CA, USA). A stationary phase consisting of an OSAKA SODA CAP-CELL PAK C_{18} column ($4.6 \times 250 \text{ mm}$, particle size = $5 \text{ }\mu\text{m}$) sourced from Chinese Taipei, China, was utilized. The guard column of the same stationary phase was positioned before

the separation columns. Before use, a column was preconditioned following the manufacturer's instructions. The pH value of the mobile phase in the HPLC was adjusted using a Mettler Toledo FiveEasy Plus pH meter (Zurich, Switzerland). Chromatographic data were collected, stored, and processed using the Agilent software MassHunter (version B.01.03). Even though no significant memory effect was detected, monitoring was conducted by periodically measuring a blank solution to ensure the absence of any memory effect or cross-contamination during the analysis. Table 3 summarizes the typical operating parameters of the ICP-MS system.

Table 3. Operating conditions of the HPLC-ICP-MS system.

ICP-MS
RF powder: 1550 W
Carrier gas: Ar 0.8 mL/min
Reaction gas: H ₂ , 4 mL/min
Isotope monitored: ⁷⁸ Se ⁺ , ⁸⁰ Se ⁺
Integration time: 0.1 s (spectrum) per point
Points per peak: 3
HPLC
Column: OSAKA SODA CAPCELL PAK C ₁₈ column
Dimensions: 250 × 4.6 mm, particle size: 5 μm
Mobile phase: 10 mmol/L sodium 1-butanefulfonic acid, 8 mmol/L tetramethylammonium hydroxide pentahydrate, 5 mmol/L malonic acid, and 5% MeOH; pH 4.0
Injection volume: 20 μL
Flow rate: 1.0 mL/min
Mode: isocratic

3.6. Determination of SeMet by ESI-HPLC-MS/MS

The chromatographic column employed for the ESI-HPLC-MS/MS system was a CAPCELL CORE C₁₈ column with the dimensions of 3.0 × 100 mm and a particle size of 2.7 μm, manufactured in Chinese Taipei. The mobile phase was operated in the isocratic mode, which consisted of 2 mmol L⁻¹ ammonium formate and 5% methanol. The flow rate was 0.25 mL min⁻¹. The column temperature was maintained at 30 °C, and a sample injection volume of 2 μL was used. The mass spectrometry analysis was carried out in the positive ion mode with a capillary voltage set at 1.0 kV and a temperature of 550 °C. The selected SeMet ions were monitored using the multiple reaction monitoring (MRM) mode, specifically at m/z 198.0 → 181.0 and 198.0 → 152.0 for SeMet (Figure 2a).

3.7. Homogeneity Test

To assess the homogeneity of the SeMet content in the yeast powder and supplement, 11 packets of the samples were randomly selected. Within each packet, two subsamples were subjected to analysis using the HPLC-ICP-MS method to determine the SeMet concentration. The obtained data were subjected to a one-way analysis of variance (ANOVA) at a 95% confidence level. The homogeneity of the property value of the yeast powder and supplement CRMs were evaluated using the *F*-test.

3.8. Stability Test

The stability outcomes of the SeMet content in the yeast powder and supplement were assessed by analyzing samples stored at −20 °C for 12 months and subjecting them to conditions simulating possible transportation (at 50 °C) for 0, 1, 2, and 5 days, respectively. For each specified time, three samples were chosen and analyzed using HPLC-ICP-MS. The significance of the observed slope (β_1) was tested using a *t*-test at a confidence level of 95%.

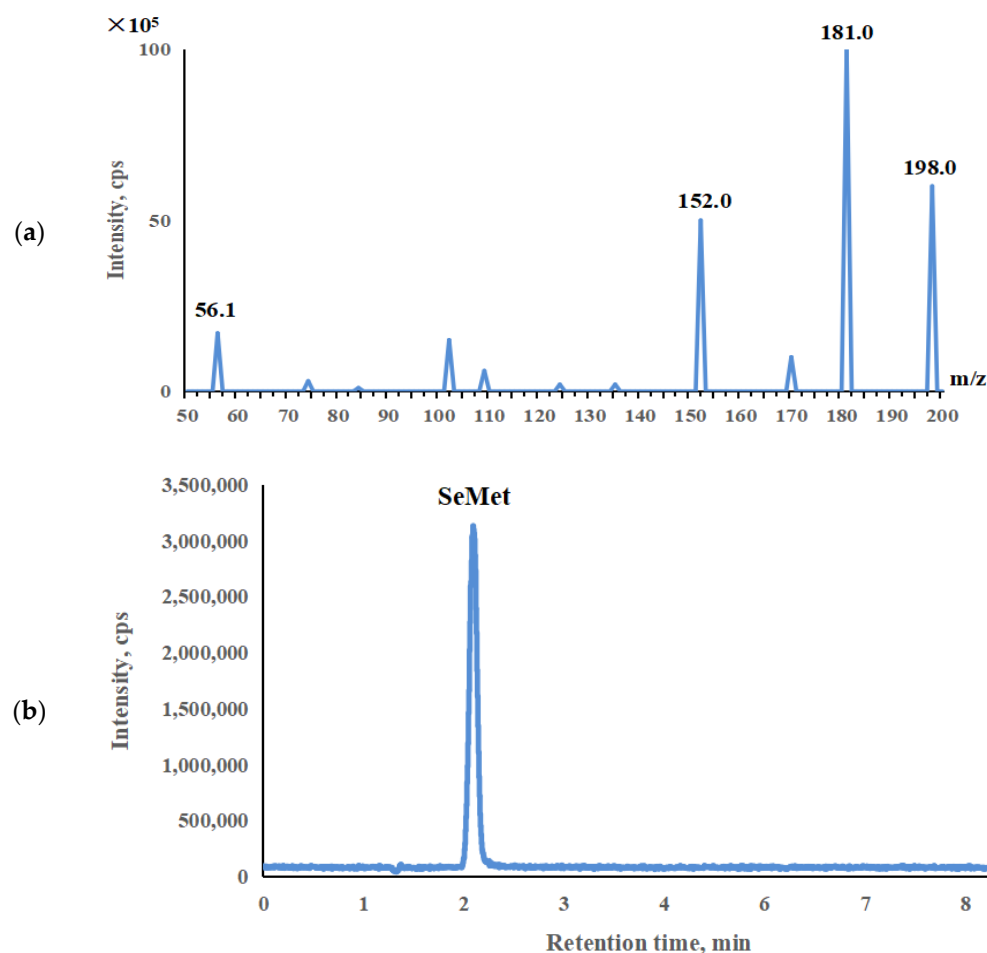


Figure 2. (a) MS/MS spectrum of SeMet; (b) ESI-HPLC-MS/MS for SeMet in the selenium-enriched yeast powder samples.

3.9. Value Assignment

According to ISO Guide 35, the value assignment for SeMet was conducted using two distinct analytical methods founded on different principles. For characterization purposes, 9 subsamples were extracted from 3 bottles and analyzed using both HPLC-ICP-MS and ESI-HPLC-MS/MS methods. The obtained measurement results were subjected to the Dixon's and Cochran's tests in accordance with the JFJ 1343–2022 General and Statistical Principles for the Characterization of Reference Materials.

4. Conclusions

In this paper, we successfully developed two novel certified reference materials for SeMet from selenium-enriched yeast powder and supplement. The investigation initially focused on optimizing and comparing various chromatographic conditions for HPLC-ICP-MS. Additionally, for ESI-HPLC-MS/MS, an innovative approach of rapid release of SeMet from the matrix was achieved by implementing an ultrasound-assisted enzymatic hydrolysis method, which ensured the stability of the target analyte while mitigating the potential contamination of the liquid chromatography-mass spectrometry ion source by the extraction solvent. Consequently, the accuracy of the CRMs' property values was ensured by the integration of both organic and inorganic mass spectrometry techniques in this study.

The certified values of SeMet in the yeast powder and supplement were $716 \text{ mg SeMet kg}^{-1}$ and $59 \text{ mg SeMet kg}^{-1}$, with expanded uncertainty outcomes of $36 \text{ mg SeMet kg}^{-1}$ ($k = 2$) and $5 \text{ mg SeMet kg}^{-1}$ ($k = 2$), respectively. These uncertainties revealed the state of the art of the measurement capabilities of SeMet in the matrices of the CRMs. Meanwhile, the results

indicate that the SeMet contents in our yeast powder and supplement CRMs are closely aligned with those found in real samples. Therefore, these CRMs will serve as important quality controls for the analysis of SeMet in a wide variety of Se nutritional supplements.

Author Contributions: Conceptualization, Methodology, Formal analysis, Data curation, Investigation, and Writing—original draft, X.L. (Xiao Li); Methodology and Data curation, L.S.; Writing—review and editing, P.S.; Methodology and Data curation, W.C.; Writing—review and editing, X.L. (Ximing Luo); Writing—review and editing B.Z. All authors have read and agreed to the published version of the manuscript.

Funding: This work was supported by the National Key R&D Program of China (2019YFC1604803) and the Fundamental Research Funds of National Institute of Metrology (AKYZZ2021).

Institutional Review Board Statement: Not applicable.

Informed Consent Statement: Not applicable.

Data Availability Statement: Data is contained within this article.

Conflicts of Interest: The authors declare no conflict of interest.

References

- Santi, C.; Santoro, S.; Battistelli, B. Organoselenium Compounds as Catalysts in Nature and Laboratory. *Curr. Org. Chem.* **2010**, *14*, 2442–2462. [CrossRef]
- Ruggeri, R.M.; D’Ascola, A.; Vicchio, T.M.; Campo, S.; Gianì, F.; Giovinazzo, S.; Frasca, F.; Cannavò, S.; Campenni, A.; Trimarchi, F. Selenium exerts protective effects against oxidative stress and cell damage in human thyrocytes and fibroblasts. *Endocrine* **2020**, *68*, 151–162. [CrossRef] [PubMed]
- Whanger, P.D. Metabolism of selenium in humans. *J. Trace Elem. Exp. Med.* **1998**, *11*, 227–240. [CrossRef]
- Zhang, K.; Guo, X.; Zhao, Q.; Han, Y.; Zhan, T.; Li, Y.; Tang, C.; Zhang, J. Development and application of a HPLC-ICP-MS method to determine selenium speciation in muscle of pigs treated with different selenium supplements. *Food Chem.* **2020**, *302*, 125371. [CrossRef] [PubMed]
- Faye, B.; Saleh, S.K.; Konuspayeva, G.; Musaad, A.; Bengoumi, M.; Seboussi, R. Comparative effect of organic and inorganic selenium supplementation on selenium status in camel. *J. King Saud Univ.-Sci.* **2014**, *26*, 149–158. [CrossRef]
- de Paiva, E.L.; Ruttens, A.; Waegeneers, N.; Laing, G.D.; Morgano, M.A.; Cheyns, K.; Ariseto-Bragotto, A.P. Selenium in selected samples of infant formulas and milk commercialized in Belgium and Brazil: Total content, speciation and estimated intake. *Food Res. Int.* **2023**, *164*, 112289. [CrossRef]
- Bodnar, M.; Konieczka, P. Evaluation of candidate reference material obtained from selenium-enriched sprouts for the purpose of selenium speciation analysis. *LWT* **2016**, *70*, 286–295. [CrossRef]
- Chen, N.; Zhao, C.; Zhang, T. Selenium transformation and selenium-rich foods. *Food Biosci.* **2021**, *40*, 100875. [CrossRef]
- Ali, W.; Mao, K.; Zhang, H.; Junaid, M.; Xu, N.; Rasool, A.; Feng, X.; Yang, Z. Comprehensive review of the basic chemical behaviours, sources, processes, and endpoints of trace element contamination in paddy soil-rice systems in rice-growing countries. *J. Hazard. Mater.* **2020**, *397*, 122720. [CrossRef]
- He, X.; Huangfu, K.; Zhao, J.; Lei, H.; Li, X.; Liu, W.; Gu, X. An efficient and low-cost method for the determination of selenium in selenium-enriched tea by high-performance liquid chromatography coupled with 3,3’-Diaminobenzidine derivatization. *Talanta* **2024**, *268*, 125335. [CrossRef]
- Guo, Y.; Luo, Y.; Wang, N.; Tang, M.; Xiao, J.; Chen, S.W.; Wang, J. Au nanoparticle-based probe for selenol in living cells and selenium-rich tea and rice. *Talanta* **2020**, *212*, 120583. [CrossRef] [PubMed]
- Sohrabi, M.; Mehrjerdi, M.Z.; Karimi, S.; Tavallali, V. Using gypsum and selenium foliar application for mineral biofortification and improving the bioactive compounds of garlic ecotypes. *Ind. Crop. Prod.* **2020**, *154*, 112742. [CrossRef]
- Kieliszek, M.; Serrano Sandoval, S.N. The importance of selenium in food enrichment processes. A comprehensive review. *J. Trace Elem. Med. Biol.* **2023**, *79*, 127260. [CrossRef] [PubMed]
- Pilarczyk, B.; Tomza-Marciniak, A.; Pilarczyk, R.; Kuba, J.; Hendzel, D.; Udała, J.; Tarasewicz, Z. Eggs as a source of selenium in the human diet. *J. Food Compos. Anal.* **2019**, *78*, 19–23. [CrossRef]
- Zhao, Y.; Tu, T.; Tang, X.; Zhao, S.; Qie, M.; Chen, A.; Yang, S. Authentication of organic pork and identification of geographical origins of pork in four regions of China by combined analysis of stable isotopes and multi-elements. *Meat Sci.* **2020**, *165*, 108129. [CrossRef] [PubMed]
- Gu, Y.; Qiu, Y.; Wei, X.; Li, Z.; Hu, Z.; Gu, Y.; Zhao, Y.; Wang, Y.; Yue, T.; Yuan, Y. Characterization of selenium-containing polysaccharides isolated from selenium-enriched tea and its bioactivities. *Food Chem.* **2020**, *316*, 126371. [CrossRef]
- Kieliszek, M.; Błażej, S.; Kurek, E. Binding and Conversion of Selenium in *Candida utilis* ATCC 9950 Yeasts in Bioreactor Culture. *Molecules* **2017**, *22*, 352. [CrossRef] [PubMed]

18. Hadrup, N.; Ravn-Haren, G. Toxicity of repeated oral intake of organic selenium, inorganic selenium, and selenium nanoparticles: A review. *J. Trace Elem. Med. Biol.* **2023**, *79*, 127235. [CrossRef]
19. Güler, N.; Maden, M.; Bakırdere, S.; Yavuz Ataman, O.; Volkan, M. Speciation of selenium in vitamin tablets using spectrofluorometry following cloud point extraction. *Food Chem.* **2011**, *129*, 1793–1799. [CrossRef]
20. Malvestio, C.; Onor, M.; Bramanti, E.; Pagliano, E.; Campanella, B. Determination of methionine and selenomethionine in food matrices by gas chromatography mass spectrometry after aqueous derivatization with triethyloxonium salts. *Food Chem.* **2024**, *433*, 137341. [CrossRef]
21. Kápolna, E.; Shah, M.; Caruso, J.A.; Fodor, P. Selenium speciation studies in Se-enriched chives (*Allium schoenoprasum*) by HPLC-ICP-MS. *Food Chem.* **2007**, *101*, 1398–1406. [CrossRef]
22. Yan, L.; Deng, B.; Shen, C.; Long, C.; Deng, Q.; Tao, C. Selenium speciation using capillary electrophoresis coupled with modified electrothermal atomic absorption spectrometry after selective extraction with 5-sulfosalicylic acid functionalized magnetic nanoparticles. *J. Chromatogr. A* **2015**, *1395*, 173–179. [CrossRef] [PubMed]
23. Chen, Y.W.; Belzile, N. High performance liquid chromatography coupled to atomic fluorescence spectrometry for the speciation of the hydride and chemical vapour-forming elements As, Se, Sb and Hg: A critical review. *Anal. Chim. Acta* **2010**, *671*, 9–26. [CrossRef] [PubMed]
24. Aoyama, C.; Tsunoda, M.; Funatsu, T. Determination of selenomethionine by high-performance liquid chromatography-fluorescence detection coupled with on-line oxidation. *Anal. Sci.* **2009**, *25*, 63–65. [CrossRef]
25. Rastogi, L.; Prasad, A.D.; Sai Krishna, D.; Yadlapalli, S.; Dash, K. Certified reference material (CRM) of tea powder (BARC-D3201) for K, Ca, P, Mg, Mn, Al, Fe, Ba, Zn, Cu, Sr, Pb, As, Cd, and Hg: Method validation and its production. *Food Control* **2024**, *158*, 110241. [CrossRef]
26. Ma, Q.; Zhang, Q.; Li, X.; Gao, Y.; Wei, C.; Li, H.; Jiao, H. The compound-independent calibration of five selenium species in rice using ion-pairing reversed phase chromatography coupled to inductively coupled plasma tandem mass spectrometry. *J. Chromatogr. A* **2022**, *1674*, 463134. [CrossRef]
27. Sun, L.; Liu, G.; Xu, D.; Wu, Z.; Ma, L.; Victoria, S.-F.M.; Baumgard, L.H.; Bu, D. Milk selenium content and speciation in response to supranutritional selenium yeast supplementation in cows. *Anim. Nutr.* **2021**, *7*, 1087–1094. [CrossRef]

Disclaimer/Publisher's Note: The statements, opinions and data contained in all publications are solely those of the individual author(s) and contributor(s) and not of MDPI and/or the editor(s). MDPI and/or the editor(s) disclaim responsibility for any injury to people or property resulting from any ideas, methods, instructions or products referred to in the content.

Article

Residue Levels and Dietary Intake Risk Assessments of 139 Pesticides in Agricultural Produce Using the m-PFC Method Based on SBA-15-C₁₈ with GC-MS/MS

Yue Wang ^{1,2,†}, Tingjie Huang ^{2,†}, Tao Zhang ^{2,†}, Xiaoping Ma ², Guangshuo Zhou ², Meiyao Chi ², Xinjie Geng ², Chunhao Yuan ^{1,*} and Nan Zou ^{2,*}

¹ School of Chemistry and Pharmaceutical Engineering, Shandong First Medical University, Shandong Academy of Medical Sciences, Tai'an 271016, China

² Key Laboratory of Pesticide Toxicology & Application Technique, College of Plant Protection, Shandong Agricultural University, Tai'an 271018, China

* Correspondence: yuanchunhao2017@163.com (C.Y.); zounan1226@163.com (N.Z.); Tel.: +86-0538-824-2611 (N.Z.)

† These authors contributed equally to this work.

Abstract: A survey was designed to investigate the pesticide residues in agricultural produce and to estimate their potential intake risks to inhabitants. A total of 314 samples of nine types of fruits and vegetables were collected from the supermarkets and vegetable markets of Shandong Province (China) from October 2020 to February 2022. An accurate and reliable multi-residue method, based on GC-MS/MS detection, as well as the multiplug filtration cleanup method, based on SBA-15-C₁₈, was prepared by a solution chemical reaction. Additionally, an in situ co-condensation method was established for the quantification of 139 pesticide residues. Residues that contained no pesticides were detected in 66.5% of the 314 samples. Moreover, of the samples, 30.6% were at or below the MRLs, and 2.9% were above the MRLs. Residues of procymidone were found to be the one that most often exceeded the MRLs (1.3% of the samples). Tebuconazole was found most frequently in 22.0% of the samples analyzed. Consumer exposure to the 139 pesticides did not exceed 100% ADI and ARfD. This led to a consideration that these pesticide residues in the nine commodities may not raise the health risk of the consumers in the long and short term. The highest value of chronic dietary intake was obtained from spirodiclofen, which resulted in a 24.1% of ADI. Furthermore, the highest exposure levels in the short term were obtained from the consumption of leeks with procymidone (58.3% ARfD).

Keywords: multiplug filtration cleanup; SBA-15-C₁₈; pesticide residue; dietary risk assessment



Citation: Wang, Y.; Huang, T.; Zhang, T.; Ma, X.; Zhou, G.; Chi, M.; Geng, X.; Yuan, C.; Zou, N. Residue Levels and Dietary Intake Risk Assessments of 139 Pesticides in Agricultural Produce Using the m-PFC Method Based on SBA-15-C₁₈ with GC-MS/MS. *Molecules* **2023**, *28*, 2480. <https://doi.org/10.3390/molecules28062480>

Academic Editor: James Barker

Received: 6 February 2023

Revised: 2 March 2023

Accepted: 3 March 2023

Published: 8 March 2023



Copyright: © 2023 by the authors. Licensee MDPI, Basel, Switzerland. This article is an open access article distributed under the terms and conditions of the Creative Commons Attribution (CC BY) license (<https://creativecommons.org/licenses/by/4.0/>).

1. Introduction

Pesticides are widely used in fields during crop production to control diseases, pests, and weeds to ensure yields and the quality of agricultural crops. Despite the obvious benefits of the use of pesticides, there has been a growing concern about pesticide residues in the environment and to food [1]. In addition, the increased use of chemical pesticides has caused many associated short-term or long-term effects on human health [2]. Pesticides have been associated with a range of human health problems, ranging from acute effects, such as headaches and nausea, to chronic impacts, such as cancer, reproductive harm, and endocrine disruption [3].

Fruits and vegetables have received an increasing amount of attention in monitoring programs since most of them are eaten raw. Further, they may contain higher pesticide residue levels compared to other food groups [4–6]. Moreover, the human intake of toxic substances due to pesticide residues in food may be much higher than the intake of these substances through the acts of drinking water and inhaling air [7]. Therefore, it is very

important to monitor pesticide residues in fruits and vegetables, as well as to assess whether they pose a risk to human health [8]. Many countries have set up pesticide residue monitoring systems and there have been a number of reports on the pesticide residues detected in crops [9,10], fruits [11,12], vegetables [11,13,14], medicinal plants [15], milk, [16] and fish [17]. The monitoring has focused on the rational use of pesticides in areas of authorization and registration (pesticide application and harvest intervals), as well as in compliance with maximum residue limits (MRLs). Intake risk assessments of pesticide residue were also recorded in many countries and regions [8,11,15,17]. Shandong Province is the largest vegetable planting province and vegetable export province in China. The Shouguang Vegetable Wholesale Market in Shandong Province supplies vegetables to more than 20 provinces [18]. A case study in Anqiu City estimated that more than 50% of the vegetables produced were exported, 30% were sold to the domestic market, and 20% were sold to the local market [19]. Therefore, the monitoring and risk assessment of pesticide residues within the typical fruits and vegetables in Shandong Province is of great significance.

Multi-walled carbon nanotubes (MWCNTs) are interesting carbonaceous materials with an ultra-high specific surface area. They have been applied, in the pesticide multi-residue analysis that was conducted in our previous work, as effective cleanup sorbents for the removal of fatty acids, pigments, and other impurities of medium and high polarity [20–22]. The mesoporous material SBA-15 and its derivatives are characterized by high adsorption versatility, strong adsorption stability, and large adsorption capacity. They are widely used to separate and remove organic pollutants and heavy metals in food and environments [23–25]. In this study, SBA-15- C_{18} was prepared by introducing C_{18} groups into the active site of SBA-15, which exhibited better adsorption properties for non-polar and weakly polar compounds compared to SBA-15 [26,27]. SBA-15- C_{18} showed the characteristics of a high specific surface area, high pore volume, and uniform pore distribution, as well as had higher recovery values than were found in commercial C_{18} amorphous silica [28]. Our research group has developed a fast, simple, and effective purification process called the multi-plug filtration cleaning method (m-PFC), which has been widely used in the detection of pesticide residues in agricultural products [21,22,29]. Through the use of m-PFC, the adsorbent mixture was fixed by two layers of sieve plates and was then filled into the syringe tube. The m-PFC process uses a streamlined filtration process with a very fast purification rate of just a few seconds, eliminating the need for whirlpool, centrifugation, and solvent evaporation steps.

The aim of the present study is to develop an m-PFC method based on MWCNTs and SBA-15- C_{18} with GC-MS/MS for the multi-residue analysis of 139 pesticides. Furthermore, in this study, the presence of the selected pesticides that are commonly used on 9 agricultural products is investigated; further, their compliance with the current maximum limit standards are also assessed. Combined with the results of monitoring projects and food consumption data, the dietary intake risk of pesticide residues in agricultural consumption was assessed in order to establish practical guidelines for monitoring the use of pesticides in the agricultural industry. The results can be used to design future control precepts in the region and to take preventive measures to minimize risks to human health.

2. Results and Discussion

2.1. Characterization of SBA-15- C_{18}

The FTIR spectra (Figure 1B,C) of the synthesized SBA-15- C_{18} and C_{18} showed stretching vibration at 2926 and 2855 cm^{-1} . This was also the stretching vibration of CH_2 in the C_{18} group, indicating that the C_{18} group was successfully introduced and that SBA-15- C_{18} was successfully synthesized. The SEM figures (Figure 1D,E) showed that SBA-15- C_{18} had two-dimensional through pore and regular pore structures, and the particle sizes were uniform, cylindrical, and curved with an average particle size between 240 and 340 nm.

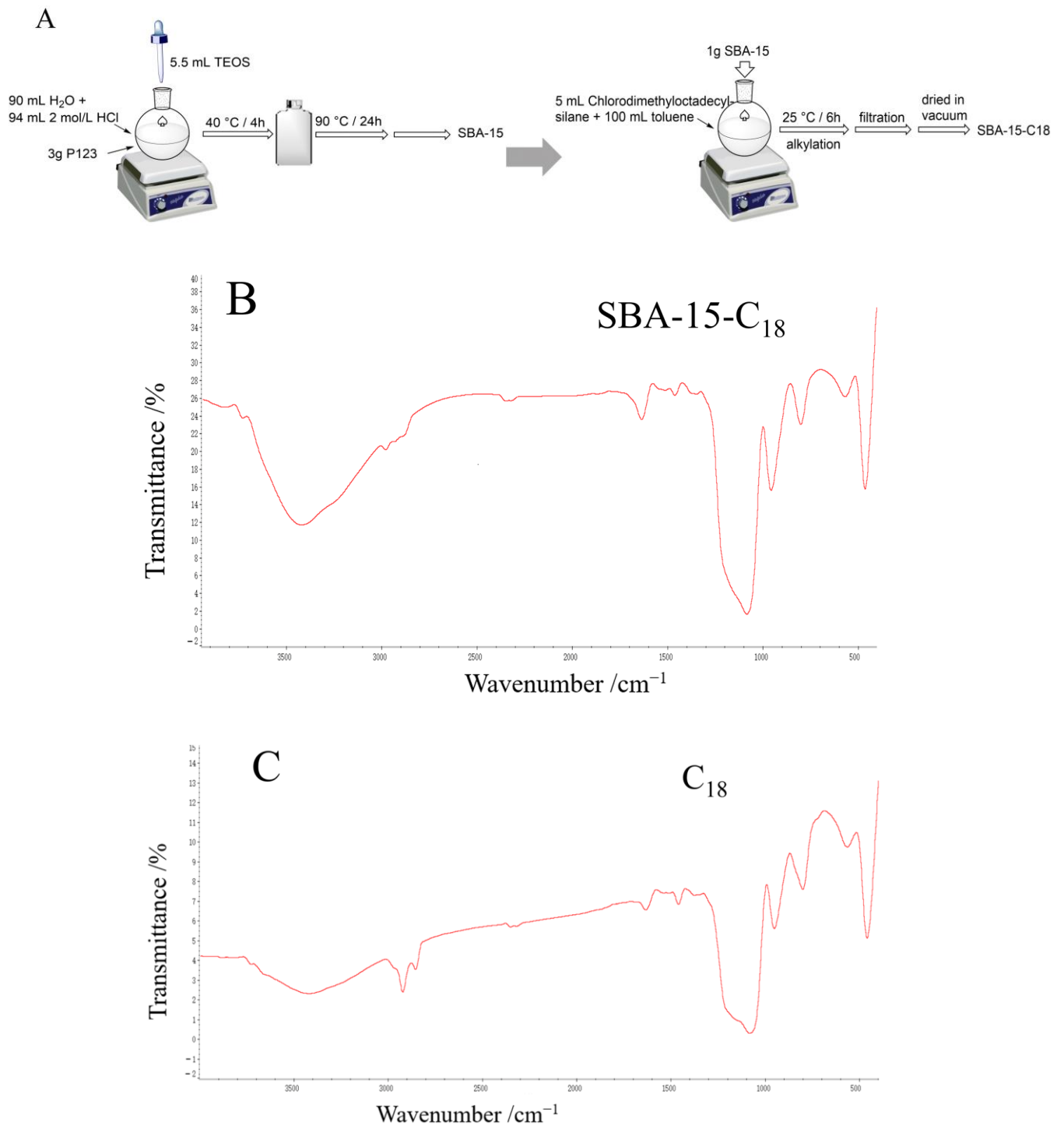
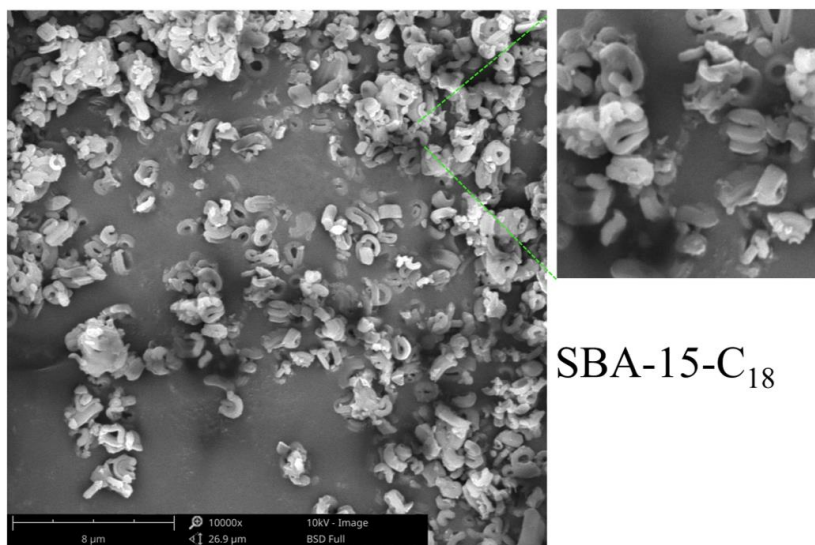
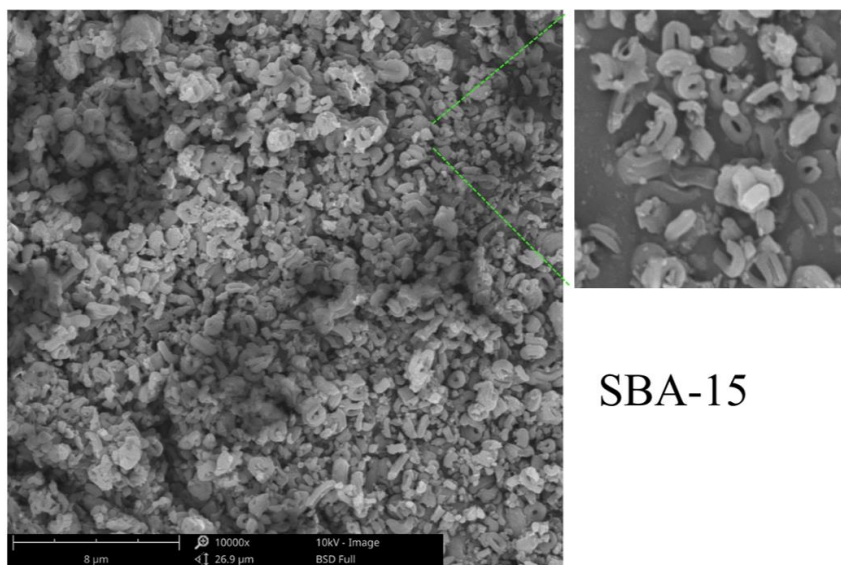


Figure 1. Cont.

D

SBA-15-C₁₈

E



SBA-15

Figure 1. Synthesis and characterization of SBA-15-C₁₈ and SBA-15. Synthesis diagram of SBA-15-C₁₈ and SBA-15 (A). FTIR spectra of synthesized SBA-15-C₁₈ (B) and C₁₈ (C), as well as the SEM images of synthesized SBA-15-C₁₈ (D) and SBA-15 (E).

2.2. Determination of Pesticide Residues

The mixtures of MWCNTs, PSA, and C₁₈ have been shown to have excellent ability in selectively removing interfering substances from the acetonitrile extracts of the troublesome leek matrices [22]. SBA-15-C₁₈ could achieve a better purification effect with less dosage compared with C₁₈. For example, for leek samples, the purification materials in the published literature were 8 mg MWCNTs, 10 mg PSA, 10 mg C₁₈, and 150 mg MgSO₄ [22], which were 8 mg of MWCNTs+, 10 mg of PSA+, 8 mg of SBA-15-C₁₈+, and 150 mg of MgSO₄ in this study. For the other matrices, the purification effect of the different combinations and proportions of purification materials was conducted on the spiked extracts. The final sorbent combination and proportion for the different matrices were as per the following: 5 mg of MWCNTs, 5 mg of SBA-15-C₁₈, and 150 mg of MgSO₄ for the

watermelon, melon, asparagus, lotus root, strawberry, and cucumber samples; 8 mg of MWCNTs, 10 mg of PSA, 8 mg of SBA-15-C₁₈, and 150 mg of MgSO₄ for the leek samples; and 8 mg of MWCNTs, 5 mg of SBA-15-C₁₈, and 150 mg of MgSO₄ for the crown daisy and leaf lettuce samples.

Matrix-matched standard calibrations for each matrix were used for the more accurate results in order to avoid the matrix effect. The standard curves of all pesticides were in the range of 10–500 µg L⁻¹ by the calculation of a five-point plot (10, 50, 100, 200, and 500 µg L⁻¹), and a good regression correlation ($R^2 > 0.99$) was achieved for all pesticides (the relevant results of the correlation equation and R^2 are presented in Table S1 (Supplementary Materials) with leek samples taken as an example). The LOQs of the proposed method were determined by the lowest accepted fortification level, which was analyzed by the Xcalibur Data System. The LOQs ranged from 1 to 10 µg kg⁻¹, and the LOQs of each compound were detailed in Table S2. Average recoveries were conducted at one fortification level (10 µg kg⁻¹) for all the pesticides in the nine types of fruits and vegetables, and were in the range from 71.1 to 120.6% with the relative standard deviations below 16.5% (Tables S3 and S4). Therefore, through the validation results of accuracy, precision, and sensitivity, the method met the requirements for the detection of multiple pesticide residues in the nine kinds of agricultural products.

2.3. Pesticide Residues in Samples

2.3.1. Evaluation by Samples

The overview of the data obtained after the analysis of the 314 samples is shown in Figure 2. A total of 209 samples (66.5%) showed that no pesticide residues were detected. A total of 96 (30.6%) analyzed samples contained pesticide residues at or below the MRLs of China (GB 2763-2021). In addition, 9 samples (2.9%) contained pesticide residues above the MRLs. The order of percentages of pesticides above the MRLs was as follows: leek (7.1%) > leaf lettuce (5.6%) > cucumber (4.8%) > strawberry (3.1%) > melon (2.9%). No pesticide residues in the watermelon and leaf lettuce products exceeded the MRLs.

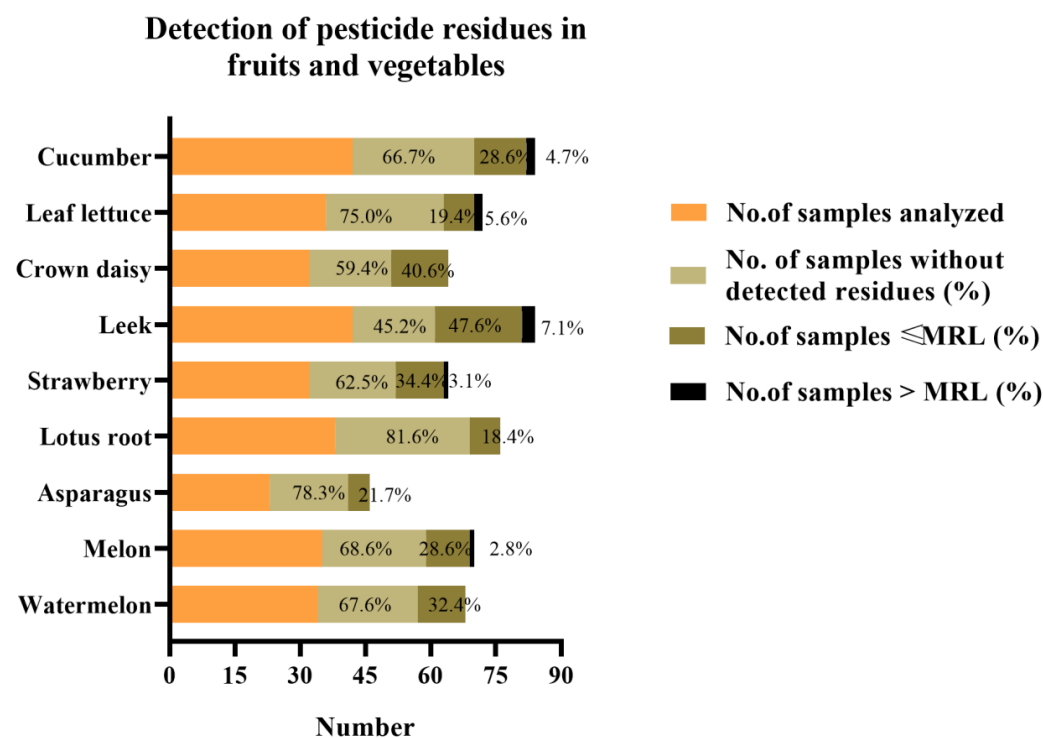


Figure 2. Frequency of samples with and without detected pesticide residues, as well as the samples containing residues above the MRLs for fruits and vegetables.

2.3.2. Evaluation by Pesticides

In this monitoring program, 4 pesticide residues were found to exceed MRLs in 9 samples, which were triadimenol in 1 melon sample and 1 cucumber sample; procymidone in 3 leek samples and 1 cucumber sample; chlorpyrifos in 1 leaf lettuce sample; and cypermethrin in 1 strawberry sample and 1 cucumber sample. The residues of procymidone were found to be the ones most often exceeding the Chinese MRLs (1.3% of the samples). Table 1 shows the specific detected amounts of several pesticides exceeding the MRL. The order of percentage of pesticides exceeding the MRLs was as follows: procymidone (1.3%) > cypermethrin (0.6%) = triadimenol (0.6%) > chlorpyrifos (0.3%). The mean levels of residues and concentration ranges of 139 pesticide in 9 agricultural products are presented in Table S3. Procymidone is a fungicide used as a seed dressing, pre-harvest spray, or post-harvest dip for the control of various fungal diseases, and it is likely to be commonly used in many countries.

Table 1. The standards and samples that exceed MRLs.

Samples	Triadimenol	Procymidone	Chlorpyrifos	Cypermethrin
	MRL/Detected Quantity (mg/kg)	MRL/Detected Quantity (mg/kg)	MRL/Detected Quantity (mg/kg)	MRL/Detected Quantity (mg/kg)
Melon	0.2/0.320	-	-	-
Strawberry	-	-	-	0.07/0.340
Leek1	-	0.2/11.270	-	-
Leek 2	-	0.2/10.560	-	-
Leek 3	-	0.2/5.430	-	-
Leaf lettuce 1	-	-	0.02/0.933	-
Leaf lettuce 2	-	-	-	2/2.344
Cucumber 1	-	2/2.334	-	-
Cucumber 2	0.2/0.510	-	-	-

Residues were found most frequently of tebuconazole (22.0%), followed by procymidone (20.4%), chlorpyrifos (18.5%), boscalid (17.2%), triadimenol (16.2%), pyriproxyfen (11.5%), butachlor (9.9%), cyfluthrin (9.2%), fenpropathrin (8.6%), etc. Tebuconazole was detected in the concentration range of lower than the detection limit (DL) to 1.599 mg kg⁻¹, most were from the leek and crown daisy samples. As the pesticide with the highest detection rate, tebuconazole is an efficient and broad-spectrum triazole bactericide with a good internal absorption. This pesticide has good efficacy and wide application range in China, so the detection frequency is relatively high, but it does not exceed the limit standard [30].

The detected 139 pesticides obtained for the mean, maximum, and minimum values (mg kg⁻¹) are listed in Table S3. The mean concentrations of pesticides in the total samples were the highest for chlorfenapyr (2.853 mg kg⁻¹). The maximum concentrations of pesticides found in the total samples were the highest for procymidone (11.27 mg kg⁻¹). In this study, the procymidone in the three leek samples exceeded the MRL. In fact, the phenomenon of procymidone exceeding the MRL in leek often occurs [31,32]. This is related to the application method of procymidone with a smoke generator that is commonly used in China. The MRL of procymidone in Chinese leeks is 0.2 mg/kg, which refers to the standard of CAC. According to the actual production in China, the residue of procymidone in leeks is seriously excessive, resulting in procymidone not being registered in leeks. To solve the problem, relevant departments of the Ministry of Agriculture of China have started to revise the standards.

2.3.3. The Results of Multiple Pesticide Residues

Figure 3 shows the commodities that presented multiple residues. The residues of two or more pesticides were found in 87 (75.2%) of the positive samples. Cucumber was the agricultural product with the highest number of samples with multiple residues (85.7%

of the positive cucumber samples), followed by leek (83.3%), and then by watermelon (81.8%). With the exception of asparagus and lotus root, all samples had mainly two or three residues present. Two leek samples had six residues, one had eight residues, and one strawberry sample had seven different residues.

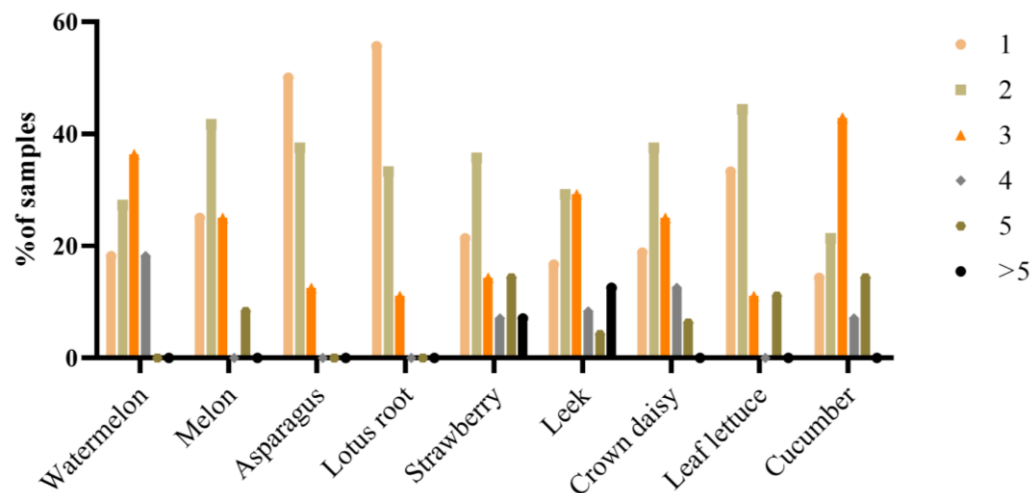


Figure 3. Commodities with multiple pesticide residues in the samples analyzed.

2.4. Risk Assessment of the Long-Term Intake and Chronic Exposure

The chronic intake risk was evaluated by Equation (1). The chronic intake risk assessment of the monitored agricultural product was based on the reported calculations, which are presented in Table 2. The chronic intakes of all the selected pesticide residues considered were rather low compared to the ADI, indicating that the pesticide residues in the agricultural products were within the acceptable range. The highest value of chronic exposure was obtained from spirodiclofen, which resulted in 24.1% of the ADI. Consequently, the safety of the Shandong Province consumer generally seems to be under control in terms of the pesticides that are consumed through the long-term consumption of the monitored fruits and vegetables.

Table 2. Results of the long-term intake and chronic exposure of pesticide residues.

Pesticide	ADI (mg/kg·bw·d)	Long-Term Risk		Pesticide	ADI (mg/kg·bw·d)	Long-Term Risk	
		IEDI (µg/kg·bw·d)	ADI%			IEDI (µg/kg·bw·d)	ADI%
Acetochlor	0.02	0.30	1.5	Flusilazole	0.007	0.00	0.0
Alachlor	0.01	0.01	0.1	Flutolanil	0.09	0.00	0.0
Ametryn	0.072	0.00	0.0	Kresoxim-methyl	0.4	0.02	0.0
Anilofos	0.001	0.02	2.2	Mefenacet	0.007	0.01	0.2
Atrazine	0.02	0.30	1.5	Mepronil	0.05	0.00	0.0
Azoxystrobin	0.2	0.01	0.0	Methidathion	0.001	0.00	0.0
Cypermethrin	0.02	0.32	1.6	Myclobutanil	0.03	0.01	0.0
Bifenthrin	0.01	0.01	0.1	DDT	0.01	0.01	0.1
Boscalid	0.04	0.00	0.0	Oxyfluorfen	0.03	0.14	0.5
Bromoxynil	0.01	0.00	0.0	Parathion	0.004	0.00	0.0
Butachlor	0.1	0.03	0.0	Pendimethalin	0.03	0.01	0.0
Butralin	0.2	0.00	0.0	Phenthoate	0.003	0.01	0.3
Chlorfenapyr	0.03	0.04	0.1	Pirimicarb	0.02	0.00	0.0
Chlorpropham	0.05	0.00	0.0	Probenazole	0.07	0.01	0.0
Chlorpyrifos	0.01	0.04	0.4	Procymidone	0.1	0.11	0.1
Clodinafop-propargyl	0.0003	0.17	5.5	Profenofos	0.03	0.09	0.3
Cyfluthrin	0.04	0.23	0.6	Prometryn	0.04	0.03	0.1
Cyhalothrin	0.02	0.07	0.3	Propachlor	0.54	0.29	0.1

Table 2. Cont.

Pesticide	ADI (mg/kg·bw·d)	Long-Term Risk		Pesticide	ADI (mg/kg·bw·d)	Long-Term Risk	
		IEDI (µg/kg·bw·d)	ADI%			IEDI (µg/kg·bw·d)	ADI%
Cyprodinil	0.03	0.00	0.0	Propargite	0.01	0.00	0.0
Deltamethrin	0.01	0.04	0.4	Propiconazole	0.07	0.02	0.0
Diclofop-methyl	0.0023	0.00	0.1	Diethofencarb	0.004	0.01	0.2
Difenzoquat	0.25	0.03	0.1	Pyriproxyfen	0.1	0.02	0.0
Endosulfan	0.006	0.04	0.6	Quinalphos	0.0005	0.01	1.4
Endrin	0.0002	0.02	9.5	Quizalofop	0.0009	0.01	0.6
Famoxadone	0.006	0.00	0.0	Spirodicofen	0.01	2.42	24.2
Fenarimol	0.01	0.01	0.1	Tebuconazole	0.03	0.07	0.2
Fenbuconazole	0.03	0.01	0.0	Terbufos	0.0006	0.00	0.0
Fenobucarb	0.06	0.23	0.4	Tolfenpyrad	0.006	0.00	0.0
Fenpropathrin	0.03	0.03	0.1	Triadimefon	0.03	0.03	0.1
Fipronil	0.0002	0.00	0.0	Triadimenol	0.03	0.10	0.3
Fenthion	0.007	0.00	0.0	Triallate	0.025	0.02	0.1
Fluazifop-P-butyl	0.004	0.17	2.3	Trifloxystrobin	0.04	0.02	0.0
Fluroxypyr	1	0.03	0.0	Trifluralin	0.025	0.03	0.1

2.5. Risk Assessment of the Short-Term Intake and Acute Exposure

The results for the short-term exposure risk assessment regarding the intake of the monitored fruits and vegetables were calculated, as shown in Table 3. The consumer acute exposure to pesticides does not exceed the value of 100% ARfD. The highest values of short-term exposure were obtained in the case of the consumption of leeks with procymidone (58.3% ARfD), followed by leeks with chlorfenapyr (49.2% ARfD), and then leaf lettuce with procymidone (46.8% ARfD). In the remaining cases, the ARfD% values from the other pesticides were between 0.0 and 21.2%, indicating that the acute exposure risk is within an acceptable range. The residue level could not be considered a serious public health problem in the short-term exposure. The only noted possible risk was connected with procymidone residues in the leek and leaf lettuce.

Table 3. Results of the short-term intake and acute exposure of pesticide residues.

Pesticide	ARfD (mg/kg·bw·d)	Commodity	Short-Term Risk		Pesticide	ARfD (mg/kg·bw·d)	Commodity	Short-Term Risk	
			UESTI (µg/kg·bw·d)	ARfD%				UESTI (µg/kg·bw·d)	ARfD%
Atrazine	0.1	Melon	0.37	0.4	Fenpropathrin	0.03	Leaf lettuce	0.44	1.5
		Watermelon	0.49	0.5			Melon	0.25	0.8
		Asparagus	0.07	0.1			Leek	0.04	0.4
Cypermethrin	0.04	Strawberry	0.32	0.8	Flusilazole	0.02	Asparagus	0.05	0.5
		Leek	0.62	1.6			Melon	0.55	2.8
		Melon	5.23	13.1			Leaf lettuce	0.15	1.5
		Cucumber	1.04	2.6			Strawberry	8.57	2.9
		Leaf lettuce	0.53	1.3			Cucumber	0.30	0.1
Bifenthrin	0.01	Melon	1.22	12.2	Myclobutanil	0.3	Leaf lettuce	0.90	0.3
		Leaf lettuce	1.21	12.1			Asparagus	0.04	0.0
		Asparagus	0.19	1.9			Strawberry	2.90	2.9
Chlorfenapyr	0.03	Leek	14.76	49.2	Procymidone	0.1	Leek	58.30	58.3
		Asparagus	0.05	0.0			Melon	13.56	13.6
Chlorpropham	0.5	Strawberry	0.37	0.4	Profenofos	1	Cucumber	2.67	2.7
		Leek	1.60	1.6			Watermelon	4.34	4.3
Chlorpyrifos	0.1	Melon	8.09	8.1	Cyhalothrin	0.02	Leaf lettuce	46.81	46.8
		Cucumber	0.45	0.5			Asparagus	0.08	0.1
		Leaf lettuce	0.17	0.2			Strawberry	5.24	0.5
		Asparagus	5.89	5.9			Cucumber	2.32	5.8
		Strawberry	0.32	0.8			Leaf lettuce	0.55	1.4
		Leek	0.59	1.5			Strawberry	0.17	0.9
		Melon	1.65	4.1			Leek	0.08	0.4
		Melon	0.40	2.0			Watermelon	10.20	1.0
Leaf lettuce	0.32	1.6	Propiconazole	0.3	Leaf lettuce	0.83	0.3		

Table 3. Cont.

Pesticide	ARfD (mg/kg·bw·d)	Commodity	Short-Term Risk		Pesticide	ARfD (mg/kg·bw·d)	Commodity	Short-Term Risk	
			IESTI ($\mu\text{g}/\text{kg}\cdot\text{bw}\cdot\text{d}$)	ARfD%				IESTI ($\mu\text{g}/\text{kg}\cdot\text{bw}\cdot\text{d}$)	ARfD%
Deltamethrin	0.05	Strawberry	0.16	0.3	Tebuconazole	0.3	Strawberry	2.21	0.7
		Leek	0.09	0.2			Melon	0.88	0.3
		Melon	0.37	0.7			Cucumber	0.20	0.1
Endosulfan	0.02	Leaf lettuce	0.22	0.4	Watermelon		Watermelon	1.19	0.4
		Strawberry	3.80	19.0			Leaf lettuce	2.81	0.9
		Leek	0.06	0.3			Asparagus	10.11	3.4
		Melon	0.67	3.4	Tolfenpyrad	0.01	Cucumber	0.07	0.7
		Cucumber	1.47	7.4			Strawberry	0.08	0.1
Famoxadone buconazole	0.6 0.2	Leaf lettuce	0.85	4.3	Triadimefon	0.08	Leaf lettuce	0.08	0.1
		Leaf lettuce	0.50	0.1	Triadimenol	0.08	Leaf lettuce	0.44	0.6
Cucumber	0.34	0.2	Melon	9.83			12.3		
Watermelon	0.60	0.3	Watermelon	16.96			21.2		
		Melon	3.57	0.4					

3. Materials and Methods

3.1. Standards, Reagents and Materials

The pesticide standards, with a purity of 95~99%, used in this work (Table S4) were provided by the Institute of the Control of Agrochemicals, Ministry of Agriculture (Beijing, China). The working standard mixture containing 10 mg L⁻¹ of each pesticide was formulated with acetone and stored at -20 °C. The PSA and C₁₈ were purchased from Tianjin Bonna-Agela Technologies Co., Ltd. (Tianjin, China). The MWCNTs, with average diameters of 5–10 nm, were purchased from the National Center for Nanoscience and Technology. The P123, TEOS, and octadecyldimethylchlorosilane were purchased from Sinopharm Chemical Reagent Co., Ltd., (Shanghai, China). The HPLC grade acetonitrile and acetone were obtained from Fisher Chemicals (Fair Lawn, NJ, USA). The NaCl and MgSO₄ were purchased from Sinopharm Chemical Reagent (Beijing, China).

3.2. Sample Collection

A total of 314 agricultural product samples were collected from October 2020 to February 2022. The samples were collected from randomly selected supermarkets, markets, and vegetable bases from each of the 10 cities of Shandong province. All samples were obtained from local production, and the specific information of samples are shown in Table S5. The sampling was carried out with the assistance of authorized personnel from the food control authorities in the districts involved. The fresh agricultural product samples analyzed in this study included watermelon, melon, asparagus, lotus root, strawberry, leek, crown daisy, leaf lettuce, and cucumber.

The sampling was conducted in accordance with the guidelines in China (SAC, 2014) for the official control of pesticide residues. All samples were comminuted after being transported to the laboratory and stored at -20 °C until analysis was carried out.

3.3. GC-MS/MS Analytical Conditions

The analysis was carried out on a Thermo Scientific™ TSQ™ 8000 Evo triple quadrupole mass spectrometer. Samples were injected with an AI 1310 auto-sampler into a split/splitless injector. The capillary column was analyzed with a Thermo Fisher Scientific TR-5MS (30 m × 250 μm × 0.25 μm).

At 0.75 min, the split mode was switched, and the split flow was 60 mL min⁻¹. At 2 min, the gas protector opened, and the flow rate was 20 mL min⁻¹. The column temperature was initially at 80 °C (held for 1 min), increased to 150 °C at a rate of 30 °C min⁻¹, then to 210 °C at a rate of 3 °C min⁻¹, and finally increased to 290 °C at a rate of 10 °C min⁻¹, holding for 12 min. The injection temperature was 260 °C and the injection volume with the splitless mode was 1 μL . The total running time was 43 min. The carrier gas was helium at 1.2 mL min⁻¹ with constant flow. The collision gas was argon, and the pressure was in the range of 1.0 mTorr. The QqQ mass spectrometer was run at 70 eV EI in

the selected reaction monitoring (SRM) mode. The specific MS/MS conditions are shown in Table S4.

3.4. Preparation and Characterization of SBA-15-C₁₈

SBA-15 and SBA-15-C₁₈ were synthesized according to the method described by Casado, N. et al. [28].

Preparation of SBA-15: Pluronic 123 (3 g) was dissolved in the mixture of water (90 mL) and 2.0 M HCl solution (94 mL). TEOS (5.5 mL) was then added, and the resulting mixture was stirred vigorously at 40 °C for 4 h for the purposes of prehydrolysis. Next, the mixture was transferred into a polypropylene bottle and stirred at 90 °C for 24 h. The solid compound was obtained by filtration, washed with water, and dried for 12 h at room temperature. The template was removed from the obtained material by refluxing in 95% EtOH for 24 h. Finally, the material was filtered and washed several times with water and EtOH, then dried at 50 °C (Figure 1A).

Preparation of SBA-15-C₁₈: SBA-15 was functionalized with chlorodimethyl -octadecylsilane. Prior to the reaction, SBA-15 was dehydrated at 150 °C in vacuum for 2 h. Then, chlorodimethyl-octadecylsilane (5 mL) was dissolved in toluene (100 mL) and, after stirring well, SBA-15 (1 g) powder was added. The alkylation was completed after about 6 h. At the end of the reaction, the powder was filtered and rinsed with a large quantity of toluene solution to remove the chlorodimethyl -octadecylsilane, and then dried in a vacuum to obtain SBA-15-C₁₈ powder (Figure 1A).

SBA-15-C₁₈ was characterized by Fourier transform infrared spectroscopy (FTIR) and scanning electron microscopy (SEM) (Figure 1B,C).

3.5. Sample Extraction and Cleanup

An appropriate sample (10.0 ± 0.1 g) was weighed into a 50 mL centrifuge tube, and then 10 mL acetonitrile was added. Then 3 g NaCl was added, shaken vigorously for 1 min, and centrifuged at 3800 rpm for 5 min. The supernatant was used for the further m-PFC process.

The principle and purification process of the m-PFC syringe are shown in Figure 4A. The m-PFC syringe contains two polymethylene sieve plates and adsorption materials. The adsorbent materials used in this study contain (Figure 4B): 5 mg of MWCNTs, 5 mg of SBA-15-C₁₈, and 150 mg of MgSO₄ for the watermelon, melon, asparagus, lotus root, strawberry, and cucumber samples; 8 mg of MWCNTs, 10 mg of PSA, 8 mg of SBA-15-C₁₈, and 150 mg of MgSO₄ for the leek samples; 8 mg of MWCNTs, 5 mg of SBA-15-C₁₈, and 150 mg of MgSO₄ for the crown daisy and leaf lettuce samples. Next, 1 mL of the initial extract was introduced into the m-PFC syringe tube for purification. When the syringe piston was pushed, all of the extract filtered through the adsorbent at a rate of 1 drop s⁻¹. At the same time, the purified extract was synchronously filtered through the 0.22 µm filter membrane under the syringe, and finally introduced into the automatic sampling vial for GC-MS/MS analysis.

3.6. Method Performances

The validation process of the analytical method was performed using the following parameters: linearity, LOQs, accuracy, and precision. An external standard method was used for quantitative analysis. Linearity was studied using matrix-matched calibration by analyzing samples. Five recoveries and reproducibility tests were performed for each sample at one fortification level (10 µg kg⁻¹). The LOQs of the proposed method were determined by the lowest accepted fortification level.

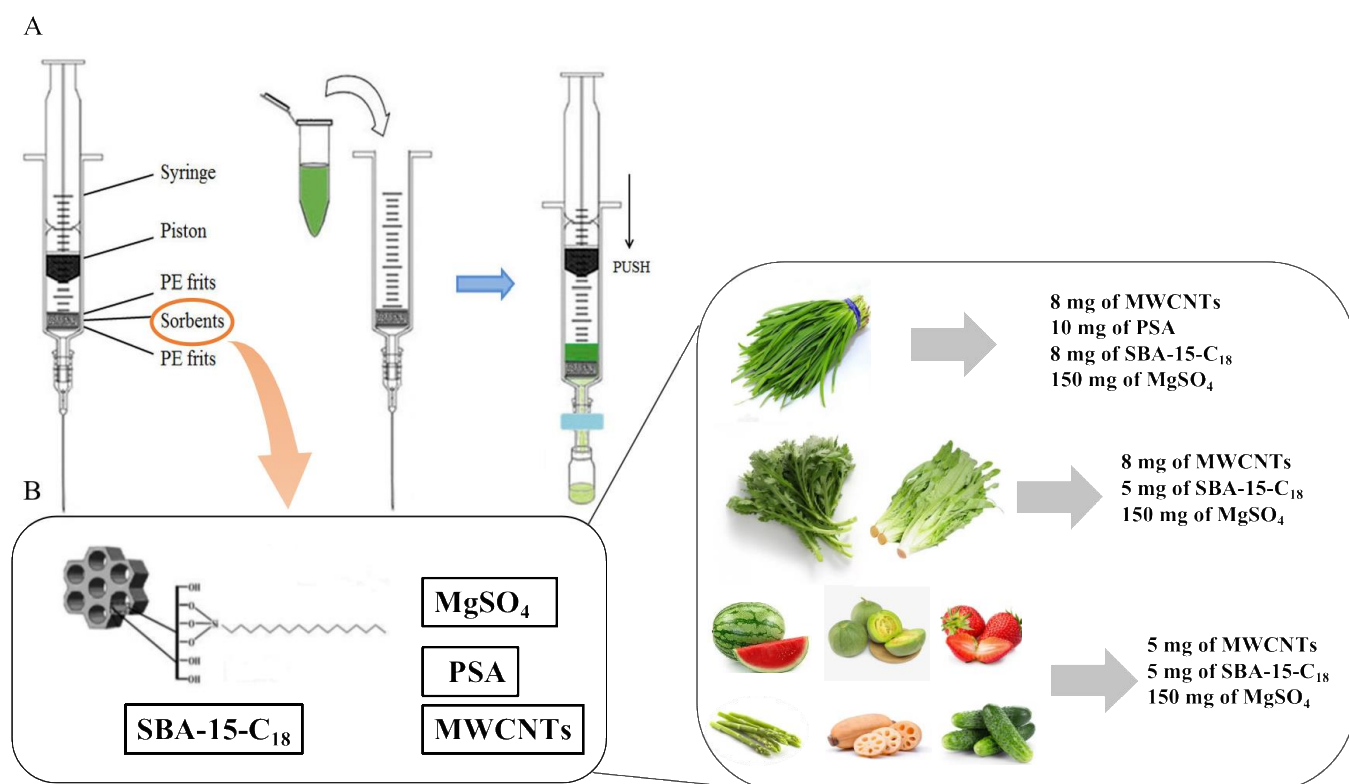


Figure 4. Schematic diagram of the m-PFC syringe and cleanup procedure (A), as well as the final sorbent combination and proportion for the different matrices (B).

3.7. Intake Risk Assessment

Dietary intake risk assessment combines the data on food consumption with chemical concentrations in food, including the assessment of dietary intake risk for acute and chronic exposures (corresponding to short- and long-term exposures). Short-term exposure mainly refers to periods of up to 24 h, while long-term exposure mainly refers to the average daily exposure over a life cycle.

For a chronic intake risk assessment, international estimated daily intakes (IEDI) were calculated by Equation (1) and then compared with acceptable daily intakes (ADI).

$$\text{IEDI} = \sum \frac{\text{Food chemical concentration} \times \text{Fi}}{\text{bw}} \quad (1)$$

where Fi is the average food consumption (kg) and bw is the average body weight (kg). When the IEDI is less than the ADI, then the risk is acceptable; if it is the opposite, then it poses an unacceptable risk.

For the acute exposure assessment, additional information is required on residual information in a single sample or a single unit of crop. The calculation of acute dietary exposure varies from case to case depending on the food commodity. The international estimated short-term intakes (IESTI) were calculated by Equations (2)–(4) and compared with the acute reference doses (ARfD).

Case 1. The residue in a composite sample (raw or processed) reflects the residue level in a meal-sized portion of the commodity (unit weight less than 25 g). Strawberries, leek, and crown daisy belong to Case 1 in this study.

$$\text{IESTI} = \frac{\text{LP} \times \text{HR}}{\text{bw}} \quad (2)$$

LP is the largest portion consumed (97.5th percentile of eaters), kg/d. HR is the highest residue, mg/kg.

Case 2. The residue of a meal-sized portion might be higher than the composite residue (where the whole fruit or vegetable unit weight is above 25 g).

Case 2a. The unit edible weight of the commodity is less than the largest portion weight. Melon, lotus root, asparagus, leaf lettuce, and cucumber belong to Case 2a in this study.

$$\text{IESTI} = \frac{U \times \text{HR} \times v + (\text{LP} - U) \times \text{HR}}{\text{bw}} \quad (3)$$

where U is the unit weight of the edible portion and kg. v is the variability factor, which is applied to the composite residue to estimate the residue level in a high residue unit. Further, it is assigned a value of 3 according to WHO and JMPR.

Case 2b. The unit edible weight of the raw commodity exceeds the largest portion weight. The watermelon belongs to Case 2b in this study.

$$\text{IESTI} = \frac{\text{LP} \times \text{HR} \times v}{\text{bw}} \quad (4)$$

When the IESTI is less than the ARfD, then the risk is acceptable; if it is the opposite, then it poses an unacceptable risk.

4. Conclusions

A novel m-PFC method based on SBA-15-C18 with GC-MS/MS was developed for a multi-residue analysis of 139 pesticides in agricultural produce. In 2020–2022, a total of 314 samples of different matrices, including watermelon, melon, asparagus, lotus root, strawberry, leek, crown daisy, leaf lettuce, and cucumber—which were collected from Shandong Province (China)—were analyzed. No pesticide residues were detected in 66.5% of the 341 samples, but 30.6% were at or below the MRLs, and 2.9% were above the MRLs. The residues of procymidone were found to most often exceed the Chinese MRLs (1.3% of the samples). Tebuconazole was found most frequently in 22.0% of the samples analyzed; most were from the leek and crown daisy samples. Multiple residues of pesticide (i.e., the residues of two or more pesticides) were found in 87 (75.2%) of the positive samples. The evaluation of consumer health risk connected with pesticide residues in agricultural products shows that the chronic and acute risk of pesticide residues are in an acceptable range, and they do not pose a serious health problem.

Supplementary Materials: The following are available online at <https://www.mdpi.com/article/10.3390/molecules28062480/s1>, Table S1. Recoveries (%) ($n = 5$) and repeatability (RSD %) from samples spiked at $10 \mu\text{g kg}^{-1}$ of target pesticides in other eight types of fruits and vegetables. Table S2. Recoveries (%) ($n = 5$) and repeatability (RSD %) from samples spiked at $10 \mu\text{g kg}^{-1}$, LOD, LOQ, correlation equation, R2 of target pesticides in leek samples. Table S3. Pesticides detected in fruits and vegetables from Shandong, China. Table S4. MRM Transitions and Other GC-MS/MS Parameters for the Compounds. Table S5. Sample collection in each city of Shandong Province.

Author Contributions: Conceptualization, C.Y.; methodology, Y.W.; software, T.Z.; validation, X.M., G.Z. and M.C.; formal analysis, X.M. and X.G.; investigation, M.C. and G.Z.; resources, C.Y. and T.Z.; data curation, T.H. and T.Z.; writing—original draft preparation, Y.W. and T.H.; writing—review and editing, N.Z., T.H. and Y.W.; visualization, C.Y. and T.H.; supervision, N.Z.; project administration, C.Y.; and funding acquisition, C.Y. and N.Z. All authors have read and agreed to the published version of the manuscript.

Funding: This research was funded by the National Natural Science Foundation of China, grant number 31801781, 21801180, as well as the Academic Promotion Programme of Shandong First Medical University (2019QL008) and the Incubation Program of Youth Innovation of Shandong Province.

Institutional Review Board Statement: Not applicable.

Informed Consent Statement: Not applicable.

Data Availability Statement: Data is available on request from the corresponding author.

Conflicts of Interest: The authors declare no conflict of interest.

Sample Availability: Samples of the compounds are not available from the authors.

References

- Walorczyk, S.; Drożdżyński, D.; Kowalska, J.; Remlein-Starosta, D.; Ziółkowski, A.; Przewoźniak, M.; Gnusowski, B. Pesticide residues determination in Polish organic crops in 2007–2010 applying gas chromatography-tandem quadrupole mass spectrometry. *Food Chem.* **2013**, *139*, 482–487. [CrossRef] [PubMed]
- Bhanti, M.; Taneja, A. Contamination of vegetables of different seasons with organophosphorous pesticides and related health risk assessment in northern India. *Chemosphere* **2007**, *69*, 63–68. [CrossRef] [PubMed]
- Berrada, H.; Fernández, M.; Ruiz, M.; Moltó, J.; Mañes, J.; Font, G. Surveillance of pesticide residues in fruits from Valencia during twenty months (2004/05). *Food Control* **2010**, *21*, 36–44. [CrossRef]
- Chen, C.; Qian, Y.Z.; Chen, Q.; Tao, C.J.; Li, C.Y.; Li, Y. Evaluation of pesticide residues in fruits and vegetables from Xiamen, China. *Food Control* **2011**, *22*, 1114–1120. [CrossRef]
- Philippe, V.; Neveen, A.; Marwa, A.; Basel, A.Y.A. Occurrence of pesticide residues in fruits and vegetables for the Eastern Mediterranean Region and potential impact on public health. *Food Control* **2021**, *119*, 107457. [CrossRef]
- Mac Loughlin, T.M.; Peluso, M.L.; Etchegoyen, M.A.; Alonso, L.L.; de Castro, M.C.; Percudani, M.C.; Marino, D.J. Pesticide residues in fruits and vegetables of the Argentine domestic market: Occurrence and quality. *Food Control* **2018**, *93*, 129–138. [CrossRef]
- Juraske, R.; Antón, A.; Castells, F.; Huijbregts, M. Human intake fractions of pesticides via greenhouse tomato consumption: Comparing model estimates with measurements for Captan. *Chemosphere* **2007**, *67*, 1102–1107. [CrossRef]
- Park, D.W.; Yang, Y.S.; Lee, Y.U.; Han, S.J.; Kim, H.J.; Kim, S.H.; Kim, J.P.; Cho, S.J.; Lee, D.; Song, N.J.; et al. Pesticide residues and risk assessment from monitoring programs in the largest production area of leafy vegetables in South Korea: A 15-year study. *Foods* **2021**, *10*, 425. [CrossRef]
- Lozowicka, B.; Kaczynski, P.; Paritova, A.; Kuzembekova, G.; Abzhaliyeva, A.; Sarsembayeva, N.; Alihan, K. Pesticide residues in grain from Kazakhstan and potential health risks associated with exposure to detected pesticides. *Food Chem. Toxicol.* **2014**, *64*, 238–248. [CrossRef]
- Yu, J.; Wang, X.; Yao, X.; Wu, X. Safety Evaluation of Heavy Metal Contamination and Pesticide Residues in Coix Seeds in Guizhou Province, China. *Foods* **2022**, *11*, 2286. [CrossRef]
- Claeys, W.L.; Schmit, J.-F.; Bragard, C.; Maghuin-Rogister, G.; Pussemier, L.; Schiffers, B. Exposure of several Belgian consumer groups to pesticide residues through fresh fruit and vegetable consumption. *Food Control* **2011**, *22*, 508–516. [CrossRef]
- Liu, Y.; Li, S.; Ni, Z.; Qu, M.; Zhong, D.; Ye, C.; Tang, F. Pesticides in persimmons, jujubes and soil from China: Residue levels, risk assessment and relationship between fruits and soils. *Sci. Total Environ.* **2016**, *542*, 620–628. [CrossRef]
- Shoiful, A.; Fujita, H.; Watanabe, I.; Honda, K. Concentrations of organochlorine pesticides (OCPs) residues in Foodstuffs collected from traditional markets in Indonesia. *Chemosphere* **2013**, *90*, 1742–1750. [CrossRef] [PubMed]
- Jallow, M.F.; Awadh, D.G.; Albaho, M.S.; Devi, V.Y.; Ahmad, N. Monitoring of pesticide residues in commonly used fruits and vegetables in Kuwait. *Int. J. Env. Res. Public Health* **2017**, *14*, 833. [CrossRef] [PubMed]
- Wu, P.; Wang, P.; Gu, M.; Xue, J.; Wu, X. Human health risk assessment of pesticide residues in honeysuckle samples from different planting bases in China. *Sci. Total Environ.* **2021**, *759*, 142747. [CrossRef] [PubMed]
- Tsakiris, I.N.; Goumenou, M.; Tzatzarakis, M.N.; Alegakis, A.K.; Tsitsimpikou, C.; Ozcagli, E.; Vynias, D.; Tsatsakis, A.M. Risk assessment for children exposed to DDT residues in various milk types from the Greek market. *Food Chem. Toxicol.* **2015**, *75*, 156–165. [CrossRef] [PubMed]
- Wu, W.-J.; Qin, N.; Zhu, Y.; He, Q.-S.; Ouyang, H.-L.; He, W.; Xu, F.-L. The residual levels and health risks of hexachlorocyclohexanes (HCHs) and dichloro-diphenyl-trichloroethanes (DDTs) in the fish from Lake Baiyangdian. *Environ. Sci. Pollut. Res.* **2013**, *20*, 5950–5962. [CrossRef]
- OECD. *China OECD Review of Agricultural Policies, Organisation for Economic Co-Operation and Development*; OECD: Paris, France, 2005.
- Liu, Y.M.; Jinsong, C.; XiaoYong, X.Z.; Kamphuis, B.M. *The Vegetable industry in China; Developments in Policies, Production, Marketing and International Trade*; Report 6.04.14; Agricultural Economics Research Institute: Den Haag, The Netherlands, 2004.
- Zhao, P.; Wang, L.; Zhou, L.; Zhang, F.; Kang, S.; Pan, C. Multi-walled carbon nanotubes as alternative reversed-dispersive solid phase extraction materials in pesticide multi-residue analysis with QuEChERS method. *J. Chromatogr. A* **2012**, *1225*, 17–25. [CrossRef]
- Zhao, P.; Huang, B.; Li, Y.; Han, Y.; Zou, N.; Gu, K.; Pan, C. Rapid Multiplug Filtration Cleanup with Multiple-Walled Carbon Nanotubes and Gas Chromatography—Triple-Quadruple Mass Spectrometry Detection for 186 Pesticide Residues in Tomato and Tomato Products. *J. Agr. Food Chem.* **2014**, *62*, 3710–3725. [CrossRef]
- Zou, N.; Han, Y.; Li, Y.; Qin, Y.; Gu, K.; Zhang, J.; Pan, C.; Li, X.S. Multi-residue method for determination of 183 pesticide residues in leeks by rapid multiplug filtration cleanup and gas chromatography-tandem mass spectrometry. *J. Agr. Food Chem.* **2016**, *64*, 6061–6070. [CrossRef]

23. Castiglioni, M.; Onida, B.; Rivoira, L.; Del Bubba, M.; Ronchetti, S.; Bruzzoniti, M.C. Amino groups modified SBA-15 for dispersive-solid phase extraction in the analysis of micropollutants by QuEChERS approach. *J. Chromatogr. A* **2021**, *1645*, 462107. [CrossRef] [PubMed]
24. Hu, Q.; Li, J.J.; Hao, Z.P.; Li, L.D.; Qiao, S.Z. Dynamic adsorption of volatile organic compounds on organofunctionalized SBA-15 materials. *Chem Eng. J.* **2009**, *149*, 281–288. [CrossRef]
25. Mureseanu, M.; Reiss, A.; Stefanescu, I.; David, E.; Parvulescu, V.; Renard, G.; Hulea, V. Modified SBA-15 mesoporous silica for heavy metal ions remediation. *Chemosphere* **2008**, *73*, 1499–1504. [CrossRef] [PubMed]
26. Casado, N.; Pérez-Quintanilla, D.; Morante-Zarcero, S.; Sierra, I. Evaluation of bi-functionalized mesoporous silicas as reversed phase/cation-exchange mixed-mode sorbents for multi-residue solid phase extraction of veterinary drug residues in meat samples. *Talanta* **2017**, *165*, 223–230. [CrossRef]
27. Casado, N.; Pérez-Quintanilla, D.; Morante-Zarcero, S.; Sierra, I. Current development and applications of ordered mesoporous silicas and other sol-gel silica-based materials in food sample preparation for xenobiotics analysis. *TrAC Trend Anal. Chem.* **2017**, *88*, 167–184. [CrossRef]
28. Casado, N.; Morante-Zarcero, S.; Pérez-Quintanilla, D.; Sierra, I. Application of a hybrid ordered mesoporous silica as sorbent for solid-phase multi-residue extraction of veterinary drugs in meat by ultra-high-performance liquid chromatography coupled to ion-trap tandem mass spectrometry. *J. Chromatogr. A* **2016**, *1459*, 24–37. [CrossRef]
29. Han, Y.; Song, L.; Liu, S.; Zou, N.; Li, Y.; Qin, Y.; Pan, C. Simultaneous determination of 124 pesticide residues in Chinese liquor and liquor-making raw materials (sorghum and rice hull) by rapid multi-plug filtration cleanup and gas chromatography-tandem mass spectrometry. *Food Chem.* **2018**, *241*, 258–267. [CrossRef]
30. Wang, X.; Wang, X.; Zhang, H.; Wu, C.; Wang, X.; Xu, H.; Li, Z. Enantioselective degradation of tebuconazole in cabbage, cucumber, and soils. *Chirality* **2012**, *24*, 104–111. [CrossRef]
31. Chen, L.; Li, X.S.; Wang, Z.Q.; Pan, C.P.; Jin, R.C. Residue dynamics of procymidone in leeks and soil in greenhouses by smoke generator application. *Ecotoxicol. Environ. Saf.* **2010**, *73*, 73–77. [CrossRef]
32. He, Z.; Chen, S.; Wang, L.; Peng, Y.; Luo, M.; Wang, W.; Liu, X. Multiresidue analysis of 213 pesticides in leek and garlic using QuEChERS-based method and gas chromatography-triple quadrupole mass spectrometry. *Anal. Bioanal. Chem.* **2015**, *407*, 2637–2643. [CrossRef]

Disclaimer/Publisher’s Note: The statements, opinions and data contained in all publications are solely those of the individual author(s) and contributor(s) and not of MDPI and/or the editor(s). MDPI and/or the editor(s) disclaim responsibility for any injury to people or property resulting from any ideas, methods, instructions or products referred to in the content.

Article

Fragmentation Pathway of Organophosphorus Flame Retardants by Liquid Chromatography–Orbitrap-Based High-Resolution Mass Spectrometry

Kangcong Li ^{1,2}, Yan Gao ^{1,3}, Xiuqin Li ^{1,3,*}, Yan Zhang ^{1,4}, Benfeng Zhu ² and Qinghe Zhang ^{1,3,*}

¹ Division of Chemical Metrology and Analytical Science, National Institute of Metrology, Beijing 100029, China; 13097513253@163.com (K.L.); gaoyan@nim.ac.cn (Y.G.); yanzhang_larissa@163.com (Y.Z.)

² College of Materials and Chemistry, China Jiliang University, Hangzhou 310018, China; zhubenfeng88@cjl.edu.cn

³ Key Laboratory of Chemical Metrology and Applications on Nutrition and Health for State Market Regulation, Beijing 100029, China

⁴ China Key Laboratory of Groundwater Conservation of MWR, China University of Geosciences, Beijing 100083, China

* Correspondence: lixq@nim.ac.cn (X.L.); zhangqh@nim.ac.cn (Q.Z.); Tel.: +86-10-64524784 (Q.Z.)

Abstract: Organophosphorus flame retardants (OPFRs) have been widely used in polymeric materials owing to their flame retardant and plasticizing effects. Investigating the fragmentation pathway of OPFRs is of great necessity for further discovering and identifying novel pollutants using orbitrap-based high-resolution mass spectrometry (HRMS). A total of 25 OPFRs, including alkyl, halogenated, and aromatic types, were analyzed in this study. The fragmentation pathways of the OPFRs were investigated using orbitrap-based HRMS with high-energy collision dissociation (HCD) in positive mode. The major fragmentation pathways for the three types of OPFRs are greatly affected by the substituents. In detail, the alkyl and halogenated OPFRs underwent three McLafferty hydrogen rearrangements, wherein the substituents were gradually cleaved to form the structurally stable $[\text{H}_4\text{PO}_4]^+$ ($m/z = 98.9845$) ions. In contrast, the aromatic OPFRs would cleave not only the C-O bond but also the P-O bond, depending on the substituents, to form fragment ions such as $[\text{C}_6\text{H}_7\text{O}]^+$ ($m/z = 95.0495$) or $[\text{C}_7\text{H}_7]^+$ ($m/z = 91.0530$), among others. Using HRMS improved the accuracy of fragment ion identification, and the pathway became more evident. These fragmentation laws can provide identification information in pollutant screening work and theoretical references for the structural characterization of compounds with diverse substituent structures.

Keywords: organophosphorus flame retardant; fragmentation pathway; liquid chromatography; high resolution mass spectrometry



Citation: Li, K.; Gao, Y.; Li, X.; Zhang, Y.; Zhu, B.; Zhang, Q. Fragmentation Pathway of Organophosphorus Flame Retardants by Liquid Chromatography–Orbitrap-Based High-Resolution Mass Spectrometry. *Molecules* **2024**, *29*, 680. <https://doi.org/10.3390/molecules29030680>

Academic Editor: Gavino Sanna

Received: 10 December 2023

Revised: 25 January 2024

Accepted: 26 January 2024

Published: 1 February 2024



Copyright: © 2024 by the authors. Licensee MDPI, Basel, Switzerland. This article is an open access article distributed under the terms and conditions of the Creative Commons Attribution (CC BY) license (<https://creativecommons.org/licenses/by/4.0/>).

1. Introduction

Organophosphorus flame retardants (OPFRs) are common polymer additives employed for flame retardation and plasticization [1–3]. In recent years, OPFRs and related degradation products and analogues have been commonly found in water [4], dust [5], sludge [6], and various foods [7–11], and are distributed worldwide [12–14]. Investigations have demonstrated that certain OPFRs possess neurotoxic and carcinogenic properties, which can substantially reduce human immunity [15,16]. As a result, OPFRs are gaining increasing attention as potential health hazards.

At present, the detection of OPFRs mainly relies on gas or liquid chromatography-mass spectrometry techniques, wherein the qualitative and quantitative analysis of a limited range of targets can be carried out with reference materials [17–19]. However, with thousands of OPFRs and derivatives currently available and continuing to expand, it is crucial to

perform both suspect and non-target screening, while the requirements for mass spectrometry information related to OPFRs are becoming increasingly stringent. There are many types of organophosphorus flame retardants (OPFRs), mainly including organophosphate esters, organophosphonates, organophosphate salts, phosphine oxides, and organophosphate heterocycles compounds. Organophosphate esters with $P(=O)(OR)_3$ as their characteristic structure account for 84.2% of the available OPFRs monomers [20]. These compounds may produce the same characteristic fragment ions during mass spectrometry cleavage because they contain the same phosphate skeleton, and these characteristic ions can be used as a basis for non-target screening of organophosphorus compounds. There are some variations in the type and abundance of fragment ions produced by different types of organophosphorus compounds, and these differential features are a tool for further differentiation and identification of the target. According to the substituents, OPFRs are currently classified as alkyl, halogenated, and aromatic [21]: alkyl OPFRs substituents are mainly straight or branched composed of C and H elements, halogenated OPFRs substituents are usually H substituted by chlorine or bromine on alkane chains, and aromatic OPFRs substituents generally contain one or more aromatic rings. Lesage et al. [22] used a deuterium label to study the fragmentation of tri-*n*-butyl phosphate. Deuterium labeling makes the fragmentation mechanism more obvious. However, it is still difficult to obtain relevant deuterium-labeled products for the increasing variety of organophosphorus flame retardants. Ma et al. [23] used gas chromatography tandem mass spectrometry to explain the common fragmentation pathways of 13 OPFRs under electron ionization (EI) sources. They found that alkyl OPFRs follow a rearrangement reaction from the precursor $[M]^+$ to $[M - R + 2H]^+$, $[M - 2R + 3H]^+$, and $[M - 3R + 4H]^+$ patterns. Yang et al. [24] optimized the ionization energy of the EI source and summarized the fragmentation pathways and characteristic fragment ion database of 17 OPFRs, which provided a basis for determining OPFRs in complex matrix samples. The high-resolution mass spectrometry (HRMS) screening technique can provide higher index parameters in terms of screening accuracy and sensitivity, improve the accuracy of fragment ion identification, effectively perform high-throughput detection, and reduce false positive and false negative rates. Ye et al. [25] used liquid chromatography tandem HRMS with an atmospheric pressure chemical ionization (APCI) source for target, suspect, and non-target screening of OPFRs in Taihu sediments, using characteristic fragment ions for qualitative analysis of emerging OPFRs, which significantly simplifies the information processing during non-target screening but also requires the researcher to learn the target well enough to remove interferences during subsequent analysis effectively. Since there are many different types of OPFRs substituents and the physicochemical properties of the various OPFRs vary widely [24], the study of the fragmentation pathways of the target compounds and the summary of the relevant mass spectrometry information are a crucial step before the screening process.

This study aims to analyze the main characteristic fragment ions generated during the fragmentation of OPFRs by LC-Orbitrap-HRMS technology using an electrospray ionization (ESI) source. The selected OPFRs include alkyl, halogenated, and aromatic classes, which are widely representative considering the chain length and substituent structure. The fragmentation laws were investigated, and the effective information was applied to the screening of OPFRs in rice samples to provide a basis for detecting and accurately characterizing the targets.

2. Results and Discussion

2.1. Fragmentation Pathway and Characteristic Ions of Three Types of OPFRs

To analyze the fragmentation pathway of the three types of OPFRs, each compound was injected separately at 200 $\mu\text{g}/\text{kg}$, and precursor ions were fragmented under the step-collision energy by HCD.

2.1.1. Fragmentation Pathway and Characteristic Ions of Alkyl OPFRs

In this study, nine representative alkyl OPFRs were selected (Table 1), including straight chain substituents (TMP, TEP, TnPP, TnBP, TPeP, TBOEP) and branched substituents (TiPP, TiBP, TEHP), corresponding to the substituent groups in the order of methyl, ethyl, *n*-propyl, *n*-butyl, *n*-pentyl, 2-butoxyethyl, isopropyl, isobutyl, and 2-ethylhexyl. Among them, TiPP and TnPP, TiBP and TnBP are two pairs of isomers.

Table 1. OPFRs' material information.

Number	Compound	Abbreviation	M_r	Molecular Formula	CAS Number
1	Trimethyl phosphate	TMP	140.0233	C ₃ H ₉ PO ₄	512-56-1
2	Triethyl phosphate	TEP	182.0702	C ₆ H ₁₅ PO ₄	78-40-0
3	Tri- <i>n</i> -propyl phosphate	TnPP	224.1177	C ₉ H ₂₁ PO ₄	513-08-6
4	Tri- <i>n</i> -butyl phosphate	TnBP	266.1641	C ₁₂ H ₂₇ PO ₄	126-73-8
5	Tri-iso-butyl phosphate	TiBP	266.1641	C ₁₂ H ₂₇ PO ₄	126-71-6
6	Tri-pentyl phosphate	TPeP	308.2111	C ₁₅ H ₃₃ PO ₄	2528-38-3
7	Tris(2-methylpropyl) phosphate	TiPP	224.1177	C ₉ H ₂₁ PO ₄	513-02-0
8	Tris(2-ethylhexyl) phosphate	TEHP	434.3519	C ₂₄ H ₅₁ PO ₄	78-42-2
9	Tris(2-butoxyethyl) phosphate	TBOEP	398.2428	C ₁₈ H ₃₉ PO ₇	78-51-3
10	Tris(chloroethyl) phosphate	TCEP	283.9533	C ₆ H ₁₂ Cl ₃ PO ₄	115-96-8
11	Tris(chloropropyl) phosphate	TCPP	326.0008	C ₉ H ₁₈ Cl ₃ PO ₄	1067-98-7
12	Tris(2-chloroisopropyl) phosphate	TCIPP	326.0008	C ₉ H ₁₈ Cl ₃ PO ₄	13674-84-5
13	Tris(2,3-dichloro-2-propyl)phosphate	T23DCPP	427.8834	C ₉ H ₁₅ Cl ₆ PO ₄	78-43-3
14	Tris(1,3-dichloro-2-propyl)phosphate	TDCIPP	427.8834	C ₉ H ₁₅ Cl ₆ PO ₄	13674-87-8
15	Tris(2,3-dibromopropyl) phosphate	T23DBPP	691.5803	C ₉ H ₁₅ Br ₆ PO ₄	126-72-7
16	Triphenyl phosphate	TPHP	326.0702	C ₁₈ H ₁₅ PO ₄	115-86-6
17	2-Ethylhexyl-diphenyl phosphate	EHDPP	362.1641	C ₂₀ H ₂₇ PO ₄	1241-94-7
18	Tris- <i>o</i> -tolyl-phosphate	<i>o</i> -TCP	368.1172	C ₂₁ H ₂₁ PO ₄	78-30-8
19	Tris- <i>m</i> -tolyl-phosphate	<i>m</i> -TCP	368.1172	C ₂₁ H ₂₁ PO ₄	563-04-2
20	Tri- <i>p</i> -tolyl-phosphate	<i>p</i> -TCP	368.1172	C ₂₁ H ₂₁ PO ₄	78-32-0
21	Dibutyl phenyl phosphate	dBPhP	286.1328	C ₁₄ H ₂₃ PO ₄	2528-36-1
22	Butyl diphenyl phosphate	BdPhP	306.1015	C ₁₆ H ₁₉ PO ₄	2752-95-6
23	Tris(3,5-dimethylphenyl) phosphate	T35DMPP	410.1641	C ₂₄ H ₂₇ PO ₄	25653-16-1
24	Cresyl diphenyl phosphate	CDPP	340.0859	C ₁₉ H ₁₇ PO ₄	26444-49-5
25	Isodecyl diphenyl phosphate	IDDP	390.1954	C ₂₂ H ₃₁ PO ₄	29761-21-5

1–9 are alkyl OPFRs, 10–15 are halogenated OPFRs, 16–25 are aromatic OPFRs.

In general, alkyl OPFRs underwent three successive McLafferty hydrogen rearrangements within the HCD collision cell. $[M - R + 2H]^+$, $[M - 2R + 3H]^+$ and $[M - 3R + 4H]^+$ ions were produced through repeated rearrangements. Figure 1 shows the possible fragmentation pathway of TnPP. Three rearrangements occurred throughout the process, with each cleavage more likely to occur at the lower bond energy C-O bond (about 326 kJ/mol) compared to the P-O bond (about 410 kJ/mol). The fragmentation process sequentially produced the $[C_6H_{16}PO_4]^+$ ($m/z = 183.0783$), $[C_3H_{10}PO_4]^+$ ($m/z = 141.0313$), and $[H_4PO_4]^+$ ($m/z = 98.9847$) ions. The abundance ratio and accurate mass of fragment ions were effective bases for qualitative analysis. Among the alkyl OPFRs, most of the compounds had $[H_4PO_4]^+$ ($m/z = 98.9847$) as the base peak, which was a common characteristic fragment ion of alkyl OPFRs. It was very stable in the mass spectrum and could be used as an identifying feature for alkyl OPFRs during screening. However, for TBOEP (Figure 2a), the precursor ion $[M + H]^+$ was the base peak. This may be due to the fact that the substituent group of TBOEP was 2-butoxyethyl, and the TBOEP precursor ion was stabilized by the presence of oxygen in the side chain, which led to difficulty in McLafferty hydrogen rearrangement. This feature, in combination with the abundance of fragment ions, could be a basis for screening TBOEP. High-resolution mass spectrometry can provide the accurate mass of the characteristic fragment ions, which provides a guarantee for eliminating interferences and accurately matching molecular formulae during the screening process.

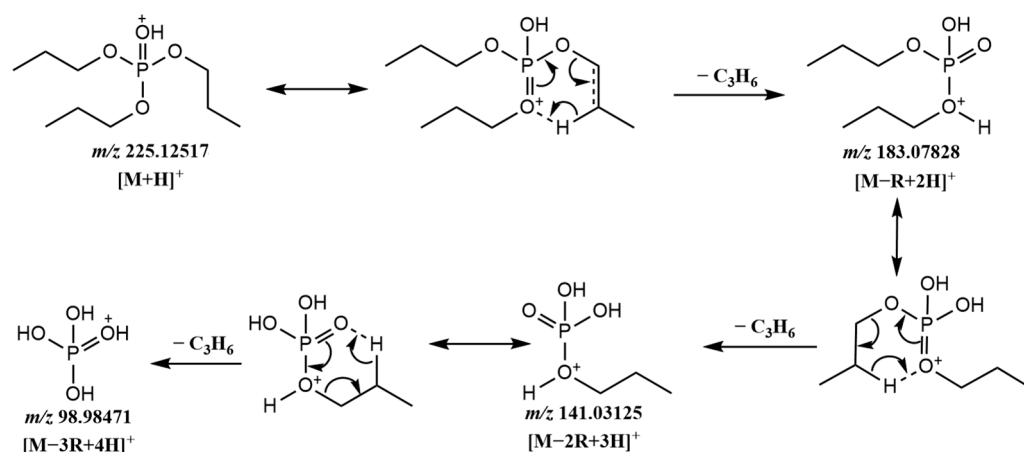


Figure 1. Possible fragmentation pathway of TnPP.

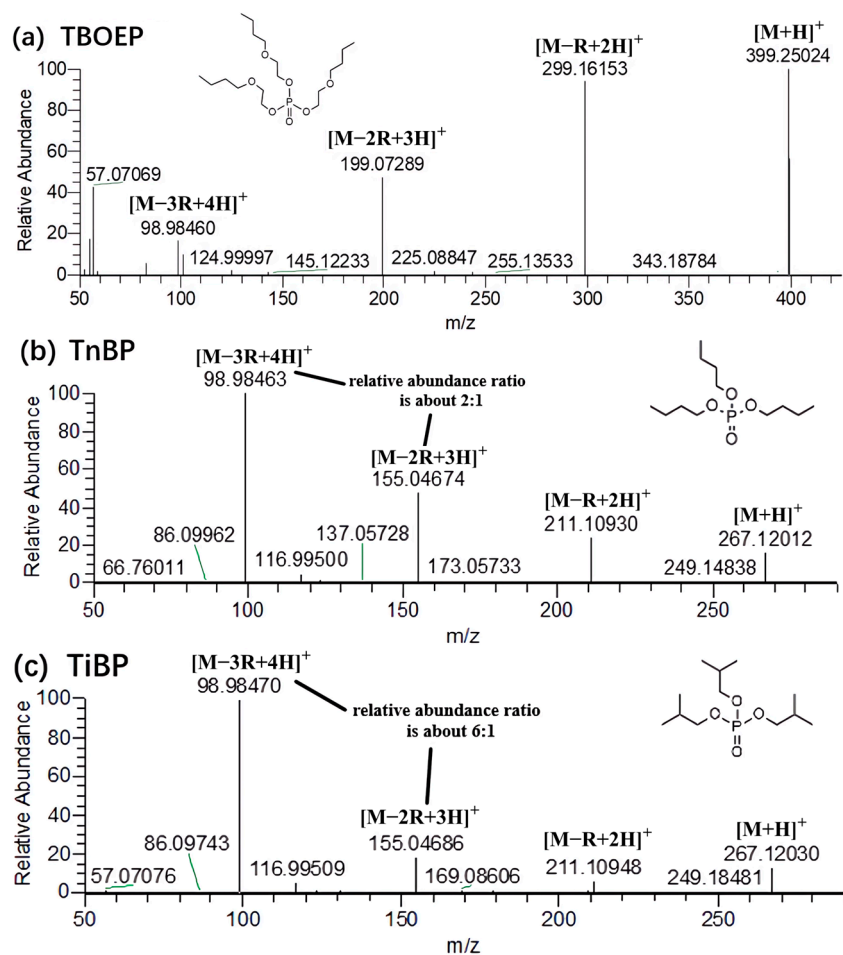


Figure 2. Cont.

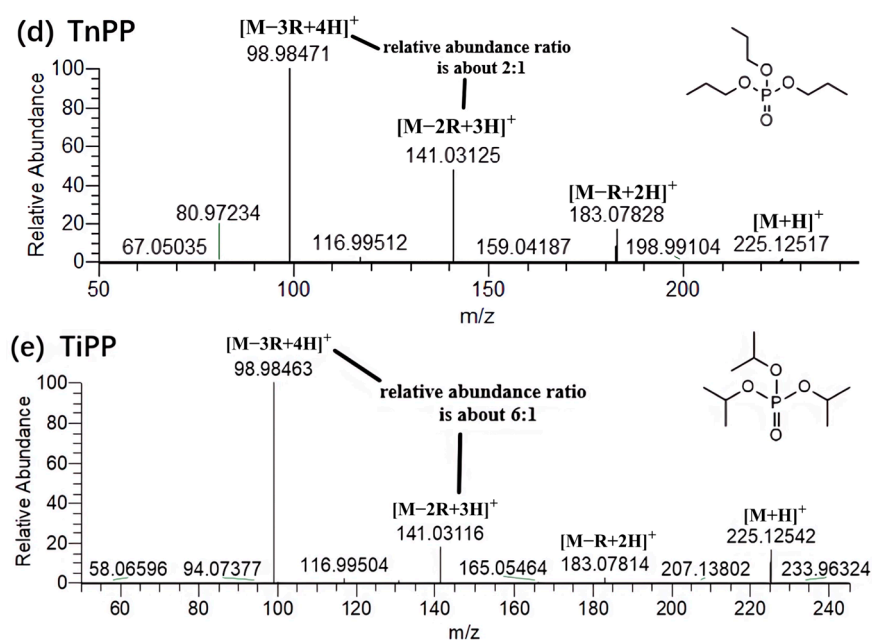


Figure 2. MS² spectra of 5 alkyl OPFR compounds.

Isomers are difficult to distinguish in qualitative analysis due to their similar structures and same molecular weights but some isomers differ in the type or abundance of fragment ions, which can be used as tools for further identification. Among the alkyl OPFRs, TnBP and TiBP, TnPP and TiPP are two pairs of isomers (Figure 2b–e), in which TiBP and TiPP are branched compounds, and TnBP and TnPP are straight-chain compounds. A comparison of their mass spectra revealed a higher relative abundance ratio of $[M - 3R + 4H]^+$ to $[M - 2R + 3H]^+$ fragments for the branched compounds and a lower ratio for the straight-chain compounds. For example, the relative abundance ratio of the fragments $[M - 3R + 4H]^+$ ($m/z = 98.9846$) to $[M - 2R + 3H]^+$ ($m/z = 141.0312$) of the branched compound TiPP was about 6:1, while the fragments $[M - 3R + 4H]^+$ ($m/z = 98.9847$) to $[M - 2R + 3H]^+$ ($m/z = 141.0313$) of the straight-chain compound TnPP was about 2:1. This may be because branched alkanes are more stable than straight-chain alkanes, and when used as substituents, the rearrangement reaction of branched OPFRs mainly occurs in the oxygen atoms connecting the substituent groups, while the energy of straight-chain compounds is dispersed during fragmentation, so the branched compounds are more prone to the formation of $[M - 3R + 4H]^+$, and the proportion of the fragments produced is relatively higher. This conclusion can provide a reference for distinguishing isomers during the qualification of compounds.

2.1.2. Fragmentation Pathway and Characteristic Ions of Halogenated OPFRs

In this study, six representative halogenated OPFRs were selected (Table 1), including five chlorinated OPFRs (TCEP, TCIPP, TCPP, T23DCIPP, and TDCIPP) and one brominated OPFR (T23DBPP). The substituents are chloroethyl, 2-chloroisopropyl, chloropropyl, 2,3-dichloropropyl, 1,3-dichloropropyl, and 2,3-dibromopropyl, in which TCIPP and TCPP, T23DCIPP and TDCIPP are two pairs of isomers.

Due to the high natural abundance of chlorine and bromine isotopes, halogenated OPFRs produce unique ion clusters during ionization. According to the relative abundance ratios of the isotope peaks in the MS¹ spectrum (Figure S5), the type and amount of halogens can be deduced, which facilitates the characterization of the compounds. The two halogenated OPFRs, TDCIPP and T23DBPP, both had distinctive isotope peaks in the MS¹ spectrum. For TDCIPP, the relative abundance ratio of the isotope peaks $[M + H]^+ : [M + 2 + H]^+ : [M + 4 + H]^+ : [M + 6 + H]^+ : [M + 8 + H]^+ : [M + 10 + H]^+$ was 51.63:100.00:81.46:34.68:7.53:1.06; For T23DBPP, the relative abundance ratio of the isotope

peaks $[M + H]^+ : [M + 2 + H]^+ : [M + 4 + H]^+ : [M + 6 + H]^+ : [M + 8 + H]^+ : [M + 10 + H]^+ : [M + 12 + H]^+$ was 5.53:31.95:74.54:100.00:73.73:27.96:4.06. The natural abundance ratio of ^{35}Cl and ^{37}Cl is about 75.77%:24.23%, and the natural abundance ratio of ^{79}Br and ^{81}Br is about 50.60%:49.31%. After calculation, when a compound contains six Cl elements, the theoretical relative abundance ratio of the isotope peaks $[M + H]^+ : [M + 2 + H]^+ : [M + 4 + H]^+ : [M + 6 + H]^+ : [M + 8 + H]^+ : [M + 10 + H]^+$ is 50.00:100.00:83.33:37.04:9.26:1.23, which is essentially identical to the isotope peaks generated by TDCIPP in the experiment. When a compound contains six Br elements, the theoretical relative abundance ratio $[M + H]^+ : [M + 2 + H]^+ : [M + 4 + H]^+ : [M + 6 + H]^+ : [M + 8 + H]^+ : [M + 10 + H]^+ : [M + 12 + H]^+$ of the isotope peaks is 5.00:30.00:75.00:100.00:75.00:30.00:5.00. This also matches the experimental isotopic peaks produced by T23DBPP. In the MS^1 spectrum of TDCIPP, the highest isotopic abundance was observed for the molecular formula $\text{C}_9\text{H}_{15}\text{Cl}^{37}\text{Cl}^{35}\text{PO}_4$ ($[M + 2 + H]^+$ $m/z = 430.8880$), and multiple $[M + \text{Na}]^+$ peaks were also observed. In the MS^1 spectrum of T23DBPP, the highest isotopic abundance of the molecular formula $\text{C}_9\text{H}_{15}\text{Br}^{81}\text{Br}^{79}\text{PO}_4$ ($[M + 6 + H]^+$ $m/z = 698.5812$) was observed along with numerous $[M + \text{NH}_4]^+$ peaks.

It was found that the fragmentation process of halogenated OPFRs was similar to alkyl OPFRs. The compounds were also gradually fragmented through the McLafferty hydrogen rearrangement reaction to form $[M - R + 2H]^+$, $[M - 2R + 3H]^+$, and $[M - 3R + 4H]^+$ fragment ions, finally generating $[\text{H}_4\text{PO}_4]^+$ ($m/z = 98.9845$). Taking TCPP as an example, the possible fragmentation pathway of TCPP is shown in Figures 3 and 4a. The whole fragmentation process also involved three rearrangements. During the fragmentation process, the chloropropyl group was fragmented and combined with the surrounding hydrogen to form $[\text{C}_6\text{H}_{14}\text{Cl}_2\text{PO}_4]^+$ ($m/z = 250.9999$), $[\text{C}_3\text{H}_9\text{ClPO}_4]^+$ ($m/z = 174.9921$), and $[\text{H}_4\text{PO}_4]^+$ ($m/z = 98.9846$) ions. Unlike the alkyl OPFRs, the $[M + H]^+$ and $[M - R + 2H]^+$ ions were often more prominent in the spectrum. This suggested that halogenated OPFRs were more stable than alkyl OPFRs and less likely to be destroyed at the same collision energy. This may be because the bond length of the C–Cl bond (about 177×10^{-12} m) is longer, making it easier to cleave than the C–O bond (about 143×10^{-12} m). Among the characteristic fragment ions of some halogenated OPFRs, $[M - \text{Cl} + H]^+$, $[M - R - \text{Cl} + 2H]^+$, and $[M - 2R - \text{Cl} + 3H]^+$ ions are included. Taking TCEP as an example (Figure 4b), except for the common ions $[M - R + 2H]^+$ ($m/z = 222.9685$), $[M - 2R + 3H]^+$ ($m/z = 160.9763$), and $[M - 3R + 4H]^+$ ($m/z = 98.9845$), it also appeared that the loss of chlorine led to the formation of $[M - R - \text{Cl} + 2H]^+$ ($m/z = 186.9919$) and $[M - 2R - \text{Cl} + 3H]^+$ ($m/z = 124.9999$) ions.

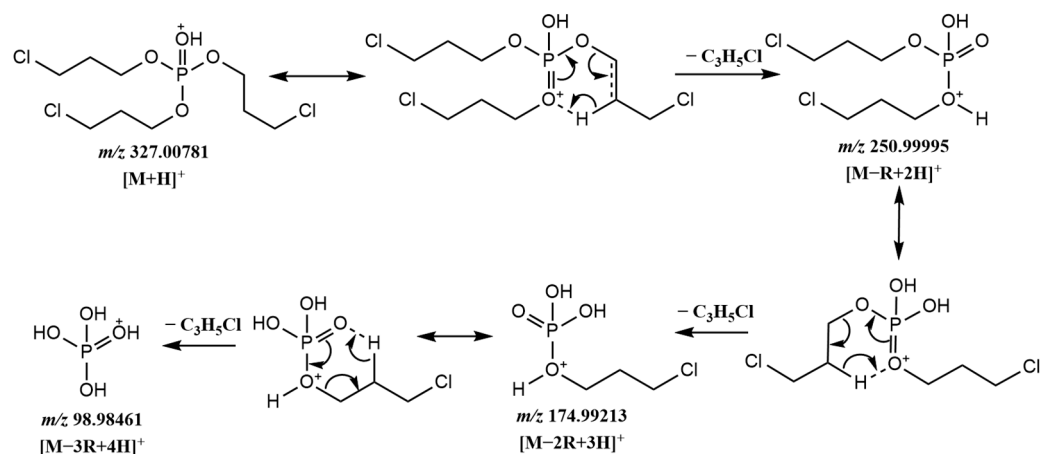


Figure 3. Possible fragmentation pathway of TCPP.

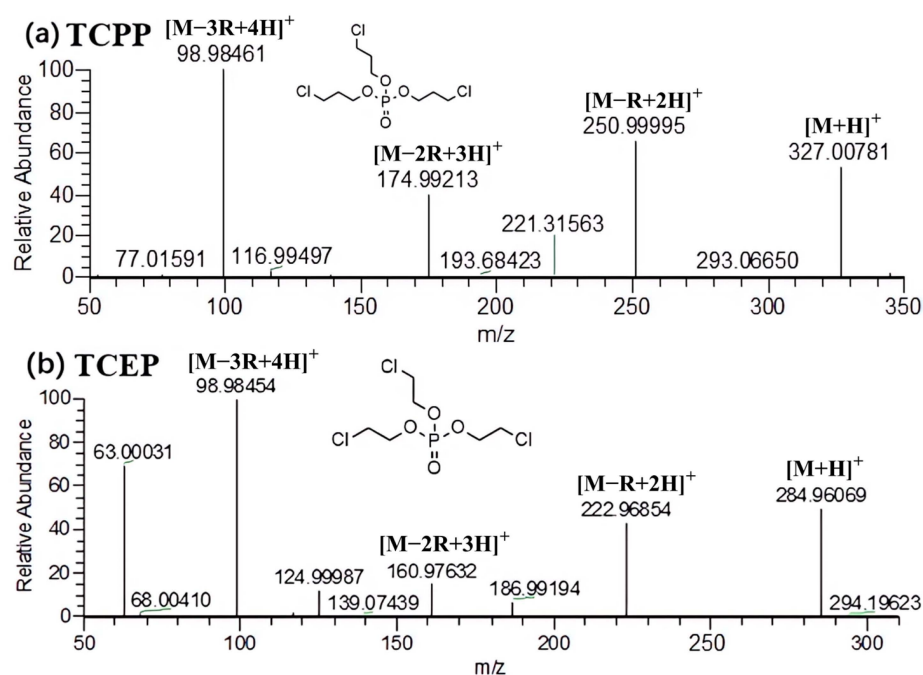


Figure 4. MS² spectra of two halogenated OPFR compounds.

2.1.3. Fragmentation Pathway and Characteristic Ions of Aromatic OPFRs

The structures of aromatic OPFRs usually contain one or more aromatic rings. Different from the above-mentioned two types of OPFRs, the substituent types of aromatic OPFRs are more abundant. The experiment involved dBPhP and BdPhP with a benzene ring and *n*-butyl; EHDPP with a benzene ring and 2-ethylhexyl; IDDP with isodecyl; CDPP with benzene and toluene; TPHP with a benzene ring; T35DMPP with xylene; and isomers *o*-TCP, *m*-TCP, and *p*-TCP with toluene.

Experiments have shown that the aromatic ring had an influence on the fragmentation of the compound, and its fragmentation pathways and characteristic fragments were different from those of alkyl and halogenated OPFRs. For aromatic OPFRs containing alkane chains in the substituents, such compounds would preferentially cleave the C–O bond connected to the alkane chain during the fragmentation process to form a stable structure. The structure of dBPhP contains one benzene ring and two alkane chains, and the possible fragmentation process and MS² spectra are shown in Figures 5 and 6a. The characteristic fragment ions [C₁₀H₁₆PO₄]⁺ (*m/z* = 231.0778) and [C₆H₈PO₄]⁺ (*m/z* = 175.0154) were formed by cleavage of the C–O bonds on the two alkane chains, followed by cleavage of the P–O bonds to form the ion [C₆H₇O]⁺ (*m/z* = 95.0496).

The structures of BdPhP, EHDPP, and IDDP contain two benzene rings and an alkane chain. These compounds formed characteristic fragment ions [C₁₂H₁₂PO₄]⁺ (*m/z* = 251.0465) with two benzene rings by the cleavage of the C–O bond on the alkane chain, and gradually formed [C₁₂H₈]⁺ (*m/z* = 152.0620) ions and [C₆H₇O]⁺ (*m/z* = 95.0496) ions in the subsequent fragmentation process. It was observed that when the substituent of aromatic OPFRs contained an alkane chain, the alkane chain was very easily cleaved, and the structure with a benzene ring was relatively stable, which could be used as characteristic fragment ions in screening.

For aromatic OPFRs in which the three substituents were all aromatic rings, the compounds had a stable structure due to the conjugation effect. Therefore, the precursor peak was the base peak in the MS² spectrum. If the substituent was a benzene ring (TPHP), [C₁₂H₈]⁺ (*m/z* = 152.0620) and [C₆H₇O]⁺ (*m/z* = 95.0496) characteristic fragment ions would be generated; if the aromatic ring was toluene (*o*-TCP, *m*-TCP, *p*-TCP), [C₁₃H₉]⁺ (*m/z* = 165.0698), [C₇H₇]⁺ (*m/z* = 91.0547) and [C₅H₅]⁺ (*m/z* = 65.0393) characteristic fragment ions would be generated; for compounds containing both toluene and benzene

rings like CDPP (Figure 6b), all five characteristic fragment ions would appear. The substituent of T35DMPP was xylene, and its characteristic fragment ions were $[C_{16}H_{18}PO_3]^+$ ($m/z = 289.0984$), $[C_{14}H_{11}]^+$ ($m/z = 179.0853$) and $[C_6H_7]^+$ ($m/z = 79.0548$).

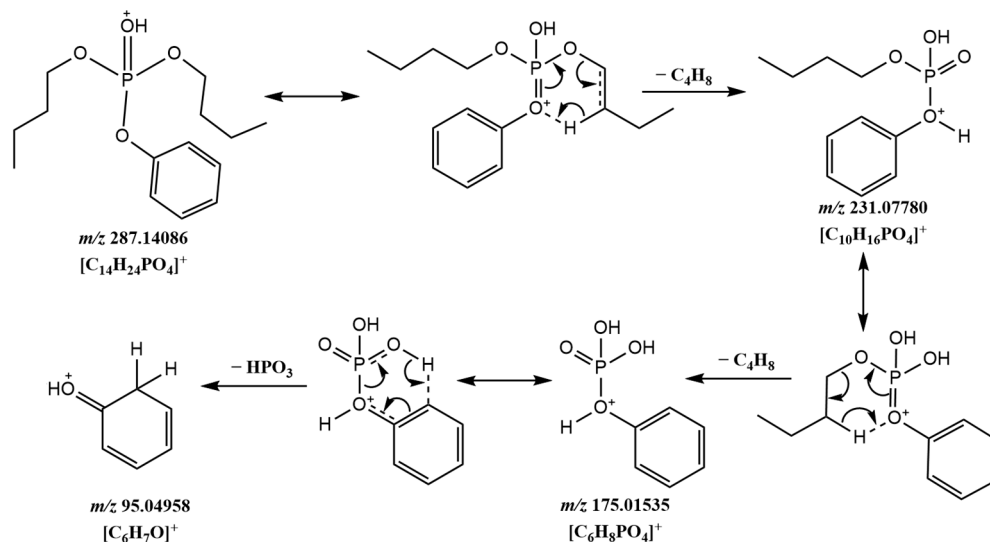


Figure 5. Possible fragmentation pathway of dBPhP.

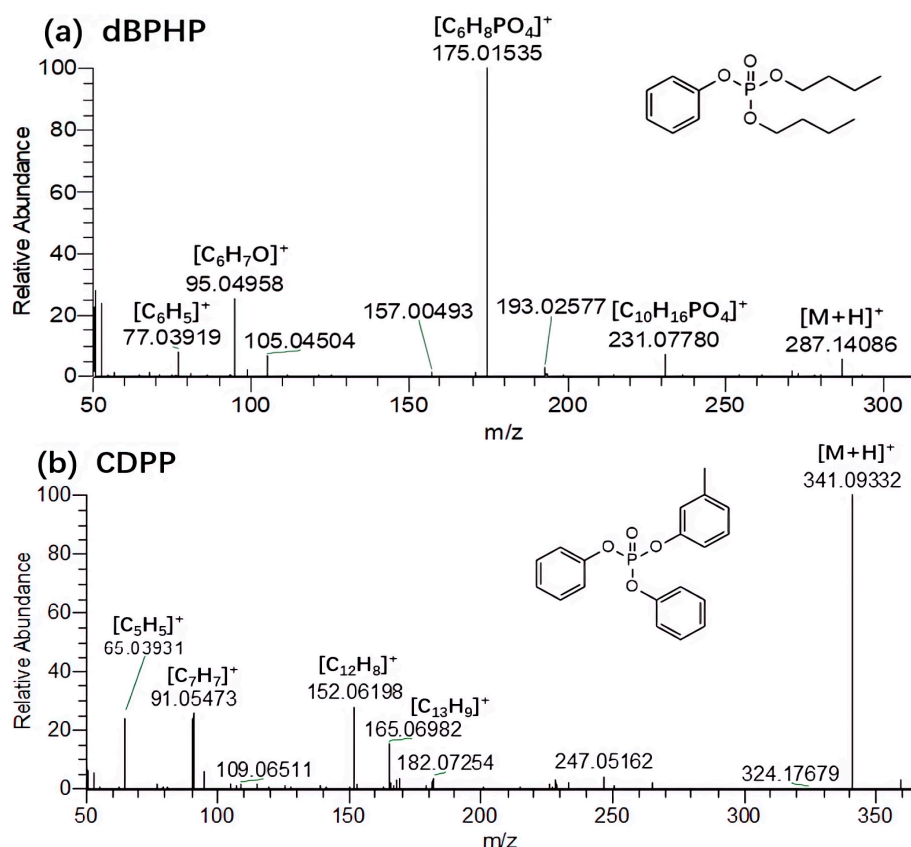


Figure 6. MS^2 spectra of two aromatic OPFR compounds.

2.2. Comparison with Fragmentation Pathways under the EI Source

The full MS spectra of OPFRs under the EI source are shown in Figures 7a and S6. This paper compared the precursor and fragment ions of OPFRs under the two instruments to study the differences in their ionization and fragmentation characteristics. It was found that after ESI ionization, alkyl and aromatic OPFRs would generate precursors $[M + H]^+$, while

some halogenated OPFRs would generate $[M + \text{NH}_4]^+$ in addition to $[M + \text{H}]^+$. This may be because the proton affinity of this compound is close to that of ammonium. $[M + \text{Na}]^+$ was found in the MS^1 spectrum of most OPFRs, usually due to impurities in the sample vial, liquid phase line, or solvent [26]. The ion clusters characteristic of the halogenated OPFRs made the $[M + \text{NH}_4]^+$ and $[M + \text{Na}]^+$ more prominent. The ionization voltage of the EI source was usually 70 eV, and the precursors were often fragmented by ionization. So, the precursor ion information could not be presented in the mass spectrum. By comparing the fragment ions under the two instruments, it was found that the fragmentation pathways of most alkyl and halogenated OPFRs were similar, and usually underwent McLafferty hydrogen rearrangement after generating precursors. $[M - \text{R} + 2\text{H}]^+$, $[M - 2\text{R} + 3\text{H}]^+$, $[M - 3\text{R} + 4\text{H}]^+$ fragment ions were formed after the chemical bond was cleaved. However, there were still significant differences in the ionization and fragmentation of some compounds between the two instruments, such as TMP (Figure 7), which followed the above rearrangement rules under the ESI ionization and HCD fragmentation, producing $[\text{C}_2\text{H}_8\text{PO}_4]^+$ ($m/z = 127.0156$), $[\text{CH}_6\text{PO}_4]^+$ ($m/z = 113.0001$), and $[\text{H}_4\text{PO}_4]^+$ ($m/z = 98.9846$) fragment ions. While under the EI ionization and fragmentation, TMP lost the methyl group by the C–O bond cleavage to form $[\text{CH}_3\text{PO}_4]^+$ ($m/z = 110.0124$) and $[\text{PO}_4]^+$ ($m/z = 94.9559$) fragment ions. For aromatic OPFRs, due to the relatively stable structure, precursor peaks could be observed in the fragmentation spectrum under the EI source. The characteristic fragment ion of OPFRs with a benzene ring as the substituent was $[\text{C}_6\text{H}_7\text{O}]^+$ ($m/z = 95.0495$) under the ESI ionization and HCD fragmentation, and $[\text{C}_6\text{H}_6\text{O}]^+$ ($m/z = 94.0409$) under the EI source; the OPFR compound whose substituent was toluene would produce characteristic fragment ions of $[\text{C}_7\text{H}_7]^+$ ($m/z = 91.0530$) and $[\text{C}_5\text{H}_5]^+$ ($m/z = 65.0393$) in both fragmentation modes.

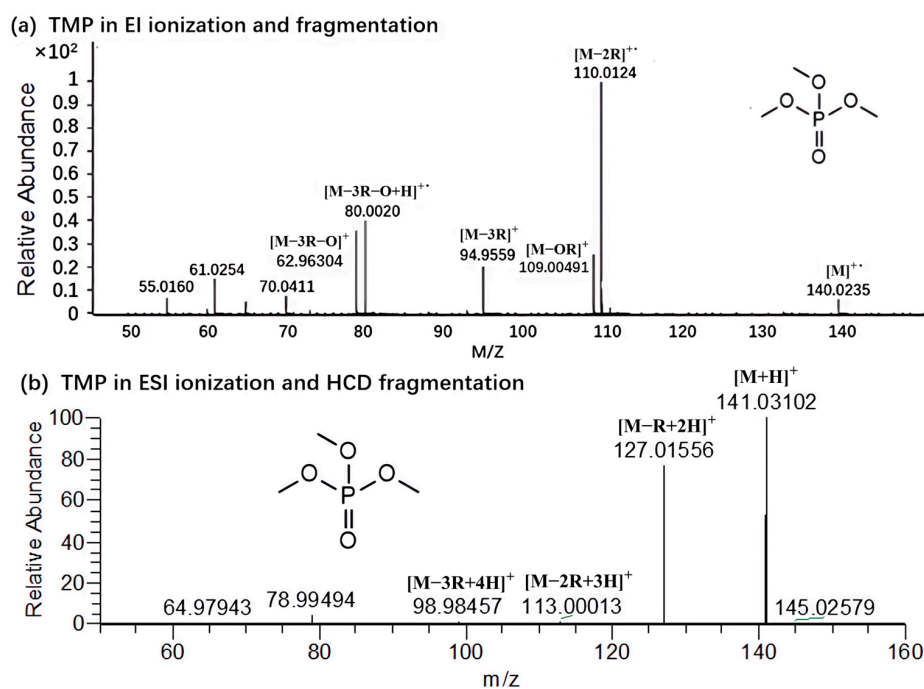


Figure 7. Mass spectra of TMP under two instruments.

In general, due to the different ionization methods and fragmentation principles, there will be some differences in the fragmentation pathways and fragment ions generated under the two instruments. The fragmentation spectrum of the EI source usually cannot display the precursor ion information, which makes some references missing in the screening process. However, this ion source is easy to use and obtains abundant fragment ions, often used to establish a standard spectrum. Compared with the EI ionization and fragmentation, the ESI ionization and HCD fragmentation have wider applicability. The soft ionization

method can retain the information of the precursor ions, acquire the accurate mass of the precursor ions in high-resolution mass spectrometry to achieve the accurate matching of molecular formulae, and combine with the HCD, which can be fragmented at different collision energies, to further confirm the structure of the compounds by fragment ions and provide a complete basis for the screening experiments. Although the ion fragmentation through the collision cell increases the complexity of the experimental operation, it is beneficial for the experimenter to discover more rules by adjusting the parameters. The comparison of the two instruments has greatly contributed to the target mass spectrum database, providing strong support for the screening of new pollutants.

2.3. Screening of Organophosphorus Flame Retardants in Actual Samples

Mass spectrometry information that can be used for qualitative analysis was obtained by exploring the fragmentation pathways of organophosphorus compounds under LC-HRMS, and in order to preliminarily verify the suitability of the relevant mass spectrometry information, an experiment was conducted to screen OPFR in rice samples under the same chromatographic and mass spectrometry conditions as those described in Section 3.2 in the text. Firstly, the target chromatographic peaks were extracted from the tested rice samples by the accurate mass of the precursor ions. Then, the extracted precursor ions were sent to the HCD collision cell for fragmentation, and the MS² spectrum was matched to the standard solution spectrum. Compounds with less than two characteristic fragmentation ions were identified as false positives and further analyzed based on the mass spectrometry information generated by fragmentation.

As shown in Figure 8, two undetermined compounds, TEP ($m/z = 183.0779$) and CDPP ($m/z = 341.0936$), were extracted from rice samples by the accurate mass of precursor ions. The four characteristic ions in the MS² spectrum of TEP are consistent with the standard solution spectrum, and the mass deviation of the characteristic ions is less than 5 ppm, with a relative abundance deviation of less than 20%, indicating the actual detected compound. However, according to the MS² spectrum, the undetermined CDPP cannot generate corresponding fragment ions in HCD, making it difficult to accurately identify. Even with the use of HRMS, screening based solely on the accurate mass of precursor ions may still result in some false positives. In order to make more accurate judgments, it is necessary to study the fragment pathways and fragment ions of compounds.

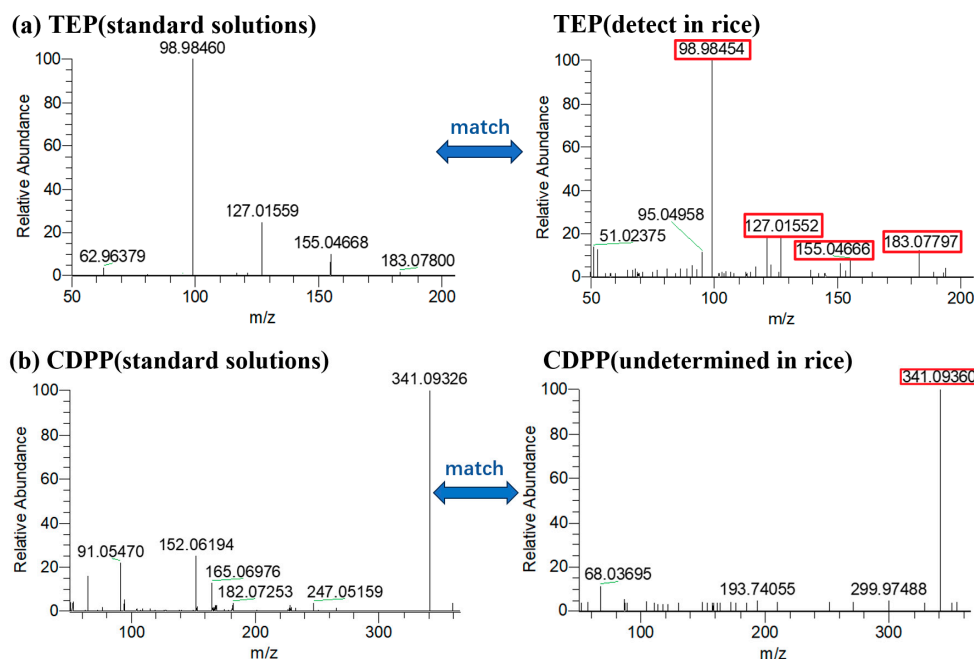


Figure 8. Matching of MS² spectra of (a) TEP and (b) CDPP in standard solutions and rice samples.

3. Materials and Methods

3.1. Main Materials and Reagents

Basic information on OPFRs is provided in Table 1. The structure of these OPFRs is shown in Figure S1 in the Supporting Information (SI). Standards of the 25 OPFRs were purchased from Chemservice (West Chester, PA, USA), Dr. Ehrenstorfer (Ausburg, Germany), BePure (Beijing, China), Sigma-Aldrich (Steinheim, Germany), or TRC Inc. (Ontario, ON, Canada). All solvents were HPLC grade: formic acid was purchased from ThermoFisher Scientific (Waltham, MA, USA), methanol (MeOH) was purchased from Merck (Darmstadt, Germany), ultrapure water was prepared with a Milli-Q system (Millipore, MA, USA). Primary secondary amine (PSA), octadecylsilane (C18), and zirconium dioxide-coated silica (Z-sep) were purchased from Sigma-Aldrich (Darmstadt, Germany). Magnesium sulfate (MgSO_4), sodium chloride (NaCl), disodium hydrogen citrate ($\text{C}_6\text{H}_6\text{Na}_2\text{O}_7$), and sodium citrate ($\text{C}_6\text{H}_5\text{Na}_3\text{O}_7$) were purchased from Agela Technologies (Torrance, CA, USA). Rice samples were collected from various regions in China (Dongbei, Hubei, and Guangxi) and stored in sealed containers at $-20\text{ }^\circ\text{C}$ until analysis.

3.2. Analytical Methods

These compounds were analyzed on Thermo Vanquish-Q Exactive Plus HRMS with an ESI source. Chromatographic separations were achieved on the Thermo Hypersil GOLD column ($100\text{ mm} \times 2.1\text{ mm}$, $1.9\text{ }\mu\text{m}$): $2\text{ }\mu\text{L}$ of the solution was injected at a flow rate of 0.25 mL/min and a column temperature of $30\text{ }^\circ\text{C}$. The mobile phase consisted of water (A) and methanol (B) (both with 0.01% formic acid and 5 mM ammonium formate). The LC gradient elution conditions were as follows: $0\text{--}1\text{ min}$ (1% B), $1\text{--}3\text{ min}$ ($1\text{--}39\%$ B), $3\text{--}14\text{ min}$ ($39\text{--}99\%$ B), $14\text{--}17\text{ min}$ (99% B), $17.1\text{--}21\text{ min}$ (1% B). The total run time was 21 min . Data acquisition was performed using the full mass-parallel reaction monitor (PRM) in positive mode with a mass range of m/z $100\text{--}1500$. MS^1 resolution was $70,000$, and MS^2 resolution was $35,000$. The step-collision energy (CE) of HCD was set to 10 , 40 , and 80 eV , and the spray voltage was set to 3 kV . The capillary temperature was $350\text{ }^\circ\text{C}$, the auxiliary gas heater temperature was $300\text{ }^\circ\text{C}$, the automatic gain control of the number of ions entering the orbitrap (AGC target) was 1×10^6 , and the maximum injection time was 100 ms .

The analysis of OPFR under EI source was performed by a GC-QTOF/MS system. Details of parameters and MS^2 spectra are given in Text S1 and Figure S6 of the Supplementary Materials.

3.3. Sample Preparation and Pretreatment

Stock standard solutions of OPFRs were prepared in methanol in amber vials, and working standard solutions of lower concentrations were obtained by serial dilution with methanol. All standard solutions were stored at $4\text{ }^\circ\text{C}$.

The rice samples were ground to a powder. Then, 10 mL of an acetonitrile solution containing 0.5% formic acid was added to 1 g of the sample. After that, 4 g of MgSO_4 , 1 g of NaCl, 0.5 g of $\text{C}_6\text{H}_6\text{Na}_2\text{O}_7$, and 1 g of $\text{C}_6\text{H}_5\text{Na}_3\text{O}_7$ were added. The mixture was shaken well and ultrasonicated for 5 min in a water bath. The mixture was vortexed for 1 min and centrifuged at $10,000\text{ rpm}$ for 5 min . The supernatant was extracted and transferred to a centrifuge tube containing 50 mg of PSA, 50 mg of C18, and 150 mg of MgSO_4 . The mixture was vortexed for 1 min and centrifuged at $10,000\text{ rpm}$ for 5 min . The supernatant was filtered with a PTFE membrane ($0.22\text{ }\mu\text{m}$) and dried under mild nitrogen. After the solution was reconstituted with 1 mL of methanol and centrifuged at $10,000\text{ rpm}$ for 5 min , 0.8 mL of the supernatant was taken for analysis.

4. Conclusions

In this study, the LC-HRMS method was used to investigate the fragmentation laws of 25 OPFR compounds, which were divided into three types: alkyl, halogenated, and aromatic. Each compound's fragmentation pathways and characteristic fragment ions were analyzed to provide a basis for results processing during the screening process. It was found

that the collision stability of alkyl OPFRs was the worst, followed by halogenated OPFRs and aromatic OPFRs. In terms of characteristic fragment ions, both alkyl and halogenated types could form structurally stable $[\text{H}_4\text{PO}_4]^+$ ($m/z = 98.9845$) ions, but aromatic OPFRs produced characteristic fragment ions such as $[\text{C}_6\text{H}_8\text{PO}_4]^+$ ($m/z = 175.0155$), $[\text{C}_{12}\text{H}_{12}\text{PO}_4]^+$ ($m/z = 251.0465$), and $[\text{C}_{12}\text{H}_8]^+$ ($m/z = 152.0620$) according to different substituents. These characteristic fragment ions provide identification signals in follow-up screening work and theoretical references for the rapid recognition of OPFRs' targets. Through the analysis of several isomers, it was found that in alkyl OPFR compounds, the relative abundance ratio of $[\text{M} - 3\text{R} + 4\text{H}]^+$ to $[\text{M} - 2\text{R} + 3\text{H}]^+$ fragment ions produced by compounds with branched substituents was higher, which was about 6:1. In contrast, the ratio of $[\text{M} - 3\text{R} + 4\text{H}]^+$ to $[\text{M} - 2\text{R} + 3\text{H}]^+$ fragment ions with straight substituents was lower, about 2:1. This ratio can be used as an index to distinguish several kinds of isomers in the subsequent screening process, assist in judging the structural types of substituents, and make more detailed qualitative analysis of the compounds found. The application of OPFRs' fragmentation laws in food and environmental samples will be further investigated to expand the scope of our research in the future.

Supplementary Materials: The following supporting information can be downloaded at: <https://www.mdpi.com/article/10.3390/molecules29030680/s1>, Figure S1: The structure of 25 OPFRs; Figures S2–S4: MS² spectrums of OPFRs under the ESI source; Figure S5: MS¹ spectra of TDCIPP and T23DBPP; Text S1: Instrument parameter details under the EI source; Figure S6: MS² spectrums of OPFRs under the EI source.

Author Contributions: Formal analysis, writing—original draft preparation, K.L.; data curation, K.L. and Y.Z.; writing—review and editing, X.L.; validation, B.Z. and Y.G.; conceptualization, methodology, X.L. and Q.Z.; All authors have read and agreed to the published version of the manuscript.

Funding: This work was supported by the National Key Research and Development Program of China (2022YFF0710404); the National R&D Infrastructure and Facility Development Program of China (APT2201-5); the National Natural Science Foundation of China (22006145); and the Fundamental Research Funds for Central Public Welfare Scientific Research Institutes (AKYJJ2102).

Institutional Review Board Statement: Not applicable.

Informed Consent Statement: Not applicable.

Data Availability Statement: The data presented in this study are available in article and Supplementary Materials.

Conflicts of Interest: The authors declare no conflicts of interest.

References



- Davidson, D.J.; McKay, A.P.; Cordes, D.B.; Woollins, J.D.; Westwood, N.J. The Covalent Linking of Organophosphorus Heterocycles to Date Palm Wood-Derived Lignin: Hunting for New Materials with Flame-Retardant Potential. *Molecules* **2023**, *28*, 7885. [CrossRef]
- Chen, C.; Wang, X.; Luo, T.; Zhen, H.; Yang, X.; Yang, L.; Yan, Z. Synthesis of solid reactive organophosphorus-nitrogen flame retardant and its application in epoxy resin. *J. Appl. Polym. Sci.* **2023**, *140*, e54282. [CrossRef]
- Konstantinova, A.; Yudaev, P.; Orlov, A.; Loban, O.; Lukashov, N.; Chistyakov, E. Aryloxyphosphazene-Modified and Graphite-Filled Epoxy Compositions with Reduced Flammability and Electrically Conductive Properties. *J. Compos. Sci.* **2023**, *7*, 417. [CrossRef]
- Zhong, M.; Wang, T.; Qi, C.; Peng, G.; Lu, M.; Huang, J.; Yu, G. Automated online solid-phase extraction liquid chromatography tandem mass spectrometry investigation for simultaneous quantification of per-and polyfluoroalkyl substances, pharmaceuticals and personal care products, and organophosphorus flame retardants in environmental waters. *J. Chromatogr. A* **2019**, *1602*, 350–358. [CrossRef]
- Vykoukalová, M.; Venier, M.; Vojta, Š.; Melymuk, L.; Bečanová, J.; Romanak, K.; Klánová, J. Organophosphate esters flame retardants in the indoor environment. *Environ. Int.* **2017**, *106*, 97–104. [CrossRef]
- Liu, S.L.; Zhang, H.; Hu, X.H.; Qiu, Y.L.; Zhu, Z.L.; Zhao, J.F. Analysis of organophosphate esters in sediment samples using gas chromatography-tandem mass spectrometry. *Chin. J. Anal. Chem.* **2016**, *44*, 192–197. [CrossRef]

7. Zhao, L.; Jian, K.; Su, H.; Zhang, Y.; Li, J.; Letcher, R.J.; Su, G. Organophosphate esters (OPEs) in Chinese foodstuffs: Dietary intake estimation via a market basket method, and suspect screening using high-resolution mass spectrometry. *Environ. Int.* **2019**, *128*, 343–352. [CrossRef]
8. Du, J.; Li, H.; Xu, S.; Zhou, Q.; Jin, M.; Tang, J. A review of organophosphorus flame retardants (OPFRs): Occurrence, bioaccumulation, toxicity, and organism exposure. *Environ. Sci. Pollut. Res.* **2019**, *26*, 22126–22136. [CrossRef] [PubMed]
9. Ding, J.; Deng, T.; Xu, M.; Wang, S.; Yang, F. Residuals of organophosphate esters in foodstuffs and implication for human exposure. *Environ. Pollut.* **2018**, *233*, 986–991. [CrossRef] [PubMed]
10. Zheng, X.B.; Wu, J.P.; Luo, X.J.; Zeng, Y.H.; She, Y.Z.; Mai, B.X. Halogenated flame retardants in home-produced eggs from an electronic waste recycling region in South China: Levels, composition profiles, and human dietary exposure assessment. *Environ. Int.* **2012**, *45*, 122–128. [CrossRef] [PubMed]
11. Santín, G.; Eljarrat, E.; Barceló, D. Simultaneous determination of 16 organophosphorus flame retardants and plasticizers in fish by liquid chromatography-tandem mass spectrometry. *J. Chromatogr. A* **2016**, *1441*, 34–43. [CrossRef]
12. Li, J.; Zhao, L.; Letcher, R.J.; Zhang, Y.; Jian, K.; Zhang, J.; Su, G. A review on organophosphate Ester (OPE) flame retardants and plasticizers in foodstuffs: Levels, distribution, human dietary exposure, and future directions. *Environ. Int.* **2019**, *127*, 35–51. [CrossRef]
13. Poma, G.; Sales, C.; Bruyland, B.; Christia, C.; Goscinny, S.; Van Loco, J.; Covaci, A. Occurrence of organophosphorus flame retardants and plasticizers (PFRs) in Belgian foodstuffs and estimation of the dietary exposure of the adult population. *Environ. Sci. Technol.* **2018**, *52*, 2331–2338. [CrossRef] [PubMed]
14. Kim, J.W.; Isobe, T.; Muto, M.; Tue, N.M.; Katsura, K.; Malarvannan, G.; Tanabe, S. Organophosphorus flame retardants (PFRs) in human breast milk from several Asian countries. *Chemosphere* **2014**, *116*, 91–97. [CrossRef] [PubMed]
15. Fang, H.; Tong, W.; Branham, W.S.; Moland, C.L.; Dial, S.L.; Hong, H.; Sheehan, D.M. Study of 202 natural, synthetic, and environmental chemicals for binding to the androgen receptor. *Chem. Res. Toxicol.* **2003**, *16*, 1338–1358. [CrossRef] [PubMed]
16. Dishaw, L.V.; Powers, C.M.; Ryde, I.T.; Roberts, S.C.; Seidler, F.J.; Slotkin, T.A.; Stapleton, H.M. Is the PentaBDE replacement, tris (1,3-dichloro-2-propyl) phosphate (TDCPP), a developmental neurotoxicant? Studies in PC12 cells. *Toxicol. Appl. Pharm.* **2011**, *256*, 281–289. [CrossRef] [PubMed]
17. Tokumura, M.; Miyake, Y.; Wang, Q.; Nakayama, H.; Amagai, T.; Ogo, S.; Ogawa, K. Methods for the Analysis of Organophosphorus Flame Retardants—Comparison of GC-EI-MS, GC-NCI-MS, LC-ESI-MS/MS, and LC-APCI-MS/MS. *J. Environ. Sci. Health Part A* **2018**, *53*, 475–481. [CrossRef]
18. Xu, F.; García-Bermejo, Á.; Malarvannan, G.; Gómara, B.; Neels, H.; Covaci, A. Multi-contaminant analysis of organophosphate and halogenated flame retardants in food matrices using ultrasonication and vacuum assisted extraction, multi-stage cleanup and gas chromatography–mass spectrometry. *J. Chromatogr. A* **2015**, *1401*, 33–41. [CrossRef]
19. Chen, D.; Letcher, R.J.; Chu, S. Determination of non-halogenated, chlorinated and brominated organophosphate flame retardants in herring gull eggs based on liquid chromatography–tandem quadrupole mass spectrometry. *J. Chromatogr. A* **2012**, *1220*, 169–174. [CrossRef]
20. Huang, J.; Ye, L.; Fang, M.; Su, G. Industrial production of organophosphate flame retardants (OPFRs): Big knowledge gaps need to be filled? *Bull. Environ. Contam. Toxicol.* **2022**, *108*, 809–818. [CrossRef]
21. Van der Veen, I.; de Boer, J. Phosphorus flame retardants: Properties, production, environmental occurrence, toxicity and analysis. *Chemosphere* **2012**, *88*, 1119–1153. [CrossRef]
22. Lesage, D.; Virelizier, H.; Tabet, J.C.; Jankowski, C.K. Study of mass spectrometric fragmentations of tributyl phosphate via collision-induced dissociation. *Rapid Commun. Mass. Sp.* **2001**, *15*, 1947–1956. [CrossRef]
23. Ma, Y.; Hites, R.A. Electron impact, electron capture negative ionization and positive chemical ionization mass spectra of organophosphorus flame retardants and plasticizers. *J. Mass. Spectrom.* **2013**, *48*, 931–936. [CrossRef] [PubMed]
24. Yang, J.S.; Zhang, Q.H.; Su, L.Q. Fragmentation mechanism of organic phosphorus flame retardant by gas chromatography–quadrupole time of flight mass spectrometry. *J. Mass. Spectrom.* **2019**, *42*, 36–47. [CrossRef]
25. Ye, L.; Meng, W.; Huang, J.; Li, J.; Su, G. Establishment of a target, suspect, and functional group-dependent screening strategy for organophosphate esters (OPEs): “Into the Unknown” of OPEs in the sediment of Taihu Lake, China. *Environ. Sci. Technol.* **2021**, *55*, 5836–5847. [CrossRef]
26. Kostianen, R.; Kauppila, T.J. Effect of eluent on the ionization process in liquid chromatography–mass spectrometry. *J. Chromatogr. A* **2009**, *1216*, 685–699. [CrossRef]

Disclaimer/Publisher’s Note: The statements, opinions and data contained in all publications are solely those of the individual author(s) and contributor(s) and not of MDPI and/or the editor(s). MDPI and/or the editor(s) disclaim responsibility for any injury to people or property resulting from any ideas, methods, instructions or products referred to in the content.

Article

Comprehensive Investigation of Ginsenosides in the Steamed *Panax quinquefolius* with Different Processing Conditions Using LC-MS

Jiali Fan ^{1,2}, Feng Liu ^{1,2}, Wenhua Ji ^{1,2}, Xiao Wang ^{1,2}  and Lili Li ^{1,2,*} 

¹ Key Laboratory for Applied Technology of Sophisticated Analytical Instruments of Shandong Province, Shandong Analysis and Test Center, Qilu University of Technology (Shandong Academy of Sciences), Jinan 250014, China; 17731638714@163.com (J.F.); liufeng8109@163.com (F.L.); jwh519@163.com (W.J.); wangx@sdas.org (X.W.)

² School of Pharmaceutical Sciences, Qilu University of Technology (Shandong Academy of Sciences), Jinan 250014, China

* Correspondence: liliouc@126.com; Tel./Fax: +86-531-82605319

Abstract: *Panax quinquefolius* (PQ) has been widely used in traditional Chinese medicine and functional food. Ginsenosides are the important functional components of PQ. The ginsenosides' diversity is deeply affected by the processing conditions. The ginsenosides in the steamed PQ have been not well-characterized yet because of the complexity of their structure. In the study, the comprehensive investigation of ginsenosides was performed on the steamed PQ with different steaming times and temperatures by UPLC-Q-TOF-MS. Based on the molecular weight, retention time and characterized fragment ions, 175 ginsenosides were unambiguously identified or tentatively characterized, including 45 protopanaxatriol type, 49 protopanaxadiol type, 19 ocellolol type, 6 oleanolic acid type ginsenosides, and 56 other ginsenosides. Ten new ginsenosides and three new aglycones were discovered in the steamed PQ samples through searching the database of CAS SciFinderⁿ. Principal component analysis showed the significant influence on the chemical components of PQ through different processing conditions. The steaming temperature was found to promote the transformation of ginsenosides more than the steaming time. The protoginsenosides were found to transform into the rare ginsenosides by elimination reactions. The malonyl ginsenosides were degraded into acetyl ginsenosides, and then degraded into neutral ginsenosides. The sugar chain experienced degradation, with position changes and configuration inversions. Furthermore, 20 (*S/R*)-ginsenoside Rh1, Rh2, Rg2, and Rh12 were found to transform from the *S*-configuration to the *R*-configuration significantly. This study could present a comprehensive ginsenosides profile of PQ with different steaming conditions, and provide technical support for the development and utilization of PQ.

Keywords: steamed *Panax quinquefolius*; ginsenosides; identification; processing; LC-MS



Citation: Fan, J.; Liu, F.; Ji, W.; Wang, X.; Li, L. Comprehensive Investigation of Ginsenosides in the Steamed *Panax quinquefolius* with Different Processing Conditions Using LC-MS. *Molecules* **2024**, *29*, 623. <https://doi.org/10.3390/molecules29030623>

Academic Editors: Xianjiang Li and Wen Ma

Received: 31 December 2023

Revised: 24 January 2024

Accepted: 25 January 2024

Published: 28 January 2024



Copyright: © 2024 by the authors. Licensee MDPI, Basel, Switzerland. This article is an open access article distributed under the terms and conditions of the Creative Commons Attribution (CC BY) license (<https://creativecommons.org/licenses/by/4.0/>).

1. Introduction

Panax quinquefolius (PQ) belongs to the genus *Panax* in the family Araliaceae. It has been widely used in traditional Chinese medicine, dietary supplements, and functional food [1,2]. It is native to the south of Canada and the northern USA, and has been widely planted in China. In vivo and in vitro studies have shown that PQ has many biological activities, including antioxidative, antidiabetic, anti-inflammatory, anti-cancer, etc., [3,4]. It has been demonstrated to have a positive impact on the treatment of various diseases such as in the central nervous system, endocrine system, cardiovascular system, as well as cancer [5]. In particular, PQ has unique advantages in treating chronic diseases because of its better compatibility with the human body and fewer side effects [3]. It was found that steamed PQ has been reported to exhibit enhanced antiproliferative activity and antioxidant capacity [6,7]. PQ contains many chemical components, including ginsenosides,

polyacetylenes, polyphenolic compounds, etc. Ginsenosides are the most important active ingredients [8,9]. More than 500 ginsenosides have been discovered from *Panax* species [10], but only a few have been characterized in the steamed PQ samples. A comprehensive investigation of ginsenosides is essential for the further development and utilization of the steamed PQ.

Based on the structure difference of the aglycone, ginsenosides are divided into protopanaxadiol (PPD-type), protopanaxatriol (PPT-type), octillol (OT-type), oleanolic (OA-type), and other types [11]. OT-type ginsenosides are characteristic in the PQ, differing from other *Panax* species [12]. The ginsenosides Rb1, Rb2, Rc, Rd, Re, and Rg1 are generally considered as the main protoginsenosides. Protoginsenosides have a larger molecular structure that is difficult to be absorbed by the human body, whereas less-polar ginsenosides are easily absorbed by the intestinal microflora [13,14]. These ginsenosides are called rare ginsenosides, and they have been found to have special pharmacological activities [15]. Compared to ginsenoside Rb1, ginsenoside Rg5 has been demonstrated to have stronger antiproliferative activity against breast cancer [16,17]. Ginsenoside Rh4 has been reported to have anti-esophageal cancer effects through inhibiting aerobic glycolysis [18,19]. Rare ginsenosides can be prepared by physical, chemical, and biological methods [20]. The chemical method has usually the disadvantage of a long reaction time and the production of byproducts. The biotransformation of rare ginsenosides needs to solve the problems of low specific activities, unidentified enzymes, and uncovered catalytic mechanisms [21]. The physical method commonly refers to the steaming method. It is a green and efficient method to regulate the transformation of ginsenosides [22]. Ginsenosides undergo chemical modifications and generate rare ginsenosides during the steaming process [23]. There have been several reports on steamed PQ. Twelve ginsenosides were determined in the roots of steamed PQ, and the anticancer activities of the extract from roots steamed for 2 h were greater than 1 h [24]. Twenty-nine major ginsenosides have been studied in the multi-steamed PQ samples and a possible chemical conversion was deduced [25]. Fifty-nine ginsenosides of PPT, PPD, OA, and OT types have been analyzed in PQ with different steaming processes [26]. However, a few known ginsenosides cannot meet the needs of holistic studies or the discovery of chemical markers in the PQ steaming process [27]. Further studies of the steam processing mechanism will be of great significance for the rational utilization of PQ.

The development of analytical technologies has made it possible for an holistic study. LC-MS has been widely used in secondary metabolite analysis for its high sensitivity and high throughput, such as for flavonoids, phenolic acids, and ginsenosides [28,29]. In the study, ginsenosides profiling has been established for the steamed PQ samples based on LC-MS. The in-depth identification of PQ was performed, the aglycone and the sugar chains were annotated, and new ginsenosides were discovered. The structure and content changes of the ginsenosides were analyzed with the different steaming processes, and the transformation mechanisms of ginsenosides were further investigated. The study could present the comprehensive ginsenoside profiling of steamed PQ with different times and temperatures.

2. Results and Discussion

2.1. Identification of Ginsenosides in PQ Samples

The total ion chromatogram of the PQ sample with LC-MS is shown in Figure 1. For ginsenosides, there were specific fragmentation rules in the MS/MS analysis [30]. The identification of ginsenosides was based on the accurate molecular weight, retention time, and MS/MS fragment ions. With different collision energies in the MS/MS analysis, ginsenosides were fragmented into aglycone and sugar chains. Characterized aglycone ions, sugar chain ions, and the neutral loss of sugar chains were found. For the PPT-, PPD-, OT-, or OA-type, the characterized aglycone ions were 475, 459, 491, and 455 (m/z), respectively. The chemical structures of the PPT-, PPD-, OT-, or OA-type aglycones are shown in Figure 2. The aglycone ions of other types of ginsenosides were complicated and varied. The charac-

teristic ions for different sugar chains of *O*-glucose, *O*-rhamnose, *O*-xylose/arabinose, *O*-glucose-glucose, *O*-glucose-rhamnose, and *O*-glucose-xylose/arabinose were 161, 145, 131, 221/323, 205/307, and 191/293, respectively. In addition, acetyl and malonyl ginsenosides were characterized as having a neutral loss of 42 and 86. Then, a total of 175 ginsenosides were identified from the extracts of the PQ samples, which included 45 PPT-type, 49 PPD-type, 19 OT-type, 6 OA-type ginsenosides, and 56 other ginsenosides. The ginsenosides were then validated with the standards available. The detailed molecular weight, retention time, aglycone, sugar chains, and MS/MS fragment ions of the ginsenosides are listed in Table 1.

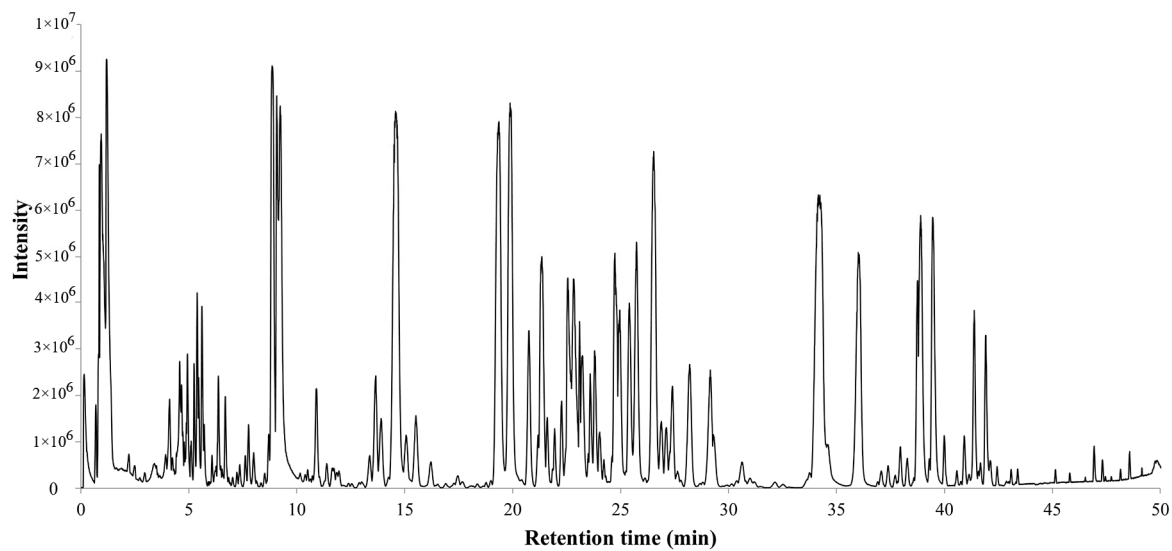


Figure 1. Total ion chromatogram of steamed PQ with LC-MS in the negative ion mode.

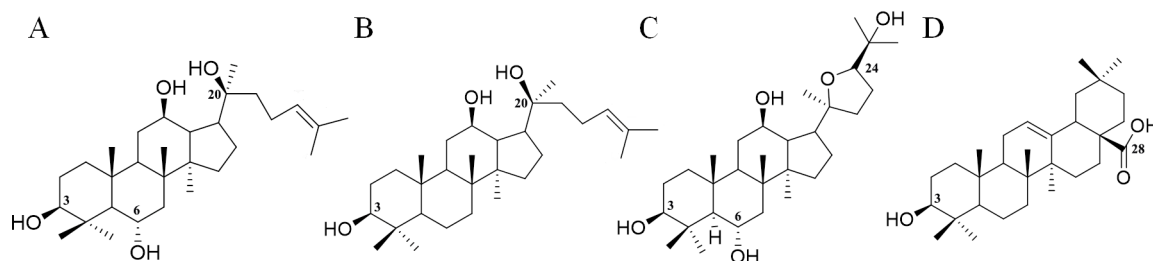


Figure 2. The chemical structures of PPT- (A), PPD- (B), OT- (C), and OA- (D) type aglycones. Numbers represent the typical glycosylation sites.

Table 1. Ginsenosides identified in the steamed PQ samples.

No.	<i>m/z</i>	<i>t_R</i> /min	Ion Adducts	Formula	Aglycone	Sugar Chains	Proposed Name	Type
1	793.4388	29.4	[M – H] [–]	C ₄₂ H ₆₆ O ₁₄	455	<i>O</i> -176/ <i>O</i> -162	Chikusetsusaponin Iva	OA
2	793.4388	33.8	[M – H] [–]	C ₄₂ H ₆₆ O ₁₄	455	<i>O</i> -162/ <i>O</i> -176	Chikusetsusaponin Iva isomer I	OA
3	793.4388	24.1	[M – H] [–]	C ₄₂ H ₆₆ O ₁₄	455	<i>O</i> -176-162	Zingibroside R1	OA
4	955.4896	22.3	[M – H] [–]	C ₄₈ H ₇₆ O ₁₉	455	<i>O</i> -162-162/ <i>O</i> -176	Ginsenoside Ro isomer	OA
5	955.4896	21.4	[M – H] [–]	C ₄₈ H ₇₆ O ₁₉	455	<i>O</i> -176-162/ <i>O</i> -162	Ginsenoside Ro *	OA
6	663.4108	39.8	[M + HCOO] [–]	C ₃₆ H ₅₈ O ₈	455	<i>O</i> -162	OA- <i>O</i> -glc	OA
7	699.4323	12.2	[M + HCOO] [–]	C ₃₆ H ₆₂ O ₁₀	491	<i>O</i> -162	Pseudoginsenoside Rt4 isomer I	OT
8	699.4323	15.2	[M + HCOO] [–]	C ₃₆ H ₆₂ O ₁₀	491	<i>O</i> -162	Pseudoginsenoside Rt4 isomer II	OT
9	699.4323	11.1	[M + HCOO] [–]	C ₃₆ H ₆₂ O ₁₀	491	<i>O</i> -162	Pseudoginsenoside Rt4	OT
10	785.4693	14.0	[M – H] [–]	C ₄₁ H ₇₀ O ₁₄	491	<i>O</i> -162/ <i>O</i> -132	Presudoginsenoside FT2	OT

Table 1. Cont.

No.	<i>m/z</i>	<i>t_R</i> /min	Ion Adducts	Formula	Aglycone	Sugar Chains	Proposed Name	Type
11	825.4634	26.1	[M + HCOO] [−]	C ₄₂ H ₆₈ O ₁₃	455	O-162-162	OA-O-glc-glc	OT
12	831.4743	13.8	[M + HCOO] [−]	C ₄₁ H ₇₀ O ₁₄	491	O-162-132	Majonoside R2	OT
13	831.4743	10.4	[M + HCOO] [−]	C ₄₁ H ₇₀ O ₁₄	491	O-162-132	Pseudoginsenoside Rt2	OT
14	845.4900	9.3	[M + HCOO] [−]	C ₄₂ H ₇₂ O ₁₄	491	O-162-146	Pseudoginsenoside F11 isomer III	OT
15	845.4900	11.0	[M + HCOO] [−]	C ₄₂ H ₇₂ O ₁₄	491	O-162-146	Pseudoginsenoside F11 isomer I	OT
16	845.4900	12.0	[M + HCOO] [−]	C ₄₂ H ₇₂ O ₁₄	491	O-162-146	Pseudoginsenoside F11 isomer II	OT
17	845.4900	15.0	[M + HCOO] [−]	C ₄₂ H ₇₂ O ₁₄	491	O-162-146	24(R)-Pseudoginsenoside F11	OT
18	845.4900	14.7	[M + HCOO] [−]	C ₄₂ H ₇₂ O ₁₄	491	O-162-146	24(S)-Pseudoginsenoside F11 *	OT
19	861.4845	11.7	[M + HCOO] [−]	C ₄₂ H ₇₂ O ₁₅	491	O-162-162	Majonoside R1	OT
20	861.4845	6.4	[M + HCOO] [−]	C ₄₂ H ₇₂ O ₁₅	491	O-162/O-162	Majonoside R1 isomer	OT
21	885.4851	17.8	[M − H] [−]	C ₄₅ H ₇₄ O ₁₇	491	O-162-146	Malonyl-Pseudoginsenoside F11	OT
22	887.4991	21.2	[M + HCOO] [−]	C ₄₄ H ₇₄ O ₁₅	491	O-162-146	24(R)-Vinaginsenoside R1	OT
23	887.4991	20.6	[M + HCOO] [−]	C ₄₄ H ₇₄ O ₁₅	491	O-162-146	24(S)-Vinaginsenoside R1	OT
24	977.5322	7.2	[M + HCOO] [−]	C ₄₇ H ₈₀ O ₁₈	491	O-132/O-162-146	OT-O-glc-rha-/O-xyl/ara	OT
25	815.4793	19.8	[M + HCOO] [−]	C ₄₁ H ₇₀ O ₁₃	491	O-146/O-132	OT-O-rha-xyl/ara	OT
26	667.4426	41.6	[M + HCOO] [−]	C ₃₆ H ₆₂ O ₈	459	O-162	20(R)-Ginsenoside Rh2 *	PPD
27	667.4426	40.9	[M + HCOO] [−]	C ₃₆ H ₆₂ O ₈	459	O-162	20(S)-Ginsenoside Rh2 *	PPD
28	799.4845	37.8	[M + HCOO] [−]	C ₄₁ H ₇₀ O ₁₂	459	O-162-132	20(S)-Gypenoside XIII	PPD
29	799.4845	38.6	[M + HCOO] [−]	C ₄₁ H ₇₀ O ₁₂	459	O-162-132	20(R)-Gypenoside XIII	PPD
30	829.4943	34.1	[M + HCOO] [−]	C ₄₂ H ₇₂ O ₁₃	459	O-162-162	20(S)-Ginsenoside Rg3 *	PPD
31	829.4943	34.6	[M + HCOO] [−]	C ₄₂ H ₇₂ O ₁₃	459	O-162-162	20(R)-Ginsenoside Rg3 *	PPD
32	829.4943	37.5	[M + HCOO] [−]	C ₄₂ H ₇₂ O ₁₃	459	O-162-162	Ginsenoside Rg3 isomer II	PPD
33	829.4943	36.2	[M + HCOO] [−]	C ₄₂ H ₇₂ O ₁₃	459	O-162-162	Ginsenoside Rg3 isomer I	PPD
34	829.4943	27.6	[M + HCOO] [−]	C ₄₂ H ₇₂ O ₁₃	459	O-162-162	Ginsenoside Rg3 isomer III	PPD
35	869.489	35.8	[M − H] [−]	C ₄₅ H ₇₄ O ₁₆	459	O-162-162	Malonyl-Ginsenoside Rg3	PPD
36	869.489	37.1	[M − H] [−]	C ₄₅ H ₇₄ O ₁₆	459	O-162-162	Malonyl-Ginsenoside Rg3 isomer I	PPD
37	869.489	37.5	[M − H] [−]	C ₄₅ H ₇₄ O ₁₆	459	O-162-162	Malonyl-Ginsenoside Rg3 isomer II	PPD
38	871.5054	38.0	[M + HCOO] [−]	C ₄₄ H ₇₄ O ₁₄	459	O-162-162	Acetyl-Ginsenoside Rg3	PPD
39	961.5385	30.9	[M + HCOO] [−]	C ₄₇ H ₈₀ O ₁₇	459	O-162-132/O-162	Gypenoside IX	PPD
40	961.5385	29.2	[M + HCOO] [−]	C ₄₇ H ₈₀ O ₁₇	459	O-162-132/O-162	Notoginsenoside Fe	PPD
41	961.5385	30.3	[M + HCOO] [−]	C ₄₇ H ₈₀ O ₁₇	459	O-162-132/O-162	Saponin Ia	PPD
42	961.5385	27.2	[M + HCOO] [−]	C ₄₇ H ₈₀ O ₁₇	459	O-162-162/O-132	Vinaginsenoside R17	PPD
43	991.5466	25.2	[M + HCOO] [−]	C ₄₈ H ₈₂ O ₁₈	459	O-162-162/O-162	Gypenoside XVII	PPD
44	991.5466	24.7	[M + HCOO] [−]	C ₄₈ H ₈₂ O ₁₈	459	O-162/O-162-162	Ginsenoside Rd *	PPD
45	1031.5432	26.0	[M − H] [−]	C ₅₁ H ₈₄ O ₂₁	459	O-162-162/O-162	Malonyl-Ginsenoside Rd	PPD
46	1031.5432	27.2	[M − H] [−]	C ₅₁ H ₈₄ O ₂₁	459	O-162-162/O-162	Malonyl-Ginsenoside Rd isomer I	PPD
47	1031.5432	25.6	[M − H] [−]	C ₅₁ H ₈₄ O ₂₁	459	O-162-162/O-162	Malonyl-Ginsenoside Rd isomer II	PPD
48	1031.5432	28.3	[M − H] [−]	C ₅₁ H ₈₄ O ₂₁	459	O-162-162/O-162	Malonyl-Ginsenoside Rd isomer III	PPD
49	1033.5566	30.8	[M + HCOO] [−]	C ₅₀ H ₈₄ O ₁₉	459	O-162-162/O-162	Acetyl-Ginsenoside Rd isomer II	PPD
50	1033.5566	34.0	[M + HCOO] [−]	C ₅₀ H ₈₄ O ₁₉	459	O-162-162/O-162	Acetyl-Ginsenoside Rd isomer I	PPD
51	1033.5566	29.3	[M + HCOO] [−]	C ₅₀ H ₈₄ O ₁₉	459	O-162-162/O-162	Acetyl-Ginsenoside Rd	PPD
52	1107.5945	22.6	[M − H] [−]	C ₅₄ H ₉₂ O ₂₃	459	O-162-162/O-162-162	Ginsenoside Rb1 *	PPD
53	1107.5945	22.9	[M − H] [−]	C ₅₄ H ₉₂ O ₂₃	459	O-162-162/O-162-162	Ginsenoside Rb1 isomer I	PPD
54	1123.5897	23.3	[M + HCOO] [−]	C ₅₃ H ₉₀ O ₂₂	459	O-162-132/O-162-162	Ginsenoside Rb3	PPD
55	1123.5897	23.6	[M + HCOO] [−]	C ₅₃ H ₉₀ O ₂₂	459	O-162-132/O-162-162	Ginsenoside Rc	PPD
56	1123.5897	23.9	[M + HCOO] [−]	C ₅₃ H ₉₀ O ₂₂	459	O-162-132/O-162-162	Ginsenoside Rb2 *	PPD
57	1137.6053	24.0	[M + HCOO] [−]	C ₅₄ H ₉₂ O ₂₂	459	O-162-162/O-162-146	PPD-O-glc-glc/O-glc-rha	PPD
58	1163.5850	24.4	[M − H] [−]	C ₅₆ H ₉₂ O ₂₅	459	O-162-162/O-162-132	Malonyl-Ginsenoside Rb2	PPD
59	1163.5850	23.7	[M − H] [−]	C ₅₆ H ₉₂ O ₂₅	459	O-162-162/O-162-132	Malonyl-Ginsenoside Rb3	PPD
60	1163.5850	24.2	[M − H] [−]	C ₅₆ H ₉₂ O ₂₅	459	O-162-162/O-162-132	Malonyl-Ginsenoside Rc	PPD
61	1163.5850	24.7	[M − H] [−]	C ₅₆ H ₉₂ O ₂₅	459	O-162-162/O-162-132	Malonyl-Ginsenoside Rb2 isomer	PPD
62	1165.5992	27.0	[M + HCOO] [−]	C ₅₅ H ₉₂ O ₂₃	459	O-162-162/O-162-132	Acetyl-Ginsenoside Rc	PPD
63	1165.5992	25.9	[M + HCOO] [−]	C ₅₅ H ₉₂ O ₂₃	459	O-162-162/O-162-132	Acetyl-Ginsenoside Rb3	PPD

Table 1. Cont.

No.	<i>m/z</i>	<i>t_R</i> /min	Ion Adducts	Formula	Aglycone	Sugar Chains	Proposed Name	Type
64	1165.5992	30.0	[M + HCOO] [−]	C ₅₅ H ₉₂ O ₂₃	459	O-162-162/O-162-132	Acetyl-Ginsenoside Rb2	PPD
65	1193.5959	24.6	[M − H] [−]	C ₅₇ H ₉₄ O ₂₆	459	O-162-162/O-162-162	Malonyl-Ginsenoside Rb1 isomer II	PPD
66	1193.5959	23.2	[M − H] [−]	C ₅₇ H ₉₄ O ₂₆	459	O-162-162/O-162-162	Malonyl-Ginsenoside Rb1	PPD
67	1193.5959	24.1	[M − H] [−]	C ₅₇ H ₉₄ O ₂₆	459	O-162-162/O-162-162	Malonyl-Ginsenoside Rb1 isomer I	PPD
68	1195.6107	25.0	[M + HCOO] [−]	C ₅₆ H ₉₄ O ₂₄	459	O-162-162/O-162-162	Acetyl-Ginsenoside Rb1	PPD
69	1195.6107	25.7	[M + HCOO] [−]	C ₅₆ H ₉₄ O ₂₄	459	O-162-162/O-162-162	Acetyl-Ginsenoside Rb1 isomer I	PPD
70	1195.6107	27.5	[M + HCOO] [−]	C ₅₆ H ₉₄ O ₂₄	459	O-162-162/O-162-162	Acetyl-Ginsenoside Rb1 isomer II	PPD
71	975.5534	30.4	[M + HCOO] [−]	C ₄₈ H ₈₂ O ₁₇	459	O-162-162/O-146	PPD-O-glc-glc/O-rha	PPD
72	975.5534	31.3	[M + HCOO] [−]	C ₄₈ H ₈₂ O ₁₇	459	O-162-162/O-146	PPD-O-glc-glc/O-rha isomer I	PPD
73	975.5534	29.9	[M + HCOO] [−]	C ₄₈ H ₈₂ O ₁₇	459	O-162-162/O-146	PPD-O-glc-glc/O-rha isomer II	PPD
74	825.4975	36.0	[M + HCOO] [−]	C ₄₃ H ₇₂ O ₁₂	459	O-162/O-162	Acetyl-PPD-O-glc/O-glc	PPD
75	631.3842	38.3	[M − H] [−]	C ₃₆ H ₅₆ O ₉	475	O-176	PPT-O-glcA	PPT
76	683.4366	15.5	[M + HCOO] [−]	C ₃₆ H ₆₂ O ₉	475	O-162	Chikusetsusaponin L10	PPT
77	683.4366	17.0	[M + HCOO] [−]	C ₃₆ H ₆₂ O ₉	475	O-162	Ginsenoside Rh1 isomer	PPT
78	683.4366	19.3	[M + HCOO] [−]	C ₃₆ H ₆₂ O ₉	475	O-162	20(S)-Ginsenoside Rh1 *	PPT
79	683.4366	20.7	[M + HCOO] [−]	C ₃₆ H ₆₂ O ₉	475	O-162	20(R)-Ginsenoside Rh1	PPT
80	683.4366	22.9	[M + HCOO] [−]	C ₃₆ H ₆₂ O ₉	475	O-162	Ginsenoside F1	PPT
81	815.4793	20.4	[M + HCOO] [−]	C ₄₁ H ₇₀ O ₁₃	475	O-162-132	Ginsenoside F5	PPT
82	815.4793	19.1	[M + HCOO] [−]	C ₄₁ H ₇₀ O ₁₃	475	O-162-132	Ginsenoside F3	PPT
83	815.4793	17.4	[M + HCOO] [−]	C ₄₁ H ₇₀ O ₁₃	475	O-162-132	Notoginsenoside R2	PPT
84	815.4793	11.5	[M + HCOO] [−]	C ₄₁ H ₇₀ O ₁₃	475	O-162/O-132	PPT-O-xyl/ara/O-glc	PPT
85	815.4793	18.1	[M + HCOO] [−]	C ₄₁ H ₇₀ O ₁₃	475	O-162/O-132	PPT-O-xyl/ara/O-glc isomer	PPT
86	829.4943	19.3	[M + HCOO] [−]	C ₄₂ H ₇₂ O ₁₃	475	O-162-146	20(S)-Ginsenoside Rg2 *	PPT
87	829.4943	20.0	[M + HCOO] [−]	C ₄₂ H ₇₂ O ₁₃	475	O-162-146	20(R)-Ginsenoside Rg2 *	PPT
88	829.4943	15.5	[M + HCOO] [−]	C ₄₂ H ₇₂ O ₁₃	475	O-162-146	Ginsenoside Rg2 isomer I	PPT
89	829.4943	16.3	[M + HCOO] [−]	C ₄₂ H ₇₂ O ₁₃	475	O-162-146	Ginsenoside Rg2 isomer II	PPT
90	845.4913	8.8	[M + HCOO] [−]	C ₄₂ H ₇₂ O ₁₄	475	O-162/O-162	Ginsenoside Rg1 *	PPT
91	845.4913	16.6	[M + HCOO] [−]	C ₄₂ H ₇₂ O ₁₄	475	O-162-162	Ginsenoside Rf	PPT
92	845.4913	21.9	[M + HCOO] [−]	C ₄₂ H ₇₂ O ₁₄	475	O-162/O-162	Ginsenoside La	PPT
93	869.4890	21.3	[M − H] [−]	C ₄₅ H ₇₄ O ₁₆	475	O-162-146	Malonyl-Ginsenoside Rg2	PPT
94	885.4851	10.5	[M − H] [−]	C ₄₅ H ₇₄ O ₁₇	475	O-162-162	Malonyl-Ginsenoside Rf	PPT
95	887.4991	13.7	[M + HCOO] [−]	C ₄₄ H ₇₄ O ₁₅	475	O-162-162	Acetyl-20(R)-Ginsenoside Rg2	PPT
96	887.4991	13	[M + HCOO] [−]	C ₄₄ H ₇₄ O ₁₅	475	O-162/O-162	Acetyl-20(S)-Ginsenoside Rg1	PPT
97	887.4991	14.4	[M + HCOO] [−]	C ₄₄ H ₇₄ O ₁₅	475	O-162/O-162	Acetyl-20(R)-Ginsenoside Rg1	PPT
98	961.5385	10.4	[M + HCOO] [−]	C ₄₇ H ₈₀ O ₁₇	475	O-162-146/O-132	Cyclofoetoside A isomer	PPT
99	961.5385	11.7	[M + HCOO] [−]	C ₄₇ H ₈₀ O ₁₇	475	O-162-146/O-132	Cyclofoetoside A	PPT
100	977.5322	17.8	[M + HCOO] [−]	C ₄₇ H ₈₀ O ₁₈	475	O-162/O-162-132	Quinquenoside L3	PPT
101	977.5322	7.7	[M + HCOO] [−]	C ₄₇ H ₈₀ O ₁₈	475	O-162-132/O-162	Ginsenoside Re4	PPT
102	977.5322	8.1	[M + HCOO] [−]	C ₄₇ H ₈₀ O ₁₈	475	O-162-132/O-162	20(S)-Quinquenoside L17	PPT
103	977.5322	8.4	[M + HCOO] [−]	C ₄₇ H ₈₀ O ₁₈	475	O-162-132/O-162	20(R)-Quinquenoside L17	PPT
104	991.5466	8.7	[M + HCOO] [−]	C ₄₈ H ₈₂ O ₁₈	475	O-162-146/O-162	Ginsenoside Re isomer	PPT
105	991.5466	27.5	[M + HCOO] [−]	C ₄₈ H ₈₂ O ₁₈	475	O-162/O-162-162	Chikusetsusaponin FK1	PPT
106	991.5466	9.5	[M + HCOO] [−]	C ₄₈ H ₈₂ O ₁₈	475	O-162-146/O-162	Ginsenoside Re *	PPT
107	1007.5416	6.9	[M + HCOO] [−]	C ₄₈ H ₈₂ O ₁₉	475	O-162/O-162-162	Ginsenoside Re1	PPT
108	1007.5416	13.4	[M + HCOO] [−]	C ₄₈ H ₈₂ O ₁₉	475	O-162/O-162-162	Ginsenoside Re2	PPT
109	1007.5416	7.4	[M + HCOO] [−]	C ₄₈ H ₈₂ O ₁₉	475	O-162/O-162-162	Ginsenoside Re3	PPT
110	1031.5432	10.7	[M − H] [−]	C ₅₁ H ₈₄ O ₂₁	475	O-162-146/O-162	Malonyl-Ginsenoside Re	PPT
111	1031.5432	11.4	[M − H] [−]	C ₅₁ H ₈₄ O ₂₁	475	O-162-146/O-162	Malonyl-Ginsenoside Re isomer I	PPT
112	1031.5432	12.0	[M − H] [−]	C ₅₁ H ₈₄ O ₂₁	475	O-162-146/O-162	Malonyl-Ginsenoside Re isomer II	PPT
113	1031.5432	12.5	[M − H] [−]	C ₅₁ H ₈₄ O ₂₁	475	O-162-146/O-162	Malonyl-Ginsenoside Re isomer III	PPT
114	1033.5566	15.4	[M + HCOO] [−]	C ₅₀ H ₈₄ O ₁₉	475	O-162-146/O-162	Acetyl-Ginsenoside Re	PPT
115	1033.5566	14.0	[M + HCOO] [−]	C ₅₀ H ₈₄ O ₁₉	475	O-162-146/O-162	Acetyl-Ginsenoside Re isomer	PPT
116	1139.5848	11.1	[M + HCOO] [−]	C ₅₃ H ₉₀ O ₂₃	475	O-162-162/O-162-132	Floralginsenoside P	PPT
117	1123.5897	7.9	[M + HCOO] [−]	C ₅₃ H ₉₀ O ₂₂	475	O-162-132/O-162-146	Floralquiquenoside E	PPT

Table 1. Cont.

No.	<i>m/z</i>	<i>t_R</i> /min	Ion Adducts	Formula	Aglycone	Sugar Chains	Proposed Name	Type
118	799.4845	23.4	[M + HCOO] [−]	C ₄₁ H ₇₀ O ₁₂	475	O-146-132	PPT-O-rha-xyl/ara	PPT
119	975.5534	15.3	[M + HCOO] [−]	C ₄₈ H ₈₂ O ₁₇	475	O-162-146/O-146	PPT-O-glc-rha/O-rha **	PPT
120	665.4265	28.3	[M + HCOO] [−]	C ₃₆ H ₆₀ O ₈	457	O-162	Ginsenoside Rh4	OTHER
121	665.4265	27.0	[M + HCOO] [−]	C ₃₆ H ₆₀ O ₈	457	O-162	Ginsenoside Pk3	OTHER
122	665.4265	26.7	[M + HCOO] [−]	C ₃₆ H ₆₀ O ₈	457	O-162	Ginsenoside Pk3 isomer	OTHER
123	665.4265	40.3	[M + HCOO] [−]	C ₃₆ H ₆₀ O ₈	457	O-162	Ginsenoside Rh16	OTHER
124	665.4265	42.0	[M + HCOO] [−]	C ₃₆ H ₆₀ O ₈	457	O-162	Ginsenoside Rh16 isomer	OTHER
125	701.4475	8.6	[M − H] [−]	C ₃₆ H ₆₄ O ₁₀	493	O-162	20(S)-Ginsenoside Rh12	OTHER
126	701.4475	9.3	[M − H] [−]	C ₃₆ H ₆₄ O ₁₀	493	O-162	20(R)-Ginsenoside Rh12	OTHER
127	703.4207	17.2	[M + HCOO] [−]	C ₃₅ H ₆₂ O ₁₁	495	O-162	Floralginsenoside Tb	OTHER
128	717.4421	6.6	[M + HCOO] [−]	C ₃₆ H ₆₄ O ₁₁	509	O-162	Dammarane-3,6,12,24,25-pentol, 20-(β-D-glucopyranosyloxy)-, (3β,6β,12β)-(ACI) isomer	OTHER
129	717.4421	7.8	[M + HCOO] [−]	C ₃₆ H ₆₄ O ₁₁	509	O-162	Dammarane-3,6,12,24,25-pentol, 20-(β-D-glucopyranosyloxy)-, (3β,6β,12β)-(ACI)	OTHER
130	781.4734	40.7	[M + HCOO] [−]	C ₄₁ H ₆₈ O ₁₁	441	O-162-132	Notoginsenoside ST11	OTHER
131	811.4839	25.4	[M + HCOO] [−]	C ₄₂ H ₇₀ O ₁₂	457	O-162-146	Ginsenoside Rg6 isomer I	OTHER
132	811.4839	25.8	[M + HCOO] [−]	C ₄₂ H ₇₀ O ₁₂	457	O-162-146	Ginsenoside Rg6 isomer II	OTHER
133	811.4839	26.4	[M + HCOO] [−]	C ₄₂ H ₇₀ O ₁₂	457	O-162-146	Ginsenoside Rg6	OTHER
134	811.4839	38.6	[M + HCOO] [−]	C ₄₂ H ₇₀ O ₁₂	441	O-162-162	Ginsenoside Rg5 isomer I	OTHER
135	811.4839	39.5	[M + HCOO] [−]	C ₄₂ H ₇₀ O ₁₂	441	O-162-162	Ginsenoside Rg5 *	OTHER
136	811.4839	39.0	[M + HCOO] [−]	C ₄₂ H ₇₀ O ₁₂	441	O-162-162	Ginsenoside Rg5 isomer II	OTHER
137	827.4783	38.4	[M + HCOO] [−]	C ₄₂ H ₇₀ O ₁₃	457	O-162-162	20(R)-5,6-Didehydroginsenoside Rg3	OTHER
138	827.4783	32.2	[M + HCOO] [−]	C ₄₂ H ₇₀ O ₁₃	457	O-162-162	20(S)-5,6-Didehydroginsenoside Rg3	OTHER
139	827.4783	28.0	[M + HCOO] [−]	C ₄₂ H ₇₀ O ₁₃	457	O-162-162	Ginsenoside Rh15	OTHER
140	847.5047	8.6	[M + HCOO] [−]	C ₄₂ H ₇₄ O ₁₄	493	O-162-146	20(S)-25-OH-Ginsenoside Rg2	OTHER
141	847.5047	23.3	[M + HCOO] [−]	C ₄₂ H ₇₄ O ₁₄	477	O-162-162	20(S)-25-OH-Ginsenoside Rg3	OTHER
142	847.5047	24.0	[M + HCOO] [−]	C ₄₂ H ₇₄ O ₁₄	477	O-162-162	20(R)-25-OH-Ginsenoside Rg3	OTHER
143	849.4843	6.5	[M + HCOO] [−]	C ₄₁ H ₇₂ O ₁₅	509	O-162/O-132	β-D-Glucopyranoside, (3β,12β)-3,12,24,25-tetrahydroxy-20-(D-xylopyranosyloxy)dammaran-6-yl (ACI)	OTHER
144	853.4949	42.0	[M + HCOO] [−]	C ₄₄ H ₇₂ O ₁₃	441	O-162-162	Ginsenoside Rs4	OTHER
145	863.501	6.7	[M + HCOO] [−]	C ₄₂ H ₇₄ O ₁₅	509	O-162-146	Quinquenoside L9	OTHER
146	975.5534	24.3	[M + HCOO] [−]	C ₄₈ H ₈₂ O ₁₇	443	O-162-162/O-162	Vinaginsenoside R3	OTHER
147	989.5324	24.0	[M + HCOO] [−]	C ₄₈ H ₈₀ O ₁₈	457	O-162-162/O-162	5,6-Didehydroginsenoside Rd	OTHER
148	989.5324	13.0	[M + HCOO] [−]	C ₄₈ H ₈₀ O ₁₈	473	O-162/O-162-146	Ginsenoside Rh18	OTHER
149	989.5324	20.8	[M + HCOO] [−]	C ₄₈ H ₈₀ O ₁₈	457	O-162-162/O-162	Quinquenoside L1	OTHER
150	1005.527	10.7	[M + HCOO] [−]	C ₄₈ H ₈₀ O ₁₉	473	O-162-162/O-162	Vinaginsenoside R20	OTHER
151	1007.5416	6.3	[M + HCOO] [−]	C ₄₈ H ₈₂ O ₁₉	491	O-162-146/O-146	Majoroside F5	OTHER
152	1007.5416	10.2	[M + HCOO] [−]	C ₄₈ H ₈₂ O ₁₉	491	O-162/O-162-146	Majoroside F6	OTHER
153	1009.559	5.7	[M + HCOO] [−]	C ₄₈ H ₈₄ O ₁₉	493	O-162/O-162-146	β-D-Glucopyranoside, (3β,6α,12β)-20-(β-D-glucopyranosyloxy)-3,12,25-trihydroxydammaran-6-yl 2-O-(6-deoxy-α-L-mannopyranosyl)- (ACI)	OTHER
154	1025.5541	10.6	[M + HCOO] [−]	C ₄₈ H ₈₄ O ₂₀	493	O-162-162/O-162	Vinaginsenoside R13 isomer	OTHER
155	1025.5541	12.0	[M + HCOO] [−]	C ₄₈ H ₈₄ O ₂₀	493	O-162/O-162-162	Vinaginsenoside R13	OTHER
156	1137.6053	21.9	[M + HCOO] [−]	C ₅₄ H ₉₂ O ₂₂	443	O-162-162/O-162-162	Notoginsenoside I	OTHER
157	1151.5848	22.0	[M + HCOO] [−]	C ₅₄ H ₉₀ O ₂₃	457	O-162-162/O-162-162	5,6-Didehydroginsenoside Rb1	OTHER
158	1167.5913	8.5	[M + HCOO] [−]	C ₅₄ H ₉₀ O ₂₄	473	O-162-162/O-162-162	Notoginsenoside B	OTHER
159	1169.5943	10.2	[M + HCOO] [−]	C ₅₄ H ₉₂ O ₂₄	475	O-162-162/O-162-162	Koryoginsenoside R2	OTHER
160	1169.5943	12.6	[M + HCOO] [−]	C ₅₄ H ₉₂ O ₂₄	475	O-162-162/O-162-162	Notoginsenoside A	OTHER
161	781.4734	41.3	[M + HCOO] [−]	C ₄₁ H ₆₈ O ₁₁	441	O-162-132	Notoginsenoside ST11 isomer	OTHER
162	843.4948	19.7	[M + HCOO] [−]	C ₄₂ H ₇₀ O ₁₄	473	O-162-162	11-Oxomogroside II A1	OTHER

Table 1. Cont.

No.	<i>m/z</i>	<i>t_R</i> /min	Ion Adducts	Formula	Aglycone	Sugar Chains	Proposed Name	Type
163	973.5373	16.2	[M + HCOO] [−]	C ₄₈ H ₈₀ O ₁₇	473	O-162-146/O-146	(3β,16β,22α)-28-[(6-Deoxy-α-L-mannopyranosyl)oxy]-16,22-dihydroxyolean-12-en-3-yl 6-deoxy-3-O-β-D-glucopyranosyl-α-L-mannopyranoside	OTHER
164	973.5373	15.0	[M + HCOO] [−]	C ₄₈ H ₈₀ O ₁₇	473	O-162-146/O-146	(3β,16β,22α)-28-[(6-Deoxy-α-L-mannopyranosyl)oxy]-16,22-dihydroxyolean-12-en-3-yl 6-deoxy-3-O-β-D-glucopyranosyl-α-L-mannopyranoside isomer	OTHER
165	1009.5575	19.1	[M + HCOO] [−]	C ₄₈ H ₈₄ O ₁₉	477	O-162-162/O-162	(3β,12β)-20-(β-D-Glucopyranosyloxy)-12,25-dihydroxydammaran-3-yl 2-O-β-D-glucopyranosyl-β-D-glucopyranoside (3β,12β)-20-(β-D-Glucopyranosyloxy)-3,12,24,25-	OTHER
166	1025.5541	5.1	[M + HCOO] [−]	C ₄₈ H ₈₄ O ₂₀	509	O-162/O-162-146	tetrahydroxydammaran-6-yl 2-O-(6-deoxy-α-L-β-D-mannopyranosyl)-β-D-glucopyranoside	OTHER
167	803.4426	34.1	[M + HCOO] [−]	C ₃₉ H ₆₆ O ₁₄	433	O-162-162	PQ-ginsenoside A **	OTHER
168	803.4426	36.0	[M + HCOO] [−]	C ₃₉ H ₆₆ O ₁₄	433	O-162-162	PQ-ginsenoside A isomer **	OTHER
169	803.4426	19.3	[M + HCOO] [−]	C ₃₉ H ₆₆ O ₁₄	449	O-162-146	PQ-ginsenoside B **	OTHER
170	785.4322	26.4	[M + HCOO] [−]	C ₄₀ H ₆₆ O ₁₅	431	O-162-146	PQ-ginsenoside C **	OTHER
171	785.4322	39.0	[M + HCOO] [−]	C ₄₀ H ₆₆ O ₁₅	415	O-162-162	PQ-ginsenoside D **	OTHER
172	827.4438	41.7	[M + HCOO] [−]	C ₄₁ H ₆₆ O ₁₄	415	O-162-162	Acetyl-PQ-ginsenoside D **	OTHER
173	827.4438	41.3	[M + HCOO] [−]	C ₄₁ H ₆₆ O ₁₄	415	O-162-162	Acetyl-PQ-ginsenoside D isomer I **	OTHER
174	827.4438	42.0	[M + HCOO] [−]	C ₄₁ H ₆₆ O ₁₄	415	O-162-162	Acetyl-PQ-ginsenoside D isomer II **	OTHER
175	845.4536	40.0	[M + HCOO] [−]	C ₄₁ H ₆₈ O ₁₅	433	O-162-162	Acetyl-PQ-ginsenoside A **	OTHER

* represents ginsenosides validated with standards. ** represents new ginsenosides.

For the structures of the ginsenosides, the database CAS SciFinderⁿ was searched. Among them, 10 ginsenosides were identified in the steamed PQ for the first time. The aglycone or sugar chains were different compared with the ginsenosides reported previously. There was one new ginsenoside classified as the PPT-type, and it was named PPT-O-glc-rha/O-rha. PPT-O-glc-rha/O-rha (*m/z* 975.5534, [M+HCOO][−]) was identified by fragment ions of 929, 783, 621, 475, 205, 163, 161, and 145 (Figure 3A). The fragment ion of 475 is the characteristic aglycone ion of PPT-type ginsenosides. The neutral loss of 929/783, 783/621, and 621/475 indicated two rhamnose and a glucose in the sugar chains. The fragment ion of 205 indicated a sugar chain of O-glucose-rhamnose.

There were nine new ginsenosides classified as the other type, and they were named PQ-ginsenoside A, B, C, D, acetyl-PQ-ginsenoside A, and acetyl-PQ-ginsenoside D isomers. Three new aglycones were discovered in PQ-ginsenoside B, C, and D, and the *m/z* of them were 449, 431, and 415 in the MS/MS analysis. For example, the fragmentation rules of PQ-ginsenoside C were consistent with the general ginsenosides, and a new aglycone with *m/z* 431 was discovered. The *m/z* of the aglycone in PQ-ginsenoside A was 433. The aglycone with *m/z* 433 has been reported to be degraded from 459 in the PPD-type, and it was characterized as 25-, 26-, and 27-trinor-PPD-type in the floralginsenoside Kb from *Panax ginseng* [31,32]. The sugar chain of PQ-ginsenoside A was different from floralginsenoside Kb, and it was not found in the database of CAS SciFinderⁿ, so it was defined as a new ginsenoside. The sugar chains of PQ-ginsenoside A were the same as Rg3, and they were eluted at the same retention time. Rg3 is a PPD-type ginsenoside. Therefore, the aglycone

structure in PQ-ginsenoside A were deduced as 25-, 26-, and 27-trinor-PPD-type degraded from Rg3 (Figure 3B). For PQ-ginsenoside B (aglycone, m/z , 449, Figure 3C), it has the same sugar chains and retention time with Rg2 (aglycone, m/z , 475). For PQ-ginsenoside C (aglycone, m/z , 431, Figure 3D), it has the same sugar chains and retention time with Rg6 (aglycone, m/z , 457). For PQ-ginsenoside D (aglycone, m/z , 415, Figure 3E) it has the same sugar chains and retention time with Rg5 (aglycone, m/z , 441). The molecular weight difference of 449/475, 431/457, and 415/441 were the same as the 433/459. Therefore, the aglycone structures of 449, 431, and 415 in PQ-ginsenoside B, C, and D were deduced to be degraded from 475, 457, and 441 in the Rg5, Rg6, and Rg5, characterized as 25-, 26-, and 27-trinor.

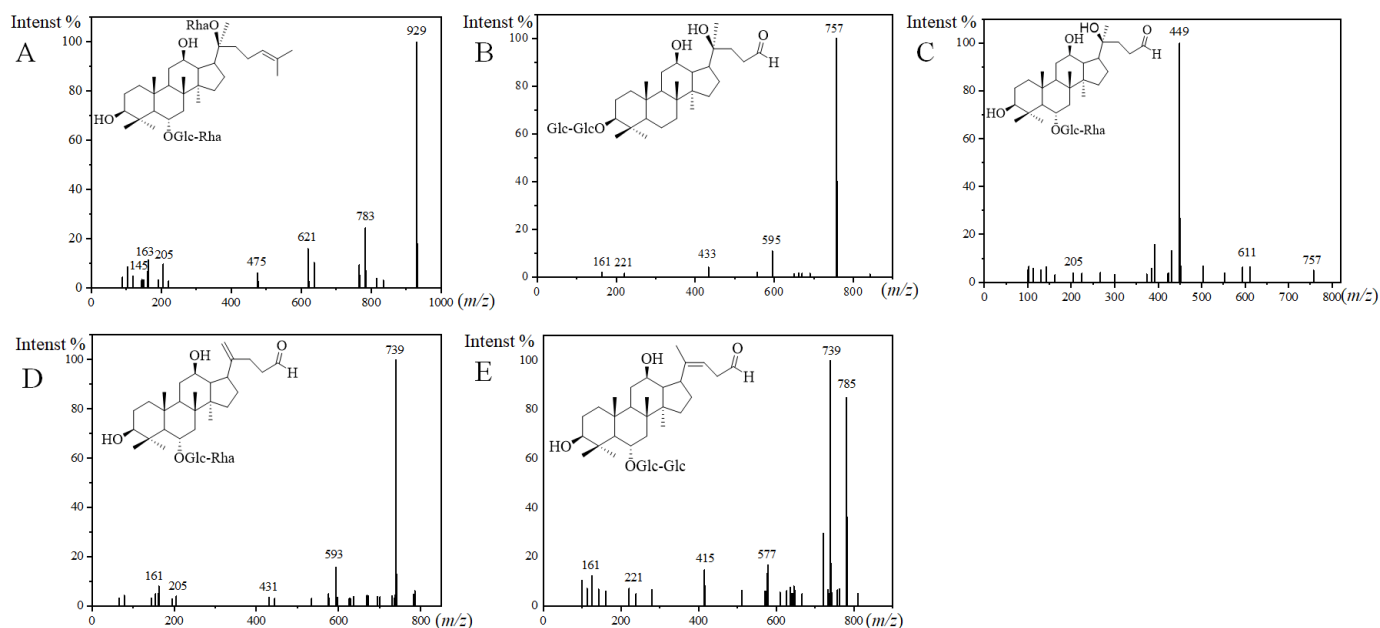


Figure 3. MS² spectra and the presumed structures of PPT-O-glc-rha/O-rha ((A), 50 eV), PQ-ginsenoside A ((B), 40 eV), PQ-ginsenoside B ((C), 70 eV), PQ-ginsenoside C ((D), 40 eV), and PQ-ginsenoside D ((E), 40 eV).

There were also many isomers identified. For the isomers, the fragmentation ions in the MS/MS analysis were the same. The aglycone and sugar chains of them were the same as the previous ginsenosides, but the attaching positions of the sugar chain and aglycone were different. The extracted ion chromatograms of 829.4943 (m/z) in the freeze-dried sample, the (100 °C, 2 h) sample, and the (130 °C, 2 h) sample are shown in Figure 4A. It was obvious that the ginsenosides contents and varieties were changed with the increase in steaming temperature. The ginsenoside Rg2 and Rg3 were PPT-type and PPD-type, respectively. The ginsenoside Rg2 isomers (No. 1, 2, 5, and 6) were identified by product ions of 783, 637, 475, 205, 161, and 145 (Figure 4B). The ginsenoside Rg3 isomers (No. 3, 4, 7, 8, and 9) were identified by product ions of 783, 621, 459, 221, and 161 (Figure 4C). The No. 1, 2, 3, and 4 were confirmed by standards as 20(S)-ginsenoside Rg2, 20(R)-ginsenoside Rg2, 20(S)-ginsenoside Rg3, and 20(R)-ginsenoside Rg3. For PPT-type ginsenosides, the glycosidic bonds were commonly at the aglycone C-6 and C-20 hydroxyl groups [33]. Ginsenoside Rg2 was C-6 linked. Therefore, No. 5 and 6 were deduced as sugar chains linking to the C-20 position, named as the ginsenoside Rg2 isomer. For PPD-type ginsenosides, the glycosidic bonds were commonly at the aglycone C-3 and C-20. Ginsenoside Rg3 was C-3 linked. Therefore, No. 7, 8, and 9 were speculated as sugar-chain-linking to the C-20 position, named the ginsenoside Rg3 isomers.

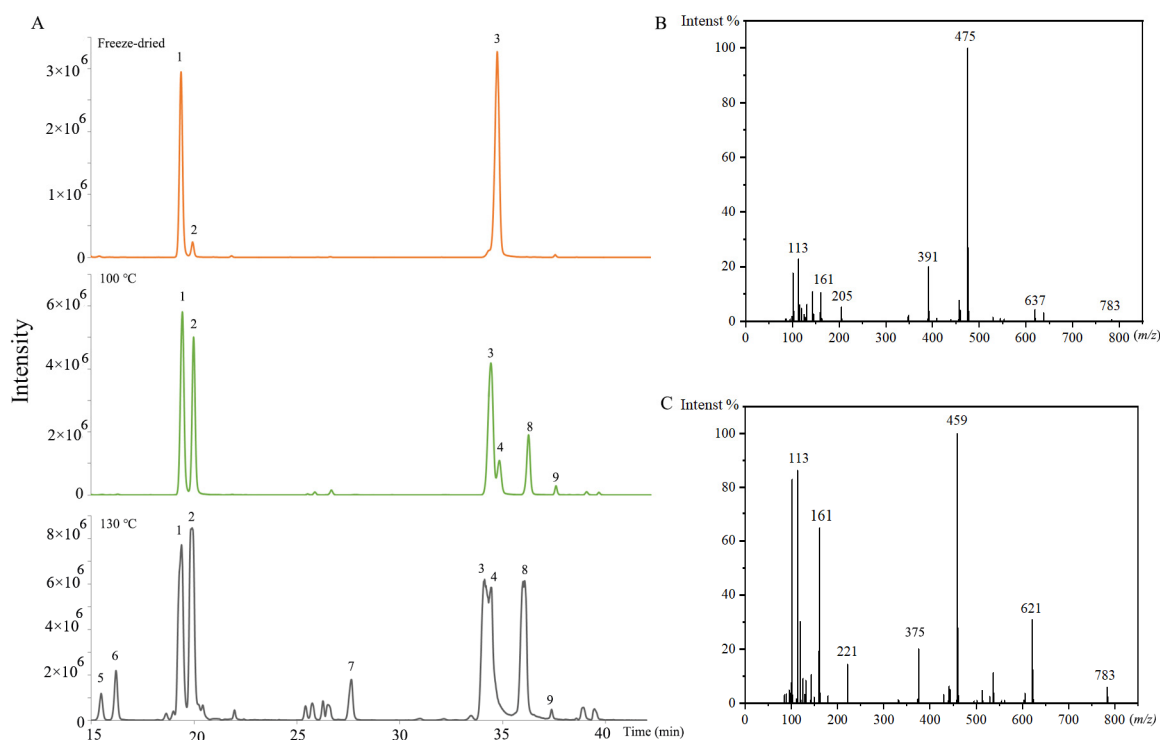


Figure 4. (A) The extracted ion chromatogram of 829.4943 (m/z) in the freeze-dried sample, and steamed samples (100 °C, 2 h), and (130 °C, 2 h), No. 1, 2, 5, and 6 represent the ginsenoside Rg2 and its isomers, No. 3, 4, 7, 8, and 9 represent the ginsenoside Rg3 and its isomers. (B) MS² spectrum of 20(S)-Ginsenoside Rg2. (C) MS² spectrum of 20(S)-Ginsenoside Rg3 (70 eV).

2.2. Method Validation

The repeatability and precision of the analytical method were investigated by QC samples. The repeatability was investigated by six QC samples. The QC samples were analyzed continuously. The RSD of each peak was calculated among the six QC samples. The peak number and area were counted within different RSD ranges (0–10%, 10–20%, 20–30%, and >30%). In total, 98.2% of the peaks had an RSD value of less than 20%, while the accumulated peak area accounted for 99.3% of the total area (Figure S1A). For the intra-day precision analysis, six QC samples were analyzed every 4 h, and 98.1% of the peaks had an RSD less than 20%, while the accumulated peak area accounted for 99.3% of the total peak area (Figure S1B). For the inter-day precision analysis, 18 QC samples were analyzed for 3 days. The results show that 96.0% of the peaks had an RSD of less than 20%, while the accumulated peak area accounted for 98.6% of the total peak area (Figure S1C). These results indicated the good stability of the analytical method.

2.3. Difference between Steamed and Freeze-Dried Samples

Principal component analysis (PCA) was carried out in PQ samples with different steaming times and temperatures with UV scaling. In Figure 5A, PC1 and PC2 were 0.608 and 0.245. In Figure 5B, PC1 and PC2 were 0.636 and 0.208. The score plots show that there was obvious separation among the freeze-dried samples and steamed samples.

A non-parametric test was then performed, and the ratio was calculated between each of the two groups. $p < 0.05$ and ratio > 5 were set as the criteria to screen the differential ginsenosides (Tables S1 and S2). There were 51, 55, 58, 63, 67, and 75 differential ginsenosides found between the steamed samples of 2 h, 4 h, 6 h, 8 h, 10 h, and 12 h and freeze-dried samples, respectively. There were 48, 60, 74, and 89 differential ginsenosides found between steamed samples of 100 °C, 110 °C, 120 °C, and 130 °C and freeze-dried samples, respectively. This indicated that the steam temperature and time had a significant influence on the steamed PQ samples.

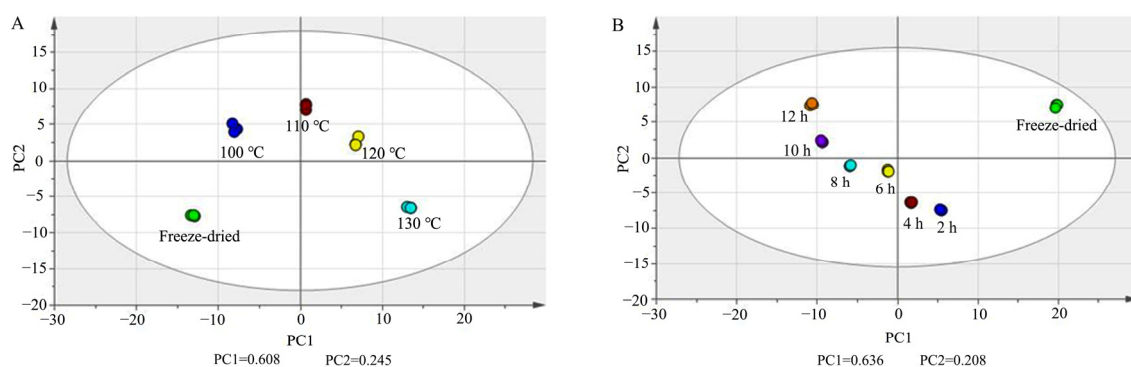


Figure 5. PCA score plots of ginsenosides in PQ samples with different steaming temperatures (A) and times (B).

2.4. Influence of Steam Temperature and Time on the Ginsenosides Composition

The hierarchical cluster analysis was carried out on the differential ginsenosides. The data were normalized, and the heat map is shown in Figures 6 and S2. There were 104 and 86 differential ginsenosides screened for PQ samples with different steaming temperatures and times, respectively. With the increase in the steaming temperature, the content of 37 ginsenosides increased gradually, while the content of 36 ginsenosides decreased gradually. With the increase in the steaming time, the content of 42 ginsenosides increased gradually, while the content of 15 ginsenosides decreased gradually. In addition, there were some ginsenosides that changed with the steaming time and temperature, for example, climbing up and then declining. The steaming process not only changed the ginsenosides content, but also influenced their structure.

For the PPD-ginsenosides, the difference was shown in Figures 6A and S2A. Firstly, the malonyl-ginsenosides Rb1, Rb2, Rb3, Rd, and Re decreased significantly with the steaming time and temperature. The rate among different samples was calculated. The content of malonyl-ginsenoside Rb3 in the freeze-dried sample was 2-, 323-, and 574-fold more than in the samples (100 °C, 2 h), (100 °C, 12 h), and (130 °C, 2 h), respectively. Malonyl-ginsenoside Rg3 was accumulated after the steaming process, and then decreased with the increase in the steaming time and temperature. Malonyl-ginsenoside Rg3 was increased by 5-fold in the sample (100 °C, 2 h), and then decreased by 26- and 47-fold in the samples (100 °C, 12 h) and (130 °C, 2 h), respectively. Secondly, the acetyl-ginsenosides showed a significant increase after the steaming process. Then, the acetyl-ginsenosides Rc, Rb3, Rb1, and Rd changed slightly with the steaming time, but showed an obviously decline with the increase in the steaming temperature. Acetyl-ginsenoside Rg3 was enhanced from steaming for 8 h at 120 °C. Thirdly, the levels of ginsenosides Rh2, Rg3, and Rb3 and gypenoside XIII were enhanced with the steaming process, while PPD-*O*-glc-glc/*O*-glc-rha and saponin Ia were decreased. And, the steaming time was not significant with the ratios. The content of 20(*R*)-ginsenoside Rh2 was extremely low in the freeze-dried sample, and then increased quickly after the steaming process. Although the content of 20(*S*)-ginsenoside Rh2 was also rising, the increase rate was low. The contents of 20(*R*)-ginsenoside Rh2 and 20(*S*)-ginsenoside Rh2 in the sample (100 °C, 2 h) were 22- and 4-fold more than in the freeze-dried sample, indicating the transformation from the *S*-configuration to the *R*-configuration. The contents of 20(*R*)-ginsenoside Rh2 in the samples (100 °C, 12 h) and (130 °C, 2 h) were 8 and 18 times more than in the sample (100 °C, 2 h), respectively. This shows that a high temperature enhances configuration transformation. The malonyl ginsenosides were sensitive to the heat process. The acetyl-ginsenoside could be produced by the decarboxylation of the malonyl group [34]. Therefore, with the decrease in the malonyl ginsenosides, the level of acetyl ginsenosides was enhanced. With the rise in temperature, acetyl ginsenosides were then degraded into neutral ginsenosides. The ginsenoside Rg3 could be produced from acetyl-ginsenoside Rg3, and could be further converted into ginsenoside Rh2 through the

elimination of glucose at C-3 [35]. The acetyl-ginsenoside Rg3 could be produced from malonyl-ginsenoside Rg3. The possible transformation pathways are shown in Figure S3.

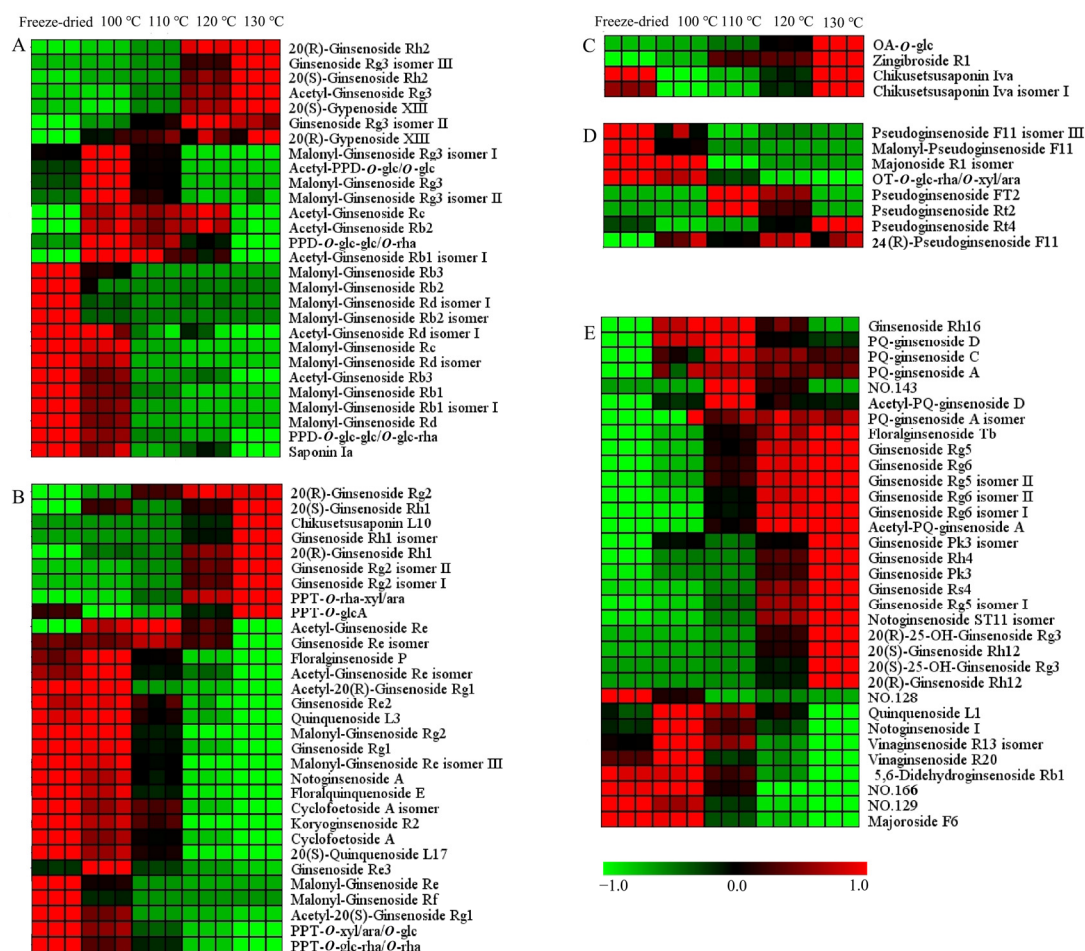


Figure 6. Heat map of differential ginsenosides in PQ samples with different steaming temperatures. (A) PPD-type. (B) PPT-type. (C) OA-type. (D) OT-type. (E) Other type. No. 128 and 129 represent Dammarane-3,6,12,24,25-pentol, 20-(β -D-glucopyranosyloxy)-, (3 β ,6 β ,12 β)-(ACI), and isomer. No. 143 represents β -D-Glucopyranoside, (3 β ,12 β)-3,12,24,25-tetrahydroxy-20-(D-xylopyranosyloxy)dammaran-6-yl (ACI). No. 166 represents (3 β ,12 β)-20-(β -D-Glucopyranosyloxy)-3,12,24,25-tetrahydroxydammaran-6-yl 2-O-(6-deoxy- α -L- β -D-mannopyranosyl)- β -D-glucopyranoside.

In the PPT-type (Figures 6B and S2B), the malonyl ginsenosides Re, Rf, and Rg2 decreased with the steaming time and temperature. Acetyl-ginsenoside Re and its isomer showed a rising and then declining tendency, indicating the conversion of malonyl-ginsenosides Re. Configuration transformations were also found in the 20(S/R)-ginsenoside Rh1 and 20(S/R)-ginsenoside Rg2. The contents of 20(S)-ginsenoside Rh1 and 20(R)-ginsenoside Rh1 in the sample (130 °C, 2 h) were 15- and 750-fold more than in the freeze-dried sample, respectively. The contents of 20(S)-ginsenoside Rg2 and 20(R)-ginsenoside Rg2 in the sample (130 °C, 2 h) were 4- and 59-fold more than in the freeze-dried sample, respectively. PPT-O-rha-xyl/ara, chikusetsusaponin L10 and PPT-O-glcA were also increased, while ginsenoside Rg1, Re2, quinquenoside L3, PPT-O-xyl/ara/O-glc, PPT-O-glc-rha/O-rha, floralginsenoside P, floralquinquenoside E, Cyclofoetoside A, and 20(S)-quinquenoside L17 were decreased. The decreased ginsenosides had three or four sugars in the sugar chain, while the increased ginsenosides had one or two sugars. The sugar chains experienced hydrolysis and dehydration. The ginsenoside Re lost the C-6 sugar to generate ginsenoside Rg2 [36]. The PPT-O-glc-rha/O-rha lost the C-20 sugar to generate ginsenoside Rg2. The

ginsenoside Rg2 lost the C-6 sugar to generate Rh1. The possible transformation pathways are shown in Figure S4.

For the OA-type ginsenosides, chikusetsusaponin Iva and isomer I had the same sugar chains (a glucose and a glucuronic acid attached to different positions of the aglycone). They were decreased after the steaming process (Figures 6C and S2C). The content of chikusetsusaponin Iva and isomer I in the freeze-dried sample were 10 and 14 times higher than in the sample (100 °C, 2 h), respectively. Zingibroside R1 was different at the sugar chains in the structure compared with chikusetsusaponin Iva and isomer I. It had a disaccharide chain of glucose and glucuronic acid. OA-O-glc had glucose in the sugar chain. The contents of OA-O-glc and zingibroside R1 were increased after the steaming process. The contents of OA-O-glc and zingibroside R1 in the sample (100 °C, 2 h) were 12 and 6 times more than in the freeze-dried sample. The sugar chain of ginsenoside Ro has been reported to experience degradation to form the zingibroside R1 and chikusetsusaponin Iva [27]. Moreover, it has been deduced that the sugar chain of chikusetsusaponin Iva experiences degradation at C-3 to form OA-O-glc. With the increase in the steaming time and temperature, the content of them were also increased. From 2 h to 10 h, the contents of them increased continuously. At the 12 h, their content showed a little decline. The contents of chikusetsusaponin Iva, chikusetsusaponin Iva isomer I, zingibroside R1, and OA-O-glc in the sample (100 °C, 10 h) were 4, 3, 4, and 5 times more than in the sample (100 °C, 2 h), respectively. From 100 °C to 130 °C, the contents of them increased continuously. The contents of chikusetsusaponin Iva, chikusetsusaponin Iva isomer I, zingibroside R1, and OA-O-glc in the sample (130 °C, 2 h) were 9, 12, 4, and 29 times more than in the sample (100 °C, 2 h), respectively. The steaming temperature had a larger impact on the OA-type ginsenosides' conversion than the steaming time. The possible transformation pathways are shown in Figure S5A.

OT-type ginsenosides are characteristic ingredients of PQ which different from other *Panax* species [27]. The differences are shown in Figures 6D and S2D. In Figure 6D, Pseudoginsenoside F11 isomer III, malonyl-pseudoginsenoside F11, and OT-O-glc-rha/O-xyl/ara show a declining tendency, and pseudoginsenoside Rt4, Rt2, Ft2, and 24(R)-pseudoginsenoside F11 show a rising tendency. The contents of malonyl-pseudoginsenoside F11 and OT-O-glc-rha/O-xyl/ara in the sample (100 °C, 2 h) were 69 and 28 times more than in the sample (130 °C, 2 h). The content of malonyl-pseudoginsenoside F11 in the sample (100 °C, 2 h) was 27 times more than in the sample (100 °C, 12 h). The malonyl-pseudoginsenoside F11 and OT-O-glc-rha/O-xyl/ara underwent demalonylation and hydrolysis reactions to produce the pseudoginsenoside F11, respectively. Pseudoginsenoside Rt4 increased with the time and temperature. The contents of pseudoginsenoside Rt4 in the sample (100 °C, 12 h) and (130 °C, 2 h) was 5 and 10 times more than in the sample (100 °C, 2 h), respectively. The content of 24(R)-pseudoginsenoside F11 in the sample (130 °C, 2 h) was six times more than in the freeze-dried sample. The content of pseudoginsenoside Rt2 was the highest at 110 °C, and then declined. The sugar chain of 24(R)-pseudoginsenoside F11 (the sugar chain of glucose-rhamnase) and pseudoginsenoside Rt2 (the sugar chain of a glucose-xylose) underwent degradation to form the pseudoginsenoside Rt4 (the sugar chain of a glucose). These results indicate the degradation of the sugar chains with the steaming process, and the high temperature facilitated the degradation process. The possible transformation pathways are shown in Figure S5B.

In Figures 6E and S2E, most other-type ginsenosides increase with the steaming process. Firstly, the steaming time and temperature have little difference in their influence on ginsenoside Rg5, floralginsenoside Tb, ginsenoside Rg6, ginsenoside Rg5 isomer II, and ginsenoside Rg6 isomer II. The contents of ginsenoside Rg5 in the samples (100 °C, 12 h) and (130 °C, 2 h) were five and four times more than in the sample (100 °C, 2 h), respectively. The contents of ginsenoside Rg6 in the samples (100 °C, 12 h) and (130 °C, 2 h) was four- and three-fold higher than in the sample (100 °C, 2 h), respectively. Secondly, the effect of the steaming temperature on the contents of ginsenoside Rs4, ginsenoside Rh4, ginsenoside Rg6 isomer I, 20(R)-ginsenoside Rh12, PQ-ginsenoside A, C, D, and acetyl-

PQ-ginsenoside D was greater than that of the steaming time. The contents of ginsenoside Rs4 in the sample (100 °C, 12 h) and temperature sample (130 °C, 2 h) was 8 and 40 times that in the sample (100 °C, 2 h). Thirdly, the effect of the steaming time on the contents of ginsenoside Pk3, ginsenoside Rg5 isomer I, and 20(S)-ginsenoside Rh12 was greater than that of the steaming temperature. The increased rate of 20(S)-ginsenoside Rh12 was less than 20(R)-ginsenoside Rh12, indicating the transformation from an S-configuration to an R-configuration. With the steaming process, the protoginsenosides could be transformed into rare ginsenosides. The dehydration of the side chain of C17 resulted in the degradation of ginsenoside Rg3 to ginsenoside Rg5, respectively. Acetyl-ginsenoside Rg3 could be transformed into ginsenoside Rs4 by dehydration in the side chain of C17. Ginsenoside Rg2 could be transformed to ginsenoside Rg6 by dehydration in the side chain of C17. Then, the hydrolysis of the rhamnosyl residue at C-6 of ginsenoside Rg6 can lead to its degradation into ginsenoside Rh4. The other types ginsenosides were mostly changed in the side chain at C17 of the aglycone (Figures S3 and S4). The ginsenosides underwent a series of chemical reactions, including dehydration, hydrolysis, isomerization, demalonylation, and deacetylation during the steaming process.

3. Materials and Methods

3.1. Chemical and Reagents

Acetonitrile and methanol were purchased from Merck (HPLC grade, Darmstadt, Germany). Formic acid was purchased from Honeywell (for mass spectrometry, Seelze, Germany). Ultrapure water was produced by a Direct-Q 8 UV-R water purification system (Millipore, Billerica, MA, USA). Ginsenosides Rb1, Ro, Rb2, Rd, Rg1, Rg5, Re, 20(S)-ginsenoside Rh1, 20(S)-ginsenoside Rg3, 20(R)-ginsenoside Rg3, 20(S)-ginsenoside Rg2, 20(R)-ginsenoside Rg2, 20(R)-ginsenoside Rh2, 20(S)-ginsenoside Rh2, and 24(S)-pseudoginsenoside F11 were purchased from Chengdu Desite Co., Ltd. (Chengdu, China).

3.2. Sample Information and Preparation

Four-year-old PQ roots were collected in the plantation farm of Weihai city, Shandong province, China. Fresh PQ roots were steamed at 100 °C for 2 h, 4 h, 6 h, 8 h, 10 h, and 12 h, respectively. And fresh PQ roots were steamed at 100 °C, 110 °C, 120 °C, and 130 °C for 2 h, respectively. Then the steamed PQ roots were cut into 2–3 mm slices and dried at 60 °C. The dried slices were then ground into powder. A batch of fresh roots were cut into 2–3 mm slices and freeze-dried as raw samples. Quality control (QC) samples were prepared by mixing equal weight of all samples.

PQ powder of 100 mg was accurately weighed into the Eppendorf tubes. Next, 1.5 mL extraction solution of methanol/water (1:1, *v/v*) was added. The mixture was vortexed for 5 min by the vortex oscillator (Digital Vortex-Genie 2, Scientific Industries, Bohemia, NY, USA). Then, the mixture was centrifuged for 10 min and the supernatant was taken out for LC-MS analysis. Three parallel samples were prepared.

3.3. LC-MS Analysis

The extract was analyzed by the UPLC system (Water, H-Class, Miford, MA, USA) coupled to a Q-TOF mass spectrometer equipped with an electrospray ionization interface (Bruker Impact II, Bremen, Germany). The LC separation was performed on an Agilent SB-Aq column (2.1 × 100 mm, 1.8 μm) with mobile phase A (0.1% formic acid in water) and mobile phase B (100% acetonitrile). The elution gradient was as follows: 0 min, 5% B; to 2 min, 7% B; to 3 min, 20% B; to 9 min, 24% B, and kept for 4 min; to 16 min, 26% B; to 18 min, 28% B; to 22 min, 34% B, and kept for 8 min; to 34 min, 36% B; to 35 min, 40% B; to 40 min, 50% B; to 50 min, 100% B, and kept for 5 min; to 55.1 min, 5%, and maintained for 5 min. The total run time was 60 min. The flow rate was 0.3 mL/min and column temperature was controlled at 35 °C. The mass data were acquired in the negative mode. The scan was set at a range of 50 to 1500 *m/z*. The capillary voltage was set at 3000 v for negative ion mode. The dry flow was set to 8 L/min, the nebulizer pressure was 2.0 bar,

and the drying gas temperature was 200 °C. The prepulse storage was 8 μ s, the collision RF was 750 Vpp, and the transfer time was 80 μ s. The collision energies were set at 40–70 eV.

3.4. Data Analysis

MS-DIAL software (version 4.9.0) was used for data deconvolution and peak alignment. A dataset containing m/z , retention time and peak area was obtained. Principal component analysis (PCA) was performed using Simca 14.0 (Umetrics, Umeå, Sweden). The hierarchical cluster analysis and non-parametric test were performed using MultiExperiment Viewer software (version 4.9, Dana-Farber Cancer Institute, Boston, MA, USA). The select mode for non-parametric test was Wilcoxon and Mann–Whitney test (one factor, two experimental groups).

4. Conclusions

A comprehensive investigation was carried out on the ginsenoside identification and transformation of PQ samples with different steaming conditions. In total, 175 ginsenosides were identified, and the sugar chains were annotated based on UHPLC-QTOF-MS. New ginsenosides and isomers were discovered. The steaming process was an effective method to increase the chemical diversity of the ginsenosides. The types and contents of the ginsenosides were found to vary greatly. The content of acylated ginsenosides and protoginsenosides decreased, while the content of the rarest ginsenosides significantly increased after the steaming process. This study can deepen the understanding of the ginsenosides' conversion in PQ during the steaming process. Since the definite functions of the individual ginsenoside have not been revealed clearly, further research is needed.

Supplementary Materials: The following supporting information can be downloaded at: <https://www.mdpi.com/article/10.3390/molecules29030623/s1>, Figure S1: The peak number and accumulated peak area with different RSD ranges for the repeatability (A), intra-day (B), and inter-day (C) precision. Figure S2: Heat map of differential ginsenosides in PQ samples with different steaming time. A, PPD-type. B, PPT-type. C, OA-type. D, OT-type. E, Other type. Figure S3: The deduced transformation pathways of PPD-type ginsenosides. Figure S4: The deduced transformation pathways of PPT-type ginsenosides. Figure S5: The deduced transformation pathways of OA-type ginsenosides (A) and OT-type ginsenosides (B). Table S1: The p and ratio of differential ginsenosides in the samples with different steaming times. Table S2: The p and ratio of differential ginsenosides in the samples with different steaming temperatures.

Author Contributions: Conceptualization, L.L. and X.W.; Methodology, J.F.; Validation, W.J. and F.L.; Formal Analysis, L.L.; Investigation, J.F.; Resources, X.W.; Data Curation, F.L.; Writing—Original Draft, J.F. and L.L.; Writing—Review and Editing, L.L. and X.W.; Visualization, W.J.; Supervision, F.L.; Project Administration, L.L.; Funding Acquisition, L.L. and X.W. All authors have read and agreed to the published version of the manuscript.

Funding: The work was funded by the National Natural Science Foundation of China (21904080), the New Innovation Team of Jinan (202228020), the Shandong Province Taishan Scholar Program (tstp20221138), the Key Research and Development Program of the Shandong Province (2022TZXD0034), and the Science, Education, and Industry Integration Innovation Pilot Project from Qilu University of Technology (Shandong Academy of Sciences) (2023PY048).

Data Availability Statement: Data are contained within the article and Supplementary Materials.

Conflicts of Interest: The authors have declared no conflicts of interest.

References

1. Xiong, H.; Zhang, A.; Zhao, Q.; Yan, G.; Sun, H.; Wang, X. Discovery of quality-marker ingredients of *Panax quinquefolius* driven by high-throughput chinmedomics approach. *Phytomedicine* **2020**, *74*, 152928. [CrossRef]
2. Yang, Z.; Deng, J.; Liu, M.; He, C.; Feng, X.; Liu, S.; Wei, S. A review for discovering bioactive minor saponins and biotransformative metabolites in *Panax quinquefolius* L. *Front. Pharmacol.* **2022**, *13*, 972813. [CrossRef]
3. Liu, L.; Xu, F.; Wang, Y. Traditional uses, chemical diversity and biological activities of *Panax* L. (Araliaceae): A review. *J. Ethnopharmacol.* **2020**, *263*, 112792. [CrossRef]


4. Hong, H.; Kim, J.; Lim, T.; Song, Y.; Cho, C.; Jang, M. Mixing ratio optimization for functional complex extracts of rhodiola crenulata, Panax quinquefolius, and astragalus membranaceus using mixture design and verification of immune functional efficacy in animal models. *J. Funct. Foods*. **2018**, *40*, 447–454. [CrossRef]
5. Wei, G.; Yang, F.; Wei, F.; Zhang, L.; Gao, Y.; Qian, J.; Chen, Z.; Jia, Z.; Wang, Y.; Su, H.; et al. Metabolomes and transcriptomes revealed the saponin distribution in root tissues of Panax quinquefolius and Panax notoginseng. *J. Ginseng Res.* **2020**, *44*, 757–769. [CrossRef]
6. Huang, L.; Ren, C.; Li, H.; Wu, Y. Recent progress on processing technologies, chemical components, and bioactivities of Chinese red ginseng, American red ginseng, and Korean red ginseng. *Food Bioprocess Technol.* **2022**, *15*, 47–71. [CrossRef]
7. Yoo, K.; Lee, C.; Lo, M.; Moon, B. The hypoglycemic effects of American red ginseng (*Panax quinquefolius* L.) on a diabetic mouse model. *J. Food Sci.* **2012**, *77*, 147–152. [CrossRef] [PubMed]
8. Guo, N.; Bai, Y.; Huang, X.; Liu, X.; Cai, G.; Liu, S.; Guo, Y.; Gong, J. Comparison of the saponins in three processed American ginseng products by ultra-high performance liquid chromatography-quadrupole orbitrap tandem mass spectrometry and multivariate statistical analysis. *Int. J. Anal. Chem.* **2022**, *2022*, 6721937. [CrossRef]
9. Wang, Y.; Li, H.; Li, Y.; Zhu, H.; Jin, Y. Identification of natural compounds targeting Annexin A2 with an anti-cancer effect. *Protein Cell.* **2018**, *9*, 568–579. [CrossRef] [PubMed]
10. Liu, M.; Xu, X.; Wang, X.; Wang, H.; Mi, Y.; Gao, X.; Guo, D.; Yang, W. Enhanced identification of ginsenosides simultaneously from seven Panax herbal extracts by data-dependent acquisition including a preferred precursor ions list derived from an in-house programmed virtual library. *J. Agric. Food Chem.* **2022**, *70*, 13796–13807. [CrossRef] [PubMed]
11. Li, X.; Liu, J.; Zuo, T.; Hu, Y.; Li, Z.; Wang, H.; Xu, X.; Yang, W.; Guo, D. Advances and challenges in ginseng research from 2011 to 2020: The phytochemistry, quality control, metabolism, and biosynthesis. *Nat. Prod. Rep.* **2022**, *39*, 875–909. [CrossRef]
12. Chen, W.; Balan, P.; Popovich, D. Comparison of ginsenoside components of various tissues of new zealand forest-grown Asian ginseng (*Panax Ginseng*) and American ginseng (*Panax Quinquefolium* L.). *Biomolecules* **2020**, *10*, 372. [CrossRef] [PubMed]
13. Xu, Q.; Fang, X.; Chen, D. Pharmacokinetics and bioavailability of ginsenoside Rb1 and Rg1 from Panax notoginseng in rats. *J. Ethnopharmacol.* **2003**, *84*, 187–192. [CrossRef]
14. Fu, L.; Zhang, W.; Zhou, X.; Fu, J.; He, C. Tumor cell membrane-camouflaged responsive nanoparticles enable MRI-guided immuno-chemodynamic therapy of orthotopic osteosarcoma. *Bioact. Mater.* **2022**, *17*, 221–233. [CrossRef] [PubMed]
15. Chen, C.; Chiou, W.; Zhang, J. Comparison of the pharmacological effects of Panax ginseng and Panax quinquefolium. *Acta Pharmacol. Sin.* **2008**, *29*, 1103–1108. [CrossRef]
16. Kim, S.; Kim, A. Anti-breast cancer activity of fine black ginseng (*Panax ginseng* Meyer) and ginsenoside Rg. *J. Ginseng Res.* **2015**, *39*, 125–134. [CrossRef]
17. Liu, Y.; Fan, D. The preparation of ginsenoside Rg5, its antitumor activity against breast cancer cells and its targeting of PI3K. *Nutrients* **2020**, *12*, 246. [CrossRef] [PubMed]
18. Yue, G.; Lee, J.; Li, L.; Chan, K.; Wong, E.; Chan, J.; Fung, K.; Lui, V.; Chiu, P.; Lau, C. Andrographis paniculata elicits anti-invasion activities by suppressing TM4SF3 gene expression and by anoikis-sensitization in esophageal cancer cells. *Am. J. Cancer Res.* **2015**, *5*, 3570–3587. [PubMed]
19. Deng, X.; Zhao, J.; Qu, L.; Duan, Z.; Fu, R.; Zhu, C.; Fan, D. Ginsenoside Rh4 suppresses aerobic glycolysis and the expression of PD-L1 via targeting AKT in esophageal cancer. *Biochem. Pharmacol.* **2020**, *178*, 114038. [CrossRef]
20. Huang, L.; Li, H.; Wu, Y. Processing technologies, phytochemistry, bioactivities and applications of black ginseng—a novel manufactured ginseng product: A comprehensive review. *Food Chem.* **2023**, *407*, 134714. [CrossRef]
21. Zheng, M.; Xu, F.; Li, Y.; Xi, X.; Cui, X.; Han, C.; Zhang, X. Study on transformation of ginsenosides in different methods. *BioMed. Res. Int.* **2017**, *2017*, 8601027. [CrossRef]
22. Liu, Z.; Wen, X.; Wang, C.; Li, W.; Huang, W.; Xiao, J.; Ruan, C.; Yuan, C. Remarkable impact of amino acids on ginsenoside transformation from fresh ginseng to red ginseng. *J. Ginseng Res.* **2020**, *44*, 424–434. [CrossRef]
23. Hu, J.; Xu, X.; Li, W.; Wang, Y.; Liu, Y.; Wang, Z.; Wang, Y. Ginsenoside Rk1 ameliorates paracetamol-induced hepatotoxicity in mice through inhibition of inflammation, oxidative stress, nitrativestress and apoptosis. *J. Ginseng Res.* **2019**, *43*, 10–19. [CrossRef]
24. Wang, C.; Aung, H.; Ni, M.; Wu, J.; Tong, R.; Wicks, S.; He, T.; Yuan, C. Red American ginseng: Ginsenoside constituents and antiproliferative activities of heat-processed Panax quinquefolius roots. *Planta Med.* **2007**, *73*, 669–674. [CrossRef]
25. Sun, B.; Xu, M.; Li, Z.; Wang, Y.; Sung, C. UPLC-Q-TOF-MS/MS analysis for steaming times-dependent profiling of steamed Panax quinquefolius and its ginsenosides transformations induced by repetitious steaming. *J. Ginseng Res.* **2012**, *36*, 277–290. [CrossRef]
26. Huang, X.; Liu, Y.; Zhang, Y.; Li, S.; Yue, H.; Chen, C.; Liu, S. Multicomponent assessment and ginsenoside conversions of Panax quinquefolium L. roots before and after steaming by HPLC-MSn. *J. Ginseng Res.* **2019**, *43*, 27–37. [CrossRef]
27. Fan, W.; Yang, Y.; Li, L.; Fan, L.; Wang, Z.; Yang, L. Mass spectrometry-based profiling and imaging strategy, a fit-for-purpose tool for unveiling the transformations of ginsenosides in Panax notoginseng during processing. *Phytomedicine* **2022**, *103*, 154223. [CrossRef] [PubMed]
28. Wu, W.; Sun, L.; Zhang, Z.; Guo, Y.; Liu, S. Profiling and multivariate statistical analysis of Panax ginseng based on ultra-high-performance liquid chromatography coupled with quadrupole-time-of-flight mass spectrometry. *J. Pharm. Biomed. Anal.* **2015**, *107*, 141–150. [CrossRef] [PubMed]

29. Shi, Y.; Guo, Y.; Wang, Y.; Li, M.; Li, K.; Liu, X.; Fang, C.; Luo, J. Metabolomic Analysis Reveals Nutritional Diversity among Three Staple Crops and Three Fruits. *Foods* **2022**, *11*, 550. [CrossRef] [PubMed]
30. Li, L.; Wang, D.; Sun, C.; Li, Y.; Lu, H.; Wang, X. Comprehensive lipidome and metabolome profiling investigations of *Panax quinquefolius* and application in different growing regions using liquid chromatography coupled with mass spectrometry. *J. Agric. Food Chem.* **2021**, *69*, 6710–6719. [CrossRef] [PubMed]
31. Yang, W.; Hu, Y.; Wu, W.; Ye, M.; Guo, D. Saponins in the genus *Panax* L. (Araliaceae): A systematic review of their chemical diversity. *Phytochemistry* **2014**, *106*, 7–24. [CrossRef] [PubMed]
32. Tung, N.; Song, G.; Nhiem, N.; Ding, Y.; Tai, B.; Jin, L.; Lim, C.; Hyun, J.; Park, C.; Kang, H.; et al. Dammarane-type saponins from the flower buds of *Panax ginseng* and their intracellular radical scavenging capacity. *J. Agric. Food Chem.* **2010**, *58*, 868–874. [CrossRef] [PubMed]
33. Lee, Y.; Park, H.; Lee, D.; Jayakodi, M.; Kim, N.; Koo, H.; Lee, S.; Kim, Y.; Kwon, S.; Yang, T. Integrated transcriptomic and metabolomic analysis of five *Panax ginseng* cultivars reveals the dynamics of ginsenoside biosynthesis. *Front. Plant Sci.* **2017**, *8*, 1048. [CrossRef] [PubMed]
34. Mao, Q.; Bai, M.; Xu, J.; Kong, M.; Zhu, L.; Zhu, H.; Wang, Q.; Li, S. Discrimination of leaves of *Panax ginseng* and *P. quinquefolius* by ultrahigh performance liquid chromatography quadrupole/time-of-flight mass spectrometry based metabolomics approach. *J. Pharm. Biomed. Anal.* **2014**, *97*, 129–140. [CrossRef]
35. Xu, X.; Gao, Y.; Xu, S.; Liu, H.; Xue, X.; Zhang, Y.; Zhang, H.; Liu, M.; Xiong, H.; Lin, R.; et al. Remarkable impact of steam temperature on ginsenosides transformation from fresh ginseng to red ginseng. *J. Ginseng Res.* **2018**, *42*, 277–287. [CrossRef]
36. Wu, W.; Qin, Q.; Guo, Y.; Sun, J.; Liu, S. Studies on the chemical transformation of 20(S)-protopanaxatriol (PPT)-type ginsenosides Re, Rg2, and Rf using rapid resolution liquid chromatography coupled with quadruple-time-of-flight mass spectrometry (RRLC-Q-TOF-MS). *J. Agric. Food Chem.* **2012**, *60*, 10007–10014. [CrossRef]

Disclaimer/Publisher’s Note: The statements, opinions and data contained in all publications are solely those of the individual author(s) and contributor(s) and not of MDPI and/or the editor(s). MDPI and/or the editor(s) disclaim responsibility for any injury to people or property resulting from any ideas, methods, instructions or products referred to in the content.

Article

Determination of A1 and A2 β -Casein in Milk Using Characteristic Thermolytic Peptides via Liquid Chromatography-Mass Spectrometry

Zeyang Liu ^{1,2}, Susu Pan ³, Peize Wu ², Ming Li ^{2,*}  and Dapeng Liang ^{1,*}

¹ Key Laboratory of Groundwater Resources and Environment of the Ministry of Education, Jilin University, Changchun 130012, China

² Division of Chemical Metrology & Analytical Science, National Institute of Metrology, Beijing 100029, China

³ Division of Ecology Environment and Energy Resources, Beijing Institute of Metrology, Beijing 100012, China

* Correspondence: mingutah@hotmail.com (M.L.); liangdp@jlu.edu.cn (D.L.)

Abstract: β -casein, a protein in milk and dairy products, has two main variant forms termed as A1 and A2. A1 β -casein may have adverse effects on humans. The fact that there is only one amino acid variation at the 67th position between A1 and A2 β -casein makes it difficult to distinguish between them. In this study, a novel method using characteristic thermolytic peptides is developed for the determination of A1 and A2 β -casein in milk. Firstly, caseins extracted from milk samples are thermolytic digested at 60 °C without any denaturing reagents required for unfolding proteins, which simplifies the sample pretreatment procedure. The characteristic thermolytic peptides (i.e., fragments 66–76 and 59–76 for A1 and A2 β -casein, respectively) selected to specifically distinguish A1 and A2 β -casein only have eleven or eighteen amino acid moieties. Compared with tryptic characteristic peptides with a length of 49 amino acid moieties, these shorter thermolytic characteristic peptides are more suitable for LC-MS analysis. This novel method, with the advantages of high specificity, high sensitivity, and high efficiency, was successfully applied for the analysis of six milk samples collected from a local supermarket. After further investigation, it is found that this method would contribute to the development of A2 dairy products for a company and the quality inspection of A2 dairy products for a government.



Citation: Liu, Z.; Pan, S.; Wu, P.; Li, M.; Liang, D. Determination of A1 and A2 β -Casein in Milk Using Characteristic Thermolytic Peptides via Liquid Chromatography-Mass Spectrometry. *Molecules* **2023**, *28*, 5200. <https://doi.org/10.3390/molecules28135200>

Academic Editor: Francesco Cacciola

Received: 25 May 2023

Revised: 2 July 2023

Accepted: 2 July 2023

Published: 4 July 2023



Copyright: © 2023 by the authors. Licensee MDPI, Basel, Switzerland. This article is an open access article distributed under the terms and conditions of the Creative Commons Attribution (CC BY) license (<https://creativecommons.org/licenses/by/4.0/>).

Keywords: β -casein; A2 milk; thermolysin; liquid chromatography; tandem mass spectrometry

1. Introduction

The ingestion of milk protein plays an indispensable role in human metabolism, nutrition acquisition and physical health [1]. About 80% of milk protein is casein [2], mainly including α , β and κ -casein, among which β -casein (β -CN) accounts for about 40% [3]. More than ten variant forms of β -CN exist in milk, and A1 β -CN and A2 β -CN are the two main forms [4]. The only difference between these two variants is the amino acid moiety at the 67th position, i.e., there is a proline moiety in A2 β -CN, while there is histidine moiety in A1 β -CN [5]. Although this difference is very slight, the bioactive peptides produced by the digestion of these two variants have significantly different effects on humans [6]. A1 β -CN, when digested, produces β -casomorphin-7 (BCM-7) [7], which can cause many diseases [8]. Conversely, BCM-7 is not generated from A2 β -CN [9]. In addition, BCM-7 is more easily absorbed by infants and young children compared with adults [10]. It was also found that the BCM-7 level in the urine of children with autism was significantly higher than that in healthy children, and the severity of illness was positively correlated with the BCM-7 level [11]. In many countries, milk and dairy product containing only A2 β -CN are labeled as A2 products for the consumer to make targeted choices. Therefore, the determination of the β -CN variant is of great significance for food manufacturers as well as consumers.

Originally, milk and dairy products with different β -CN variants were directly traced to milk collected from different cattle populations [12]. Several methods based on different principles have also been developed to determine different β -CN variants in milk or various dairy products. For example, an electrophoresis coupled with multiple linear regression (MLR) method could initially predict various caseins in cheese [13]. A urea–polyacrylamide electrophoresis method was developed to distinguish A1 and A2 β -CN variants in milk [14]. A polymerase chain reaction (PCR) combined with the high-resolution melting method has also been applied to identify β -CN variants [15,16]. In recent years, liquid chromatography–mass spectrometry with advantages of high sensitivity, high accuracy, and high specificity is widely used in various fields. Liquid chromatography has the capability of separating different proteins in milk, while high-resolution mass spectrometry has the advantages of high specificity and high sensitivity in determining the molecular weights of intact proteins. However, it is very difficult to completely separate intact β -CN variants using liquid chromatography because their physical and chemical properties are extremely similar. In addition, direct detection of the molecular weights for intact caseins [17] creates high requirements for the mass range and ionization performance of a mass spectrometer. Alternatively, it is more feasible to determine β -CN variants through detecting characteristic peptides after enzyme digestion [18]. Recently, characteristic peptides with a length of 49 amino acid moieties, produced by trypsin digestion, were reported to determine A1 and A2 β -CN in milk [19]. The molecular weights of these characteristic tryptic peptides are much higher than the ideal mass range (i.e., 700–1500 daltons) [20] for mass spectrometric analysis.

In this study, thermolysin was adopted for use in protein digestion. Considering that the difference between A1 and A2 β -CN variants is the amino acid moiety at 67th position in the sequence, the observed β -CN fragments 66–76 and 59–76 after digestion were selected as characteristic peptides for A1 and A2 β -CN, respectively. The characteristic thermolytic peptides of A1 and A2 β -CN were obviously different in both composition and length, which facilitates liquid chromatography separation. Meanwhile, the shorter characteristic peptides could be beneficial for mass detection and peptide standard synthesis [21]. A method based on liquid chromatography–mass spectrometry (LC-MS) has been established to determine characteristic thermolytic peptides of A1 and A2 β -CN variants in milk. These characteristic peptides were analyzed by means of MS/MS experiments under collision-induced dissociation (CID) mode, which further increases the specificity of the method, and thus the reliability of the result. For application demonstration, six commercial milk samples (i.e., four normal milk samples and two A2 milk samples) were analyzed using this method. The results prove that this method has the advantages of high specificity, high sensitivity, and high efficiency, and thus would contribute to the development of A2 dairy products for a company and the quality inspection of A2 dairy products for a government.

2. Results and Discussion

2.1. Choice of Thermolytic Characteristic Peptides

To fully dissolve the proteins, a buffer solution is usually prepared with urea, dithiothreitol, or inorganic salts added [22], which contributes to protein unfolding and thus improves the efficiency of extraction and enzymatic digestion. The sample should be desalted before being subjected to LC-MS analysis, avoiding contamination of the mass spectrometer. To improve extraction efficiency and reduce sample preparation time, a protein extraction method based on isoelectric precipitation was developed in this study. A Tris-HCl buffer solution was used to extract caseins. After sufficient precipitation, caseins were isolated by means of centrifugation at 4 °C. The low-temperature centrifugation can reduce the interaction between hydrophobic groups in the milk protein, preventing the aggregation of whey protein and casein.

Thermolysin preferentially cleaves the amide bond positioned at the N-terminus of the hydrophobic residues such as leucine, phenylalanine, valine, isoleucine, alanine, and methionine. Thermolysin still maintains activity at 60 °C [23], which facilitates protein unfolding without additional denaturing reagents being required, and it thus is conducive

to digestion [24]. Therefore, thermolysin was chosen as a digestion enzyme in this study. Thermolytic fragments containing different amino acid moieties at the 67th position in β -caseins were selected as the characteristic peptides distinguishing A1 and A2 β -caseins, and the sequences of A1 peptide and A2 peptide are listed in Table 1.

Table 1. Detailed information of A1 peptide and A2 peptide.

Peptide	Amino Acid Sequence	Theoretical Mass (Da) [M + H] ⁺	Observed Mass (Da) [M + H] ⁺	Error (ppm)
A1	IHNSLPQNIPP	1229.664	1229.671	6.3
A2	VYPPFGPIPNSLPQNIPP	1947.038	1947.049	6.1

One of the favored cleavage sites is the N-terminus of position P1', Ile66 in this case. However, thermolytic cleavage is blocked when proline is located at position P2', as reported previously [25], e.g., Pro67 for A2 protein. This is the reason that different lengths of A1 and A2 peptides were observed. Similarly, cleavage of Ile74 was not blocked because of the presence of Pro75. Therefore, no other peptide in the Pro/His67 area was observed in this study. The digestion experimental conditions were carefully optimized using a β -casein standard. The relative abundances of A1 peptide, which was generated after enzyme digestion, against reaction time, and the amount of thermolysin are shown in Figure 1a,b, respectively. When the incubation time and amount of thermolysin added were optimized, the same trends for the A2 peptide level were also observed under the same condition. Finally, a digestion reaction time of 4 h and a protein to enzyme ratio of 1:20 were adopted for the experiments. Under optimized digestion conditions, no intact proteins were detected using the mass spectrometer, which proved that the reaction had been completed.

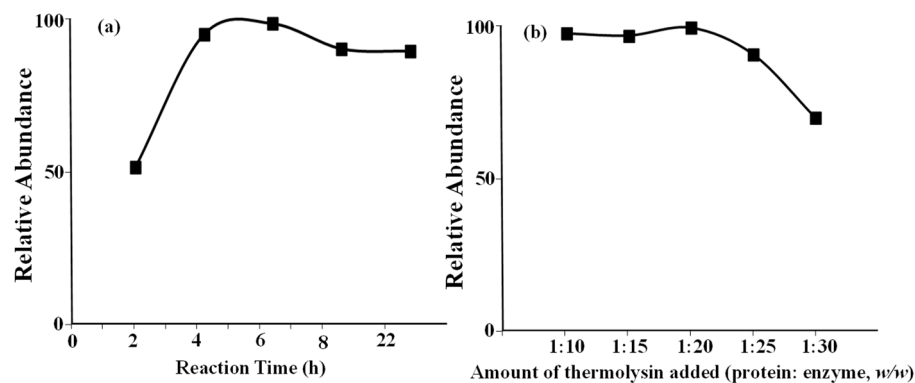


Figure 1. Optimization of experimental conditions. (a) Reaction time. (b) Amount of thermolysin added.

2.2. Chromatographic Separation and MS/MS Analysis

A mixture solution of synthetic A1 peptide and A2 peptide standards (15 μ g/mL) was used to optimize the liquid chromatography gradient. A core-shell LC column, which was previously found to be suitable for the separation of peptides [26,27], was chosen for the separation of β -CN digestion products. A1 peptide and A2 peptide can be completely separated, as shown in Figure 2.

A relatively long LC gradient of 30 min was adopted in this study, reducing the matrix effect as much as possible. When a shorter LC gradient is developed, analytical efficiency will be significantly increased, while slightly compromising the measurement accuracy. After liquid chromatographic separation, the peptides were analyzed using a high-resolution mass spectrometer and the full mass spectra of A1 peptide and A2 peptide are shown in Figure 3a,b, respectively.

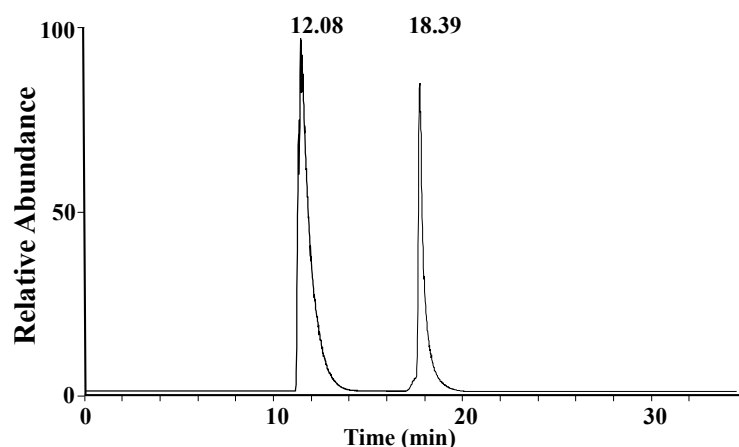


Figure 2. Overlap of extracted ion chromatograms of the A1 peptide and A2 peptide in a mixture standard solution (15 µg/mL).

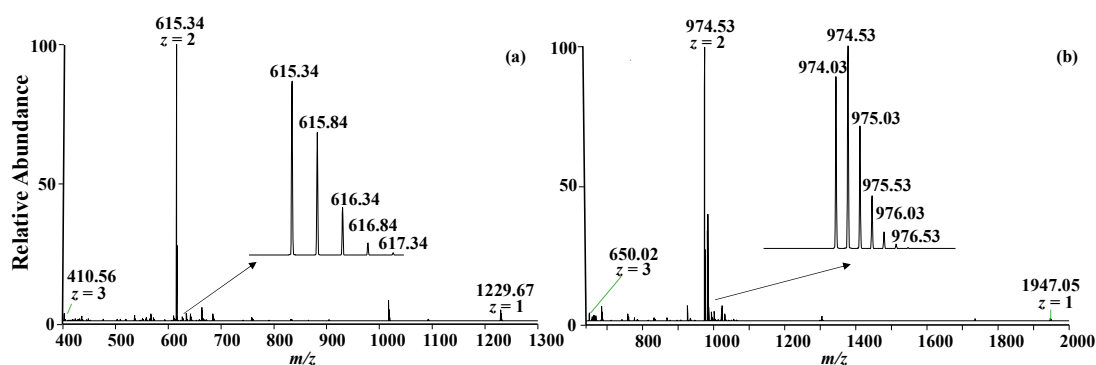


Figure 3. (a) Full mass spectrum of A1 peptide—the insert shows the isotope distribution. (b) Full mass spectrum of A2 peptide—the insert shows the isotope distribution.

In the full mass spectra, several multiple charge states were clearly observed as expected [28]. The most intense peaks correspond to the doubly charged species for A1 peptide (m/z : 615.34) and A2 peptide (m/z : 974.03). The isotope distributions exhibited in the inserts of Figure 3a,b are consistent with the theoretical data obtained from a program on a website (<https://www.sisweb.com/mstools/isotope.htm>, accessed on 16 June 2023). The relative errors of the exact masses are less than 6.3 ppm, as listed in Table 1. The experimental MS/MS spectra of the peptides upon collision-induced dissociation are also consistent with the theoretical data.

2.3. Method Validation

A soybean milk was chosen as a blank for the negative control study, no thermolytic characteristic peptides were detected after the sample preparation process. Thermolysis experiments were performed six times in six days, and the characteristic peptides (i.e., A1 β -CN fragment 66–76 and A2 β -CN fragment 59–76) were always observed. The relative standard deviations ($n = 6$) of reproducibility were calculated to be 3.1% and 2.9% for A1 peptide and A2 peptide, respectively. Several methods using isotope-labelled peptides or heavy-labelled peptides are available for accurate protein quantification after enzyme digestion. This study mainly aims to report novel characteristic thermolytic peptides for the determination of A1 and A2 β -casein in milk. Therefore, the standard addition method, which is relatively simple, was performed for quantitative analysis of characteristic peptides in the thermolytic digestion solution. After a series of A1 peptide and A2 peptide stock solutions were added, the total amounts of A1 peptide and A2 peptide in the digestion solution were measured by using the established LC-MS² method. A calibration curve for measuring A1 peptide was obtained with a satisfactory linearity ($R^2 = 0.998$), and

acceptable relative standard deviations (RSD) of 3.6~4.5% ($n = 6$). A calibration curve for measuring A2 peptide was obtained with a satisfactory linearity ($R^2 = 0.992$) and relative standard deviations (RSD) of 3.2~4.8% ($n = 6$). Consequently, the original concentrations of A1 peptide and A2 peptide were calculated based on the linear responds against total peptide concentrations. Finally, the amounts of A1 protein and A2 protein in the milk samples were calculated, assuming that they were equal to the amounts of A1 peptide and A2 peptide, respectively. The limits of detection (LOD, $S/N = 3$) for A1 peptide and A2 peptide were determined to be 25 ng/mL, and 31 ng/mL, respectively. Therefore, LODs for A1 protein and A2 protein in the digestion sample were calculated to be 0.48 $\mu\text{g/mL}$, and 0.38 $\mu\text{g/mL}$, respectively. With the dilution steps during sample preparation considered, the LODs for A1 protein and A2 protein in a milk sample were calculated to be 0.22 mg/mL and 0.18 mg/mL, respectively. Notably, the LODs for A1 protein and A2 protein in a milk sample could be significantly improved by slightly reducing the dilution fold during the sample preparation process.

2.4. Determination of A1 and A2 β -CN in Milk

For the application demonstration, six commercial milk samples (i.e., four normal milk samples and four A2 milk samples) collected from a local supermarket were analyzed using this novel method. For the negative control, a soybean milk sample was analyzed using the same method.

With an LC-MS method, A1 and A2 peptides could be determined based on their retention times and exact masses, distinguishing β -CN variants. However, false signals could be generated if an isobaric peptide with the same retention time is present in the digestion solution sample. Alternatively, tandem mass spectrometry can further increase the specificity of the LC-MS method, and thus improve the reliability of the result. In this study, the characteristic peptides containing varied amino acid moieties at the 67th position were subjected to fragmentation upon collision-induced dissociation. The fragmental ions were clearly annotated, as shown in Figure 4, and are consistent with the theoretical MS/MS data.

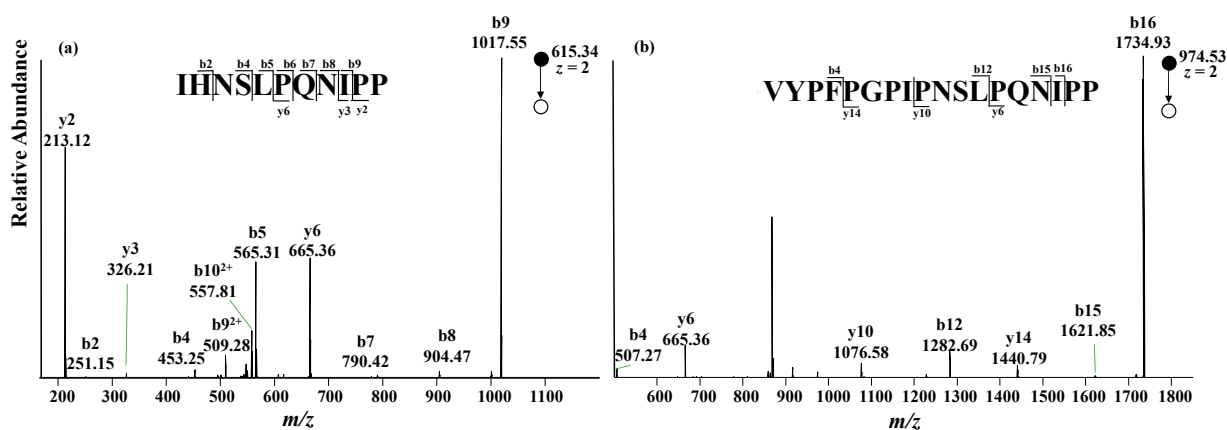


Figure 4. MS/MS spectra of A1 peptide (a) and A2 peptide (b) in the milk samples analyzed.

An extracted ion chromatogram constructed from the tandem mass spectrum, instead of the full mass spectrum, could avoid the possible false signals from the isobaric peptides with the same retention time as characteristic peptides, which greatly increases the specificity and sensitivity of the analytical method. Given that the fragmental ions annotated as b_9 for A1 peptide and b_{16} for A2 peptide (shown in Figure 4) are the two most abundant product ions, b_9 (A1) and b_{16} (A2) were chosen to quantitatively analyze A1 peptide and A2 peptide. Meanwhile, the fragmental ions y_6 (A1) and y_6 (A2) were chosen to assess peptide identity, increasing method specificity. A standard addition method was adopted for quantitative analysis by adding A1 and A2 peptide mixed standard solutions in the

thermolytic digestion solution. The mass spectrometer was set to the MS² mode with a collision energy of 18 arb. Integrated areas of b₉ (A1) and b₁₆ (A2) peaks in the extracted ion chromatogram from the tandem mass spectrum were used as quantitative signals for establishing standard addition curves. As listed in Table 2, both A1 peptide and A2 peptide were detected for all four normal milk samples. The A1 β-CN level is approximately two to four times higher than the A2 β-CN level in the normal milk samples analyzed.

Table 2. Contents of A1 β-casein and A2 β-casein detected in 6 commercially available milk samples (mg/mL).

Milk Sample	A1 β-Casein	A2 β-Casein
Normal 1	5.98	3.13
Normal 2	6.81	1.98
Normal 3	8.68	2.62
Normal 4	5.59	1.51
A2 sample 1	<0.22	4.87
A2 sample 2	0.66	3.15

For A2 milk sample 1, an A2 peptide signal exclusively appeared in the overlay of EIC for A1 and A2 peptides, as expected. For A2 milk sample 2, an A1 peptide signal with small intensity also appeared in the overlay of EIC for A1 and A2 peptides. Compared with the four normal milk samples, the A1 peptide signal in A2 milk sample 2 is significantly lower than the A2 peptide signal, indicating that only a small amount of the A1 β-CN variant exists in A2 milk sample 2. Although the manufacturer states that the A2 milk product exclusively contains A2 β-CN variant, the existence of a very small amount of A1 β-CN variant still can be detected using the characteristic thermolytic peptides based on LC-MS/MS.

3. Experimental Section

3.1. Reagents

Triton X-100, β-casein standard from bovine milk, and thermolysin were purchased from Sigma-Aldrich (St. Louis, MO, USA). Sodium chloride was purchased from Suprapur (Merck, Darmstadt, Germany). Tris(hydroxymethyl) aminomethane was purchased from GPC Biotechnology (Beijing, China). Formic acid was purchased from Fluka (Buchs, Switzerland). Ultrapure water (18.2 MΩ·cm⁻¹) was produced using a Milli-Q system (Fisher Scientific, San Jose, CA, USA). The peptide standards of A1 and A2 β-CN fragments 66–76 and 59–76 (named as A1 peptide, A2 peptide, respectively) were synthesized by SBS (Beijing, China). Six commercial milk samples including four normal milk samples and two A2 milk samples were purchased from a local supermarket.

3.2. Instrument

A high-speed refrigerated centrifuge (CR 21GIII, Hitachi, Hitachinaka, Japan), pH meter (FE20-K, Mettler Toledo, Zurich, Switzerland) and orbital incubator (SI500, Stuart, Stone, UK) were used for sample pretreatment. A series 1250 liquid chromatograph coupled with a linear quadrupole ion trap (LTQ)-Orbitrap Velos Pro mass spectrometer (Thermo Fisher Scientific, San Jose, CA, USA) was used for peptide separation and detection. An electrospray ionization source (ESI) was used for ion generation. The mass spectrometer was operated in positive ion mode. Collision-induced dissociation (CID) in an ion trap was adopted for tandem mass spectrometry (MS/MS) experiments.

3.3. LC Parameters

Liquid chromatographic separation was performed using a core-shell LC column (Kinetex C18, 150 × 4.6 mm, 2.6 μm, 100 Å; Phenomenex, Torrance, CA, USA). The injection volume was set at 10 μL, and the flow rate was set at 0.3 mL/min. Eluent A consisted of water:formic acid (1000:1, v/v) and eluent B consisted of acetonitrile:formic acid (1000:1,

v/v). The LC mobile phase gradient was started at 5% eluent B, then gradually increased to 55% eluent B in 25 min, and then gradually increased to 95% eluent B in 10 min.

3.4. MS Parameters

To obtain optimal signal intensities for the peptides, four parameters (source voltage, sheath gas flow rate, auxiliary gas, and capillary temperature) were carefully optimized. The optimized MS parameters were set as: ESI needle position D (vertical), 2 (forward–backward); source voltage, 3.5 kV; sheath gas flow rate, 5 arb (arbitrary units); auxiliary gas flow rate, 20 arb for A1 peptide, 5 arb for A2 peptide; capillary temperature, 300 °C. The mass resolution of the Orbitrap was set at 30,000. The data type was set to “profile”, and the mass range was set at m/z 150–2000 Th. For MS/MS experiments, the normalized collision energy was set at 18 arb for A1 peptide and 21 for A2 peptide under CID mode.

3.5. Sample Preparation

Caseins in milk were isolated by means of isoelectric precipitation from crude mixtures. Firstly, 10 mL of the milk sample was dissolved in 40 mL of tris-HCl solution (50 mmol/L). Then, 10 mL of the abovementioned solution and 10 mL of a NaCl solution (0.5 mol/L) were mixed using a vortex mixer. The pH of this mixture solution was adjusted to 4.6–4.8 with a 10% formic acid aqueous solution. The sample solution was stored at 4 °C in a freezer overnight, waiting for caseins to be completely precipitated. Then, the sample was centrifuged for 15 min (4 °C, 10,000 r/min). The precipitate collected was dissolved in 10 mL of tris-HCl solution (50 mmol/L). Then, 500 µL of the casein solution mentioned above was diluted two-fold with ultrapure water, and a suitable amount of thermolysin (1 mg/mL) was added to perform an enzymatic digestion reaction at 60 °C for 4 h. The digestion reaction was terminated by adding 20 µL of a 10% formic acid aqueous solution. The digestion product was centrifuged for 10 min (4 °C, 10,000 r/min) and the supernatant was collected for subsequent LC-MS analysis.

3.6. Standard Addition Method

In the standard addition method, 0 µL, 5 µL, 10 µL, 15 µL, and 20 µL of A1 and A2 peptide mixed standard solution (15 µg/mL) were separately spiked into five 250 µL digestion samples. Then, ultrapure water was added into the spiked samples, reaching a constant volume of 500 µL. Finally, contents of A1 peptide and A2 peptide in the abovementioned samples were measured by using the established LC-MS² method. Extracted ion chromatogram was constructed from a tandem mass spectrum using b_9 (A1) and b_{16} (A2). Areas of b_9 (A1) and b_{16} (A2) peaks in the extracted ion chromatogram from the tandem mass spectrum were manually integrated to establish standard addition curves. The x-intercept of the extrapolated line was calculated as the original concentration of the analyte in the sample solution. Given that the digestion sample was diluted twice during the standard addition process, the contraction of the analyte in the original digestion sample can be obtained by multiplying it by a factor of 2.

3.7. Data Evaluation

All the mass spectra were recorded using Xcalibur[®] software (version 2.2) equipped in the instrument (Thermo Fisher Scientific, San Jose, CA, USA). Theoretical data of MS/MS product ions of peptides produced by enzymatic digestion were calculated using the MS-Product tool available from a website (<https://prospector2.ucsf.edu/prospector/cgi-bin/msform.cgi?form=msproduct>, accessed on 16 June 2023). The possible sequences of peptides generated from thermolytic digestion of β -casein were predicted using the Peptide-Cutter tool available from a website (https://web.expasy.org/peptide_cutter/, accessed on 16 June 2023).

4. Conclusions

In this study, a novel method has been developed to determine A1 and A2 β -CN variants in milk using characteristic thermolytic peptides. Casein extraction from milk samples was achieved by means of isoelectric precipitation with a tris-HCl buffer solution at pH 4.6–4.8. Thermolysin, chosen as an enzyme for casein digestion, maintains activity at a higher temperature of 60 °C, which facilitates protein unfolding and thus improves the efficiency of enzymatic digestion. After thermolytic digestion, characteristic peptides containing the varied amino acid moiety at the 67th position in the β -CN sequence were selected as signatures determining A1 and A2 β -CN variants in milk samples. Compared with tryptic characteristic peptides with a length of 49 amino acid moieties, these thermolytic characteristic peptides (i.e., fragments 66–76 and 59–76 for A1 and A2 β -CN, respectively) are relative shorter, which are more suitable for LC-MS analysis. Under the optimized liquid chromatography gradient, A1 peptide and A2 peptide could be separated completely. With the information regarding the retention times, molecular weights obtained from full mass spectra, and fragmental behaviors of characteristic peptides from tandem mass spectra, unambiguous determination of β -CN variants can be successfully accomplished. Finally, six commercially available milk samples including four normal milk samples and two A2 milk samples were analyzed for the application demonstration of this novel method. The A1 β -CN variant in all of the normal milk samples tested accounts for the majority. No A1 β -CN variant was detected in one A2 labeled milk sample, and a small amount of an A1 β -CN variant was clearly detected in another A2-labeled milk sample. Although the amount of this A1 β -CN variant in this A2-labeled milk product is very low, it may still cause adverse effects in humans. To reduce the potential risk to customers, it would be very helpful to develop a method to determine A1 and A2 β -casein in milk.

This novel method developed here has the advantages of high sensitivity, high specificity, and high efficiency. After further investigation, it would contribute to the development of A2 dairy products for a company and the quality inspection of A2 dairy products for a government.

Author Contributions: Conceptualization, M.L.; Methodology, M.L. and D.L.; Validation, P.W.; Investigation, Z.L., S.P. and P.W.; Data curation, Z.L., S.P. and D.L.; Writing—Original draft, Z.L. and S.P.; Writing—Review and editing, M.L.; Project administration, M.L.; Funding acquisition, M.L. All authors have read and agreed to the published version of the manuscript.

Funding: This work was supported by National Key R&D Program of China (No. 2021YFF0600701 and 2017YFF0205403).

Institutional Review Board Statement: Not applicable.

Informed Consent Statement: Not applicable.

Data Availability Statement: The data that support the findings of this study will be available from the corresponding authors upon reasonable request.

Conflicts of Interest: The authors declare no conflict of interest.

Sample Availability: Samples of the compounds are not available from the authors.

References

1. Borad, S.G.; Kumar, A.; Singh, A.K. Effect of processing on nutritive values of milk protein. *Crit. Rev. Food Sci. Nutr.* **2017**, *57*, 3690–3702. [CrossRef] [PubMed]
2. Nguyen, D.D.; Solah, V.A.; Busetti, F.; Smolenski, G.; Cooney, T. Application of ultra-high performance liquid chromatography coupled to high-resolution mass spectrometry (Orbitrap) for the determination of beta-casein phenotypes in cow milk. *Food Chem.* **2020**, *307*, 125532. [CrossRef] [PubMed]
3. Asledottir, T.; Le, T.T.; Petrat-Melin, B.; Devold, T.G.; Larsen, L.B.; Vegarud, G.E. Identification of bioactive peptides and quantification of β -casomorphin-7 from bovine β -casein A1, A2 and I after ex vivo gastrointestinal digestion. *Int. Dairy J.* **2017**, *71*, 98–106. [CrossRef]
4. Farrell, H.M.; Jimenez-Flores, R.; Bleck, G.T.; Brown, E.M.; Butler, J.E.; Creamer, L.K.; Hicks, C.L.; Hollar, C.M.; Ng-Kwai-Hang, K.F.; Swaisgood, H.E. Nomenclature of the proteins of cows' milk—Sixth revision. *J. Dairy Sci.* **2004**, *87*, 1641–1674. [CrossRef]

5. Gigliotti, R.; Gutmanis, G.; Katiki, L.M.; Okino, C.H.; de Sena Oliveira, M.C.; Filho, A.E.V. New high-sensitive rhAmp method for A1 allele detection in A2 milk samples. *Food Chem.* **2020**, *313*, 126167. [CrossRef]
6. Boutrou, R.; Gaudichon, C.; Dupont, D.; Jardin, J.; Airinei, G.; Marsset-Baglieri, A.; Benamouzig, R.; Tomé, D.; Leonil, J. Sequential release of milk protein-derived bioactive peptides in the jejunum in healthy humans. *Am. J. Clin. Nutr.* **2013**, *97*, 1314–1323. [CrossRef]
7. Asledottir, T.; Le, T.T.; Poulsen, N.A.; Devold, T.G.; Larsen, L.B.; Vegarud, G.E. Release of β -casomorphin-7 from bovine milk of different β -casein variants after ex vivo gastrointestinal digestion. *Int. Dairy J.* **2018**, *81*, 8–11. [CrossRef]
8. Bell, S.J.; Grochoski, G.T.; Clarke, A.J. Health implications of milk containing beta-casein with the A2 genetic variant. *Crit. Rev. Food Sci. Nutr.* **2006**, *46*, 93–100. [CrossRef]
9. Ho, S.; Woodford, K.; Kukuljan, S.; Pal, S. Comparative effects of A1 versus A2 beta-casein on gastrointestinal measures: A blinded randomised cross-over pilot study. *Eur. J. Clin. Nutr.* **2014**, *68*, 994–1000. [CrossRef]
10. Duarte-Vázquez, M.Á.; García-Ugalde, C.; Villegas-Gutiérrez, L.M.; García-Almendárez, B.E.; Rosado, J.L. Production of Cow's Milk Free from Beta-Casein A1 and Its Application in the Manufacturing of Specialized Foods for Early Infant Nutrition. *Foods* **2017**, *6*, 50. [CrossRef]
11. Sokolov, O.; Kost, N.; Andreeva, O.; Korneeva, E.; Meshavkin, V.; Tarakanova, Y.; Dadayan, A.; Zolotarev, Y.; Grachev, S.; Mikheeva, I.; et al. Autistic children display elevated urine levels of bovine casomorphin-7 immunoreactivity. *Peptides* **2014**, *56*, 68–71. [CrossRef] [PubMed]
12. Olenski, K.; Kamiński, S.; Szyda, J.; Cieslinska, A. Polymorphism of the beta-casein gene and its associations with breeding value for production traits of Holstein–Friesian bulls. *Livest. Sci.* **2010**, *131*, 137–140. [CrossRef]
13. Rodríguez-Nogales, J.M.; Vázquez, F. Application of electrophoretic and chemometric analysis to predict the bovine, ovine and caprine milk percentages in Panela cheese, an unripened cheese. *Food Control* **2007**, *18*, 580–586. [CrossRef]
14. Duarte-Vázquez, M.Á.; García-Ugalde, C.R.; Álvarez, B.E.; Villegas, L.M. Use of urea-polyacrylamide electrophoresis for discrimination of A1 and A2 beta casein variants in raw cow's milk. *J. Food Sci. Technol.* **2018**, *55*, 1942–1947. [CrossRef]
15. Royo, L.J.; del Cerro, A.; Vicente, F.; Carballal, A.; de la Roza-Delgado, B. An accurate high-resolution melting method to genotype bovine β -casein. *Eur. Food Res. Technol.* **2013**, *238*, 295–298. [CrossRef]
16. Dobosy, J.R.; Rose, S.D.; Beltz, K.R.; Rupp, S.M.; Powers, K.M.; Behlke, M.A.; Walder, J.A. RNase H-dependent PCR (rhPCR): Improved specificity and single nucleotide polymorphism detection using blocked cleavable primers. *BMC Biotechnol.* **2011**, *11*, 80. [CrossRef] [PubMed]
17. Fuerer, C.; Jenni, R.; Cardinaux, L.; Andetson, F.; Wagnière, S.; Moulin, J.; Affolter, M. Protein fingerprinting and quantification of beta-casein variants by ultra-performance liquid chromatography-high-resolution mass spectrometry. *J. Dairy Sci.* **2020**, *103*, 1193–1207. [CrossRef]
18. Miralles, B.; Leaver, J.; Ramos, M.; Amigo, L. Mass mapping analysis as a tool for the identification of genetic variants of bovine β -casein. *J. Chromatogr. A* **2003**, *1007*, 47–53. [CrossRef]
19. De Poi, R.; De Dominicis, E.; Gritti, E.; Fiorese, F.; Saner, S.; de Laureto, P.P. Development of an LC-MS Method for the Identification of beta-Casein Genetic Variants in Bovine Milk. *Food Anal. Methods* **2020**, *13*, 2177–2187. [CrossRef]
20. Laskay, Ü.A.; Lobas, A.A.; Srzentić, K.; Gorshkov, M.V.; Tsybin, Y.O. Proteome Digestion Specificity Analysis for Rational Design of Extended Bottom-up and Middle-down Proteomics Experiments. *J. Proteome Res.* **2013**, *12*, 5558–5569. [CrossRef]
21. Okada, Y. Synthesis of Peptides by Solution Methods. *Curr. Org. Chem.* **2001**, *5*, 1–43. [CrossRef]
22. Mansor, M.; Al-Obaidi, J.R.; Jaafar, N.N.; Ismail, I.H.; Zakaria, A.F.; Abidin, M.A.Z.; Selamat, J.; Radu, S.; Jambari, N.N. Optimization of Protein Extraction Method for 2DE Proteomics of Goat's Milk. *Molecules* **2020**, *25*, 2625. [CrossRef]
23. N'Negue, M.A.; Miclo, L.; Girardet, J.M.; Campagna, S.; Mollé, D.; Gaillard, J.L. Proteolysis of bovine α -lactalbumin by thermolysin during thermal denaturation. *Int. Dairy J.* **2006**, *16*, 1157–1167. [CrossRef]
24. Ohta, Y.; Ogura, Y.; Wada, A. Thermostable Protease from Thermophilic Bacteria. *J. Biol. Chem.* **1966**, *241*, 5919–5925. [CrossRef] [PubMed]
25. Keil, B. *Specificity of Proteolysis*; Springer: Berlin/Heidelberg, Germany; New York, NY, USA, 1992; p. 335.
26. Cheng, Y.; Wu, P.; Kan, Y.; Li, M.; Li, H. Identification and determination of structurally related peptide impurities in thymalfasin by liquid chromatography-high-resolution mass spectrometry. *Anal. Bioanal. Chem.* **2022**, *414*, 8035–8045. [CrossRef] [PubMed]
27. Wu, P.; Li, M.; Kan, Y.; Wu, X.; Li, H. Impurities identification and quantification for calcitonin salmon by liquid chromatography-high resolution mass spectrometry. *J. Pharm. Biomed. Anal.* **2020**, *186*, 113271. [CrossRef]
28. Liu, H.; Zhang, J.; Sun, H.; Xu, C.; Zhu, Y.; Xie, H. The Prediction of Peptide Charge States for Electrospray Ionization in Mass Spectrometry. *Procedia Environ. Sci.* **2011**, *8*, 483–491. [CrossRef]

Disclaimer/Publisher's Note: The statements, opinions and data contained in all publications are solely those of the individual author(s) and contributor(s) and not of MDPI and/or the editor(s). MDPI and/or the editor(s) disclaim responsibility for any injury to people or property resulting from any ideas, methods, instructions or products referred to in the content.

MDPI
St. Alban-Anlage 66
4052 Basel
Switzerland
www.mdpi.com

Molecules Editorial Office
E-mail: molecules@mdpi.com
www.mdpi.com/journal/molecules



Disclaimer/Publisher's Note: The statements, opinions and data contained in all publications are solely those of the individual author(s) and contributor(s) and not of MDPI and/or the editor(s). MDPI and/or the editor(s) disclaim responsibility for any injury to people or property resulting from any ideas, methods, instructions or products referred to in the content.



Academic Open
Access Publishing

mdpi.com

ISBN 978-3-7258-0699-7